Fracture Mechanics
and Its Application in Rock Excavation Engineering

Chaoshui Xu **BSc, MSc**

Submitted in accordance with the requirements for the degree of

Doctor of Philosophy

The University of Leeds

Department of Mining and Mineral Engineering

May 1993

The candidate confirms that the work submitted is my own and that appropriate credit has been given where reference has been made to the work of others

Fracture Mechanics
and Its Application in Rock Excavation Engineering

Chaoshui Xu

PhD, May 1993

Abstract

The two chevron notched specimen geometries for rock **Mode I** fracture toughness measurement, CB and SR, recommended by the ISRM have several disadvantages, such as very low loads required to initiate failure, complicated loading fixtures, difficult to be developed for rock mixed mode fracture testing, relatively large amounts of intact rock core needed for the test and complex specimen preparation for the SR geometry. The cracked chevron notched Brazilian disc (CCNBD) and the cracked straight through Brazilian disc (CSTBD) specimen geometries overcome these problems and they are believed to be ideal geometries for rock fracture investigations.

The general case for the cracked Brazilian disc fracture problem is when the specimen is loaded diametrically with the crack inclined at an angle to the loading direction. Different combinations of **Mode I** and **Mode II** fracture intensities can be obtained simply by changing this angle and the loading fixture still remains as simple as for a normal Brazilian test.

A special superimposition technique is developed to theoretically solve the stress intensity factor (SIF) values for the CSTBD fracture problem with the help of dislocation and complex stress function methods. This evaluation can generate accurate SIF results for the problem with any crack length α**(a/R) = 0.05-0.95**, while the mixed mode SIF solution for $\alpha > 0.60$ has not been reached by previous researchers. The relative theoretical SIF solution for the corresponding CCNBD fracture problem (single or mixed fracture modes) is obtained by using Bluhm's slice model proposed for general crack problems.

Numerical calibrations for **Mode I** fracture problems of the CSTBD and the CCNBD specimens have been conducted by using 194 different specimen geometries and the results prove the correctness of the theoretical evaluations. The valid CCNBD geometrical range for a valid rock **Mode I** fracture toughness test is numerically investigated and then experimentally validated based on 40 different CCNBD geometries by using 42 different rocks. Experimental studies on the minimum specimen size requirement for a valid CCNBD rock **Mode I** fracture toughness test are also carried out and the approximate critical criteria is given. The great advantages of using the CCNBD specimens for rock fracture toughness measurement have been investigated and the documentation for recommending the CCNBD specimen geometry to the ISRM as the third suggested method for rock **Mode I** fracture toughness test is presented. The rock **Mode I** fracture toughness values are then related to rock conventional properties for the purpose of prediction.

Rock cutting mechanics is analyzed by probabilistic fracture mechanics and Weibull's distribution model is found to better express the characteristics of rock cutting performance parameters. Some initial predictions for these parameters based on this mode are then presented.

I

Keys to the Abbreviations

BEASY	-	Boundary Element Analysis SYstem soft package
BEM	-	Boundary Element Method
BT	-	Burst Test specimen
C.D.	-	diamond saw Cutting Depth
CB	-	Chevron Bend specimen
CCNBD	-	Cracked Chevron-Notched Brazilian Disc
CM	-	Compliance Method
CMOD	-	Crack Mouth Opening Displacement
COD	-	Crack mouth Opening Displacement
CS	-	Cutting Strength in rock cutting
CSTBD	-	Cracked Straight-Through Brazilian Disc
CT	-	Compact Tension
DCB	-	Double Cantilever Beam
DI	-	Direct Indentation method
DSM	-	Direct Stress Method
DT	-	Double Torsion
EPFM	-	Elastic-Plastic Fracture Mechanics
FEM	-	Finite Element Method
FS	-	Fracture Strength in rock cutting
FSMA	-	MAjor chipping fracture strength in rock cutting
FSMI	-	MInor chipping Fracture Strength in rock cutting
IDM	-	Immediate Displacement Method
IS	-	Indentation Strength in rock cutting
LEFM	-	Linear Elastic Fracture Mechanics
LPD	-	Loading Point Displacement
LVDT	-	Linear Variable Differential Transformer transducer
MA	-	MAjor chipping in rock cutting
MI	-	MInor chipping in rock cutting
PFM	-	Plastic Fracture Mechanics
SCB	-	Semi-Circle Bending specimen
SE	-	rock cutting Specific Energy
SECRBB	-	Single Edge Cracked Round Bar in Bending
SENBB	-	Single Edge Notched Beam in Bending
SIF	-	Stress Intensity Factor
SR	-	Short Rod Specimen
TBM	-	Tunnel Boring Machine
VCEM	-	Virtual Crack Extension Method

II

Common Nomenclature

a	-	semi-crack length
a_0	-	semi-initial length of a chevron crack for a CCNBD specimen
a_1	-	semi-final length of a chevron crack for a CCNBD specimen
a_m	-	semi-critical crack length
α	-	dimensionless crack length
α_0, α_1,	-	dimensionless expressions of a_0 and a_1
α_R, α_s	-	dimensionless expressions of B and R_s
α_{II}, θ_{II}	-	critical crack length and critical crack inclination angle for pure Mode II fracture condition for the CSTBD fracture problem
θ	-	crack inclination angle with the loading direction in the mixed mode CSTBD and CCNBD fracture problems
γ	-	crack surface energy per unit area
ϱ	-	density
ν	-	Poisson's ratio
σ_c	-	rock uniaxial compressive strength
σ_t	-	rock tensile strength
σ_s	-	rock shear strength
σ_N	-	normal stress acting on a crack surafce along the normal direction
σ_T	-	tangential stress acting on a crack surface along the tangential direction
σ_{xx},σ_{yy},σ_{xy}	-	stress components (stress field) at any arbitrary point inside the media considered
ϵ_z	-	strain value at the crack front along the specimen thickness direction
ϕ	-	dislocation variable
A_{min}	-	critical (minimum) dimensionless SIF for the CB and SR specimens
B	-	thickness of the CSTBD or the CCNBD specimens
b	-	width of the crack front of a propagating crack
$C(\alpha)$	-	dimensional compliance of a cracked system
CBE'	-	dimensionless compliance of a crack system
D	-	disc diameter of the CSTBD or the CCNBD specimens
D_{min}	-	minimum valid specimen size (diameter) of CCNBD specimens for rock K_{IC} test.
E	-	Young's modulus
$f(\alpha)$	-	dimensionless SIF for the CSTBD specimens under Mode I fracture condition
$f(\alpha,\theta)$	-	dimensionless SIF for the CSTBD specimens under mixed mode fracture

condition

$f_I(\alpha, \theta)$ - Mode I dimensionless SIF component of $f(\alpha, \theta)$

$f_{II}(\alpha, \theta)$ - Mode II dimensionless SIF component of $f(\alpha, \theta)$

$f(\zeta)$, $g(\zeta)$ - edge dislocation densities

$F(\phi)$, $G(\phi)$ - nominal edge dislocation densities

F_C, F_N - rock cutting and normal forces

G - crack strain energy release rate

h - rock cutting depth by mechanical tools

h_c - diamond saw cutting depth for the CCNBD specimen preparation

k_B - SIF recalibration constant for the Mode I CCNBD fracture problem

K - dimensional stress intensity factor, or SIF

K_I, K_{II} - dimensional Mode I and Mode II SIF values

K_C - rock fracture toughness for any fracture mode

K_{IC} - rock Mode I fracture toughness

M_G - rock shear modulus

P - external force or load

P_{max} - failure (maximum) external load for a cracked system

P_X, P_Y - disc boundary traction loads along the X and Y directions

P(S) - probability of failure when the system is under the action of the external stress S

P_s, P_n - boundary tangential and normal forces

r, β - polar coordinates

R - disc radius of the CSTBD or the CCNBD specimens

r_c - size of the micro-cracking process zone

r_p - size of the plastic process zone

r_{mc} - size of the micro-cracking zone in the vicinity of crack tips for rock materials

R_s, D_s - diamond saw radius and diameter for the CCNBD specimen preparation

s - crack coordinate, $s \in [-a, +a]$

SD - standard deviation

SE - rock cutting specific energy

S_U, S_0, m - Weibull distribution constants for rock cutting performance parameters

T_X, T_Y - disc boundary traction stresses along the X and Y directions

u, v - geometrical constants for the Y^*_m evalution of the CCNBD specimens

U - energy term of a cracked system

x, y - Cartesian coordinates

$Y(\alpha)$ - dimensionless SIF for the CSTBD specimens under Mode I fracture condition

$Y(\alpha,\theta)$ - dimensionless SIF for the CSTBD specimens under mixed mode fracture condition

$Y_I(\alpha, \theta)$ - Mode I dimensionless SIF component of $Y(\alpha, \theta)$

$Y_{II}(\alpha, \theta)$ - Mode II dimensionless SIF component of $Y(\alpha, \theta)$

$Y^*(\alpha)$ - dimensionless SIF for the CCNBD specimens under Mode I fracture condition

Y^*_I, Y^*_{II} - Mode I and Mode II dimensionless SIF components of the mixed mode dimensionless SIF Y^*_{mix} for the CCNBD specimens under mixed fracture condition

Y^*_{mix} - mixed mode dimensionless SIF for the CCNBD specimens

Y^*_m - critical (minimum) dimensionless SIF values of the CCNBD specimens under Mode I fracture condition

Z - complex coordinate, $Z = x + i \cdot y = r \cdot e^{i \cdot \beta}$

Acknowledgement

The Author would like to express his sincere gratitude to all those without whose help much of this research work would have been impossible, especially the followings:

The British Council and The State Education Commission, PRC for their generous financial support through the scholarship.

Professor D.J.Fray, Head of the Department of Mining and Mineral Engineering, University of Leeds and Professor J.Tunnicliffe, Head of the Department of Mining Engineering, University of Newcastle upon Tyne, for providing the research facilities.

Dr. R.J.Fowell, Reader Mining Engineering, for his excellent supervision of the research work, his generous support with the machining equipment and rock samples, and his kindness and hospitality.

The Computing Laboratory of The University of Newcastle upon Tyne, for providing the excellent computing facilities, which were vitally important for this research.

Professor Tiangui Ren and Professor Minghan Feng in the Mining Research Institute, University of Science and Technology Beijing, PRC, for their encouragement, support and understanding during this research.

Dr. N.Brook for his kindness and interest in this research.

Mr. P. Doran, Mr. C. Hudson, Mr. P. Townhill-Rewston, Mr. J.Haigh, Mr. P. Jarvis and other technicians of the department, for their valuable help during the specimen preparation and the experiment. It was a great pleasure to work with them. Thanks are also directed to Mr. P.M. Davey and Mr. A.V. Greenhalgh for their help during the research.

Mr. M. McKenna, chief technician of the Department of Civil Engineering, University of Newcastle upon Tyne, for his help in the transportation of rock samples from Newcastle to Leeds.

Mrs. P. Kirwan and Ms. J. Rriestley, secretaries of the department, for their kind help, and most importantly, for their smiles.

Dr. J. Martin, Dr. T. Gillani, Dr. J. Searle, Dr. A. Young and Mr. D. Author for their helpful discussions and friendship. I will miss those days when working together with them.

Mr. C. Christie and Mrs. R. Christie, Mr. R. Scott amd Mrs. S. Scott for their hospitality and following the progress of my research.

Last but not least, Lijuan Wang, my wife, for her patience and understanding.

Contents

Lists of Figures and Illustrations

Chapter 6

Lists of Tables

Chapter 1
Introduction

The key to solving rock engineering problems is rock mechanics. Unlike the mechanics of other materials, rock mechanics is dealing with a media where discontinuities, heterogeneity and anisotropy have often to be dealt with. Different from man-made materials, rock is a historical material. It survives and therefore records the long term history of *in-situ* geological events which have been undergone for millions of years. It suffers from being deformed, fractured, weathered, acted on thermally and chemically, permeated, changed in contents and affected by any geological influence. It then turns out to be a kind of media which, when considered at large scale, will commonly possess arbitrarily distributed faults, joints, cracks, voids in the forms of pore spaces or elongated cavities and any other possible mechanical weaknesses. These existing weaknesses within the media will form the mechanical discontinuities which will then operate as the dominant stress concentrators for stress redistribution when the media is subjected to further mechanical actions. Therefore the theories of continuum mechanics will become inapplicable.

Besides, when considered at small scale, rock is an aggregate composed of more than one mineral. These minerals commonly come in the form of individual crystals or as amorphous particles (generally referred to as mineral grains) jointed by varying amounts of cementious materials to form the rock solid. In sedimentary rock, one can always find that different types of rock in the shape of pebbles are cemented together to form this new rock. A microstructural study of rock materials has shown that intergranular cracks (grain boundary cracks) and transgranular cracks (cracks across mineral grains) are often present in rock materials [Whittaker, 1992]. It is generally the case that the sizes and directions of these mineral grains are arbitrarily distributed over the whole media, so will be the sizes and the directions of these micro-cracks.

Therefore it seems more suitable to treat the rock as some sort of discrete media disintegrated by all the discontinuities mentioned above. As a result, discrete rock mechanics has been developed. Amongst them, rock fracture mechanics has made great progress and gained in popularity since the middle 1960's when significant early investigations were carried out by a few researchers [Bieniawski, 1967]. With a sound background knowledge of fracture mechanics for metallic and other man-made materials accumulated over half of a century, we can now reach some solutions for rock fracture mechanics by combining the existing theories with the specialities of rock materials both flexibly and critically.

It is then essential to appreciate some of the basic special characteristics of rock which are different to metallic and other man-made materials which classic fracture mechanics deals with. These differences have to be in one's mind when adapting the existing theories for rock fracture mechanics studies.

1) As mentioned, rock is intrinsically (naturally) discontinuous, heterogeneous and anisotropic, which generally means that the pre-existing discontinuities and variations in crystal structure and strength ahead of the extending crack will affect the local stress distributions and crack propagation behaviour. Therefore crack propagation in rock materials will include irregularities, random characteristics and a tendency to wander along grain boundaries and the pre-existing discontinuity (weakness) planes. The crack propagation procedure is normally complicated. Crack bifurcation and branching, random propagation, self-arrest and dramatic variations of propagation stability status can always be observed.

2) Fracture problems for most rock materials are brittle or quasi-brittle in almost all rock engineering applications of interest to man. Rock plastic fracturing is only a special case when rock is subjected to some particular environoment, extremely high temperature thermal action for instance. Therefore the concept of the plastic fracture process zone in metallic materials has to be changed when dealing with the crack tip fracture status of rock materials. The micro-cracking fracture process zone concept is always the substitution when dealing with rock.

3) On the large scale, rock masses may behave dramatically different to the mechanical characteristics of small scale rock samples coming from the rock mass and measured in the laboratory. Therefore when applying laboratory research results to practical rock engineering, one should always be critical about the scale factor for mechanical behaviour.

4) Rock specimens for laboratory testing are mostly available in the form of rock cores. Therefore core based testing methods are to be preferred.

Apart from the above rock specialities, in rock engineering, rock fracture mechanics is applied for two opposite purpose. One is concerned with the prevention of failure, i.e., fracture growth or movement along the pre-existing cracks of excavated rock structures such as rock slopes and underground openings where structural stability has to be guaranteed. The other is concerned with the initiation of failure, i.e., generation and propagation of new fractures in rock fragmentation by cutting , drilling or blasting where methods are often sought to optimize the fracture fragmentation effect. However for either of them, the state when the crack propagation starts governs their turning points. At this turning point, the fracture intensity **K** within the cracked body will reach its critical value, rock fracture toughness $\mathbf{K_C}$, or fracture strength of the material. This will put the rock fracture toughness in an important

position in rock fracture research.

Fracture toughness has been found to be the most important parameter to describe the rock materials ability to resist fracturing. Its value is applied widely in rock engineering such as:

1) A parameter for fracture classification of rock materials;

2) A material property to be used in the assessment of the stability of rock structures and in the interpretation of geological features.

3) An index to be used in modelling the rock fragmentation process by cutting, drilling or blasting.

It is believed that, similar to metallic materials, rock fracture toughness $\mathbf{K_C}$ is an intrinsic material constant if it is properly measured. It will not be dependent on the test specimen and the external loading conditions. Efforts have been spent on trying to find proper test methods for rock materials for many years. It was Schmidt (1975,1976) who was the first to determine the **Mode I** (the definition of different fracture modes is given in Figure 2.1) fracture toughness of rock materials following the standard testing method suggested by the ASTM for measuring the plane strain fracture toughness of metallic materials. Thereafter the fracture toughness measurement for rocks with different specimen configurations by researchers was reported [Clifton, 1976]. However the methods used were originally designed for metallic materials, and therefore when used for rock materials, the specimen configurations required unreasonably large size rock samples and extensive machining, which in most cases were impractical or some times found to be impossible.

Meanwhile it had been found that the chevron notched short bar was an ideal specimen for measuring the **Mode I** fracture toughness of high strength brittle materials [Barker, 1977, 1979, 1983] as the difficult measurement of the critical crack length does not have to be undertaken. With this significant knowledge it was soon found that core based specimens with chevron notches have numerous advantages over other forms for determining rock fracture toughness [Ouchterlony, 1986]. As a result, two suggested standard methods, the chevron bend specimen (CB) and the short rod specimen (SR), for measuring the plain strain fracture toughness of rock materials were recommended in 1988 by the Testing Commission of the ISRM. Therefore consistent and comparable results of fracture toughness values of any rock material can be obtained.

However some disadvantages exist with these two specimen configurations. The following three points always make the testing inconvenient, difficult and sometimes impossible.

1) The failure loads $\mathbf{P_{max}}$ for these two specimens are generally very low for most of the rock materials ($\mathbf{P_{max}}$ normally less than 1 kN). This puts a high requirement on the low load range testing ability of the apparatus and will induce large system error at the same time.

Sometimes it will cause problems if there is a certain preload applied by the testing machine.

2) The sample preparation for SR specimens is complicated. The machining tolerance for both of the specimens is low and therefore the specimen preparation is inconvenient and it is easy to generate useless specimens because of this tolerance.

3) Both of the testing methods involve complicated loading fixtures, especially the SR method. This is always unwelcome for engineering purposes.

In addition, in rock engineering it is clear that a pure **Mode I** form of loading seldom represents real conditions. Rock fracturing more commonly occurs under **Mode II** and mixed **Mode I** and **Mode II** loading. As a result, there is an increasing trend for rock fracture mechanics researches to be directed to the investigation of the fracture behaviour of **Mode II** and mixed **Mode I** and **Mode II** loadings of rock materials under complicated external loads. Therefore it is equally important to develop methods for measuring the **Mode II** fracture toughness and the mixed mode fracture strength locus of rock materials. Unfortunately there is little potential for extending the CB and SR specimens for this purpose as the loading fixtures will become very complicated and therefore impractical.

The introduction of the cracked straight through Brazilian disc (CSTBD) and the chevron cracked notched Brazilian disc (CCNBD) seems to possess great potential for current and future applications and overcomes the disadvantages of the CB and SR specimens. The CCNBD geometry was first used by Shetty [1985, 1986, 1987] for ceramic fracture research and then adopted by Fowell and Chen [1989] for rock materials. Our current researches have shown that many natural advantages are associated with CCNBD specimen for rock fracture investigations over the other chevron notched specimens. Among them, the following are some of the important points:

1) The failure load of CCNBD specimen for Mode I fracture toughness test is at least six times greater compared with the CB specimen and twelve times with the SR specimen. This certainly means that it is convenient, low cost and suitable for testing on most compression testing machines available in rock mechanics laboratories.

2) Larger tolerances for the specimen dimensions are allowed. Thus specimen preparation for the CCNBD is made a simple job.

3) No special loading fixture is required. The testing procedure will be just the same as for the Brazilian disc test to measure the tensile strength of rock materials which is a very common test procedure.

4) Quite interestingly, if the CB, SR and CCNBD specimens are machined from the same rock core, their crack orientations can be selected to be perpendicular to each other in 3-D space. Therefore they together compose a complete specimen set to be used for rock

anisotropic fracture studies. In fact, the CSTBD and the CCNBD themself only are believed to be the ideal specimens for this purpose.

5) In addition, great potential exists for the CSTBD and the CCNBD to be developed for **Mode II** fracture toughness, mixed mode fracture strength locus measurement and other mixed mode rock fracture investigations. Different combinations of different **Mode I** and **Mode II** fracture intensities can easily be obtained simply by altering the crack orientation to the loading direction and the whole testing procedure will still remain unchanged.

It is the purpose of developing the CSTBD and the CCNBD specimens for **Mode I**, **Mode II** and mixed mode rock fracture tests that is the principal aim of this research. The results presented in this thesis are only a single step away from practical application of the CSTBD and the CCNBD specimens. It is considered that it is now the time to recommend the CCNBD testing method as the third suggested method for **Mode I** rock fracture toughness testing to the ISRM. Even though we are satisfied with our test results, the usage of the method by other researchers, or some sort of round robin test are vitally important as the method needs to be substantiated by a large amount of independent testing and the repeatability of the test results under different circumstances needs to be determined.

For pure **Mode II** fracture toughness measurement and the rock fracture strength locus test by the CSTBD and the CCNBD specimens, much more needs to be done before the same draft documentation as for **Mode I** by the CCNBD method can be drawn up. However the theoretical evaluations of the CSTBD specimen with the crack length $\alpha > 0.6$ under mixed mode fracture conditions has been solved numerically, which has not yet been reached by the previous researchers. Therefore the **Mode I** and **Mode II** stress intensity factors for CSTBD and CCNBD specimens of any crack length ($\alpha = 0.01$-0.95) under the action of any combinations of mixed mode fracture intensities can be theoretically obtained.

Chapter 2 presents an overview of fracture mechanics, rock fracture mechanics and the principal rock fracture toughness measurement tests. The theories, their origination and development history are briefly described.

Chapter 3 concentrates on the theoretical solutions of the pure **Mode I** fracture problems for the CSTBD and the CCNBD specimens. A stepwise superimposition technique is developed which helps to obtain the theoretical solution of the CSTBD fracture problem numerically. The result is expressed by the best fit polynomial and comparison with the limited existing results shows it to be satisfactory. The theoretical solutions for the CCNBD **Mode I** fracture problem is also given numerically using two different compliance models, Munz's identical compliance changing rate model and Bluhm's compliance superimposition slice model. It is found that the later one can yield more reasonable results for the case of the

CCNBD fracture problem.

The numerical calibration by boundary element and finite element methods of the CSTBD and the CCNBD fracture problems described in Chapter 2 is presented in Chapter 4, where satisfactory agreement between the theoretical, BEM and FEM calibration results are shown. The CCNBD specimen geometrical requirements for a plain strain fracture environment around the crack front are also studied and it was found that the CCNBD geometries have to be within a certain range in order to have a valid test for the rock plane strain fracture toughness. The critical dimensionless stress intensity factors for any CCNBD specimens with the geometries within the valid range, which have to be used for the fracture toughness calculations when the specimen is used for the test, are finally presented numerically in a tabulated form.

Research then moves on to the experimental calibrations of CCNBD specimens for **Mode I** rock fracture toughness measurement, by comparison with the test results by the CB and the SR methods. The results are presented in Chapter 5. The experiments substantiated the CCNBD method as a satisfactory test method. The valid range argument reached in Chapter 4 is also proved experimentally. The CCNBD minimum size requirement for a valid plane strain fracture toughness test is studied as well. The samples tested are still far too limited but some sort of approximate conclusions have been reached. More test have to be carried out in order to have a more precise minimum size requirement estimation. Furthermore, the rock **Mode I** fracture toughness values are correlated with conventional rock mechanical properties, Young's modulus, tensile strength and uniaxial compressive strength. The data is based on the current test results and on the large database presented in [Chen, 1989] and therefore is believed to be able to predict the rock **Mode I** fracture toughness by these conventional mechanical properties more precisely.

Based on the theoretical, numerical and experimental evaluations mentioned, it is believed that CCNBD is an improved chevron specimen to be used for rock Mode I fracture toughness measurement. It is time to recommend it as the third ISRM suggested standard method. The first draft documentation for this recommendation is presented as Chapter 6 in this thesis.

Due to the importance of **Mode II** and mixed mode fracture testing and the good features of the CSTBD and the CCNBD geometries for these tests, theoretical investigations for mixed mode CSTBD and CCNBD fracture problems have been carried out in Chapter 7. The existing solutions are only available for the mixed mode CSTBD fracture problem for crack lengths up to $\alpha = 0.6$, but unfortunately the CSTBD with such a short crack can hardly be of any use in practical applications due to machining difficulties. Solution methods for these mixed mode fracture problems have been developed by combining the dislocation method and complex stress function methods with the stepwise superimposition technique developed in Chapter 3, and the solutions for the CSTBD with crack lengths up to $\alpha = 0.95$ have been

reached. The evaluated results are presented graphically and evaluation programs for any cases are listed in Appendix B. The critical crack inclination angles with the loading direction for pure **Mode II** CSTBD problem and the corresponding stress intensity factor (SIF) are then evaluated and the results are presented by a best fit polynomial for convenience of application. Based on these results, it is believed that pure **Mode II** fracture toughness of rock materials can be easily measured by this method. Mixed mode fracture strength locus problem of the CSTBD structure have then been theoretically investigated and some typical results are presented graphically. It is believed that with the help of these ideas, the mixed mode fracture test for rock materials can be carried out. At the end of the chapter, the mixed mode CCNBD problem is theoretically investigated. Solutions have been obtained but again the results need numerical and experimental validation. Obviously this chapter is just an opening for further research.

Rocks possess random characteristics, as mentioned above, all rock property "constants" are actually variables changing from point to point within the rock and the external loading conditions are generally uncertain as well. However when a long term and a large number of observations have been made, these uncertainties can turn out to follow certain statistical (probabilistic) distributions. Therefore when applying rock fracture research results to practical rock engineering, these random characteristics have to be carefully considered. Chapter 8 deals with the rock cutting problem by using rock fracture toughness as one of the most important indices to determine cutting efficiency by probabilistic fracture mechanics. The Weibull probabilistic distribution is introduced to describe the "strength" of rock materials. Cutting performance parameter predictions based on the above considerations are presented. It is believed this probabilistic approach can more suitably describe the rock cutting (fracturing) mechanism. However it is only just an initial theoretical approach to the problem and many mathematically imperfect definitions are still involved. More validation investigations have to be carried out before it can be applied with the confidence required for practical applications.

In the final chapter, Chapter 9, overall conclusions and further research recommendations are summarised.

Chapter 2

Overview of Fracture Toughness Measurement

§2.1 Introduction

The differences between brittle and plastic failure has led to the development of a branch of fracture mechanics dealing particularly with brittle fracturing of engineering materials, such as ceramics, concrete and rock. Fracture toughness test techniques have developed correspondingly and have become one of the most important aspects in this area.

As a material property, the fracture toughness plays a critical principal role in the analysis of material fracture. It provides the foundation for evaluating the strength of materials from the fracture point of view. Therefore, its importance has led to a wide range of investigations into methods of measuring its values to be most suitable for solving practical problems.

§2.2 Overview of Fracture Mechanics Literature

§2.2.1 Origins of Fracture Mechanics

The significance of intense and localized concentration of stress around sharp notches was first emphasized by Inglis (1913). He obtained expressions for the maximum stress $(\sigma_y)_{max}$ at the apex of the major axis of an ellipse, where the radius of curvature $\varrho = b_e^2/a_e$ is a minimum. He also derived expressions for stress concentrations for cracks with a length of **2a** and a notch radius ϱ, in the two dimensional plane condition. They are (Figure 2.1):

$$\begin{cases} (\sigma_y)_{max} = P\cdot\left(1 + \dfrac{2\cdot a_e}{b_e}\right) & \textit{for an ellipse,} \\ (\sigma_y)_{max} = 2\cdot P\cdot\left(\dfrac{a}{\rho}\right)^{\frac{1}{2}} & \textit{for a crack} \end{cases} \qquad (2.1)$$

Where **P** -- applied stress at a distance far away, in the **Y** direction,

a_e -- major semi-axis of the ellipse,

b_e -- minor semi-axis of the ellipse,

a -- semi-length of a crack

ϱ -- radius of curvature of the crack tip, and

Y -- the direction of the short axis a_e of the ellipse, or the direction perpendicular

to the crack line.

As can be seen from Equation (2.1), the actual stress $(\sigma_y)_{max}$ at the apex could be extremely large, at least several times larger than the applied stress since **b** is very small compared with the **a** value. That offered the first clue to the mechanism of fracture mechanics.

However the problem was approached only from the point of view of stress concentration analysis and the results can hardly be used to solve practical fracture problems.

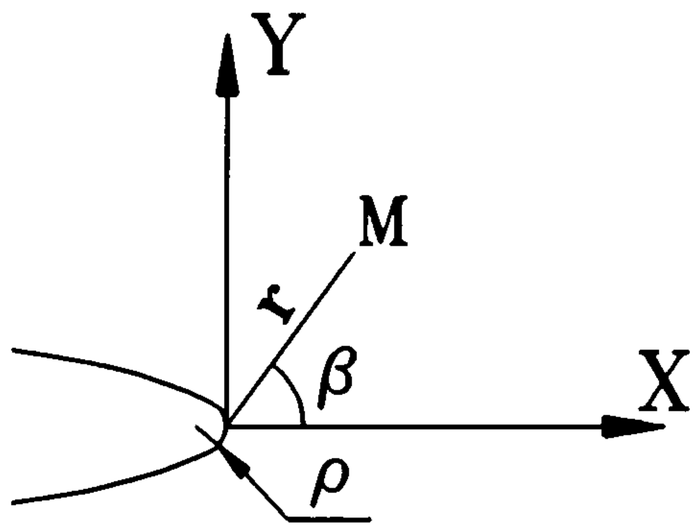

Figure 2.1 Inglis' Solution

§2.2.2 Energy Balance Approach

Griffith (1921,1924) postulated that brittle materials contained submicroscopic defects (or flaws) from which micro cracks originate and propagate to form the catastrophic macro cracks under the external applied force. He approaches the problem of fracture from the point of thermodynamics or energy balance at the crack tip and assumed the existence of surface energy on two opposite crack surfaces. The crack can only propagate when the dynamic energy (coming from the strain energy release, the work done by the external force) exceeds the newly-created crack surface energy.

From Griffith's theory, the total energy of a strained specimen can be expressed as:

$$U = U_0 + (U_a - F) + U_\gamma \qquad (2.2)$$

where **U** -- total energy,

$\mathbf{U_0}$ -- elastic (strain) energy of the loaded but uncracked specimen, which is a constant for a given load,

$\mathbf{U_a}$ -- change in the elastic energy caused by introducing the crack with length **2a** into the specimen,

$\mathbf{U_\gamma}$ -- change in the elastic surface energy caused by the formation of the new crack surface, and

F -- work performed by external forces, which is not part of the potential energy. Therefore this must be subtracted from the total energy.

The sum in the bracket is the total change of the strain energy of the system (referred to as the crack extension force), which provides the energy needed for the crack to propagate. The

change of surface energy term U_γ represents the cohesive molecular forces (referred to as the crack resistance force) which should be overcome by introducing some work while creating the new crack surfaces. Equilibrium is achieved when these two opposite energies are balanced, or when the total energy **U** reaches a critical value, i.e.,

$$\frac{\partial U}{\partial a} = 0 \tag{2.3}$$

Griffith's theory makes it possible to obtain a numerical criterion for crack propagation. However, it is only concerned with changes in energy as a crack grows and hence ignores the details of the fracture process at the crack tip. This may not be sufficient although it gives reasonable predictions when only the initial and the final states of the extension are considered.

Nevertheless, Griffith's theory quickly achieved great popularity and has since provided the basis for newer methods through the critical concept of treating fracture in terms of changes in energy. Some of the related theories and formulas for linear fracture mechanics have already been widely accepted.

§2.2.3 Energy Balance Modification

Since Griffith's theory neglected all forms of energy dissipations other than the surface energy, Irwin (1948) and Orowan (1949) modified the theory by taking account of the small scale plasticity (still in the range of Linear Elastic Fracture Mechanics, or LEFM) around the crack tip and suggested that the analysis for ideally-brittle materials could be modified and applied to slightly-plastic fracture. Then they proposed that the Griffth-type energy balance must be between:

1) the stored strain energy, and

2) the surface energy plus the work done in plastic deformation.

Most importantly, Irwin postulated the ideas and further presented the definitions of the strain energy release rate (crack extension force) **G** and the crack resistance force **R** based on the above knowledge. For an infinitesimal crack extension **∂a**, **G** and **R** can be expressed as:

$$\begin{cases} G = \dfrac{\partial}{\partial a}(U_a - F) \\ R = \dfrac{\partial}{\partial a} U_\gamma = 4 \cdot \Delta a \cdot \gamma \end{cases} \tag{2.4}$$

where **G** -- strain (elastic) energy release rate or crack extension force, which represents the stored (elastic) energy per unit crack surface area that is available for infinitesimal extension,and

R -- crack resistance force which represents the surface energy increase that could occur owing to the crack propagation, or the energy needed (absorbed) during this process.

The factor **4** in the equation implies that four new surfaces will be created in association with any infinitesimal crack extension **Δa**. In Equation (2.4), γ is the material-dependent constant which represents the surface energy per unit crack surface area. Originally Griffth designated:

$$\gamma = \gamma_e \tag{2.5}$$

where γ_e is the elastic surface energy. Irwin modified γ by introducing another term signifying the plastic deformation around the crack tip, i.e.,

$$\gamma = \gamma_e + \gamma_p \tag{2.6}$$

where γ_p is the plastic work, which is accompanying the crack extension and consumed irreversibly by the plastic deformation. For relatively ductile materials, $\gamma_p >> \gamma_e$, which means that **R** is mainly plastic energy and the elastic surface energy can be neglected.

Furthermore, Irwin (1958a) and Orowan (1955) demonstrated that the thermodynamic surface energy was not only determined by elastic and plastic energy. Other processes such as micro-cracking, acoustic emission, micro-plasticity, heat generation, and some other energy-needed micro-movement around the crack tip should also be taken into account when calculating the value of the practical surface energy γ.

However, although the theory is reasonably modified, there still exists problems which cannot be solved simply by the energy balance approach, such as the slow crack growth problem, the crack propagation path and the stress field around the crack.

§2.2.4 Stress Intensity Factor Approach

Instead of considering the energy of the entire crack system, Irwin (1957,1958b) proposed to examine the stress field in the immediate vicinity of the crack tip. In 1946, Sneddon and Elliott took advantage of the Westergaard complex stress function [Westergaard, 1939] and solved the stress field analytically around a crack in an infinite continuum media by means of the Fourier transform technique. The solution can be expressed:

$$\sigma_{ij} = P_0 \cdot (\frac{a}{2r})^{\frac{1}{2}} f_{x,y}(\beta) + \mu_{x,y}(\frac{r^2}{a^2}) \qquad (2.7)$$

where P_0 -- applied external force,

a -- semi-length of the crack,

r, β -- the polar coordinates with the origin set at the apex of the crack (Figure 2.1),

i, j -- designating x, y,

x, y -- the Cartesian coordinates with the origin set at the centre of the crack,

$f_{x,y}$ -- function of β,

$\mu_{x,y}$ -- higher order error term, which takes a much smaller value compared with the first term in the equation when considering the immediate vicinity of the crack tip, i.e., $r \ll a$, hence for approximation it can be neglected.

With the knowledge of Sneddon's results, Irwin derived and analyzed thoroughly the stress state around the immediate vicinity of the crack apex and pointed out that the crack tip stress under the condition of generalized plane stress or plane strain can be expressed by a two parameter equation:

$$\sigma_{ij} = \frac{K}{\sqrt{2 \cdot \pi \cdot r}} f_{ij}(\beta) + \mu_{ij}(r) \qquad (2.8)$$

where K is a constant which gives the magnitude of the elastic stress field. It is then referred to as a Stress Intensity Factor (SIF) of the stress field by Irwin, and it is this concept that provides the important foundation for fracture mechanics.

Obviously, the SIF K should be a function of both the crack geometry and the external load value. For two dimensional problems, it takes the form (Irwin):

$$K = \sigma \cdot \sqrt{\pi \cdot a} \cdot Y(a) \qquad (2.9)$$

where σ -- applied external load,

a -- crack geometry, and

Y -- a geometrical constant depending on the given specimen configuration only.

Therefore, all the details of the loading and crack geometry are embodied in the constant K, which consequently determine the local stress field. The introduction of this index overcomes the difficulties in describing and comparing the stress field around the crack tip as the local stress will tend to infinity when $r \to 0$ by conventional analysis. In other words, when the SIF K parameter is used, the stress field state around the crack tip can be clearly and distinctly demonstrated. In fact, as $r \to 0$, the whole crack system tends to a limit value, that is the numerical definition of K (Rooke & Cartwright,1976):

$$K = \lim_{r \to 0} \{ \sqrt{2 \cdot \pi \cdot r} \cdot \sigma_{ij}(r,0) \} \tag{2.10}$$

The simplicity and convenience of the **K** description for the crack system makes possible the easier application of fracture mechanics. The critical values of the SIF **K** for the whole cracked system, which is now broadly referred to as fracture toughness, govern the conditions for crack propagation. As a result, some criterion can be hypothesized to evaluate the strength of the cracked specimen, or to estimate the tolerable flaw size from the point of fracture mechanics.

§2.2.5 Non-singularity Stress Approach

Aiming to overcome the shortcomings of continuum elastic mechanics when it is used to analyse the stress field around the crack tip, Barenblatt (1962) introduced the effect of cohesive forces acting across the faces of the crack within the range of intermolecular distances close to its tip, and proposed the theory called equilibrium cracks. It is based on the following hypotheses:

1) the end region in which the cohesive forces are active is very small compared with the crack length,
2) the stresses at the crack tip are finite,and
3) the crack surfaces close smoothly, i.e. the crack tip has a cusp shape.

He then pointed out that a non-singular stress state was obtained by the superimposition of stress due to the external loads and those due to the cohesive forces. Finally a fracture criterion was derived by putting the combined stress intensity factor equal to zero.

§2.2.6 Internal Equivalence

It is Irwin (1960) who associated the concept of stress intensity factor with the strain energy release rate. He put the work done by the stress field when moving through the displacements corresponding to the crack extension from **a** to **a + da** equal to the change of the internal strain energy **Gda** and derived the following equivalent expression between SIF **K** and strain energy release rate **G**:

$$G = \frac{K^2}{E'} \tag{2.11}$$

where,

$$E' = \begin{cases} E & \textit{for plane stress condition,} \\ \dfrac{E}{(1-\nu^2)} & \textit{for plane strain condition} \end{cases} \tag{2.12}$$

Here **E** is the Young's modulus and ν is the Poisson's ratio.

The equivalence of these two different approaches confirms that they are both reasonable and comprehensive. It is the combination that provides an more powerful tool to study fracture mechanics, especially slightly-plastic linear fracture mechanics, and the more extensive elastic-plastic fracture mechanics (EPFM).

§2.2.7 Extensive Research Areas

The introduction of **K** and **G** lead to the rapid development of fracture mechanics in the last three decades. The following are some of the main current research areas:

1) more precise solutions to the crack problem,
2) seeking solutions for more complicated crack and loading geometries,
3) investigating single mode or mixed-mode fracture criterion,
4) extending the theory of LEFM, and searching for solutions in the area of EPFM, non-linear fracture mechanics, visco-elastic fracture mechanics, and more importantly, fatigue fracture mechanics,
5) solving some practical engineering problems by applying fracture mechanics,
6) searching for more precise and more convenient techniques for measuring fracture toughness,
7) research into the crack propagation problems, i.e., fracture dynamics, the crack initiation point(s), crack path (route), as well as the extension direction(s) and speed,
8) controlling of crack extension (origination, path and rate) and its application in engineering structures,

Most importantly, the combination of fracture mechanics with probabilistic and statistical theories creates a very powerful technique to solve some engineering problems, especially when:

1) some parameters (strength, crack length, toughness) of some engineering materials (such as rock, ceramics and some other brittle materials) can not be definitely known beforehand for a particular case, but their values follow some statistical law when a large number tests are carried out,
2) the loading conditions (or the boundary conditions) of the system studied are not kept the same for one particular observation, but the large number of tests suggests that they

will follow a certain statistical distribution.

As a matter of fact, these two situations are just the cases met in rock excavation engineering, and therefore it is expected that the relative fracture problems can be better solved by probabilistic fracture mechanics.

§2.3 Brief Overview of Rock Fracture Mechanics

§2.3.1 Background

Research into rock fracture mechanics began with the investigation of rock strength criterion. It developed with general fracture mechanics during the last few decades. The common research methods used at present are by combining the basic theories of general fracture mechanics with particular rock characteristics.

Therefore the history of this subject can be traced back to as early as 1920s, when Griffth proposed his theory for brittle materials (glass). However, owing to the specialties of rock materials, up till now there still cannot be found a satisfactory theory which is encouragingly comprehensive in rock fracture mechanics. From the constitutive standpoint, most engineering materials are relatively homogeneous. However rock is an extremely variable substance no matter whether viewed on the macroscopic, microscopic or even submicroscopic scale, as mentioned in Chapter 1. A very simple block of rock may contain many different smaller elements which may be composed of different materials (minerals) having different mechanical properties, or may have different geological structures which show different mechanical response even if made of the same minerals. Furthmore, owing to its different formation and environmental conditions, any rock can enclude many mechanical structural defects, such as flaws, cleavage, crystal facets, laminations or micro-cracks. It seems this coincides with Griffith's hypothesis that all materials contain defects so that general fracture mechanics theories can be adopted directly. But it is these discontinuities that make rock media considerably less homogeneous, less continuous, and more anisotropic. As the general fracture theories are based on the hypothesis of macro- homogeneity, continuity and isotropy except for the crack flaws studied, and therefore it is obviously unsuitable to introduce these theories, without any modification, to solve the rock fracture problems. In addition, rock materials always show apparent non-linearity and large residual deformations which are obviously incompatible with basis of LEFM.

§2.3.2 Rock Fracture Strength

As a result of the complexities mentioned above, rock fracture mechanics started with the investigation of rock fracture strength criterion.

§2.3.2.1 Coulomb's Theory

Coulomb suggested that fracture will occur in rock when a maximum shear stress τ_{max} at a point in the material has reached a specific value σ_τ which is referred to as rock shear strength, i.e.,

$$\tau_{max} = \frac{1}{2}(\sigma_1 - \sigma_3) > \sigma_\tau \qquad (2.13)$$

where σ_1 and σ_3 are the maximum and the minimum principal stresses respectively:

§2.3.2.2 Coulomb-Navier Theory

Navier modified the Coulomb theory by assuming that the normal stress σ_N acting across the failure plane increased the shear resistance of the material by an amount proportional to the magnitude of the normal stress. The fracture criteria will then becomes:

$$| \tau_{max} | \geq \sigma_\tau + \mu \cdot \sigma_N \qquad (2.14)$$

where μ -- coefficient of the internal friction.

§2.3.2.3 Mohr's Theory

Mohr proposed that a material will fracture or deform permanently when the shear stress τ on the fracture plane has increased to a critical value that depends on the normal stress σ_N acting on the same plane, i.e.:

$$\tau = f(\sigma_N) \qquad (2.15)$$

where the function relationship $f(\sigma_N)$ must be determined experimentaly. Obviously this curve is the envelope to the Mohr's circles for the values of σ_3 and σ_1 at failure. For the special case when the envelope is a straight line, the Coulomb-Navier and Mohr's theories are identical.

§2.3.2.4 Griffith's Theory

Griffith hypothesized that brittle materials contain randomly oriented cracks and that stress concentrations develop at or near the end of these cracks, causing them to propagate and

ultimately contribute to macro failure. Although his theory was directed to the research of glass, however it soon was adopted to apply to other kinds of brittle materials, especially rock.

The stress analysis approach of the Griffith's theory proposed that the crack would start to extend when the tensile stress at or near its tip attained a critical value, which is referred to as molecular cohesive strength of materials by Orowan (1949). When related to the uniaxial tensile strength σ_t, the criteria can be written as:

$$\frac{(\sigma_1 - \sigma_3)^2}{(\sigma_1 + \sigma_3)} = -8\sigma_t \tag{2.16}$$

This equation is based on the results from Inglis (1913) for the solution of the stress distribution of an ellipse in an infinite stressed plate.

Furthermore, McClintock and Walsh (1962) proposed a modification to Griffth's hypothesis, taking account of the crack closure problem (closed cracks) by introducing a coefficient of internal friction between crack faces and rewrote the criterion as:

$$\sigma_1 = \frac{-4\sigma_t}{(1 - \frac{\sigma_3}{\sigma_1}) \cdot \sqrt{(1 + \mu^2) - \mu \cdot (1 + \frac{\sigma_3}{\sigma_1})}} \tag{2.17}$$

where μ is the coefficient of internal friction of the rock material.

The Griffth theory applied to brittle materials can also be approached from the viewpoint of energy balance. The results are identical in appearance to the equations mentioned in section 2.2.2. The only difference is that the specific surface energy for rock materials will mainly consist of the energy consumed by micro-cracking, energy dissipation and local micro-deformation, while the plastic surface energy will make much less contribution.

§2.3.3 Some Current Aspects

Rock fracture theories mentioned above deal with problems theoretically (Griffth) or experimentally (Mohr). However only the Griffith's energy theory analyzes the problem from the point of view of the crack fracture mechanism. Mohr's hypothesis is based on the macro-shear failure mode and does not account for the micro fracture mechanism, and hence ignores the initiation, propagation and ultimate formation of the shear plane. Griffith's stress approach theory, on the other hand, is based on the genetic concept, namely the existence of small cracks or flaws, and deals with the initiation problems of crack fracture modelled by a flat ellipse, but it is not suitable to be used for analysing a complete fracture mechanism, or the ultimate failure of the rock material.

Since the 1960s, attention has been turned to directly introducing general fracture mechanics theories for continuous media into the rock fracture mechanics research area by means of some modifications and this has proved successful. Some reasonable explanations of rock fracturing phenomenon and some rock fracture criterion have been proposed (even though not perfect) both from experimental and theoretical analysis for some relatively homogeneous rock materials.

One of the recent research branches in this area is the investigations of fracture toughness testing methods for rock materials, which advanced rapidly especially during the last decade owing to the painstaking endeavours of some researchers in this area (Barker L.M., Ouchterlony F., Atkinson B.K., Ingraffea A.R., Sun Zong Qi). As a result, two specially developed methods, the chevron bend (CB) method and the short rod (SR) method, were authenticated by the ISRM Testing Commission and recommended in 1989 as the two primary methods for rock fracture toughness measurement.

§2.4 Simple Review of Major Rock Fracture Toughness Test Methods

§2.4.1 Fracture Modes

Irwin (1958) defined three different basic modes of fracturing. They are respectively (as shown in Figure 2.2):

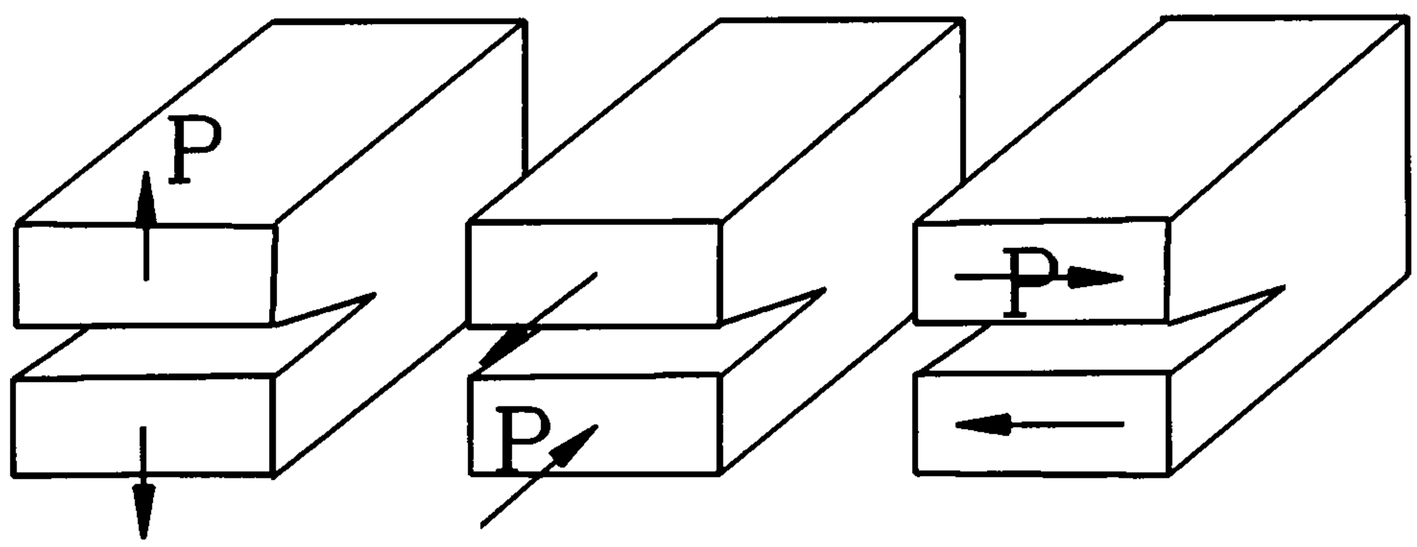

Figure 2.2 Three Fracture Modes

Mode I : opening mode, or tensile mode.

Mode II : sliding mode, or in-plane shear mode.

Mode III : tearing mode, or anti-plane shear mode.

As the basic principle, the law of superimposition is also followed in fracture mechanics so that any complicated fracture state can be split into these three basic modes and taken equivalently as the result of their combination.

Mode I and **Mode II** are by far the most pertinent to fracture problems, especially in brittle materials [Lawn and Willshaw, 1975]. The former is even more important with respect to rock fracturing and therefore attracted most of the attention for fracture toughness researches.

§2.4.2 Fracture Toughness Definitions

Fracture toughness tests were mainly developed in the late 1950s and 1960s. It started with simple geometries, then different configurations were added for different purposes, and eventually formed a large part of fracture research.

Owing to the importance of **Mode I** fracture in practice, most fracture toughness research was and is still being devoted to **Mode I** fracture toughness $\mathbf{K_{IC}}$ and crack resistance force $\mathbf{G_{IC}}$ measurements even though **Mode II**, **Mode III** and mixed modes are attracting more and more attention. For comprehensive purposes, the fracture test is no longer limited to within the range of LEFM. Some special techniques have been developed so that experimental fracture mechanics can be extended to the field of EPFM or even Plastic Fracture Mechanics (PFM) without any difficulty.

In the following definitions and discussions, if the symbols are followed by subscript "**I**", "**II**" or "**III**", that means that the definitions and discussions are only suitable for **Mode I**, **Mode II** or **Mode III** fracture condition only. If one of these subscripts is not used, the definitions and discussions will be suitable for any single mode or mixed mode fracture conditions.

§2.4.2.1 Definition I -- Stress Intensity Factor Approach

Taking advantage of the relationship between the SIF, load and the specimen geometry has resulted in this being the most common method for $\mathbf{K_c}$ measurements. The SIF **K** can be expressed as:

$$K = \Omega(P)\cdot Y(\alpha) \tag{2.18}$$

where $\Omega(P)$ -- loading or boundary condition,

$Y(\alpha)$ -- specimen geometry function, including the crack configuration,

α -- dimensionless crack length **a/R**.

Obviously the functions $\Omega(P)$ and $Y(\alpha)$ are definite for a given configuration, therefore for a particular testing system the critical values of these two functions $\Omega(P_c)$ and $Y(\alpha_c)$ can be obtained provided the critical crack length α_c is known. Hence the critical value of SIF K_c can be calculated from the above expression, and this value is defined as the fracture toughness of the material.

However, the problem lies in the determination of the critical value of crack length α_c and the corresponding critical load P_c. It is the different determinations of α_c and P_c by different criterion which results in many different calculated values as the substitution for the real fracture toughness value K_c.

1) K_Q -- apparent K_c value

$$K_Q = K(\alpha_0 , P_Q) \tag{2.19}$$

where α_0 -- dimensionless initial crack length or notch length,

P_Q -- the load magnitude of the intersection point of the load-displacement curve with the 5% offset secant line having slope equal to 0.95 of initial slope (Figure 2.3), which is supposed to correspond to 2% apparent crack growth from initial length according to the E399 K_{IC} testing method [3] recommended by ASTM for metallic materials.

This definition of fracture toughness might not be applicable to rock materials. The compliance of rock material is generally quite small and this results in a much higher slope of the load-displacement curve. In addition, there cannot be observed the obvious "pop-in" phenomenon in rock fracture experiments which is commonly the case in metals. Therefore the intersection point of the 5% offset secant line with the load-displacement curve may come well after the critical load which is to be used for the fracture toughness calculation. Furthermore, it is still uncertain that the 5% offset line is corresponding to the 2% apparent crack growth in rock materials. Thus in rock fracture research the K_Q value can only be used as a reference.

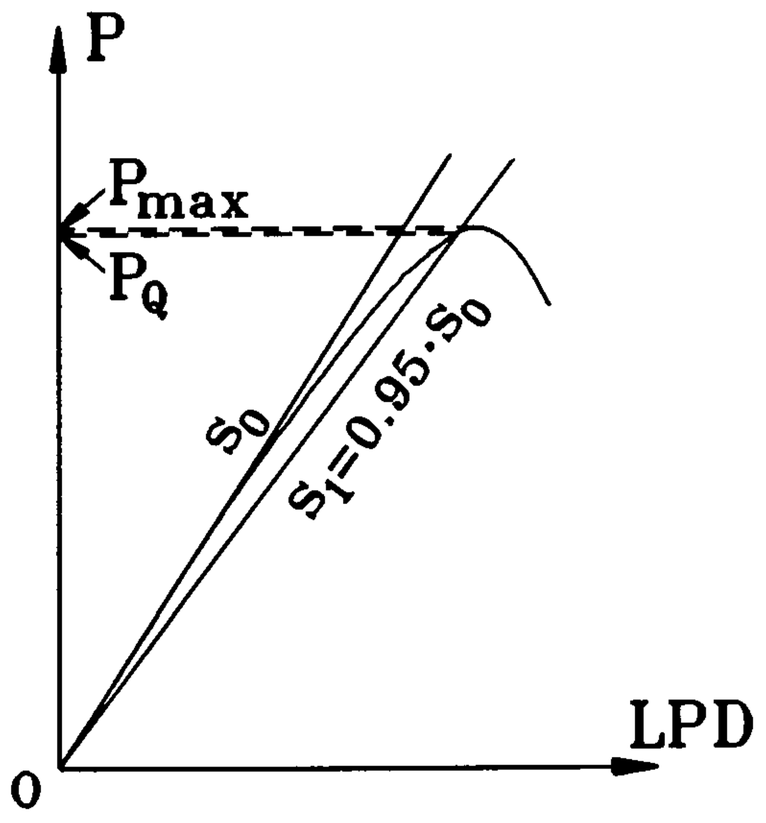

Figure 2.3 K_Q Definition

2) $\mathbf{K_m}$ -- quasi-effect $\mathbf{K_c}$ value

$$K_m = K (\alpha_0 , P_m) \tag{2.20}$$

Brown (1976) used the maximum load value $\mathbf{P_m}$ rather than $\mathbf{P_Q}$, but still used the initial crack length α_0, to approximate the $\mathbf{K_c}$ value. This is especially recommended for rock specimens with no fatigue precrack, i.e., the notch length α_0 is known.

3) $\mathbf{K_a}$ -- adjusted apparent $\mathbf{K_c}$ value

$$K_a = K (a_0 + r_{mc} , P_Q) \tag{2.21}$$

As mentioned above, the determination of $\mathbf{P_Q}$ is not definitely corresponding to the 2% apparent crack growth, but it is verified that micro-cracking, micro-plasticity, and some other non-linear behaviour will happen in the process zone immediately ahead of the crack apex before the load and the crack reach their critical values [Ouchertlony, 1982]. Therefore, Schmidt (1980) proposed a micro-cracking adjustment factor $\mathbf{r_{mc}}$ to approximate the critical crack length value, which is based on estimating the critical size of the micro-crack zone. For **Mode I** fracture condition, $\mathbf{r_{mc}}$ is:

$$r_{mc} = 0.2 \cdot (\frac{K_{IC}}{\sigma_t})^2 \tag{2.22}$$

4) $\mathbf{K_i}$ -- Initiation $\mathbf{K_c}$ value

$$K_i = K (\alpha_0 , P_i) \tag{2.23}$$

For some special cases, the rock materials are not expected to have any crack extension, i.e., the crack initiation should be prevented. Accordingly, the $\mathbf{K_i}$ value will be much more suitable to apply in this situation. Here $\mathbf{P_i}$ is the load value of any crack propagation origination, visible or invisible depending on the conditions required, and which can be determined by visual observation or by the sonic radiation detection technique. Obviously the $\mathbf{K_i}$ will be accurately representing the real $\mathbf{K_c}$ value for the kind of material having an ideal crack resistance curve **R-Δa**.

From the definition we know that $\mathbf{P_i}$ lies well below $\mathbf{P_{max}}$, therefore the $\mathbf{K_i}$ value underestimates $\mathbf{K_c}$ and hence can be considered to be a conservative toughness parameter.

5) $\mathbf{K_c}$ -- true fracture toughness value

In order to obtain the true value of $\mathbf{K_c}$, it is vitally important to know the crack length and the corresponding load at the critical unstable condition, $\mathbf{a_c}$ and $\mathbf{P_c}$. With regards to rock materials, $\mathbf{P_c}$ is generally substituted by the maximum (failure) load value $\mathbf{P_{max}}$. This is because that maximum (failure) load $\mathbf{P_{max}}$ always corresponds to the critical state, or the

difference between $\mathbf{P_{max}}$ and $\mathbf{P_C}$ is usually very small. Therefore the major problem is directed to the determination of the critical length $\mathbf{a_c}$. As a result, some special experimental measurement and estimation methods have been developed. Amongst them, chevron notched specimens proved to be the best geometries to solve the problem of α_c determination.

6) Comparison

For the purpose of convenient comparison and clear illustration, all the different definitions of $\mathbf{K_c}$ mentioned above are shown in the same diagram, Figure 2.4, where all the relationships can be easily recognized.

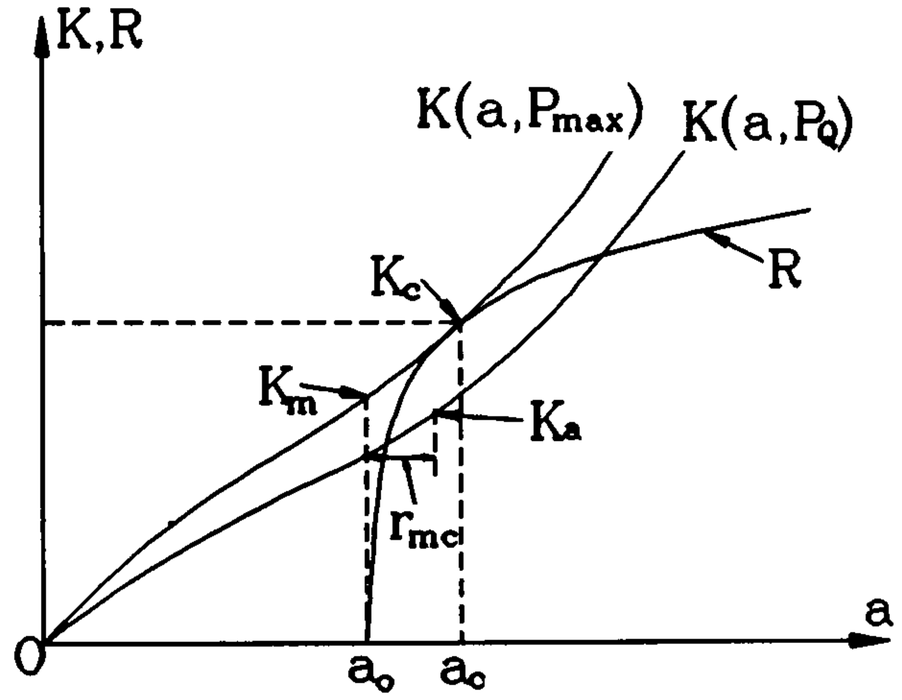

Figure 2.4 $\mathbf{K_c}$ Definitions

Here note should be taken that the above definitions are not restricted to any particular fracture mode. In other words, they could be the fracture toughness of any fracture mode or their combination.

§2.4.2.2 Definition II -- Energy Balance Approach

On the other hand, the fracture toughness can also be measured from the Griffth's energy balance concept. The crack resistance force $\mathbf{G_c}$, or $\mathbf{J_c}$ for more non-linear materials can be obtained experimentally using special techniques. Then the calculated $\mathbf{G_c}$ or $\mathbf{J_c}$ values can be used as the rock toughness parameters directly or they can be further converted into the $\mathbf{K_c}$ expression by Equation (2.11) if necessary.

Owing to the special characteristics of the energy approach method to fracture mechanics research, the fracture toughness thus defined is more suitable for fracture investigations in the range of EPFM and PFM. Followings are some of the corresponding definitions.

1) **R** -- The Specific Work of Fracture

R, as defined by the following equation, is supposed to designate the elastic surface energy parameter based on Griffth's classical theory (original idea).

$$\overline{R} = 2 \cdot \gamma_{eff} = \frac{W_f}{A} \tag{2.24}$$

where,

$$W_f = \int_0^{\infty} P \cdot du \tag{2.25}$$

and **A** -- net cross section area of the fracture surface,

u -- the loading point displacement, LPD, and

P -- load.

This is quite a simple definition and it only accounts for the average energy consumption over the whole fractured area, and is not concerned with the different stages of crack initiation, propagation and ultimately unstable fracturing. Therefore it may only be suitable when the crack growth is stable and the whole test system is non-energy-dissipative.

Furthermore, the measured **R** value varies with the initial crack length $\mathbf{a_0}$, and this results in the problem of it being used as a material-dependent-only parameter. Olofsson (1978) reached a conclusion, after comprehensive testing, that **R** only shows a nearly constant plateau value with a certain varying range of initial crack lengths, and it is only this plateau value that can be taken as the material property constant. In other words, the range of $\mathbf{a_0}$ suitable for the **R** measurement has to be decided before fracture toughness testing when **R** values have to be used in special applications.

2) **R** -- The Crack Resistance Force, The Determination of the **R**-curve

An **R**-curve is a plot of crack growth resistance as a function of actual or effective crack extension, $\mathbf{\Delta a}$, which is not characterized in the $\mathbf{K_c}$ values with respect to slow stable crack growth. The crack resistance **R** can be expressed in the same units as **G**, as it was originally proposed from the point of view of the energy consumption concept. But as it is now commonly used, it is always designated in terms of stress intensity factor $\mathbf{K_R}$, converted from **R** by the relationship of Equation (2.11). Therefore the **R**-curve diagram becomes a continuous record of fracture toughness development plotted against crack extension in the material as a crack is driven under a continuously increased stress intensity factor **K**.

The method used to determine the **R**-curve is a load control technique. Under rising load conditions, the crack extends gradually to the maximum extension $\mathbf{\Delta a}$ when unstable crack growth occurs at $\mathbf{K_c}$. This critical point is determined by the tangential point between the **R** curve and one of the lines representing a crack driving force curve, $\mathbf{K_G = f(P,a)}$, as shown in Figure 2.5. Thus by carefully monitoring the effective (or actual) crack length, the **R** curve can be obtained.

Obviously the problem may lie in the determination of the effective crack length, $\mathbf{a_e}$. It is recommended for metallic materials by ASTM E561 [4] that $\mathbf{a_e}$ consists of three parts as follows:

$$a_e = a_0 + \Delta a + r_Y \qquad (2.26)$$

where a_e -- effective crack length,

a_0 -- initial crack length,

Δa -- physical (visible) crack extension length, and

r_Y -- plastic zone adjustment, theoretically,

$$r_Y = \frac{1}{2\pi}\cdot\frac{K^2}{\sigma_Y^2} \qquad (2.27)$$

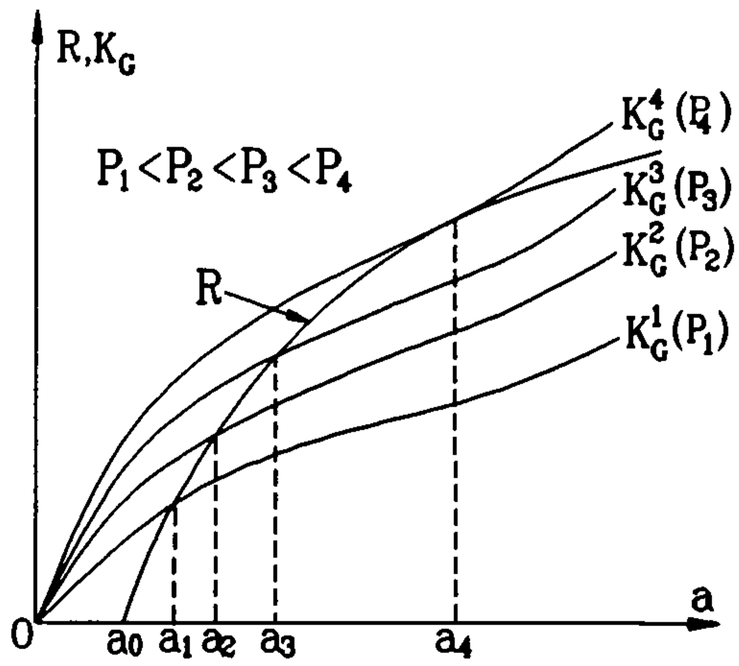

Figure 2.5 **R**-Curve Determination

However, it is not clear whether this adjustment is suitable or not for rock materials by simply changing σ_Y to σ_t, r_Y to r_t and accordingly naming r_t as the micro-cracking zone adjustment [Ouchterlony, 1982]. Hence the **R**-curve characterization is only suitable for those materials which possess less non-linear behaviour during fracturing. The difficulty of monitoring crack length makes its application in rock materials rather unrealistic.

3) J_c -- The Critical **J**-resistance Value

Owing to micro-cracking and local irreversible deformation, some rock materials show serious non-linearity before crack propagation has reached the critical situation. This makes it unreasonable to use LEFM test parameters, K_c or **R**, to designate the fracture characteristics, and the introduction of J_c characterization becomes necessary.

The application of J_c is based on its feature of path independence, which implies it is a characteristic scalar measure of the conditions around the crack tip, similar to the SIF in LEFM. As required by its definition, all the related parameters within the process zone should be single-valued functions, therefore the **J**-integral method is basically limited to non-linear elasticity. It can only be extended to elasto-plastic cases for some special conditions.

There has been no standard for rock non-LEFM test published yet, though Ouchertlony concluded in his comprehensive rock fracture toughness review (1982) that a J_c evaluation modelled on recommended metal test practice also seems effective for rock, with the exception of the size requirements. With regard to the test methods, the multiple specimen technique is cumbersome, costly and especially unrealistic as it is rather difficult to keep the mechanical parameters of several rock specimens identical as required, so the single specimen test technique seems more suitable for the rock J_c test.

The calculation equation of the **J**-integral for experimental usage can be written in the

following expression:

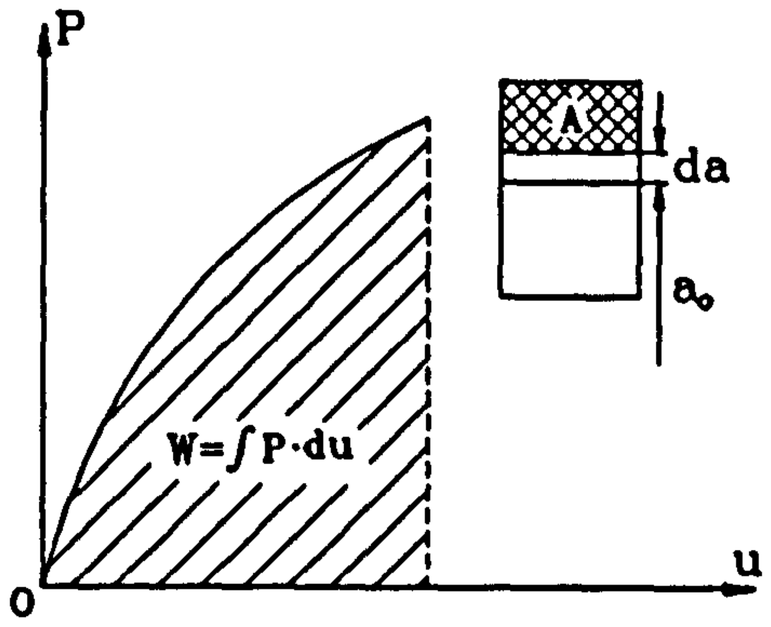

Figure 2.6 Definition of J-integration

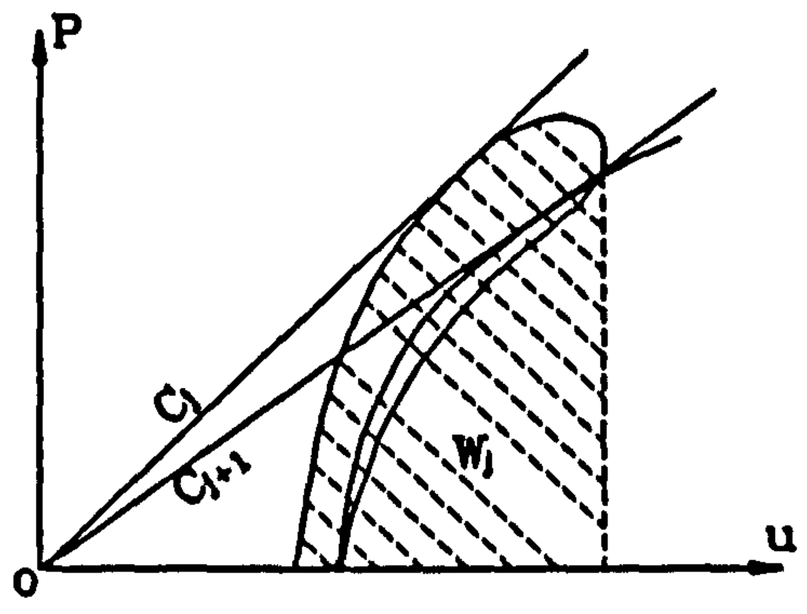

Figure 2.7 J_c by Compliance Method

$$J = \eta \cdot \frac{W}{A} \tag{2.28}$$

where W and A are shown in the Figure 2.6 and constant η usually depends both on specimen geometry (especially crack length) and material properties.

When taking the maximum load as the critical condition, by analogy with K_m, J_m is obtained:

$$J_m = J(a_0, W_C) = \left(\frac{\eta}{A}\right)_{a=a_0} \cdot W_C \tag{2.29}$$

where,

$$W_C = \int_0^{u_c} P \cdot du \tag{2.30}$$

u_c is the corresponding displacement at P_{max}.

When the crack initiation point is taken as the critical condition, the following J_i (by analogy with K_i) can be obtained:

$$J_i = J(a_0, W_i) = \left(\frac{\eta}{A}\right)_{a=a_0} \cdot W_i \tag{2.31}$$

$\mathbf{u_i}$ is the displacement when $\mathbf{P = P_i}$. As demonstrated before, $\mathbf{P_i}$ lies well below $\mathbf{P_{max}}$.

The $\mathbf{J_c}$ value can also be obtained by the compliance method technique, as shown in Figure 2.7. By loading and unloading, the different compliance values ($\mathbf{C_j}$ and $\mathbf{C_{j+1}}$) can be used to estimate the different corresponding crack lengths. For the **j**-th reloading cycle, the crack length is $\mathbf{a_j}$ and the work done by the external force $\mathbf{W_j}$. Then the **J**-integral for this reloading cycle is:

$$(J_R)_j = J(\, a_j \,,\, W_j \,) \tag{2.33}$$

and,

$$\Delta a_j = a_{j+1} - a_j \tag{2.34}$$

Then the pseudo resistance curve $\mathbf{J_R(\Delta a)}$ can be plotted and $\mathbf{J_c}$ is therefore defined as:

$$J_c = J_R^0 = \lim_{\Delta a \to 0} J_R\,(\Delta a) \tag{2.35}$$

In conclusion, different fracture toughness values can be obtained by using different definitions. Therefore it is necessary to decide before-hand which definition should be used according to the practical requirements and situation.

§2.4.3 Specimen Geometries

§2.4.3.1 Geometry I

Specimen geometry plays another important role in fracture toughness experiments. A good configuration can make the toughness determination more precise and convenient. Most of the specimen geometries for rock fracture toughness tests are directly introduced from the geometries popularly accepted for metallic materials and then combined with the characteristics of rock materials. The results are quite encouraging even though not so satisfying. The following is just a list of some of the testing methods for rock **Mode I** $\mathbf{K_{IC}}$ tests (see Figure 2.8).

1) Single Edge Notched Beam (Rectangular Bar,3-point Bending) -- SENBB

It is an idealized **2-D** toughness test geometry and probably the most widely used specimen type. In addition, it was the first standard specimen recommended by ASTM for $\mathbf{K_{IC}}$ tests of metals when **S/W = 4** and **B/W = 5**.

2) Single Edge Cracked Round Bar (3-Point Bending) -- SECRBB

Owing to the difficulty of sample preparation, a core based specimen geometry, SECRBB, was developed by Bush (1976) and Ouchertlony (1981) which is better adapted for rock samples.

3) Double Cantilever Beam -- DCB

4) Compact Tension -- CT

These two specimen variations (3 and 4) are also used for rock materials simply because of their symmetrical geometry with respect to the crack and are ideal for measuring the **Mode I** fracture toughness. However they are only used for comparison testing owing to their sample preparation complexity.

5) Double Torsion -- DT

This geometry was introduced by Henry (1977) and B.Atkinson (1979) for rock fracture studies. For this configuration, it is assumed that the stress intensity factor around the crack tip will be kept constant as the crack propagates along the shallow surface notch for a certain range. Therefore it makes the toughness calculations easier as it does not have to take into account the critical crack length, which is always very difficult to determine for rock materials.

6) Burst Test Specimen -- BT

It was first introduced by Johnson (1973) and is a test geometry used to determine the rock fracture toughness for blasting and hydrofracturing applications.

7) Semi-Circle Specimen -- SCB

This variation was proposed by Chong (1984). It is a simple configuration specimen which can be obtained from rock samples with very little machining. However the problem may lie in the complexity of the analysis of the stress field around the crack, and this results in some difficulties with the toughness calculations.

8) Direct Indentation Method -- DI

This method has been developing since 1976 as a very simple and quick way for toughness

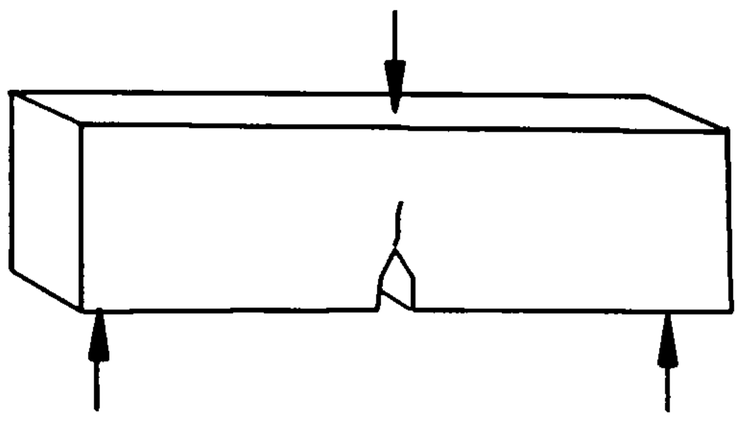

1 SENBB

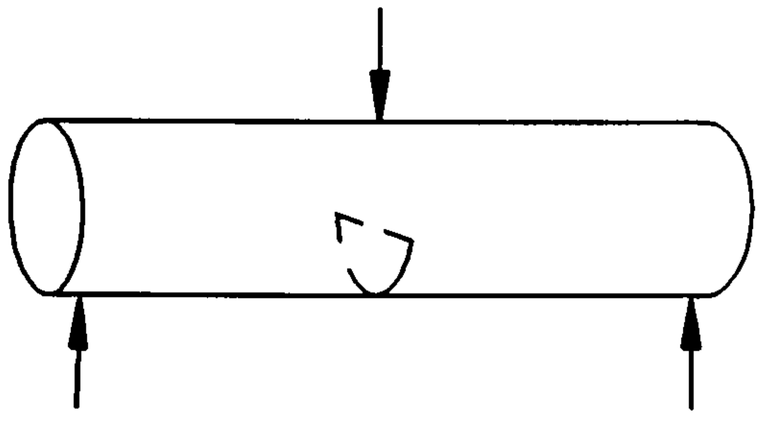

2 SECRBB

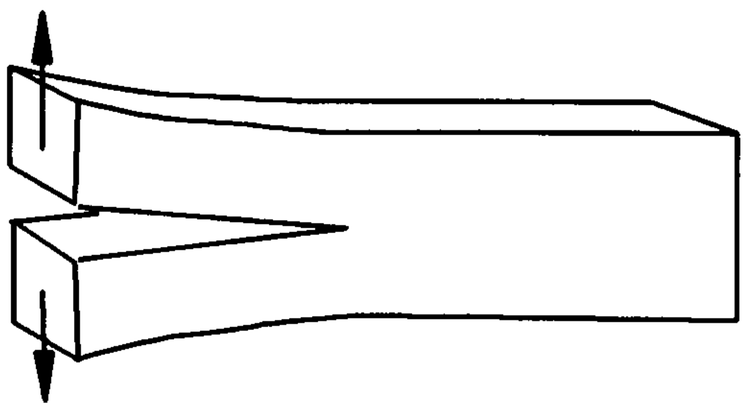

3 DCB

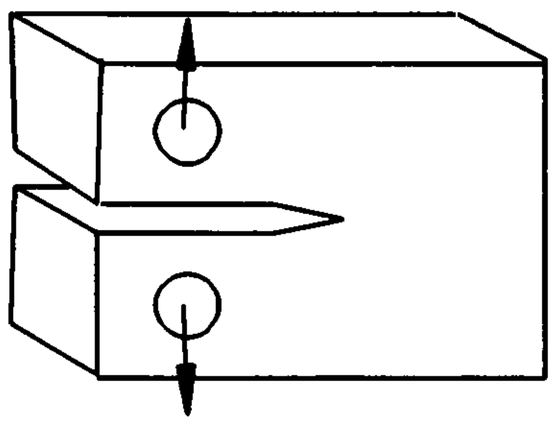

4 CT

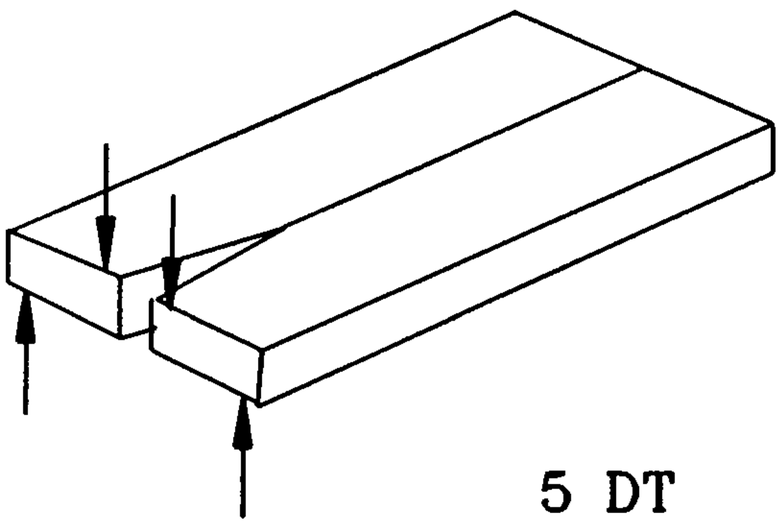

5 DT

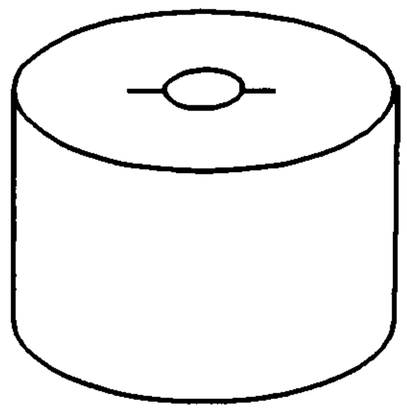

6 BT

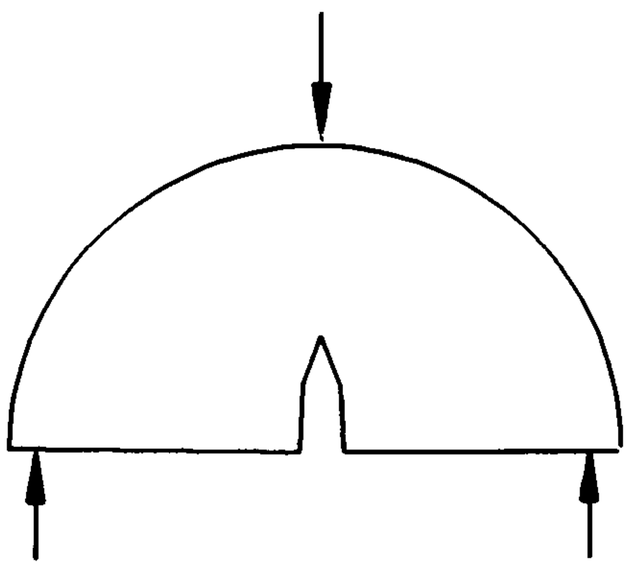

7 SCB

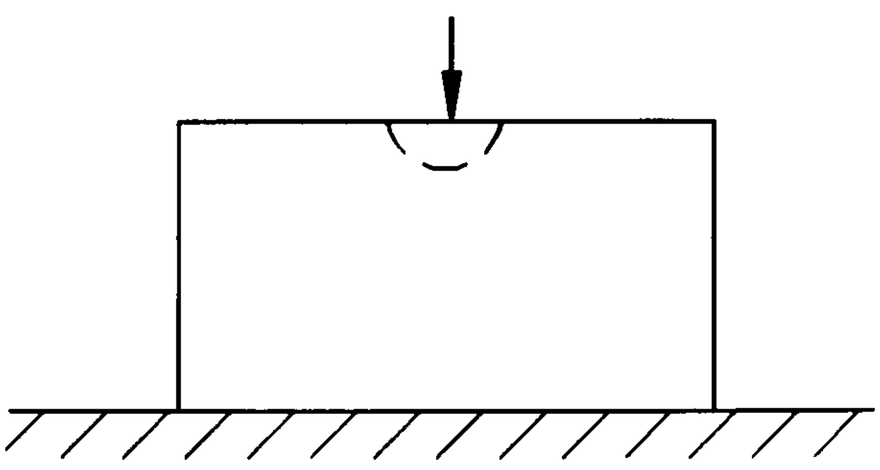

8 DI

Figure 2.8 Testing Geometry I

evaluations. Even though it is not an accurate test, it is still expected to be as a quick fracture toughness estimation method which sometimes is vital for some on site applications.

§2.4.3.2 The Introduction of the Chevron Notched Specimens

In rock fracture research, difficulties with monitoring crack growth, makes it inconvenient to conduct rock fracture toughness testing. Large errors always exist with the estimation of the critical crack length $\mathbf{a_c}$. Therefore chevron notch specimens were specially developed for rocks with satisfying results. Consequently, two kinds of chevron notched geometries, CB and SR, were quickly recommended in 1988 by the ISRM Testing Commission as basic toughness test methods for rock materials.

As expected, the introduction of the chevron notched specimen perfectly solved two difficult problems existing in the conventional geometry:

1) There will be an extremely high stress concentration at the tip of the chevron notch. Hence the crack will initiate at a low applied load and propagate stably for a certain distance before the whole specimen turns to catastrophic (unstable) fracture. This effect is exact in analogy with and is in fact precracking, therefore the costly precrack procedure (by fatigue technique for instance) is not needed.
2) The SIF for chevron notch specimens can be expressed by the following equation:

$$K = \frac{P}{\Omega(A)} \cdot Y^*(\alpha) \tag{2.36}$$

where **P** -- load,

Ω(A) -- function of specimen geometrical dimensions (excluding crack),

$Y^*(\alpha)$ -- dimensionless intensity factor which is only the function of specimen geometry (including crack).

As determined by the characteristics of chevron notch specimens, **$Y^*(\alpha)$** begins with an extremely large value, declines rapidly thereafter, passes through a minimum and then rises again as the crack grows. If we suppose the material fracture toughness $\mathbf{K_c}$ to be a constant, then from Equation (2.36) it is known that the applied load **P** obviously will attain a maximum value when **$Y^*(\alpha)$** reaches its lowest apex. This is exactly the critical state (theoretical ideal condition) so that the toughness $\mathbf{K_c}$ can be evaluated from these corresponding values. Advantageously, the critical state when the crack length **a** reaches its critical value $\mathbf{a_c}$ and **$Y^*(\alpha)$** at its minimum value $\mathbf{Y^*_{min}}$ depends only on the specimen's initial geometries for the chevron notched specimens. In other words, there is no need to monitor the crack propagation or to do the accurate load-displacement recording for fracture toughness measurement as long as the specimen

geometries are known beforehand. Certainly, that makes the whole testing procedure very simple.

Furthermore, the points of better crack propagation guidance and minimum crack "pop-in" effect, can also be added into the good features of the chevron-notch specimens over the conventional ones. The reason why we have to use the critical state value $\mathbf{P_{max}}$ and $\mathbf{Y^*_m}$ for the toughness calculation is mainly based on the following points:

1) It is not necessary to calculate the toughness using the critical values. But when using other states for the toughness evaluation, the monitoring of the load value and the corresponding crack length becomes important and this is normally difficult. However when evaluating the toughness at the critical state, the whole procedure is very simple as the only recorded value needed is the maximum test load.
2) As a material property constant, the calculated toughness values by different test methods should be identical, or very nearly the same (allowing for some error in test data manipulation). As decided by its confinement condition, the plane strain toughness value has been confirmed to show this kind of constant value much better than the plane stress one does because in the later case the stress state around the crack tip is influenced greatly by the so-called surface effect [Kanninen, 1985, Knott, 1973]. Therefore most fracture toughness tests are concentrating on the plane strain state only or trying to be close to that state. With regard to the chevron notch specimen, the state around the crack tip at the beginning of crack propagation is considered to be an unconfined condition. Only the critical state is considered to be the closest to the plane strain condition and therefore the fracture toughness value calculated by this state is believed to be better representing the material constant $\mathbf{K_c}$.
3) The toughness values measured from different specimens for the same material are expected to be unchanged. Taking the critical state as the evaluation point provides an identical criterion for the fracture toughness evaluations.

However, it is necessary to note that owing to the non-linear behaviour of rock materials there may be a small deviation between the maximum test load $\mathbf{P_{max}}$ and the critical load $\mathbf{P}$ although the difference is usually very small. But this deviation can be satisfactorily accounted for by the non-linearity correction technique proposed by Ouchertlony (1986, 1989).

§2.4.3.3 Specimen Geometry II

Chevron notch geometries did not originate in the research field of rock fracture mechanics. It was first proposed by Nakayama (1964) to measure the fracture energy of brittle, polycrystalline refractory materials by using a bend bar with a non-symmetrical chevron notch. Pook (1971) first suggested using chevron notch specimens to determine the plane strain

fracture toughness of metals, and he further theoretically analyzed the whole estimation procedure for K_{IC} evaluations and reached the important basic concept of chevron notch specimens.

The idea was quickly extended to the whole research field, especially for high-strength brittle materials. The bend bar with a chevron notch symmetrical about the centerline appeared in 1966 by Tahersall, and the chevron notch short rod and bar evolved in 1977 and 1978 by Barker. In the 1980s, these geometries were introduced in to rock fracture mechanics.

The chevron specimens suitable for and now popularly accepted for rock fracture toughness tests are short rod (developed as SR) and round bend rod (developed as CB), as these geometries can be easily obtained from rock core samples and need very little machining.

1) Short Rod -- SR (Figure 2.9)

It was first introduced by Barker in 1977 to measure the fracture toughness of high strength metal materials, such as steel, aluminum and titanium alloys. He later extended (1980) his studies to non-metallic materials, mainly rock and ceramics. Costin (1981) used this geometry to measure the toughness of oil shale. The geometry was thoroughly investigated at the beginning of the last decade both from the analytical and the experimental point of view, by using finite element, boundary element and compliance calibration methods (Barker,1983, Beech & Ingraffea, 1982, Shannon,1982, Newman,1984, Ingraffea,1984), and the basic characteristics of this geometry have been therefore defined.

2) Chevron Notch Bending Rod -- CB (Figure 2.9)

This geometry was first introduced by Bush (1976) for aluminum and then extensively developed by Ouchterlony (1980s) especially for rock materials. The complete theoretical analysis was presented by Ouchterlony (1980a, 1980b) again in 1980 and later the substantive experimental results (Ouchterlony, 1981,1986).

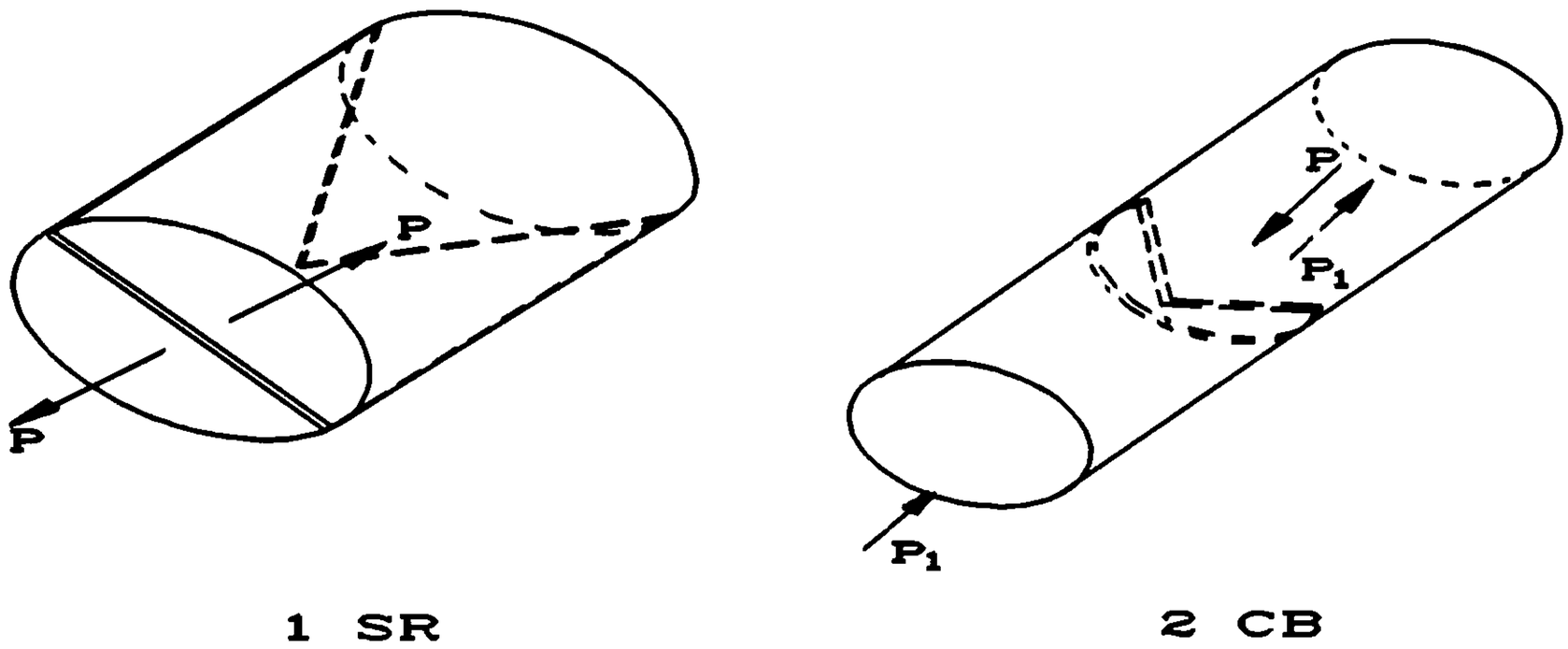

Figure 2.9 Testing Geometries II -- Chevron Notched Specimens

The theoretical and experimental results from SR and CB research have proved that they are suitable geometries which can be used to correctly measure the toughness value of rock materials. Therefore, in 1988, they were suggested by the ISRM Testing Commission as the two basic recommended methods for rock toughness testing. The requirements for the specimen size, the testing system, the whole procedure of the test and the calculation and calibration methods can be found in "**Suggested Methods for Fracture Toughness Testing of Rock Materials**", Testing Committee, ISRM, 1988 [145].

However the disadvantages of these two chevron specimens for rock materials make their applications sometimes rather difficult. It is believed that the CCNBD specimen geometry will overcome these disadvantages and it can be developed as a simple and effective chevron specimen for rock fracture toughness measurement.

Chapter 3

Stress Intensity Factor Evaluations for CSTBD and CCNBD Specimens under Mode I Fracture Condition

§3.1 The Use of Brazilian Disc Geometries for Rock Fracture Toughness Determinations

§3.1.1 Brazilian Disc, the CSTBD and the CCNBD Specimens

The Brazilian disk test technique was originally proposed by Carneiro (1947) and independently by Akazawa (1953) to measure the tensile strength of brittle materials. It then was used to determine the elastic properties of concretes by Hondros (1959), the tensile strength of coal by Berenbaum (1959) and Evans (1961), and the tensile strength of rocks by Berenbaum (1959) and Hobbs (1964). All their findings proved that it is a convenient and effective method to measure the tension related properties of brittle materials (1979, Jaeger & Cook). From these studies, the idea of adapting the geometry for tensile mode (**Mode I**) fracture toughness test originated.

A diametrical compression Brazilian disk with a central straight-through crack, referred to as CSTBD specimen was first proposed by Yarema & Krestin (1966) and Libatskii (1967) for this purpose. The geometry has then been specially developed in the field of combined mode fracture toughness tests because of its easier generation of mixed mode states. Awaji & Sato used this specimen in 1978 to evaluate the **Mode I**, combined **Mode I** and **Mode II**, as well as purely **Mode II** fracture toughness of graphite plaster and marble by varying the orientation of the straight-through notch (crack) relative to the line of loading. Atkinson (1982) and Yarema (1984) employed this geometry to measure the fracture toughness of composite materials and cemented carbide materials respectively. Shetty and co-workers also used the geometry for the single and mixed-mode fracture toughness measurement during research into ceramic materials.

Owing to the broad acceptance of the chevron notch specimen geometry and its unique features, Shetty combined this geometry with the CSTBD specimen in 1985 and introduced the cracked chevron notched Brazilian disc (CCNBD) specimen geometry. Compared with the CSTBD, the CCNBD geometry simplifies the specimen preparation, eliminates the pre-cracking and the error caused by the existence of the notch curvature at both tips of the crack,

and makes the whole testing procedure much more convenient and straight forward. Since then, the CCNBD has been mainly used for mixed mode fracture toughness measurements of ceramic materials (Shetty, 1985, 1986, 1987).

§3.1.2 The CCNBD Specimens for Rock Materials

In 1989, Fowell and Chen introduced the CCNBD technique into the field of fracture toughness testing for rock materials. Studies were carried out by means of boundary element analysis (3D) and finite element analysis (2D) and the results were supported by fracture toughness experiments for a large variety of sandstones. It is believed that many unique advantages will be gained by the application of the CCNBD geometry over other chevron notched specimens recommended by the ISRM and others for rock materials. The advantages claimed by the previous research are as follows [Chen, 1989]:

1) The testing rig, the measurement apparatus, and hence the whole test procedure are much simpler.
2) It needs a much smaller rock sample.
3) It can easily be used for mixed mode rock fracture investigations.

It is hoped that this specimen geometry will be internationaly accepted as the third ISRM suggested geometry for rock fracture toughness testing following the CB and the SR methods. Therefore it is vitally important at this stage that thorough investigations of the specimen geometry have to be both theoretically and experimentally undertaken before it can be accepted.

§3.2 Theoretical Solution of SIF for the CSTBD Specimen under Mode I Fracture Condition

§3.2.1 Solid Brazilian Disc

Hondros in 1959 solved the mechanical problem of a solid Brazilian disc (with diameter **D**, radius **R** and thickness **B**) subjected to diametrical uniform loading $\mathbf{P}_{\omega}$ over a small arc of contact 2ω (Figure 3.1.a) by suggesting a Fourier series to represent load distribution. He presented the stress distribution along the central loaded diameter line in the normal direction to this diameter as:

$$\sigma_N = \frac{2P_{\omega}}{\pi \cdot B}\left[\frac{(1-\frac{r^2}{R^2})\sin 2\omega}{1-2\cdot\frac{r^2}{R^2}\cos 2\omega+\frac{r^4}{R^4}} - \arctan\left(\frac{1+\frac{r^2}{R^2}}{1-\frac{r^2}{R^2}}\right)\tan\omega\right] \qquad (3.1)$$

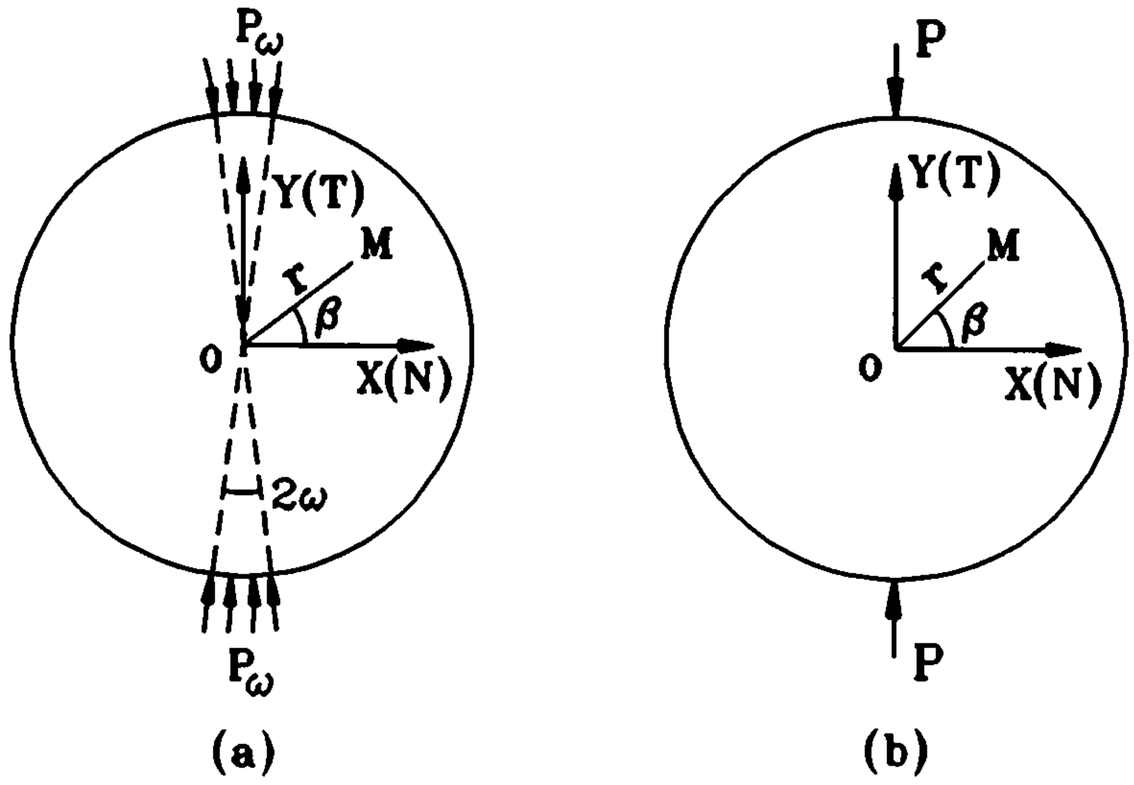

Figure 3.1 Diametrically Loaded Brazilian Disc

This relationship gives a uniform tensile stress along the central part of the loaded diameter except where the diameter approaches the loading points. When the disc is subjected to a pair of diametrically positioned concentrated loads **P** (Figure 3.1.b), this uniform tensile stress σ_N and the related tangential stress along the loaded diameter can be calculated by the following equations [Timoshenko, 1970, Frocht, 1948]:

$$\begin{cases} \sigma_N = \dfrac{2P}{\pi \cdot B \cdot D} \\ \sigma_T = 0 \end{cases} \tag{3.2}$$

where **N** and **T** signify the directions normal and tangential to the loaded diameter.

It is then assumed to be a tensile mode (pure **Mode I**) fracture problem when introducing a straight through centre crack along the loaded diameter. When the crack is orientated at a certain angle inclined to the loaded diameter (less than a critical value), a mixed mode fracture problem will be generated. Obviously the **Mode I** fracture problem of the CSTBD specimen is just a special case of its mixed mode (general) fracture problem. In this chapter and the following three chapters, the **Mode I** fracture problem will be mainly considered for the CSTBD specimen (theoretical solution of the SIF, numerical calibration and **Mode I** fracture toughness measurement). The general solutions for the mixed mode fracture problem of the CSTBD specimen will be thoroughly investigated in Chapter 7.

§3.2.2 Former Solutions

For the CSTBD specimen under **Mode I** fracture condition, some solutions of the SIF have been proposed by previous researchers.

1) Libatskii and Kovchik (1967) obtained, by integral transform technique, the SIF solution with an approximate algebraic expression:

$$\frac{K_I}{K_0} = 1 + \frac{3\cdot\zeta}{2} + \frac{3\cdot\zeta^3}{4} + \frac{3\cdot\zeta^4}{64} \tag{3.3}$$

where,

$$\zeta = \left(\frac{a}{R}\right)^2 = \alpha^2 \tag{3.4}$$

and,

$$K_0 = \frac{P}{B\cdot R}\cdot\sqrt{\frac{a}{\pi}} \tag{3.5}$$

It is pointed out that the error in this approximation is within 2% for $\alpha < 0.75$ ($\zeta < 0.56$).

2) Rooke & Tweed (1972, 1973) showed that the SIF due to the diametrical forces P are the same as those obtained when the crack is opened by an internal pressure σ_0 equal to $P/(\pi Rt)$. They used the Mellin transform technique (Tranter, 1947, Tweed, 1971, 1972) to solve the problem and expressed the SIF as:

$$\frac{K_I}{K_0} = \frac{1}{a}\cdot q(a) \tag{3.6}$$

where q(a) is a complicated function of the system geometry parameters, which includes a solution of an integral equation, and,

$$K_0 = \frac{P}{\pi\cdot B\cdot R}\sqrt{a} \tag{3.7}$$

They finally presented the SIF values in diagramatic form by solving the integral equation numerically.

3) Bowie & Neal (1970) studied the problem of a CSTBD crack subjected to an uniform internal pressure by boundary mapping and collocation methods. The result agreed well with that by Rooke & Tweed, but they did not extend their solution to the diametrical loading condition.

4) Atkinson, Smelser & Sanchez (1982) investigated the mixed mode fracturing problem of CSTBD by the edge dislocation method, and the Mode I SIF of the specimen was given as follows:

$$K_I = \frac{P}{\pi \cdot B \cdot R} \sqrt{\pi a} \cdot N_I \qquad (3.8)$$

where N_I is the dimensionless SIF and the values were presented by a curve-fit cubic polynomial.

$$N_I = 0.991 + 0.141 \cdot \alpha + 0.863 \cdot \alpha^2 + 0.886 \cdot \alpha^3 \qquad (3.9)$$

and,

$$\alpha = \frac{a}{R} \qquad (2.10)$$

As indicated, the error is less than 0.1% within the range of $\alpha = 0.1 \sim 0.6$.

5) Awaji & Sato (1978) also used dislocation and boundary collocation method to study the mixed mode fracture problem of the CSTBD specimen with the dimensionless crack length α (=**a/R**) also within the range $0.1 \sim 0.6$. The results are shown numerically.

6) Chang Shangchow (1988) studied the problem using the equivalent procedure method and presented the results numerically, which agreed well with those by Rooke & Tweed.

In order to have a more accurate solution for any crack length for the CSTBD specimen, the problem has been approached here simply by stepwise superimposition technique. The results obtained agree well with the results by previous researchers and allow more precise solutions for longer crack cases. This method satisfies the requirements for further studies, especially of interest here for being extended into investigations of the related chevron notched specimen, CCNBD.

§3.2.3 Problem Analysis

Consider a Brazilian disk , diameter **D**, radius **R** and thickness **B**, with a central straight-through crack **2a**, subjected to a pair of diametrical compressive load **P** along the crack direction (Fig. 3.2). Owing to the specialities of superimposition of mechanical states and magnitudes, this problem can be

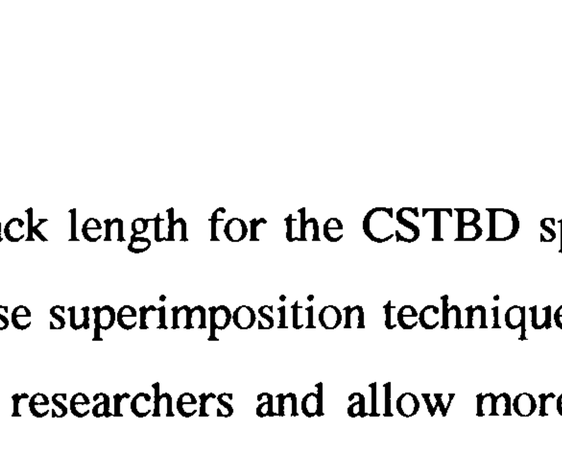

Fig. 3.2 CSTBD Subjected to **P**

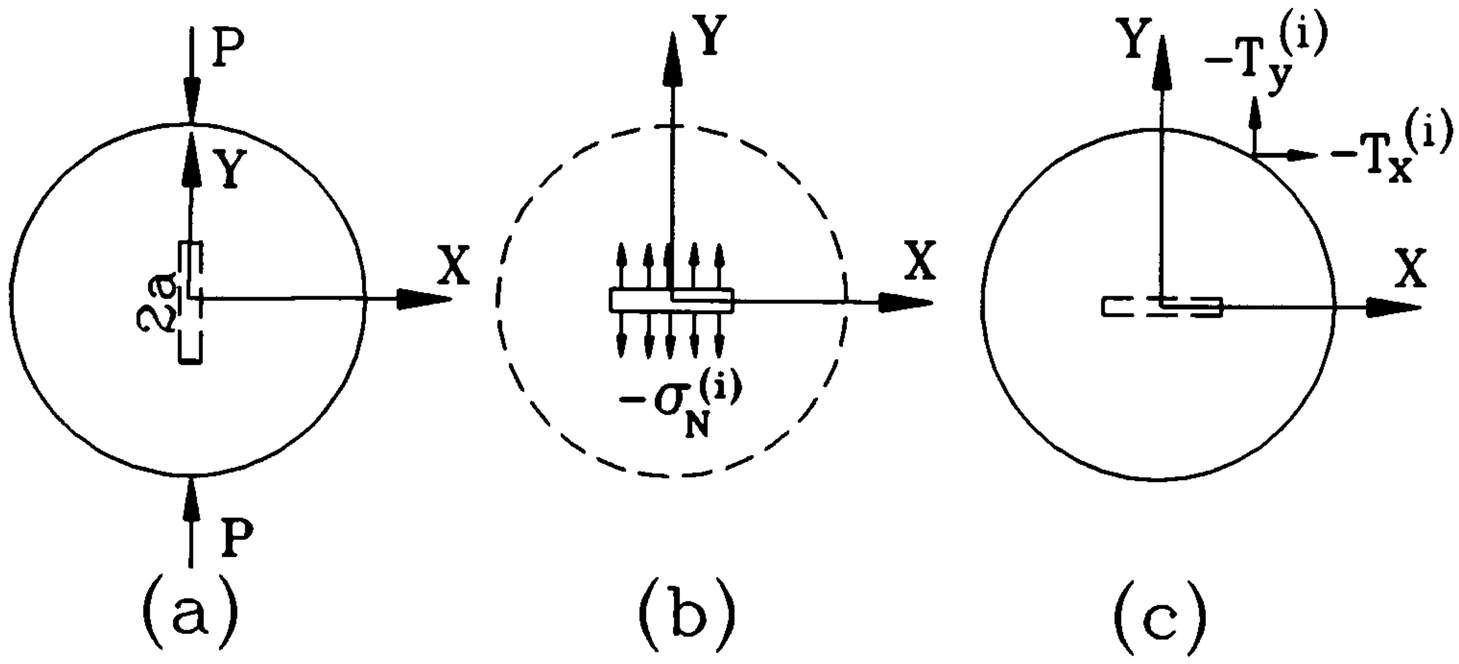

Figure 3.3 Problem Analysis of the CSTBD under Mode I Fracture Condition

divided into the following different smaller problems and the final solution can be obtained simply by summing up all the respective results.

1) A solid Brazilian disk subjected to a pair of diametrical forces **P** (Figure 3.3.a).
Boundary conditions:

$$\begin{cases} XX\ ,\ YY\ axis\ symmetry, \\ P_s = 0 \qquad r=R,\ 0\le\beta\le 2\pi, \\ P_n = \begin{cases} -P & r=R,\ \beta=\pm\dfrac{\pi}{2} \\ 0 & others \end{cases} \end{cases} \tag{3.11}$$

2) Case (1) will create a uniform tensile stress $\sigma_N^{(0)}$ along that part of the loading diameter of the solid disk $0<r<a$, $\beta=\pm\pi/2$. The direction of this tensile stress is in **X** direction and normal to the loading diameter. By introducing a traction free crack in this particular part of the specimen, this stress should be cancelled. So the second problem will be an infinite media with a central crack **2a** subjected to an internal pressure $-\sigma_N^{(0)}$ (Figure 3.3.b).
Boundary conditions:

$$\begin{cases} XX\ ,\ YY\ axis\ symmetry, \\ \sigma_{r\beta} = 0 \qquad 0<r<+\infty,\ \beta = 0,\dfrac{\pi}{2},\pi,\dfrac{3\pi}{2} \\ \sigma_r = \sigma_\beta = \sigma_{r\beta} = 0 \qquad r\to\infty \\ \sigma_\beta = -\sigma_N^{(i)},\ (i=0,1,2,\cdots) \qquad 0<r<a\ ,\ \beta = \pm\dfrac{\pi}{2} \end{cases} \tag{3.12}$$

where **i** is the step number of the stepwise superimposition and at this step, **i = 0**.

3) Case (2) certainly will produce boundary traction stresses $\mathbf{T_x}^{(0)}$ and $\mathbf{T_y}^{(0)}$ along the circle which is identical to the disk boundary. However the practical disk is traction force free along the boundary and therefore these boundary stresses should be cancelled. Thus the third problem is also a solid Brazilian disk, identical to that in case (1), but subjected to boundary traction stresses instead (Figure 3.3.c).

Boundary condition:

$$\begin{cases} XX\ ,\ YY\ \textit{axis symmetry}, & \\ \sigma_{r\beta} = 0 & 0 < r < +\infty\ ,\ \beta = 0, \dfrac{\pi}{2}, \pi, -\dfrac{\pi}{2}, \\ T_x = -T_x^{(i)} & r = R\ ,\ 0 < \beta < 2\pi\ , \\ T_y = -T_y^{(i)} & r = R\ ,\ 0 < \beta < 2\pi\ . \\ & i = 0, 1, 2, 3, \cdots \end{cases} \tag{3.13}$$

where **i** is the step number of the stepwise superimposition procedure, and at this step, **i = 0**.

In practical evaluations, for the reason of simplicity, the disc boundary is divided into **N** elements and the boundary stresses are equated by boundary concentrated forces $\mathbf{P_x}$ and $\mathbf{P_y}$ acting at the central points of each element. When the divided elements are small enough this equivalence is believed to be exact.

4) Under the action of the boundary traction forces $\mathbf{P_x}^{(0)}$ and $\mathbf{P_y}^{(0)}$, the tensile stress $\boldsymbol{\sigma_N}^{(1)}$ will be again set up (certainly $\boldsymbol{\sigma_N}^{(1)} < \boldsymbol{\sigma_N}^{(0)}$) along that part of the loading diameter $\mathbf{0 < r < a}$, $\boldsymbol{\beta = \pm \pi/2}$. As mentioned above, this needs cancelling. Hence the problem will come back to case (2) whilst changing the internal pressure from $\boldsymbol{\sigma_N}^{(0)}$ to $\boldsymbol{\sigma_N}^{(1)}$ and the step number will be **i = 1**.

5) Therefore the whole superposition procedure carries on between case (2) and (3). Obviously the superimposition is convergent due to the apparent condition:

$$\begin{cases} \sigma_N^{(i+1)} < \sigma_N^{(i)} \\ T_x^{(i+1)} < T_x^{(i)} \\ T_y^{(i+1)} < T_y^{(i)} \end{cases} \qquad i = 0\ ,\ 1\ ,\ 2\ ,\ 3\ ,\cdots \tag{3.14}$$

6) The final SIF results $\mathbf{K_I}$ can easily be obtained by summing up all the results of stress intensity factor values $\mathbf{K_I}^{(i)}$ (i=0,1,2,3,...) calculated from case (2) during the different steps of the whole stepwise superimposition procedure.

§3.2.4 Solutions of Cases (1), (2) and (3) Problems

1) The solution for the case (1) problem is well known as the Brazilian compression problem, (Timoshenko, 1970, Frocht, 1948) and here we rewrite it from Equation (3.2),

$$\sigma_N^{(0)} = \frac{2P}{\pi \cdot B \cdot D} \tag{3.15}$$

2) For the case (2) problem, however, the problem is an infinite sheet with a central crack subjected to a internal pressure $-\sigma_N^{(i)}$ (i=0,1, 2,3,...).

The problem was solved by Sneddon (1946,1969), who presented the stress distribution all over the infinite sheet using the Westergaard complex stress function method. As denoted in Figure 3.4, the stress components at any point in the infinite sheet are given by:

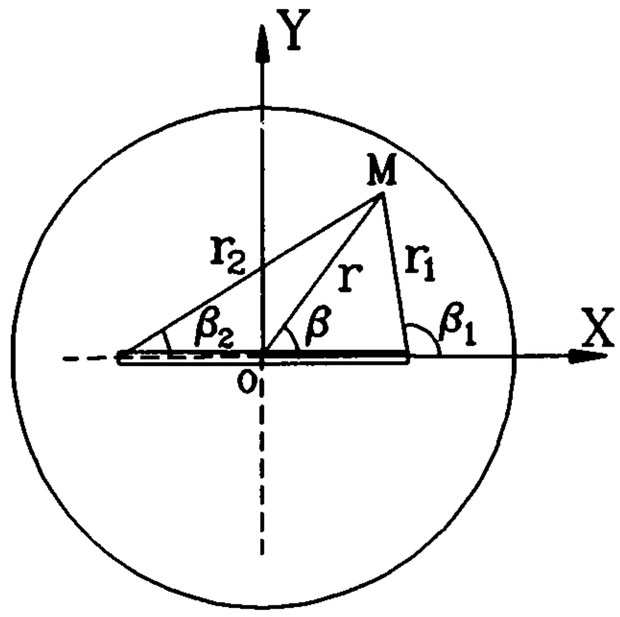

Figure 3.4 Sneddon's Solution

$$\begin{cases} \sigma_{xx} = \dfrac{r \cdot K_I}{\sqrt{a \cdot r_1 \cdot r_2}} \cdot \left[\cos(\beta - \dfrac{\beta_1}{2} - \dfrac{\beta_2}{2}) + \dfrac{a^2}{r_1 \cdot r_2} \cdot \sin\beta \cdot \sin\dfrac{3(\beta_1+\beta_2)}{2} \right] \\ \sigma_{yy} = \dfrac{r \cdot K_I}{\sqrt{a \cdot r_1 \cdot r_2}} \cdot \left[\cos(\beta - \dfrac{\beta_1}{2} - \dfrac{\beta_2}{2}) - \dfrac{a^2}{r_1 \cdot r_2} \cdot \sin\beta \cdot \sin\dfrac{3(\beta_1+\beta_2)}{2} \right] - \sigma_0 \\ \sigma_{xy} = \dfrac{r \cdot K_I}{\sqrt{a \cdot r_1 \cdot r_2}} \cdot \dfrac{a^2}{r_1 \cdot r_2} \cdot \sin\beta \cdot \cos\dfrac{3(\beta_1+\beta_2)}{2} \end{cases} \tag{3.16}$$

where $\mathbf{K_I} = \sigma_0\sqrt{a}$,

σ_0 -- internal pressure, in our case, $\sigma_0 = \sigma_t^{(i)}$ (i=0,1,2,3...).

β, β_1 and β_2 -- angles based on the crack line and its central and apex points, as shown in Figure 3.4.

$\sigma_{xx} = \sigma_{xx}^{(i)}$, $\sigma_{yy} = \sigma_{yy}^{(i)}$ and $\sigma_{xy} = \sigma_{xy}^{(i)}$ (i=0,1,2,3,...).

Thus the stress components of the elements along the circumference of the circle $\mathbf{r = R}$, $0 < \beta < 2\pi$, which symbolizes the boundary of the disk, can be calculated, and hence the pseudo "boundary" traction stresses can be obtained.

Taking one of the pseudo "boundary" elements for instance, as shown in Figure 3.5. The traction stresses acting on the inclined section face which is constructed along the pseudo disk

"boundary" can be expressed as follows:

$$\begin{bmatrix} T_x^{(i)} \\ T_y^{(i)} \end{bmatrix} = \begin{bmatrix} \sigma_{xx}^{(i)} & \sigma_{yx}^{(i)} \\ \sigma_{xy}^{(i)} & \sigma_{yy}^{(i)} \end{bmatrix} \begin{bmatrix} n_x \\ n_y \end{bmatrix} \tag{3.17}$$

where $\mathbf{n_x}$ and $\mathbf{n_y}$ are the direction cosines of the inclined section face, i.e.,

$$\begin{cases} n_x = \cos\beta \\ n_y = \sin\beta \end{cases} \tag{3.18}$$

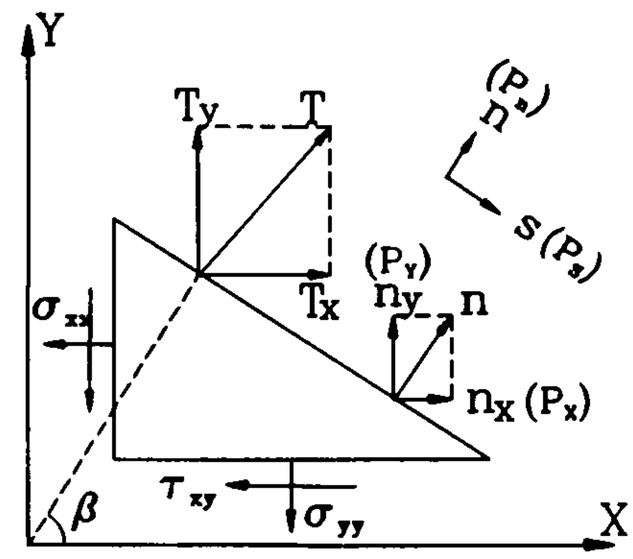

Figure 3.5 Boundary Elements

corresponding to the nomenclature in Figure 3.5.

3) The solution for the case (3) problem can be obtained from Frocht (1948). For a disk subjected to a pair of point loads $\mathbf{P_x}$ or $\mathbf{P_y}$ acting horizontally and vertically along a chord, the stress components at any point **M** within the disk can be calculated by the following equations (Figure 3.6):

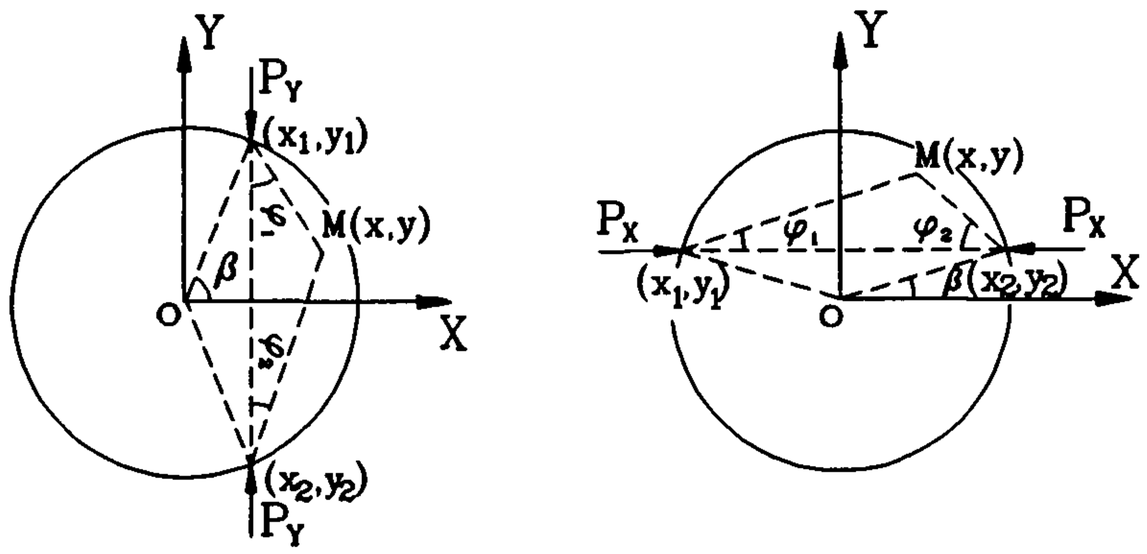

Figure 3.6 Boundary Loadings

a) Vertical Load, Figure 3.6.a

$$\begin{cases} \sigma_{xx} = -\dfrac{2\cdot P_y}{\pi\cdot B}\left[\dfrac{\cos\varphi_1\sin^2\varphi_1}{s_1} + \dfrac{\cos\varphi_2\sin^2\varphi_2}{s_2} - \dfrac{\cos\beta}{D}\right] \\ \sigma_{yy} = -\dfrac{2\cdot P_y}{\pi\cdot B}\left[\dfrac{\cos^3\varphi_1}{s_1} + \dfrac{\cos^3\varphi_2}{s_2} - \dfrac{\cos\beta}{D}\right] \\ \sigma_{xy} = \dfrac{2\cdot P_y}{\pi\cdot B}\left[\dfrac{\cos^3\varphi_1\sin\varphi_1}{s_1} - \dfrac{\cos^2\varphi_2\sin\varphi_2}{s_2}\right] \end{cases} \tag{3.19}$$

where,

$$\begin{cases} \sin\varphi_1 = \dfrac{(x - x_1)}{s_1} \\ \cos\varphi_1 = \dfrac{(y_1 - y)}{s_1} \\ \sin\varphi_2 = \dfrac{(x - x_1)}{s_2} \\ \cos\varphi_2 = \dfrac{(y - y_2)}{s_2} = \dfrac{(y + y_2)}{s_2} \\ s_1 = \sqrt{(x - x_1)^2 + (y - y_1)^2} \\ s_2 = \sqrt{(x - x_2)^2 + (y - y_2)^2} \end{cases} \tag{3.20}$$

b) Horizontal Load, Figure 3.6.b

$$\begin{cases} \sigma_{xx} = -\dfrac{2 \cdot P_x}{\pi \cdot B}\left[\dfrac{\cos^3\varphi_1}{s_1} + \dfrac{\cos^3\varphi_2}{s_2} - \dfrac{\cos\beta}{D} \right] \\ \sigma_{yy} = -\dfrac{2 \cdot P_x}{\pi \cdot B}\left[\dfrac{\cos\varphi_1 \sin^2\varphi_1}{s_1} + \dfrac{\cos\varphi_2 \sin^2\varphi_2}{s_2} - \dfrac{\cos\beta}{D} \right] \\ \sigma_{xy} = \dfrac{2 \cdot P_x}{\pi \cdot B}\left[\dfrac{\cos^3\varphi_1 \sin\varphi_1}{s_1} - \dfrac{\cos\varphi_2 \sin\varphi_2}{s_2} \right] \end{cases} \tag{3.21}$$

where,

$$\begin{cases} \sin\varphi_1 = \dfrac{(y - y_1)}{s_1} \\ \cos\varphi_1 = \dfrac{(x - x_1)}{s_1} \\ \sin\varphi_2 = \dfrac{(y - y_2)}{s_2} = \dfrac{(y - y_1)}{s_2} \\ \cos\varphi_2 = \dfrac{(x_2 - x)}{s_2} \\ s_1 = \sqrt{(x - x_1)^2 + (y - y_1)^2} \\ s_2 = \sqrt{(x - x_2)^2 + (y - y_2)^2} \end{cases} \tag{3.22}$$

However, the stress components along the **XX** axis where the crack is supposed to be introduced are particularly of interest. Therefore the equations above can be simplified by substituting $\mathbf{Y} = 0$.

§3.2.5 The Stepwise superimposition Procedure

The circumference and the crack can be discreted by dividing the circle boundary into **N** segments, and the crack into **J** segments. The superimposition iteration begins from the crack subjected to the initial internal pressure $\sigma_N^{(0)}$ in an infinite sheet. For the **i**-th step, the pressure becomes $\sigma_N^{(i)}$ (i = 0,1,2,3,...), and the traction stresses on the **n**-th element of the pseudo "boundary" can be calculated from Equation (3.17) directly, and hence the forces acting on this boundary element are:

$$\begin{cases} (P_x^{(i)})_n = (T_x^{(i)})_n \cdot l_n \\ (P_y^{(i)})_n = (T_y^{(i)})_n \cdot l_n \end{cases} \quad \begin{array}{l} i = 0,1,2,3,\cdots \\ n = 1,2,3,\cdots,N \end{array} \tag{3.23}$$

where l_n is the length of the **n**-th boundary element.

On obtaining the boundary forces, under their actions, the stresses they create in the **j**-th element of the crack can be calculated by summing up all the effects of the **N/2** pair of boundary forces, i.e.,

$$(\sigma_N^{(i)})_j = \sum_{n=1}^{\frac{N}{2}} [(\sigma_N^{(i)})_j]_n \qquad (j = 1, 2, \cdots, M) \tag{2.24}$$

where $[(\sigma_N^{(i)})_j]_n$ is the effective stress of **j**-th crack element due to the traction forces acting on the **n**-th boundary element during the **i**-th iteration step. Here the asymmetry conditions are used so that the boundary force effect is evaluated in pairs. Then the internal pressure $\sigma_N^{(i+1)}$ for the next step calculation will be their average over the total **M** crack elements. Thereafter, the procedure goes back to the calculating the pseudo "boundary" stresses again. The stepwise superimposition continues.

The SIF value around the crack tip is the sum of the stress intensity factors obtained during each step of the whole superimposition procedure:

$$K^I = \sum_{i=1}^{I} \sigma_N^{(i)} \cdot \sqrt{\pi a} \qquad (i = 0, 1, 2, \cdots, I) \tag{3.25}$$

here $\sigma_N^{(i)}\sqrt{(\pi a)}$ is the individual stress intensity factor of a crack in an infinite sheet subjected to internal pressure equal to the **i**-th iteration step stress $\sigma_N^{(i)}$.

As discussed above, the superimposition is convergent so that the accuracy can be set beforehand. In other words, $\mathbf{K^I}$ will be taken as the final **K** value as long as it satifies the following condition:

$$| K^I - K^{I-1} | \leq ESP \tag{3.26}$$

then,

$$K = K^I \tag{3.27}$$

where **ESP** is the set error of the evaluation.

In addition, it should be noted that during the evaluation procedure, the tangential stress along the crack surface do not need to be considered. In fact, for the pure **Mode I** fracture problem for the CSTBD specimen, the tangential stresses along the crack surfaces σ_T are always zero.

§3.2.6 The SIF Values of the CSTBD Specimen under Mode I Fracture Condition

Table 3.1 is the list of the **Mode I** SIF evaluation results for the CSTBD specimen. For comparison, the results by Rooke & Cartwright, Libatskii, and Atkinson are also listed. All the results are presented in the dimensionless expression defined as follows:

$$\frac{K_I}{K_0} = f(\frac{a}{R}) = f(\alpha)$$

where,

$$K_0 = \frac{P}{\pi \cdot B \cdot R}\sqrt{\pi \cdot a} = \frac{P}{B\sqrt{R}}\sqrt{\frac{\alpha}{\pi}} \tag{3.29}$$

is the stress intensity factor of a crack in an infinite sheet subjected to the internal pressure equal to $\mathbf{P/\pi RB}$, and α is the dimensionless crack length. The results are also plotted in Figure 3.7 where the differences between researchers are clearly illustrated.

Furthermore, for the sake of convenient analysis, an eighth order polynomial is used to fit the results listed in Table 3.1 by the least-square technique. Table 3.2 is the list of the coefficients of the polynomial which is the best fit, where the conversion of the SIF value from $\mathbf{f(\alpha)}$ to the more common form $\mathbf{Y(\alpha)}$ has been made by the following equation:

$$Y(\alpha) = f(\alpha)\cdot\sqrt{\frac{\alpha}{\pi}} \tag{3.30}$$

Table 3.1 K_I Evaluation Results of the CSTBD Specimen

α (a/R)	Dimensionless SIF $f(\alpha)$			
	Present Analysis	Libatskii	Rooke & Cartwright	Atkinson
0.05	0.9623	1.0038	0.9944	1.0003
0.10	1.0217	1.0150	1.0195	1.0146
0.15	1.0432	1.0338	1.0445	1.0608
0.20	1.0583	1.0600	1.0713	1.0940
0.25	1.0843	1.0939	1.1022	1.1349
0.30	1.1266	1.1356	1.1396	1.1841
0.35	1.1835	1.1851	1.1860	1.2422
0.40	1.2498	1.2431	1.2431	1.3099
0.45	1.3216	1.3106	1.3118	1.3880
0.50	1.3983	1.3869	1.3925	1.4770
0.55	1.4839	1.4749	1.4848	1.5777
0.60	1.5858	1.5758	1.5890	1.6906
0.65	1.7116	1.6918	1.7071	
0.70	1.8658	1.8259	1.8448	
0.75	2.0495	1.9819	2.0147	
0.80	2.2686		2.2403	
0.85	2.5608		2.5612	
0.90	3.0547		3.0399	

§3.3 The Mode I SIF Evaluations of the CCNBD Specimens

Owing to the complexity of the specimen geometry, there are not any existing analytical solutions for the SIF values for the CCNBD specimen under any single mode or mixed mode fracture condition. However, the solution can be reached by extending the CSTBD results obtained above and combining with some commonly accepted hypothesis, such as Munz's identical compliance changing rate model or Bluhm's slice superimposition model.

In the following theoretical derivation, if the fracture mode is particularly mentioned or if the symboles in the equations are followed by subscript "**I**", "**II**" or "**III**", then the discussions

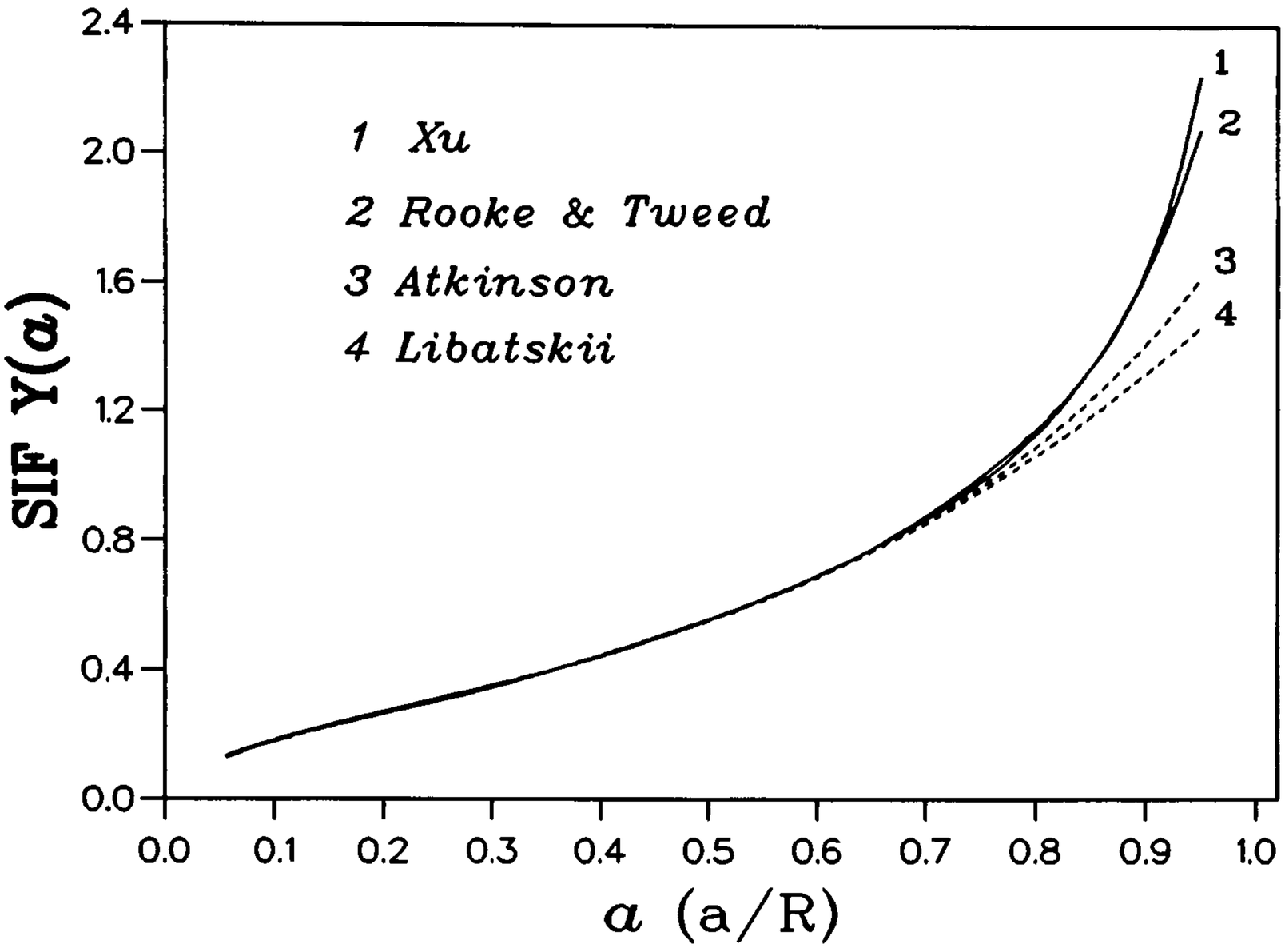

Figure 3.7 Mode I SIF Evaluation Results for the CSTBD Specimen

Table 3.2 Polynomial Best Fit for Y(α) of the CSTBD Specimen

$$Y(\alpha) = \sum_{ic=0}^{IC} c_{ic} \cdot \alpha^{ic} \qquad ic = 0, \frac{1}{2}, 1, \frac{3}{2}, \cdots, IC$$

α^{ic}	Present Results c_{ic}	α^{ic}	Libatskii c_{ic}	Rooke & Cartwright c_{ic}	Atkinson c_{ic}
α^0	0.035	$\alpha^{1/2}$	0.564	0.020	0.559
α^1	2.039	$\alpha^{3/2}$		0.297	0.080
α^2	-7.036	$\alpha^{5/2}$	0.846	-0.060	0.487
α^3	12.815	$\alpha^{7/2}$		-0.799	0.500
α^4	8.411	$\alpha^{9/2}$		5.216	
α^5	-30.742	$\alpha^{11/2}$		-1.547	
α^6	-29.496	$\alpha^{13/2}$	0.423	-5.790	
α^7	62.974	$\alpha^{15/2}$		-0.122	
α^8	66.544	$\alpha^{17/2}$	0.026	5.017	
α^9	-82.134				
α^{10}	-73.674				
α^{11}	73.847				

and the equations will be only suitable to that fracture mode condition. Otherwise if no restrictions about fracture mode conditions for the applications of the discussions and the equations are mentioned, then the analysis will be suitable to any single mode or mixed mode fracture conditions.

§3.3.1 The CCNBD Specimen Geometry -- Nomenclature and Relationships

As shown in Figure 3.8, two basic relationship equations between the geometrical parameters can be obtained from the Pythagoras' theorem:

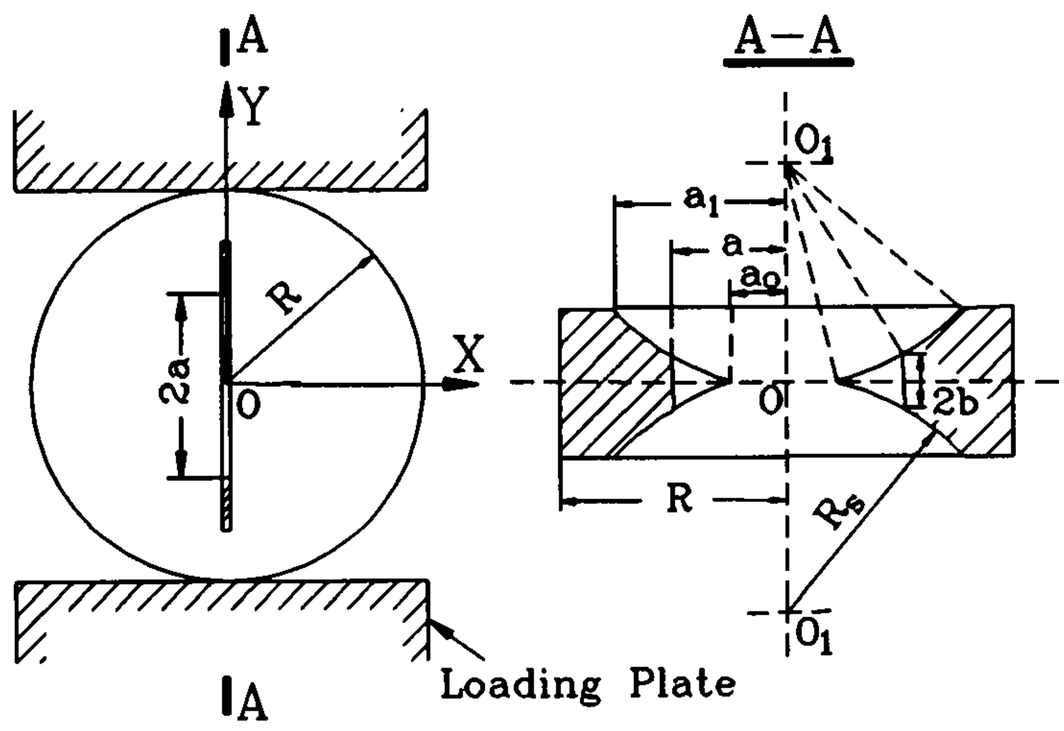

Figure 3.8 The CCNBD Nomenclature

$$\begin{cases} b = 2\cdot\left(\sqrt{R_s^2 - a_1^2} - \sqrt{R_s^2 - a^2} + \dfrac{B}{2} \right) \\ b = 2\cdot\left(\sqrt{R_s^2 - a_0^2} - \sqrt{R_s^2 - a^2} \right) \end{cases} \tag{3.31}$$

Therefore b can be easily derived:

$$b = \frac{2\cdot R^2}{B} f_1(\alpha) \tag{3.32}$$

where,

$$f_1(\alpha) = (\alpha_1^2 - \alpha_0^2) + \frac{\alpha_B^2}{4} - \sqrt{(\alpha_1^2 - \alpha^2)\cdot\alpha_B^2 + (\alpha_1^2 - \alpha_0^2 - \frac{\alpha_B^2}{4})^2} \tag{3.33}$$

and,

$$\begin{cases} \alpha = a/R \\ \alpha_0 = a_0/R \\ \alpha_1 = a_1/R \\ \alpha_B = B/R \\ \alpha_s = R_s/R \end{cases} \tag{3.34}$$

Based on the above equations, some useful relationships between the different geometry parameters can be obtained:

$$\begin{cases} \alpha_s = \sqrt{\alpha_0^2 + (\alpha_1^2 - \alpha_0^2 + \alpha_B^2/4)^2 \div \alpha_B^2} \\ h_c = (\alpha_s - \sqrt{\alpha_s^2 - \alpha_1^2})\cdot R = (\alpha_s - \sqrt{\alpha_s^2 - \alpha_0^2})\cdot R + B/2 \\ \alpha_0 = \sqrt{\alpha_s^2 - (\sqrt{\alpha_s^2 - \alpha_1^2} + \alpha_B/2)^2} \\ \alpha_1 = \sqrt{\alpha_s^2 - (\sqrt{\alpha_s^2 - \alpha_0^2} - \alpha_B/2)^2} \\ \alpha_B = 2\cdot(\sqrt{\alpha_s^2 - \alpha_0^2} - \sqrt{\alpha_s^2 - \alpha_1^2}) \end{cases} \tag{3.35}$$

As a final point in this section, it is necessary here to mention the restrictions between the specimen's structural parameters α_0, α_1 and α_B. These three variables are independent from the physical point of view. However, with respect to machining feasibility and in order to obtain a reasonable specimen geometry, the lowest limit between the saw radius $\mathbf{R_s}$ and the crack length $\mathbf{a_1}$ should be satisfied, i.e., $\mathbf{R_s \geq a_1}$. From this limit equation, restriction relations between the three variables can be derived:

$$\begin{cases} \alpha_B \leq 2\cdot\sqrt{\alpha_1^2 - \alpha_0^2} \\ \alpha_0 \leq \sqrt{\alpha_1^2 - \alpha_B^2/4} \\ \alpha_1 \geq \sqrt{\alpha_0^2 + \alpha_B^2/4} \end{cases} \tag{3.36}$$

§3.3.2 Relations between the Compliance and the Stress Intensity Factor of the CCNBD Specimens -- Compliance Method

Specimen compliance is defined as the reverse of specimen stiffness, i.e.,

$$C = u/P \tag{3.37}$$

where **P** -- external load, and

u -- related displacement.

Combined with the definition of the strain energy release rate **G** (crack driving force), it is very easy to derive the relation between **C** and **G**. Supposed when the crack propagates stably for an incremental value **da** and the change in the compliance value of the specimen is **dC**, then the relation can be expressed as (Figure 3.9):

$$G = \frac{P^2}{2 \cdot b} \cdot \frac{dC}{da} \tag{3.38}$$

This equation was also derived by Barker (1979) while he was evaluating the stress intensity factor of the chevron notch SR specimen.

Therefore, the SIF value can be obtained by the relationship between **G** and **K** (Equation 2.11):

$$K = P \cdot \left[\frac{\frac{dC}{da} \cdot E'}{2 \cdot b} \right]^{\frac{1}{2}} \tag{3.39}$$

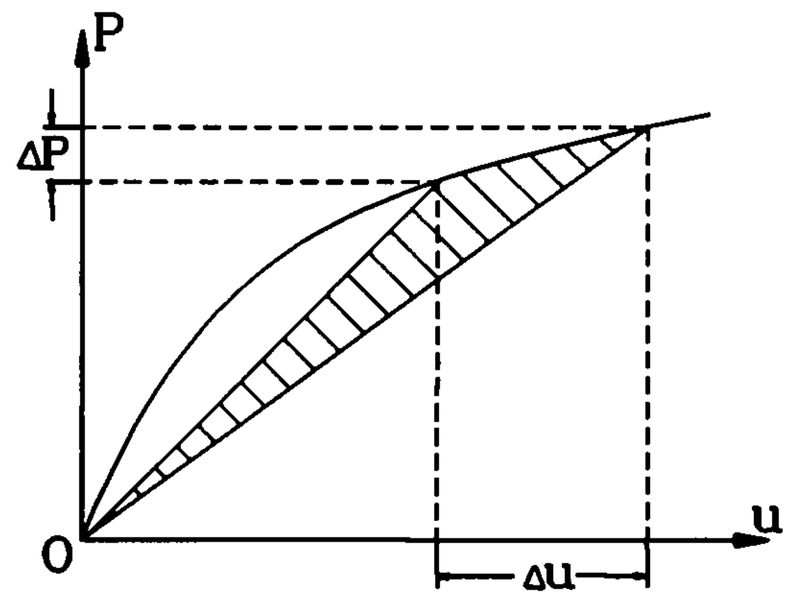

Figure 3.9 Compliance Method

Substituting Equation (3.32) into (3.39) will yield:

$$K = \frac{P}{B\sqrt{R}} \cdot \left[\frac{\frac{d(CBE')}{d\alpha} \cdot \alpha_B^2}{4 \cdot f_1(\alpha)} \right]^{\frac{1}{2}} = \frac{P}{B\sqrt{R}} \cdot Y^*(\alpha) \tag{3.40}$$

where **CBE'** is the dimensionless compliance of the CCNBD specimen with **E'** defined in Equation (2.12) and $\mathbf{Y^*(\alpha)}$ is the dimensionless stress intensity factor (SIF) of the CCNBD specimen.

§3.3.2.1 Hypothesis I and $Y^*(\alpha)$ Evaluation

As a first approximation, Munz (1980) assumed that the change in dimensionless compliance with a crack extension **da** ($d\alpha$) for the chevron notch specimen is identical to that for a straight through specimen provided the other geometrical values are identical, i.e.

$$\frac{d(C_{CN} \cdot BE')}{d\alpha} = \frac{d(C_{ST} \cdot BE')}{d\alpha} \tag{3.41}$$

This assumption has been used for the study of SR specimens and the results are convincingly satisfactory.

For the CCNBD specimen, from Equation (3.39) we can derive the compliance changing rate expression of CSTBD specimen as the following equation:

$$K_I = \frac{P}{B\sqrt{R}}\left[\frac{1}{2}\cdot\frac{d(C_{ST}BE')}{d\alpha}\right]^{\frac{1}{2}} = K_0\cdot f(\alpha) = \frac{P}{B\sqrt{R}}\cdot Y(\alpha) \tag{3.42}$$

hence,

$$\frac{d(C_{ST}BE')}{d\alpha} = 2\cdot Y^2(\alpha) \tag{3.43}$$

Combined with the above assumption,we can then obtain the dimensionless SIF expression for the CCNBD specimen as followed:

$$Y^*(\alpha) = \left[\frac{\alpha_B^2}{2f_1(\alpha)}\right]^{\frac{1}{2}}\cdot Y(\alpha) \tag{3.44}$$

§3.3.2.2 Hypothesis II and $Y^*(\alpha)$ Evaluation

Bluhm (1975) developed a quasi-analytical method to solve the general non-straight crack front problem. The basic idea is that the whole specimen can be analytically divided into a number of different slices along the direction of thickness, and the compliance C_{tl} of the total specimen is given by the sum of the reciprocals of the compliance of all the slices, i.e.,

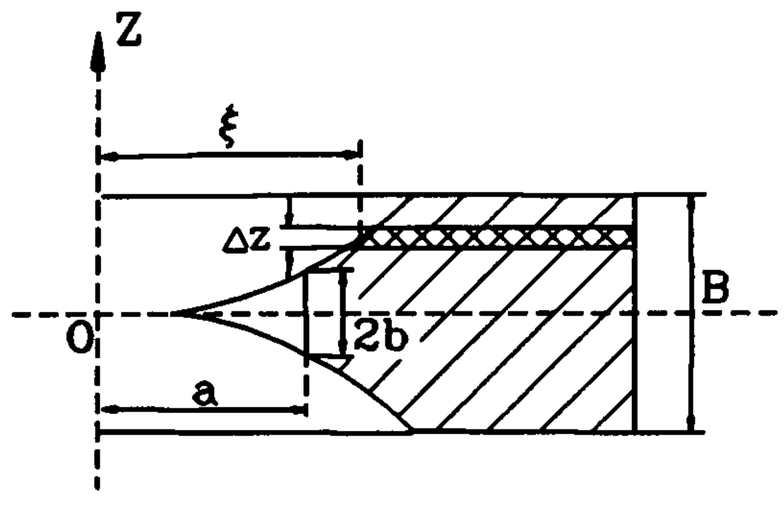

Fig. 3.10 Hypothesis II for the CCNBD

$$\frac{1}{C_{tl}} = \sum_{i=1}^{n}\frac{1}{C_s^i} \tag{3.45}$$

The effect of the interlaminar shear stress between different slices can be represented by a constant $\mathbf{c_k}$ which has to be determined by comparison of experimental and analytical results.

For the CCNBD specimen, the idea can be illustrated in Figure 3.10. Divide the specimen into **n** slices thus every slice gets a thickness $\mathbf{\Delta Z = B/n}$. Then the compliance of a slice with a dimensionless crack length $\mathbf{\xi = a_\xi/R}$ is obviously as:

$$C_s^i = C(\xi)\cdot\frac{B}{\Delta Z} \tag{3.46}$$

where $\mathbf{C(\xi)}$ is the compliance value of a CSTBD specimen with thickness **B** and a dimensionless crack length ξ. Therefore,

$$\frac{1}{C_{tl}} = \frac{b}{B}\cdot\frac{1}{C(\alpha)} + \frac{2}{B}\cdot\sum\frac{\Delta Z}{C(\xi)} \tag{3.47}$$

On the other hand, the following equations can be given from the geometry relations:

$$\begin{cases} dZ_\xi = \dfrac{1}{2}\cdot db_\xi \\ db_\xi = \dfrac{2R^2}{B}f_1'(\xi)\cdot d\xi = \dfrac{2R^2}{B}f_2(\xi)\cdot d\xi \end{cases} \tag{3.48}$$

where,

$$f_2(\xi) = \frac{\alpha_B^2\cdot\xi}{\sqrt{(\alpha_1^2-\xi^2)\cdot\alpha_B^2 + (\alpha_1^2-\alpha_0^2-\alpha_B^2/4)^2}} \tag{3.49}$$

Substituting these equations into Equation (3.47) will yield:

$$\frac{1}{C_{tl}} = \frac{2}{\alpha_B^2}\left[\frac{f_1(\alpha)}{C(\alpha)} + \sum_{\xi=\alpha}^{\alpha_1}\frac{f_2(\xi)}{C(\xi)}\cdot\Delta\xi\right] \tag{3.50}$$

Differentiating Equation (3.50) with respect to α, substituting the following relations into Equation (3.50):

$$\begin{cases} C(\alpha) = \displaystyle\int_0^\alpha \frac{2}{BE'}\cdot Y^2(\alpha)\cdot d\alpha \\ C'(\alpha) = \dfrac{2}{BE'}\cdot Y^2(\alpha) \\ \left[\displaystyle\int_\alpha^{\alpha_1}\frac{f_2(\xi)}{C(\xi)}\cdot d\xi\right]' = -\frac{f_2(\alpha)}{C(\alpha)} \end{cases} \tag{3.51}$$

and at the same time introducing the interlaminar effect constant $\mathbf{c_k}$, then the following expression can be reached:

$$\frac{dC_{tl}}{d\alpha} = \frac{\alpha_B^2}{2BE' f_3(\alpha)} f_4(\alpha) \tag{3.52}$$

where,

$$\begin{cases} f_3(\alpha) = \left[\dfrac{1}{BE'} \cdot \dfrac{f_1(\alpha)}{C(\alpha)} + \dfrac{1}{BE'} \cdot \int_{\alpha}^{\alpha_1} \dfrac{f_2(\xi)}{C(\xi)} \cdot d\xi \right]^2 \\ f_4(\alpha) = \dfrac{2}{(BE')^2} \cdot \dfrac{Y(\alpha) f_1(\alpha)}{C^2(\alpha)} - \dfrac{(1-c_k)}{BE'} \cdot \dfrac{f_2(\alpha)}{C(\alpha)} \end{cases} \tag{3.53}$$

Hence the dimensionless stress intensity factor $\mathbf{Y^*}(\alpha)$ for the CCNBD specimen can be finally obtained:

$$Y^* = \left[\frac{\alpha_B^4 f_4(\alpha)}{8 f_1(\alpha) f_3(\alpha)} \right]^{\frac{1}{2}} \tag{3.54}$$

Here note should be taken that the theoretical derivations in section §3.3.2.1 and §3.3.2.2 for $\mathbf{Y^*}(\alpha)$ of the CCNBD specimens are not restricted to a special fracture mode (**Mode I, II, III** or mixed mode). In other words, $\mathbf{Y^*}(\alpha)$ could be the dimensionless SIF values for any fracture mode depending on the represented mode of the original $\mathbf{Y}(\alpha)$ and $\mathbf{C}(\alpha)$ values. However, in the sections of this chapter that follow, unless mentioned, all the $\mathbf{Y^*}(\alpha)$ values will be concerning **Mode I** SIF values of the CCNBD specimen only.

§3.3.3 Typical SIF $\mathbf{Y^*}(\alpha)$ Results for the CCNBD Specimens

Figure 3.11 illustrates the results from Equation (3.44) and (3.54) for the dimensionless SIF $\mathbf{Y^*}(\alpha)$ of the CCNBD specimen vs crack extension for three typical cases, medium, short and long crack (distinguished by the value of $\mathbf{\Delta a_{CN} = a_1 - a_0}$). We know from this figure that as the crack propagates from $\mathbf{a = a_0}$, the $\mathbf{Y^*}(\alpha)$ starts with a high magnitude which means that a high stress concentration is generated at the tip of the chevron notched crack and hence the crack initiates at a low externally applied load. Thereafter, $\mathbf{Y^*}(\alpha)$ drops rapidly with increasing crack length. That signifies that larger increments of applied load are needed in order to keep the crack growing. In other words, the pseudo non-static crack initiation can turn into stable crack propagation under a known increasing rate for the external loads. This reduction of the $\mathbf{Y^*}(\alpha)$ value will continue until it reaches its minimum $\mathbf{Y^*_m}(\alpha_m)$, corresponding the critical crack

length $\mathbf{a_m}$. After this point, the $\mathbf{Y^*}(\alpha)$ value begins to rise, gently (slowly) at the beginning and rapidly afterwards. That demonstrates that the whole system has passed its critical state and the crack turns to unstable propagation, corresponding to the decrease in the external loads.

For the medium and long crack cases, the critical state happens within the chevron part of the crack , i.e., $\mathbf{a_0 < a_m < a_1}$. For the short crack case, that state will happen when the crack propagation front hits the uncracked part of the specimen, i.e., as long as the chevron part of the crack ends, or, $\mathbf{a_m = a_1}$. In this case the chevron notch functions no more than just as a stable pre-cracking method for the CSTBD specimens, and the CCNBD specimen will loss the good features of a chevron specimen geometry. However in practical usage, the short crack case CCNBD specimens are very difficult to machine therefore the medium or long crack case CCNBD specimens will be commonly used.

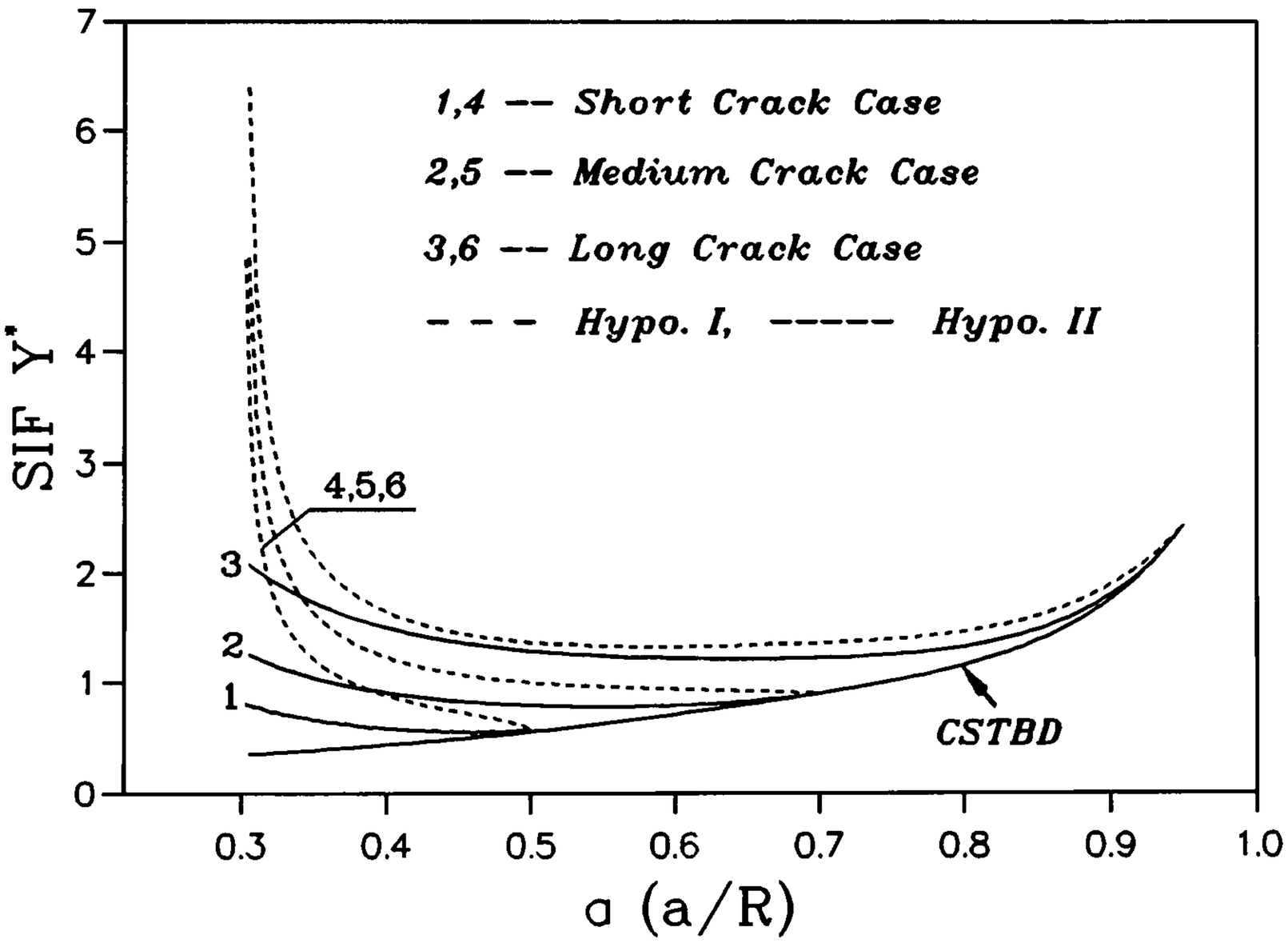

Figure 3.11 Typical $\mathbf{Y^*}(\alpha)$ Results for some CCNBD Specimens

It has been proved by numerical analysis of the CCNBD specimen (boundary element and finite element methods, next chapter) that Bluhm's model (hypothesis II) can better simulate the fracture problem of the CCNBD specimen than Munz's model (hypothesis I). The dimensionless SIF $\mathbf{Y^*}(\alpha)$ for the CCNBD specimen evaluated by Bluhm's model can yield much closer values to those obtained by the numerical methods. Therefore in the following analysis in this thesis, the theoretical dimensionless SIF $\mathbf{Y^*}(\alpha)$ for the CCNBD specimen will be referred

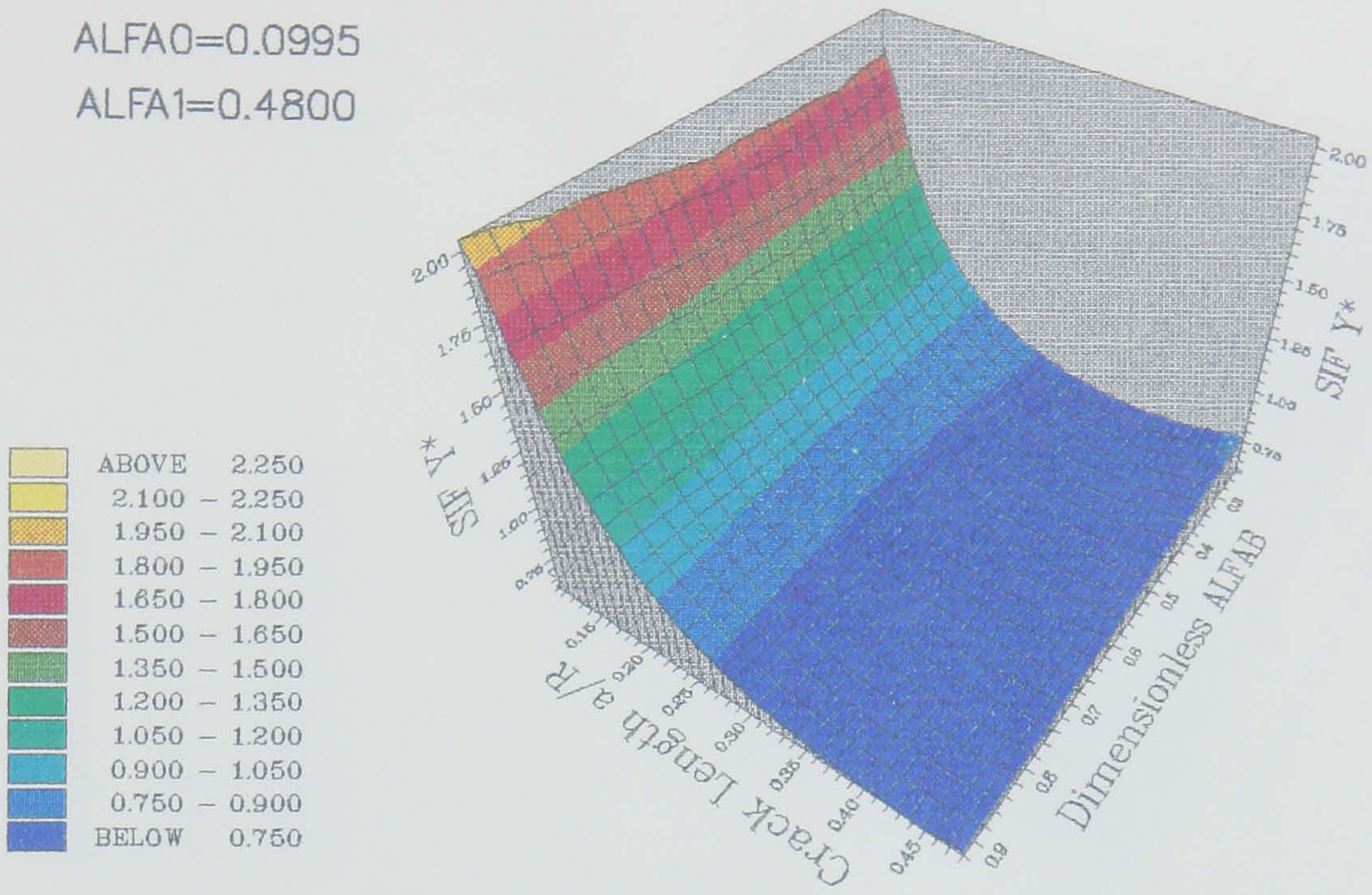

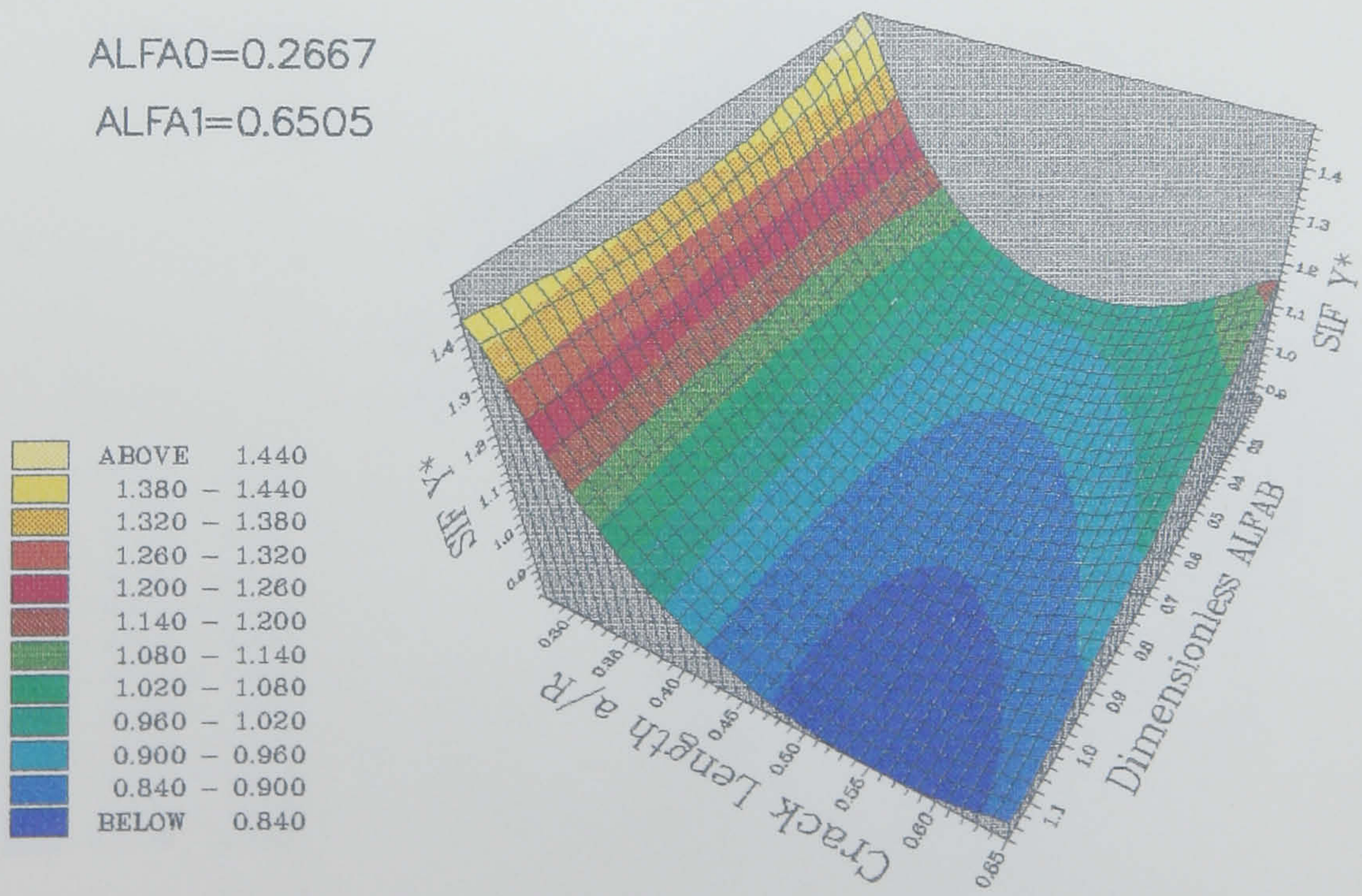

Figure 3.12 (a) and (b) $Y^*(\alpha)$ for the CCNBD (short and medium crack cases)

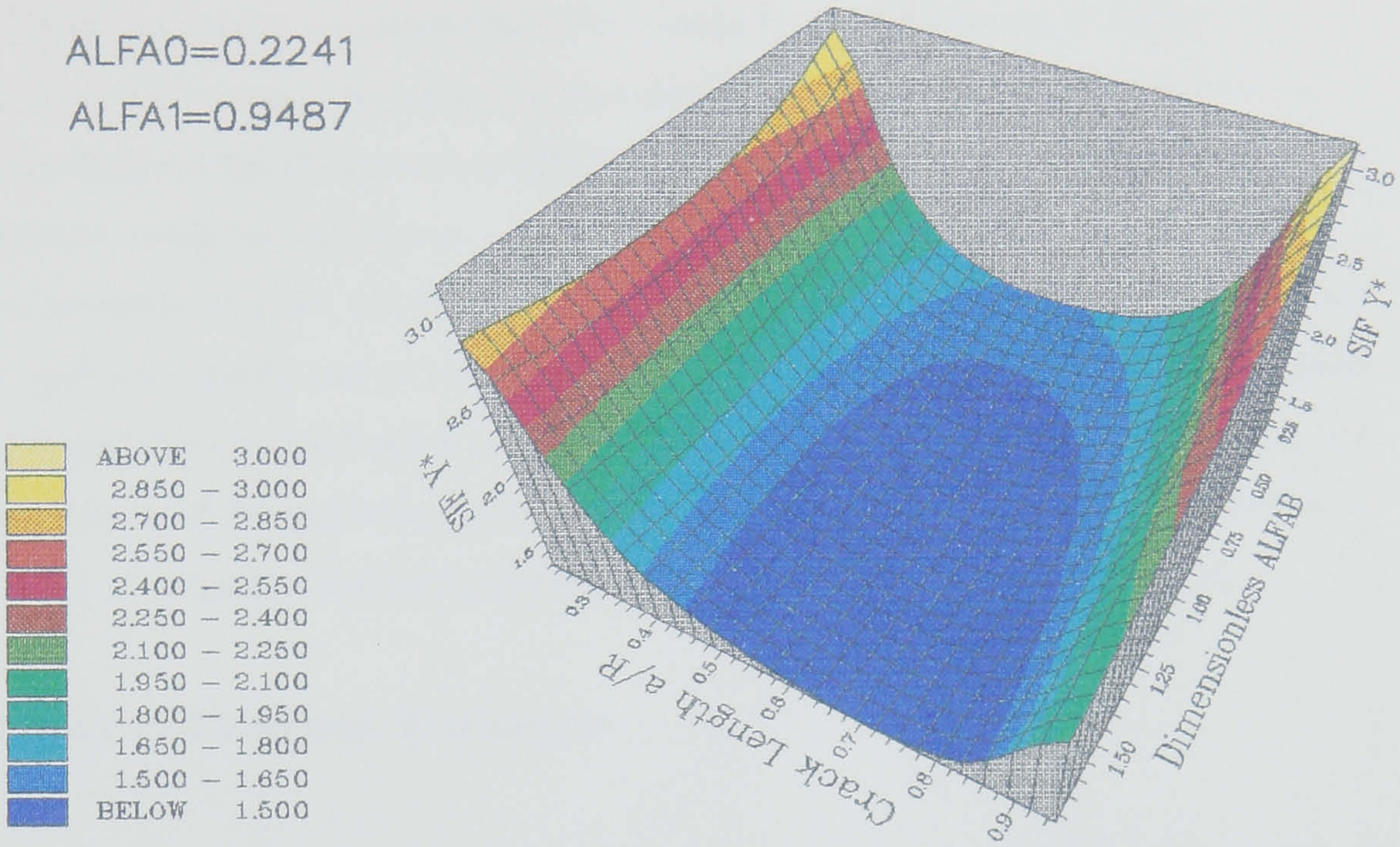

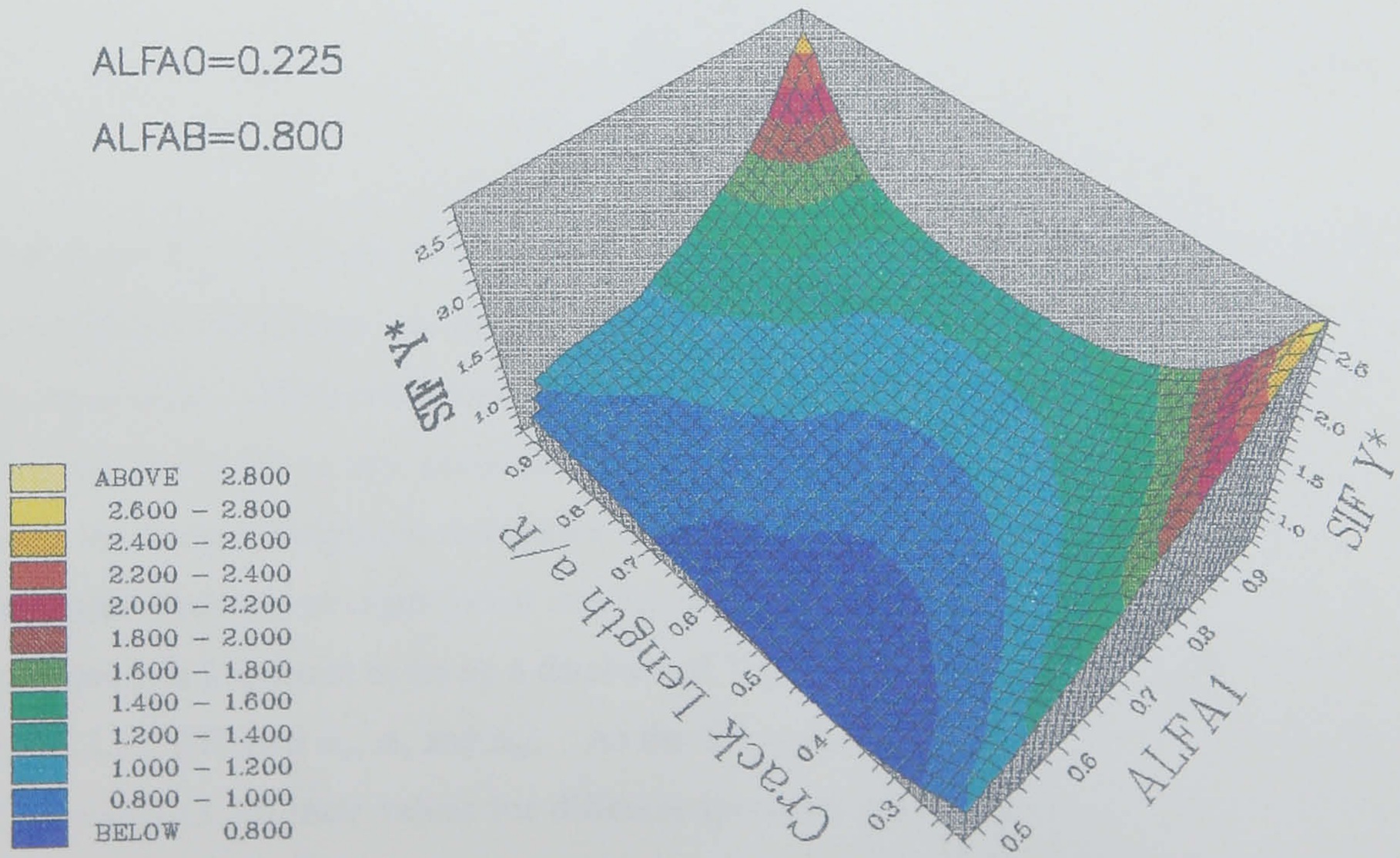

Figure 3.12 (c) and (d) $Y^*(\alpha)$ for the CCNBD (long crack and fixed B cases)

to those values evaluated by Bluhm's model only.

In order to have a much clearer illustration of the dimensionless SIY $\mathbf{Y}^*(\alpha)$ value variation for the CCNBD specimen, we present the $\mathbf{Y}^*(\alpha)$ values by Bluhm's model in Figure 3.12 (a), (b), (c) and (d) where $\Delta\mathbf{a}_{CN}$, **B** and α_1 are changing at the same time. From these figures, the relations between the dimensionless SIF $\mathbf{Y}^*(\alpha)$ of the specimen and the state of the crack propagation can easily be understood.

It is worthwhile to point out here that the critical state is determined by the CCNBD specimen geometry itself, and is nothing to do with the properties of the materials under investigation and the external loading condition. Therefore for fracture toughness testing, the critical parameters of the specimen can be obtained beforehand. This solves the problem of difficult crack propagation monitoring during conventional fracture toughness testing.

§3.4 Fracture Toughness Evaluation

From relation between the SIF **K** and the dimensionless SIF $\mathbf{Y}^*(\alpha)$ for the CCNBD specimen, Equation (3.40), one can logically conclude that the external load **P** will reach its maximum value when the $\mathbf{Y}^*(\alpha)$ hits its minimum if the $\mathbf{K}_c$ of the material is taken as a constant. During practical fracture toughness testing, the maximum external load is the easiest to obtain. Therefore what is important for fracture toughness value determinations is the specimen critical state parameter, in other words, the $\mathbf{Y}^*_m$ value.

We can rewrite Equation (3.40) in terms of fracture toughness $\mathbf{K}_c$ as followed:

$$K_C = \frac{P_{max}}{B\cdot\sqrt{R}}\cdot Y_m^* \tag{3.55}$$

Therefore if the $\mathbf{Y}^*_m$ is known, we only have to measure the maximum external load for the fracture toughness calculation, obviously it is not necessary to know the critical crack length $\mathbf{a}_m$ at the same time. Here note should be taken that the fracture toughness evaluation by this method is not restricted to any particular fracture mode condition. In other words, it is suitable for the fracture toughness calculation for any single fracture mode ($\mathbf{K}_{IC}$, $\mathbf{K}_{IIC}$ and $\mathbf{K}_{IIIC}$) or mixed mode (fracture strength locus) conditions.

At present, it is important to set up a database of $\mathbf{Y}^*_m$ values for different CCNBD specimen geometries, i.e., different α_0, α_1 and α_B. As the $\mathbf{Y}^*_m$ value is material independent, so by the help of Equation (3.55) their values for different specimen geometries can be experimentally verified. In fact, if the $\mathbf{K}_{IC}$ value of a material and its maximum failure load for a particular geometry during the test are known, the corresponding $\mathbf{Y}^*_m$ value can be obtained simply by

reversing Equation (3.55). The $\mathbf{Y^*_m}$ values can also be evaluated by numerical methods. By use of finite element or boundary element numerical analysis, the SIF value for any CCNBD specimen geometry can be numerically obtained. Hence the critical $\mathbf{Y^*_m}$ and $\mathbf{a_m}$ values can be found if a full set of numerical analysis with the same geometry but different crack extension length has been carried out. As this numerical procedure is normally cumbersome and involves a lot of data processing, it is not practical to expect numerical validation of all the different specimen geometries. Therefore in practice, the simple theoretical calculation method will still have to be used but with some modifications based on numerical analysis of limited specimen geometries.

§3.5 Conclusions and Suggestions for further Researches

Based on the above discussions, the following conclusions about the theoretical analysis of the CSTBD and the CCNBD specimens can be drawn:

1) The CSTBD fracture problem can be solved by the stepwise superimposition method from two single elastic problems: solid Brazilian disc subjected to diametrical loadings and central cracked infinite body subjected to internal pressure. The results agree well with those of previous researches within their valid range, and can also give further solutions for the problem of a longer crack case up to $\alpha = 0.95$ with the error within 2%.

2) The CCNBD fracture problem can be solved by the compliance method based on the CSTBD results combined with two hypothesis models: the Munz's identical compliance changing rate model and Bluhm's slice superimposition model. Bluhm's model can better simulate the fracture problem of the CCNBD specimen and therefore is used in the following research.

3) The CCNBD specimen geometries can be expressed and distinguished by three basic dimensionless parameters, $\alpha_0(\mathbf{a_0/R})$, $\alpha_1(\mathbf{a_1/R})$ and $\alpha_B(\mathbf{a_B/R})$. In other words, $\mathbf{a_0}$, $\mathbf{a_1}$, **B** and **R** are the basic independent CCNBD geometry dimensions. On knowing them, other CCNBD geometrical dimensions can be calculated.

4) Theoretically CCNBD geometries can vary freely. However restrictions exist between them if a reasonably proportioned and machinable CCNBD specimen is to be obtained.

Apart from the above conclusions, some suggestions for further research are drawn:

1) The theoretical results for CSTBD and CCNBD specimens need validations both numerically and experimentally. The preciseness of the results and the valid applicable crack range have to be decided.

2) Due to its simple and effective features, the stepwise superimposition solution method for the **Mode I** fracture problem for the CSTBD specimen can also be adopted to solve mixed

mode CSTBD fracture problems. The cracked Brazilian discs (CSTBD or CCNBD) under mixed fracture conditions are believed to be the simplest specimens practically applicable for mixed mode fracture investigations for rock materials.

3) Owing to the good features of the CCNBD specimen geometries and loading alignment, it is suggested that it could be an ideal specimen to be used for rock anisotropic fracture research. Therefore the CCNBD fracture problems under anisotropic conditions should be introduced and theoretically investigated.

Chapter 4

Numerical Calibration of the Mode I CSTBD and CCNBD Fracture Problems

§4.1 Introduction

The theoretical analysis of the CSTBD and the CCNBD specimen in the last chapter needs validating before the results can be used. In this chapter, Boundary Element and Finite Element methods of analyses are used for the calibration of some CSTBD and CCNBD geometries. The theoretical evaluation has been modified for practical use and some conclusions have been reached.

§4.2 Brief Review of the General Methods Used for Numerical Calibration of Stress Intensity Factor (SIF) for a Cracked Body

§4.2.1 Immediate Displacement Method - IDM

From fracture mechanics, the displacement components around the immediate area of the crack tip within the range of LEFM for the plane strain condition (**Mode I**) are:

$$\begin{cases} V_x = \dfrac{K_I}{M_G}\cdot\sqrt{\dfrac{r}{2\pi}}\cdot\cos\dfrac{\beta}{2}\cdot\left[\,1-2\cdot\nu+\sin^2\dfrac{\beta}{2}\,\right]+\cdots\cdot \\ V_y = \dfrac{K_I}{M_G}\cdot\sqrt{\dfrac{r}{2\pi}}\cdot\sin\dfrac{\beta}{2}\cdot\left[\,2\cdot(\,1-\nu\,)-\cos\dfrac{\beta}{2}\,\right]+\cdots\cdot \end{cases} \tag{4.1}$$

where the terms omitted are the components of higher derivatives which can be neglected when the point considered is near the crack tip, i.e., **r** is small. Note that only the **Mode I** fracture problem is considered here.

$\mathbf{M_G}$ in the equation is the shear modulus, its relationship with Young's modulus **E** and the Poisson's ratio ν is:

$$M_G = \frac{E}{2\cdot(\,1-\nu^2\,)} \tag{4.2}$$

Consider the vertical displacement of the two opposite points **A** and **B** (or **C** and **D**, ..., as shown in Figure 4.1) on the opposite upper and lower crack surface with the same polar coordinate component **r**. Substitute the condition of $\beta = \pm 180°$ in the displacement equation we can then reach the following equation:

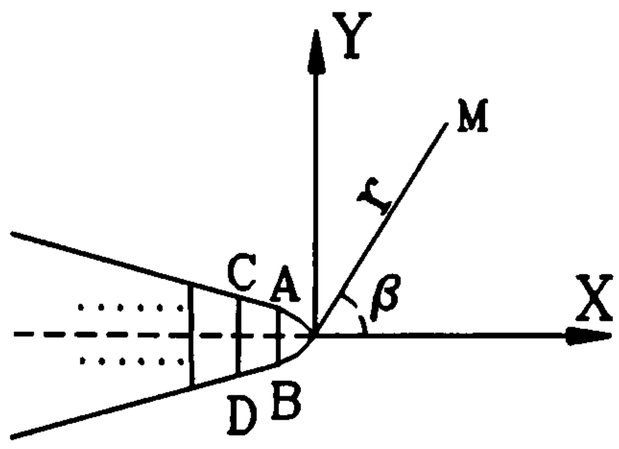

Figure 4.1 Crack Tip

$$K_I = \frac{E}{4\cdot(1-\nu^2)}\cdot\sqrt{\frac{\pi}{2r}}\cdot(V_y^A - V_y^B) \tag{4.3}$$

where the term V_y^A-V_y^B is actually the crack opening displacement, **COD(r)**, hence we can rewrite the above equation as:

$$K_I = \frac{E}{4\cdot(1-\nu^2)}\cdot\sqrt{\frac{\pi}{2\cdot r}}\cdot COD\ (r) \tag{4.4}$$

Therefore if the **COD(r)** can be evaluated by a numerical method, the stress intensity factor SIF $\mathbf{K_{IC}}$ can then be determined.

§4.2.2 Direct Stress Method - DSM

Theoretically the stress distribution around the vicinity of a **Mode I** crack tip can be expressed as:

$$\begin{cases} \sigma_{xx} = \dfrac{K_I}{\sqrt{2\pi r}}\cdot\cos\dfrac{\beta}{2}\cdot\left(1 - \sin\dfrac{\beta}{2}\cdot\sin\dfrac{3\cdot\beta}{2}\right) + \cdots \\ \sigma_{yy} = \dfrac{K_I}{\sqrt{2\pi r}}\cdot\cos\dfrac{\beta}{2}\cdot\left(1 + \sin\dfrac{\beta}{2}\cdot\sin\dfrac{3\cdot\beta}{2}\right) + \cdots \\ \sigma_{xy} = \dfrac{K_I}{\sqrt{2\pi r}}\cdot\sin\dfrac{\beta}{2}\cdot\cos\dfrac{\beta}{2}\cdot\cos\dfrac{3\cdot\beta}{2} + \cdots \end{cases} \tag{4.5}$$

Note should be taken that these equations are valid only within the range of LEFM, and when the considered points are near the crack tip.

Reversing the above equations we have:

$$K_I = \frac{\sigma_{xx}\sqrt{2\cdot\pi\cdot r}}{f_{xx}(\beta)} = \frac{\sigma_{yy}\sqrt{2\cdot\pi\cdot r}}{f_{yy}(\beta)} = \frac{\sigma_{xy}\sqrt{2\cdot\pi\cdot r}}{f_{xy}(\beta)} \tag{4.6}$$

Henceforth the stress intensity factor $\mathbf{K_I}$ can be evaluated as long as the stress component values near the crack tip are obtained by a numerical method.

However owing to inability to express the singularity stresses at the crack tips by numerical BEM or FEM methods, the exact stress intensity factor value $\mathbf{K_I^e}$ can not be obtained directly by this method. Therefore the extrapolation technique should be introduced. The $\mathbf{K_I^e}$ value can be derived from the calculated results, as shown in Figure 4.2, where the solid line is the $\mathbf{K_I}$ calculation results and the dotted line is the extrapolation line.

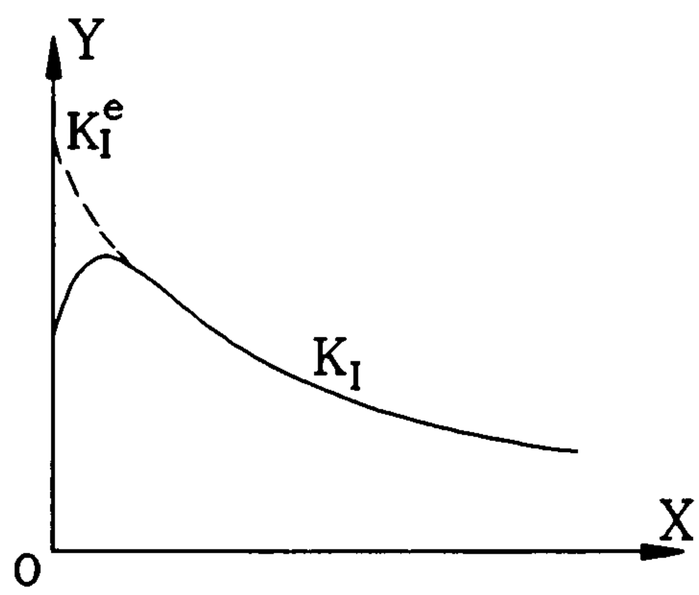

Figure 4.2 DSM Extrapolation

§4.2.3 Compliance Method - CM

As derived in the Chapter 3, the stress intensity factor can be calculated from the change in the specimen compliance as:

$$K = P\left[\frac{\frac{dC}{da}\cdot E'}{2\cdot b}\right]^{\frac{1}{2}} \tag{4.7}$$

Where **b** is the thickness of the crack front, and **dC/da** is the compliance change rate with respect to the crack extension. When dealing with the problem of the CCNBD specimen for the **Mode I** fracture conditions, the above equation can be rewritten as:

$$K_I = \frac{P}{B\cdot\sqrt{R}}\left[\frac{\frac{dCBE'}{d\alpha}\cdot\alpha_B^2}{4f_1(\alpha)}\right]^{\frac{1}{2}} \tag{4.8}$$

Therefore if the dimensionless compliance value **CBE** has been evaluated by a numerical method, the K_I value can be determined.

§4.2.4 Energy Release Rate Method - VCEM

Within the range of LEFM, the strain energy stored in a cracked body having a crack with length **a**, when it is subjected to external forces, can be calculated as:

$$U_a = \sum_{i=1}^{n} \frac{P_i \cdot u_i}{2} \tag{4.9}$$

where the P_i and u_i are the resulting load and displacement at the **i**-th node in the body, **n** is the total number of discrete nodes.

When a virtual crack extension **Δa** of the crack tip is assumed, the new strain energy $U_{a+\Delta a}$ can be recalculated again according to the new load and displacement values at the nodes. The change in the strain energy due to the virtual crack extension can then be obtained:

$$\Delta U = U_a - U_{a+\Delta a} \tag{4.10}$$

which is supposed to be a constant whenever the specimen geometry is fixed, no matter whether it is a constant loading or a fixed displacement boundary condition [Knott, 1973]. Therefore the energy release rate according to Griffith's theory will be:

$$G = \frac{\Delta U}{\Delta a} \tag{4.11}$$

After **G** is obtained, **K** can then be calculated from the relationship given as Equation (2.11).

However care should be taken here about the fracture modes of the evaluation. If it is a mixed mode problem (**Mode I + Mode II** for instance) then the contribution of both K_I and K_{II} in the **G** value should be considered, i.e.,

$$G = \frac{(K_I^2 + K_{II}^2)}{E'} \tag{4.12}$$

As this method uses the virtual crack extension assumption, it is sometimes referred to as the Virtual Crack Extension Method (VCEM).

§4.2.5 Other Methods

The four methods mentioned above are the most popular and simplest methods for estimating the SIF values of a fracture problem by numerical methods. However there are some more methods, such as Modified Crack Closure Work Method, Closed Form Displacement Method and Line Contour J-integral Method. Owing to their complexity, they are seldom used in practical calculations.

§4.3 Applications of Boundary Element and Finite Element Methods for the Evaluation of the SIF Values for the CSTBD and the CCNBD Specimens

§4.3.1 Brief Introduction to the BEASY Software Package

The BEASY (Boundary Element Analysis SYstem) is a powerful software package developed by the Computational Mechanics Corporation Ltd., USA. It is broadly used for solution of 2-D(imensional) and 3-D numerical analysis of solid and fluid mechanics problems. As far as solid mechanics is concerned, linear elastic continuum mechanics is still followed even though some plastic criteria calculations are available in the package. Therefore LEFM condition will be automatically assumed when using the package to evaluate the solid fracture mechanics problems.

Boundary element meshing can be conducted manually or automatically by the package. This makes it possible to make denser element meshing around interesting parts of the solid investigated.

The discontinuous element meshing facility in the package makes it convenient to simulate a crack in a cracked body. This is one of the biggest advantages of using BEASY in solving fracture mechanics problems as this saves a lot of time to find a suitable element meshing to simulate the crack front.

The boundary conditions accepted could be any combination of stress, displacement or their mixture in any one or mixture of the three directions **X**, **Y** and **Z**. The boundary connection could be free, fully bounded, spring bounded or some other models. This simplifies the procedure to introduce some models to simulate the problems of crack closure or a crack cohesive zone when these phenomena are to be taken into account (the Dougdale model for example).

The BEASY -IMS interface provides a very useful tool for data checking and auto-

correcting. The Post Process is powerful for plotting the calculated results (stress, strain or displacement), value graphs or contour pictures (14 selections).

§4.3.2 Applications of Boundary Element and Finite Element Methods for the Evaluation of the SIF Values for the CSTBD and the CCNBD Specimens

Owing to the symmetry of the CCNBD specimen and the loading geometry, only 1/8 of the investigated disc has to be considered, which is shown in Figure 4.3 where **ON(X)**, **OC(Y)** and **OH(Z)** are the three central axes of the specimen, the arc **AEI** is the machined notch front, **BE** is the propagating crack front and the shaded area is the uncracked body.

Area **OBED** is the cracked surface and quadrilateral element meshing is used and the following rules will be followed: in the **Z** direction the element divisions are equal, in the **Y** direction, more elements are needed near the crack front **BE** for more precise expression so that unequal meshing (denser near the crack front) will be used. The same arguments will hold for the notch area **DEIH**, and the uncracked area **BCGE**. Area **EFI** is a triangle with a side arc line, triangular element meshing will be used.

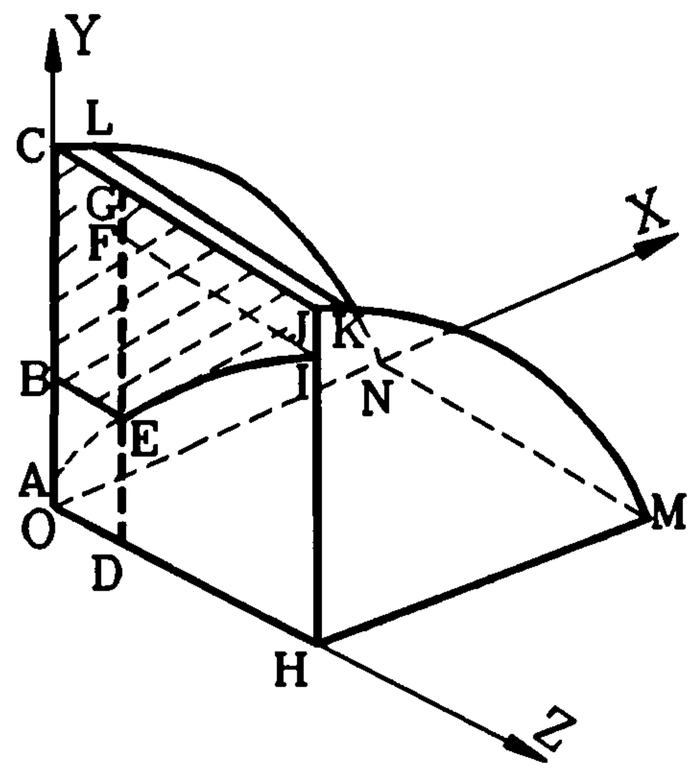

Figure 4.3 Calibrated Disc Part

Area **FGJI** can be equally meshed both along **Y** and **Z** directions as there are no special requirements for this part of the body.

One very important point should be noted is that discontinuity element meshing should be used to simulate the crack front **BE** and the notch front **EI**. Care should be taken as well to ensure that there are less than 3 common mesh points between the neighbouring elements across the crack front line.

Therefore the meshing commands for area **ACJH** will be:

```
BR 1 1 2 8 7 408 3
BR 2 7 8 5 4 408 4
BR 3 2 3 9 8 -406 2
BR 4 14 9 6 5 4 4
BD 5 8 14 5 3 2
```

which is shown in the Figure 4.4.

The surface **HIJKM** and **MKLN** are equally meshed with respect to their arc length and angle, as there are no special requirements. The external loading surface **JCLK** can be equally divided into elements as well. However care should be taken again as there is another discontinuity line **KL** (elastic condition discontinuity instead of specimen geometry discontinuity) between **JCLK** and **MKLN**. The reason we introduce this external loading surface is that BEASY does not take external loading singularities, i.e., point load. So that a load band with a central radian angle **4°** as the external loading area is introduced, and the external loads are assumed to be uniformly distributed over this band. This assumption (substitution) will generate some error, as will be shown in a later section. It will also enlarge the differences between the numerical results and the theoretical results where a point load is assumed. Therefore the error caused have to be corrected by use of special constants.

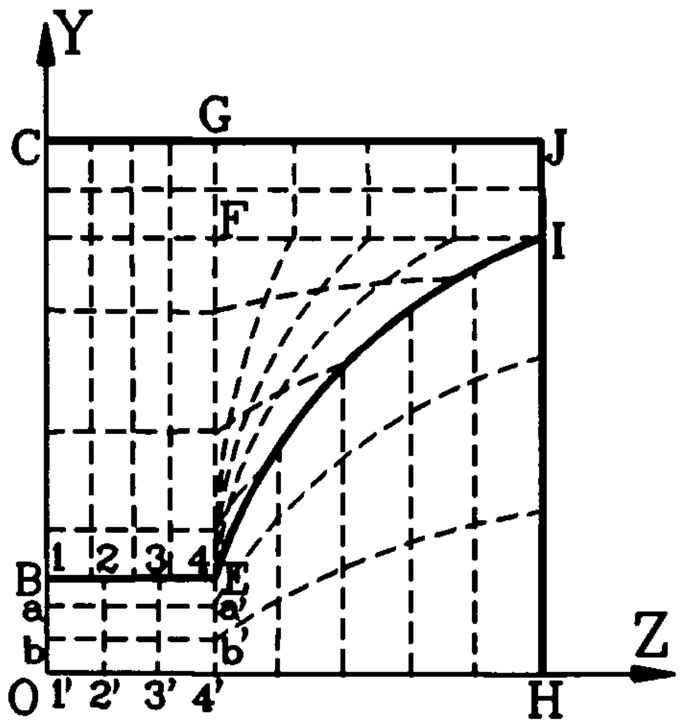

Figure 4.4 Crack Plane Meshing

Henceforth the commands for meshing the loading band and for the load set input data will be:

```
BR 7 13 6 3 12 1 5
PP 7 -1 -100 -100 -100 -100
LF 1
```

The area **OHMN** and **ONCO** are the symmetrical planes and they are made to be fully bounded by the following two commands:

```
ZX 1
ZZ 1
```

As the investigated surface **OCJH** is not taken by the BEASY as a symmetrical plane, in other words, the uncracked area **BCKIE** is not fully bounded. Therefore some additional boundary conditions should be introduced to enforce practical symmetry. The simplest way is setting the displacement of the area **BCKIE** in the **X** direction to zero as an additional boundary condition, i.e.,

```
PD 3 2 0 0 0 0
PD 4 2 0 0 0 0
```

```
PD 5 2 0 0 0 0
LF 1
```

This will be included in load set 1 as well.

For the CSTBD specimen geometry, it can be treated as a special case when the crack front line **BE** of the CCNBD specimen geometry coincides with the line **FI** (Figure 4.3). Therefore the input file will be much simpler.

A simple example of the datafile for input into the BEASY software package is given in appendix A.

In addition, the finite element method is also used to calibrate the CSTBD and CCNBD specimens. The software used is a self-compiled FEM programme, FEMFR, and the PAFEC software package. The commercial package ABAQUS was also used a few times for comparison. The results obtained are the same as those calculated by BEASY package but much more time was spent on the FEM analysis. Therefore for reasons of time, the BEASY software package was used to do most of the calibrations.

Figure 4.5 is an example of the meshing of a CCNBD specimen for the FEM analysis. The basic element types used are mainly isoparametric linear and quadratic triangular and brick elements. For the elements consisting of the crack front (Figure 4.5.b), the isoparametric quadratic tetrahedral elements are used.

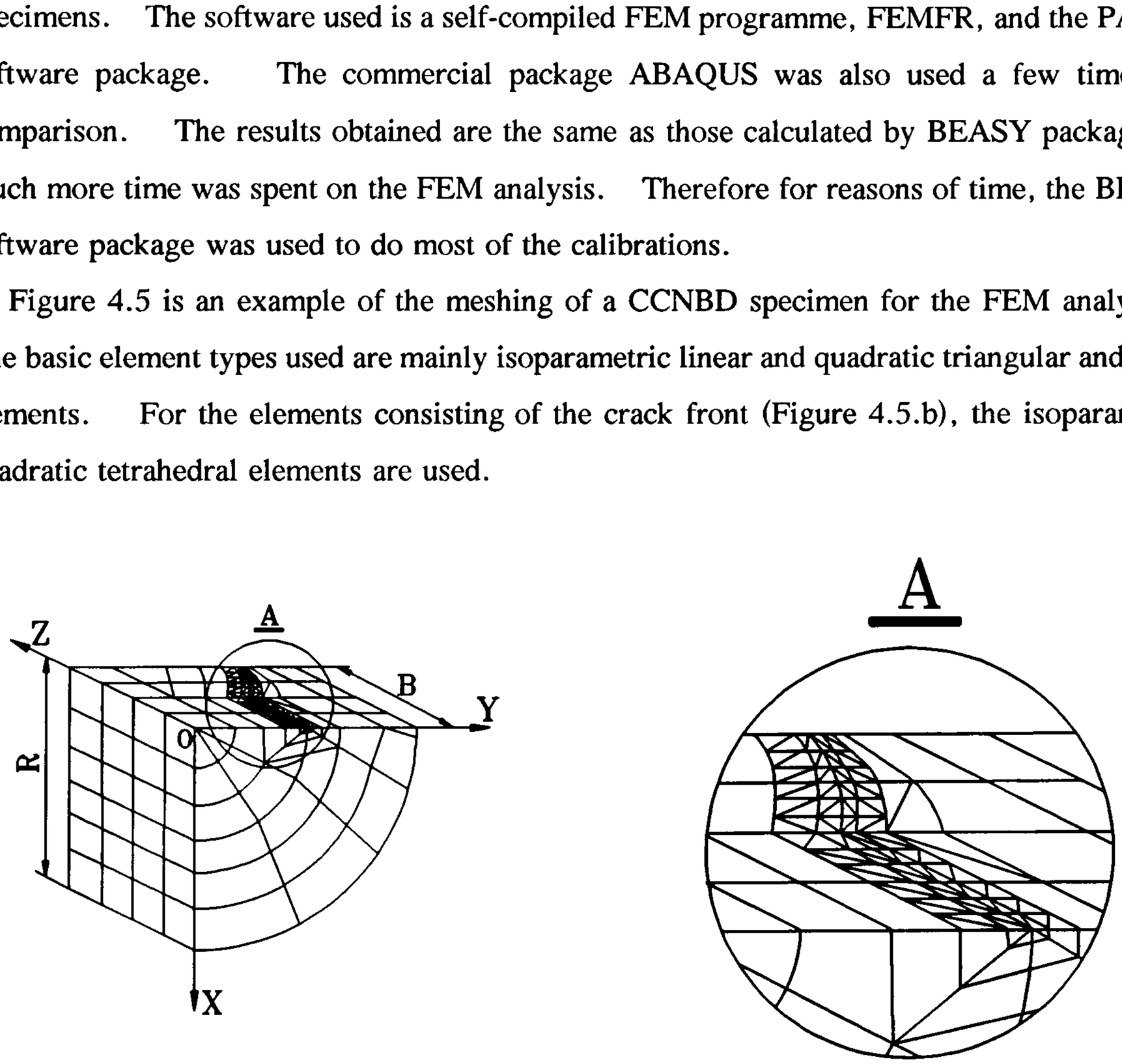

Figure 4.5 Meshing of a CCNBD Specimen for FEM analysis

§4.3.3 SIF Calculation Method for the CSTBD and the CCNBD Specimens

The crack opening displacement (COD) at any point on the crack surface can be calculated

directly by BEASY. Hence the **COD** along the lines (Figure 4.4) 1-1', 2-2', ... , a-a', b-b', ... , can be obtained. Two typical **COD**s along these lines are drawn below:

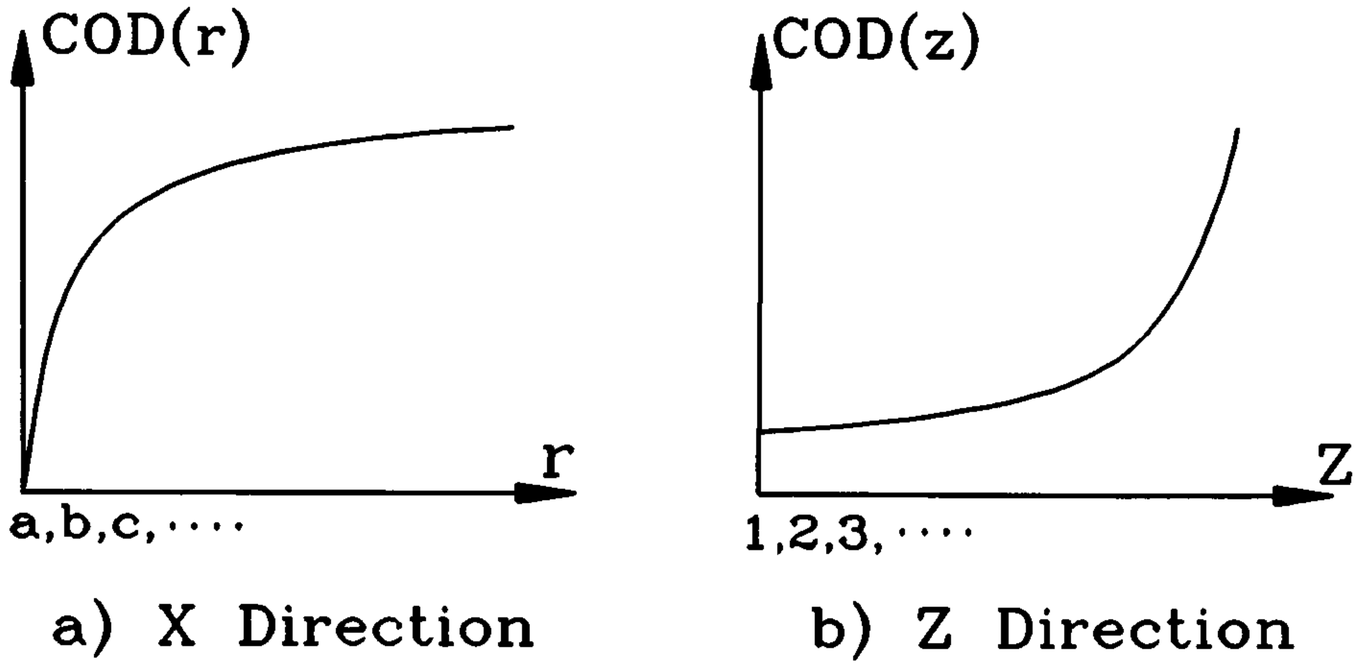

Figure 4.6 COD(r) and COD(z) of the Cracked Part of the CCNBD Specimen

where **COD(r)** is the crack opening displacement along **Y** direction and **COD(z)** is the crack opening displacement along the **Z** direction. As can be seen from the figures, the nearer the points to the free disc surface **HJ**, the greater the variation of **COD**. This is due to the limited thickness of the specimen and the plane condition is hard to keep when near the free surface. Therefore the **COD** results used for the SIF evaluations are the ones within the middle of the specimen where presumably the **COD** variation is relatively small enough. As the evaluation points for the SIF calculation should be near to the crack front, we will use the **COD** values along the a-a' line along which the node points are the nearest ones to the crack front **BE**. Then the results are averaged for the node points from a to a'.

Therefore from the above calculation equations and by using the condition of symmetry, the SIF values for the CCNBD or the CSTBD specimens can be expressed as:

$$K_I = \frac{E}{4\cdot(1-\nu^2)}\cdot\sqrt{\frac{\pi}{2\cdot r_a}}\cdot COD(r_a) \tag{4.13}$$

and the dimensionless SIF value $\mathbf{f(\alpha)}$ ($\mathbf{Y(\alpha)}$) and $\mathbf{Y^*(\alpha)}$ ($\mathbf{Y^*(\alpha)}$ for the CCNBD specimen and $\mathbf{Y(\alpha)}$ for the CSTBD specimen) can then be calculated by Equations (3.29) and (3.30).

Apart from the SIF numerical calibration for the CSTBD and the CCNBD specimens mentioned above, in the calibration which follows in this chapter, some sections will be concentrating on finding the most reasonable CCNBD geometries for practical use in order to obtain the valid (consistent) $\mathbf{K_{IC}}$ test results (or plane strain $\mathbf{K_{IC}}$ values). The influence of element meshing, loading contact angle, and Poisson's ratio can be found in Chen (1989).

Based on our calibration experience, the numerical analysis generates much closer SIF

results to those theoretical values calculated by hypothesis II theory discussed in the last chapter for the CCNBD specimen geometry. Therefore the greater suitability of this assumption for the simulation of the CCNBD fracture problem over hypothesis I is suggested. As a result, during the following discussion, the theoretical SIF values will be particularly referred to as those based on hypothesis II theory only.

§4.4 Numerical Calibration Results for the CSTBD Specimen

Table 4.1 is the list of calibration SIF results $\mathbf{Y}(\alpha)$ for the CSTBD specimens, calculated by the Immediate Displacement Method. The Young's modulus and the Poisson's ratio for the calibration are set to be 10 GPa and 0.3 respectively. The number of elements for the BEM method is between 140-170, which meets the minimum element number requirement set by Chen (1989) in order to keep the precision required. The corresponding theoretical evaluation results are also listed. Their differences are signified by the Ratio values in the table, which is the quotient of the theoretical results over the calibrated ones.

Table 4.2 lists the compliance values for the calibrated CSTBD specimens. The corresponding dimensionless SIF $\mathbf{Y}(\alpha)$ values are calculated by the Compliance Method within the same group, where α for each $\mathbf{Y}(\alpha)$ value will be the middle point between two adjacent crack length values from which the calibrated compliance values come.

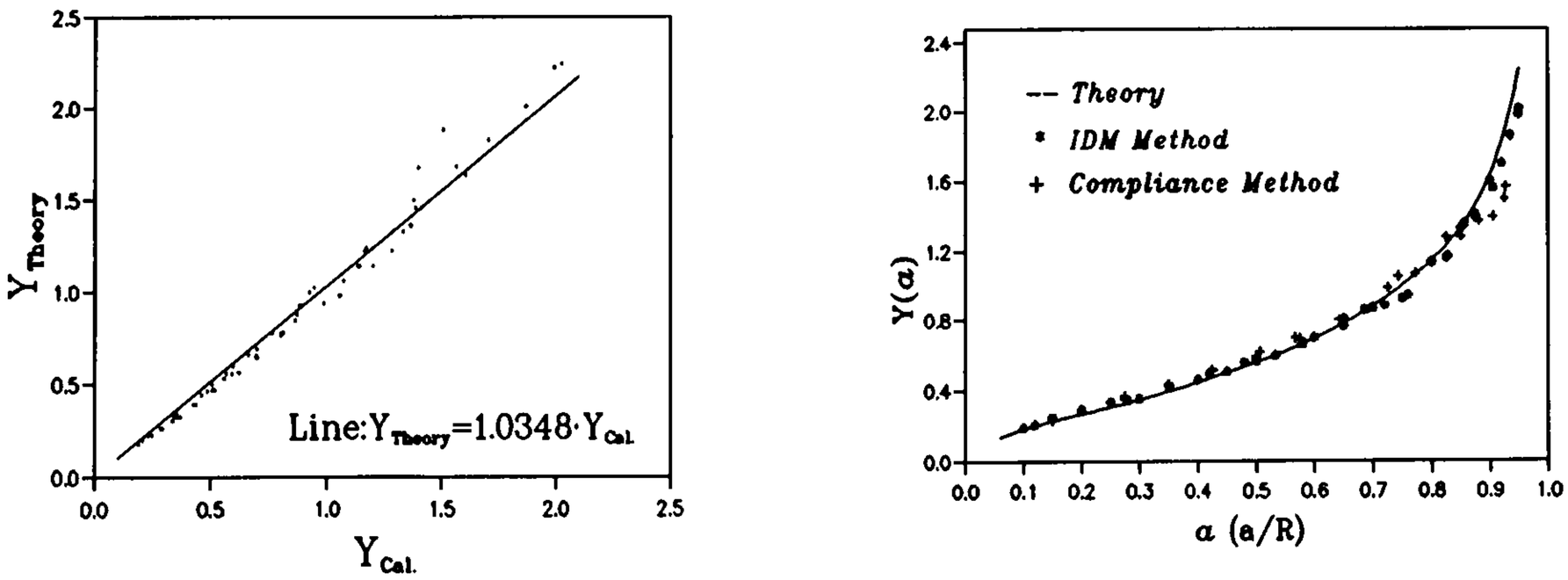

Figure 4.7 Comparison between Calibrated and Theoretical Results

Table 4.1 **Y(α)** Calibration Results for the CSTBD Specimens by IDM Method

ID	D (mm)	α	α_B	r_a (mm)	COD ($\times 10^{-3}$)	Y Cali.	Y Theory	Ratio
CS1		0.10		0.327	1.3535	0.1913	0.1823	1.0493
CS2		0.20		0.412	2.3309	0.2927	0.2670	1.0964
CS3		0.35		0.422	3.4152	0.4236	0.3950	1.0724
CS4		0.50		0.426	4.5983	0.5678	0.5579	1.0177
CS5	75.0	0.65		0.428	6.5647	0.8082	0.7785	1.0381
CS6		0.80	0.80	0.457	9.5419	1.1375	1.1448	0.9936
CS7		0.85		0.456	11.173	1.3333	1.3320	1.0010
CS8		0.90		0.454	13.420	1.6052	1.6350	0.9817
CS9		0.95		0.453	16.911	2.0249	2.2434	0.9026
CNF1	53.0	0.9057		0.496	11.495	1.5640	1.6836	0.9290
CNF2	56.0	0.8571		0.496	10.313	1.3650	1.3653	0.9998
CNF3	60.0	0.8000		0.496	9.4020	1.2023	1.1448	1.0503
CNF4	70.0	0.6857	0.70	0.496	7.2945	0.8636	0.8497	1.0164
CNF5	80.0	0.6000		0.496	6.3316	0.7012	0.6930	1.0118
CNF6	90.0	0.5333		0.496	5.7375	0.5991	0.5990	1.0001
CNF5	100.0	0.4800		0.496	5.6407	0.5587	0.5343	1.0457
CND9	78.0	0.9487	0.80	0.529	18.333	1.9909	2.2208	0.8965
CNC5	75.0	0.6500	0.80	0.554	7.0970	0.7680	0.7785	0.9866
CNG5		0.80	1.04	0.489	9.9391	1.1449	1.1448	1.0001
CNJ6		0.70	0.90	0.461	7.3611	0.8734	0.8807	0.9917
CNK6		0.75	1.00	0.459	7.7967	0.9271	1.0014	0.9258
CNL1		0.15		0.304	1.6910	0.2471	0.2279	1.0842
CNL2		0.25		0.350	2.4690	0.3362	0.3059	1.0990
CNL3		0.30		0.362	2.6483	0.3546	0.3482	1.0185
CNL4		0.40	0.80	0.424	3.7423	0.4629	0.4460	1.0380
CNL5	75.0	0.45		0.425	4.1085	0.5077	0.5002	1.0150
CNL6		0.76		0.407	7.5105	0.9483	1.0280	0.9225
CNL7		0.92		0.416	13.652	1.7051	1.8248	0.9344
CNM1		0.12		0.321	1.4576	0.2071	0.2018	1.0262
CNM2		0.28		0.392	2.6609	0.3424	0.3307	1.0353
CNM3		0.42		0.397	3.7987	0.4857	0.4673	1.0394
CNM4		0.58	0.90	0.413	5.3093	0.6655	0.6628	1.0041
CNM5		0.72		0.411	7.0616	0.8873	0.9267	0.9575
CNM6		0.825		0.417	9.3476	1.1661	1.2302	0.9479
CNM7		0.875		0.341	10.244	1.4131	1.4611	0.9671
CNM8		0.935		0.344	13.604	1.8685	2.0097	0.9297

Table 4.2 **Y(α)** Calibration Results for the CSTBD Specimens by Compliance Method

ID	α (Cali.)	CBE'	α (Midpoint)	Y (Cali.)	Y (Theory)	Ratio
CS1	0.10	3.0886				
CS2	0.20	3.0992	0.150	0.2314	0.2279	1.0154
CS3	0.35	5.1424	0.275	0.3698	0.3265	1.1325
CS4	0.50	3.2215	0.425	0.5205	0.4727	1.1011
CS5	0.65	3.3670	0.575	0.6964	0.6556	1.0623
CS6	0.80	3.6599	0.725	0.9881	0.9387	1.0526
CS7	0.85	3.8249	0.825	1.2841	1.2302	1.0438
CS8	0.90	4.0178	0.875	1.3892	1.4611	0.9508
CS9	0.95	4.2448	0.925	1.5065	1.8817	0.8006
CNF1	0.9057	4.0200				
CNF2	0.8571	3.8351	0.8814	0.6211	0.5659	1.0975
CNF3	0.8000	3.6776	0.8286	0.7013	0.6438	1.0893
CNF4	0.6857	3.4223	0.7429	0.8027	0.7654	1.0488
CNF5	0.6000	3.3118	0.6429	1.0566	0.7831	1.0747
CNF6	0.5333	3.2462	0.5667	1.1746	1.2437	0.9444
CNE5	0.4800	3.2051	0.5067	1.3793	1.5004	0.9193
CNL1	0.15	3.0534				
CNL2	0.25	3.0972				
CNL3	0.30	3.1097	0.275	0.3542	0.3265	1.0848
CNL4	0.40	3.1462	0.350	0.4272	0.3950	1.0816
CNL5	0.45	3.1721	0.425	0.5086	0.4727	1.0759
CNL6	0.76	3.5294				
CNL7	0.92	4.0263				
CNM1	0.12	3.0821				
CNM2	0.28	3.1082	0.200	0.2856	0.2670	1.0695
CNM3	0.42	3.1621	0.350	0.4386	0.3950	1.1104
CNM4	0.58	3.2745	0.500	0.5931	0.5579	1.0631
CNM5	0.72	3.4604	0.650	0.8147	0.7785	1.0465
CNM6	0.825	3.7029	0.7725	1.0745	1.0625	1.0113
CNM7	0.875	3.8685	0.850	1.2869	1.3320	0.9661
CNM8	0.935	4.1038	0.905	1.4004	1.6774	0.8349

Figure 4.7 illustrates the comparison between the calibrated and the theoretical results from Tables 4.1 and 4.2. The regression suggests that their difference is less than 5%. The calibrated and the theoretical values of $\mathbf{Y}(\alpha)$ tend to deviate as $\alpha > 0.95$, which obviously is due to the loading boundary influences. Therefore it is not suggested that the above theoretical evaluation results be used when the dimensionless crack length exceeds this limit.

§4.5 Numerical Calibration Results for the CCNBD Specimens

Ten basic groups of CCNBD specimen geometries were designed for calibration to simulate the median, long and short crack cases respectively. Table 4.3 and 4.4 are the lists of their SIF $\mathbf{Y}^*(\alpha)$ numerical calibration results by Direct Displacement Method and Compliance Method. The corresponding theoretical SIF $\mathbf{Y}^*(\alpha)$ values based on the Bluhm's model are also listed in the tables for comparison. Again during the evaluation the Young's modulus is taken to be 10 GPa and the Poisson's ratio 0.30.

In order to reach more comprehensive conclusions, another 17 groups of CCNBD specimen geometries were introduced for the numerical calibration, which were based on the calibration geometries used by Chen (1989). Table 4.5 shows the comparison of the SIF $\mathbf{Y}^*(\alpha)$ values between the calibration and the theoretical results by Bluhm's model. The Young's modulus and the Poisson's ratio used during the numerical calculation are the same as those used above.

In order to investigate the thickness effect on the SIF $\mathbf{Y}^*(\alpha)$ values of the CCNBD specimens, an extra group of CCNBD specimen geometries, TH, with the same crack front width **b**, the same crack length α and α_1 but with different specimen thicknesses, α_B, varying from $\alpha_B = 0.2667$ to $\alpha_B = 1.1733$ have been calibrated and their geometrical parameters and calibrated results are listed in Table 4.6.

From Table 4.3 to 4.6, the Ratio values between the calibrated (practical) and theoretical results point out that certain differences exist between the numerical calibrated and the theoretical SIF $\mathbf{Y}^*(\alpha)$ values of the CCNBD specimens with a range of 2% to 15%. From the basic assumptions it is suggested that the main contributory factors for these differences are as follows:

1) The effect of specimen thickness, which changes the stress-strain state within the specimen. The theory is based on the assumption of plane strain condition. However this condition can hardly be satisfied in practical CCNBD specimens. This disagreement will cause deviations of the theoretical SIF results from the practical SIF values (numerical calibrated).

2) The effect of loading contact angles. Obviously some error has to be generated owing to the differences between the point load assumption in the theory and the strip (band) loading

assumption in the numerical calibration. However in practical application of the CCNBD specimens, the strip loading assumption is believed to better represent the practical loading situation, and the point loading assumption is considered to be far too idealized.

3) The influences of different specimen geometries.

Therefore correction of the theoretical results is needed so that they can converge to the practical SIF values. After the determination of this correction relation, the practical SIF $\mathbf{Y^*}(\alpha)$ values for any CCNBD specimen geometry can be calculated directly from theory and the troublesome numerical calibration for that geometry does not have to be conducted. This makes possible the application of the CCNBD specimen geometry for practical fracture toughness measurement, as in a practical situation, the geometrical parameters of the CCNBD specimens are always different but their SIF values needs to be known instantly. It is impossible to use the above numerical methods to calibrate all the possible CCNBD specimen geometries and therefore it is only the theoretical method which can simply and quickly give the SIF value of any CCNBD specimen.

If $\mathbf{k_B}$ is used to designify the Ratio values listed in the above tables, based on the points discussed above, attempts have been made to relate $\mathbf{k_B}$ with the specimen thickness α_B, the loading contact angle, the crack front width **b**, some other specimen geometries and all their possible combinations, but only the $\mathbf{k_B} \sim \alpha_B$ shows a simple and clear relationship, as illustrated in Figure 4.8. The regression yields:

$$k_B = \frac{1.3087}{0.7982 + 0.3806 \cdot \alpha_B} \tag{4.14}$$

with regression coefficient of 0.9111. However even though $\mathbf{k_B}$ values are obtained in this way, they should be considered to be the superimposed coefficient from the three contributory factors mentioned above.

Henceforth the corrected theoretical SIF values $\mathbf{Y^*}(\alpha)$ (which will be referred to as the theoretical SIF values for the CCNBD specimens in later sections) can be calculated from the theoretical SIF values based on the hypothesis II (Bluhm's model) discussed in the last chapter as follows:

$$Y^*_{Theory}(\alpha) = Y^*_{Corrected}(\alpha) = Y^*_{Re\text{-}Cali.}(\alpha) = k_B \cdot Y^*_{Hypothesis\ II}(\alpha) \tag{4.15}$$

Table 4.3 $\mathbf{Y^*}(\alpha)$ Calibration Results for the CCNBD Specimens by IDM Method

Cases	ID	D (mm)	α_B	α_0	α_1	α	r_a (mm)	COD(r_a) ($\times 10^{-3}$)	Y^* (Cali.)	Y^* (Theo.)	Ratio	Y^* (Re-Cal.)
	CNA1					0.30	0.362	7.2058	1.2631	1.0524	1.2001	1.2490
	CNA2					0.35	0.422	6.3752	1.0351	0.8812	1.1747	1.0458
	CNA3					0.40	0.424	6.0154	0.9743	0.7851	1.2410	0.9318
	CNA4			0.2667	0.6505	0.50	0.472	5.4536	0.8372	0.7116	1.1765	0.8446
	CNA5					0.60	0.511	5.8196	0.8586	0.7421	1.1570	0.8808
	CS5		0.80			0.65			0.9571	0.8056	1.1881	0.9561
	CNC1					0.40	0.483	8.1892	1.2422	0.9433	1.3169	1.1195
	CNC2					0.45	0.543	6.9734	0.9976	0.8268	1.2066	0.9813
	CNC3			0.3795	0.6500	0.55	0.583	6.3492	0.8766	0.7429	1.1800	0.8817
	CNC4					0.60	0.567	6.1890	0.8665	0.7521	1.1521	0.8926
	CNC5					0.65	0.554	6.4220	0.9096	0.8054	1.1294	0.9559
	CNI1					0.30	0.318	5.7020	1.0659	0.9040	1.1791	1.1113
	CNI2					0.35	0.371	5.0042	0.8399	0.7610	1.1037	0.9355
	CNI3		0.70		0.6000	0.40	0.378	4.6452	0.7965	0.6839	1.1646	0.8407
Medium	CNI4	75.0				0.50	0.426	4.5408	0.7334	0.6385	1.1486	0.7849
	CNI5					0.55	0.427	4.6014	0.7423	0.6586	1.1271	0.8096
	CNI6					0.60	0.367	5.7258	0.9964	0.7157	1.3922	0.8798
	CNJ1					0.30	0.318	7.2304	1.3518	1.2179	1.1099	1.3972
	CNJ2					0.35	0.371	6.3178	1.0934	1.0148	1.0775	1.1642
	CNJ3		0.90	0.2667	0.7000	0.45	0.383	5.6226	0.9577	0.8327	1.1501	0.9553
	CNJ4					0.55	0.427	5.4846	0.8848	0.7883	1.1224	0.9044
	CNJ5					0.65	0.463	5.8848	0.9118	0.8323	1.0955	0.9548
	CNJ6					0.70	0.461	6.6610	1.0343	0.9031	1.1453	1.0361
	CNK1					0.30	0.318	8.1212	1.5182	1.3980	1.0860	1.5521
	CNK2					0.35	0.371	7.0778	1.2249	1.1633	1.0530	1.2915
	CNK3		1.00		0.75	0.45	0.383	6.1120	1.0412	0.9455	1.1012	1.0497
	CNK4					0.55	0.427	6.0352	0.9737	0.8793	1.1074	0.9762
	CNK5					0.65	0.463	6.3894	0.9899	0.8920	1.1098	0.9903
	CNK6					0.75	0.459	7.0552	1.0979	1.0148	1.0819	1.1266

Table 4.3 $\mathbf{Y^*}(\alpha)$ Calibration Results for the CCNBD Specimens by IDM Method (continued)

Cases	ID	D (mm)	α_B	α_0	α_1	α	r_a (mm)	COD(r_a) ($\times 10^{-3}$)	Y^* (Cali.)	Y^* (Theo.)	Ratio	Y^* (Re-Cal.)
Long	CNB1	75.0	0.80	0.2667	0.9487	0.30	0.318	11.130	2.0815	1.9461	1.0696	2.3097
	CNB2					0.35	0.371	9.8812	1.7110	1.6185	1.0572	1.9209
	CNB3					0.40	0.424	9.4086	1.5239	1.4286	1.0667	1.6955
	CNB4					0.50	0.472	8.9936	1.3807	1.2499	1.1047	1.4834
	CNB5					0.65	0.463	8.7626	1.3582	1.1976	1.1341	1.4214
	CNB6					0.75	0.428	8.9470	1.4423	1.2439	1.1595	1.4763
	CNB7					0.85	0.451	10.474	2.2050	1.4759	1.4940	1.7517
	CNB8					0.90	0.514	12.410	2.4473	1.7926	1.3652	2.1275
	CS9					0.95			2.3979	2.4180	0.9917	2.8698
	CND1	78.0		0.2241		0.25	0.364	11.971	2.0509	2.2123	0.9270	2.6256
	CND2					0.30	0.437	10.717	1.6759	1.7625	0.9509	2.0918
	CND3					0.40	0.393	8.9484	1.4756	1.3565	1.0878	1.6099
	CND4					0.50	0.443	8.7114	1.3531	1.2126	1.1159	1.4392
	CND5					0.60	0.484	8.9838	1.3349	1.1778	1.1334	1.3979
	CND6					0.70	0.518	9.3416	1.3418	1.1978	1.1202	1.4216
	CND7					0.80	0.547	10.641	1.4873	1.3124	1.1333	1.5576
	CND8					0.90	0.572	13.876	1.8967	1.7911	1.0590	2.1257
	CND9					0.9487	0.529	16.589	2.3578	2.4022	0.9815	2.8510

Table 4.3 $Y^*(\alpha)$ Calibration Results for the CCNBD Specimens by IDM Method (continued)

Cases	ID	D (mm)	α_B	α_0	α_1	α	r_a (mm)	COD(r_a) ($\times 10^{-3}$)	Y^* (Cali.)	Y^* (Theo.)	Ratio	Y^* (Re-Cal.)
Short	CNE1	100.0	0.70	0.0995	0.48	0.12	0.329	6.6664	0.8103	1.3934	0.5815	
	CNE2					0.20	0.549	5.7774	0.5440	0.7702	0.7063	0.9468
	CNE3					0.30	0.560	5.0714	0.4728	0.5521	0.8564	0.6787
	CNE4					0.40	0.643	5.2268	0.4547	0.4941	0.9203	0.6074
	CNE5					0.48	0.496	5.1042	0.5056	0.5338	0.9472	0.6562
	CNG1	75.0	1.04	0.6000	0.80	0.6133	0.476	10.705	1.6356	1.3279	1.2317	1.4554
	CNG2					0.65	0.504	9.0486	1.3436	1.2159	1.1050	1.3327
	CNG3					0.70	0.498	8.2108	1.2266	1.1297	1.0858	1.2382
	CNG4					0.75	0.493	7.9250	1.1899	1.1009	1.0808	1.2066
	CNG5					0.80	0.489	8.9938	1.3558	1.1593	1.1695	1.2706
	CNH1	50.0	0.80	0.3500	0.55	0.36	0.381	6.1026	1.0423	0.8026	1.2987	0.9526
	CNH2					0.40	0.424	4.9806	0.8064	0.7069	1.1408	0.8390
	CNH3					0.45	0.425	4.4428	0.7185	0.6390	1.1244	0.7584
	CNH4					0.50	0.426	4.204	0.6791	0.6149	1.1044	0.7298
	CNH5					0.55	0.336	5.0936	0.9264	0.6336	1.4621	0.7520

Table 4.4 $Y^*(\alpha)$ Calibration Results for the CCNBD Specimens by Compliance Method

ID	α	CBE'	α_{MID}	Y^* (Cali.)	Y^* (Theo.)	Ratio	Y^* (Re-Cal.)
CNA1	0.30	2.6876					
CNA2	0.35	2.6921	0.325	0.8630	0.9541	0.9045	1.1324
CNA3	0.40	2.7000	0.375	0.9499	0.8262	1.1497	0.9806
CNC1	0.40	2.6938					
CNC2	0.45	2.6988	0.425	0.9963	0.8764	1.1368	1.0401
CNC3	0.55	2.7212	0.500	0.8468	0.7669	1.1042	0.9102
CNC4	0.60	2.7460	0.575	0.8976	0.7439	1.2066	0.8829
CNB1	0.30	2.7040					
CNB2	0.35	2.7152	0.325	2.3393	1.7532	1.3343	2.0808
CNB3	0.40	2.7283	0.375	1.7745	1.5088	1.1761	1.7907
CNB4	0.50	2.7658	0.450	1.5407	1.3149	1.1717	1.5606
CNB5	0.65	2.8605	0.575	1.4041	1.2049	1.1653	1.4300
CNB6	0.75	2.9703	0.700	1.4353	1.2103	1.1859	1.4364
CNB7	0.85	2.1575	0.800	1.5821	1.3189	1.1996	1.5653
CNB8	0.90	3.2946	0.875	1.7071	1.6077	1.0618	1.9081
CS9	0.95	3.4756	0.925	1.8240	2.0547	0.8877	2.4386
CND1	0.25	2.6883					
CND2	0.30	2.6964	0.275	2.3434	1.9528	1.2000	2.3177
CND3	0.40	2.7191	0.35	1.6398	1.5091	1.0866	1.7911
CND4	0.50	2.7592	0.45	1.4895	1.2648	1.1777	1.5011
CND5	0.60	2.8191	0.55	1.4023	1.1866	1.1818	1.4083
CND6	0.70	2.9118	0.65	1.4207	1.1815	1.2025	1.4022
CND7	0.80	3.0511	0.75	1.4637	1.2348	1.1854	1.4655
CND8	0.90	3.2977	0.85	1.6701	1.4715	1.1350	1.7464
CND9	0.949	3.4659	0.924	1.7782	2.0411	0.8712	2.4225
CNE1	0.12	2.5646					
CNE2	0.20	2.5681	0.16	0.9025	0.9738	0.9268	1.1971
CNE3	0.30	2.5774	0.25	0.6982	0.6304	1.1076	0.7749
CNE4	0.40	2.5949	0.35	0.6269	0.5094	1.2307	0.6262
CNE5	0.48	2.6243	0.44	0.6610	0.5015	1.3181	0.6165

Table 4.4 $\mathbf{Y^*(\alpha)}$ Calibration Results for the CCNBD Specimens by Compliance Method

ID	α	CBE'	α_{MID}	Y^* (Cali.)	Y^* (Theo.)	Ratio	Y^* (Re-Cal.)
CNG1	0.613	2.8562					
CNG2	0.65	2.8632	0.632	1.4936	1.2663	1.1795	1.3879
CNG3	0.70	2.8838	0.675	1.3579	1.1753	1.1554	1.2882
CNG4	0.75	2.9171	0.725	1.2457	1.1176	1.1146	1.2249
CNG5	0.80	2.9773	0.775	1.2722	1.1256	1.1302	1.2337
CNH1	0.36	2.6054					
CNH2	0.40	2.6085	0.38	0.9931	0.7507	1.3229	0.8910
CNH3	0.45	2.6161	0.425	0.8340	0.6644	1.2553	0.7885
CNI1	0.30	2.5786					
CNI2	0.35	2.5851	0.325	1.1364	0.8218	1.3828	1.0102
CNI3	0.40	2.5952	0.375	0.9826	0.7168	1.3708	0.8811
CNI4	0.50	2.6244	0.45	0.8344	0.6468	1.2900	0.7951
CNI5	0.55	2.6496	0.525	0.7738	0.6449	1.1999	0.7928
CNI6	0.60	2.7193	0.575	1.1905	0.6815	1.7469	0.8377
CNJ1	0.30	2.6367					
CSJ2	0.35	2.6427	0.325	1.3514	1.1020	1.2263	1.2643
CNJ3	0.45	2.6623	0.40	1.0561	0.8989	1.1749	1.0313
CNJ4	0.55	2.6962	0.50	0.9490	0.7984	1.1886	0.9160
CNJ5	0.65	2.7566	0.60	0.9517	0.7987	1.1916	0.9163
CNJ6	0.70	2.8011	0.675	0.9410	0.8612	1.0927	0.9880
CNK1	0.30	2.6635					
CNK2	0.35	2.6694	0.325	1.4635	1.2637	1.1581	1.4030
CNK3	0.45	2.6893	0.40	1.1652	1.0259	1.1358	1.1390
CNK4	0.55	2.7221	0.50	1.0290	0.8999	1.1435	0.9991
CNK5	0.65	2.7793	0.60	1.0300	0.8769	1.1746	0.9735
CNK6	0.75	2.8854	0.70	1.0934	0.9311	1.1743	1.0337

Table 4.5 $\mathbf{Y^*}(\alpha)$ Calibration Results for the CCNBD Specimens [36]

ID	D (mm)	α_B	α_0	α_1	No.	α	Y^* (Cali.)	Y^* (Theo.)	Ratio	Y^* (Re-Cali.)
Da01	100.0	0.80	0.30	0.8454	1	0.4000	1.3675	1.2225	1.1186	1.4509
					2	0.5500	1.2862	1.0228	1.2575	1.2139
					3	0.6000	1.1519	1.0112	1.1391	1.2001
					4	0.6569	1.2063	1.0174	1.1857	1.2075
					5	0.7565	1.3166	1.0924	1.2052	1.2965
					6	0.8326	1.5210	1.2928	1.1765	1.5343
Da02	100.0	0.70	0.30	0.7970	1	0.4000	1.4390	1.0869	1.3240	1.3361
					2	0.5000	1.2014	0.9445	1.2720	1.1610
					3	0.6000	1.1123	0.9199	1.2092	1.1308
					4	0.6565	1.1738	0.9380	1.2514	1.1531
					5	0.7565	1.2756	1.0460	1.2195	1.2858
					6	0.7970	1.3697	1.1491	1.1920	1.4125
Da03	100.0	0.60	0.30	0.7564	1	0.4000	1.4418	0.9764	1.4767	1.2448
					2	0.5000	1.1441	0.8588	1.3322	1.0948
					3	0.5947	1.0741	0.8511	1.2620	1.0850
					4	0.6400	1.1314	0.8716	1.2981	1.1112
					5	0.7565	1.2975	1.0308	1.2587	1.3141
Da04	100.0	0.50	0.30	0.7102	1	0.4000	1.3470	0.8683	1.5513	1.1496
					2	0.4500	1.0734	0.8040	1.3351	1.0644
					3	0.5000	1.0564	0.7751	1.3629	1.0262
					4	0.5900	0.9447	0.7855	1.2027	1.0399
					5	0.6400	1.0840	0.8219	1.3189	1.0881
					6	0.7100	1.2000	0.9240	1.2987	1.0909
Da05	100.0	0.70	0.40	0.8240	1	0.5000	1.4439	1.1051	1.3066	1.3585
					2	0.5593	1.3124	1.0346	1.2685	1.2718
					3	0.6709	1.2601	1.0066	1.2518	1.2374
					4	0.7000	1.2636	1.0181	1.2411	1.2515
					5	0.8241	1.5472	1.2515	1.2363	1.5384

Table 4.5 $Y^*(\alpha)$ Calibration Results for the CCNBD Sopecimens (continued) [36]

ID	D (mm)	α_B	α_0	α_1	No.	α	Y^* (Cali.)	Y^* (Theo.)	Ratio	Y^* (Re-Cali.)
Da11	100.0	0.60	0.20	0.4878	1	0.3262	0.7785	0.5532	1.4073	0.7052
					2	0.3600	0.6979	0.5221	1.3367	0.6656
					3	0.4019	0.6753	0.5047	1.3380	0.6634
					4	0.4532	0.6774	0.5139	1.3182	0.6551
					5	0.4879	0.6866	0.5440	1.2621	0.6935
Da12	100.0	0.50	0.20	0.4664	1	0.3000	0.7333	0.5412	1.3550	0.7165
					2	0.3600	0.6746	0.4874	1.3841	0.6453
					3	0.4299	0.6647	0.4870	1.3649	0.6448
					4	0.4664	0.6781	0.5167	1.3124	0.6841
Da13	100.0	0.40	0.20	0.4382	1	0.2924	0.7036	0.4995	1.4086	0.6878
					2	0.3200	0.6244	0.4715	1.3243	0.6492
					3	0.3550	0.6145	0.4537	1.3544	0.6247
					4	0.4019	0.6378	0.4567	1.3965	0.6288
					5	0.4382	0.6513	0.4833	1.3476	0.6655
Da14	100.0	0.60	0.16	0.4822	1	0.3069	0.6597	0.5495	1.2006	0.7005
					2	0.3893	0.6569	0.4954	1.3260	0.6316
					3	0.4100	0.6590	0.4942	1.3335	0.6300
					4	0.4445	0.6788	0.5045	1.3455	0.6432
					5	0.4821	0.6873	0.5366	1.2808	0.6841
Db01	75.0	0.80	0.2667	0.6504	1	0.4000	0.9214	0.7852	1.1735	0.9319
					2	0.4800	0.8754	0.7172	1.2206	0.8512
					3	0.5200	0.8450	0.7098	1.1905	0.8424
					4	0.5600	0.8351	0.7175	1.1639	0.8516
					5	0.6218	0.8761	0.7637	1.1472	0.9064
					6	0.6505	0.9504	0.8062	1.1789	0.9568

Table 4.5 $Y^*(\alpha)$ Calibration Results for the CCNBD Specimens (continued) [36]

ID	D (mm)	α_B	α_0	α_1	No.	α	Y^* (Cali.)	Y^* (Theo.)	Ratio	Y^* (Re-Cali.)
Db02	75.0	0.6667	0.2667	0.6219	1	0.4000	0.9157	0.7121	1.2859	0.8859
					2	0.4800	0.8535	0.6622	1.2889	0.8238
					3	0.5200	0.8068	0.6636	1.2158	0.8256
					4	0.5600	0.8528	0.6822	1.2501	0.8487
					5	0.6218	0.9030	0.7539	1.1978	0.9379
Db03	75.0	0.5842	0.2667	0.5843	1	0.4000	0.8393	0.6431	1.3051	0.8247
					2	0.4267	0.8026	0.6234	1.2875	0.7994
					3	0.4533	0.8019	0.6129	1.3084	0.7860
					4	0.4867	0.8358	0.6114	1.3670	0.7840
					5	0.5200	0.8521	0.6227	1.3684	0.7985
					6	0.5842	0.8860	0.6889	1.2861	0.8834
Db04	75.0	0.80	0.2133	0.6429	1	0.4092	0.8443	0.7281	1.1596	0.8641
					2	0.5190	0.8174	0.6895	1.1855	0.8183
					3	0.5467	0.8443	0.6972	1.2110	0.8275
					4	0.5927	0.8796	0.7267	1.2104	0.8625
					5	0.6429	1.0649	0.7923	1.3441	0.9403
Db11	75.0	0.6667	0.1880	0.8968	1	0.3733	1.5274	1.2133	1.2589	1.5094
					2	0.4984	1.3188	1.0598	1.2444	1.3185
					3	0.6915	1.4913	1.0827	1.3774	1.3470
					4	0.7955	1.5153	1.2141	1.2481	1.5104
					5	0.8968	2.0245	1.7233	1.1748	2.1439
Db12	75.0	0.6818	0.2273	0.5544	1	0.3710	0.7510	0.6228	1.2062	0.7704
					2	0.4567	0.7396	0.5783	1.2789	0.7155
					3	0.5150	0.7510	0.5976	1.2567	0.7394
					4	0.5544	0.8103	0.6405	1.2651	0.7925

Table 4.5 $Y^*(\alpha)$ Calibration Results for the CCNBD Specimens (continued) [36]

ID	D (mm)	α_B	α_0	α_1	No.	α	Y^* (Cali.)	Y^* (Theo.)	Ratio	Y^* (Re-Cali.)
Dc01	50.0	0.80	0.40	0.8764	1	0.5000	1.6624	1.2542	1.3255	1.4885
					2	0.5848	1.3619	1.1431	1.1914	1.3567
					3	0.7099	1.4312	1.1160	1.2824	1.3245
					4	0.7600	1.4581	1.1516	1.2662	1.3668
					5	0.8038	1.5203	1.2263	1.2398	1.4554
					6	0.8764	1.8569	1.5506	1.1975	1.8403
Dc02	50.0	0.60	0.40	0.8036	1	0.5000	1.5875	1.0395	1.5272	1.3252
					2	0.5463	1.2876	0.9879	1.3034	1.2594
					3	0.6523	1.2134	0.9619	1.2615	1.2263
					4	0.7200	1.2898	1.0019	1.2874	1.2773
					5	0.8037	1.4948	1.1719	1.2755	1.4940

Table 4.6 $Y^*(\alpha)$ Calibration Results for CCNBD TH Group Specimens by IDM Method

Cases	ID	D (mm)	α_B	α_0	α_1	α	r_a (mm)	COD(r_a) ($\times 10^{-3}$)	Y^* (Cali.)	Y^* (Theo.)	Ratio	Y^* (Re-Cal.)
Medium	TH1	75.0	0.2667	0.1997	0.65	0.40	0.483	4.6568	0.7064	0.6992	1.2431	0.9140
	TH2		0.4000				0.483	5.3224	0.8074			
	TH3		0.5333				0.483	5.7300	0.8692			
	TH4		0.6667	0.2465			0.483	6.0254	0.9140	0.7439	1.2287	0.9255
	TH5		0.8000	0.2667			0.424	6.0154	0.9740	1.0092	0.9651	
	TH6		0.9333	0.2762			0.483	6.4008	0.9710	0.8266	1.1747	0.9379
	TH7		1.0667	0.2802			0.483	6.5464	0.9931	0.8708	1.1405	0.9464
	TH8		1.1733	0.2803			0.483	6.6758	1.0127	0.9199	1.1009	0.9672
	TH9		1.2800				0.483	6.7640	1.0216			

It is this value $\mathbf{Y_{Theory}}$ which will be used to represent the practical dimensionless SIF value $\mathbf{Y^*}(\alpha)$ for any CCNBD specimen geometry. It is believed that the error caused will be small enough to be neglected. Therefore in the application of CCNBD specimens, the practical (applicable) dimensionless SIF value for any specimen geometry can be easily obtained.

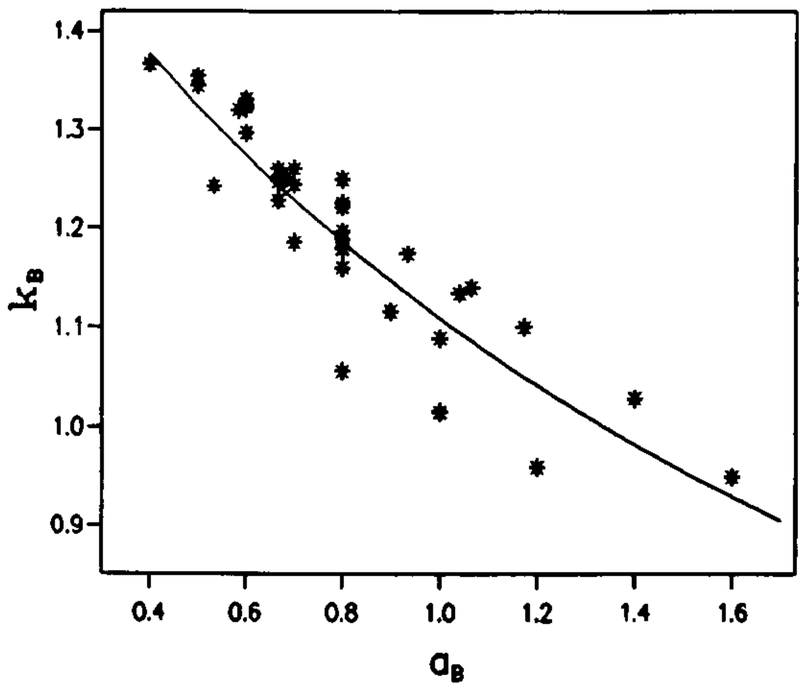

Figure 4.8 k_B - α_B Relationship

For the CCNBD specimens calibrated (Table 4.3 - Table 4.7) above, the practical (theoretical) $\mathbf{Y^*}$ values re-calculated this way are shown in the column under the heading $\mathbf{Y^*}$ (Re-Calibration). One interesting point which can be seen from Equation (4.15) is that the theoretical SIF values of the CCNBD specimens will tend to agree well with the numerical calibration ones with increasing specimen thickness values as the ratio of their difference $\mathbf{k_B}$ will tend to 1. This explains the importance of the specimen thickness effect on the validity of the theoretical evaluations.

The SIF $\mathbf{Y^*}(\alpha)$ calibration results for all the CCNBD specimens listed above in the tables are illustrated in Figure 4.9 (a) - (e2), where the variations of the dimensionless SIF values with respect to the crack extension evaluated by the theory are shown as solid lines and the numerical calibration values either by IDM method or by compliance method are shown as the discrete points.

From these figures, the generally good agreement between the theoretical and numerical calibration SIF values is illustrated, which implies the suitability of the theoretical evaluations applied. The $\mathbf{Y^*}(\alpha)$ values by the compliance method for CNA to CNH groups agreed well with the other results as. As expected, the SIF $\mathbf{Y^*}(\alpha)$ values of the CCNBD specimens vary with crack propagation in the pattern typical for chevron cracked specimens, which is discussed in section §2.4.3.2 and §3.3.3.

The theoretical evaluation method for the CSTBD specimens introduced in Chapter 3 can yield accurate SIF results $\mathbf{Y}(\alpha)$ up to a long crack case of $\alpha = 0.95$, so that the theoretical SIF values, $\mathbf{Y^*}(\alpha)$, for the CCNBD specimens based on the CSTBD SIF results agree well with the numerical calibration values up to the long crack case of $\alpha = 0.90$. This can be seen from the SIF comparison diagrams of the CNB, CND, Da01, Da02, Da05, Db11, Dc01 and Dc02 group CCNBD specimens.

For the CCNBD specimens calibrated above, after the SIF $\mathbf{Y^*}$ re-calibration, the overall difference between the theoretical values and the numerical results will be within $\pm 15\%$, as

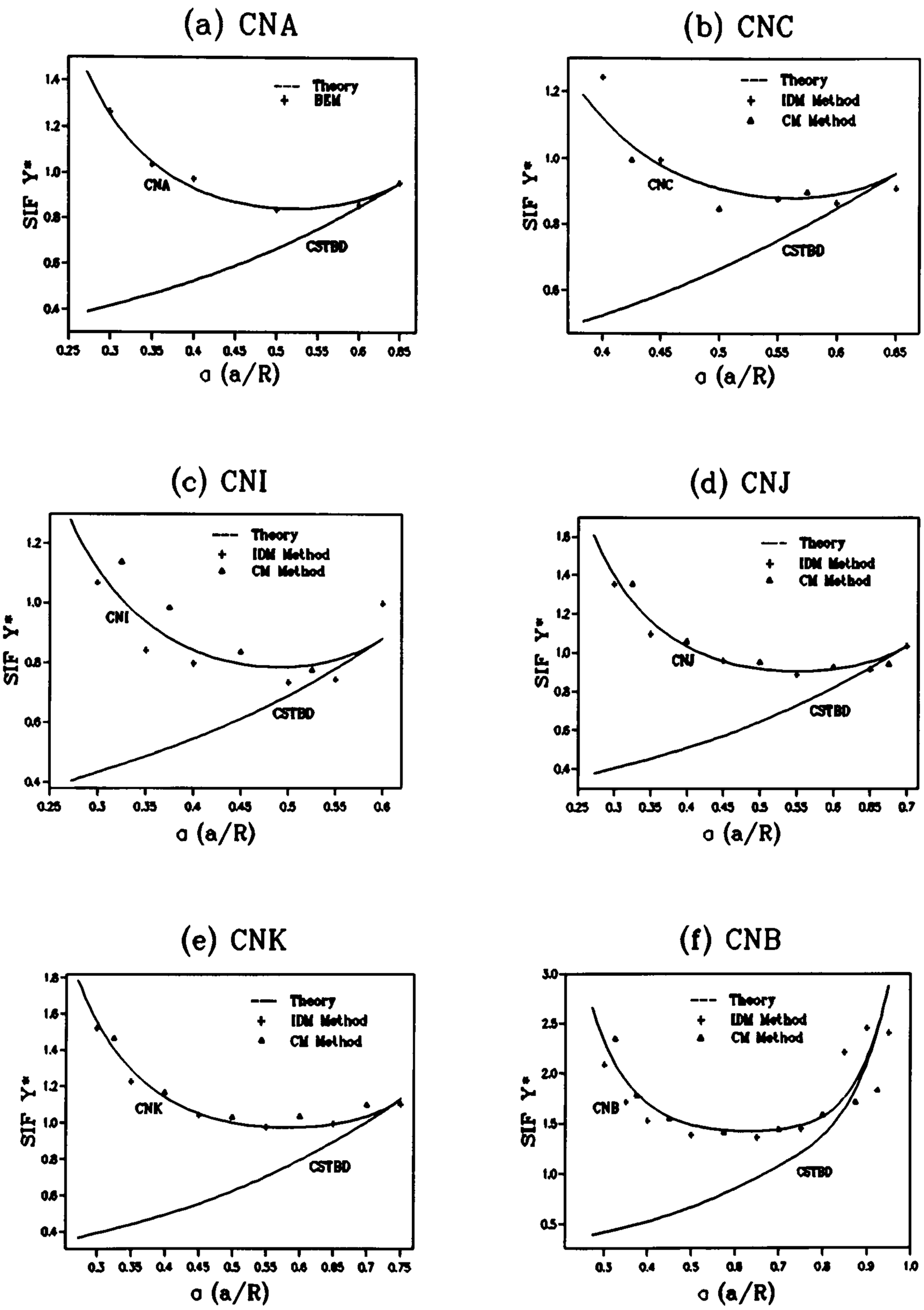

Figure 4.9 $\mathbf{Y}^*(\alpha)$ Calibration for CNA, CNC, CNI, CNJ, CNK and CNB Groups

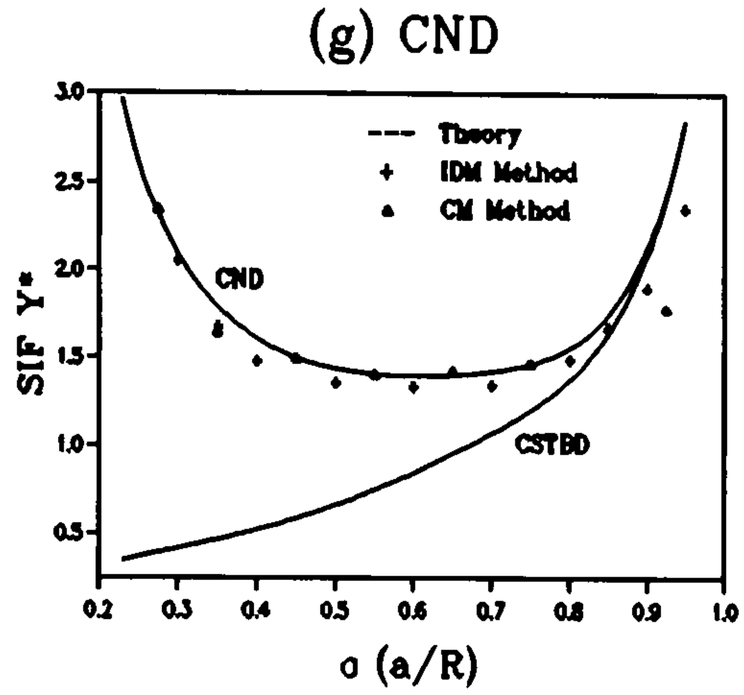

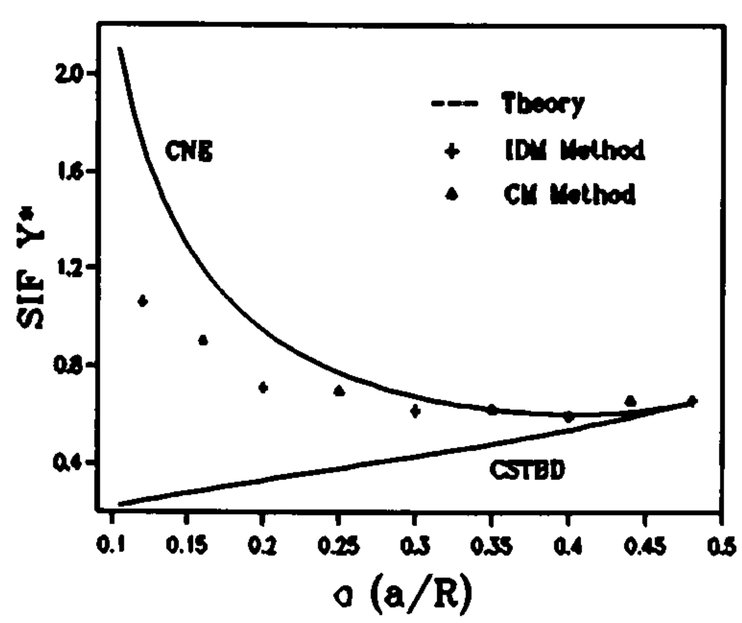

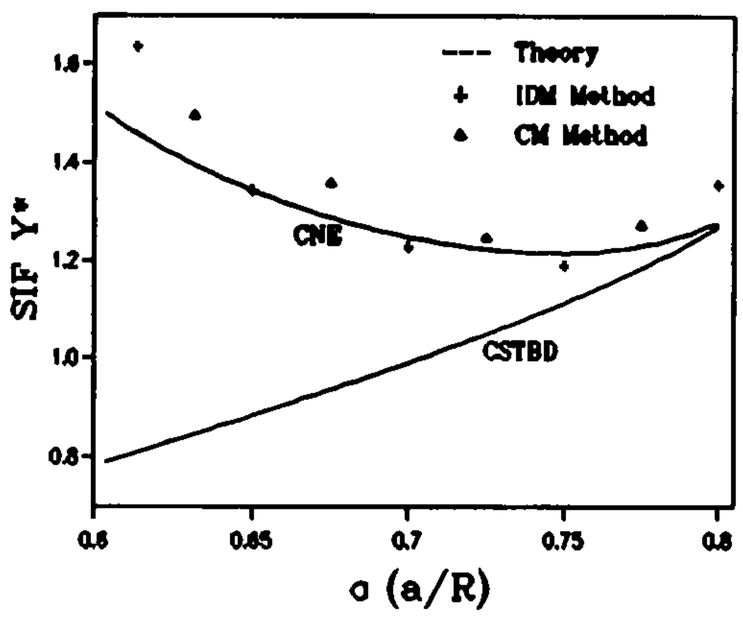

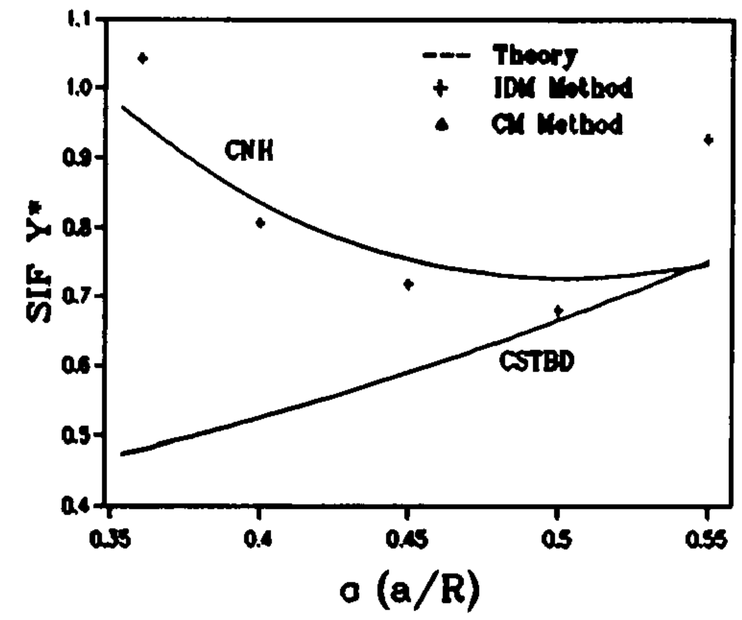

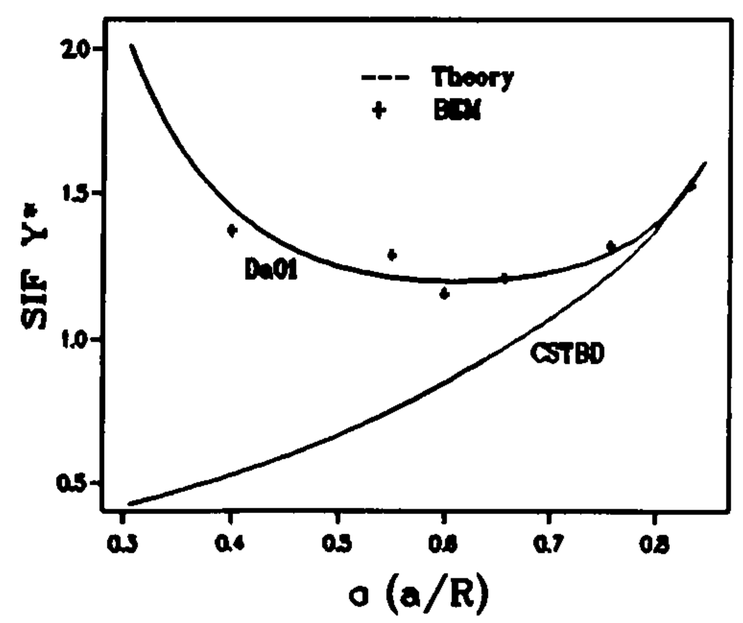

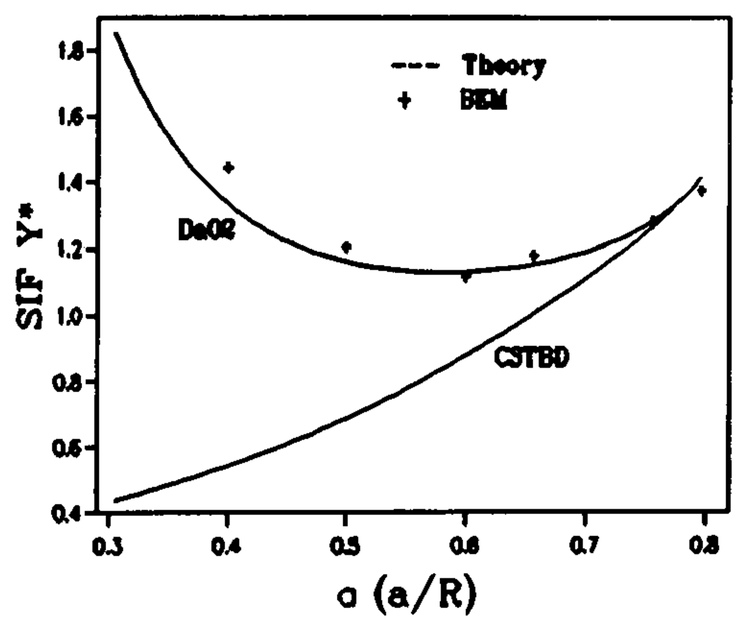

Figure 4.9 $\mathbf{Y}^*(\alpha)$ Calibration for CND, CNE, CNG, CNH, Da01 and Da02 Groups

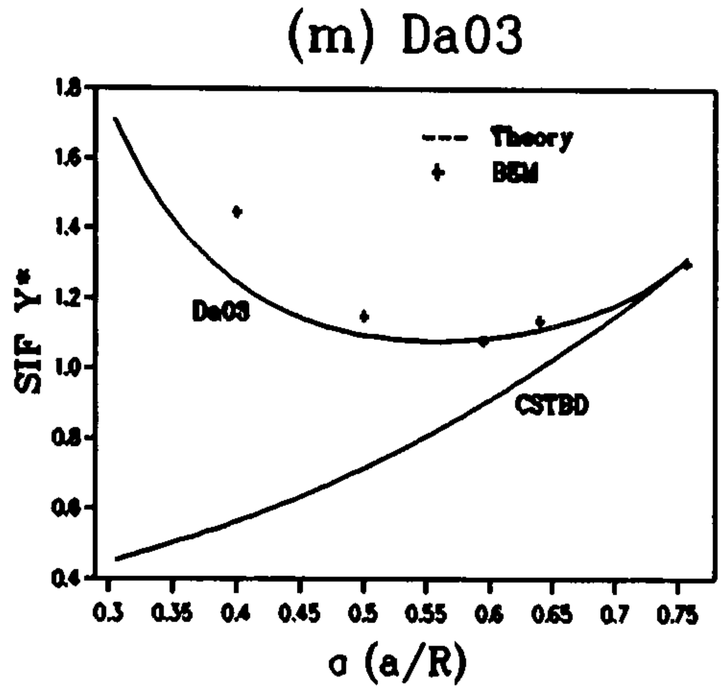

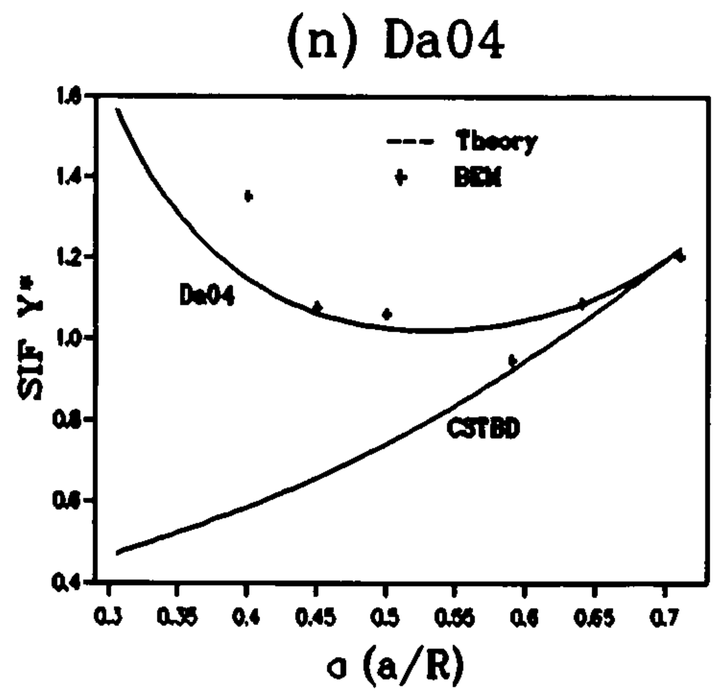

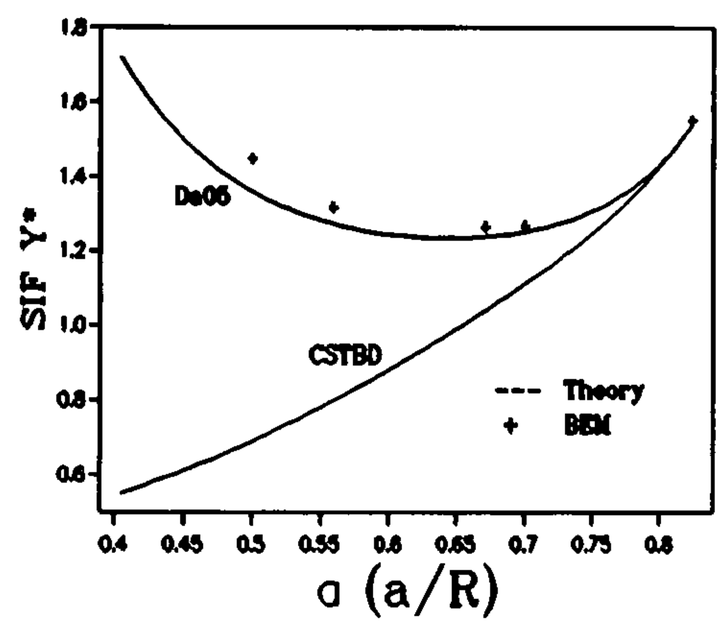

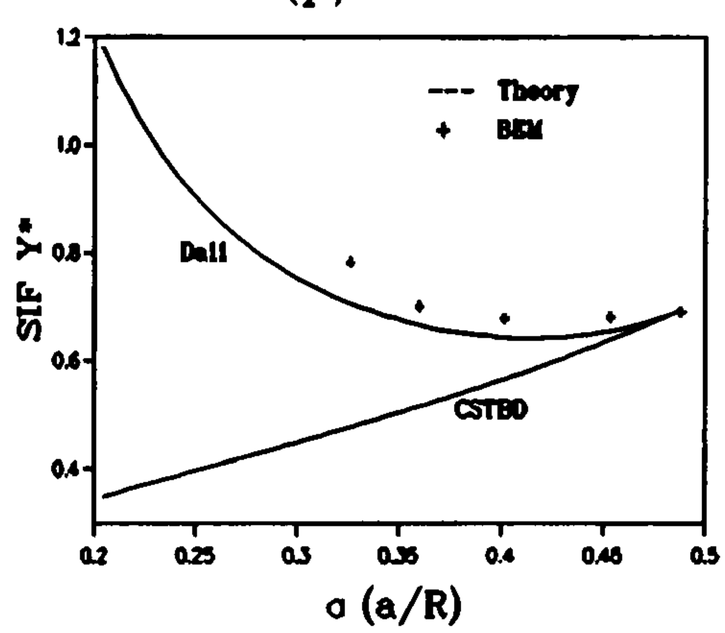

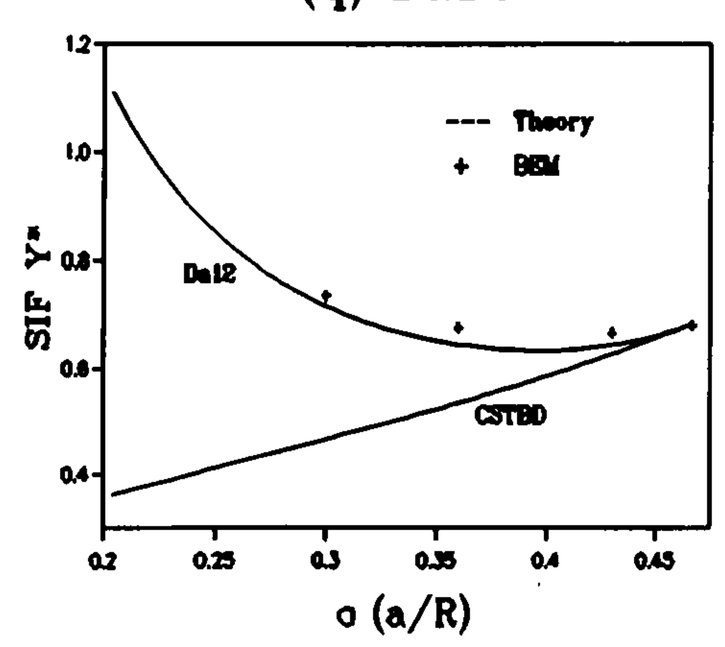

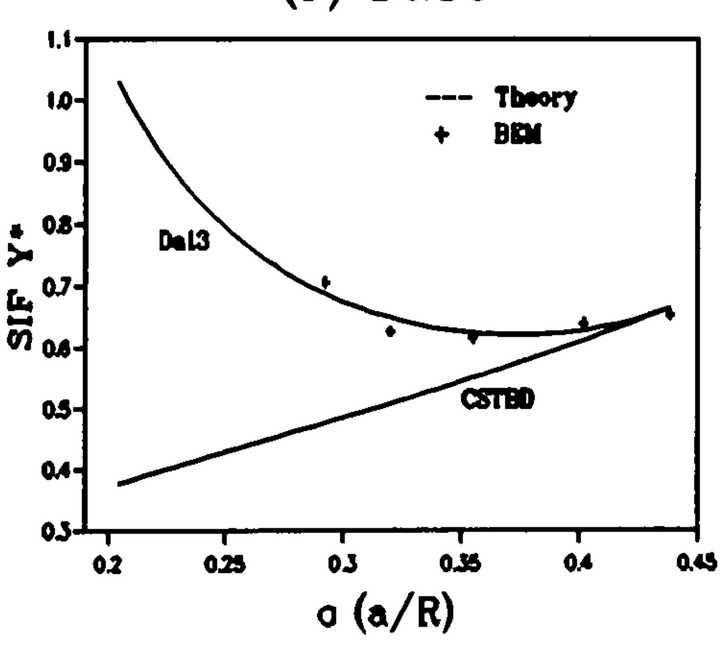

Figure 4.9 $\mathbf{Y^*}(\alpha)$ Calibration for Da03, Da04, Da05, Da11 Da12 and Da13 Groups

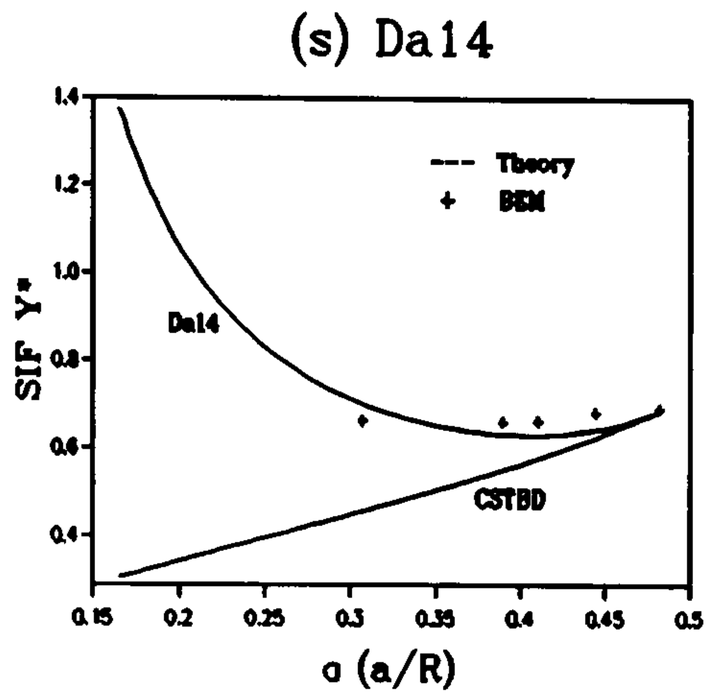

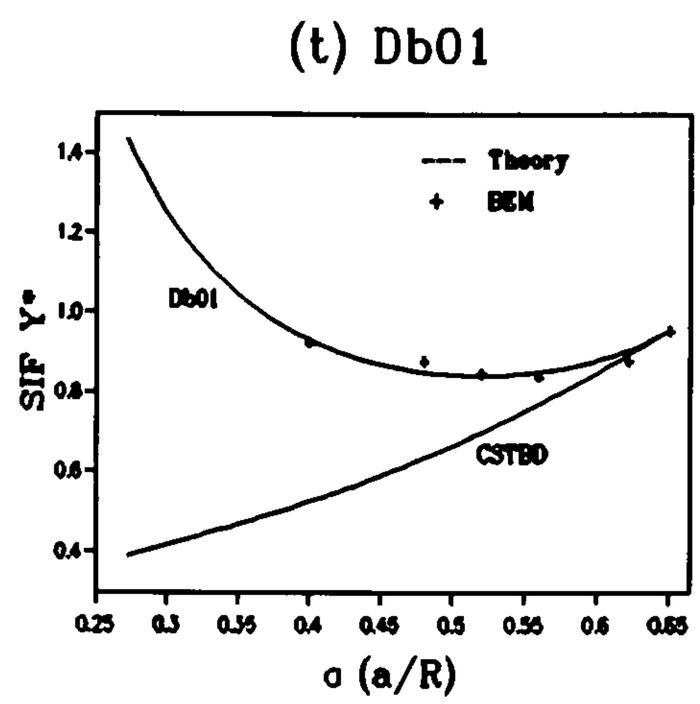

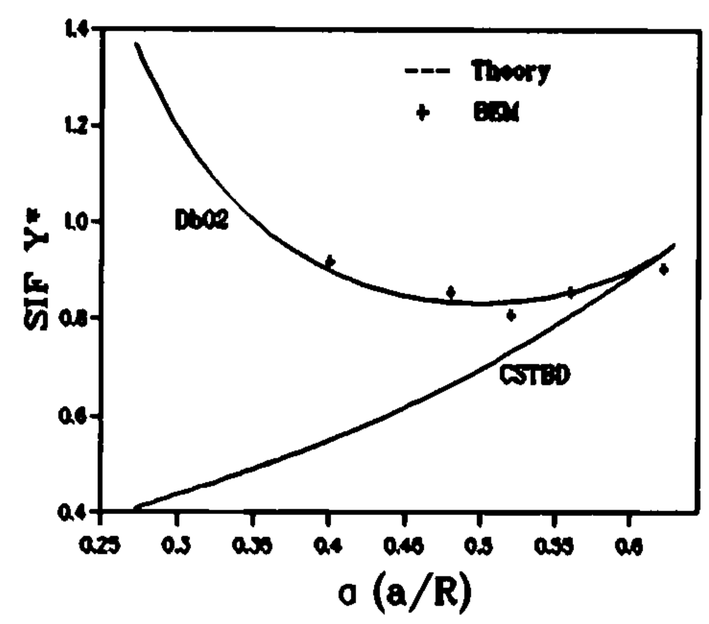

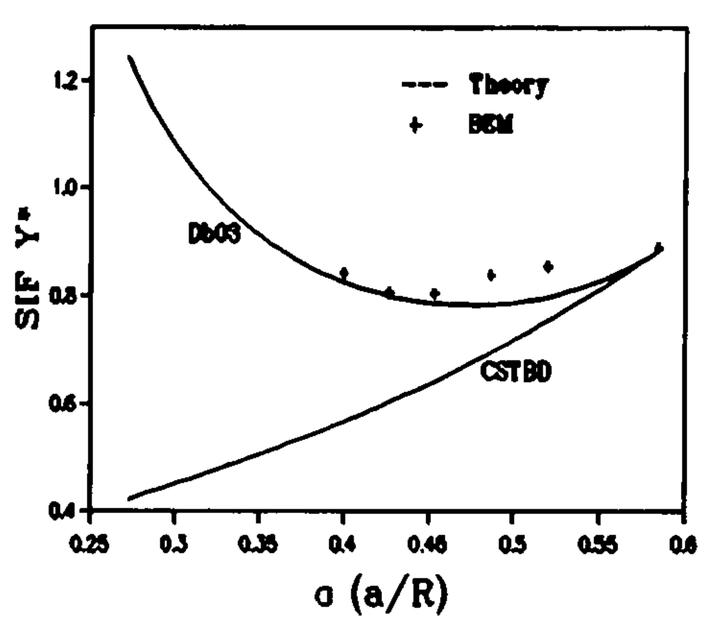

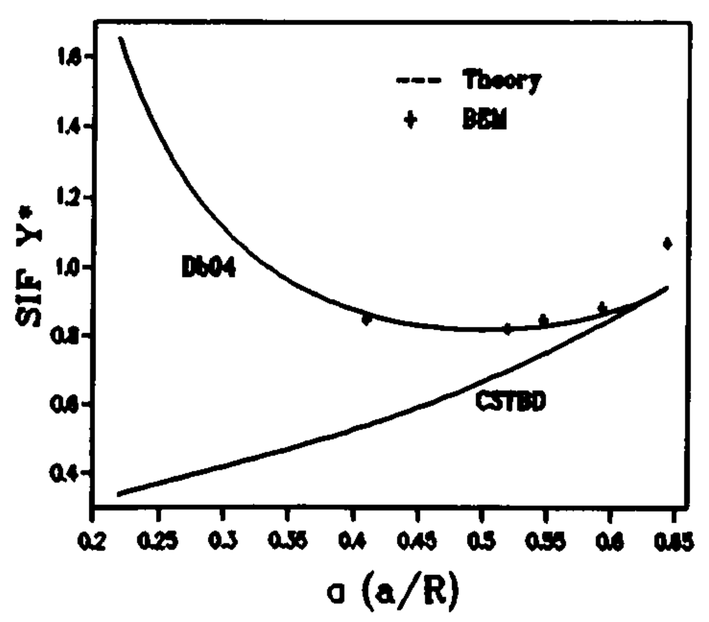

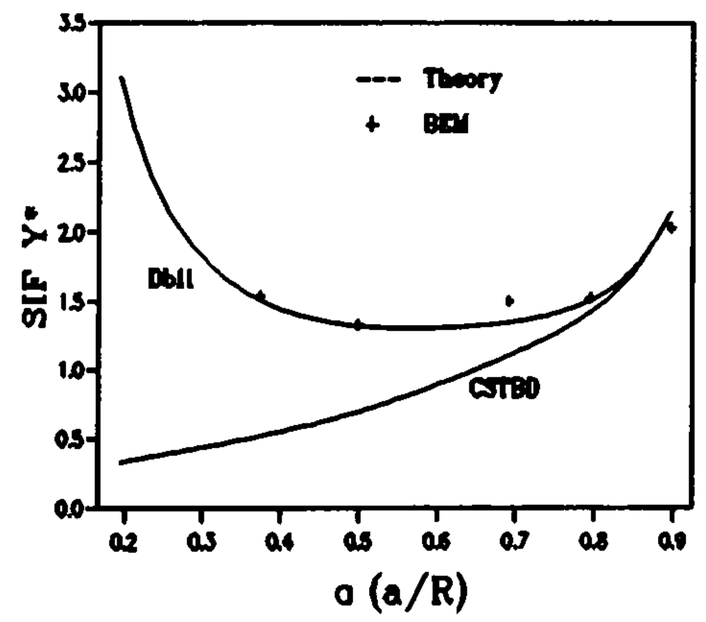

Figure 4.9 $\mathbf{Y}^*(\alpha)$ Calibration for Da14, Db01, Db02, Db03, Db04 and Db11 Groups

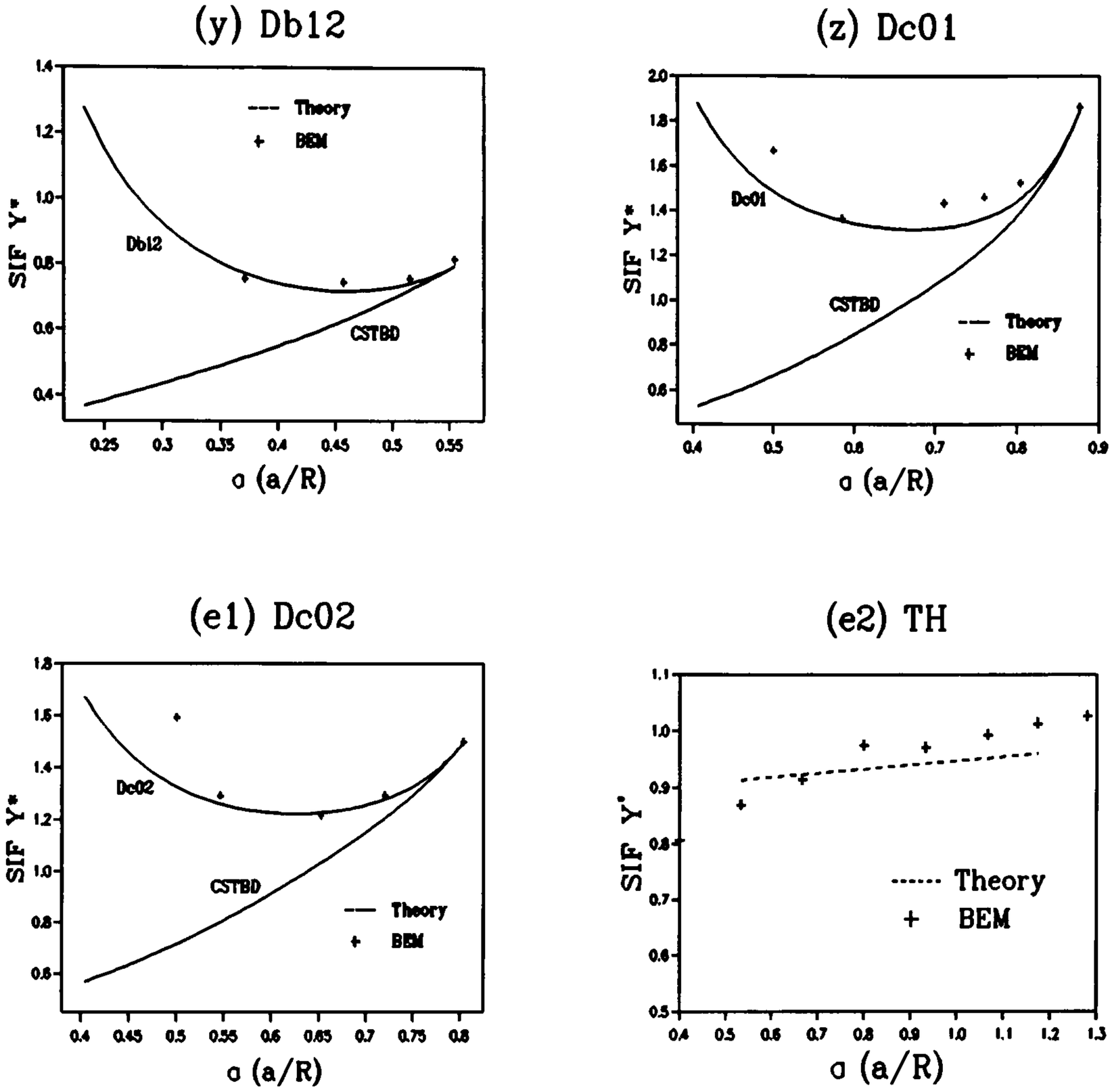

Figure 4.9 $\mathbf{Y}^*$ Calibration for Db12, Dc01, Dc02 and TH Groups

shown in Figure 4.10. However if we consider the critical SIF $\mathbf{Y}^*(\alpha)$ values $\mathbf{Y}^*_m$ only, as those will be the only values to be used for fracture toughness calculations, the difference will then be within $\pm 3\%$ for any crack cases, as is shown in Figure 4.11. For some CCNBD specimens whose geometrical parameters satisfy the valid geometrical requirement (which will be discussed in the following section) of practical use for plane strain fracture toughness testing, CNA, CNC, CNI, CNJ, CNK, CNG, CNH, Da11, Da12, Da14, Db01, Db02, Db03 and Db04 specimens for examples, the diference will be even less. Therefore, for fracture toughness measurement using the CCNBD specimen geometry, the above theoretical evaluations can be used to calculate $\mathbf{Y}^*_m$ for any CCNBD specimens with confidence.

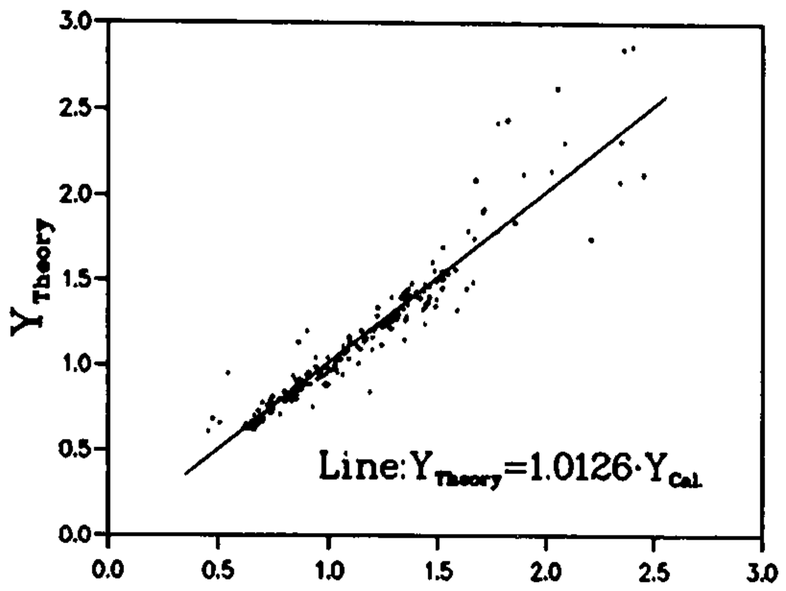

Figure 4.10 $Y^*(\alpha)$ Comparison

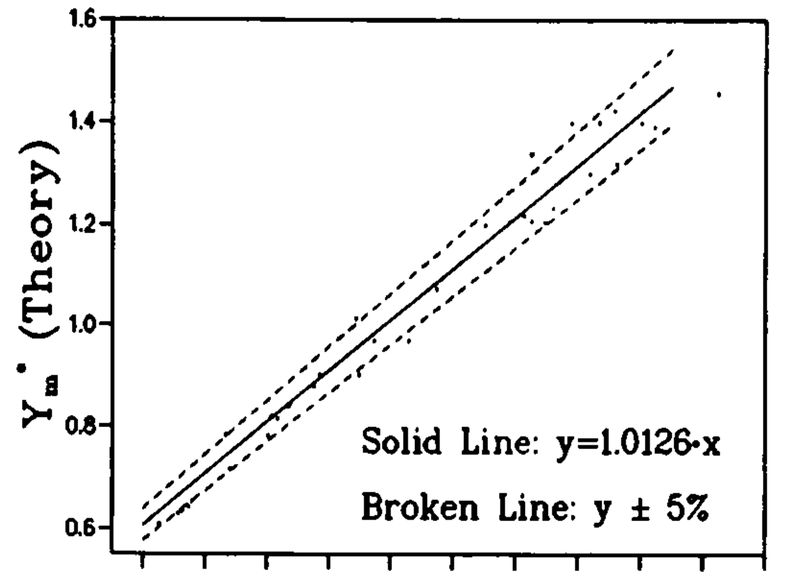

Figure 4.11 Y^*_m Comparison

§4.6 The Valid CCNBD Geometrical Range for Fracture Toughness Measurement

Even though the critical SIF $\mathbf{Y^*_m}$ for any CCNBD specimens can be solved as shown above, not all the specimens can yield valid measured fracture toughness values, $\mathbf{K_{IC}}$. Therefore some basic requirements about specimen geometrical parameters, the crack length α_0 and α_1 and the specimen thickness α_B, have to be drawn in order to have a valid fracture toughness test. These requirements have to be determined according to the stress-strain states of the crack tip areas.

In fracture mechanics studies of metallic materials, the acceptable specimen thickness is decided by comparing the plastic zone size around the crack tips with the actual specimen size. Within the range of LEFM, the plastic zone size $\mathbf{r_p}$ along the direction of the crack axis for the plane strain condition can be determined either by Von Mises or Tresca yielding criteria as follows:

$$r_p = \frac{1}{2\cdot\pi}\cdot\left(\frac{K_I}{\sigma_{ys}}\right)^2\cdot(1-2\cdot\nu)^2 \tag{4.16}$$

For the general cases, $\nu = 1/3$, then,

$$r_p = \frac{1}{18\cdot\pi}\cdot\left(\frac{K_I}{\sigma_{ys}}\right)^2 \tag{4.17}$$

However arguments exist about the exact size of the plastic zone. The above equation is supposed to underestimate the plastic zone size in metallic materials and therefore Irwin (1957) used a plastic constraint factor of 1.68 instead of 3 as used in the above equations to modify the size of the plastic zone and reached the same equation as Equation (4.17) but with 6π in the denominator instead of 18π. Experimentally determined plastic constraint factors for metallic materials are mostly between 1.5 and 2.0, which confirms the correctness of Irwin's modification.

As clearly illustrated in the metallic fracture studies, the ratio of plastic zone size to the specimen thickness is an important factor reflecting the stress-strain state of the crack front, and this state in turn will influence the size of the plastic zone. When the plastic zone is large (or of the same order) compared with the specimen thickness, yielding can take place freely in the thickness direction, and the plane stress shearing deformation and slant fracturing will be the dominant cases. When the plastic zone is very small, yielding in the thickness direction can not take place freely, i.e., the deformation in this direction is constrained by the surrounding elastic materials. In this case hinge deformation and the square fracturing, implying the plain strain state around the crack front, will be shown. Generally for any specimen, the stress-strain state will be just between these two cases discussed.

It has been determined experimentally in metallic material fracture that the cracking behaviour is typical of plane strain if $\mathbf{r_p/B}$ is in the order of 0.025 [Kanninen, 1985]. In the ASTM standard E399 [3], the requirement of $\mathbf{r_p/B}$ for a valid test is about 0.021, based on Irwin's modified calculation results.

In brittle rock material however, the plastic zone concept has to be replaced by the micro-cracking (micro tensile failure) zone concept (Figure 4.12). Ouchterlony (1982) suggested the calculation of micro cracking zone size can adopt the equations above simply by replacing the material yielding stress σ_{ys} with the rock material tensile strength σ_t and similar arguments can still be drawn. However owing to the different mechanical characteristics between metallic and rock materials, the micro-cracking zone in rock cannot "transmit" the stress and strain value from the crack apex to the uncracked body as well as the plastic zone in metal does. Therefore it is suggested that the micro-cracking zone size in rock materials will be generally much smaller so that the smaller micro-cracking size calculation is preferred, i.e., Equation (4.17) can be used. As a result, the following relationship can be obtained:

$$r_c = \frac{1}{18\pi}\cdot\left(\frac{K_{IC}}{\sigma_t}\right)^2 = \frac{1}{18\pi}\left[\frac{\frac{P_{cmax}}{B\cdot\sqrt{R}}\cdot Y^*}{\frac{P_{max}}{\pi\cdot B\cdot R}}\right]^2 = \frac{\pi\cdot R}{18}\cdot Y^{*2}\cdot\left[\frac{P_{cmax}}{P_{max}}\right]^2 \qquad (4.18)$$

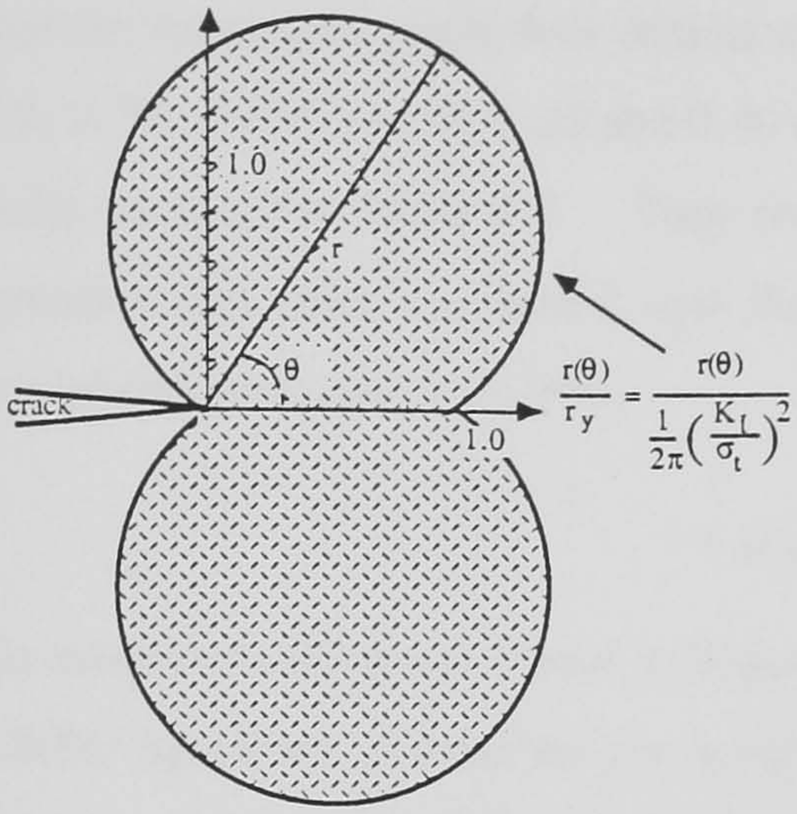

a. Plastic Zone in Metallic Materials

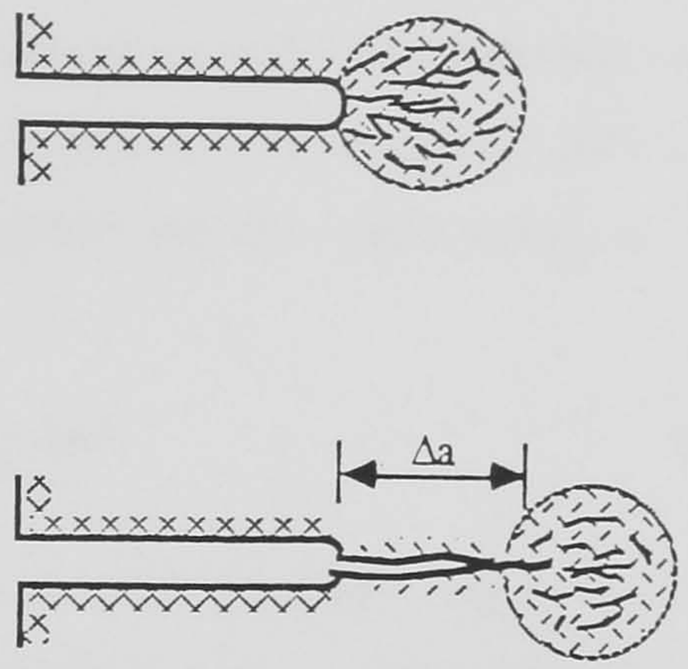

b. Micro-cracking Zone in Rock Materials

Figure 4.12 Plastic and Micro-cracking Zone

If we substitute the plain strain condition $\mathbf{r_c/B < 0.025}$ we can then reach:

$$\alpha_B > \frac{40\pi}{18} \cdot Y^{*2} \cdot [\frac{P_{cmax}}{P_{max}}]^2 \tag{4.19}$$

where the $\mathbf{P_{cmax}}$ and $\mathbf{P_{max}}$ are respectively the failure load of the cracked and the uncracked Brazilian disc with the same diameter **D**, thickness **B** and loading geometries. From experiment it is known that the ratio of $\mathbf{P_{cmax}/P_{max}}$ is normally less than 1/3 for reasonably structured geometries. Therefore this upper bound ratio (1/3) can be used for a conservative prediction of the basic requirement for α_B, and then the following equations can be obtained:

$$\begin{cases} \alpha_B \geq 0.7757 \cdot [Y^*(\alpha)]^2 , \quad or \\ (\alpha_B)_{min} = 0.7757 \cdot [Y^*(\alpha)]^2 \end{cases} \tag{4.20}$$

It is suggested that only when the CCNBD specimen geometry satisfies these relations that the stress-strain state around the crack front of the specimen can be considered approximately to be in the plane strain condition. This relation can then be used as a criterion to judge the stress-strain state around the crack front studied. However for a CCNBD specimen, the $\mathbf{Y^*}(\alpha)$ value varies as the crack front propagates and therefore the stress-strain state is changing at the same time according to the above argument. But what is important to the $\mathbf{K_{IC}}$ calculation is only the critical situation when $\mathbf{Y^*}(\alpha)$ reaches its minimum, $\mathbf{Y^*_m}$. Therefore only the stress-strain state of the crack front when the specimen reaches its critical condition has to be considered for the test validity analysis.

The minimum α_B requirements to achieve the plane strain condition around crack fronts,

when the specimens reach their critical states, for some typical CCNBD specimens with α_0 = 0.10, 0.20, 0.2667, 0.30, 0.35 and 0.40 are evaluated according to the above discussion. The results are listed in Table 4.7. They are also plotted in Figure 4.13 as discrete points. The regression has been conducted and the best fit equation for this relationship is, with a correlation coefficient $\gamma = 0.994$,

$$(\alpha_B)_{min} = 1.1729 \cdot \alpha_1^{1.6666} \tag{4.21}$$

This relation is shown as line 4 in Figure 4.13. It provides one basic requirement for the CCNBD specimen geometries for a valid fracture toughness test. Therefore during the practical application of CCNBD specimens, the specimen geometries can be designed according to this relation so that the plane strain requirement, in order to obtain a valid (consistent) rock K_{IC} test value, can be easily satisfied.

Apart from the valid specimen geometries set by the plane strain requirement discussed above, some other CCNBD specimen geometry requirements need to be drawn based on specimen machining and the SIF $Y^*(\alpha)$ calibration results. These requirements have to be strictly observed in practical applications in order to have a valid CCNBD specimen geometry for the K_{IC} test.

1) According to machining feasibility, the condition $(\alpha_B)_{max} < 2\alpha_1$ should always be followed, as discussed in the last chapter. This requirement is shown in Figure 4.13 as line 1.

2) As will be discussed in the Section §4.7, the CCNBD specimen thickness parameter α_B value is recommended to be within the range of $0.44 \sim 1.04$ in order to obtain the SIF results $Y^*(\alpha)$ coinciding (equivalent to) the practical values while using the theoretical evaluations. Furthermore, CCNBD specimens which are too thick are difficult to prepare and sometimes are impossible to machine, and based on experience of the CCNBD specimen preparation, $\alpha_B = 1.04$ should be taken as the upper limit for the specimen thickness. These two requirements are shown in Figure 4.13 as lines 5 and 2.

3) As discussed in the last section, the error in the SIF evaluations for the CSTBD and the CCNBD specimen geometries, $Y(\alpha)$ and $Y^*(\alpha)$, will tend to deviate from the practical values as the crack length α increases. As mentioned, one of the reasons for this deviation is due to the differences in the boundary loading assumption between the theory (point load loading assumption), the numerical calibration (strip load loading assumption) and the practical loading condition. Obviously the longer the crack in the CSTBD or the CCNBD specimens, or the nearer the crack tips to the boundary loading point(s), the greater the error in the SIF values caused by the differences in the boundary loading assumption. Therefore a limit of the crack length α should exist below which the correctness (or preciseness) of the evaluated SIF, $Y(\alpha)$ or $Y^*(\alpha)$, can be guaranteed. According to the calibration results shown in the last section,

this limit is around α(or α_1) = 0.90. Based on the experiments conducted by Chen (1989), the CCNBD specimens with crack length $\alpha_1 > 0.8$ always generated inconsistent $\mathbf{K_{IC}}$ values for rock materials. Therefore the restriction of $(\alpha_1)_{max} = 0.80$ is set as another CCNBD specimen geometry requirement in order to obtain a valid CCNBD $\mathbf{K_{IC}}$ test. The boundary influence of the CCNBD specimens with α_1 less than this upper limit value is assumed to be extremely small so that it can be neglected without the sacrifice of accuracy in the SIF results. This requirement is put in Figure 4.13 as line 3.

4) As mentioned in the last chapter, the CCNBD specimens with the crack length α_1 less than a certain limit will be difficult or even impossible to machine. Based on experience on CCNBD specimen preparation, this limit is around $\alpha_1 = 0.4$. Therefore another geometrical requirement for the CCNBD specimens can be concluded which is $(\alpha_1)_{min} = 0.40$ and this requirement is shown in Figure 4.13 as line 0.

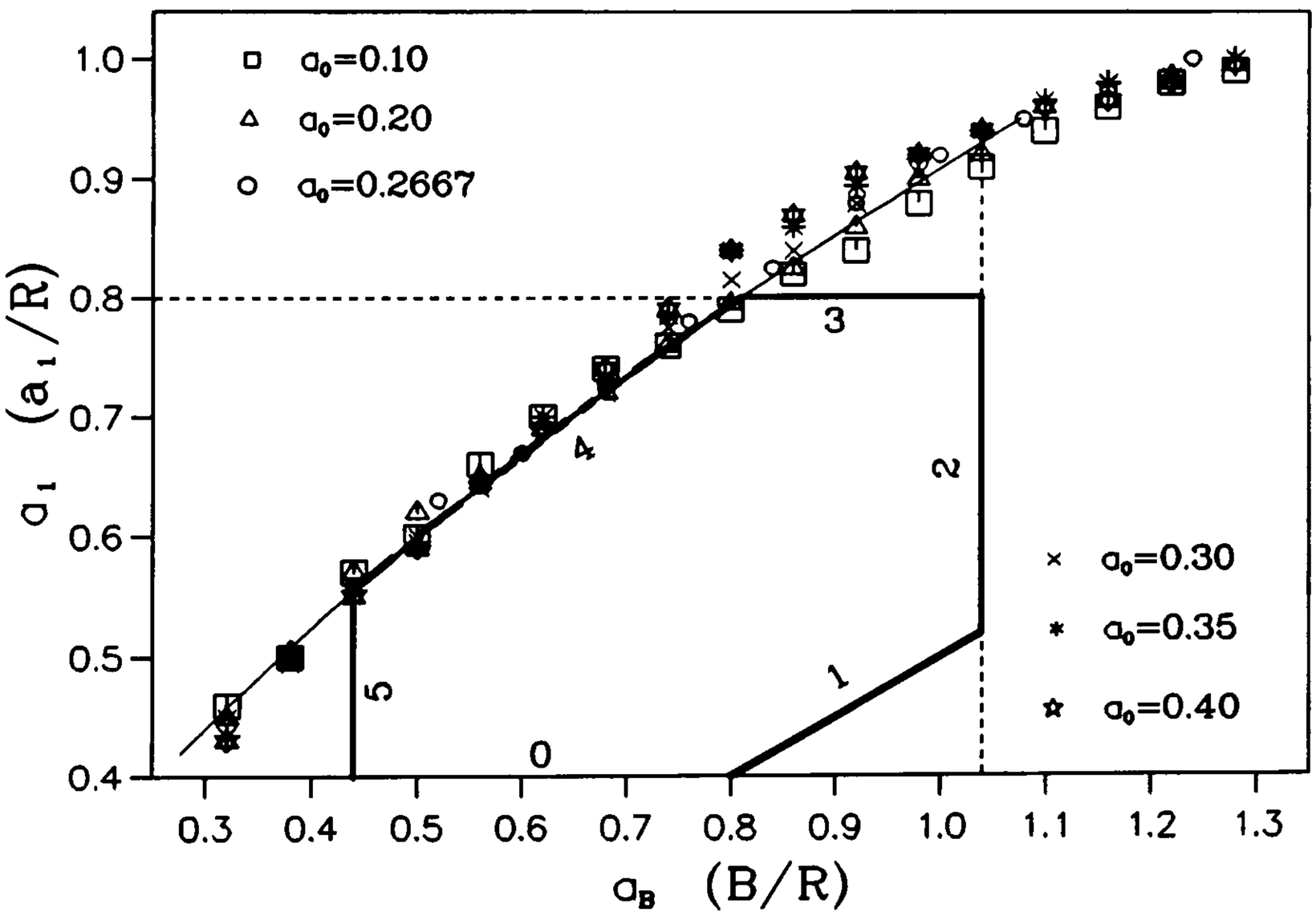

Figure 4.13 The Valid Geometrical Range for the CCNBD Specimens

Therefore theoretically, the CCNBD specimen geometry parameters α_B and α_1 should be within the range outlined by lines 0, 1, 2, 3, 4 and 5 in Figure 4.13 in order to have a valid K_{IC} test from the specimen. This range is called the valid geometrical range for CCNBD specimens. The α_0 value however, seems play little influence in the specimen geometry

Table 4.7 Minimum α_B Requirement for Plane Strain State for CCNBD Specimens

α_0	0.10	0.20	0.30	0.35	0.40	0.2667	
α_B	α_1					α_B	α_1
0.32	0.460	0.450	0.450	0.435	0.430	0.44	0.560
0.38	0.500	0.505	0.495	0.500	0.500	0.52	0.630
0.44	0.570	0.570	0.560	0.555	0.550	0.60	0.670
0.50	0.600	0.620	0.600	0.595	0.590	0.68	0.730
0.56	0.660	0.650	0.640	0.645	0.645	0.76	0.780
0.62	0.700	0.690	0.700	0.700	0.690	0.84	0.825
0.68	0.740	0.720	0.720	0.730	0.740	0.92	0.880
0.74	0.760	0.760	0.775	0.785	0.790	1.00	0.920
0.80	0.790	0.795	0.815	0.840	0.840	1.08	0.950
0.86	0.820	0.825	0.840	0.860	0.870	1.16	0.975
0.92	0.840	0.860	0.880	0.895	0.905	1.24	1.000
0.98	0.880	0.900	0.905	0.920	0.920		
1.04	0.910	0.920	0.940	0.940	0.940		
0.10	0.940	0.960		0.965	0.960		
1.16	0.960	0.965		0.980	0.965		
1.22	0.980	0.985		0.985	0.980		
1.28	0.990			1.000	0.995		

requirements for a valid test so that it can be taken as the passive parameter dependent on (determined by) the α_B, α_1 and the available saw diameter D_s.

These conclusions about the valid CCNBD specimen geometrical range are vitally important for practical application of the CCNBD specimens to rock K_{IC} tests. It will be validated extensively and intensively by experiments for rock K_{IC} tests using a large range of different CCNBD geometries in the next chapter.

Furthermore, if the strain values of the crack front of all the calibrated CCNBD specimens in the **Z** direction (Figure 4.3) are examined, Table 4.8 can be obtained, where ϵ_Z is the average strain value of the crack front in the specimen thickness direction (**Z**) at $\mathbf{r} = 0.5$mm directly calculated from the numerical calibration results. Attempts have been made to relate ϵ_Z to the geometrical parameters and only $\epsilon_Z \sim \mathbf{Y}^*/\alpha_B$ shows a clear relationship. This relation is shown in Figure 4.14 and its regression line is:

$$\varepsilon_z = 2.945 \cdot \left(\frac{Y^*}{\alpha_B}\right)^{0.435} \quad (\times 10^{-4}) \tag{4.22}$$

with the regression coefficient $\gamma = 0.974$.

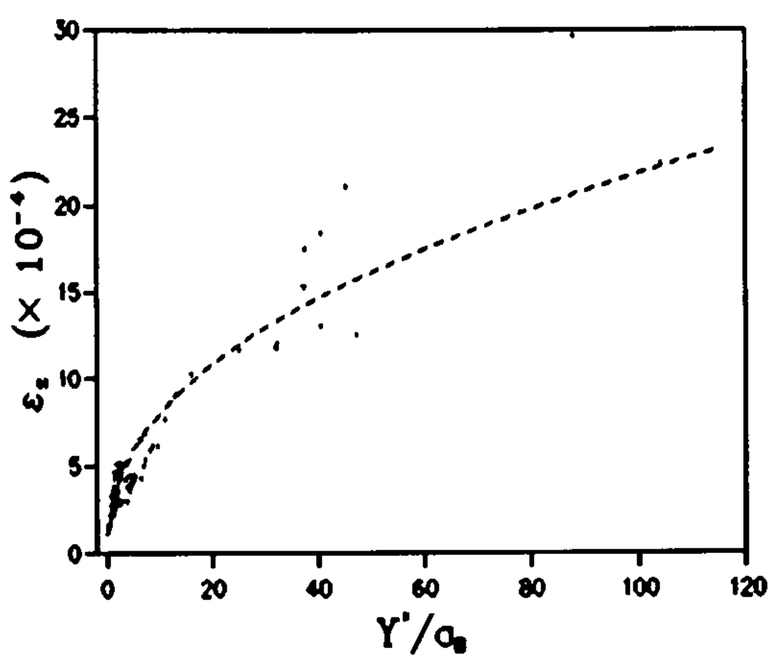

Figure 4.14 ϵ_z at r = 0.5 mm

According to this relation, it is found that, when the CCNBD specimens reach their critical states, the strain condition corresponding to the minimum α_B requirement [Equation (4.20), (4.21)] for a valid test is:

$$\varepsilon_z \leq 3.8 \times 10^{-4} \tag{4.23}$$

When the thickness of the CCNBD specimens, α_B, is changing, the ϵ_z values calculated by Equation (4.22) will vary in a pattern as shown in Figure 4.15, where the condition of Equation (4.23) is shown as well. As can be seen, there will be not much difference between the strain values ϵ_Z after its value is less than 3.8×10^{-4} for different thickness CCNBD specimens. In other words, the satisfaction of Equation (4.23) means the satisfaction of the plane strain requirement around the crack front when the specimen is at its critical state. This substantiates the valid geometrical requirement argument discussed above from the point of the strain values in the specimen thickness direction, as Equation (4.23) is actually derived from Equation (4.20).

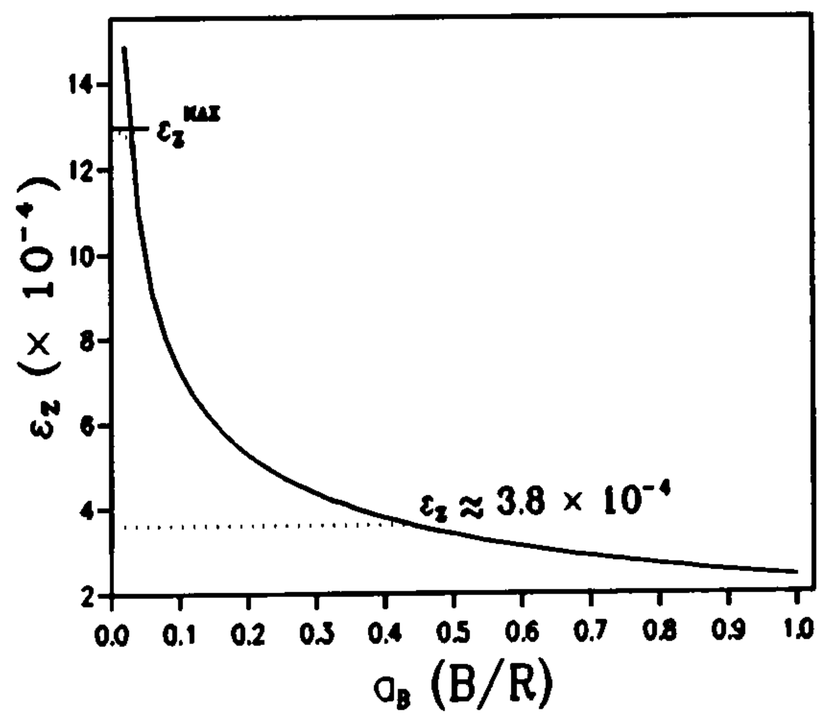

Figure 4.15 ϵ_Z vs α_B

Table 4.8 List of ϵ_z ($\times 10^{-3}$) vs Y^*/α_B

ID	Y^*/α_B	ϵ_z	ID	Y^*/α_B	ϵ_z	ID	Y^*/α_B	ϵ_z
CNA1	32.313	11.994	CNC1	32.059	11.754	CNJ1	37.412	17.458
CNA2	9.5215	6.1462	CNC2	6.7749	4.9915	CNJ2	10.918	7.6677
CNA3	5.0449	4.4920	CNC3	1.9541	3.0448	CNJ3	3.5593	4.2375
CNA4	2.0000	3.0640	CNC4	1.2854	2.9055	CNJ4	1.7324	3.2152
CNA5	1.1188	2.9091	CNC5	0.8688	3.0348	CNJ5	1.0354	3.1574
CNB1	104.04	22.390	CND1	160.96	43.826	CNJ6	0.8781	3.2963
CNB2	37.272	15.307	CND2	40.395	18.375	CNK1	45.181	21.080
CNB3	16.000	10.241	CND3	12.739	9.0215	CNK2	13.185	9.0801
CNB4	7.0896	6.8934	CND4	6.3215	6.5450	CNK3	4.2033	4.4536
CNB5	3.4370	5.1944	CND5	3.9436	5.2157	CNK4	2.0990	3.5832
CNB6	3.5357	5.1263	CND6	2.7236	5.1070	CNK5	1.2772	3.3815
CNB7	2.8190	5.0440	CND7	2.1815	5.1489	CNK6	0.8389	3.5712
CNB8	2.6977	4.7279	CND8	2.0748	4.7431	CNG1	40.390	13.015
CS1	0.2164	1.4579	CND9	2.2520	4.3590	CNG2	8.1782	5.9010
CS2	0.3311	1.6528	CNE1	87.822	29.606	CNG3	3.3045	4.2377
CS3	0.4791	1.8489	CNE2	8.5690	6.1366	CNG4	1.8134	3.8832
CS4	0.6422	2.1877	CNE3	2.6267	2,9863	CNG5	0.9962	3.8285
CS5	0.9141	3.0913	CNE4	1.1966	2.2200	CNH1	47.199	12.490
CS6	1.2866	4.3097	CNE5	0.7223	2.1004	CNH2	6.6001	4.3105
CS7	1.5080	4.6450	CNF1	2.0219	5.0711	CNH3	2.5467	2.8169
CS8	1.8156	4.6024	CNF2	1.7646	5.0800	CNH4	1.3339	2.4280
CS9	2.2904	4.3034	CNF3	1.5543	4.5566	CNH5	0.8849	2.3659
TH1	3.6642	2.9911	CNF4	1.1164	3.1873			
TH2	4.1880	3.5735	CNF5	0.9064	2.7615			
TH3	4.5083	3.8684	CNF6	0.7744	2.2964			
TH4	4.7410	4.0448	CNI1	25.013	11.641			
TH5	5.0518	4.4920	CNI2	7.0580	5.3718			
TH6	5.0362	4.2124	CNI3	3.7463	3.8018			
TH7	5.1509	4.2919	CNI4	1.5598	2.6496			
TH8	5.2526	4.3682	CNI5	1.1342	2.5684			
TH9	5.3219	4.4188	CNI6	1.0877	2.6204			

§4.7 The Evaluation of the Y^*_m Values for CCNBD Specimens for K_{IC} Calculations

As discussed above, the important part of the SIF value, $Y^*(\alpha)$, of a CCNBD specimen is its critical value Y^*_m which will be used for practical K_{IC} calculation. It is necessary then to have a list of the Y^*_m values for all the possible CCNBD specimens which satisfy the valid geometrical range requirement discussed in the last section.

Y^*_m values for the CCNBD specimens are determined by their geometries α_0, α_1 and α_B only, and are independent of the rock materials and the external loading conditions, as discussed in Chapter 3. From the calculations it is found that when the specimen geometrical parameters α_0 and α_B are fixed, the Y^*_m value of the specimen can be expressed by the exponential relation with respect to specimen crack length α_1, i.e.,

$$Y^*_m = u \cdot \exp[v \cdot \alpha_1] \tag{4.24}$$

where the coefficients **u** and **v** will be decided by α_0 and α_B of the specimen only. A large number of calculations for the **u** and **v** values have been conducted for the different CCNBD specimens with different geometrical parameters α_0 (= 0.05, 0.10, 0.15, 0.175, 0.20, 0.225, 0.25, 0.275, 0.30, 0.325, 0.35, 0.375, 0.40, 0.425, 0.45) and α_B (ranging from 0.20 to 1.46 at the interval of 0.04). The results are illustrated in Figure 4.16 (a), (b) and Figure 4.17 (a), (b), where the variations of the **u** and **v** values for a large range of CCNBD specimens with the geometrical parameters α_0 and α_B are presented. The "ALFA0" and "ALFAB" printed in Figure 4.17 are the "α_0" and "α_B" of the specimens. For the CCNBD specimens satisfying the valid geometrical range requirement, the **u** and **v** values are listed in Table 4.9. It is necessary to mention here that, for the valid CCNBD specimens, the correlation coefficients for Equation (4.24), while carrying out the evaluation of the **u** and **v** values, are normally over 0.99. In other words, the **u** and **v** values listed in Table 4.9 have 99% confidence in their preciseness. This conclusion is well illustrated in Figure 4.18, where C_r is the correlation coefficient of the regression of **u** and **v** values.

Therefore in practical use, the Y^*_m value for any valid CCNBD specimen can be calculated jointly by Equation (4.24) and Table 4.9. For those valid CCNBD specimens which α_0 and α_B are not listed in Table 4.9, the linear interpolation technique is recommended to find the **u** and **v** values corresponding to the actual α_0 and α_B.

In order to have a clear illustration of the variation of Y^*_m for CCNBD specimens with respect to the specimen geometries, the three dimensional variation diagrams have been generated for some typical groups α_0 = 0.10, 0.20, 0.30 and 0.40, which are shown in Figure

Table 4.9 Values of **u** and **v**

α_0	0.100	0.150	0.175	0.200	0.225	0.250	0.275	0.300	0.325	0.350	0.375	0.400	0.425	0.450
							u							
α_B														
0.440	0.2747	0.2774	0.2791	0.2808	0.2825	0.2844	0.2865	0.2883	0.2914	0.2943	0.2979	0.3024	0.3069	0.3120
0.480	0.2727	0.2752	0.2765	0.2782	0.2795	0.2812	0.2833	0.2856	0.2882	0.2918	0.2954	0.2994	0.3039	0.3090
0.520	0.2708	0.2727	0.2740	0.2757	0.2771	0.2788	0.2806	0.2828	0.2857	0.2887	0.2925	0.2968	0.3013	0.3060
0.560	0.2689	0.2705	0.2716	0.2733	0.2744	0.2763	0.2781	0.2805	0.2831	0.2867	0.2901	0.2943	0.2989	0.3039
0.600	0.2667	0.2684	0.2696	0.2709	0.2721	0.2739	0.2757	0.2782	0.2812	0.2844	0.2882	0.2921	0.2967	0.3015
0.640	0.2649	0.2665	0.2674	0.2685	0.2701	0.2719	0.2738	0.2764	0.2791	0.2825	0.2863	0.2905	0.2947	0.2992
0.680	0.2632	0.2646	0.2655	0.2667	0.2682	0.2704	0.2718	0.2744	0.2774	0.2807	0.2848	0.2888	0.2930	0.2971
0.720	0.2611	0.2628	0.2637	0.2650	0.2667	0.2683	0.2705	0.2727	0.2763	0.2794	0.2831	0.2871	0.2916	0.2954
0.760	0.2598	0.2612	0.2625	0.2637	0.2650	0.2668	0.2693	0.2719	0.2744	0.2781	0.2819	0.2860	0.2895	0.2934
0.800	0.2582	0.2602	0.2611	0.2625	0.2641	0.2657	0.2680	0.2706	0.2736	0.2772	0.2811	0.2845	0.2878	0.2916
0.840	0.2572	0.2586	0.2599	0.2612	0.2628	0.2649	0.2672	0.2699	0.2727	0.2763	0.2801	0.2831	0.2867	0.2891
0.880	0.2562	0.2578	0.2593	0.2602	0.2621	0.2642	0.2668	0.2691	0.2723	0.2754	0.2793	0.2816	0.2853	0.2867
0.920	0.2553	0.2572	0.2582	0.2598	0.2613	0.2634	0.2658	0.2684	0.2716	0.2747	0.2782	0.2811	0.2831	0.2856
0.960	0.2549	0.2566	0.2578	0.2593	0.2612	0.2633	0.2655	0.2685	0.2710	0.2746	0.2767	0.2799	0.2811	0.2825
1.000	0.2547	0.2564	0.2576	0.2591	0.2610	0.2630	0.2653	0.2679	0.2709	0.2738	0.2768	0.2786	0.2794	0.2794
1.040	0.2544	0.2565	0.2576	0.2593	0.2608	0.2627	0.2653	0.2678	0.2708	0.2727	0.2747	0.2769	0.2769	0.2765
1.080	0.2543	0.2561	0.2576	0.2591	0.2608	0.2630	0.2657	0.2674	0.2695	0.2718	0.2735	0.2736	0.2731	0.2721
1.120	0.2547	0.2565	0.2579	0.2591	0.2612	0.2630	0.2648	0.2672	0.2693	0.2705	0.2717	0.2712	0.2697	0.2679
1.160	0.2548	0.2572	0.2579	0.2600	0.2613	0.2627	0.2645	0.2666	0.2679	0.2684	0.2695	0.2688	0.2661	0.2628
1.200	0.2552	0.2574	0.2585	0.2598	0.2616	0.2629	0.2648	0.2650	0.2671	0.2675	0.2655	0.2633	0.2608	0.2566
1.240	0.2555	0.2572	0.2581	0.2603	0.2610	0.2619	0.2630	0.2636	0.2634	0.2633	0.2616	0.2596	0.2564	0.2513
1.280	0.2561	0.2577	0.2586	0.2595	0.2600	0.2611	0.2613	0.2616	0.2608	0.2607	0.2582	0.2549	0.2501	0.2447
							v							
0.440	1.7813	1.7820	1.7820	1.7833	1.7863	1.7893	1.7923	1.7967	1.7966	1.7977	1.7973	1.7932	1.7901	1.7850
0.480	1.7748	1.7763	1.7787	1.7800	1.7843	1.7881	1.7907	1.7934	1.7952	1.7929	1.7923	1.7901	1.7866	1.7811
0.520	1.7694	1.7734	1.7758	1.7769	1.7808	1.7845	1.7884	1.7907	1.7911	1.7920	1.7897	1.7860	1.7823	1.7784
0.560	1.7644	1.7701	1.7732	1.7748	1.7794	1.7822	1.7856	1.7877	1.7885	1.7864	1.7857	1.7820	1.7779	1.7725
0.600	1.7620	1.7668	1.7692	1.7727	1.7770	1.7792	1.7826	1.7835	1.7833	1.7831	1.7805	1.7782	1.7733	1.7689
0.640	1.7580	1.7631	1.7671	1.7707	1.7732	1.7757	1.7788	1.7794	1.7795	1.7779	1.7753	1.7716	1.7686	1.7652
0.680	1.7550	1.7602	1.7640	1.7676	1.7707	1.7711	1.7757	1.7759	1.7754	1.7741	1.7700	1.7666	1.7630	1.7612
0.720	1.7536	1.7580	1.7616	1.7647	1.7661	1.7698	1.7708	1.7722	1.7693	1.7683	1.7652	1.7617	1.7574	1.7562
0.760	1.7497	1.7553	1.7568	1.7600	1.7635	1.7656	1.7649	1.7652	1.7662	1.7624	1.7593	1.7554	1.7548	1.7528
0.800	1.7474	1.7506	1.7538	1.7557	1.7581	1.7611	1.7613	1.7603	1.7596	1.7561	1.7525	1.7512	1.7509	1.7494
0.840	1.7430	1.7487	1.7500	1.7522	1.7545	1.7547	1.7551	1.7548	1.7535	1.7499	1.7469	1.7473	1.7448	1.7497
0.880	1.7392	1.7438	1.7446	1.7487	1.7490	1.7492	1.7478	1.7487	1.7463	1.7452	1.7403	1.7434	1.7414	1.7493
0.920	1.7357	1.7390	1.7413	1.7423	1.7440	1.7446	1.7443	1.7432	1.7411	1.7389	1.7360	1.7363	1.7417	1.7448
0.960	1.7299	1.7337	1.7358	1.7370	1.7372	1.7373	1.7372	1.7346	1.7344	1.7309	1.7343	1.7331	1.7414	1.7483
1.000	1.7243	1.7279	1.7300	1.7308	1.7310	1.7307	1.7306	1.7297	1.7273	1.7270	1.7258	1.7302	1.7394	1.7525
1.040	1.7196	1.7213	1.7231	1.7232	1.7246	1.7256	1.7237	1.7231	1.7204	1.7238	1.7272	1.7293	1.7423	1.7569
1.080	1.7143	1.7167	1.7174	1.7176	1.7186	1.7172	1.7152	1.7182	1.7199	1.7202	1.7250	1.7366	1.7511	1.7681
1.120	1.7071	1.7097	1.7101	1.7118	1.7105	1.7110	1.7130	1.7120	1.7136	1.7199	1.7255	1.7401	1.7584	1.7789
1.160	1.7015	1.7016	1.7046	1.7023	1.7048	1.7076	1.7087	1.7093	1.7136	1.7225	1.7287	1.7436	1.7673	1.7942
1.200	1.6951	1.6959	1.6970	1.6989	1.6984	1.7012	1.7020	1.7105	1.7112	1.7204	1.7397	1.7611	1.7841	1.8150
1.240	1.6902	1.6925	1.6947	1.6919	1.6961	1.7007	1.7044	1.7117	1.7220	1.7332	1.7513	1.7711	1.7974	1.8332
1.280	1.6833	1.6861	1.6879	1.6910	1.6959	1.6999	1.7072	1.7151	1.7283	1.7390	1.7609	1.7865	1.8200	1.8578

(a) u Value

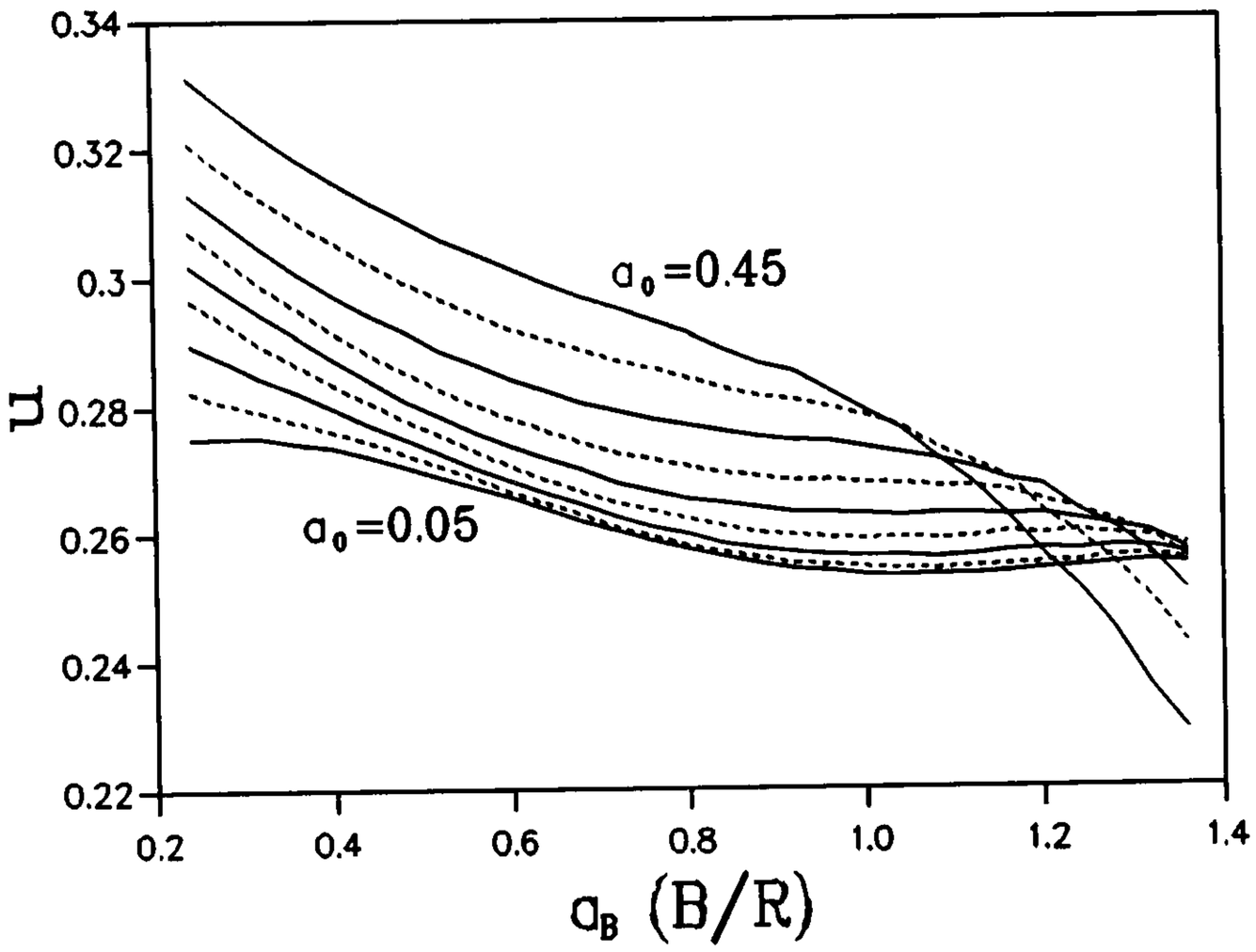

(b) v Value

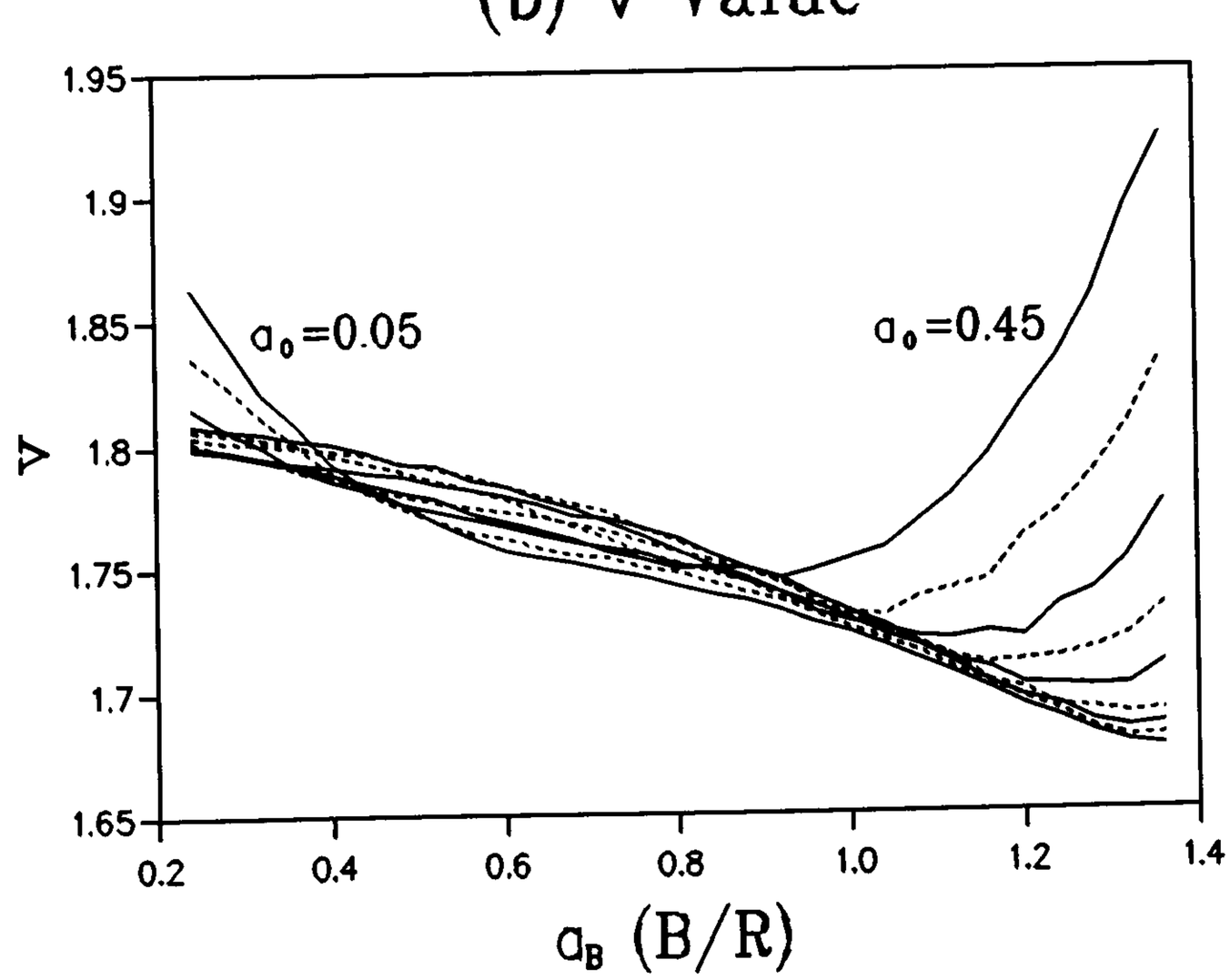

Figure 4.16 (a), (b) u and v Values

(a) u Value

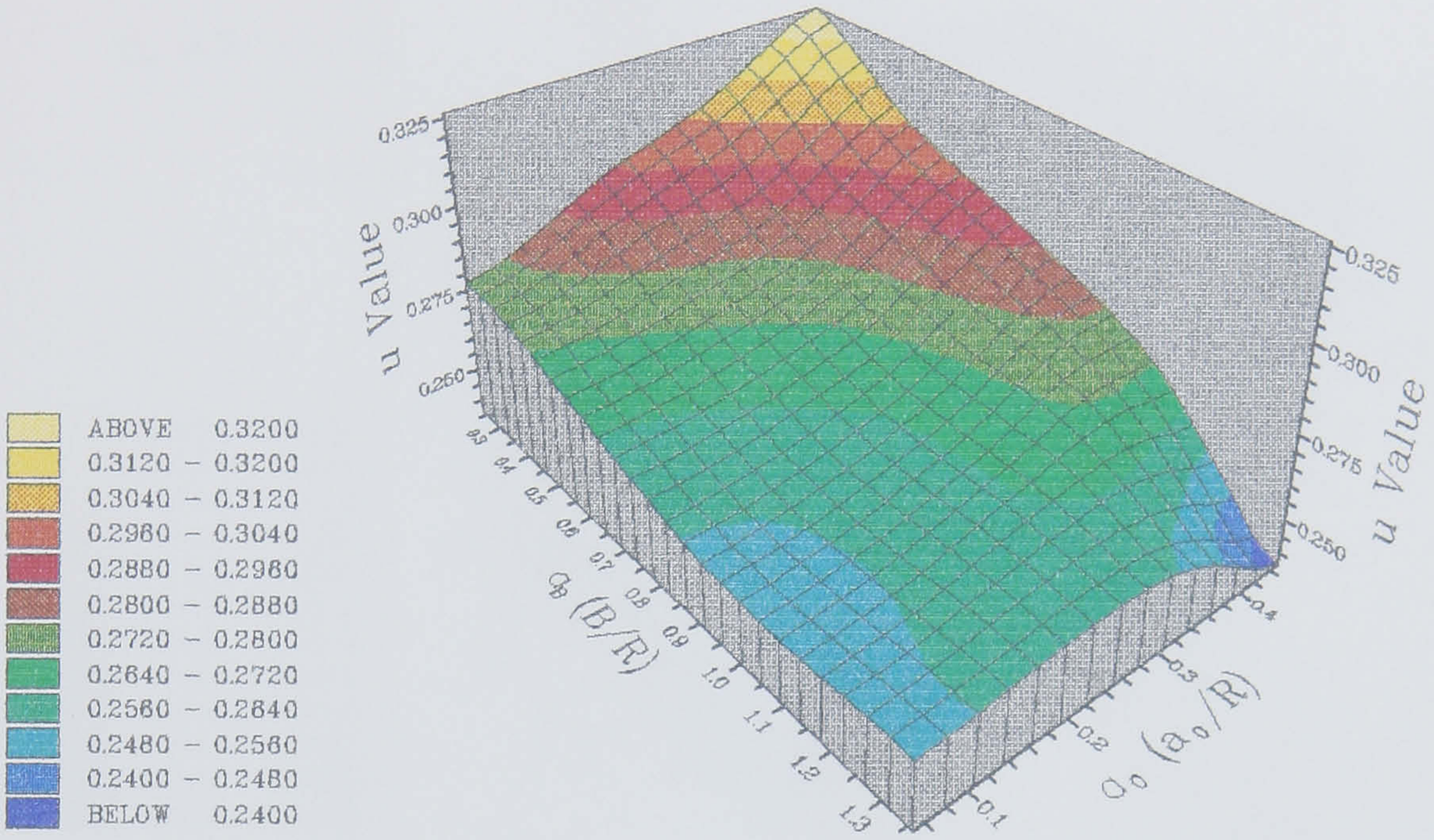

(b) v Value

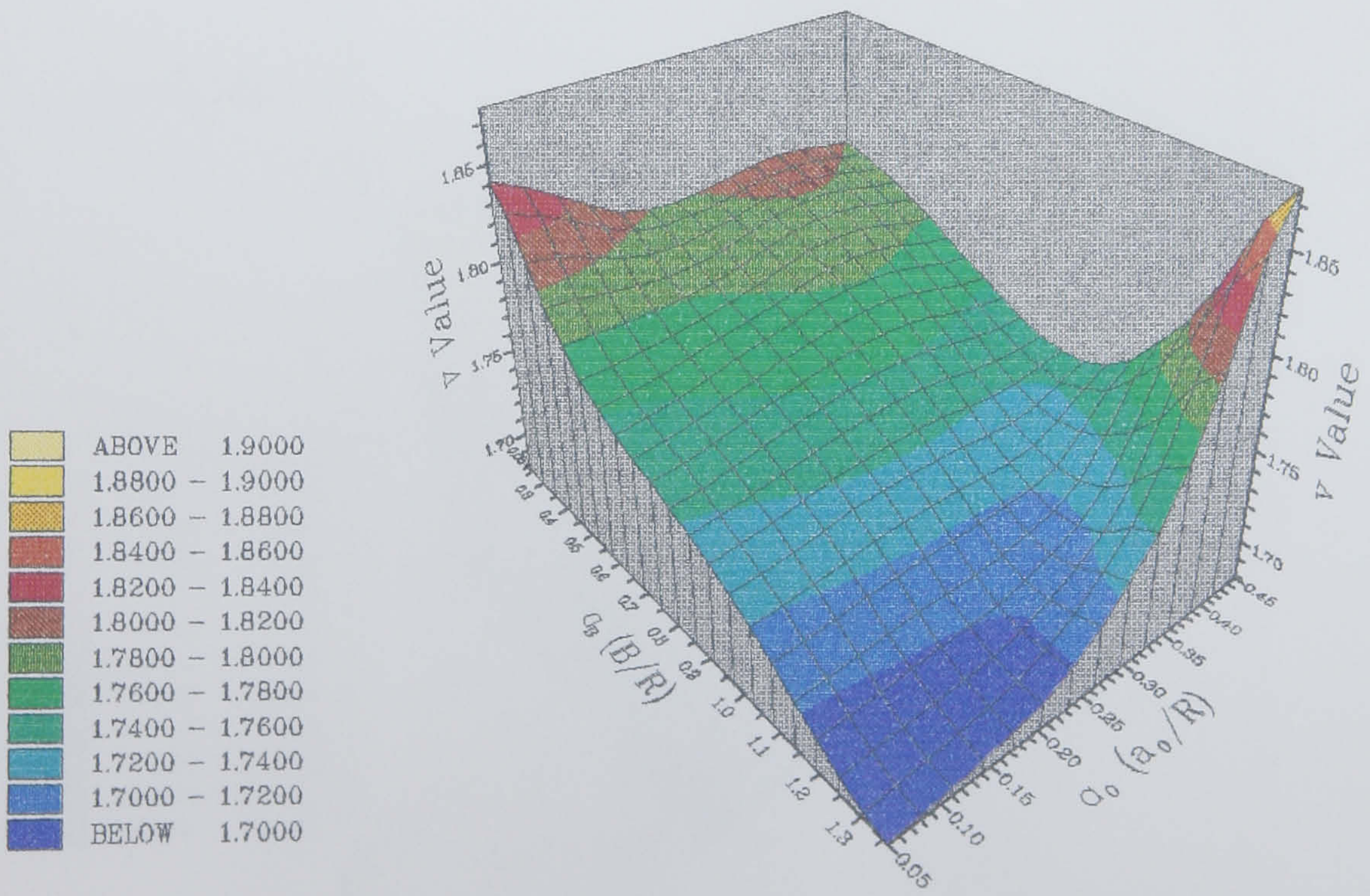

Figure 4.17 u and v vs α_0 and α_B

(a) Y^*_m vs α_1 and α_B

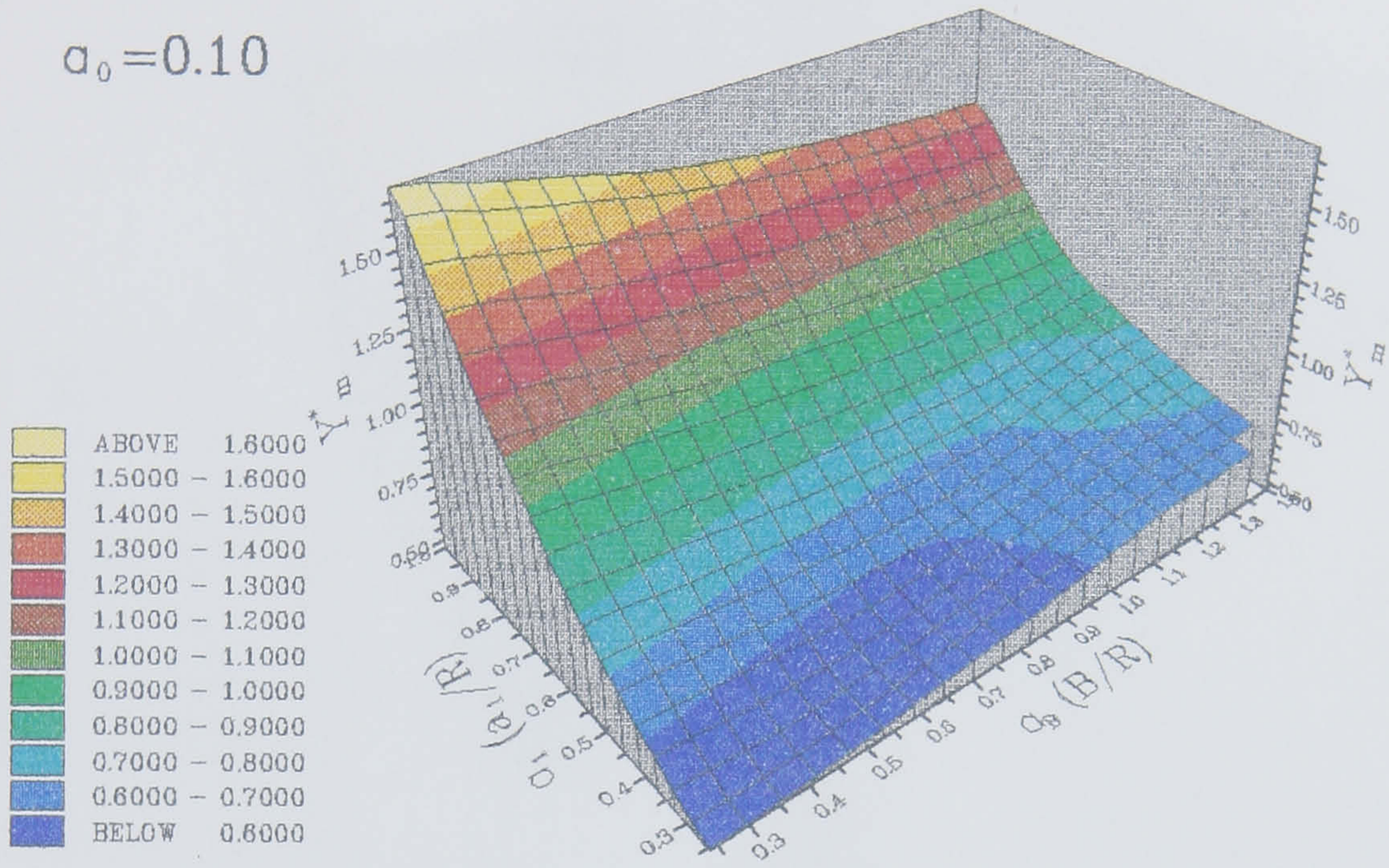

(b) Y^*_m vs α_1 and α_B

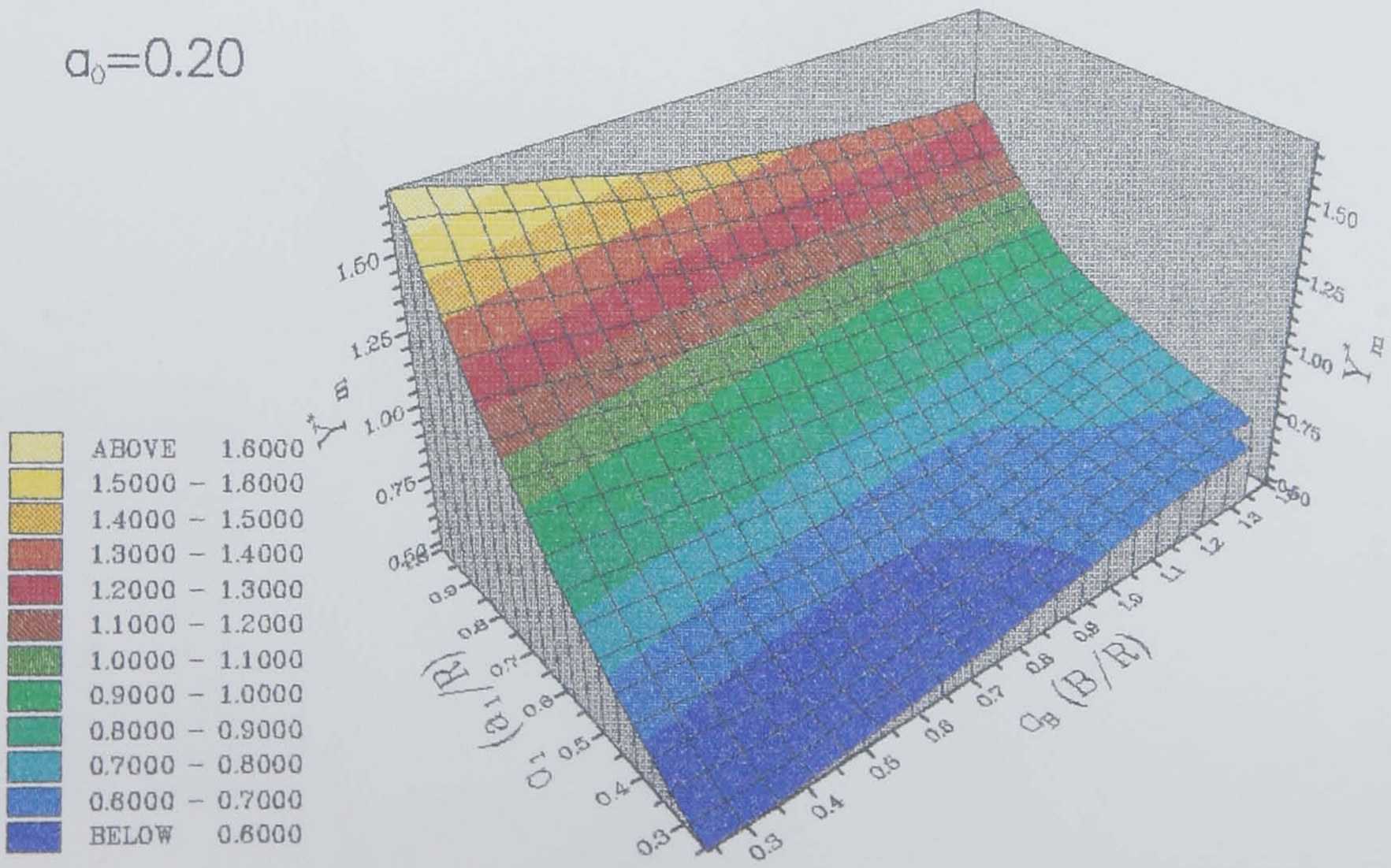

Figure 4.19 (a) and (b) Typical Y^*_m Variations ($\alpha_0 = 0.10$ and 0.20)

(c) Y^*_m vs α_1 and α_B

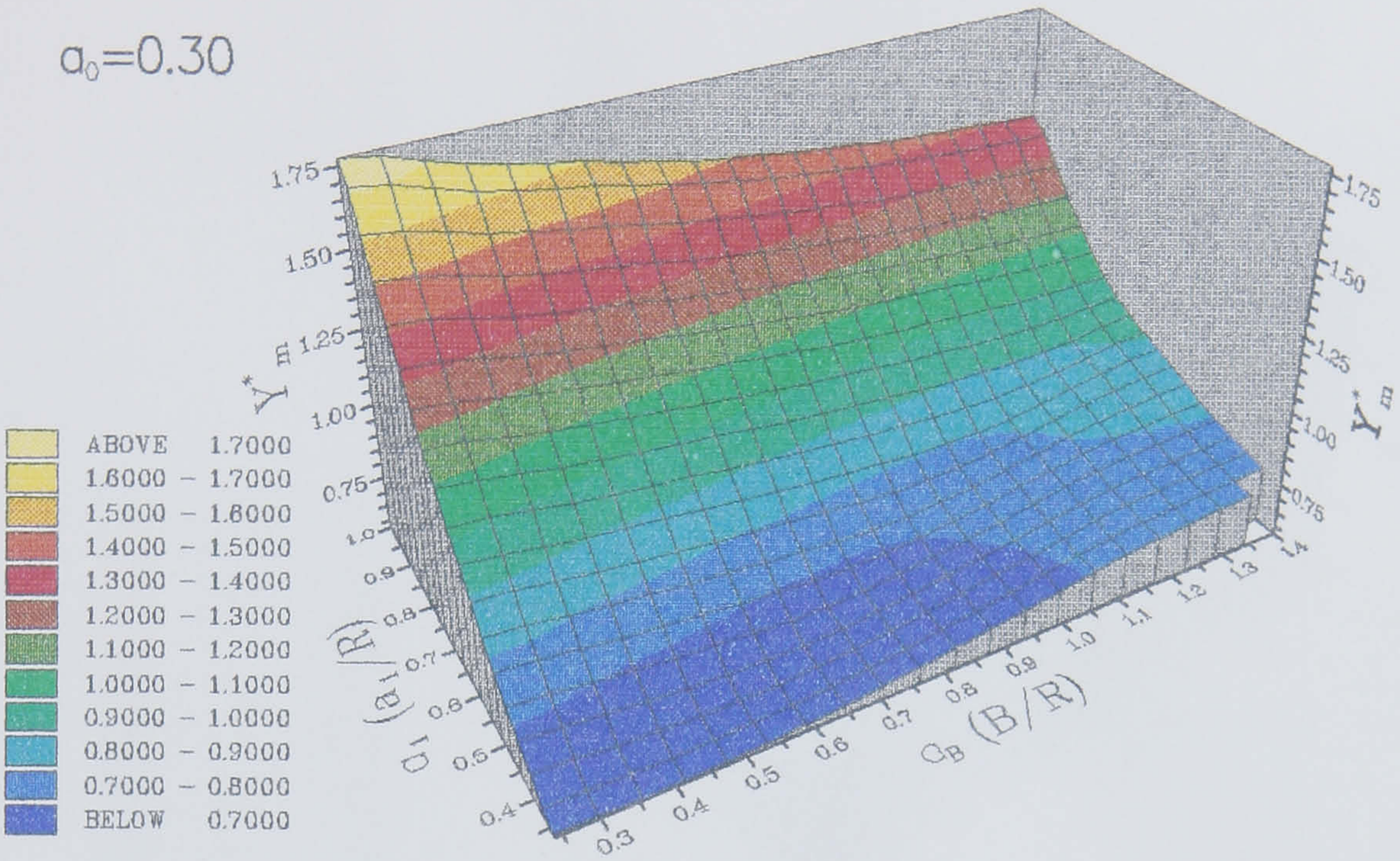

(d) Y^*_m vs α_1 and α_B

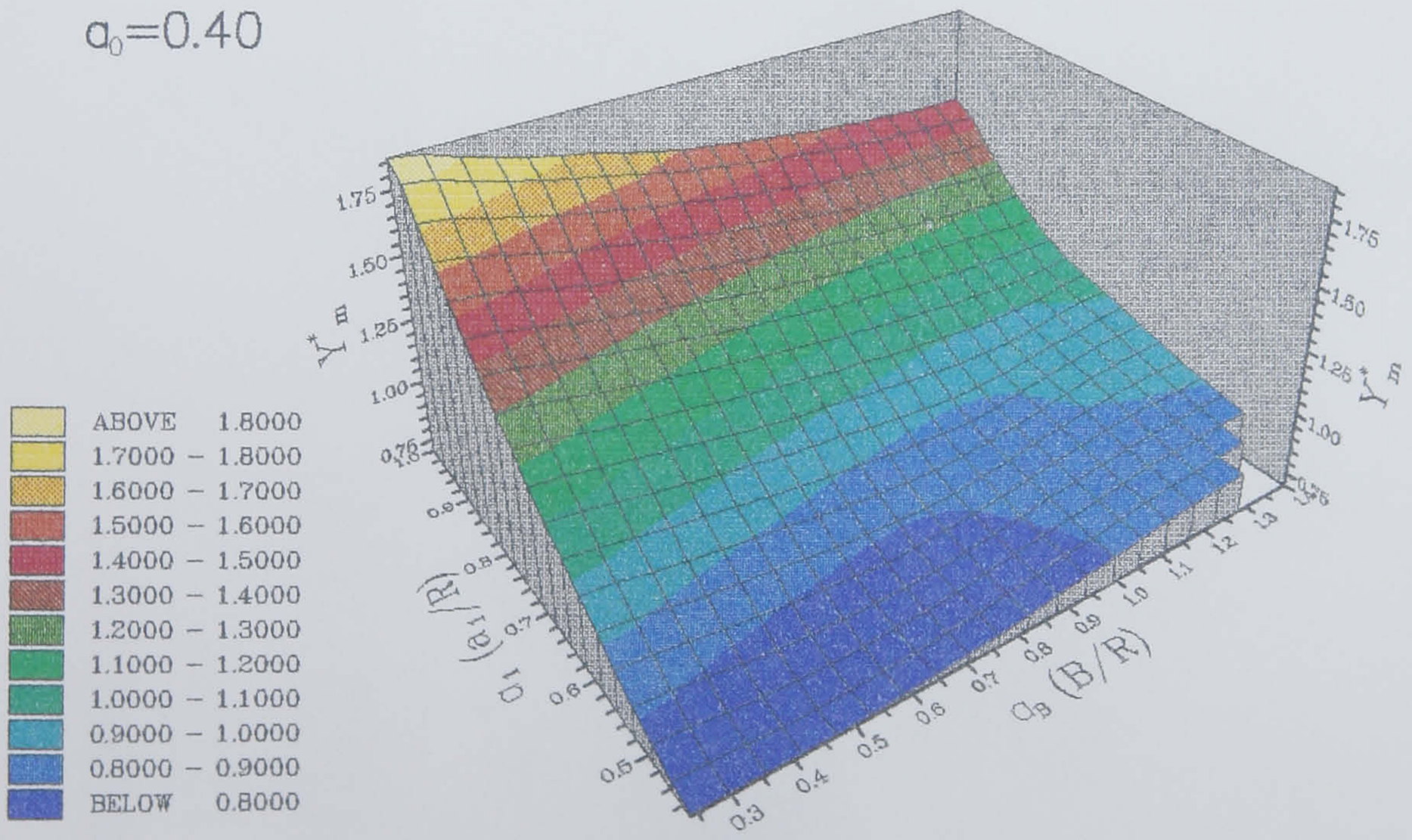

Figure 4.19 (c) and (d) Typical Y^*_m Variations ($\alpha_0 = 0.30$ and 0.40)

(a) a_m vs α_1 and α_B

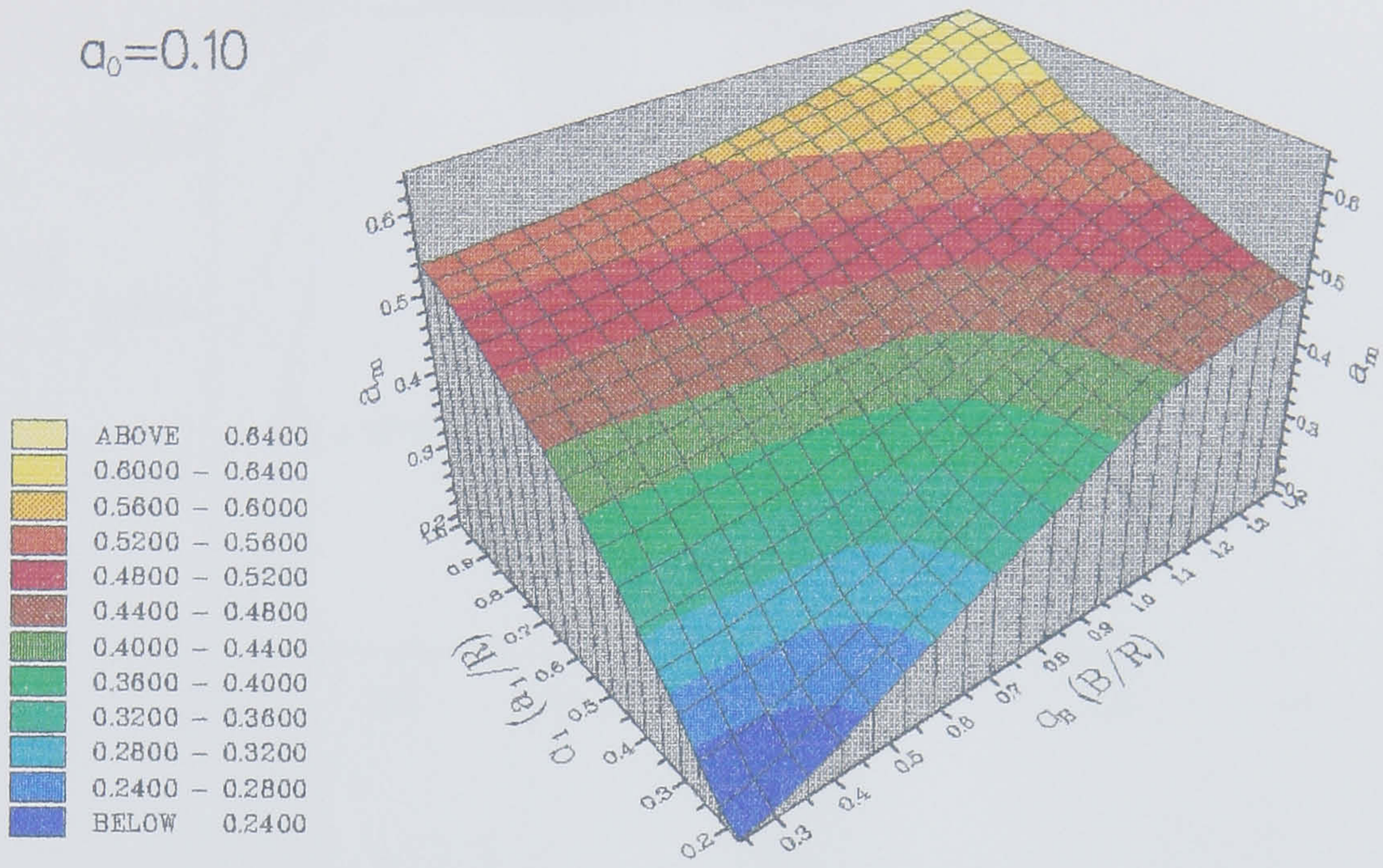

(b) a_m vs α_1 and α_B

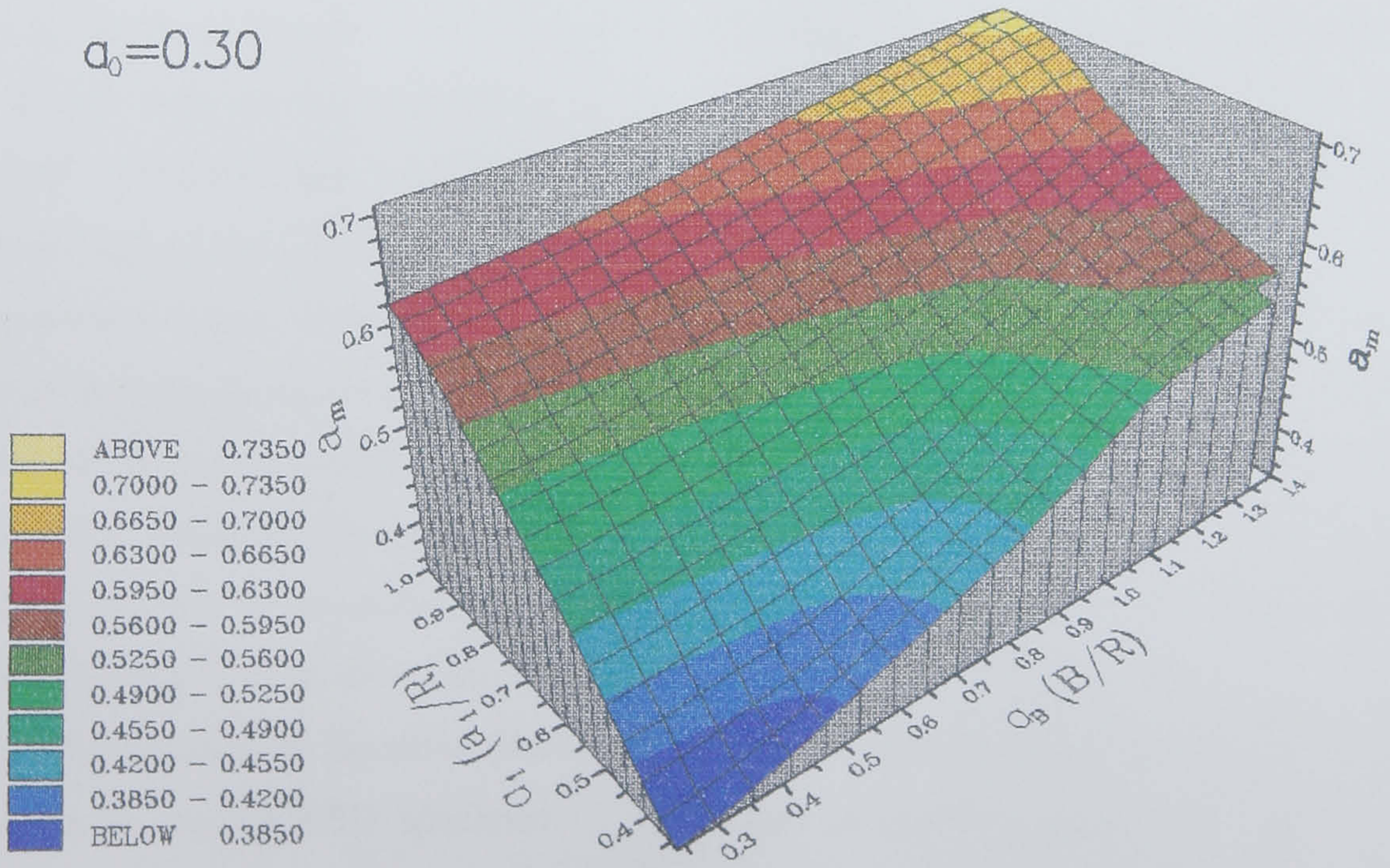

Figure 4.20 (a) and (b) Critical Crack Length a_m for $\alpha_0 = 0.10$ and 0.30

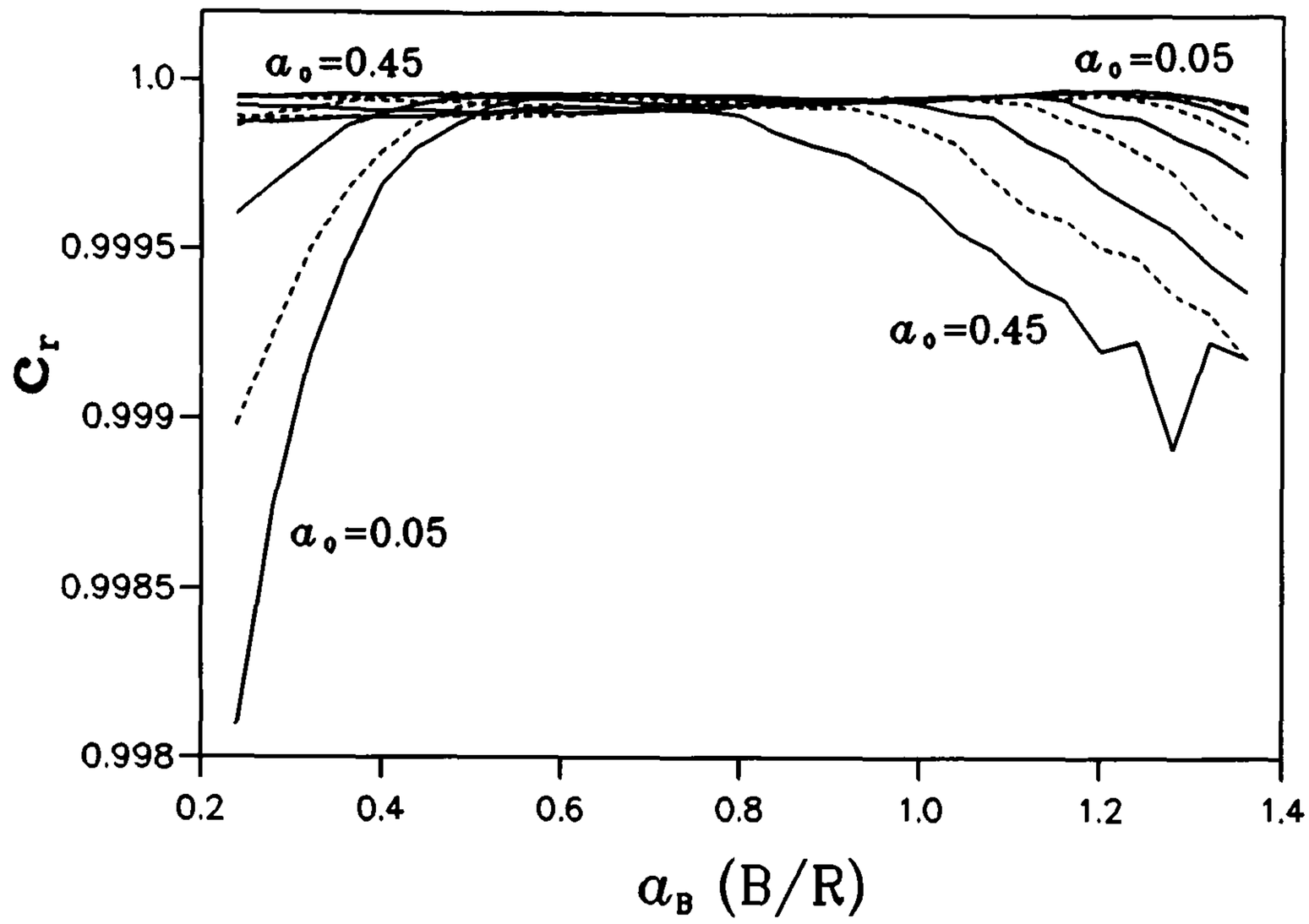

Figure 4.18 The Correlation Coefficients of the u and v values

4.19 (a), (b), (c) and (d) respectively. For reference, the critical dimensionless crack length values $\mathbf{a_m}$ for the groups of α_0 = 0.10 and 0.30 are presented in Figure 4.20 (a) and (b) as well even though they are not required to be known for $\mathbf{K_{IC}}$ calculation. The "**Ym**", "**am**", "ALFA0", "ALFA1" and "ALFAB" printed in these two figures are the "$\mathbf{Y^*_m}$", "$\mathbf{a_m}$", "α_0", "α_1" and "α_B" of the CCNBD specimens respectively.

From these figures shown above, it is found that the $\mathbf{Y^*_m}$ values vary widely when the α_B values of the specimens are outside the range of 0.44 - 1.04. This suggests the unsuitability of using the α_B values outside that range for the CCNBD specimens as larger errors could be introduced. Therefore these lower and upper bound values for the α_B requirement for a valid CCNBD specimen can be added into the valid specimen geometrical requirements and they are shown in Figure 4.13 as line 2 and line 5 respectively.

The combination of Equation (4.24) and Table 4.9 provides a simple tool for the $\mathbf{Y^*_m}$ evaluation of any CCNBD specimen. Therefore in practical application, the designed CCNBD specimen geometries do not have to be strictly controlled during the specimen machining. The actual specimen geometrical dimensions can be measured after specimen preparation or even after the test. As long as these geometrical parameters meet the valid

geometrical range requirements, the CCNBD specimens will generate valid (consistent) fracture toughness values $\mathbf{K_{IC}}$. The actual $\mathbf{Y^*_m}$ values of these valid specimens will be calculated according the practical values of α_0, α_1 and α_B. This good feature of the CCNBD specimens makes practical experiment much easier as we can always choose freely the specimen geometrical dimensions according to the availability of rock samples and the capacities of the machining equipment.

Another especially good feature of the CCNBD specimens is shown in the evaluation of the critical SIF $\mathbf{Y^*_m}$ for the specimens. The practical $\mathbf{Y^*_m}$ values for any CCNBD specimen is normally around 1.0 only, compared with 10.42 and 24.0 for the standard CB and SR specimens. If $\mathbf{K_{IC}}$ for a material is a constant, then from Equation (3.54) it is known lower $\mathbf{Y^*_m}$ values will always mean a larger failure load $\mathbf{P_{max}}$. Take the suggested standard CCNBD specimen CNC geometry (as listed in the last section) for example, $\mathbf{Y^*_m}=0.8798$, the output readings of failure load $\mathbf{P_{max}}$ in kN will be magnitudely 6.6032 times larger than the $\mathbf{K_{IC}}$ magnitude in MPa$\sqrt{m}$. The same factors will be only 1.0092 and 0.4382 for the suggested CB and SR standard geometries when D = 48.0 mm. In other words, a CCNBD specimen can work like an amplifier to increase the output reading magnitude from a generally very small input of fracture toughness value. But the output readings $\mathbf{P_{max}}$ (kN) for the standard CB specimens will remain at the same order as the $\mathbf{K_{IC}}$ (MPa$\sqrt{m}$) magnitude, while $\mathbf{P_{max}}$ (kN) for the standard SR specimens will be only around half of the $\mathbf{K_{IC}}$ (MPa$\sqrt{m}$) magnitude. Therefore when the CCNBD specimens are used for practical $\mathbf{K_{IC}}$ measurement, this good feature of the specimens will greatly reduce the extremely high requirement on the testing machine's low load range test ability set by the CB and SR methods, and will reduce the experimental measurement error at the same time. This good feature is of great significance especially for engineering purposes as it makes the test procedure cheaper, gives greater precision to the test results and allowes the test to be conducted in most rock mechanics laboratories.

§4.8 Error Evaluation

The errors in the determination of the CCNBD specimen geometrical parameters α_0, α_1 and α_B will cause a deviation of the calculated $\mathbf{Y^*_m}$ from the actual value. These geometrical errors could be due to the precision of measurement or some other random influences. If the errors in the CCNBD specimen geometrical parameters and the deviation of $\mathbf{Y^*_m}$ from the actual values are expressed as a percentage of their practical values, then their relations are illustrated in Figure 4.21. It is shown from the figure that there is generally low $\mathbf{Y^*_m}$ deviation from

its actual values caused by the error in the determination of the specimen geometrical dimensions, which implies that large tolerance in the specimen dimensions can be given in practical application. However note should be taken that deviation in $\mathbf{Y}^*_m$ value by the error in α_1 is much greater than those by the errors in α_0 and α_B. Therefore in a practical situation, a higher precision is required for the α_1 measurement than for the other two dimensions.

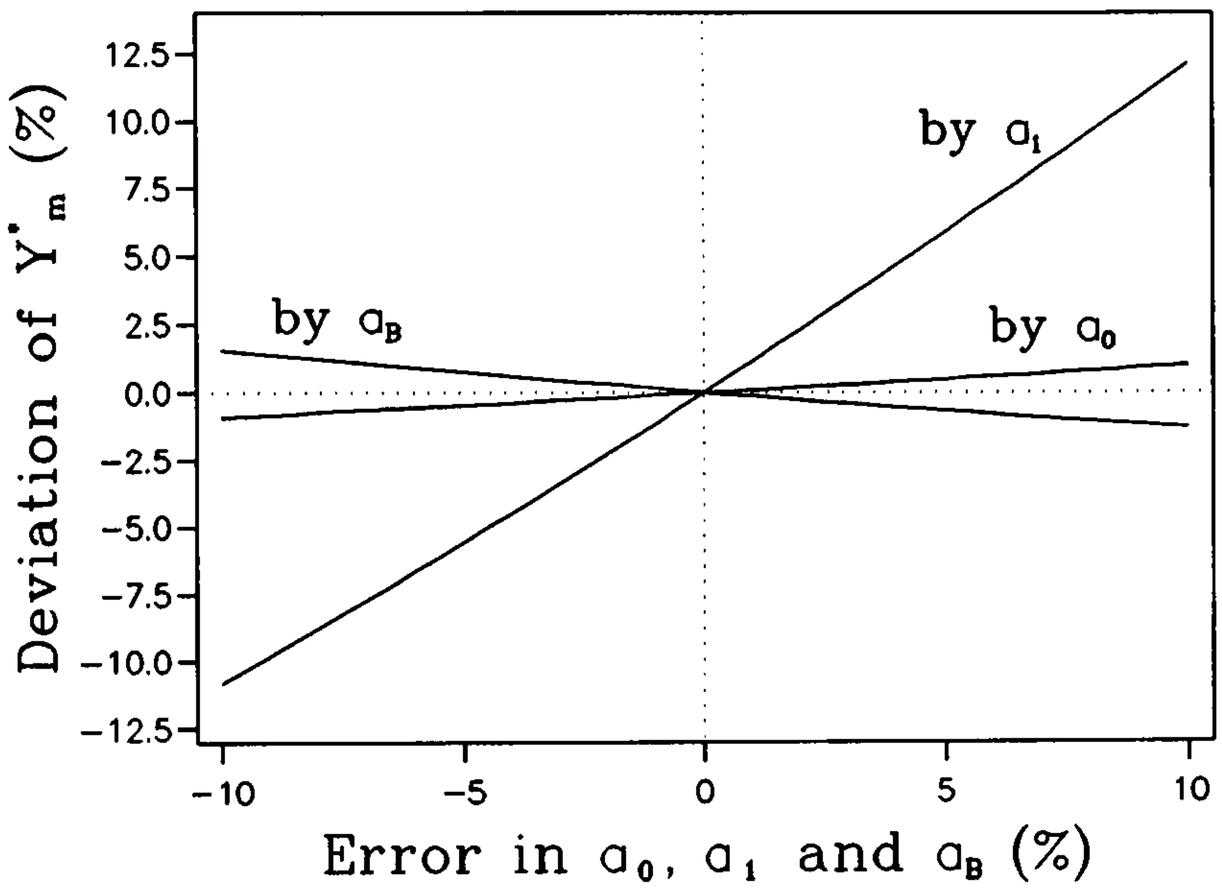

Figure 4.21 Error Evaluations

§4.9 Conclusions from the Numerical Calibrations and Suggestions for further Research

Based on the above evaluation and discussion, the following conclusions can be drawn:

1) The theoretical SIF evaluation method developed in Chapter 3 can generate SIF values which agree well with numerical calibration results up to the long crack case ($\alpha = 0.05$-0.95). This substantiates the suitability of the theory and the assumptions.

2) Bluhm's slice superimposition model is more suitable for simulating the CCNBD fracture problem compared with other models. The theoretical SIF $\mathbf{Y}^*(\alpha)$ values for the CCNBD specimens evaluated based on this model generally agree well with the numerical calibration results. Their differences , when the critical SIF values of the specimens, $\mathbf{Y}^*_m$, are concerned, have been found to be within $\pm 5\%$. Therefore this theoretical method developed

can be used to calculate the practical $\mathbf{Y^*_m}$ values for any CCNBD specimen with confidence.

3) In practical application, most of the CCNBD specimens designed for fracture toughness tests can be classified as the medium crack case. Therefore as the crack propagates, the dimensionless SIF $\mathbf{Y^*}(\alpha)$ of the specimen will reach its critical value, hence the system is at its critical state, before the crack propagation front arrives at the end of the chevron-notched part of the geometry. This reinforces the suitability of using the CCNBD as a chevron notched specimen for $\mathbf{K_{IC}}$ tests as it will keep all the advantages of a chevron notched specimen.

4) In order to have a valid rock fracture toughness test, the geometrical parameters of the CCNBD specimens should be within the valid geometrical range outlined in Figure 4.13. For a CCNBD specimen with the geometries within this range, its crack front when the specimen reaches its critical state can be considered to be under an approximate plane strain condition, and therefore it will generate valid (consistent) $\mathbf{K_{IC}}$ values for rock materials.

5) For any valid CCNBD specimen geometry, the critical (minimum) dimensionless SIF value, $\mathbf{Y^*_m}$, can be jointly calculated by Equation (4.24) and Table 4.10 according to its actual geometrical parameters. These values have been intensively and extensively calibrated and they can be used with confidence.

6) The minimum (critical) SIF values for the CCNBD specimens, $\mathbf{Y^*_m}$, are much less than those for the CB and SR specimens. Therefore in the CCNBD $\mathbf{K_{IC}}$ tests, the maximum (failure) load $\mathbf{P_{max}}$ will be much higher than those obtained in the other two test methods. In other words, a CCNBD specimen can work as an amplifier to enlarge the output readings (failure load) for small input (fracture toughness values). This considerably reduces the extremely high requirement on the testing machine's low load range test ability compared with the CB and SR methods. As a result, rock fracture toughness measurement will become a simple, convenient and low cost engineering practice which can be easily conducted in most of the rock mechanics laboratories.

7) The resulting deviation in $\mathbf{Y^*_m}$ from its actual value of a CCNBD specimen is insensitive to the errors in the geometry parameter determination. This gives greater tolerance to the determination of specimen geometries $\mathbf{a_0}$, $\mathbf{a_1}$ and $\mathbf{B}$ in the practical application and therefore more convenience and less error in the $\mathbf{K_{IC}}$ test can be expected.

8) The designed values $\mathbf{D}$, α_0, α_1 and α_B for CCNBD specimens can be used for approximate control of the specimen preparation but their values do not have to be

strictly observed during preparation. Their actual values can be measured after the specimens have been prepared or even after the test has been carried out. This is of great significance for practical application as less strict requirements for specimen preparation always means more convenient and less costly jobs. It also makes it possible for practical engineering users to always choose the specimen geometries according to the availability of rock samples and the capacities of the machining equipment.

Further research suggestions are proposed as follows:

1) The suitability of adopting metallic fracture research results to the analysis the plain strain requirement for the CCNBD specimens for rock materials has to be investigated both theoretically and experimentally. The research into this aspect is one of the areas studied in the experimental validation of the CCNBD specimens which will be presented in the next chapter.

2) It is believed that the CCNBD specimens could be the best chevron notched geometry at the present to be used for rock mixed mode fracture studies and rock anisotropic studies. Therefore numerical calibrations for these purposes are recommended.

Chapter 5

Experimental Validation of the CCNBD Geometry for Mode I Rock Fracture Toughness Measurement

§5.1 Introduction

For practical application reasons, the CCNBD specimens for $\mathbf{K_{IC}}$ measurement of brittle materials have to be experimentally validated. By comparing the $\mathbf{K_{IC}}$ results with those obtained by other testing methods, the conclusions reached by the theoretical evaluation argued in the last chapters can then be substantiated experimentally. This will provide a solid basis for recommending the CCNBD as a better $\mathbf{K_{IC}}$ measurement method for brittle materials, especially rock. According to the theoretical discussion, the validation will include the studies of the influences of specimen geometry and the investigations of minimum specimen size requirements. The reference $\mathbf{K_{IC}}$ testing methods selected are the ISRM recommended CB and SR methods for rock materials.

§5.2 Specimen Design

§5.2.1 Rock Samples

Eighteen rock samples ranging from soft sandstone to hard granite were chosen for this purpose. Some conventional rock mechanical properties, Young's modulus **E**, uniaxial compressive strength σ_c, tensile strength σ_t, Poisson's ratio ν and some other rock characteristics have been measured. They are classified into two categories according to these property parameters and the validation requirements. Table 5.1 is the list of these rock samples and their measured mechanical properties.

For uniaxial compressive strength σ_c test, two groups of specimens were prepared for each rock sample with $\phi 48 \times$ L96 (mm $\times$ mm) and $\phi 25 \times$ L50 (mm $\times$ mm) (where ϕ is the specimen diameter and **L** is the length) respectively. There were at least two test specimens in each group for each rock sample. The Young's modulus **E** and Poisson's ratio ν were measured by strain gauges glued on the $\phi 48$ mm diameter test samples. The tensile strength σ_t was determined by the Brazilian disc method. Two groups of specimen geometries of $\phi 75 \times$ B37.5

Table 5.1 Rock Samples Used for Experimental Validation

Spl.	Sample Descriptions	E (GPa)	ν	ϱ (T/m^3)	σ_c (MPa)	σ_t (MPa)
1	yellow sandstone, fine grained.	10.598	0.360	2.243	50.930	3.4766
2	red sandstone, fine grained.	15.551	0.264	2.308	73.227	3.3568
3	red sandstone, coarse grained.	11.116	0.340	2.204	47.612	4.0287
4	grey sandstone, medium grained.	13.751	0.301	2.146	48.484	3.4568
5	green sandstone, very fine grained.	12.110	0.173	2.384	102.64	7.3958
6	cream limestone, soft.	7.794		1.964	17.526	2.0194
7	anhydrite, very fine grained, fractured.	22.845	0.267	2.964	104.31	8.0132
8	Scotish white granite, very hard.	43.705	0.096	2.628	217.53	11.046
9	dolomite, fine grained, very hard.	56.702	0.256	2.928	295.55	20.857
10	dolomite, coarse grained.	40.269	0.161	2.894	191.71	13.565
11	pink mottled sandstone.	10.147		2.152	62.844	3.0599
12	pink sandstone, medium grained.	9.928		2.179	66.350	2.6733
13	grey limestone, coarse grained.	12.105		2.715	54.407	4.1511
14	white limestone, fractured.	26.082		2.524	102.28	7.9612
15	grey limestone, fined grained.	26.110		2.714	98.578	5.4919
16	cream bedded sandstone, fine grained.	18.632		2.550	147.15	13.419
17	grey limestone, fine grained.	12.644		2.470	82.803	8.3319
18	grey dolomite, fine grained, with quartz.	37.009		2.747	156.99	17.576

(mm × mm) and ϕ48 × B24 (mm × mm) (where ϕ is the disc diameter and **B** is the thickness of the disc) were prepared for each rock sample and there were at least two test specimens in each of these two groups. The property parameters presented in Table 5.1 are the average of the measured values for the tested samples.

§5.2.2 Specimen Geometry I -- Geometry Influence Studies

From the evaluations in the last chapter, any CCNBD specimens with the geometry parameters inside the range outlined in Figure 4.13 should theoretically generate the same value when used in a practical experiment. This point was to be validated by two categories of CCNBD specimens. The first category of the CCNBD specimens for this geometry influence study consists of three groups of specimens, G1, G2 and G3, with different geometrical parameters. Rock sample 1 to sample 10 were selected for this test. The geometrical dimensions for the specimens in the same groups but from different rock samples were kept identical. At least four test specimens were prepared for each group of each rock sample. The geometrical positions of these three groups are shown as G1, G2 and G3 in Figure 5.1 respectively and the details of the designed specimen dimensions are listed in Table 5.2.

The second category of CCNBD specimens for geometry influence study came from Chen [1989]. One single rock sample (block) was used to produce 24 groups of CCNBD specimens with different geometrical parameters. The geometrical dimensions of these 24 groups are identical to those of the CCNBD specimens used for the numerical calibration studies discussed in the last chapter. The geometrical positions of these 24 groups of specimens are also shown in Figure 5.1. As can be seen, they were designed to be within, around and far outside the valid geometrical range obtained from numerical calibration. They are widely distributed all over the α_1-α_B range and are intended to cover all the possible CCNBD geometrical range, therefore the characteristics for different possible CCNBD geometries can be obtained. Rock sample 20 which is listed in Table 5.9 was selected for this study.

§5.2.3 Specimen Geometry II -- Specimen Size Influence Studies

Specimen size, taken as the CCNBD diameter **D**, is another important factor, apart from the geometries, for the determination of the validity of the $\mathbf{K_{IC}}$ test. Large specimens are always recommended so that it will be easier to satisfy the plane strain conditions, which is believed to generate a consistent material property value $\mathbf{K_{IC}}$, and therefore less error will be caused by the boundary conditions. However it is not practical to use extremely large specimens, but a valid specimen size must be used instead. Therefore a valid minimum (critical) specimen

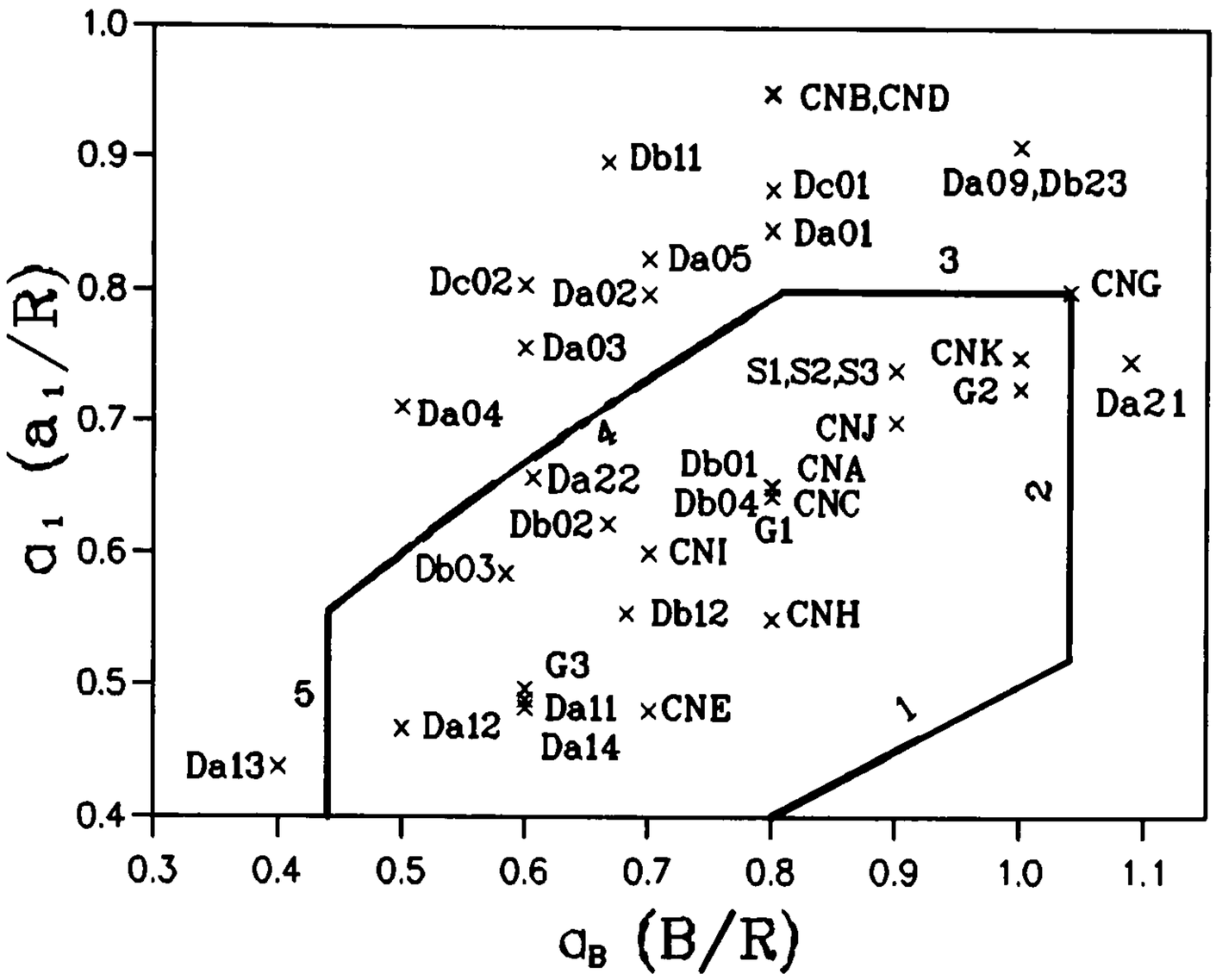

Figure 5.1 Geometrical Positions of the CCNBD Specimens Used for Experimental Validation

size needs to be determined.

Another three groups of specimens S1, S2 and S3 were designed for this size influence study. The geometrical parameters α_0, α_1, α_B and α_s of these three groups were kept identical, but different specimen diameters, **D** = 65, 75 and 100 mm, were used for these three groups respectively. The details of their dimensions are listed in Table 5.2 and their geometrical positions are shown in Figure 5.1 as points **S1**, **S2** and **S3**. Rock samples 1, 5, 6, 8, 9, 10, and 11 to 18 were chosen for this test. At least four test specimens were prepared for each size group (S1, S2 or S3) from each rock sample.

§5.2.4 Specimen Geometries Used for Reference Testing

In addition, CB and SR specimen geometries were selected for comparison testing. The diameter of **D** = 48mm and **D** = 42mm were used for these two specimens and their geometrical details are listed in Table 5.3. Their configurations are shown in Figures 5.2. The tests were conducted on every rock sample used for the CCNBD experimental validation study.

Table 5.2 Specimen Design for CCNBD Experimental Validation Studies

Name	G1	G2	G3	S1	S2	S3
D (mm)	75.0	100.0	100.0	65.0	75.0	100.0
α_0	0.2667	0.30	0.25	0.2674	0.2674	0.2674
α_1	0.6505	0.7262	0.4960	0.74	0.74	0.74
α_B	0.80	1.0	0.60	0.90	0.90	0.90
D_S (mm)	52.0	75.0	52.0	52.0	60.0	80.0
α_S	0.6933	0.75	0.52	0.80	0.80	0.80
C.D.(mm)	17.0	28.1307	18.202	16.12	18.6	24.8
Rock Samples Used	1,2,..., 10	1,2,..., 10	1,2,..., 10	1,5,6,8,9, 10,11,12, ...,18	1,5,6,8,9, 10,11,12, ...,18	1,5,6,8, 9,10, 11,12, ...,18

Table 5.3 CB and SR Geometries for Comparison Testing

Notations	CB		Notations	SR
D (mm)	48.0	42.0	D (mm)	48.0
L (mm)	200.0, 160.0	80.0, 100.0, 150.0	W (mm)	70.0
S	3.33D, 2.5D	3.33D, 2.5D, 1.5D	θ (°)	54.6
θ (°)	90.0	90.0	a_0	0.48D
a_0	0.15D ± 0.02D	0.15D ± 0.02D	W-a_1	0.02D
†C.D. (mm)	0.25D	0.25D	C.D. (mm)	0.97D

†C.D.: Diamond saw cutting depth.

For all the different test geometries mentioned in these three sections, at least four test specimens were prepared for each group for each rock sample. For the CCNBD geometry, as mentioned in the last chapter, the designed specimen geometries listed in Table 5.2 were only used as a guideline for the specimen preparation. Therefore the practical geometrical dimensions after specimen preparation were slightly different from the values of the experimental design, dependent on the rock sample's size availability and the machining condition. Their actual values were measured after specimen preparation or after the test. It is these actual values which are to be used for the actual $\mathbf{Y}^*_m$ evaluation for each tested specimen.

Figure 5.2 The Chevron Bend (CB) and the Short Rod (SR) Specimens with Basic Notations

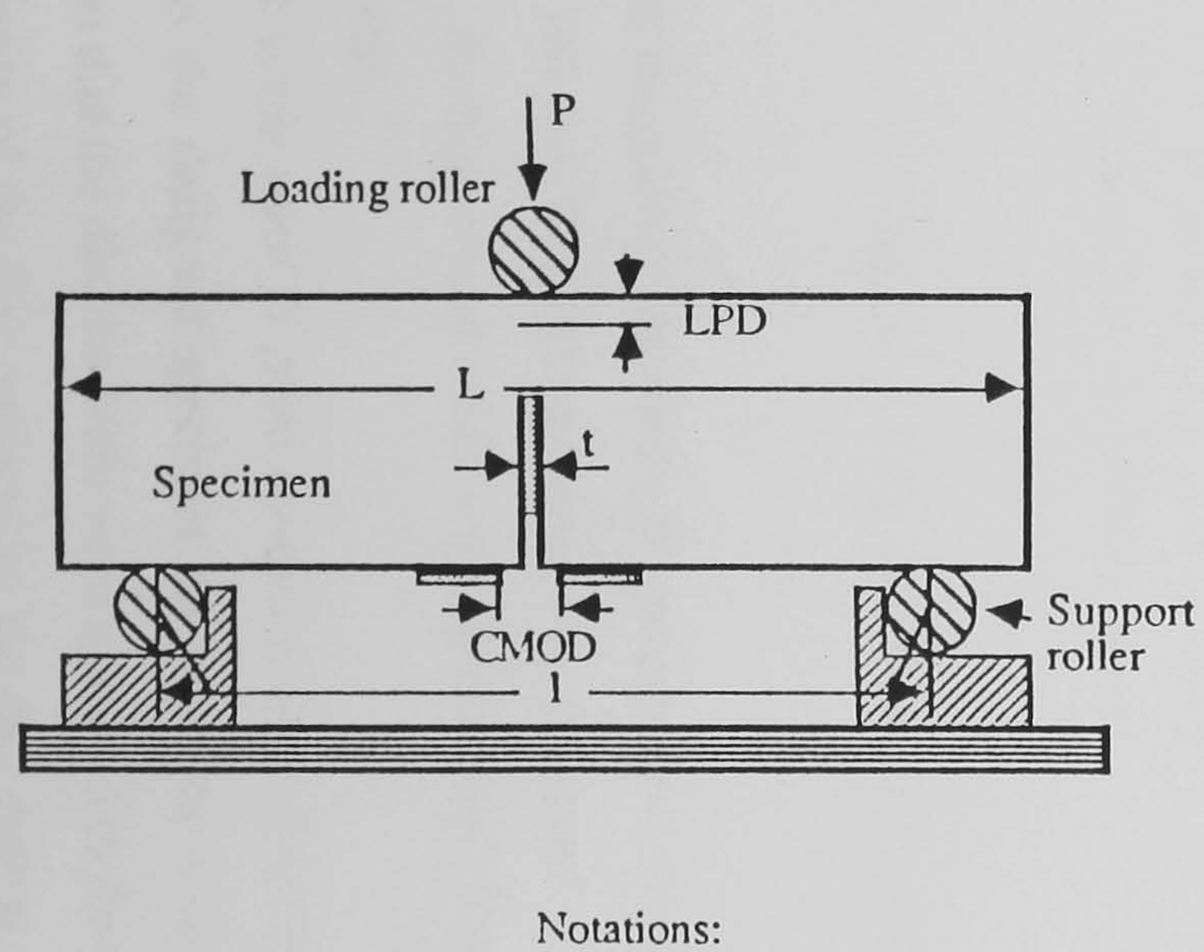

Notations:
A = Ligament area
D = Specimen diameter
l = Loading span, 3.33D
a = Crack length
a_o = Chevron tip distance from specimen surface, 0.15D
h = Depth of cut in notch flank
B = Crack front width
t = Notch width
L = Specimen length
P = Applied load
2θ = Chevron angle, 90°

(a) Chevron Bend (CB) Specimen

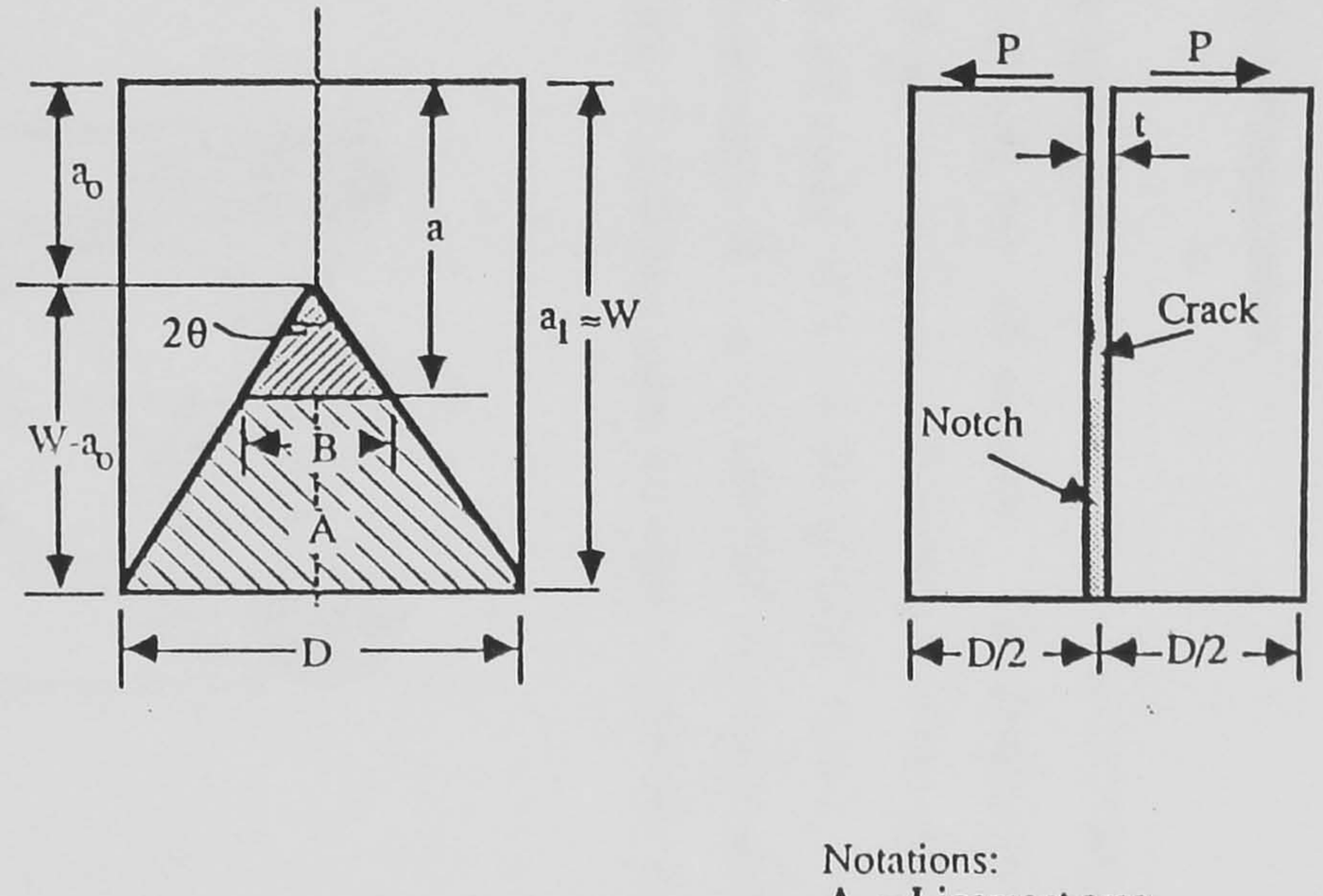

Notations:
A = Ligament area
D = Specimen diameter
a = Crack length
a_o = Chevron tip distance from load line, 0.48D
a_1 = Maximum depth of chevron flanks, $a_1 \approx W$
B = Crack front width
t = Notch width
W = Specimen height
P = Applied load at the notch mouth
2θ = Chevron angle, 54.6°

(b) Short Rod (SR) Specimen

§5.3 Testing Methodology and Equipment

§5.3.1 Specimen Preparation

A workshop milling machine was used for the CCNBD specimen preparation. Simple jigs were required to hold the rock sample. The dimensions of the jig are shown in Figure 5.3, where **D** and **B** are the diameter and thickness of the specimen to be machined, **L** is the width of the jig and the range of $\mathbf{L > 1.5D}$ is used, $\angle\mathbf{A}$ is the angle of slot for holding the rock specimen and the range of $\angle\mathbf{A} = 110^{o}\text{-}130^{o}$ was used, and **H** is the thickness of the jig and the range of $0.25D \sim 0.35D$ was used in order to provide a good guide for specimen machining alignment.

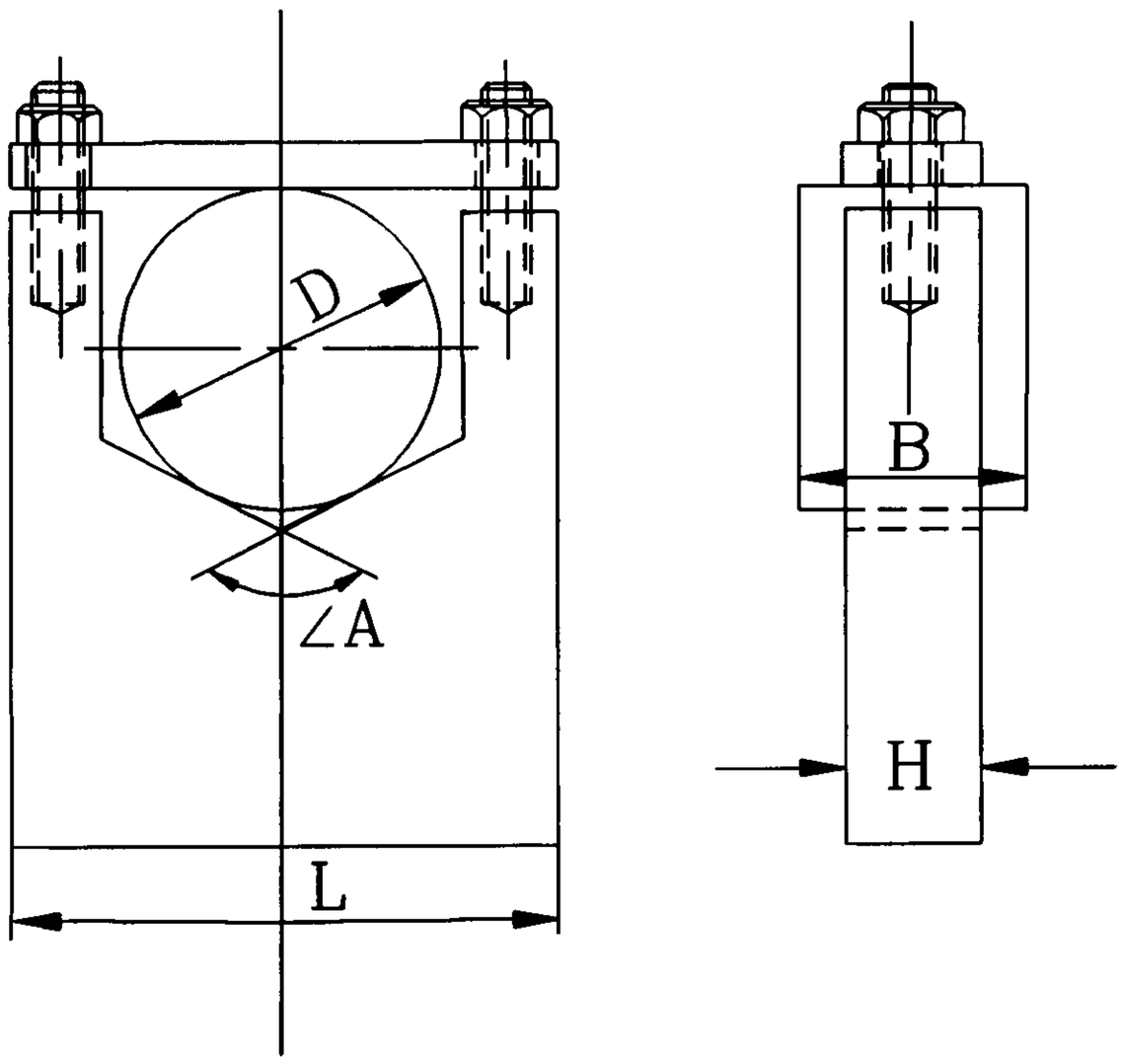

Figure 5.3 Jig for CCNBD Specimen Preparation

For a rock mechanics laboratory preparing these specimens, a series of these jigs for $\mathbf{D} = 65$, 75, 85 and 100 mm CCNBD specimens is suggested. It is recommended that for the jig's thickness **H**, the high bound value $\sim 0.35D$ for small **D** and low bound value $\sim 0.20D$ for large **D** is to be used.

The rock cores were in good condition when they were used. They were cut into discs according to the designed specimen thickness by a diamond saw. The cutting speed is controlled so that the disc surfaces were smooth and there were no rough cutting traces. The perpendicularity of the disc surfaces to the disc central axis (rock sample core axis) was well controlled to within the recommended 1%. If these conditions were not met a grinding

machine was then used to ensure the satisfaction of these requirements.

Thereafter the designed crack orientations were decided and clearly marked on both sides of the disc surfaces. The disc was then mounted in a jig and then fixed on to the milling machine. The mounted disc surfaces were kept perpendicular to the plane of the surface of the cutting saw. The starting cut point was right in the centre of the disc. Then cutting continues to the cutting depth C.D. = $\mathbf{h_c}$ which can be calculated by the following equation from the designed geometrical values,

$$h_c = (\alpha_s - \sqrt{\alpha_s^2 - \alpha_1^2})\cdot R = (\alpha_s - \sqrt{\alpha_s^2 - \alpha_0^2})\cdot R + \frac{B}{2} \qquad (5.1)$$

Then the other side of the disc was turned to the cutting saw and the same cutting depth $\mathbf{h_c}$ was taken. The cutting procedure is shown in Figure 5.4, where $\mathbf{D_s}$ is the diamond saw diameter, $\mathbf{d_s}$ is the diameter of the rotating axis holding the diamond saw and in our machining requirement $\mathbf{d_s} = 10$ mm was used. Clean tap water was used as the cutting cooling liquid.

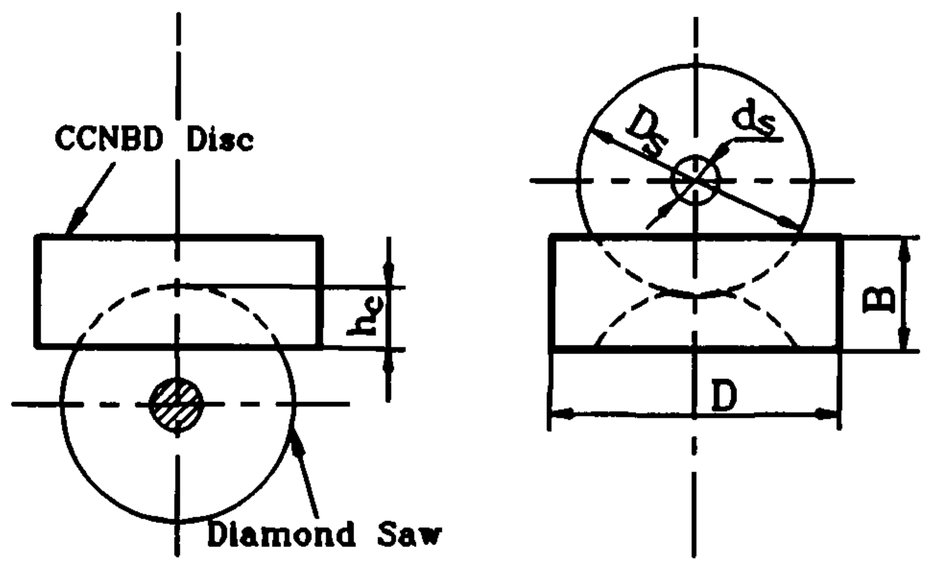

Figure 5.4 CCNBD Specimen Cutting

The specimen was removed from the jig and the mud inside the notch slot were washed away using clean tap water. After 24 hours of drying in the oven at a temperature of 104° the specimens were ready to be tested.

The following dimensions were then measured: specimen diameter **D**, thickness **B** and crack length $\mathbf{a_1}$. The error in the measurement was kept within ± 0.01 mm for the dimensions measured, especially for the $\mathbf{a_1}$ measurement according to the discussion in section §4.8. Generally the measured geometrical dimensions will be slightly different from the original designed values. The dimensions $\mathbf{a_1}$ and **B** were then converted into dimensionless expressions α_1 and α_B.

It is worth here to point out that by careful design of the crack orientations, the CB, SR and CCNBD specimens can be machined from the same cores and their crack orientations can be arranged to signify three perpendicular planes of the rock sample respectively. In other words, the rock anisotropic fracture characteristics can be easily modelled by a set of these three specimens from a single core. Therefore they together will compose a complete set of specimens for $\mathbf{K_{IC}}$ measurement for rock materials.

§5.3.2 Testing and Recording Equipment

The testing alignment used in our experiment is shown in Figure 5.5. The CCNBD specimen was placed between the upper and the lower loading plates. The crack plane was kept perpendicular to the loading plates within 0.5%. A specimen setting up and alignment checking aid was designed which is shown in Figure 5.6, where the thickness of the thin metal plate is equal to the chevron notch slot width in order to keep the perpendicularity requirement. The checks were carried out each time before loading.

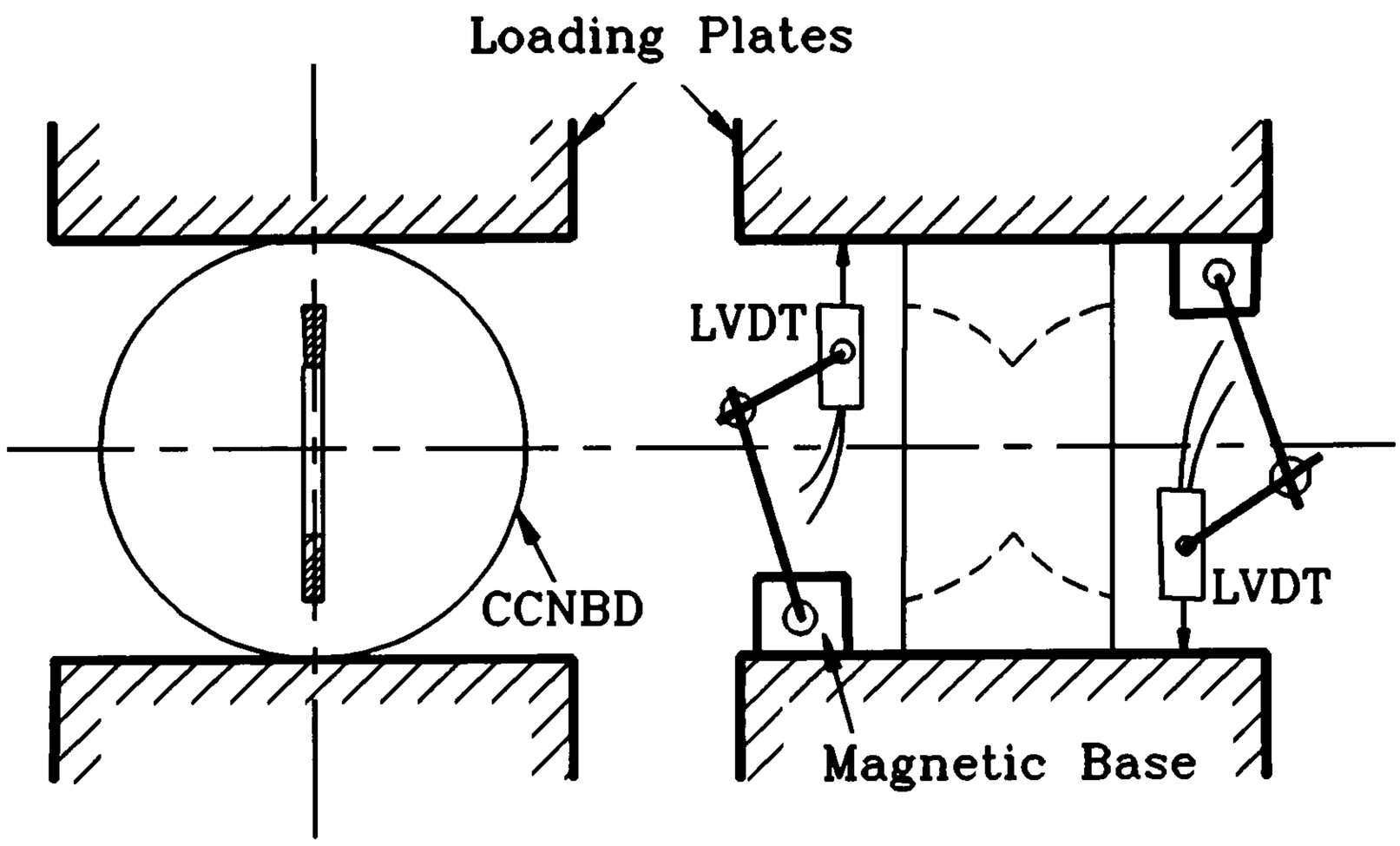

Figure 5.5 Testing Fixture

As an alternative, two LVDT displacement transducer can be mounted on each side of the specimen to measure the relative displacement of the upper and lower plates if both the load and the displacement are to be recorded.

A MAND testing machine was used for our experiment. The main features related to our studies are listed as follows:

1. Load Range: 0-25, 0-50, 0-100, 0-250 kN
2. Loading Control:

   Manual Control

   Servo Control: Displacement Control: Rate Range:0.001-1.0 mm/s

   Preload: 0 kN

   Load Control: Rate Range: 0.1-10 kN/s

   Preload: 0.76 kN
3. Displacement Range: ±5 mm, ±50 mm

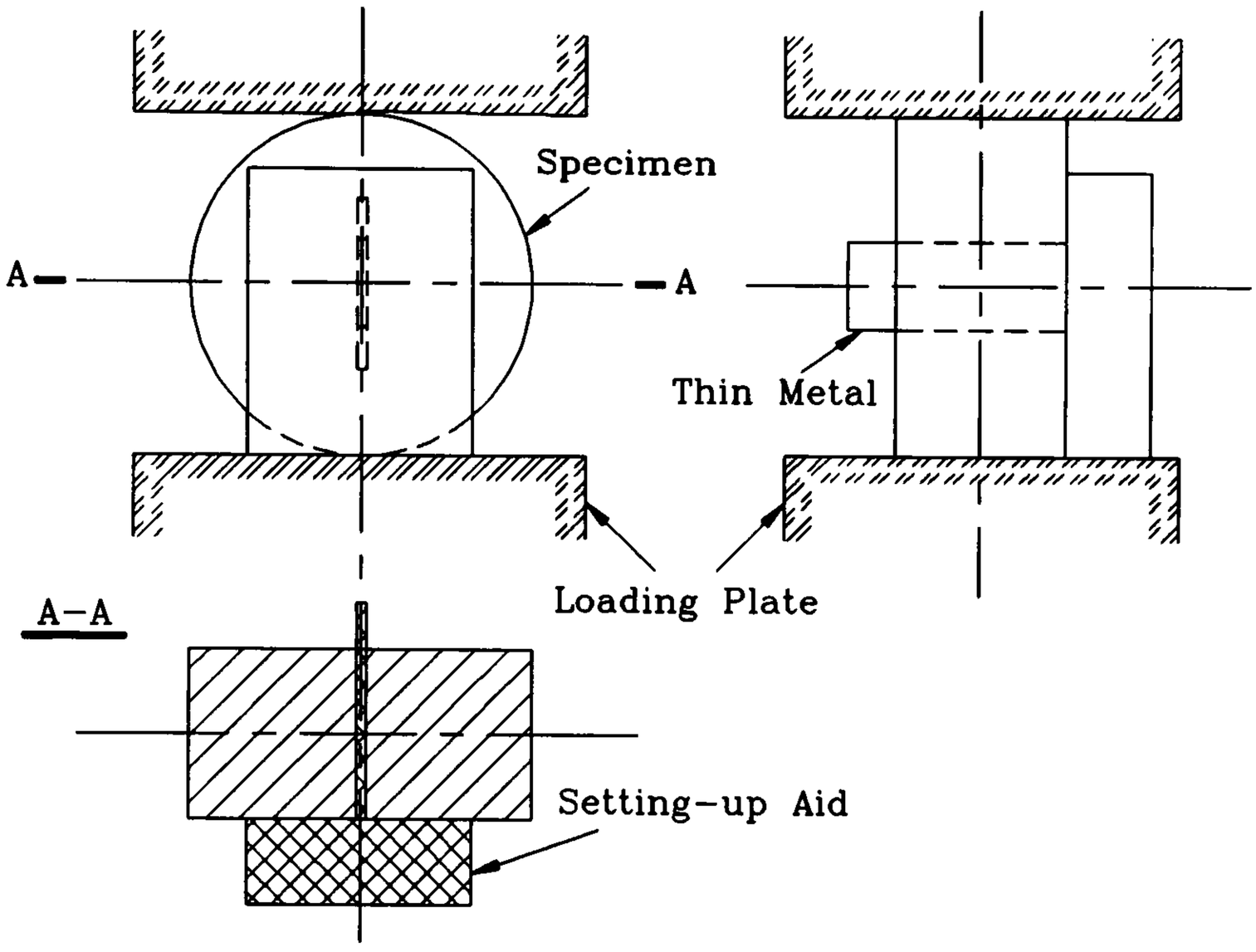

Figure 5.6 Setting-up Aid

The load **P** vs loading point displacement **u** was recorded by an X-Y plotter. Then the recorded traces were analyzed with the help of a data scanner machine connected to a PC computer, where the maximum (failure) load $\mathbf{P_{max}}$ and the compliance value **CBE'** corresponding to the different load magnitudes were calculated.

One important point about the testing is the determination of the loading rate. As suggested by Ouchterlony [1989], the crack propagation rate for rock fracture toughness tests should be higher than 0.01 mm/s in order to have a valid result. If we still use this criteria for the CCNBD test, the loading rate for the tests should be over 0.007 mm/s for displacement control or 0.10 kN/s for load control. Too low a loading rate will initiate the fatigue propagation of the crack and should be avoided. As different $\mathbf{K_{IC}}$ will correspond to different failure loads therefore the loading rate should be related to the $\mathbf{K_{IC}}$ value for each rock sample. Further investigation on the loading rate effect on $\mathbf{K_{IC}}$ is recommended.

§5.3.3 The Calculations of the Fracture Toughness Values

After the test on the CCNBD specimen was conducted, the disc was broken into two halves along the cracked diameter. Then another specimen dimension $\mathbf{a_0}$ was measured and converted into dimensionless expression α_0. This α_0 value, together with the α_1 and α_B values

obtained before are the specimen geometrical parameters to be used to calculate the dimensionless critical (minimum) SIF values, $\mathbf{Y}^*_m$, for the CCNBD specimens. The calculations of the $\mathbf{Y}^*_m$ values are based on Equation (4.24) and Table 4.9. After the determination of the $\mathbf{Y}^*_m$ value for the CCNBD specimen, the rock fracture toughness value is then obtained from the following calculation:

$$K_{IC} = \frac{P_{max}}{B\cdot\sqrt{D}} \cdot \underline{Y}^*_m \qquad (5.2)$$

where $\mathbf{P_{max}}$ is the maximum (failure) load of the tested CCNBD specimen.

§5.4 The Analysis of the CCNBD Geometry Influences on Rock K_{IC} Testing

§5.4.1 Geometry Influence Analysis -- Category I

In the first category of geometry influence studies, each of the rock samples 1-10 was machined into three groups of specimens according to the G1, G2 and G3 designed geometrical dimensions listed in Table 5.2. Table 5.4 is the list of their $\mathbf{K_{IC}}$ experimental results where the unit for $\mathbf{K_{IC}}$ is MPa$\sqrt{m}$. The fracture toughness average and standard deviation values for each group, $\mathbf{K_{IC}}^G$ and $\mathbf{SD_{IC}}^G$, were calculated and are listed in Table 5.5. Listed in Table 5.5 are also the sample average and standard deviation values, $\mathbf{K_{IC}}$ and $\mathbf{SD_{IC}}$. The sample average fracture toughness value means the $\mathbf{K_{IC}}$ value averaged over all the <u>valid</u> $\mathbf{K_{IC}}$ test results obtained by the CCNBD, CB and SR tests (the later two tests will be discussed in a later section) conducted on this rock sample. These valid tests include some of the tests on the CCNBD specimens used for the size requirement study which will be presented in the next section. The comparison between the group and the sample average are also listed in the Table 5.5, where the deviation means the deviation of group average, $\mathbf{K_{IC}}^G$, from the sample average, $\mathbf{K_{IC}}$.

As expected, the actual geometrical dimensions of the specimens in the same group are slightly different. This is due to the fact that the specimens are machined according to the size of the rock cores available. This slight difference will not affect their common characteristics of the specimens in the same group. In other words, the CCNBD specimens in the same group, even though slightly different in geometrical dimensions, will still show the same behaviour.

Figure 5.7 (a)-(j) clearly shows the comparison between the $\mathbf{K_{IC}}$ values measured by different groups for rock samples 1-10, where the error bars show the scatter of the

experimental results. For reason of comparison, the $\mathbf{K_{IC}}$ values measured by the CB method for all the rock samples are also plotted in Figure 5.7 (their values and calculations will be discussed in section §5.6). As expected, the $\mathbf{K_{IC}}$ values generally agree well between the three groups. The deviations of $\mathbf{K_{IC}}$ values from sample averages are within 10%. For samples 3,4,5,6, the deviations are only within 5%. Compared with the $\mathbf{K_{IC}}$ value measured by the CB method, it can be concluded that the $\mathbf{K_{IC}}$ values measured by these two methods are varying in the same range (a more detailed discussion is given in Section §5.6).

§5.4.2 Geometry Influence Analysis -- Category II

In the second specimen geometry study, 24 different CCNBD specimens with different geometrical dimensions were designed and taken from a single rock sample, sample 20, the mechanical properties of which are listed in Table 5.9. At least four test specimens were prepared for each designed geometry. The geometrical positions of the 24 different designs are shown in Figure 5.1, where note should be taken that geometries Da06, Da07, Da08, Db21 and Db22 are not shown because their dimensions are outside the limit plotted in the figure. These designs are widely spread over the α_1-α_B range investigated and they are considered to be comprehensively representative, i.e., their behaviour should outline the characteristics of all CCNBD specimens with all possible dimensional combinations.

Table 5.6 gives the $\mathbf{K_{IC}}$ test results from the specimens in this category, where the group and sample averages and standard deviations have the same meaning as those discussed in the first category and $\mathbf{K_{IC}}^{ISRM}$ is the average test values by both CB and SR methods. Figure 5.8 clearly shows the comparison between the different geometries, where the sample average and the $\pm 10\%$ deviations from the average are also shown.

By comparison of the $\mathbf{K_{IC}}$ deviations from the sample average for different geometries, one will soon find out that the measured fracture toughness values generally agree well as long as the tested geometries are within the valid geometrical range outlined in Figure 5.1 by lines 0-5. This is the same conclusion as that reached by the analysis of the $\mathbf{K_{IC}}$ test results in the first geometry influence study.

On the contrary, the specimens with a geometry outside the valid geometrical range generated $\mathbf{K_{IC}}$ results greatly deviated from the sample average value. For some geometries, these deviations are even around 50%. The further the distance between the geometrical position of the specimen and the valid geometrical boundary, the larger the $\mathbf{K_{IC}}$ deviation from the sample average. Obviously the invalidity of the test will automatically be assumed if too

Table 5.4 K_{IC} Test Results by G1, G2 and G3 Group Specimens

Rock	Grup.	D (mm)	α_R	α_0	α_1	α_B	Y^*_m	P_{max} (KN)	K_{IC}
1	G1-1	74.05	0.689	0.256	0.648	0.808	0.833	4.201	0.609
	2	74.05		0.263	0.648	0.802	0.836	3.942	0.577
	3	74.03		0.311	0.652	0.767	0.854	4.019	0.632
	4	74.03		0.295	0.648	0.778	0.848	4.119	0.632
	G2-1	99.7	0.752	0.303	0.727	0.996	0.949	7.639	0.653
	2			0.321	0.732	0.979	0.958	6.777	0.598
	3			0.326	0.727	0.996	0.949	7.439	0.639
	4			0.303	0.727	0.997	0.948	7.989	0.682
	5			0.191	0.727	1.074	0.907	8.074	0.612
	G3-1	99.5	0.513	0.251	0.491	0.599	0.654	6.131	0.603
	2			0.261	0.491	0.593	0.656	6.573	0.656
	3			0.251	0.491	0.603	0.653	7.639	0.745
	4			0.251	0.493	0.595	0.655	6.867	0.683
	5			0.201	0.489	0.657	0.635	8.864	0.774
	6			0.201	0.489	0.651	0.636	6.651	0.586
2	G1-1	74.3	0.686	0.256		0.832	0.818	3.769	0.521
	2			0.276		0.800	0.834	3.982	0.582
	3			0.276	0.646	0.795	0.837	4.036	0.594
	4			0.269		0.810	0.829	3.845	0.551
	5			0.276		0.797	0.836	4.004	0.588
	G2-1	99.7	0.752	0.316	0.727	0.975	0.960	7.221	0.637
	2	99.8	0.752	0.316	0.726	0.978	0.957	6.655	0.582
	3	99.8	0.752	0.306	0.727	0.995	0.948	7.845	0.673
	4	99.6	0.753	0.306	0.727	0.976	0.960	8.365	0.737
	5	99.9	0.751	0.240	0.726	1.051	0.917	7.949	0.622
	G3-1	99.0	0.515	0.258	0.490	0.594	0.658	4.895	0.492
	2			0.253	0.495	0.593	0.658	6.195	0.626
	3			0.248	0.492	0.606	0.654	6.186	0.606
	4			0.253	0.490	0.594	0.658	6.364	0.639
	5			0.131	0.490	0.699	0.623	8.704	0.703
3	G1-1	74.0	0.689	0.277	0.649	0.796	0.840	5.107	0.759
	2			0.270		0.800	0.837	5.132	0.756
	3			0.274		0.796	0.840	4.971	0.738
	4			0.280		0.789	0.843	4.653	0.699
	G2-1	99.7	0.752	0.301	0.727	0.997	0.948	8.003	0.683
	2			0.306		0.991	0.951	7.929	0.683
	3			0.306		0.992	0.951	7.884	0.678
	G3-1	99.5	0.513	0.261	0.493	0.587	0.659	7.089	0.718
	2			0.256	0.488	0.597	0.655	7.832	0.773
	3			0.256	0.489	0.598	0.655	7.371	0.727

Table 5.4 K_{IC} Test Results by G1, G2 and G3 Group Specimens (continued)

Rock	Grup.	D (mm)	α_R	α_0	α_1	α_B	Y^*_m	P_{max} (kN)	K_{IC}
4	G1-1	74.0	0.689	0.257	0.649	0.808	0.833	4.597	0.667
	2			0.288	0.649	0.789	0.843	3.769	0.567
	3			0.291	0.660	0.781	0.847	3.915	0.604
	4			0.278	0.649	0.789	0.843	4.472	0.671
	G2-1	99.8	0.752	0.306	0.724	0.992	0.950	8.297	0.710
	2	99.8		0.298	0.725	1.000	0.946	7.714	0.653
	3	99.7		0.321	0.727	0.979	0.958	7.475	0.656
	4	99.7		0.296	0.727	1.005	0.944	6.351	0.536
	G3-1	99.7	0.512	0.256	0.492	0.602	0.652	6.414	0.626
	2			0.261		0.688	0.656	7.166	0.721
	3			0.261		0.590	0.656	5.516	0.553
	4			0.266		0.582	0.659	6.456	0.658
5	G1-1	74.2	0.687	0.276	0.647	0.798	0.836	6.040	0.888
	2					0.790	0.841	6.911	1.030
	3					0.796	0.837	6.613	0.974
	4					0.798	0.840	6.568	0.968
	G2-1	99.9	0.751	0.301	0.726	0.998	0.947	11.34	0.963
	2	99.9	0.751	0.300	0.726	0.995	0.947	11.44	0.974
	3	99.8	0.752	0.291	0.727	1.003	0.944	11.00	0.927
	4	100.0	0.750	0.373	0.735	0.976	0.986	9.247	0.837
	G3-1	99.9	0.511	0.253	0.491	0.601	0.652	9.909	0.965
	2			0.250	0.491	0.593	0.654	9.936	0.983
	3			0.245	0.486	0.595	0.653	9.396	0.924
	4			0.243	0.486	0.593	0.654	10.15	0.999
6	G1-1	74.0	0.689	0.284	0.649	0.795	0.840	2.325	0.347
	2			0.264		0.811	0.832	1.914	0.277
	3			0.270		0.797	0.839	2.397	0.355
	4			0.270		0.800	0.837	2.344	0.345
	G2-1	99.4	0.755	0.290	0.731	1.006	0.947	4.673	0.397
	2			0.282	0.732	1.013	0.943	4.063	0.342
	3			0.287	0.732	1.006	0.947	4.396	0.374
	4			0.317	0.729	0.979	0.961	3.395	0.301
	G3-1	99.3	0.514	0.257	0.491	0.600	0.654	3.738	0.369
	2			0.242	0.488	0.596	0.656	3.688	0.365
	3			0.252	0.494	0.601	0.654	3.525	0.348
	4			0.262	0.494	0.592	0.657	2.995	0.301
7	G1-1	74.15	0.688	0.263	0.647	0.797	0.838	6.965	1.025
	2			0.270		0.798	0.838	8.814	1.296
	3			0.263		0.804	0.834	9.096	1.324

Table 5.4 K_{IC} Test Results by G1, G2 and G3 Group Specimens (continued)

Rock	Grup.	D (mm)	α_R	α_0	α_1	α_B	Y^*_m (kN)	P_{max}	K_{IC}
7	G2-1	99.9	0.751	0.355	0.736	0.995	0.947	13.57	1.177
	2			0.305	0.730	1.001	0.944	12.28	1.041
	3			0.305	0.730	0.993	0.948	14.24	1.220
	G3-1	99.9	0.511	0.250	0.489	0.596	0.653	14.89	1.462
	2			0.250	0.491	0.597	0.653	12.73	1.250
	3			0.255	0.491	0.591	0.655	14.92	1.483
	4			0.245	0.491	0.594	0.654	12.26	1.209
8	G1-1	74.3	0.686	0.269	0.646	0.798	0.835	12.36	1.807
	2					0.787	0.841	11.43	1.702
	3					0.794	0.837	12.68	1.867
	G2-1	100.2	0.749	0.300	0.728	0.999	0.945	18.91	1.597
	2			0.295	0.727	1.001	0.948	20.27	1.705
	3			0.280	0.724	1.007	0.954	22.53	1.869
	G3-1	100.2	0.509	0.243	0.489	0.589	0.654	19.89	1.969
	2			0.255		0.579	0.658	19.97	2.022
	3			0.256		0.579	0.658	20.12	2.034
	4			0.245		0.579	0.658	20.89	2.113
9	G1-1	74.3	0.686	0.283	0.646	0.791	0.839	17.80	2.639
	2			0.281		0.786	0.841	18.04	2.696
	3			0.262		0.814	0.827	13.77	1.960
	4			0.267		0.808	0.830	17.05	2.455
	G2-1	100.0	0.750	0.300	0.728	0.998	0.945	30.91	2.620
	2			0.305		0.992	0.948	30.34	2.595
	3			0.316		0.980	0.954	31.40	2.735
	G3-1	100.0	0.510	0.253	0.490	0.588	0.655	27.85	2.778
	2			0.260		0.580	0.658	28.52	2.897
	3			0.263		0.576	0.658	28.37	2.904
10	G1-1	74.3	0.686	0.262	0.646	0.805			
	2			0.296	0.650	0.775	0.847	12.60	1.931
	3			0.283	0.646	0.791	0.839	12.27	1.820
	4			0.269	0.646	0.794	0.837	12.89	1.898
	G2-1	100.0	0.75	0.323	0.728	0.977	0.956	20.95	1.835
	2			0.300	0.728	1.000	0.944	22.62	1.912
	3			0.305	0.727	0.992	0.948	23.71	2.026
	4			0.300	0.728	1.000	0.944	22.13	1.871
	G3-1	100.0	0.510	0.250	0.490	0.591	0.655	21.70	2.149
	2			0.253	0.487	0.587	0.656	20.65	2.058
	3			0.251	0.490	0.591	0.655	21.30	2.111
	4			0.243	0.485	0.593	0.654	21.76	2.135
	5			0.200	0.485	0.634	0.640	25.80	2.317

Table 5.5 Group Averages and Comparisons

Rock	Groups	Group Average	Sample Average	Deviation from Sample Average (%)
		$K_{IC}{}^{G} \pm SD_{IC}{}^{G}$(MPa$\sqrt{m}$)	$K_{IC} \pm SD_{IC}$(MPa$\sqrt{m}$)	
1	G1	0.6125 ± 0.0223	0.6567 ± 0.0290	-6.7306
	G2	0.6367 ± 0.0300		-3.0455
	G3	0.6745 ± 0.0687		2.7105
2	G1	0.5671 ± 0.0274	0.6100 ± 0.0339	-7.0328
	G2	0.6500 ± 0.0521		6.5574
	G3	0.6130 ± 0.0688		0.4918
3	G1	0.7380 ± 0.0237	0.7197 ± 0.0271	2.5427
	G2	0.6813 ± 0.0024		-5.3356
	G3	0.7397 ± 0.0184		2.7789
4	G1	0.6273 ± 0.0438	0.6352 ± 0.0056	-1.2437
	G2	0.6389 ± 0.0636		0.5825
	G3	0.6394 ± 0.0606		0.6612
5	G1	0.9650 ± 0.0505	0.9452 ± 0.0258	2.0948
	G2	0.9251 ± 0.0539		-2.1265
	G3	0.9675 ± 0.0280		2.3593
6	G1	0.3310 ± 0.0314	0.3435 ± 0.0195	-3.6390
	G2	0.3532 ± 0.0363		2.8239
	G3	0.3458 ± 0.0268		0.6696
7	G1	1.2150 ± 0.1349	1.2374 ± 0.0851	-1.8102
	G2	1.1462 ± 0.0763		-7.3703
	G3	1.3510 ± 0.1228		9.1805
8	G1	1.7923 ± 0.0682	1.9058 ± 0.1461	-5.9555
	G2	1.7234 ± 0.1120		-9.5708
	G3	2.0345 ± 0.0514		6.7531
9	G1	2.4372 ± 0.2899	2.8028 ± 0.0916	-13.044
	G2	2.6499 ± 0.0614		-5.4553
	G3	2.8595 ± 0.0578		2.0230
10	G1	1.8828 ± 0.0467	2.0449 ± 0.1088	-7.9270
	G2	1.9108 ± 0.0718		-6.5578
	G3	2.1541 ± 0.0872		5.3401

Table 5.6 $\mathbf{K_{IC}}$ Test Results for Rock Sample 20 by Different CCNBD Specimens

ID	Y^*_m	K_{IC}^{ISRM}	Group Average $K_{IC}^G \pm SD_{IC}^G$ (MPa$\sqrt{m}$)	Sample Average $K_{IC} \pm SD_{IC}$ (MPa$\sqrt{m}$)	K_{IC}^G Deviation from K_{IC} (%)
Da01	1.1519		0.598 ± 0.012		-1.5314☜?
Da02	1.1123		0.615 ± 0.006		1.2679☜?
Da03	1.0741		0.610 ± 0.004		0.4446☜?
Da04	0.9447		0.619 ± 0.005		1.9266☜?
Da05	1.2601		0.616 ± 0.012		1.4326☜?
Da06	1.4220		0.451 ± 0.005		-25.7370☜
Da07	1.5245		0.462 ± 0.021		-23.9256☜
Da08	1.2891		0.436 ± 0.006		-28.2068☜
Da09	1.2261		0.430 ± 0.002		-29.1950☜
Da21	1.1766		0.620 ± 0.003		2.0912☜?
Da22	1.0939		0.617 ± 0.008		1.5972
Da11	0.6689	0.6250	0.599 ± 0.006	0.6073 ± 0.0114	-1.3667
Da12	0.6647		0.625 ± 0.010		2.9145
Da13	0.6145		0.587 ± 0.002		-3.3427☜?
Da14	0.6590		0.608 ± 0.010		0.1153
Db01	0.8351		0.605 ± 0.010		-0.3787
Db02	0.8068		0.616 ± 0.013		1.4326
Db03	0.8019		0.618 ± 0.007		1.7619
Db04	0.8174		0.600 ± 0.004		-1.2020
Db21	1.5245		0.420 ± 0.015		-30.8414☜
Db22	1.2891		0.325 ± 0.013		-46.4844☜
Db23	1.2261		0.358 ± 0.012		-41.0500☜
Dc01	1.3619		0.558 ± 0.026		-8.1179☜
Dc02	1.2134		0.526 ± 0.015		-13.3870☜

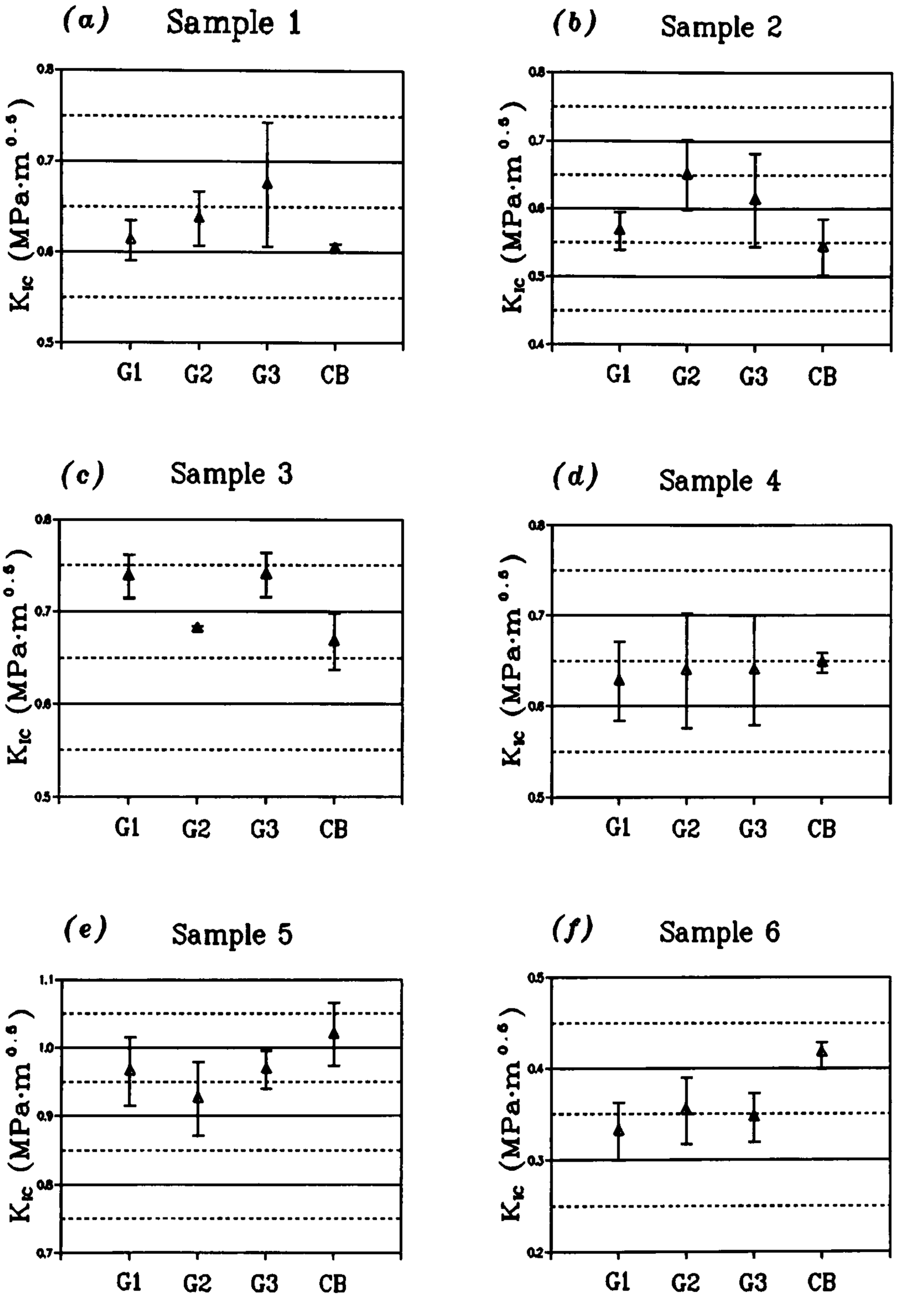

Figure 5.7 a) Geometry Influence Testing Results for Rock Samples 1 - 6

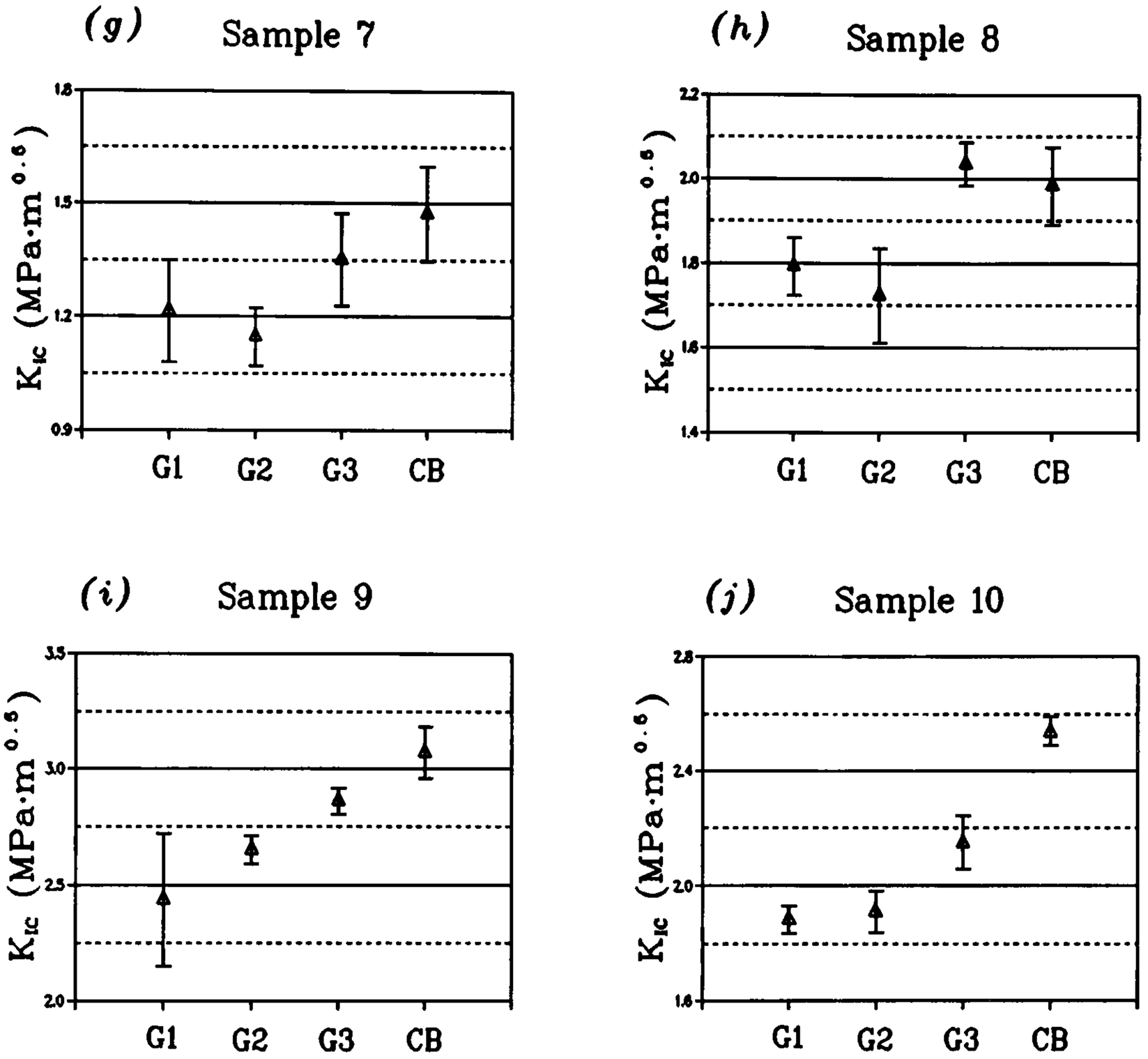

Figure 5.7 b) Geometry Influence Testing Results for Rock Samples 7 - 10

large a deviation is the situation. These invalid K_{IC} tests are marked with a "☜" in Table 5.6 and their K_{IC} values will not be counted when conducting the sample average evaluation.

However some exceptions exist for specimen groups Da01-Da05, Da21 and Da13 where the measured K_{IC} values do not deviate considerably from the sample average even though their geometrical positions are outside the valid range boundary. They are marked with a "☜?" in the table. A simple interpretation is that their geometries are just outside the valid range boundaries and are not far enough to definitely produce invalid results. That suggests a transitional geometrical band between the valid and invalid geometrical range starting from the valid boundary outlined in Figure 5.1 instead of a sudden change of validity over the border. Interestingly this point has to be true as mathematically the variations of CCNBD specimen

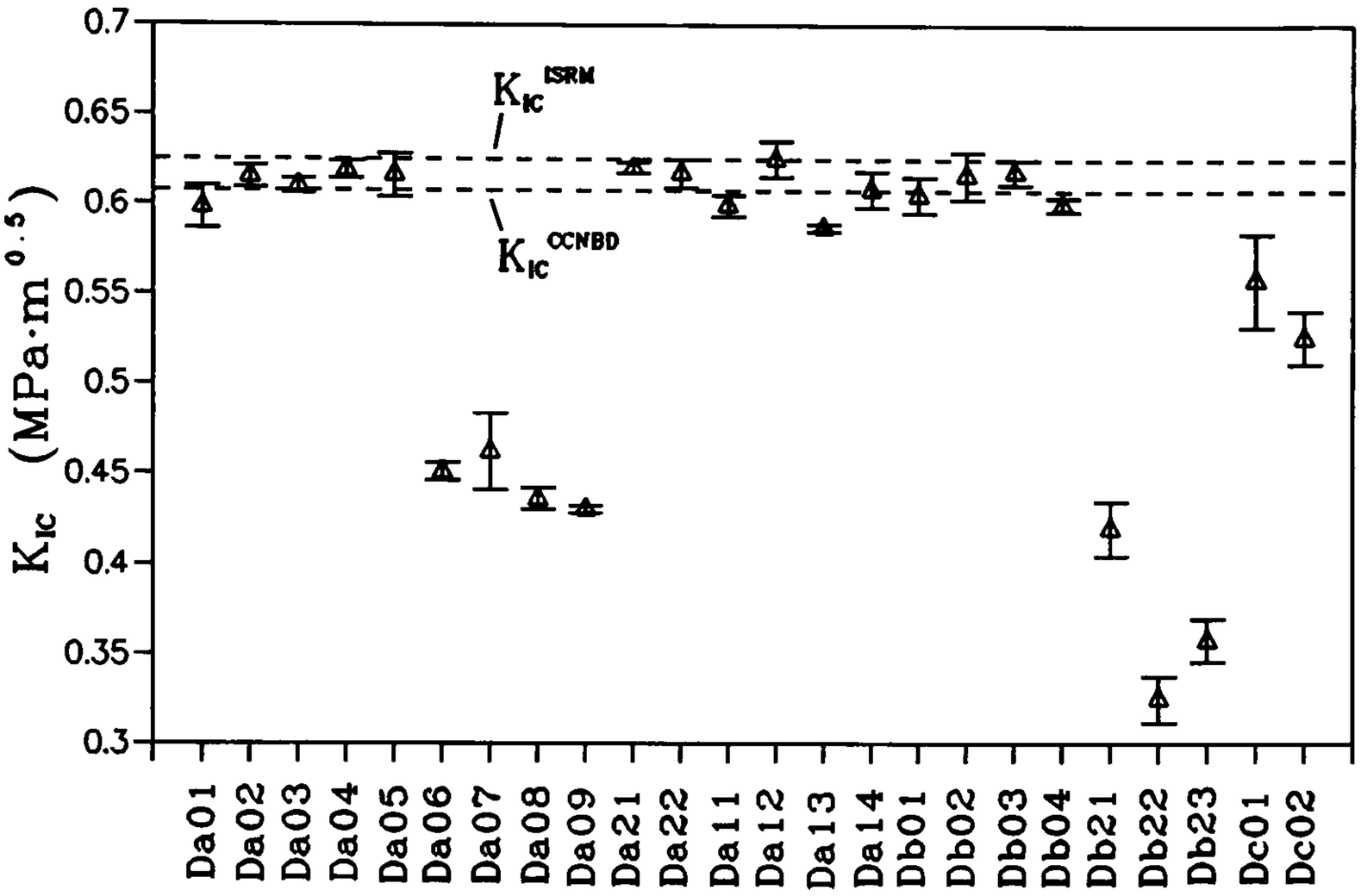

Figure 5.8 $\mathbf{K_{IC}}$ Results by Different CCNBD Geometries of Sample 20

geometries are all continuous functions and there should not be any sudden change in the specimen behaviour characteristics. However in practice, this transitional band should be avoided as the validity for different rock samples cannot be theoretically guaranteed.

Based on the above analysis on the two categories for the geometrical influence studies, it can be concluded that CCNBD specimens with geometrical parameters within the valid geometrical range outlined in Figure 5.1 (or Figure 4.13) will generate valid consistent $\mathbf{K_{IC}}$ values. This will provide CCNBD users with a greater choice for their practical geometry design. They can always design the specimen geometries according to the availability of their rock cores and their machine capacity. On the other hand, according to this conclusion, the designed CCNBD geometrical dimensions do not have to be strictly controlled during the machining. As long as the final geometrical parameters of the specimens are still within the valid geometrical range, they will generate the same (consistent) $\mathbf{K_{IC}}$ results. In practical situations, one will soon find out that less strict requirements for geometrical dimensions always mean easier machining, more productivity in terms of specimen production and higher utilization of rock samples.

Furthermore, another good feature of the CCNBD specimens was shown during the $\mathbf{K_{IC}}$ tests for the geometry influence studies. The magnitude ratio (neglecting the units) $\mathbf{P_{max}/K_{IC}}$ for all the valid CCNBD specimens tested are normally over 10.0, while the same ratios will be just about 1.5 for the CB specimens and about 1.0 for the SR specimens (as discussed in the last chapter). This ratio physically signifies the output reading of the maximum (failure) load, $\mathbf{P_{max}}$, in kN per unit rock fracture toughness value, $\mathbf{K_{IC}}$, in MPa$\sqrt{m}$ for a particular test geometry. The ratio values shown above suggest that the CCNBD specimen geometry works as an amplifier to enlarge the output reading $\mathbf{P_{max}}$ from the generally small $\mathbf{K_{IC}}$ input, while the CB and the SR specimen geometries will just maintain the same order of magnitude. Therefore the strict requirements on the testing apparatus' ability for low load range testing, set by the CB and the SR test methods, can be reduced when the CCNBD specimen geometry is used. From this point of view, it is believed that the CCNBD test method is much more practical for engineering purposes.

§5.5 Minimum Size Requirement Studies for Valid CCNBD K_{IC} Tests

Specimen size, reflected by diameter **D** for the CCNBD specimen geometry, affect the stability of the measured $\mathbf{K_{IC}}$ values. Large specimens can generally generate the desired stable $\mathbf{K_{IC}}$ results as the crack front at its critical condition can easier meet the plain strain condition and the surface effect can be neglected. However too large a specimen is uneconomical, and sometimes impractical due to the availability of the sample core sizes. Therefore there should exist a valid minimum specimen size for each rock. The CCNBD specimens with sizes over this minimum value will yield valid (stable) plain strain $\mathbf{K_{IC}}$ result, which is believed to be precise enough to represent the true material constant $\mathbf{K_{IC}^T}$.

The relation between the valid specimen geometry study and the valid specimen minimum size study for the CCNBD is dependent, i.e., validity study for one is based on the knowledge of the satisfaction of the validity for the other. In other words, the investigation of the valid minimum CCNBD specimen size is based on the assumption that the specimen geometries used have already met the requirements of valid geometrical range outlined in Figure 4.13 (or Figure 5.1), and vice-versa.

The actual geometrical dimensions **D**, **B**, $\mathbf{a_0}$ and $\mathbf{a_1}$ (hence α_0, α_1 and α_B) of the CCNBD specimens in the three designed groups, S1, S2 and S3, for the size influence study are measured after specimen preparation and the corresponding $\mathbf{Y_m^*}$ values are calculated from Equation (4.24). Again there was not much difference between the dimensions of the CCNBD specimens in the same group so that each of them can behave in the same pattern. After the maximum (failure) load $\mathbf{P_{max}}$ for each specimen was obtained from the test, the $\mathbf{K_{IC}}$

value was then calculated from Equation (5.2).

Care should be taken while conducting the validity analysis as the smallest specimen size used in our research is only **D** = 65 mm (S1) due to the limitation of our machining ability for specimen preparation. This size sometimes may not be small enough to represent the minimum specimen size for a valid test for some rock materials.

Table 5.7 is the list of all the test details for rock samples 1, 5, 6, 8, and 9 to 18. The results are illustrated in Figure 5.9 (a)-(n) where the error bars show the scatter for the measured $\mathbf{K_{IC}}$ values. The group averages and their comparisons with sample averages are listed in Table 5.8. The average $\mathbf{K_{IC}}$ values measured from the geometrical influence studies discussed in the last section are listed in the table as well.

Some information can be drawn from these test results. For samples 5, 6, 9, 10, 11 and 15, the $\mathbf{K_{IC}}$ values generally agree well within the three size groups. In other words, the size range used is suggested to be already large enough to generate stable (consistent) $\mathbf{K_{IC}}$ values for these six samples. For samples 1, 12, 13 and 14, it is quite obvious that the $\mathbf{K_{IC}}$ values will tend to be stable only after size **D** is larger than 75 mm (S2). In other words, the valid $\mathbf{K_{IC}}$ results can only be obtained when **D** > 75 mm. From the $\mathbf{K_{IC}}$ test results of these four samples, we know that smaller sized specimens always produce smaller $\mathbf{K_{IC}}$ values. This is just on the contrary to the results obtained in metallic material fracture toughness measurement studies where small specimen sizes (signifying plain stress condition) can always generate larger $\mathbf{K_{IC}}$ values than the plain strain material property values $\mathbf{K_{IC}}^{T}$. Similar conclusions were obtained for some other rock materials by Oucterlony (1991) while doing the CB and SR round-robin investigations. The investigation on the reason for this difference is therefore suggested.

For sample 16 however, it is certain that the CCNBD specimens with size **D** over 75 mm will produce stable (consistent) $\mathbf{K_{IC}}$ values, but the $\mathbf{K_{IC}}$ values obtained by smaller sized specimens **D** = 65 mm appear larger. The explanation is being investigated but obviously the CCNBD specimens with size **D** less than 75 mm are not recommended for valid tests for this sample. For sample 8, the results do not show a clear trend of a stable $\mathbf{K_{IC}}$ so that a clear valid statement about this sample can not be made. But from the deviation values of the group averages from the sample average (Table 5.8), -5% (S1), 2% (S2) and 12% (S3), it is suggested that the valid specimen size should be lying somewhere between 65 mm - 100 mm, and most possibly around 75 mm. For the last two samples 17 and 18, only the specimens of the S2 and S3 groups were tested due to the shortage of sample blocks for machining the S1 group specimens. However clear trends are already shown for both of the samples that **D** over 75 mm will produce stable (consistent) $\mathbf{K_{IC}}$ values. It is suggested that the minimum valid size $\mathbf{D_{min}}$ for both samples may be less than 75 mm but without any further proof this

Table 5.7 K_{IC} Test Results by S1, S2 and S3 Group Specimens

Rock	Grup.	D (mm)	α_R	α_0	α_1	α_B	Y^*_m	P_{max}	K_{IC}
1	S1-1	63.2	0.807	0.158	0.736	0.889	0.937	2.572	0.483
	2			0.190		0.899	0.931	2.580	0.479
	3			0.206		0.889	0.937	2.574	0.486
	S2-1	74.1	0.810	0.173	0.738	0.924	0.941	4.741	0.677
	2			0.202	0.737	0.903	0.940	4.226	0.620
	3			0.189	0.742	0.912	0.933	4.814	0.698
	S3-1	99.05	0.808	0.202	0.734	0.900	0.940	7.644	0.627
	2			0.242		0.881	0.952	6.908	0.680
	3			0.222		0.886	0.948	6.965	0.678
5	S1-1	63.15	0.808	0.206	0.738	0.887	0.939	4.904	0.933
	2			0.139	0.733	0.890	0.937	5.291	0.990
	3			0.206	0.738	0.885	0.940	4.847	0.925
	S2-1	74.1	0.810	0.259	0.736	0.866	0.969	5.686	0.890
	2			0.229		0.877	0.961	5.912	0.906
	S3-1	99.8	0.802	0.261	0.728	0.865	0.956	9.734	0.966
6	S1-1	63.0	0.810	0.159	0.738	0.911	0.921	1.432	0.262
	2			0.151		0.908	0.923	1.956	0.359
	3			0.143		0.913	0.920	1.737	0.316
	S2-1	74.0	0.811	0.216	0.741	0.907	0.938	2.256	0.332
	2			0.216		0.895	0.946	2.312	0.346
	3			0.189		0.911	0.935	2.411	0.351
	S3-1	99.4	0.805	0.221	0.733	0.892	0.941	3.694	0.354
	2			0.221		0.888	0.944	4.068	0.392
	3			0.206		0.897	0.938	4.036	0.382
8	S1-1	63.25	0.806	0.253	0.735	0.851	0.962	8.298	1.676
	2			0.174	0.737	0.898	0.930	9.760	0.810
	3			0.174	0.737	0.898	0.930	10.39	1.926
	S2-1	74.2	0.807	0.239	0.734	0.872	0.964	12.08	1.862
	2	74.2	0.807	0.191	0.733	0.902	0.944	13.03	1.902
	3	74.25	0.808	0.280	0.741	0.862	0.979	12.80	2.041
	4	74.25	0.808	0.267	0.739	0.862	0.965	12.48	1.969
	S3-1	100.0	0.80	0.205	0.725	0.894	0.935	22.15	2.069
	2			0.215		0.882	0.943	23.14	2.205
9	S1-1	63.25	0.806	0.174	0.738	0.900	0.929	13.81	2.559
	2			0.174	0.738	0.904	0.926	15.72	2.891
	3			0.213	0.737	0.885	0.939	15.32	2.914

Table 5.7 K_{IC} Test Results by S1, S2 and S3 Group Specimens (continued)

Rock	Grup.	D (mm)	α_R	α_0	α_1	α_B	Y^*_m	P_{max}	K_{IC}
9	S2-1	74.2	0.809	0.263	0.735	0.861	0.971	18.39	2.895
	2			0.249	0.737	0.873	0.965	18.28	2.826
	3			0.222	0.740	0.890	0.947	18.93	2.844
	4			0.175	0.739	0.896	0.943	21.26	3.136
	S3-1	99.9	0.801	0.210	0.727	0.889	0.939	31.18	2.948
	2			0.220		0.883	0.943	27.55	2.635
10	S1-1	63.25	0.806	0.206	0.737	0.885	0.939	11.67	2.216
	2			0.190	0.738	0.893	0.933	10.98	2.059
	3			0.174	0.737	0.901	0.928	11.67	2.154
	S2-1	74.2	0.807	0.270	0.735	0.849	0.979	13.03	2.093
	2			0.276	0.739	0.860	0.979	12.13	1.932
	3			0.202	0.740	0.898	0.942	13.78	2.039
	4			0.155	0.740	0.919	0.927	15.40	2.191
	S3-1	99.8	0.802	0.253	0.730	0.866	0.955	21.74	2.155
	2			0.234		0.878	0.947	21.41	2.075
11	S1-1	63.2	0.807	0.222	0.736	0.862	0.955	3.101	0.613
	S2-1	74.1	0.810	0.270	0.736	0.858	0.974	3.219	0.511
	2			0.250	0.734	0.870	0.965	4.050	0.628
	3			0.256	0.734	0.864	0.970	4.606	0.724
	4			0.250	0.734	0.872	0.965	4.189	0.642
	S3-1	99.3	0.806	0.217	0.729	0.886	0.951	6.491	0.625
	2			0.224	0.730	0.856	0.970	5.244	0.535
12	S1-1	63.2	0.807	0.248	0.737	0.880	0.943	3.283	0.635
	S2-1	74.1	0.810	0.286	0.736	0.846	0.982	4.176	0.678
	2			0.243	0.733	0.875	0.963	5.064	0.779
	S3-1	99.3	0.806	0.240	0.729	0.880	0.950	7.711	0.753
	2			0.237	0.730	0.879	0.951	6.940	0.679
13	S1-1	63.25	0.806	0.198	0.740	0.898	0.930	1.918	0.358
	2			0.168	0.738	0.909	0.923	2.543	0.464
	3			0.231	0.738	0.885	0.939	2.452	0.468
	S2-1	74.1	0.810	0.283	0.736	0.850	0.979	3.761	0.607
	2			0.266	0.737	0.858	0.974	3.311	0.526
	3			0.290	0.736	0.838	0.978	3.989	0.654
	S3-1	100.0	0.800	0.240	0.725	0.876	0.947	6.478	0.626
	2			0.250	0.726	0.872	0.949	6.609	0.644
	3			0.255	0.729	0.869	0.951	6.074	0.597

Table 5.7 K_{IC} Test Results by S1, S2 and S3 Group Specimens (continued)

Rock	Grup.	D (mm)	α_R	α_0	α_1	α_B	Y^*_m	P_{max}	K_{IC}
14	S1-1	63.25	0.806	0.213	0.738	0.884	0.940	6.318	1.206
	2			0.253	0.738	0.904	0.926	5.156	0.960
	3			0.258	0.743	0.889	0.966	5.222	1.016
	S2-1	74.0	0.811	0.223	0.737	0.884	0.958	9.165	1.393
	2			0.234		0.878	0.962	9.116	1.399
	3			0.254		0.866	0.970	8.507	1.335
	4			0.230		0.881	0.960	8.803	1.345
	5			0.264		0.872	0.962	8.787	1.375
	S3-1	99.80	0.802	0.254	0.728	0.864	0.956	14.86	1.476
	2			0.263	0.728	0.862	0.958	14.10	1.406
	3			0.256	0.727	0.864	0.956	11.85	1.176
	4			0.246	0.726	0.870	0.952	14.04	1.376
15	S1-1	63.20	0.807	0.182	0.739	0.900	0.930	6.909	1.285
	2			0.190	0.737	0.896	0.933	7.268	1.358
	3			0.182	0.739	0.900	0.930	6.595	1.224
	4			0.190	0.744	0.899	0.931	6.820	1.276
	S2-1	74.1	0.810	0.297	0.736	0.837	0.988	9.298	1.537
	2			0.270	0.734	0.862	0.971	10.36	1.634
	3			0.277	0.734	0.849	0.980	7.692	1.241
	4			0.236	0.736	0.869	0.967	11.72	1.820
	S3-1	100.0	0.80	0.230	0.725	0.875	0.947	15.64	1.511
	2			0.210	0.725	0.891	0.937	15.35	1.441
	3			0.245	0.728	0.872	0.949	12.49	1.218
16	S1-1	63.2	0.807	0.166	0.737	0.907	0.925	8.686	1.591
	2			0.214	0.739	0.885	0.940	8.331	1.592
	4			0.182	0.737	0.894	0.934	10.39	1.945
	5			0.201	0.741	0.886	0.939	9.958	1.898
	S2-1	74.05	0.810	0.230	0.736	0.881	0.960	9.125	1.393
	2			0.216		0.886	0.956	9.815	1.482
	3			0.230		0.883	0.958	8.563	1.302
	4			0.257		0.864	0.970	8.634	1.358
	S3-1	99.8	0.802	0.236	0.727	0.880	0.946	14.23	1.373
	2			0.200		0.897	0.935	15.42	1.441
	3			0.224		0.883	0.944	13.58	1.302
17	S1								
	S2-1	74.1	0.810	0.256	0.736	0.864	0.970	5.595	0.879
	2			0.259		0.864	0.970	5.953	0.936
	3			0.256		0.869	0.967	5.348	0.833

Table 5.7 K_{IC} Test Results by S1, S2 and S3 Group Specimens (continued)

Rock	Grup.	D (mm)	α_R	α_0	α_1	α_B	Y^*_m	P_{max}	K_{IC}
17	S3-1 2	99.6	0.803	0.231 0.263	0.728	0.880 0.861	0.948 0.960	9.131 8.279	0.885 0.830
18	S1								
	S2-1 2 3	74.2	0.809	0.216 0.293 0.169	0.732 0.733 0.735	0.881 0.837 0.914	0.957 0.987 0.936	14.85 14.12 17.76	2.241 2.322 2.539
	S3-1 2	100.1	0.799	0.200 0.157	0.723	0.891 0.915	0.936 0.920	24.90 23.94	2.326 2.144

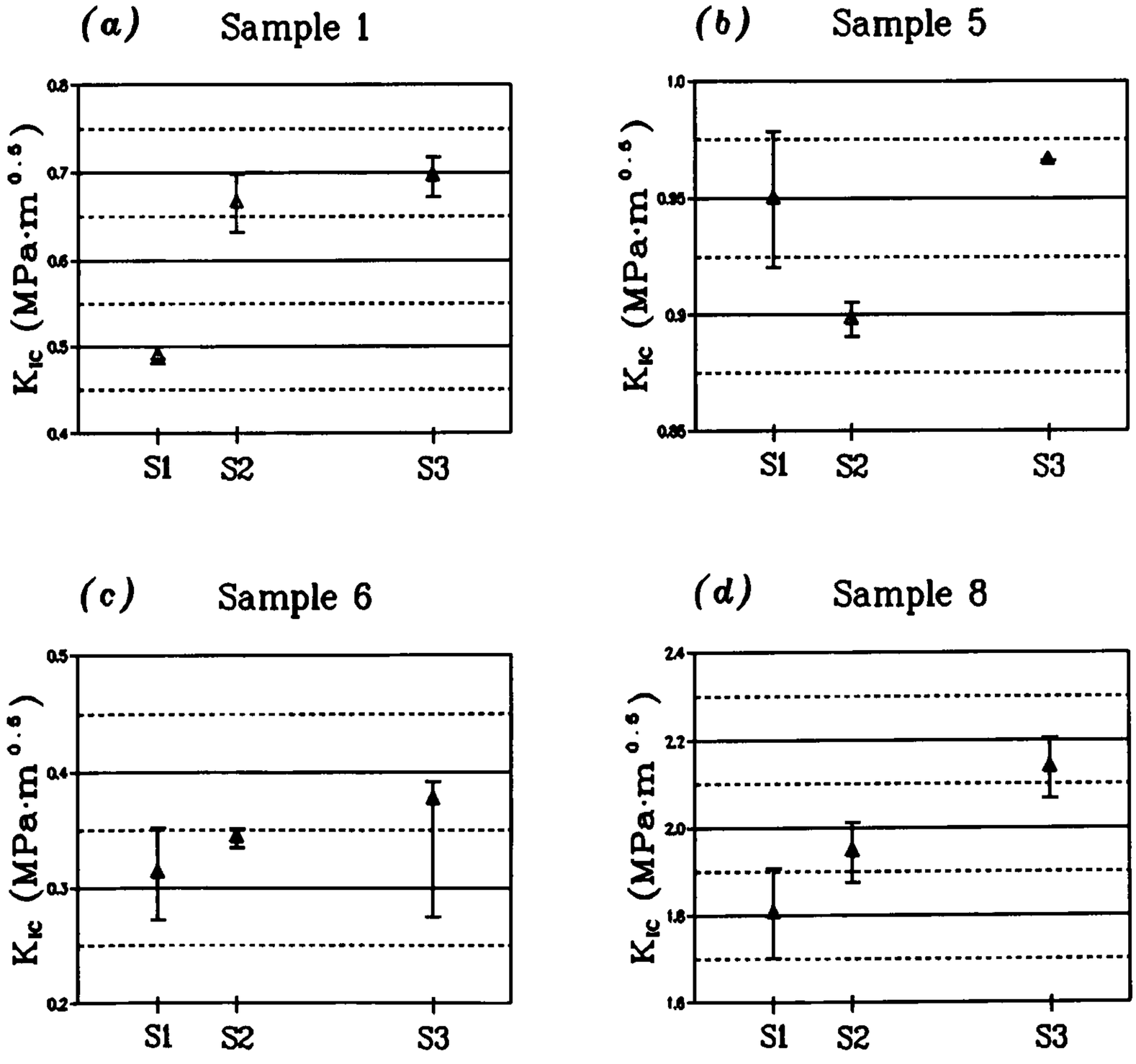

Figure 5.9 (a) Size Influence Test Results for Rock Samples 1, 5, 6 and 8

Table 5.8 Group Averages and Comparisons

Rock Groups	Group Average	Sample Average	Deviation from K_{IC} (%)	K_{IC} by G_i Groups (MPa$\sqrt{m}$)
	$K_{IC}^G \pm SD_{IC}^G$(MPa$\sqrt{m}$)	$K_{IC} \pm SD_{IC}$(MPa$\sqrt{m}$)		
1 - S1	0.4829 ± 0.0029	0.6567 ± 0.0290	-26.466☜	0.6412
S2	0.6651 ± 0.0328		1.2791	
S3	0.6948 ± 0.0226		5.8017	
5 - S1	0.9495 ± 0.0289	0.9452 ± 0.0258	0.4549	0.9525
S2	0.8979 ± 0.0076		-5.0042	
S3	0.9661		2.2112	
6 - S1	0.3121 ± 0.0397	0.3435 ± 0.0195	-9.1412	0.3433
S2	0.3429 ± 0.0082		-0.1747	
S3	0.3757 ± 0.0162		9.3741	
8 - S1	1.8039 ± 0.1022	1.9058 ± 0.1461	-5.3468	1.8501
S2	1.9433 ± 0.0679		1.9677	
S3	2.1371 ± 0.0679		12.136	
9 - S1	2.7879 ± 0.1623	2.8028 ± 0.0916	-0.5316	
S2	2.9252 ± 0.1245		4.3671	
S3	2.7916 ± 0.1565		-0.3996	
10 - S1	2.1427 ± 0.0646	2.0449 ± 0.1088	4.7826	1.9826
S2	2.0636 ± 0.0937		0.9145	
S3	2.1151 ± 0.0399		3.4329	
11 - S1	0.6129	0.6065 ± 0.0193	1.0552	
S2	0.6263 ± 0.0758		2.8195	
S3	0.5804 ± 0.0450		-4.3034	
12 - S1	0.6347	0.7223	-12.128☜	
S2	0.7286 ± 0.0501		0.8722	
S3	0.7160 ± 0.0370		-0.8722	
13 - S1	0.4299	0.6088	-29.386☜	
S2	0.5956 ± 0.0527		-2.1682	
S3	0.6220 ± 0.0195		2.1682	
14 - S1	1.0606	1.3640	-22.243☜	
S2	1.3694 ± 0.0254		0.3959	
S3	1.3586 ± 0.1115		-0.3959	
15 - S1	1.2858 ± 0.0479	1.4113 ± 0.1121	-8.8925	
S2	1.5580 ± 0.2093		10.3947	
S3	1.3900 ± 0.1246		-1.5092	
16 - S1	1.7564 ± 0.1656	1.3778	27.479☜	
S2	1.3837 ± 0.0656		0.4282	
S3	1.3719 ± 0.0564		-0.4282	
17 - S2	0.8827 ± 0.0420	0.8702	1.4365	
S3	0.8576 ± 0.0277		-1.4479	
18 - S2	2.3673 ± 0.1258	2.3012	2.8724	
S3	2.2350 ± 0.0910		-2.8768	

(e) Sample 9

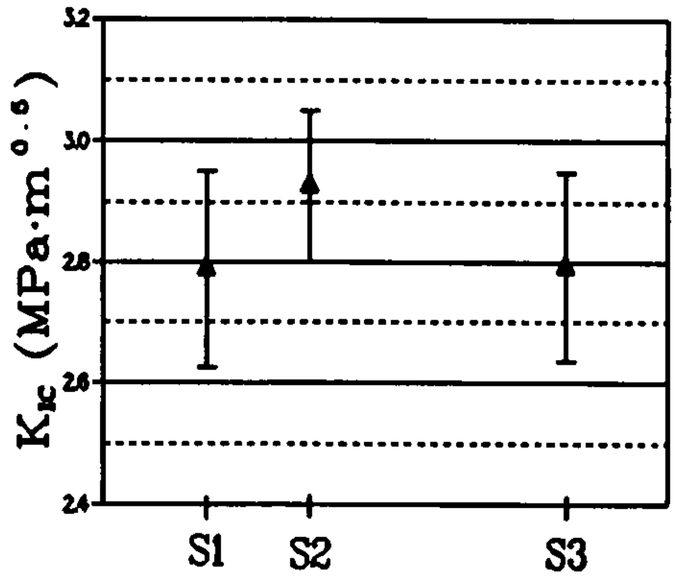

(f) Sample 10

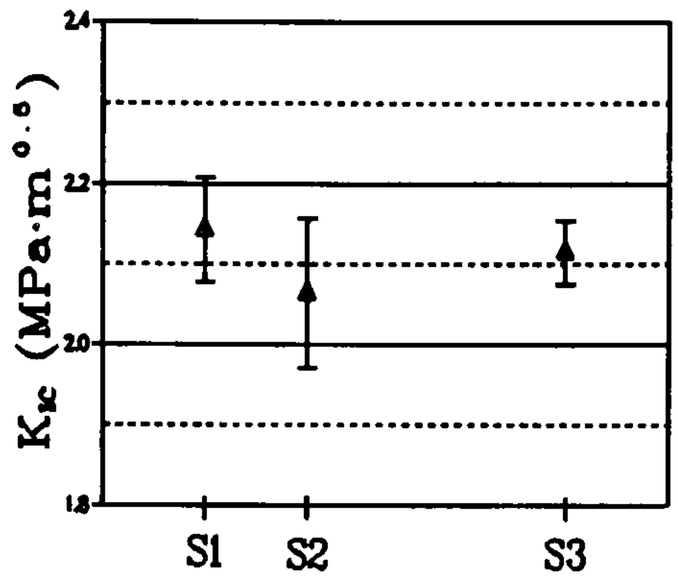

(g) Sample 11

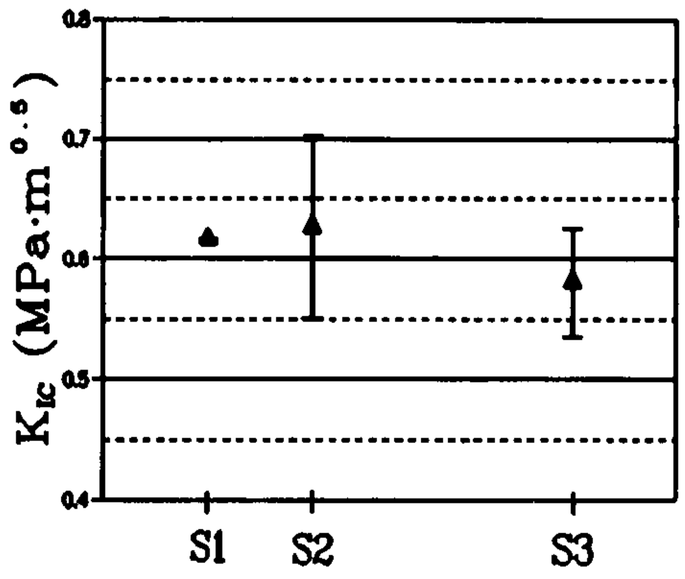

(h) Sample 12

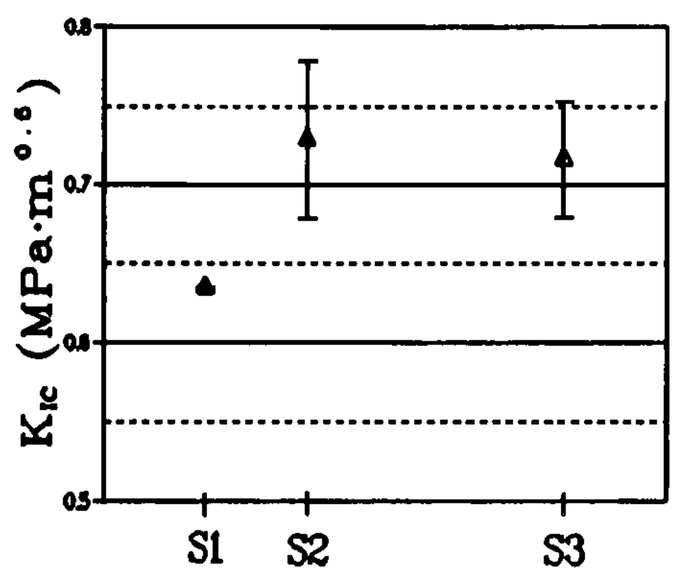

(i) Sample 13

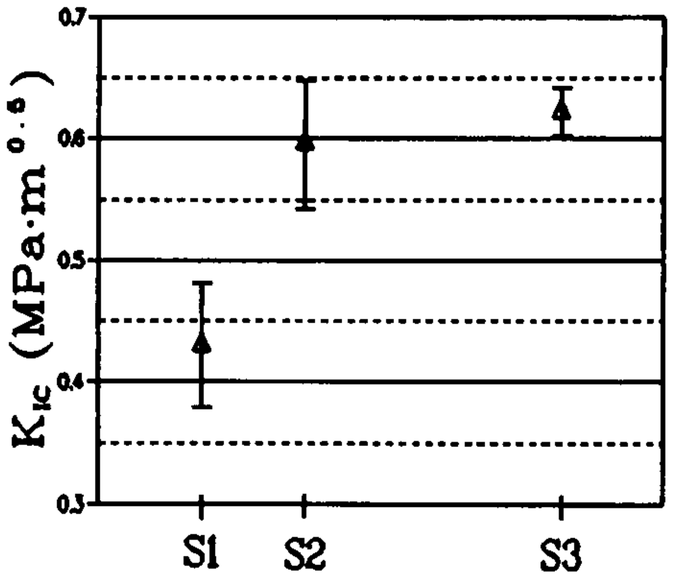

(j) Sample 14

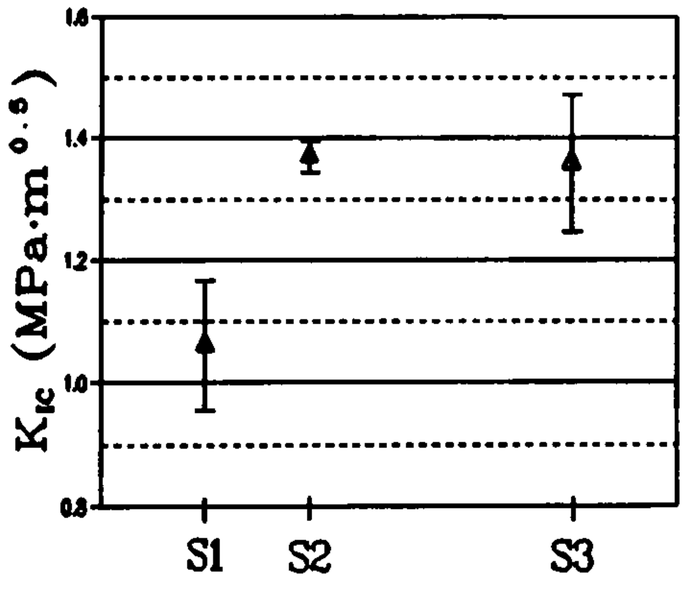

Figure 5.9 b) Size Influence Test Results for Rock Samples 9 to 14

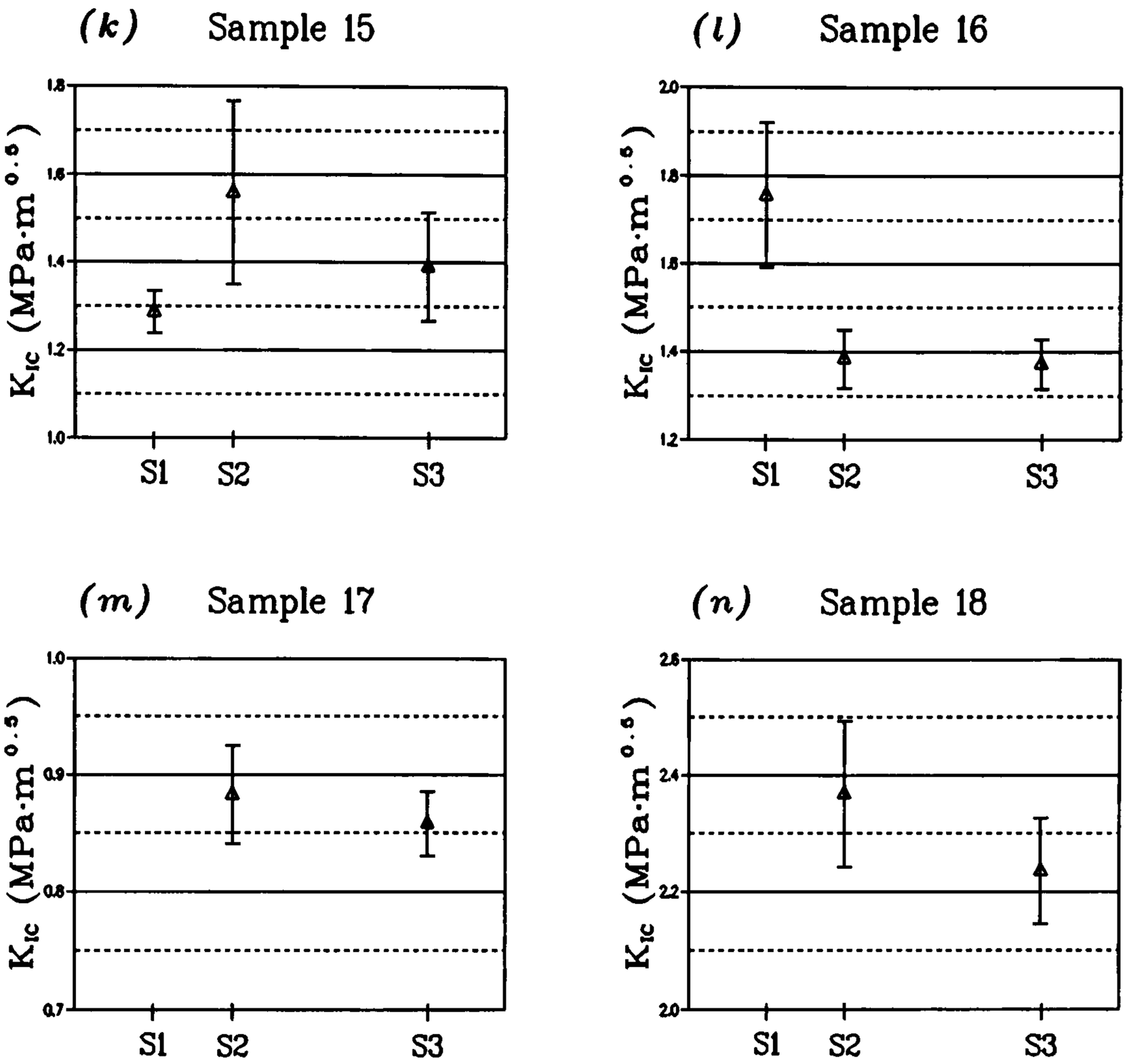

Figure 5.9 c) Size Influence Test Results for Rock Samples 15 to 18

limit can be used.

Based on the above discussions on the stability of the measured $\mathbf{K_{IC}}$ values, it is concluded that there is a certain minimum size limit for each rock when using the CCNBD specimens for fracture toughness measurement. The CCNBD specimens with the sizes over this minimum limit will generate stable (consistent) $\mathbf{K_{IC}}$ values which can then be taken as the material constant property values $\mathbf{K_{IC}}^{T}$, and on the other hand, the specimens with sizes below this limit will yield invalid (unstable) $\mathbf{K_{IC}}$ values which should be discarded when evaluating the material fracture properties. For the CCNBD tests conducted above, the invalid tests will be marked with a "☜" in the tables.

For most of the rock materials, this valid minimum specimen size is believed to be around

75 mm and therefore in practical usage $D \geq 75$ mm should always be the first choice. The CCNBD specimens with $D < 75$mm are not recommended unless a smaller minimum valid size for that particular rock is known beforehand. Furthermore, validity of any test always has to be checked each time after the test. The most effective way for this checking is by comparing the measured K_{IC} values from different CCNBD specimens with different sizes. Or alternatively, it can be conducted according the following approximate validity criteria.

It is rather difficult to reach a precise criteria about the minimum size requirement for the CCNBD K_{IC} testing with these initial experimental results on a limited number of rock samples. Nevertheless approximation can always be made. If the valid minimum specimen size D_{min} discussed above for the 14 rock samples tested is related to the K_{IC}/σ_t values for each sample (where K_{IC} takes the sample average), then the following approximate criteria for valid minimum size requirement can be obtained:

$$D_{min} \sim 8.88 + 1.4744 \cdot \left(\frac{K_{IC}}{\sigma_t}\right)^2 \tag{5.3}$$

At this stage, Equation (5.3) will be accepted for the approximate judgement of the valid minimum size requirement for a valid K_{IC} test by the CCNBD specimens, on condition that no other more precise criteria exists. The K_{IC} for this purpose should use the sample average values.

One extra point needs to be made is that if the ratios of P_{max}/K_{IC} for the tests in these three groups are examined, the same conclusion, as drawn in the last section, about the relations of the output maximum (failure) load readings P_{max} and the input fracture toughness values K_{IC} for the CCNBD specimens will be reached.

§5.6 The Validation Analysis for the CCNBD K_{IC} Test

Apart from the validation studies of the specimen geometries and the specimen sizes for the valid CCNBD K_{IC} tests, in this section the CCNBD method is validated by comparing its results with those obtained by the CB and the SR methods based on 41 different rock samples.

The specimens for the CB and the SR test groups were machined according to the dimensions designed in Table 5.3. The minimum dimensionless SIF A_{min} of the specimens were then calculated according to the suggested method [145] as follows:

$$\begin{aligned} A_{min} &= [\ 1.835 + 7.15 \cdot a_0/D + 9.85 \cdot (\ a_0/D\ )^2\ ] \cdot (\ S/D\ ) \qquad [CB] \\ A_{min} &= 24.0 \cdot [\ 1 - 0.6 \cdot \Delta W/D + 1.4 \cdot \Delta a_0/D - 0.01 \cdot \Delta(\ 2\theta\ )\ ] \qquad [SR] \end{aligned} \tag{5.4}$$

The experimental level I $\mathbf{K_{IC}}$ values for the rock samples were then calculated by the following equation:

$$K_{IC} = \frac{A_{\min} \cdot P_{\max}}{D^{1.5}} \qquad [\ CB,\ SR\ ] \tag{5.5}$$

Some similar comparison tests are introduced from Chen (1989) to substantiate the validation arguments here. There was a total of 23 rock samples. One valid single CCNBD specimen geometry is used for the test which is the CNA geometry listed in Table 4.4, except rock sample 20. Table 5.9 is the list of the rock samples' related mechanical properties. For reason of clarity, these samples are renumbered here starting from number 20.

Table 5.10 presents the comparison results between the $\mathbf{K_{IC}}$ values for each rock sample (samples 1 to 43) by the CCNBD method and the ISRM suggested methods (CB and SR). The comparison results are plotted in Figure 5.10. The $\mathbf{K_{IC}}^{\mathbf{ISRM}}$ values shown here are the averaged values over those obtained by the CB and SR methods. Owing to the limitation of our testing equipment only the first step test results (level I tests) are used. The best fit regression yields the following relationship between $\mathbf{K_{IC}}^{\mathbf{CCNBD}}$ and $\mathbf{K_{IC}}^{\mathbf{ISRM}}$:

$$K_{IC}^{CCNBD} = 0.0521 + 0.8788 \cdot K_{IC}^{ISRM} \tag{5.7}$$

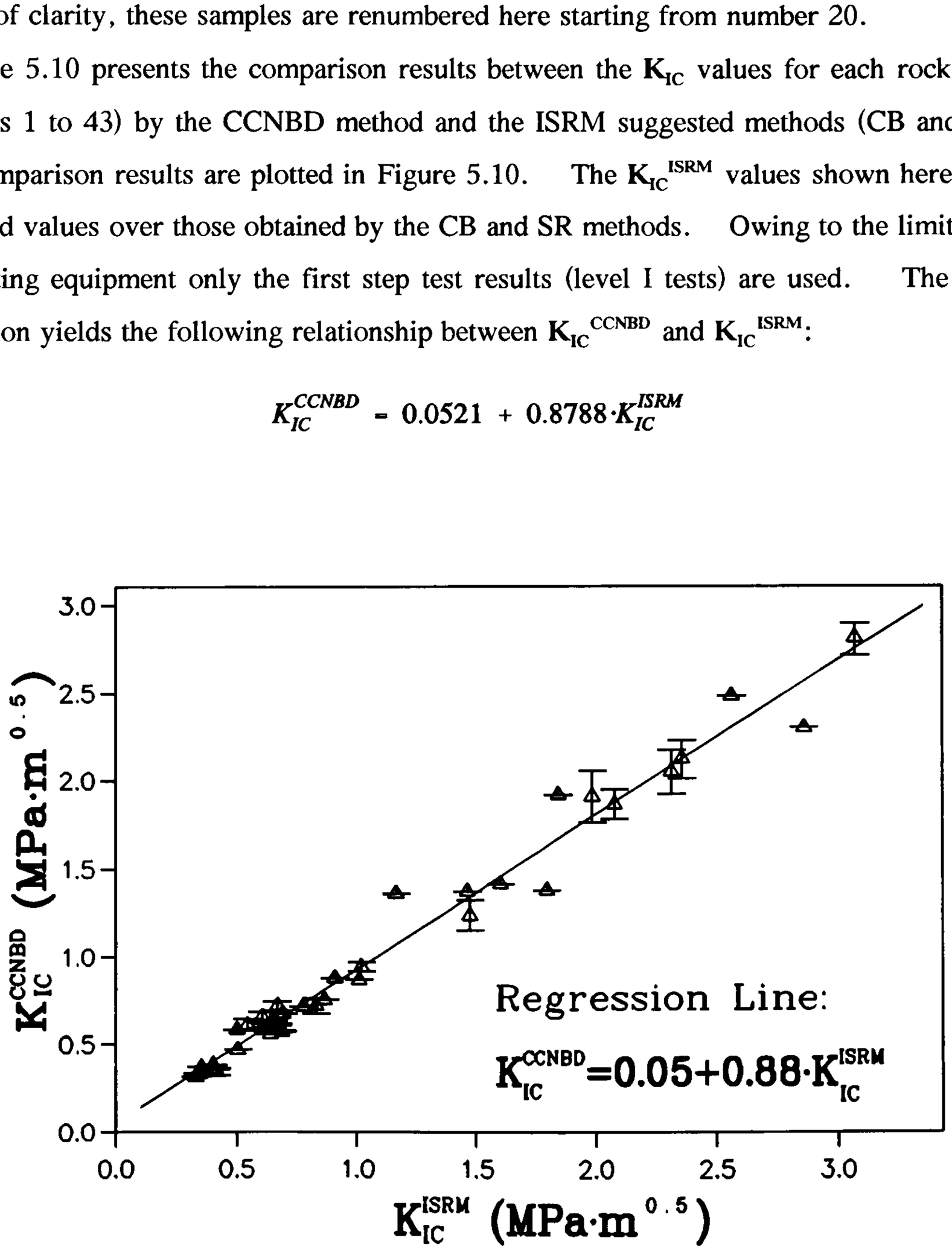

Figure 5.10 Comparison between $\mathbf{K_{IC}}^{\mathbf{CCNBD}}$ and $\mathbf{K_{IC}}^{\mathbf{ISRM}}$

Table 5.9 Extra Samples Used for Experimental Validation [36]

Spl.	Sample Descriptions	E (GPa)	ν	ϱ (T/m^3)	σ_c (MPa)	σ_t (MPa)
20	Sandstone - 1	11.26	0.23	2.32	47.25	2.87
21	Pennant Sandstone	17.86	0.23		197.17	11.22
22	Sandstone - DOS	13.58	0.24		69.35	2.58
23	Sandstone - DISC	11.26	0.23		47.03	2.87
24	Limestone - EIM				62.91	2.72
25	Limestone - 2	10.28			58.21	
26	Limestone - Hard	31.23				
27	Gneiss - Eim5				292.66	12.40
28	Rhyolite - Eim4	30.74			126.42	8.81
29	Gypsum - DOS				34.47	2.30
30	Ore - Eim				133.38	3.82
31	Sandstone - Fai	9.26			47.21	
32	Sandstone - 7	9.73			58.71	
33	Sandstone - 9	11.28			63.21	
34	Sandstone - 31	12.86			71.34	4.58
35	Sandstone - 33	11.76			27.46	2.54
36	Sandstone - 34	12.13			68.21	
37	Sandstone - Spr. 41	11.90	0.28		38.30	3.02
38	Gypsum - Pink 48	13.19			63.31	
39	Limestone - 54	19.26			121.27	
40	Sandstone - 15				33.53	
41	Sandstone - 18				37.85	
42	Sandstone - 25				29.34	
43	Sandstone - 26				21.23	

Table 5.10 Comparison between K_{IC}^{CCNBD} and K_{IC}^{ISRM}

Sample	$K_{IC}^{CCNBD} \pm SD^{CCNBD}$	$K_{IC}^{ISRM} \pm SD^{ISRM}$	$K_{IC}^{CCNBD}/K_{IC}^{ISRM}$
1	0.6567 ± 0.0290	0.6041 ± 0.0045	1.0871
2	0.6100 ± 0.0339	0.5433 ± 0.0413	1.1228
3	0.7197 ± 0.0271	0.6677 ± 0.0304	1.0779
4	0.6352 ± 0.0056	0.6479 ± 0.0107	0.9804
5	0.9452 ± 0.0258	1.0195 ± 0.0463	0.9304
6	0.3435 ± 0.0195	0.4166 ± 0.0170	0.8245
7	1.2374 ± 0.0851	1.4727 ± 0.1257	0.8402
8	1.9058 ± 0.1461	1.9824 ± 0.0917	0.9761
9	2.8028 ± 0.0916	3.0704 ± 0.1133	0.9128
10	2.1189 ± 0.1088	2.3544 ± 0.0462	0.9000
13	0.6088		
14	1.3640	1.1641	1.1717
15	1.4113 ± 0.1121		
16	1.3778	1.7931	0.7684
17	0.8702	1.0088	0.8626
18	2.3012	2.8606	0.8044
20	0.6073 ± 0.0114	0.6300 ± 0.0900	0.9640
21	1.9165	1.8400 ± 0.2230	1.0416
22	0.4715	0.5042 ± 0.0490	0.9351
23	0.6140 ± 0.0042	0.6685 ± 0.0641	0.9185
24	0.7560	0.8648 ± 0.1317	0.8742
25	0.7200 ± 0.0441	0.8293 ± 0.1134	0.8682
26	2.4790	2.5615	0.9678
27	2.0463 ± 0.1269	2.3115	0.8853
28	1.8617 ± 0.0833	2.0743 ± 0.1243	0.8975
29	0.5580	0.6383 ± 0.0689	0.8742
30	1.4150	1.5990 ± 0.0900	0.8849
31	0.3845	0.4000 ± 0.0200	0.9613
32	0.5825	0.5008 ± 0.0110	1.1631
33	0.7170	0.7770 ± 0.0568	0.9228
34	0.5743 ± 0.0048	0.6873 ± 0.0904	0.8356
35	0.3700	0.3520 ± 0.0225	1.0511
36	0.5915	0.6080 ± 0.0316	0.9729
37	0.6765	0.6918 ± 0.0298	0.9779
38	0.8790	0.9083 ± 0.0436	0.9677
39	1.3735	1.4605 ± 0.1444	0.9404
40	0.3325	0.3455	0.9624
41	0.3580	0.4085 ± 0.0611	0.9764
42	0.3345	0.3375	0.9911
43	0.3155	0.3285	0.9604

Therefore the $\mathbf{K_{IC}}$ values measured by the CCNBD specimens turn out to be around 10% lower than those by the ISRM suggested methods (level I). However according to recent reports by Ouchterlony (1991) where some new calibrations have been added, the ISRM suggested methods seem to generate the $\mathbf{K_{IC}}$ values around 10% higher than the "true" values. So that it is suggested that the CCNBD method may be just the one to produce closer $\mathbf{K_{IC}}$ values to the actual ones compared with the first step $\mathbf{K_{IC}}$ results by the ISRM suggested method. Certainly this point needs to be carefully investigated in more details in the future.

Sample 1-18 are the same samples used above for the geometry and size influence studies, and the $\mathbf{K_{IC}}$ values shown in the tables are the averages of all the valid test results from different specimens.

If only the standard CCNBD specimen geometry (the CNA geometry listed in Table 4.3) was used, as was the case for rock samples 20 to 43, then the scatter of the $\mathbf{K_{IC}}$ test results came out to be much less than that by the standard CB or SR specimen geometries. Therefore it is suggested that if the practical situation allows the use of the standard CCNBD geometry only, a more reliable $\mathbf{K_{IC}}$ test value can be obtained with less test specimens. This is another good feature which is of great significance for practical applications.

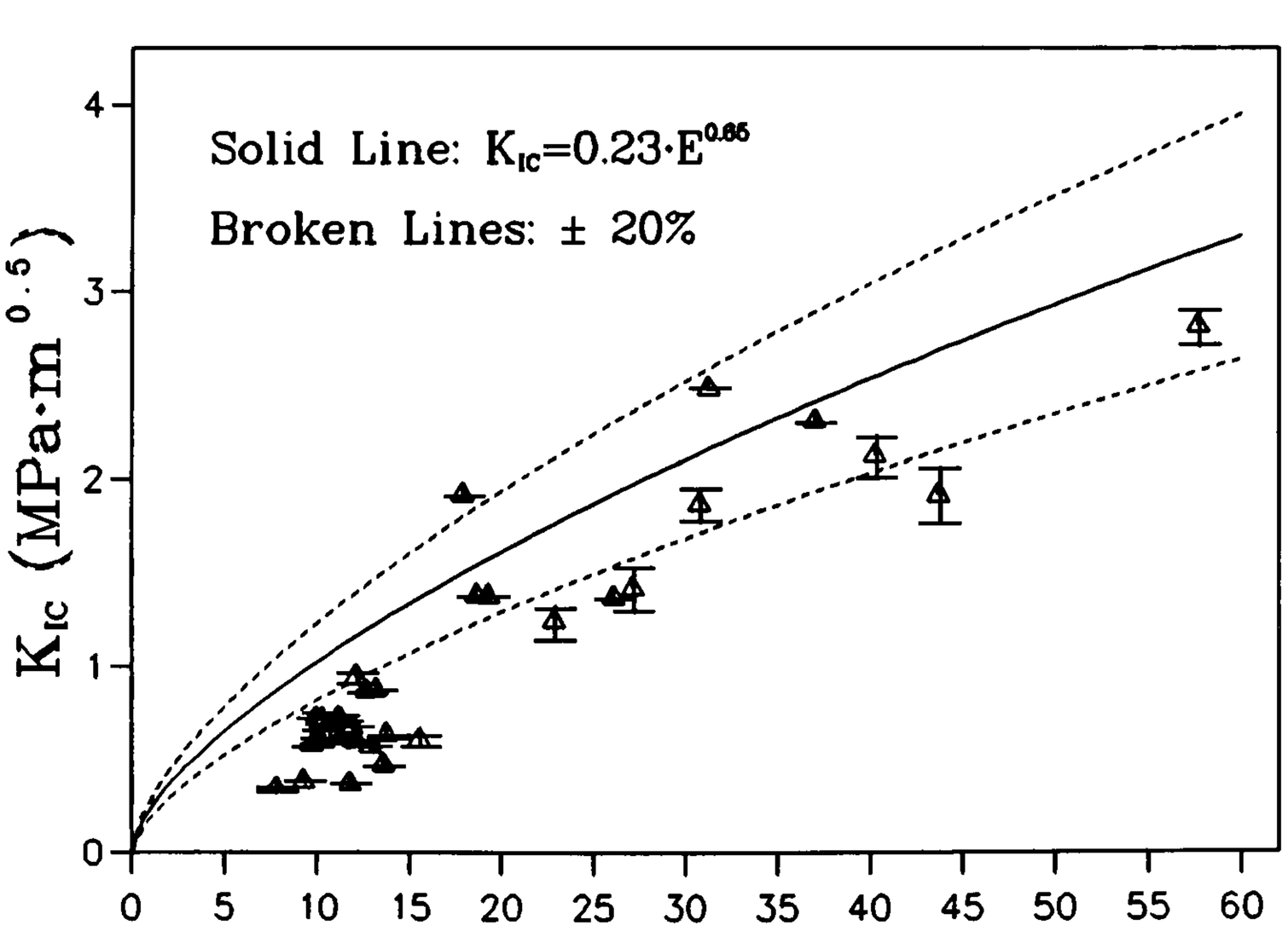

Figure 5.11 $\mathbf{K_{IC}}$ vs **E**

Based on the $\mathbf{K_{IC}}$ test results on some limited particular rock materials, Ouchterlony (1991) concluded that for rock materials the relationship between the second step (level II) $\mathbf{K_{IC}}$ test values by the ISRM suggested method and the rock Young's modulus **E** will roughly follow the following equation:

$$K_{IC} = 0.23 \cdot E^{0.65} \tag{5.7}$$

Plotting the $\mathbf{K_{IC}}$ test results by the CCNBD specimens against **E** for all the rock samples tested in the current investigation, Figure 5.11 was obtained, where Equation (5.7) is plotted as well. Again differences exist between them. The $\mathbf{K_{IC}}$ values by the CCNBD method turn out to follow the trend of -80% of the values by Equation (5.7) shown as the lower dotted line, which is supposed to be around the first step (level I) $\mathbf{K_{IC}}$ values by the CB and SR methods [Ouchterlony, 1991]. The regression relation for $\mathbf{K_{IC}}$ test results in the current research is:

$$K_{IC} = 0.054 \cdot E^{1.0143} \tag{5.8}$$

However, Equation (5.7) is based on the test results on a few rock samples, therefore Equation (5.8) is believed to be the better prediction for rock $\mathbf{K_{IC}}$ values from rock Young's modulus **E**.

If the $\mathbf{K_{IC}}$ values are related to the rock compressive strength σ_c and tensile strength σ_t, the relationships shown in Figure 5.12 a) and b) will be obtained. The best fit regressions for these relations will yield:

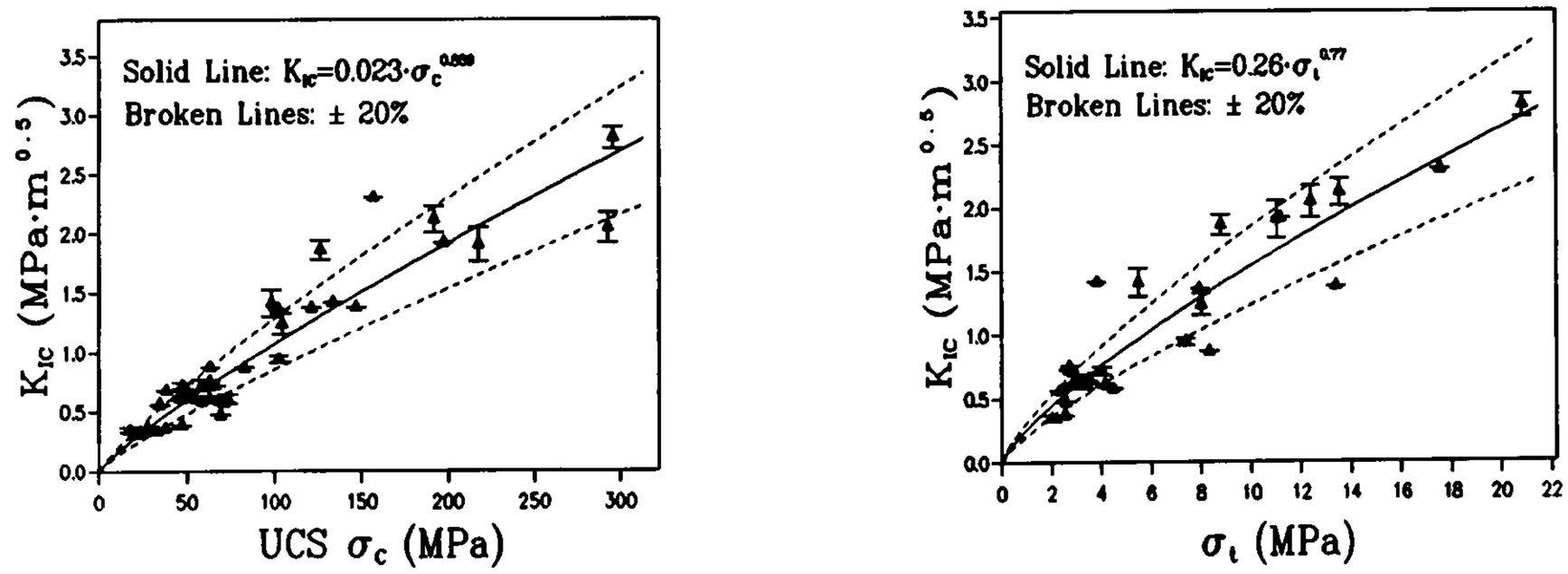

Figure 5.12 (a) and (b) Relationships between K_{IC} and σ_c, σ_t

$$\begin{cases} K_{IC} = 0.0225 \cdot \sigma_c^{0.8390} \\ K_{IC} = 0.2598 \cdot \sigma_t^{0.7728} \end{cases} \tag{5.9}$$

Equations (5.8) and (5.9) are only the regressed relationships based on the available results. They should not be taken as definite analytical relations. In other words they can only be used as some sort of prediction. For practical use, the minimum valid specimen size prediction for instance, it is suggested that the $\mathbf{K_{IC}}$ value for a particular rock be jointly predicted by these three equations, i.e.,

$$K_{IC}^{Pred.} = \frac{K_{IC}^{E} + K_{IC}^{\sigma_c} + K_{IC}^{\sigma_t}}{3} \tag{5.10}$$

where $\mathbf{K_{IC}}^{E}$, $\mathbf{K_{IC}}^{\sigma c}$ and $\mathbf{K_{IC}}^{\sigma t}$ are the predicted values from **E**, σ_c and σ_t respectively. This prediction is normally very useful as, in order to have the valid experimental results, the specimen size and the testing loading rate should be designed according to the most liable $\mathbf{K_{IC}}$ value before conducting the testing.

§5.7 Conclusions and Suggestions for Further Research

The following conclusions have been made from the CCNBD experimental validation studies based on the above test results:

1) It has been experimentally proven that CCNBD specimens with the geometrical dimensions inside the range outlined by lines 1, 2, 3, 4 and 5 in Figure 4.13 (or Figure 5.1) will generate valid stable (consistent) $\mathbf{K_{IC}}$ values for rock materials. This range is referred to as the valid geometrical range. The CCNBD specimens with geometrical dimensions within the transitional band immediately outside the valid range boundary and within the invalid geometrical range far away from the boundary will produce invalid inconsistent $\mathbf{K_{IC}}$ values and therefore they should be avoided for practical applications.

2) The tested specimen geometries show that for CCNBD specimen preparation, the designed geometrical dimensions do not have to be strictly controlled as long as the finished specimens' dimensions are still within the valid geometrical range in order to have a valid test. Certainly the minimum (critical) dimensionless SIF $\mathbf{Y^*_m}$ will change according to the practical dimensions however they will still generate valid consistant fracture toughness values. This will make the CCNBD specimen preparation much easier and much more productive.

3) In order to obtain a valid material constant plain strain $\mathbf{K_{IC}}$ value of rock materials, the CCNBD specimen size **D** is recommended to be at least 75 mm unless a smaller size has been

validated beforehand. For any specimen size, the validation study should be checked each time before the $\mathbf{K_{IC}}$ value can be taken as a valid material constant. The studies can be carried out easier by comparing the results for different specimen sizes, or alternatively can be approximately evaluated by Equation (5.3) as the former way is always troublesome, costly and sometime impossible due to the limited rock available and the machining ability.

4) The CCNBD specimens can generate less scatter and closer "true" $\mathbf{K_{IC}}$ values compared with the first step (level I) testing of the ISRM suggested CB and SR methods, so that the CCNBD testing method can be recommended as an engineering simple and accurate $\mathbf{K_{IC}}$ measurement method. It has been proved that the CCNBD specimens will produce less scattered $\mathbf{K_{IC}}$ results if one single geometry is used. This suggests that the CCNBD testing is less influenced by the outside conditions and can always generate more consistent results.

5) Valid CCNBD specimens will generate 10% lower $\mathbf{K_{IC}}$ values compared with the first step (level I) $\mathbf{K_{IC}}$ values by current ISRM suggested CB and SR methods.

6) Based on the relations obtained, rock $\mathbf{K_{IC}}$ values for experimental design or for prediction purposes can be jointly predicted by the rock Young's modulus **E**, the tensile strength σ_t and the compressive strength σ_c by Equation (5.8), (5.9) and (5.10).

7) Owing to the much lower dimensionless SIF values for the CCNBD geometry, the specimen can work like an amplifier when used for rock fracture toughness testing. It will enlarge the low $\mathbf{K_{IC}}$ value input and give a high $\mathbf{P_{max}}$ reading output. In other words, it is much less sensitive compared with CB and SR methods, while too sensitive testing method for material property measurement purposes always means much larger induced system error. This certainly will reduce the costly requirement on the testing machines' low load range capability and will also greatly reduce the induced error due to testing machines' resolution.

8) Based on the experience of using the CCNBD specimens for rock fracture toughness studies, there are no complicated machining, no difficult setting up, no high and costly requirement on the testing system and no troublesome calculations.

9) Quite interestingly, if the CCNBD, CB and SR specimens are machined from the same rock cores, their crack orientation plane can be constructed perpendicular to each other in 3-D space. In other words, they together form a complete set of specimens for rock anisotropic fracture studies. Therefore by carefully selecting the coring direction with the rock anisotropic plane, the rock anisotropic fracture problems can be ideally modelled jointly by these three specimen geometries from a single core. This will greatly reduce the error caused by testing the rock cores from different blocks.

Apart from the conclusions above, some further research into aspects of this work are strongly recommended:

1) More rock samples and a larger specimen size range are suggested to investigate the size effect on the $\mathbf{K_{IC}}$ test results so that a more accurate minimum size requirement criteria for a valid CCNBD test can be reached.

2) Some attention should be paid to the loading rate effect on $\mathbf{K_{IC}}$ test results so that the valid loading rate can be decided before the test.

3) Compared with the second step (level II) $\mathbf{K_{IC}}$ values by the ISRM suggested CB and SR methods, the $\mathbf{K_{IC}}$ values by the CCNBD method are much lower. Further investigations into this aspect are strongly recommended.

4) A database is suggested to be set up to establish the relations between rock $\mathbf{K_{IC}}$ values and some other rock properties so that rock $\mathbf{K_{IC}}$ values can be more precisely predicted. Furthermore the relations for rock $\mathbf{K_{IC}}$ values with some engineering practice performance parameters (the specific energy in rock cutting engineering for instance) should be investigated.

5) It is believed that the cracked Brazilian discs (the CSTBD or the CCNBD specimens) are ideal specimens to be used for rock mixed mode fracture studies and rock anisotropic fracture studies. Therefore further theoretical and experimental investigations in this area are strongly recommended.

Chapter 6

Draft for the Third Suggested Method for Determining the Mode I Fracture Toughness of Rock

Suggested Method for Determining Mode I Fracture Toughness Using Cracked Chevron Notched Brazilian Disc (CCNBD) Specimens

1 INTRODUCTION

Historically a large variety of specimen types and methods have been used for the rock fracture toughness $\mathbf{K_{IC}}$ test, and the results generated were normally not comparable [145]. Therefore in 1988, the ISRM Testing Commission recommended two suggested methods aiming to provide testing methods which would yield consistent fracture toughness values. These two methods very soon achieved general acceptance.

The introduction of the Cracked Chevron Notched Brazilian Disc (CCNBD) specimen into the suggested methods would form a complete set of specimens for a full rock anisotropic fracture toughness investigation since the crack orientations of these three suggested specimen geometries can be easily arranged to be orthogonal to each other if they are machined from the same rock core. Additional advantages are much higher failure loads, fewer restrictions on the testing apparatus, larger tolerance on the specimen machining error, simpler testing procedure and lower scatter of test results. It is suggested that this method is even more suitable for practical purposes.

Furthermore, the CCNBD specimen and its original model Cracked Straight Through Brazilian Disc (CSTBD) are both ideal specimens for pure mode II or mixed mode fracture studies of rock materials. Different combinations of mode I and mode II fracture intensities can be easily obtained and the test can be carried out just as simply as that in the pure mode I fracture toughness test. Other documentation for this purpose is under preparation.

In this version of the document for the CCNBD test method, only one level of experiment is presented. It is anticipated that some research results for the non-linearity influences on fracture toughness value measured by CCNBD specimen will be added in a future version.

2 SCOPE

1.(a) This test is intended to measure the fracture toughness of rock materials. The main use of this property is for the classification and characterization of intact rock with respect to its resistance to crack propagation. Other important uses are either as an index for rock fragmentation processes such as crushing and tunnel boring, or in the analysis of hydraulic or explosive fracturing and stability.

(b) The test uses rock material in the form of core specimens. The core axis should be oriented either parallel or perpendicular to any anisotropy features such as planes of weakness. The present method uses a specimen, called a Cracked Chevron Notched Brazilian Disc (CCNBD) specimen (Figure 1), with a chevron or V-shaped notch cut along the core diameter direction.

(c) The testing requires only the recording of the maximum load.

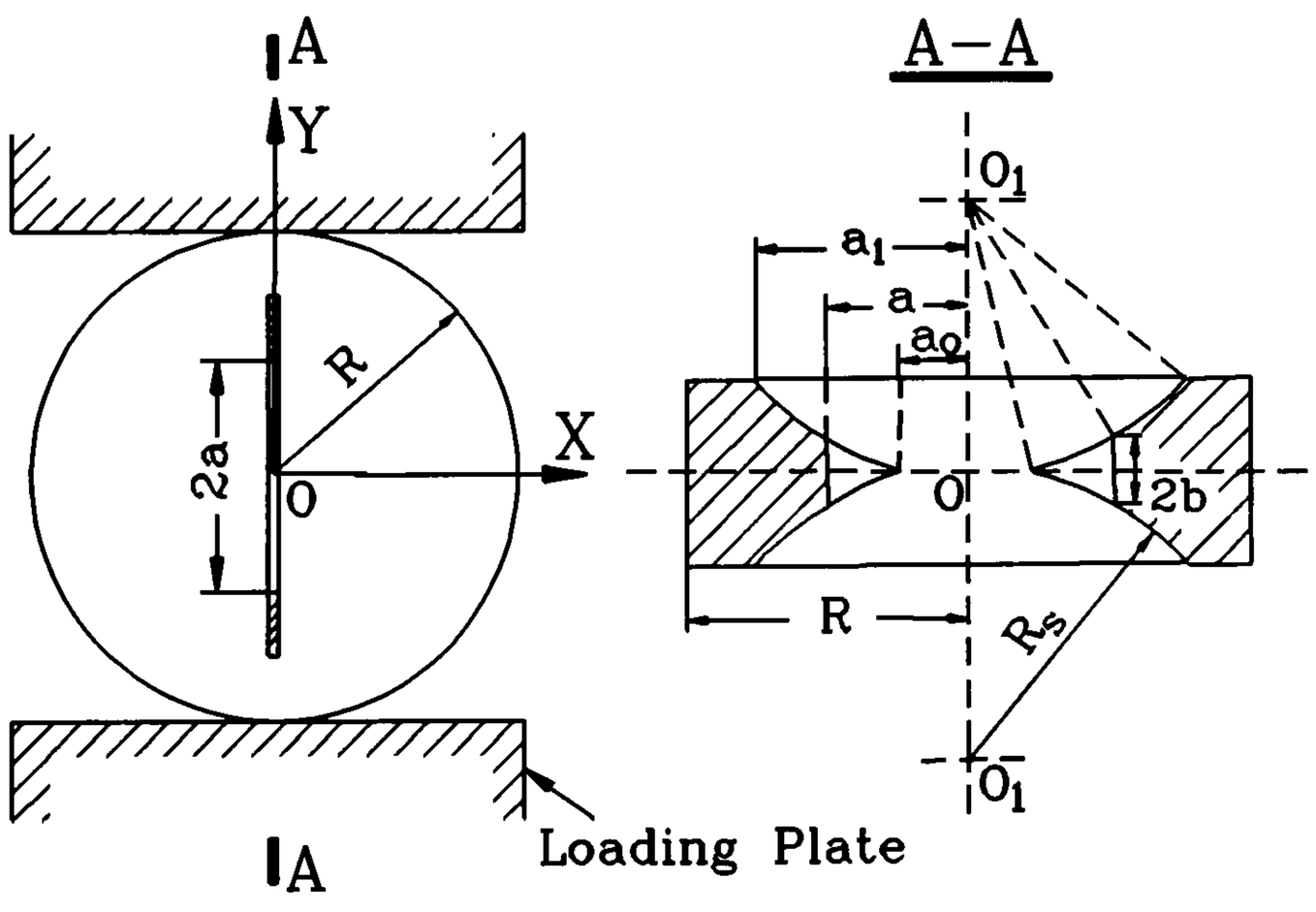

Figure 1. The CCNBD Specimen Geometry with Recommended Test Fixture

3 SPECIMEN DESCRIPTION

2. (a) The geometry of the CCNBD specimen is illustrated in Figure 1. The chevron notch causes crack propagation to start at the tip of the V aligment and to proceed radially outwards in a stable fashion until the point where the fracture toughness is evaluated.

(b) All the geometry dimensions should be converted into dimensionless parameters with respect to the specimen radius **R** and diameter **D** as follows:

$$\begin{cases} \alpha_0 = a_0 / R \\ \alpha_1 = a_1 / R \\ \alpha_B = B / R \\ \alpha_s = D_s / D \end{cases} \tag{1}$$

(c) The suggested standard specimen geometry dimensions are to be as in Table 1. Other selections of specimen geometry dimensions are possible, but in order to have a valid test, the selected geometry dimensions α_1 and α_B should satisfy the following restrictions, which are shown in Figure 2.

$$\begin{cases} \alpha_1 \geq 0.4 , & Line\ 0 \\ \alpha_1 \geq \alpha_B / 2 , & Line\ 1 \\ \alpha_B \leq 1.04 , & Line\ 2 \\ \alpha_1 \leq 0.8 , & Line\ 3 \\ \alpha_B \geq 1.1729 \cdot \alpha_1^{1.6666} , & Line\ 4 \\ \alpha_B \geq 0.44 , & Line\ 5 \end{cases} \tag{2}$$

Table 1 Standard CCNBD Geometrical Dimensions (Figure 1)

Descriptions	Values	Dimensionless Expression
Diameter **D** (mm)	75.0	
Thickness **B** (mm)	30.0	$\alpha_B = B/R = 0.80$
Initial Chevron Notched Crack Length $\mathbf{a_0}$ (mm)	9.89	$\alpha_0 = a_0/R = 0.2637$
Final Chevron Notched Crack Length $\mathbf{a_1}$ (mm)	24.37	$\alpha_1 = a_1/R = 0.65$
Saw Diameter $\mathbf{D_s}$ (mm)	52.0	$\alpha_s = D_s/R = 0.6933$
Cutting Depth $\mathbf{h_c}$ (mm)	16.95	
$\mathbf{Y^*_{min}}$ (dimensionless)	0.84	
$\mathbf{a_m}$ (mm)	19.31	$\alpha_m = a_m/R = 0.5149$

(d) The initial crack length a_0 for specimen preparation purpose in practical applications could be arbitrarily set between (0.20-0.30)**R**.

(e) $\alpha_0(a_0)$, $\alpha_1(a_1)$ and $\alpha_B(B)$ are the three basic dimensions in the CCNBD geometrical parameters. When known, the other geometrical dimensions (Figure 1) can then be calculated from the following interrelations:

$$\begin{cases} \alpha_s = R_s/R = \sqrt{\alpha_0^2 + (\alpha_1^2 - \alpha_0^2 + \alpha_B^2/4)^2 \div \alpha_B^2} \\ h_c = (\alpha_s - \sqrt{\alpha_s^2 - \alpha_1^2})\cdot R = (\alpha_s - \sqrt{\alpha_s^2 - \alpha_0^2})\cdot R + B/2 \\ \alpha_0 = \sqrt{\alpha_s^2 - (\sqrt{\alpha_s^2 - \alpha_1^2} + \alpha_B/2)^2} \\ \alpha_1 = \sqrt{\alpha_s^2 - (\sqrt{\alpha_s^2 - \alpha_0^2} - \alpha_B/2)^2} \\ \alpha_B = 2\cdot(\sqrt{\alpha_s^2 - \alpha_0^2} - \sqrt{\alpha_s^2 - \alpha_1^2}) \end{cases} \quad (3)$$

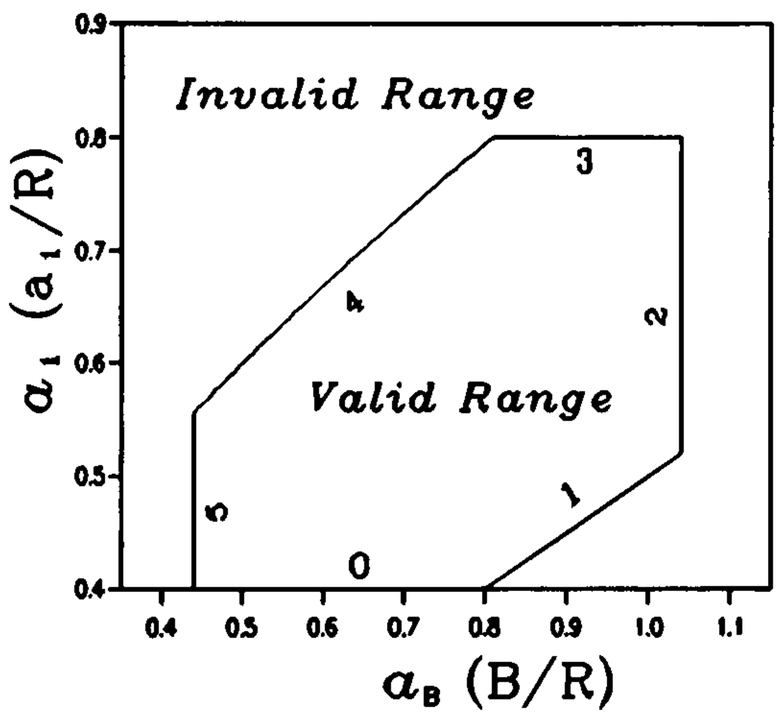

Figure 2 Valid Geometrical Range

4 APPARATUS

Specimen preparation equipment

3. A circular diamond saw shall be used to cut the required notch. The flanks of the chevron notch shall be straight, which requires a saw with a linear cutting motion. A preparation fixture should be used for cutting the notch, which will help to ensure that the chevron notches are exactly in the centre of the disc and the geometrical dimensions conform to the given tolerances. A specimen preparation fixture is shown in Figure 3. **D** and **B** values are the diameter and thickness of the specimen to be machined. **L** is the width of the jig and the range of **L > 1.5D** is used. ∠**A** is the angle of slot for locating the rock specimen and the range of ∠**A** is 110°-130°. **H** is the thickness of the jig and the range 0.25D ~ 0.35D is suggested in order to provide a good guide for specimen machining alignment. For a rock mechanics laboratory, a series of these jigs for **D** = 65, 75, 85 and 100 mm specimens are suggested. For the jig's thickness **H**, it is recommended to use the high bound value of ~0.30D for small **D** and low bound value of ~0.20D for large **D**.

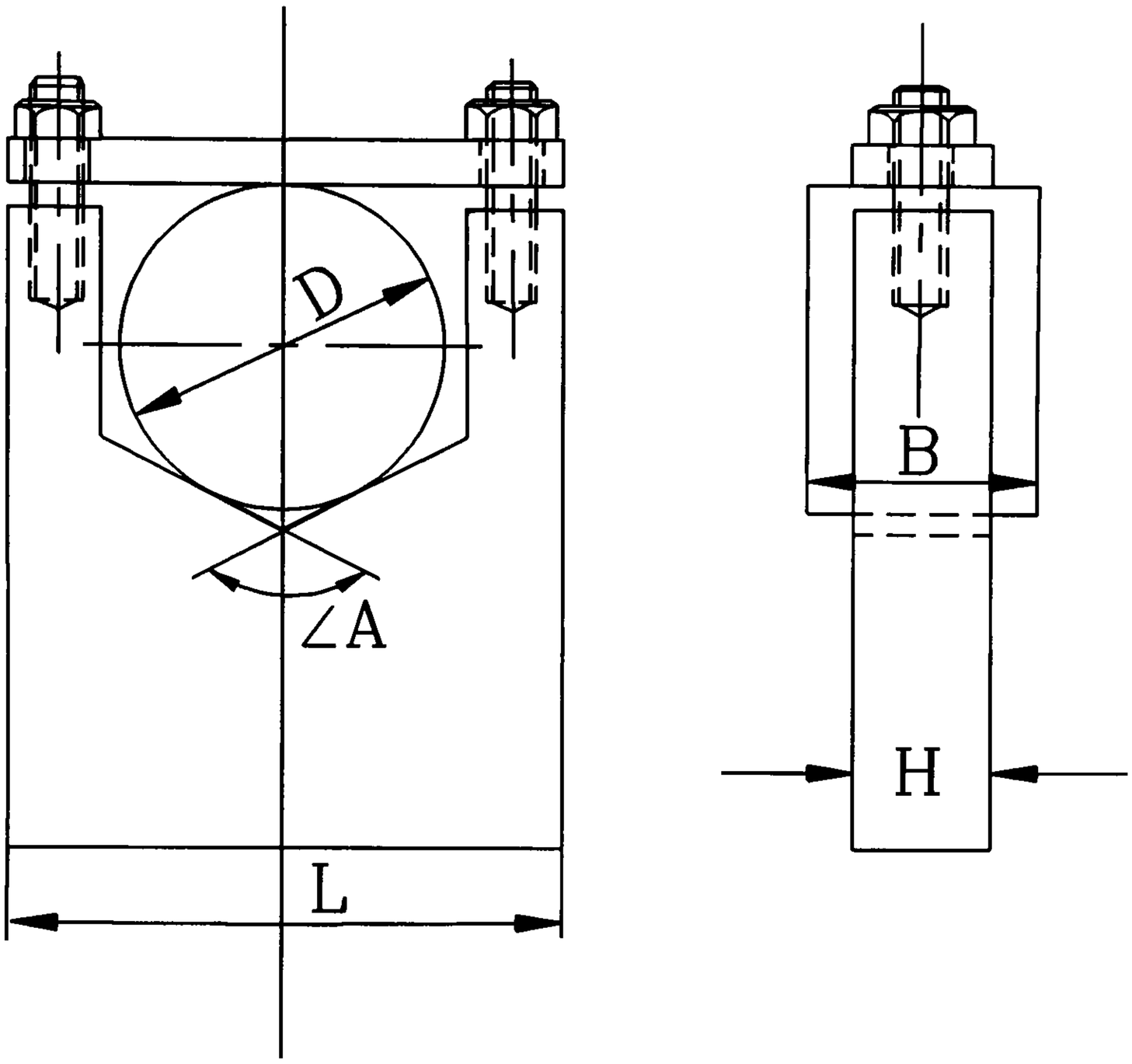

Figure 3 Jig for the CCNBD Sample Preparation

Testing machine and load fixtures

4. (a) The testing shall have sufficient capacity for the peak load required and shall be capable of applying load at the rate conforming to the requirements of paragraph 11 below. It shall be calibrated at regular time intervals and shall comply with accepted national requirements.

(b) At the present test level, the testing prescribes the recording of the maximum load only. This requires a testing machine in which the loading rate can be controlled. Such equipment could be portable. However a testing machine with displacement servo control is preferred as it will help the specimen alignment set-up and it has the advantage of zero preload.

(c) The loading fixture should be as shown in Figure 1, where the lower and the upper loading plates should be rigid and should be parallel to each other to ensure a concentrated vertical loading.

Specimen alignment aids

5. (a) No special setting up aid is required for the CCNBD test. However simple aids can be used to help make the setting up easier.

(b) A simple right angle level is always required. This will help to ensure that the loading plates are perpendicular to the crack orientation. Two small smooth wedges could be used at the same time to help the setting-up by simply putting them on both sides of the specimen to prevent the CCNBD disc from rolling.

(c) The design of any setting up aid should be such that the alignment aid can be removed easily when the specimen has been secured in position.

(d) Checks should be carried out each time before loading. The checks should include the perpendicularity of the crack orientation to the loading plates and the alignment of the crack orientation with the loading direction. The error should be controlled within 0.5%.

Displacement measuring equipment

6. (a) The loading point displacement (LPD) and crack mouth opening displacement (CMOD) could be measured during the test for the compliance studies even though they unnecessary at this stage for the fracture toughness calculation. The equipment shall use a transducer with electric output signals. The LPD should be the primary displacement variable measured on the disc specimen.

(b) A recommended arrangement of displacement measurements uses two linear variable differential transformer (LVDT) transducers mounted on two magnetic supports. They should be arranged on both sides of the specimen, with each sitting on one loading platen but pointing to the other. The LVDTs should be set up straight and should touch the point as close to the loading point as possible (Figure 4).

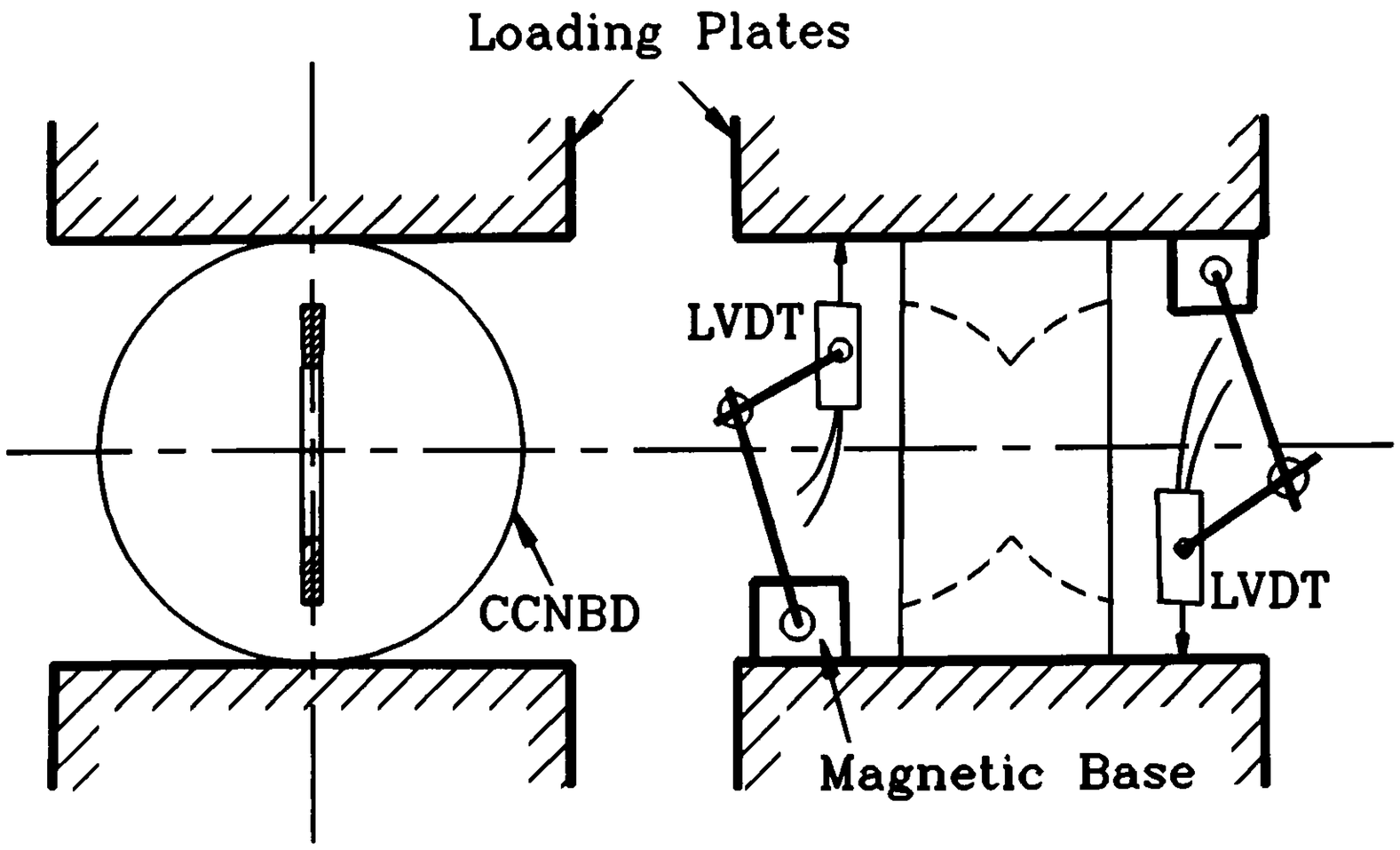

Figure 4 Displacement Measurement

(c) The equipment for the displacement measurement should possess the capability of measuring accurately within 0.001 mm.

Recording

7. An analogue or digital recording system is required such that the accuracies specified for force and displacement systems can be realized. A testing machine recording maximum load only is also acceptable for the fracture toughness determination provided it has good recording accuracy.

5 PROCEDURE

Specimen selection and preparation

8. (a) A test sample is defined as a set of core pieces (specimens) with the same diameter, same thickness, similar properties and identical orientation of the core axis (see 8b below) for which the fracture toughness is to be determined. Each set of specimens with identical loading direction (see 8l below) forms a sub-sample that is to be treated separately.

(b) The core pieces shall be marked with a reference, using a waterproof pen, before specimen preparation so that core axes and rotation angles relative to the material fabric and to block sample faces are known. They should be stored in such a way as to preserve their natural water content, as far as possible, until the time of specimen preparation.

(c) The moisture content of each test sample should be measured and reported.

(d) At least one thin section should be made from each test sample set in order to describe mineral content, grain size, texture and pore volume and configuration. The accuracy of these determinations should be better than $\pm 3\%$ for model analysis, $\pm 5\%$ for grain size, and $\pm 0.2\%$ for porosity. If the core pieces appear anisotropic or are found to be anisotropic as a result of later testing, then three mutually perpendicular thin sections should be cut, parallel and perpendicular to the anisotropy, and analyzed.

(e) The direct tensile strength of the rock material, σ_t, should be measured.

(f) The diameter, **D**, of the core should be related to the size of the largest grain in the rock by the ratio of at least 10:1. A smooth piece of core without abrupt irregularities and straight to within 0.5 mm shall be chosen for specimen preparation. The diameter could be roughly measured at this stage.

(g) The core should be cut to the desired length according to the specimen thickness required and notched using a diamond saw with clean water as coolant. Though the preparation of the specimen thickness does not have to follow exactly the original design, a deviation within 10% is recommended.

(h) The disc surfaces of the cut specimen should be smooth and flat and shall not depart from perpendicularity to the disc axis by more than 0.25 mm in 100 mm. Surface grinding should be applied if these requirements are not satisfied. The required crack orientation should be clearly marked on both sides of the surfaces by a waterproof pen.

(i) The notch width, **t**, should be measured and it should not exceed 1.5 mm.

(j) The notch shall be made with two cuts from both sides of the disc along the disc rotating axis on the same diametrical cutting plane, which is to be the designed crack orientation direction (Figure 5). The fixture shown in Figure 3 holds the disc straight up with the disc surface facing the diamond wheel. Before each cut, a check should be made to ensure that the cut is going to be exactly in the centre of the disc surface, vertically and horizontally. This could be made by matching the diamond wheel with the centre mark of the disc surface circle, or automatically set by the mechanical settings of the machine. The error for the centre alignment should not exceed 0.5 mm. The disc central axis line should match the diamond wheel rotating plane, which will ensure the perpendicularity of the cutting plane to the disc surfaces. The error in this matching shall be within 0.25 mm in 100 mm.

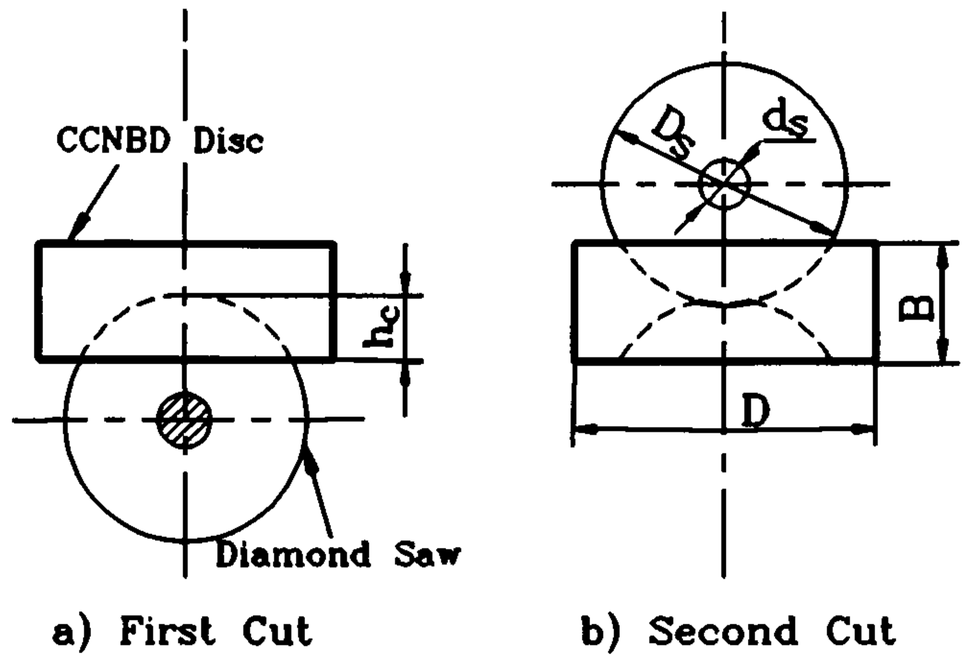

Figure 5 Cutting Procedure

(k) Set the gap between the disc surface and the rotating wheel to zero. The first cut is made by moving the disc toward the rotating wheel up to the designed cutting depth h_c, which can be calculated from the designed values as follows:

$$h_c = (\alpha_s - \sqrt{\alpha_s^2 - \alpha_1^2})\cdot R = (\alpha_s - \sqrt{\alpha_s^2 - \alpha_0^2})\cdot R + \frac{B}{2} \qquad (4)$$

After this cut, the specimen together with the fixture are removed from the fixing vice and turned 180° with the other disc surface facing the diamond wheel. After the centre alignment and the cutting plane perpendicularity checks have been made, the specimen is cut to the same depth $\mathbf{h_c}$ as the first cut.

(l) The angle of the chevron notch plane with respect to the core reference shall be recorded so that both the plane of the crack and its direction of propagation relative to material fabric

and to block sample faces are known. This angle must coincide with the intended direction of loading (crack propagation direction), which may be inclined to the rock anisotropic features at the desired angle (parallel, perpendicular or some defined angle).

(m) After machining, the specimen is removed from the fixture and the silt trapped inside the notch crack is washed away.

(n) Two lines are drawn on both sides of the disc along the notch plane direction. The two loading lines contacting the lower and upper loading plates can be obtained by joining the four end points of the two lines drawn. Along these two loading lines, the rock surface should be flat and smooth in order to ensure full contact with the loading platens. The parallelarity of these two lines to the disc axis, or their perpendicularity to both sides of the disc surfaces should meet the basic requirement mentioned above, i.e., within 0.25 mm in 100 mm.

(o) After machining, the specimen should be dried at 104° for 24 hours to remove the water absorbed during preparation.

(p) At this stage, the specimen geometry dimensions, disc diameter **D**, disc thickness **B**, and maximum chevron notch crack length $2a_1$ should be precisely measured to the nearest 0.1 mm. **D** should be measured by averaging two diameters at right angles near both sides of the disc surfaces. **B** should be measured by averaging four measured values obtained at the four end points of a pair of orthogonal diameters. $2a_1$ should be measured as the mean of the two values measured on both sides of the disc surfaces. After the measurement, the geometry should be converted into dimensionless expressions α_B and α_1.

(q) The specimens should be discarded if the measured geometries α_1 and α_B do not meet the valid geometrical requirement outlined in Equation (3) and illustrated in Figure 2.

Calibration

9. (a) The load cell calibration shall be checked at regular intervals.

(b) If the LPD or the CMOD is measured, the displacement measuring equipment shall be checked for linearity and calibrated before each series of tests.

Setting up

10. (a) The specimen shall be carefully installed in the testing machine in such a way that the load transfer system is properly aligned. Alignment aids (see 5) should be used to help the setting up of the specimen and the perpendicularity requirement (see 5) of the crack plane to the loading plates should be checked as the last step before the actual load is applied. A small holding load should be used to secure the specimen in the correct position. The contact loading lines on both the lower and upper loading plates should be checked to ensure that full contact is made between the plates and the specimen.

(b) The setting of the ram or cross-head position and position limits should be chosen so that no damage to the machine or displacement gauges can occur if the specimen should fail prematurely in a sudden or unexpected manner.

Testing

11. (a) The test can be run both under the load or displacement control. The load history shall be recorded and test shall be run until the specimen fails. The average stress intensity loading rate during the test shall be not less than 0.25 MPa$\sqrt{m}$/sec or such that failure occurs within 20 sec of initial load application.

(b) At least two unloading-reloading cycles should be performed at the load point of about 20% of the maximum load to ensure a perfect contact between the loading plates and the specimen.

(c) The maximum load on the specimen should be recorded with an error less than $\pm 1.0\%$.

(d) If the LPD and the CMOD displacements are measured, they should be determined to the accuracy of 0.001mm.

(e) The results shall be considered invalid and a further test conducted if the crack deviates from symmetrical crack plane defined by the notch plane by more than 0.05**D** within 0.5**D** from the centre of the disc surface.

(f) After the test, the geometrical dimension $\mathbf{2a_0}$ shall be measured from the broken sample and conveted into a dimensionless expression (see 3) α_0.

6 CALCULATIONS FOR FRACTURE TOUGHNESS

12. (a) The fracture toughness of the specimen shall be calculated by the following formula:

$$K_{IC} = \frac{P_{\max}}{B\sqrt{D}} \cdot Y^*_{\min} \qquad (5)$$

where $\mathbf{Y^*_{min}}$ is the critical dimensionless stress intensity value for the specimen, which is determined by the specimen geometry dimensions α_0, α_1 and α_B only.

(b) $\mathbf{Y^*_{min}}$ shall be calculated by the following formula:

$$Y^*_{\min} = u \cdot e^{v \cdot \alpha_1} \qquad (6)$$

Table 2 Values of **u** and **v**

α_0	0.100	0.150	0.175	0.200	0.225	0.250	0.275	0.300	0.325	0.350	0.375	0.400	0.425	0.450
							u							
α_B														
0.440	0.2747	0.2774	0.2791	0.2808	0.2825	0.2844	0.2865	0.2883	0.2914	0.2943	0.2979	0.3024	0.3069	0.3120
0.480	0.2727	0.2752	0.2765	0.2782	0.2795	0.2812	0.2833	0.2856	0.2882	0.2918	0.2954	0.2994	0.3039	0.3090
0.520	0.2708	0.2727	0.2740	0.2757	0.2771	0.2788	0.2806	0.2828	0.2857	0.2887	0.2925	0.2968	0.3013	0.3060
0.560	0.2689	0.2705	0.2716	0.2733	0.2744	0.2763	0.2781	0.2805	0.2831	0.2867	0.2901	0.2943	0.2989	0.3039
0.600	0.2667	0.2684	0.2696	0.2709	0.2721	0.2739	0.2757	0.2782	0.2812	0.2844	0.2882	0.2921	0.2967	0.3015
0.640	0.2649	0.2665	0.2674	0.2685	0.2701	0.2719	0.2738	0.2764	0.2791	0.2825	0.2863	0.2905	0.2947	0.2992
0.680	0.2632	0.2646	0.2655	0.2667	0.2682	0.2704	0.2718	0.2744	0.2774	0.2807	0.2848	0.2888	0.2930	0.2971
0.720	0.2611	0.2628	0.2637	0.2650	0.2667	0.2683	0.2705	0.2727	0.2763	0.2794	0.2831	0.2871	0.2916	0.2954
0.760	0.2598	0.2612	0.2625	0.2637	0.2650	0.2668	0.2693	0.2719	0.2744	0.2781	0.2819	0.2860	0.2895	0.2934
0.800	0.2582	0.2602	0.2611	0.2625	0.2641	0.2657	0.2680	0.2706	0.2736	0.2772	0.2811	0.2845	0.2878	0.2916
0.840	0.2572	0.2586	0.2599	0.2612	0.2628	0.2649	0.2672	0.2699	0.2727	0.2763	0.2801	0.2831	0.2867	0.2891
0.880	0.2562	0.2578	0.2593	0.2602	0.2621	0.2642	0.2668	0.2691	0.2723	0.2754	0.2793	0.2816	0.2853	0.2867
0.920	0.2553	0.2572	0.2582	0.2598	0.2613	0.2634	0.2658	0.2684	0.2716	0.2747	0.2782	0.2811	0.2831	0.2856
0.960	0.2549	0.2566	0.2578	0.2593	0.2612	0.2633	0.2655	0.2685	0.2710	0.2746	0.2767	0.2799	0.2811	0.2825
1.000	0.2547	0.2564	0.2576	0.2591	0.2610	0.2630	0.2653	0.2679	0.2709	0.2738	0.2768	0.2786	0.2794	0.2794
1.040	0.2544	0.2565	0.2576	0.2593	0.2608	0.2627	0.2653	0.2678	0.2708	0.2727	0.2747	0.2769	0.2769	0.2765
1.080	0.2543	0.2561	0.2576	0.2591	0.2608	0.2630	0.2657	0.2674	0.2695	0.2718	0.2735	0.2736	0.2731	0.2721
1.120	0.2547	0.2565	0.2579	0.2591	0.2612	0.2630	0.2648	0.2672	0.2693	0.2705	0.2717	0.2712	0.2697	0.2679
1.160	0.2548	0.2572	0.2579	0.2600	0.2613	0.2627	0.2645	0.2666	0.2679	0.2684	0.2695	0.2688	0.2661	0.2628
1.200	0.2552	0.2574	0.2585	0.2598	0.2616	0.2629	0.2648	0.2650	0.2671	0.2675	0.2655	0.2633	0.2608	0.2566
1.240	0.2555	0.2572	0.2581	0.2603	0.2610	0.2619	0.2630	0.2636	0.2634	0.2633	0.2616	0.2596	0.2564	0.2513
1.280	0.2561	0.2577	0.2586	0.2595	0.2600	0.2611	0.2613	0.2616	0.2608	0.2607	0.2582	0.2549	0.2501	0.2447
							v							
0.440	1.7813	1.7820	1.7820	1.7833	1.7863	1.7893	1.7923	1.7967	1.7966	1.7977	1.7973	1.7932	1.7901	1.7850
0.480	1.7748	1.7763	1.7787	1.7800	1.7843	1.7881	1.7907	1.7934	1.7952	1.7929	1.7923	1.7901	1.7866	1.7811
0.520	1.7694	1.7734	1.7758	1.7769	1.7808	1.7845	1.7884	1.7907	1.7911	1.7920	1.7897	1.7860	1.7823	1.7784
0.560	1.7644	1.7701	1.7732	1.7748	1.7794	1.7822	1.7856	1.7877	1.7885	1.7864	1.7857	1.7820	1.7779	1.7725
0.600	1.7620	1.7668	1.7692	1.7727	1.7770	1.7792	1.7826	1.7835	1.7833	1.7831	1.7805	1.7782	1.7733	1.7689
0.640	1.7580	1.7631	1.7671	1.7707	1.7732	1.7757	1.7788	1.7794	1.7795	1.7779	1.7753	1.7716	1.7686	1.7652
0.680	1.7550	1.7602	1.7640	1.7676	1.7707	1.7711	1.7757	1.7759	1.7754	1.7741	1.7700	1.7666	1.7630	1.7612
0.720	1.7536	1.7580	1.7616	1.7647	1.7661	1.7698	1.7708	1.7722	1.7693	1.7683	1.7652	1.7617	1.7574	1.7562
0.760	1.7497	1.7553	1.7568	1.7600	1.7635	1.7656	1.7649	1.7652	1.7662	1.7624	1.7593	1.7554	1.7548	1.7528
0.800	1.7474	1.7506	1.7538	1.7557	1.7581	1.7611	1.7613	1.7603	1.7596	1.7561	1.7525	1.7512	1.7509	1.7494
0.840	1.7430	1.7487	1.7500	1.7522	1.7545	1.7547	1.7551	1.7548	1.7535	1.7499	1.7469	1.7473	1.7448	1.7497
0.880	1.7392	1.7438	1.7446	1.7487	1.7490	1.7492	1.7478	1.7487	1.7463	1.7452	1.7403	1.7434	1.7414	1.7493
0.920	1.7357	1.7390	1.7413	1.7423	1.7440	1.7446	1.7443	1.7432	1.7411	1.7389	1.7360	1.7363	1.7417	1.7448
0.960	1.7299	1.7337	1.7358	1.7370	1.7372	1.7373	1.7372	1.7346	1.7344	1.7309	1.7343	1.7331	1.7414	1.7483
1.000	1.7243	1.7279	1.7300	1.7308	1.7310	1.7307	1.7306	1.7297	1.7273	1.7270	1.7258	1.7302	1.7394	1.7525
1.040	1.7196	1.7213	1.7231	1.7232	1.7246	1.7256	1.7237	1.7231	1.7204	1.7238	1.7272	1.7293	1.7423	1.7569
1.080	1.7143	1.7167	1.7174	1.7176	1.7186	1.7172	1.7152	1.7182	1.7199	1.7202	1.7250	1.7366	1.7511	1.7681
1.120	1.7071	1.7097	1.7101	1.7118	1.7105	1.7110	1.7130	1.7120	1.7136	1.7199	1.7255	1.7401	1.7584	1.7789
1.160	1.7015	1.7016	1.7046	1.7023	1.7048	1.7076	1.7087	1.7093	1.7136	1.7225	1.7287	1.7436	1.7673	1.7942
1.200	1.6951	1.6959	1.6970	1.6989	1.6984	1.7012	1.7020	1.7105	1.7112	1.7204	1.7397	1.7611	1.7841	1.8150
1.240	1.6902	1.6925	1.6947	1.6919	1.6961	1.7007	1.7044	1.7117	1.7220	1.7332	1.7513	1.7711	1.7974	1.8332
1.280	1.6833	1.6861	1.6879	1.6910	1.6959	1.6999	1.7072	1.7151	1.7283	1.7390	1.7609	1.7865	1.8200	1.8578

where **u** and **v** are constants determined by α_0 and α_B only. Their values can be found in Table 2 if the dimensionless specimen geometrical parameters α_0 and α_B are matching the values listed in the table. Otherwise linear interpolation should be used to calculate their values.

7 VALIDITY ANALYSIS

Specimen size

13. (a) Since no distinct validity criterion relating to specimen size can be given at this stage, a valid specimen size for a valid experimental fracture toughness test shall be obtained from the comparison of the $\mathbf{K_{IC}}$ values by different specimen diameters **D**. The minimum valid **D** value $\mathbf{D_{min}}$ will be the specimen diameter of the CCNBD which generates $\mathbf{K_{IC}}$ values consistent to larger diameter specimens. At this stage, $\mathbf{D_{min}}$ can be estimated by the following equation:

$$D_{\min} = 8.88 + 1.4744\cdot(\frac{K_{IC}}{\sigma_t})^2 \qquad (7)$$

where σ_t is the tensile strength of the rock sample. Generally for rock materials $\mathbf{D_{min}} = 75\text{mm}$.

(b) There is no guarantee at the present that a fracture toughness value determined according to the present method accurately represents a material property. However current research has shown that the value obtained will be closer to the real material property value for more brittle rocks.

Use of the fracture toughness value obtained

14. The fracture toughness values obtained using this method are considered to be conservative for design analysis, provided that the defects analyzed are much smaller than structural dimensions and much larger than the characteristic microstructure of the material. If this is not the case, then such values should be used to assess the relative fracture resistance of different materials.

8 REPORTING OF RESULTS

15. All reports of results should contain the following information:

General data

16. Details of testing equipment and procedures employed. Reference may be made to the present method, describing the departures from recommended procedure and the reasons for these.

Test sample data

17. (a) The sample number, source location and rock type, and the nature and *in situ* orientation of any planes of anisotropy and weakness.

(b) Core axis with respect to *in situ* geology and structures, in the case of sub-samples, the direction of loading.

(c) Storage history and environment, water content and degree of saturation at the time of testing.

(d) A tabulation of specimen data related to the fracture toughness determination, including auxiliary parameters (see 18 below).

(e) For each sub-sample a summary tabulation of mean fracture toughness values ± standard deviation.

(f) Index properties obtained by other types of testing, and physical data such as specific gravity, grain size, porosity, and permeability, citing the method of determination for each.

Specimen data

18. For each specimen in the sample the information should contain the following:

(a) Specimen dimensions **D**, $\mathbf{D_s}$, **B**, $\mathbf{a_0}$, $\mathbf{a_1}$, and $\mathbf{h_c}$.

(b) The loading rate $\mathbf{p_r}$ or the time to failure **t**.

(c) Maximum load $\mathbf{P_{max}}$.

(d) Critical SIF $\mathbf{Y^*_m}$.

(e) Fracture toughness value $\mathbf{K_{IC}}$.

Chapter 7

Theoretical Analysis of Mixed Mode Fracture Problems for CSTBD and CCNBD Specimens

§7.1 Introduction

In this chapter, theoretical solutions for mixed mode fracture problems for the CSTBD and CCNBD specimens are presented using dislocation theory and complex stress function methods. It is believed that these results will provide a theoretical foundation for the development of these two specimens for mixed mode fracture research of rock materials.

§7.2 Background to the Research

Mixed **Mode I** and **Mode II** fracture situations can simply obtained by inclining the crack orientation [**A-A**] in the CSTBD or CCNBD geometry to the diametrical loading direction [**Y**] to a certain angle θ, as shown in Figure 7.1. By changing this inclined angle, combinations of different fracture intensities for the two different fracture modes can be obtained by which mixed mode fracture problems, such as the mixed mode fracture initiation, mixed mode crack propagation and mixed mode fracture strength locus for different materials can be examined.

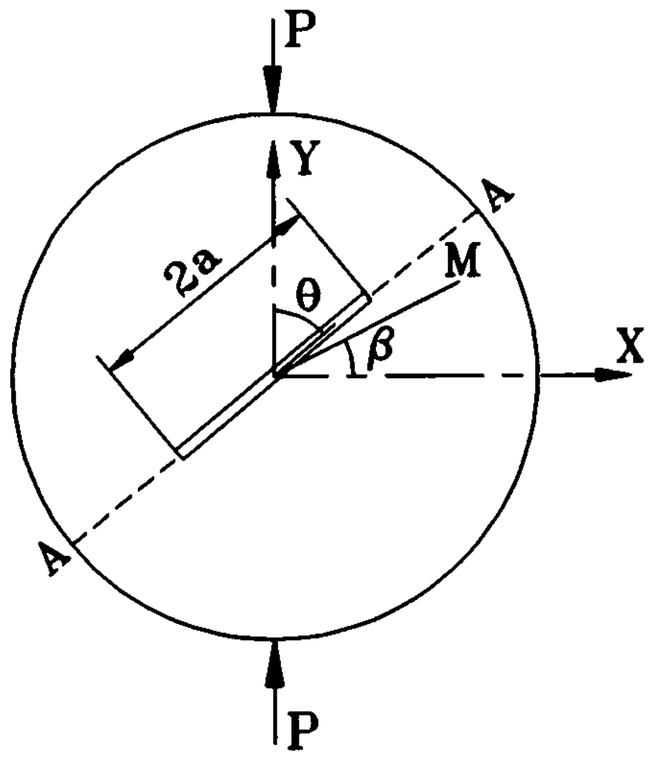

Fig. 7.1 Mixed Mode Brazilian Disc

The mixed mode fracture problems for the CSTBD specimen geometry has been investigated by Awaji & Sato (1978), Sanchez (1979) and Atkinson (1982) using dislocation and boundary collocation methods. They studied short crack cases by assuming the crack in the CSTBD specimen behaves like a crack in an infinite sheet [Whittaker, 1992] and therefore the higher order components describing crack behaviour and the interaction between the crack and the boundary can be neglected. As a result, this approximation will only be valid for crack cases

with length $\alpha < 0.6$ [Whittaker, 1992]. Based on our experience of using the CCNBD specimen for Mode I fracture toughness measurement, a CSTBD specimen with $\alpha < 0.6$ or a CCNBD with $\alpha_1 < 0.6$ will be difficult to machine and the upper limit of $(\alpha \text{ or } \alpha_1)_{upper} = 0.65$-$0.80$ are considered to be appropriate for practical applications. Therefore theoretical evaluations of the SIF for the mixed mode CSTBD geometry with a crack length $\alpha > 0.6$ has to be obtained.

The stepwise superimposition technique developed in Chapter 3 has been successfully used for the **Mode I** CSTBD SIF evaluations for any crack length, as shown in the last few chapters. By taking advantages of this technique, we develop three different evaluation methods in this chapter based on dislocation theory and complex stress function theories, which are believed to be able to calculate correctly the SIF values for the mixed mode CSTBD geometry with any crack lengths up to $\alpha = 0.95$ and with an error of less than 1% for each evaluation.

§7.3 Theoretical Analysis of the Problem and the Method of Solution

§7.3.1 Problem Analysis

As for the method given in Chapter 3, we consider a Brazilian disk , diameter **D**, radius **R** and thickness **B**, subjected to a pair of diametrical compressive loads **P**, with a central straight-through crack **2a** inclined to the loading direction with an angle of θ (Figure 7.1). The problem can then be divided into the following three different problems and the solution can be obtained simply by summing up all the respective results.

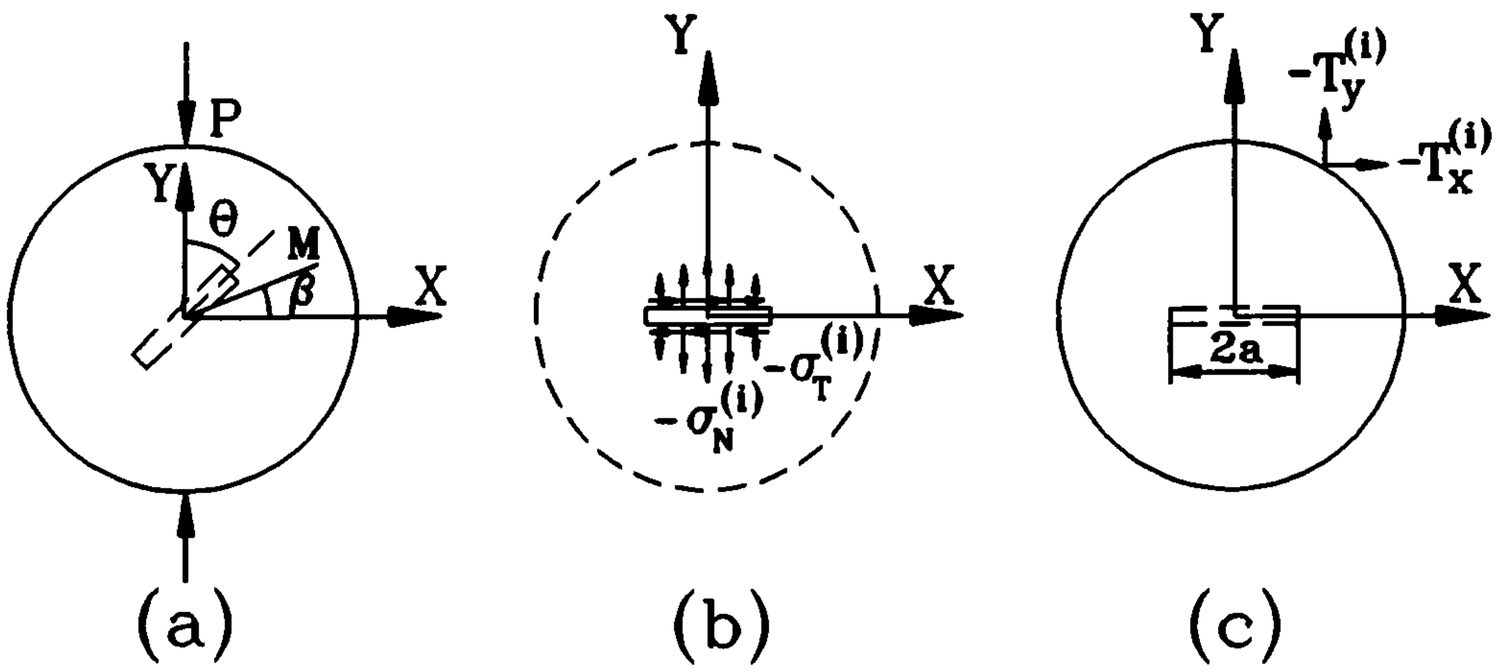

Figure 7.2 Numerical Solution Procedure

1) A solid Brazilian disk subjected to a pair of diametrical loads **P** (Figure 7.2.a).

Boundary conditions:

$$\begin{cases} P_s = 0 & r=R,\ 0\le\beta\le 2\pi, \\ P_n = \begin{cases} -P & r=R,\ \beta=\pm\dfrac{\pi}{2} \\ 0 & others \end{cases} \end{cases} \tag{7.1}$$

2) Case (1) will create a distributed normal and tangential stresses $\sigma_N^{(0)}$ and $\sigma_T^{(0)}$ along the pseudo crack part of the solid disk diameter $0 < r < a$, $\beta = \pm\pi/2-\theta$. By introducing a traction free crack in this part, the stresses should be cancelled. So the second problem will be an infinite region with a central crack **2a** subjected to internal distributed normal and tangential stresses $-\sigma_N^{(0)}$ and $-\sigma_T^{(0)}$ (Figure 7.2.b).

Boundary conditions:

$$\begin{cases} \sigma_r = \sigma_\beta = \sigma_{r\beta} = 0 & r\to\infty \\ \sigma_N = -\sigma_N^{(i)},\ (i=0,1,2,\cdots) & 0 < r < a,\ \beta = \pm\dfrac{\pi}{2} \\ \sigma_T = -\sigma_T^{(i)},\ (i=0,1,2,\cdots) & 0 < r < a,\ \beta = \pm\dfrac{\pi}{2} \end{cases} \tag{7.2}$$

where **i** is the step number of the stepwise superimposition and at this step, $\mathbf{i}=0$.

3) Case (2) will produce stresses $T_x^{(0)}$ and $T_y^{(0)}$ along the pseudo circumference which is identical to the disc boundary. However the practical disk is traction force free along the boundary and therefore these stresses should be cancelled. Thus the third problem is also a solid Brazilian disk, identical to that in case (1), but subjected to boundary traction stresses instead (Figure 7.2.c).

Boundary condition:

$$\begin{cases} T_x = -T_x^{(i)} & r = R,\ 0 < \beta < 2\pi, \\ T_y = -T_y^{(i)} & r = R,\ 0 < \beta < 2\pi \\ & i = 0,1,2,3,\cdots \end{cases} \tag{7.3}$$

where **i** is the step number of the stepwise superimposition procedure, and at this stage, $\mathbf{i}=0$.

4) Under the action of the boundary traction stresses $-T_x^{(0)}$ and $-T_y^{(0)}$, the normal and tangential stresses $\sigma_N^{(1)}$ and $\sigma_T^{(1)}$ will be again set up ($\sigma_N^{(1)} < \sigma_N^{(0)}$ and $\sigma_T^{(1)} < \sigma_T^{(0)}$) along that part of the diameter $0 < r < a$, $\beta = \pm\pi/2-\theta$. As mentioned above, these need cancelling.

Hence the problem will come back to case (2) while changing the internal pressure from $\sigma_N^{(0)}$ to $\sigma_N^{(1)}$ and $\sigma_T^{(0)}$ to $\sigma_T^{(1)}$ and the step number will be $\mathbf{i = 1}$.

5) Therefore the whole superimposition procedure carries on between case (2) and (3). Obviously the iteration is convergent due to the apparent condition:

$$\begin{cases} \sigma_N^{(i+1)} < \sigma_N^{(i)} \\ \sigma_T^{(i+1)} < \sigma_T^{(i)} \\ T_x^{(i+1)} < T_x^{(i)} \\ T_y^{(i+1)} < T_y^{(i)} \\ i = 0,1,2,3,\cdots \end{cases} \tag{7.4}$$

6) The final SIF results can then be obtained by summing up all the results of the SIF values calculated from case (2) during the different steps of the whole iteration.

§7.3.2 Basic Theoretical Solutions for Case (1), (2) and (3) Problems

§7.3.2.1 Case (1) Problem (Figure 7.2.a)

The solutions for case (1) problem can be derived from the basic solutions of a solid disc subjected to an arbitrary boundary loading presented by Timoshenko (1970). As shown in Figure 7.3, we derived the normal and tangential stresses at any point **M** with $\mathbf{r = s}$ along the **A-A** diameter where the crack will lie within the range of $\mathbf{-a \le s \le +a}$ as given by the following equations:

$$\begin{cases} \sigma_N = -\dfrac{2 \cdot P \cdot \cos\varphi_1}{\pi \cdot r_1} \cdot \sin^2(\theta+\varphi_1) - \dfrac{2 \cdot P \cdot \cos\varphi_2}{\pi \cdot r_2} \cdot \sin^2(\theta-\varphi_2) + \dfrac{2 \cdot P}{\pi \cdot D} \\ \sigma_T = -\dfrac{2 \cdot P \cdot \cos\varphi_1}{\pi \cdot r_1} \cdot \dfrac{\sin[2 \cdot (\theta+\varphi_1)]}{2} - \dfrac{2 \cdot P \cdot \cos\varphi_2}{\pi \cdot r_2} \cdot \dfrac{\sin[2 \cdot (\theta+\varphi_2)]}{2} \end{cases} \tag{7.5}$$

where,

$$\begin{cases} r_1 = \sqrt{s^2 \cdot \sin^2\theta + (s \cdot \cos\theta - R)^2} \\ r_2 = \sqrt{s^2 \cdot \sin^2\theta + (s \cdot \cos\theta + R)^2} \\ \varphi_1 = \arcsin\dfrac{s \cdot \sin\theta}{r_1} \\ \varphi_2 = \arcsin\dfrac{s \cdot \sin\theta}{r_2} \end{cases} \tag{7.6}$$

Figure 7.4 is the distribution of σ_N and σ_T along a diameter of the disc with inclined angle θ to the loading direction varying from 0° to 90°. Uneven stress distributions are shown except for the special case of $\theta = 0°$.

Atkinson (1982) used polynomial lines to fit the above normal and tangential stress distributions so that the solutions of the equations in his theoretical evaluation can be reached. Certainly this approximation will cause error in the final results especially when the stresses vary considerably. In our analysis, the diameters are divided into small segments and the stresses acting on the segments are stored in the form of arrays according their actual values instead of in the form of an approximate functional relation.

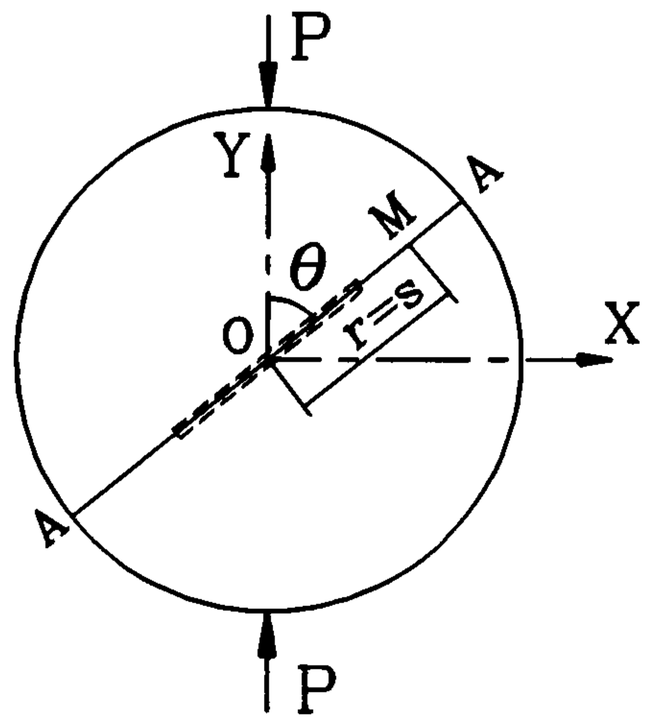

Figure 7.3 Loaded Brazilian Disc

Therefore no approximation for the distribution has been made and the results are believed to

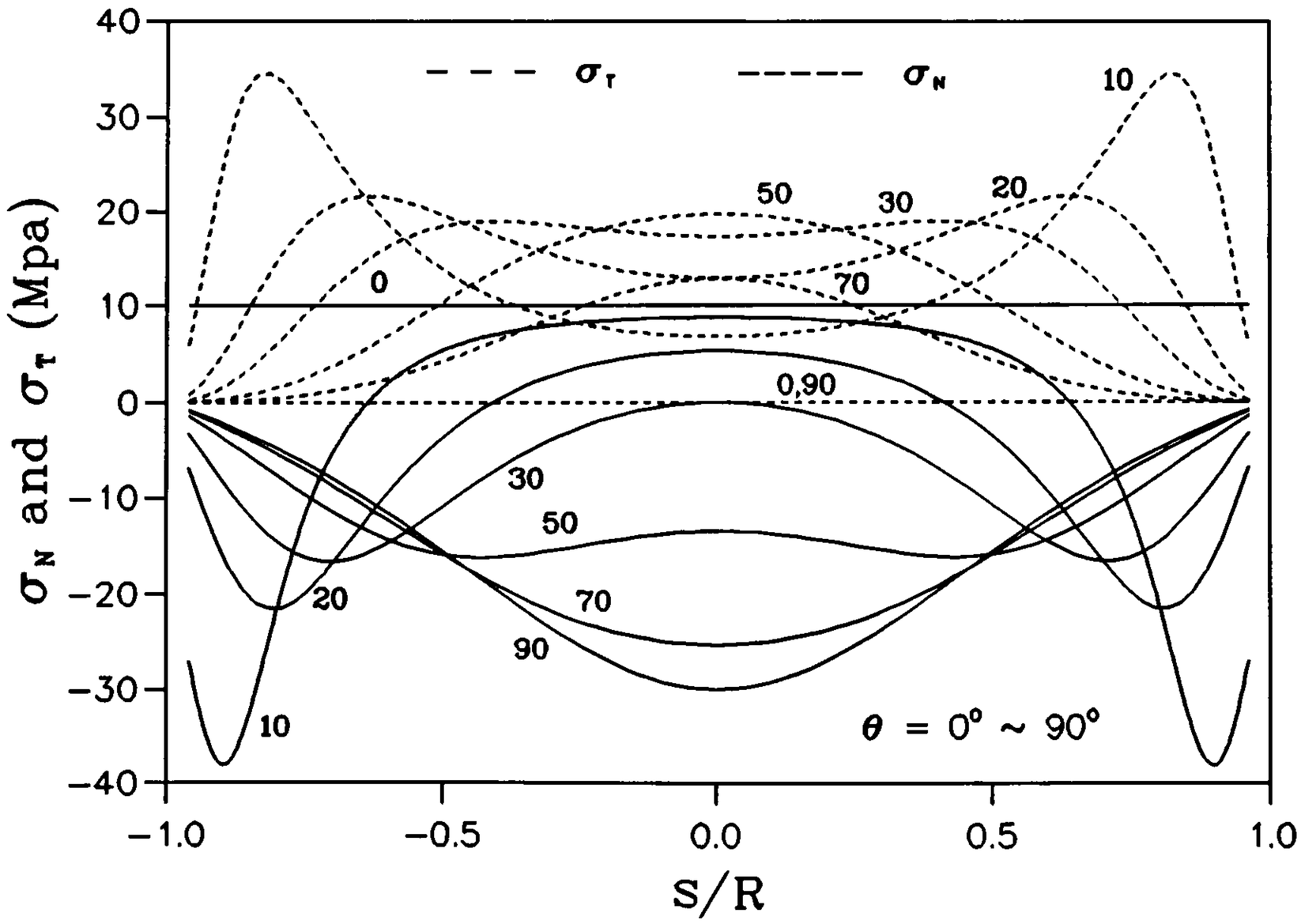

Figure 7.4 Normal and Tangential Stress Distributions along Disc Diameters

be accurate when the segments are small enough.

§7.3.2.2 Case (2) Problem

The Case (2) problem is an infinite sheet with a central crack subjected to internal normal and tangential stresses $\sigma_N^{(i)}$ and $\sigma_T^{(i)}$ $[i = 0,1,2,3,....]$. Sneddon's results used in Chapter 3 can no longer be used as the internal loads are not evenly distributed. Therefore we seek solutions from dislocation and complex stress function methods. In the following sections, unless otherwise defined, variable **s** will be referred to as the local coordinate along the crack line with the origin point sitting at the central point of the crack (Figure 7.6 - 7.8 below). For instance, the coordinates of the tips of a crack with length **2a** will then be $s = \pm a$.

1. <u>Dislocation Method</u>

One of the common methods to solve the problem of an infinite region with a central crack (two dimensional, mixed **Mode I** and **Mode II**) subjected to arbitrary surface normal and tangential stresses σ_N and σ_T is by assuming that the problem can be solved by introducing two distributional infinitesimal edge dislocation densities $f(\zeta)$ and $g(\zeta)$ ($\zeta \in [-a, +a]$) between the crack tips **-a** and **a**, which simulate the normal and tangential behaviour of the crack respectively [Atkinson, 1972] [Awaji & Sato, 1978] [Ioakimidis, 1982]. For the basic theories and its application to macro-fracture mechanics of dislocation theory, the following references can be consulted, [Hull & Bacon, 1984] and [H.Liebowitz, 1971].

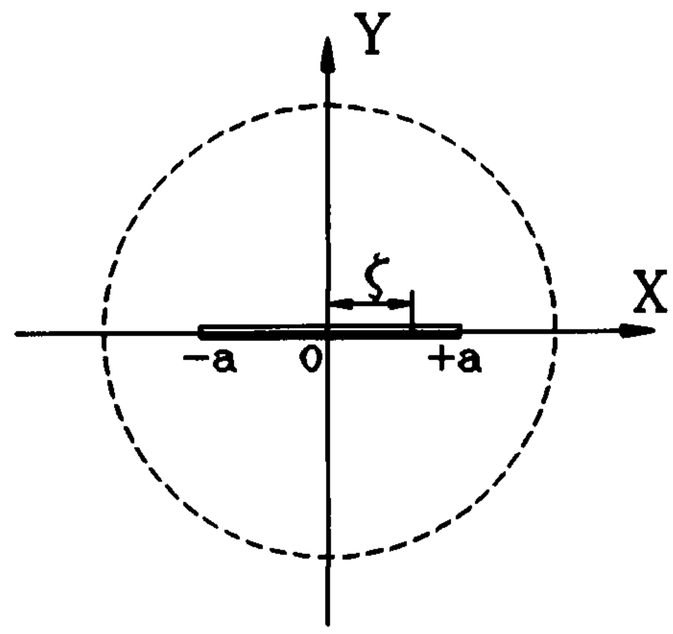

Figure 7.5 Dislocation Coordinates

The origin of the **x-y** coordinates is set at the centre of the crack and the **x**-axis in the crack direction, as shown in Figure 7.5. Under the action of the continuous edge dislocations $f(\zeta)$ and $g(\zeta)$, the total Burgers vector [Hull, 1984] of dislocation intensities between ζ and $\zeta + d\zeta$ will be $b_I \cdot f(\zeta) \cdot d\zeta$ and $b_{II} \cdot g(\zeta) \cdot d\zeta$ respectively for the two different dislocations. The stresses they produce are $\mathscr{E}_I \cdot f(\zeta) \cdot d\zeta/(x-\zeta)$ and $\mathscr{E}_{II} \cdot g(\zeta) \cdot d\zeta/(x-\zeta)$, where,

$$\mathscr{E}_I \text{ or } \mathscr{E}_{II} = \frac{G \cdot b_I \ (or \ G \cdot b_{II})}{2 \cdot \pi \cdot (1 - \nu)} \tag{7.7}$$

$\mathbf{b_I}$ and $\mathbf{b_{II}}$ are the material intrinsic Burgers vectors related to Mode I and Mode II fracture simulations respectively, **G** is the shear modulus and ν is the Poisson's ratio. Then from the requirements of equilibrium of the dislocations, $\mathbf{f}(\zeta)$ and $\mathbf{g}(\zeta)$ should satisfy the following equations:

$$\begin{cases} \mathscr{E}_I \cdot \int_{-a}^{a} \dfrac{f(\zeta)}{x-\zeta} \cdot d\zeta + \sigma_N(x) = 0 \\ \mathscr{E}_{II} \cdot \int_{-a}^{a} \dfrac{g(\zeta)}{x-\zeta} \cdot d\zeta + \sigma_T(x) = 0 \end{cases} \tag{7.8}$$

These integration equations are of the Cauchy type and are solved by Muskhelishvili (1953a, 1953b) by the inverse theorem. The solutions of $\mathbf{f}(\zeta)$ and $\mathbf{g}(\zeta)$ can be expressed as follows:

$$\begin{bmatrix} f(\zeta) \\ g(\zeta) \end{bmatrix} = \frac{1}{\mathscr{E} \cdot \pi^2 \sqrt{a^2 - \zeta^2}} \cdot \int_{-a}^{a} \frac{\sqrt{a^2 - \zeta^2}}{x - \zeta} \cdot \begin{bmatrix} \sigma_N(x) \\ \sigma_T(x) \end{bmatrix} \cdot dx \tag{7.9}$$

where for the reason of simplicity, $\mathscr{E}_I$ and $\mathscr{E}_{II}$ are expressed by $\mathscr{E}$ only.

From Equation (7.9) it is very easy to see that the values of $\mathbf{f}(\zeta)$ and $\mathbf{g}(\zeta)$ will tend to infinity at the two extreme points $\zeta = \pm a$ when the right hand side integration exists. To avoid this mathematical difficulty for numerical analysis we make a substitution of the dislocation density functions in the following forms:

$$\begin{bmatrix} F_o(\zeta) \\ G_o(\zeta) \end{bmatrix} = \sqrt{a^2 - \zeta^2} \cdot \begin{bmatrix} f(\zeta) \\ g(\zeta) \end{bmatrix} \tag{7.10}$$

Take $\mathbf{F_o}(\zeta)$ and $\mathbf{G_o}(\zeta)$ as the new dislocation density functions and from the above relations we can obtain their expression as followed:

$$\begin{bmatrix} F_o(\zeta) \\ G_o(\zeta) \end{bmatrix} = \frac{1}{\mathscr{E} \cdot \pi^2} \cdot \int_{-a}^{a} \frac{\sqrt{a^2 - x^2}}{x - \zeta} \cdot \begin{bmatrix} \sigma_N(x) \\ \sigma_T(x) \end{bmatrix} \cdot dx \tag{7.11}$$

After this substitution, $\mathbf{F_o}(\zeta)$ and $\mathbf{G_o}(\zeta)$ will then become finite continuous functions within the range of $\zeta \in [-a, a]$. It will be proved later that this substitution will yield equivalent results.

For the reason of greater convenience, we make a transformation of variable ζ into variable ϕ by the relation of $\zeta = a \cdot \sin\phi$, then functions $\mathbf{F}(\phi) = \mathbf{F_o}(\zeta) = \mathbf{F_o}(a \cdot \sin\phi)$ and $\mathbf{G}(\phi) = \mathbf{G_o}(\zeta) = \mathbf{G_o}(a \cdot \sin\phi)$ will become continuous functions with a constant variation range $\phi \in [-\pi/2, +\pi/2]$ independent of the crack length. From the above equations we can write the expressions for $\mathbf{F}(\phi)$ and $\mathbf{G}(\phi)$ in the following equations:

$$\begin{bmatrix} F(\phi) \\ G(\phi) \end{bmatrix} = \frac{1}{\mathscr{E}\cdot\pi^2}\cdot\int_{-a}^{a} \frac{\sqrt{a^2 - x^2}}{x - a\cdot\sin\phi}\begin{bmatrix} \sigma_N(x) \\ \sigma_T(x) \end{bmatrix}\cdot dx \tag{7.12}$$

For an edge dislocation with Burgers vector value **b** in the two dimensional condition, the stress field caused is presented by Hull & Bacon (1984) as follows. Suppose the dislocation is in the **x** direction, i.e., Mode II fracture simulation,

$$\begin{cases} \sigma_{xx} = -\mathscr{E}_{II}\, y\cdot\dfrac{3\cdot x^2 + y^2}{(x^2 + y^2)^2} \\ \sigma_{yy} = \mathscr{E}_{II}\, y\cdot\dfrac{x^2 - y^2}{(x^2 + y^2)^2} \\ \sigma_{xy} = \sigma_{yx} = \mathscr{E}_{II}\cdot x\cdot\dfrac{x^2 - y^2}{(x^2 + y^2)^2} \end{cases} \tag{7.13}$$

For the edge dislocation in **y** direction, simulating Mode I fracture, the stress field can be obtained simply by changing **x** to **y**, **y** to **x** and $\mathscr{E}_{II}$ to $\mathscr{E}_{I}$ in Equation (7.13).

Under the action of the dislocations suggested for the case (2) problem, the basic dislocation Burgers vector intensities are $\mathbf{b_I}\cdot\mathbf{f}(\zeta)\cdot\mathbf{d}\zeta$ and $\mathbf{b_{II}}\cdot\mathbf{g}(\zeta)\cdot\mathbf{d}\zeta$ acting at the point $(\zeta,\mathbf{0})$. By replacing the dislocation value $\mathbf{b_I}$ and $\mathbf{b_{II}}$ (implied in the $\mathscr{E}_{I}$ and $\mathscr{E}_{II}$) in Equation (7.13) by these two dislocation intensities and changing **x** to $(\mathbf{x}\text{-}\mathbf{a}\cdot\mathbf{sin}\boldsymbol{\phi})$ in the equations, the resulting stress field at any arbitrary point (**x**,**y**) in the region can be obtained by summing up all the stress components caused by all the individual dislocations distributed over the crack line **[-a, + a]**, i.e.,

$$\begin{bmatrix} \sigma_{xx} \\ \sigma_{yy} \\ \sigma_{xy} \end{bmatrix} = \sum_{\zeta=-a}^{a} \left\{ \begin{bmatrix} \sigma_{xx}^{I} \\ \sigma_{yy}^{I} \\ \sigma_{xy}^{I} \end{bmatrix}_{\zeta}\cdot f(\zeta)\cdot d\zeta + \begin{bmatrix} \sigma_{xx}^{II} \\ \sigma_{yy}^{II} \\ \sigma_{xy}^{II} \end{bmatrix}_{\zeta}\cdot g(\zeta)\cdot d\zeta \right\} \tag{7.14}$$

where $\boldsymbol{\sigma}_{xx}^{I,II}$, $\boldsymbol{\sigma}_{yy}^{I,II}$ and $\boldsymbol{\sigma}_{xy}^{I,II}$ are the stress field caused by dislocation Burgers vectors $\mathbf{b_I}$ and $\mathbf{b_{II}}$ in **y** (**Mode I**) and **x** (**Mode II**) directions acting at the crack point of $\mathbf{s}=\zeta$, $\zeta\in\mathbf{[-a, + a]}$ respectively, and their values can be calculated from Equation (7.13) above. Substitute Equation (7.9), (7.13) and $\zeta=\mathbf{a}\cdot\mathbf{sin}\boldsymbol{\phi}$ into Equation (7.14) we can finally reach the following calculation integrations:

$$\begin{cases} \sigma_{xx} = \int_{-\frac{\pi}{2}}^{\frac{\pi}{2}} \dfrac{F(\phi)\cdot(x-a\sin\phi)\cdot[y^2-(x-a\sin\phi)^2]-G(\phi)y\cdot[3\cdot(x-a\sin\phi)^2+y^2]}{[(x-a\sin\phi\ )^2+y^2]^2}\cdot d\phi \\ \sigma_{yy} = \int_{-\frac{\pi}{2}}^{\frac{\pi}{2}} \dfrac{-F(\phi)\cdot(x-a\sin\phi)\cdot[3y^2+(x-a\sin\phi)^2]+G(\phi)y\cdot[(x-a\sin\phi)^2-y^2]}{[(x-a\sin\phi)^2+y^2]^2}\cdot d\phi \\ \sigma_{xy} = \int_{-\frac{\pi}{2}}^{\frac{\pi}{2}} \dfrac{F(\phi)y\cdot[y^2-(x-a\sin\phi)^2]+G(\phi)\cdot(x-a\sin\phi)\cdot[(x-a\sin\phi)^2-y^2]}{[(x-a\sin\phi)^2+y^2]^2}\cdot d\phi \end{cases}$$

(7.15)

As can be seen from these equations, the final expression is only concerned with the substituted version of the dislocation densities $\mathbf{F}(\phi)$ and $\mathbf{G}(\phi)$. The actual version of the dislocation density $\mathbf{f}(\zeta)$ and $\mathbf{g}(\zeta)$ originally defined do not have to be calculated. This eliminates the difficulties of express the infinity values of the $\mathbf{f}(\zeta)$ and $\mathbf{g}(\zeta)$ when $\zeta = \pm \mathbf{a}$ during the numerical evaluation procedure.

For the superimposition procedure, during the **i**-th iteration step, the cancelling stresses acting on the crack line **[-a, + a]** are $\sigma_N^{(i)}$ and $\sigma_T^{(i)}$ [**i** = **0,1,2,3,....**]. Substituting the σ_N and σ_T in the above equations by $\sigma_N^{(i)}$ and $\sigma_T^{(i)}$ values the corresponding dislocation densities in the **i**-th iteration step $\mathbf{F}^{(i)}(\phi)$ and $\mathbf{G}^{(i)}(\phi)$ can be obtained from Equation (7.12) and then the stress field in the infinite region during this step $\sigma_{xx}^{(i)}$, $\sigma_{yy}^{(i)}$ and $\sigma_{xy}^{(i)}$ can be solved by Equation (7.15).

2. Complex Stress Function Method -- I (Z1 Method)

For an infinite sheet containing a central crack subjected to a pair of arbitrary concentrated loads **P** and **Q** acting on its surface at point (**s**,**0**) (Figure 7.6), Erdogan propose a complex stress function to solve the stress and displacement filed in the region, which originated from Hilbert's problem of stresses in plates with straight cuts [Erdogan, 1962]. By defining two complex stress functions $\mathbf{\Phi(Z)}$ and $\mathbf{\Omega(Z)}$, the stress field in the region can then be expressed as:

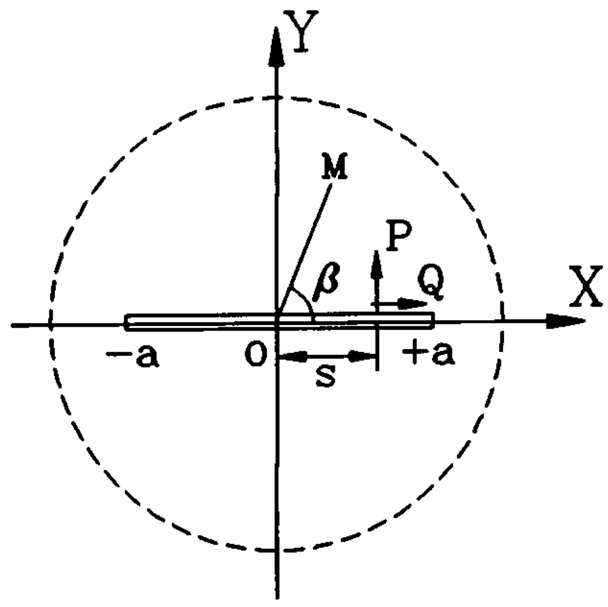

Figure 7.6 Z1 Method

$$\begin{cases} \sigma_{xx} + \sigma_{yy} = 2\cdot[\ \Phi(Z) + \overline{\Phi(Z)}\ ] \\ \sigma_{yy} - \sigma_{xx} + 2\cdot i\cdot\sigma_{xy} = 2\cdot[\ (\ \bar{Z} - Z\ )\cdot\Phi'(Z) - \Phi(Z) + \overline{\Omega(Z)}\ ] \end{cases} \qquad (7.16)$$

Erdogan then proposed the complex stress function expressions for the problem shown in Figure 7.6 as followed:

$$\begin{cases} \Phi(Z) = \dfrac{P - i\cdot Q}{4\cdot\pi\cdot i\cdot(Z - s)}\left[\sqrt{\dfrac{s^2 - a^2}{Z - a^2}} + 1\right] - \dfrac{\kappa - 1}{\kappa + 1}\cdot\dfrac{P - i\cdot Q}{4\cdot\pi\cdot i\sqrt{Z^2 - a^2}} \\ \Omega(Z) = \dfrac{P - i\cdot Q}{4\cdot\pi\cdot i\cdot(Z - s)}\left[\sqrt{\dfrac{s^2 - a^2}{Z^2 - a^2}} - 1\right] - \dfrac{\kappa - 1}{\kappa + 1}\cdot\dfrac{P - i\cdot Q}{4\cdot\pi\cdot i\sqrt{Z^2 - a^2}} \end{cases} \tag{7.17}$$

where $\mathbf{Z = x + i\cdot y = r\cdot e^{i\cdot\beta}}$ is the complex coordinate. κ is a constant and it is defined as follows $\kappa = 3\text{-}4\cdot\nu$.

With the help of the following relationship between the coordinates (Figure 7.7):

$$\begin{cases} Z = r\cdot e^{i\cdot\beta} \\ Z - a = r_1\cdot e^{i\cdot\beta_1} \\ Z + a = r_2\cdot e^{i\cdot\beta_2} \\ Z - s = r_3\cdot e^{i\cdot\beta_3} \end{cases} \tag{7.18}$$

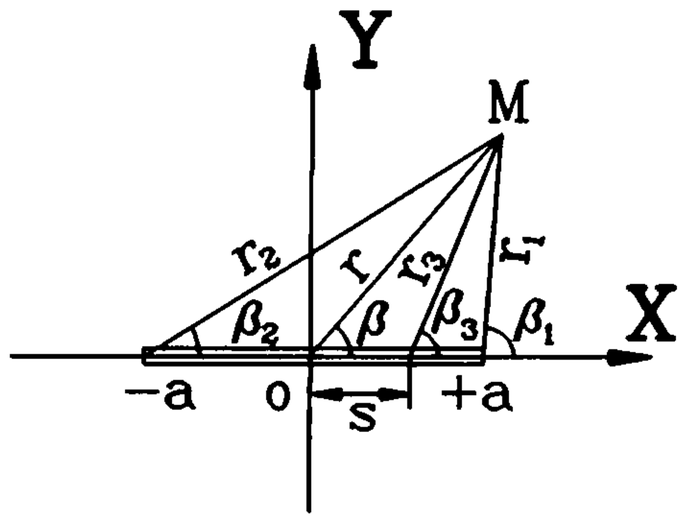

Fig. 7.7 Polar Coordinates

the explicit expressions for $\Phi'(Z)$, $\Phi(Z)$ can be derived as Equation (7.19) and Equation (7.20). $\Omega(Z)$ comes out in the same form as Equation (7.20) but the signs in lines 3 and 4 have to be changed from "+" to "-" and from "-" to "+".

After obtaining these expressions, the stress field can therefore be determined. During the superimposition procedure, for the **i**-th iteration step of an infinite region with a central crack subjected to internal normal and tangential surface stress $\sigma_N^{(i)}$ and $\sigma_T^{(i)}$ $[\mathbf{i = 0,1,2,3,....}]$ within the crack range $\mathbf{s \in [-a, +a]}$, the crack line can be divided into **J** small segments and the stress field in the region caused by the stresses $(\sigma_N^{(i)})_j$ and $(\sigma_T^{(i)})_j$ acting on a segment **ds [s,0]** is equal to that caused by the resulting concentrated loads $P_j^{(i)}$ and $Q_j^{(i)}$ acting at the central point of that segment, where $P_j^{(i)} = (\sigma_N^{(i)})_j\cdot ds$ and $Q_j^{(i)} = (\sigma_T^{(i)})_j\cdot ds$. The final stress field in the whole region can then be obtained by summing up all the stress components caused by the forces acting on each of the **J** crack segments, i.e. (Equation (7.21)),

$$\Phi'(Z) = -\frac{P\sqrt{a^2 - s^2}}{4\cdot\pi\cdot r_3^2\cdot\sqrt{r_1\cdot r_2}}\cdot\cos\frac{\beta_1 + \beta_2 + 4\cdot\beta_3}{2}$$

$$+ i\cdot\frac{P\sqrt{a^2 - s^2}}{4\cdot\pi\cdot r_3^2\cdot\sqrt{r_1\cdot r_2}}\cdot\sin\frac{\beta_1 + \beta_2 + 4\cdot\beta_3}{2}$$

$$-\frac{Q\sqrt{a^2 - s^2}}{4\cdot\pi\cdot r_3^2\cdot\sqrt{r_1\cdot r_2}}\cdot\sin\frac{\beta_1 + \beta_2 + 4\cdot\beta_3}{2}$$

$$- i\cdot\frac{Q\sqrt{a^2 - s^2}}{4\cdot\pi\cdot r_3^2\cdot\sqrt{r_1\cdot r_2}}\cdot\cos\frac{\beta_1 + \beta_2 + 4\cdot\beta_3}{2}$$

$$-\frac{P\sqrt{a^2 - s^2}}{4\cdot\pi\cdot r_3\cdot\sqrt{(r_1\cdot r_2)^3}}\cdot r\cdot\cos\frac{2\cdot\beta - 3\cdot\beta_1 - 3\cdot\beta_2 - 2\cdot\beta_3}{2}$$

$$- i\cdot\frac{P\sqrt{a^2 - s^2}}{4\cdot\pi\cdot r_3\cdot\sqrt{(r_1\cdot r_2)^2}}\cdot r\cdot\sin\frac{2\cdot\beta - 3\cdot\beta_1 - 3\cdot\beta_2 - 2\cdot\beta_3}{2}$$

$$+\frac{Q\sqrt{a^2 - s^2}}{4\cdot\pi\cdot r_3\cdot\sqrt{(r_1\cdot r_2)^3}}\cdot r\cdot\sin\frac{2\cdot\beta - 3\cdot\beta_1 - 3\cdot\beta_2 - 2\cdot\beta_3}{2}$$

$$- i\cdot\frac{Q\sqrt{a^2 - s^2}}{4\cdot\pi\cdot r_3\cdot\sqrt{(r_1\cdot r_2)^2}}\cdot r\cdot\cos\frac{2\cdot\beta - 3\cdot\beta_1 - 3\cdot\beta_2 - 2\cdot\beta_3}{2}$$

$$+\frac{P}{4\cdot\pi\cdot r_3^2}\cdot\sin 2\cdot\beta_3 + i\cdot\frac{P}{4\cdot\pi\cdot r_3^2}\cdot\cos 2\cdot\beta_3$$

$$-\frac{Q}{4\cdot\pi\cdot r_3^2}\cdot\cos 2\cdot\beta_3 + i\cdot\frac{Q}{4\cdot\pi\cdot r_3^2}\cdot\sin 2\cdot\beta_3$$

$$-\frac{\kappa - 1}{\kappa + 1}\cdot\frac{P\cdot r}{4\cdot\pi\cdot\sqrt{(r_1\cdot r_2)^3}}\cdot\sin\frac{2\cdot\beta - 3\cdot\beta_1 - 3\cdot\beta_2}{2}$$

$$+ i\cdot\frac{\kappa - 1}{\kappa + 1}\cdot\frac{P\cdot r}{4\cdot\pi\cdot\sqrt{(r_1\cdot r_2)^3}}\cdot\cos\frac{2\cdot\beta - 3\cdot\beta_1 - 3\cdot\beta_2}{2}$$

$$-\frac{\kappa - 1}{\kappa + 1}\cdot\frac{Q\cdot r}{4\cdot\pi\cdot\sqrt{(r_1\cdot r_2)^3}}\cdot\cos\frac{2\cdot\beta - 3\cdot\beta_1 - 3\cdot\beta_2}{2}$$

$$- i\cdot\frac{\kappa - 1}{\kappa + 1}\cdot\frac{P\cdot r}{4\cdot\pi\cdot\sqrt{(r_1\cdot r_2)^3}}\cdot\sin\frac{2\cdot\beta - 3\cdot\beta_1 - 3\cdot\beta_2}{2}$$

(7.19)

$$\Phi(Z) = +\frac{P\sqrt{a^2 - s^2}}{4\cdot\pi\cdot r_3\cdot\sqrt{r_1\cdot r_2}}\cdot\cos\frac{\beta_1+\beta_2+2\cdot\beta_3}{2} - i\cdot\frac{P\sqrt{a^2 - s^2}}{4\cdot\pi\cdot r_3\cdot\sqrt{r_1\cdot r_2}}\cdot\sin\frac{\beta_1+\beta_2+2\cdot\beta_3}{2}$$
$$+\frac{Q\sqrt{a^2 - s^2}}{4\cdot\pi\cdot r_3\cdot\sqrt{r_1\cdot r_2}}\cdot\sin\frac{\beta_1+\beta_2+2\cdot\beta_3}{2} + i\cdot\frac{Q\sqrt{a^2 - s^2}}{4\cdot\pi\cdot r_3\cdot\sqrt{r_1\cdot r_2}}\cdot\cos\frac{\beta_1+\beta_2+2\cdot\beta_3}{2}$$
$$-\frac{P}{4\cdot\pi\cdot r_3}\cdot\sin\beta_3 - i\cdot\frac{P}{4\cdot\pi\cdot r_3}\cdot\cos\beta_3$$
$$-\frac{Q}{4\cdot\pi\cdot r_3}\cdot\cos\beta_3 - i\cdot\frac{Q}{4\cdot\pi\cdot r_3}\cdot\sin\beta_3$$
$$+\frac{\kappa - 1}{\kappa + 1}\cdot\frac{P}{4\cdot\pi\cdot\sqrt{r_1\cdot r_2}}\cdot\sin\frac{\beta_1+\beta_2}{2} + i\cdot\frac{\kappa - 1}{\kappa + 1}\cdot\frac{P}{4\cdot\pi\cdot\sqrt{r_1\cdot r_2}}\cdot\cos\frac{\beta_1+\beta_2}{2}$$
$$+\frac{\kappa - 1}{\kappa + 1}\cdot\frac{P}{4\cdot\pi\cdot\sqrt{r_1\cdot r_2}}\cdot\sin\frac{\beta_1+\beta_2}{2} + i\cdot\frac{\kappa - 1}{\kappa + 1}\cdot\frac{P}{4\cdot\pi\cdot\sqrt{r_1\cdot r_2}}\cdot\cos\frac{\beta_1+\beta_2}{2} \qquad (7.20)$$

$$\begin{bmatrix}\sigma_{xx}^{(i)}\\ \sigma_{yy}^{(i)}\\ \sigma_{xy}^{(i)}\end{bmatrix} = \sum_{j-1}^{J}\begin{bmatrix}(\sigma_{xx}^{(i)})_j\\ (\sigma_{yy}^{(i)})_j\\ (\sigma_{xy}^{(i)})_j\end{bmatrix}\Bigg|\begin{array}{l}j\text{-}th\ segment,\\ Coordinate:\ (s,0),\ and\\ P_j^{(i)} = (\sigma_N^{(i)})_j\cdot ds,\quad Q_j^{(i)} = (\sigma_T^{(i)})_j\cdot ds\end{array} \qquad (7.21)$$

where $(\sigma_{xx}^{(i)})_j$, $(\sigma_{yy}^{(i)})_j$ and $(\sigma_{xy}^{(i)})_j$ are the stress fields caused by the resulting concentrated forces $P_j^{(i)}$ and $Q_j^{(i)}$ acting at the central point of the crack segment **ds (s,0)** during the **i**-th iteration step. They can be calculated by the above equations (7.16) to (7.20) while changing **P** and **Q** to $P_j^{(i)}$ and $Q_j^{(i)}$ respectively.

3 Complex Stress Function Method --II (Z2 Method)

Another complex stress function solution for an infinite region containing a central crack had been proposed by Irwin in 1957 which takes care of the situation as shown in Figure 7.8, i.e., infinite region with central crack opened by a pair of wedge forces **P** acting at point **(s,0)**. The complex stress function proposed for this case is:

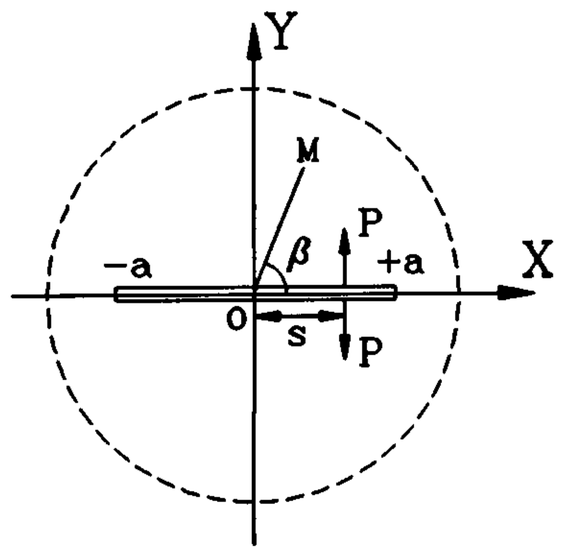

Fig.7.8 A Crack with Wedge Forces

$$\Phi(Z) = \frac{P\sqrt{a^2 - s^2}}{\pi\cdot(Z - s)\sqrt{Z^2 - a^2}} \qquad (7.22)$$

Then the stress field caused will be

$$\begin{cases} \sigma_{xx} = \Re\Phi(Z) - y\cdot\Im\Phi'(Z) \\ \sigma_{yy} = \Re\Phi(Z) + y\cdot\Im\Phi'(Z) \\ \sigma_{xy} = -y\cdot\Re\Phi'(Z) \end{cases} \tag{7.23}$$

where $\Re$ and $\Im$ means the real and the imaginary values of the complex functions respectively. With the help of the relationship shown in Equation (7.18), the expressions for $\mathbf{\Phi(Z)}$ and $\mathbf{\Phi'(Z)}$ can be derived as followed:

$$\Phi(Z) = \frac{P\sqrt{a^2 - s^2}}{\pi\cdot r_3\cdot\sqrt{r_1\cdot r_2}}\cdot\left[\cos\frac{\beta_1 + \beta_2 + 2\cdot\beta_3}{2} - i\cdot\sin\frac{\beta_1 + \beta_2 + 2\cdot\beta_3}{2}\right] \tag{7.24}$$

and,

$$\begin{aligned}\Phi'(Z) = &-\frac{P\sqrt{a^2 - s^2}}{\pi\cdot r_3^2\cdot\sqrt{r_1\cdot r_2}}\cdot\left[\cos\frac{\beta_1+\beta_2+4\cdot\beta_3}{2} - i\sin\frac{\beta_1+\beta_2+4\cdot\beta_3}{2}\right] \\ &-\frac{P\cdot r\sqrt{a^2-s^2}}{\pi\cdot r_3\sqrt{(r_1\cdot r_2)^3}}\cdot\left[\cos\frac{2\cdot\beta-3\cdot\beta_1-3\cdot\beta_2-2\cdot\beta_3}{2} + i\sin\frac{2\cdot\beta-3\cdot\beta_1-3\cdot\beta_2-2\cdot\beta_3}{2}\right]\end{aligned} \tag{7.25}$$

From these equations, the stress field can then be determined. During the superimposition procedure, the solutions for the case when the crack is subjected to distributed normal and tangential surface stresses $\sigma_N^{(i)}$ and $\sigma_T^{(i)}$ (i=0,1,2,3,...) during the i-th step can be treated the same as for the **Z1** method as mentioned in the last section. As can be seen, the complex stress function proposed by Irwin is much simpler. Unfortunately it doesn't include the case when the acting force is tangential to the crack surface. Therefore while evaluating the stress field caused by the tangential surface stress $\sigma_T^{(i)}$ acting on the crack surface, the solutions from Erdogan's complex functions have to be used, in other words, Erdogan's solutions will be used for evaluating the Mode II $\mathbf{K_{II}}$ SIF values in the **Z2** method.

After the stress field for case (2) problem during the i-th iteration step (i=0,1,2,3,...) is obtained, the stress components along the pseudo disc boundary in this infinite region can then be calculated. The corresponding traction stresses $T_x^{(i)}$ and $T_y^{(i)}$ can then be obtained by Equation (3.17) described in Chapter 3.

During the superimposition procedure, the disc boundary is divided into N elements and the boundary traction stresses T_x and T_y are equated by N pairs of boundary concentrated forces $(P_x)_n$ and $(P_y)_n$ (n=1,2,3,...,N) acting at the central points (x_n,y_n) of each element. When the

divided elements are small enough, this equivalence is believed to be exact. Again these boundary forces need cancelling as the real disc is traction force free along its boundary. This is the case (3) problem to be discussed in the next section.

§7.3.2.3 Case (3) Problem

For the problem of a solid disc subjected to arbitrary boundary concentrated forces $-\mathbf{P}_x$ and $-\mathbf{P}_y$ the normal and tangential stress set up over the pseudo crack line $s \in [-a, +a]$ can be calculated with the help of the basic solutions presented by Timoshenko (1970), who presented the stress components at any arbitrary point inside the disc when the disc boundary is subjected to one arbitrary concentrated load.

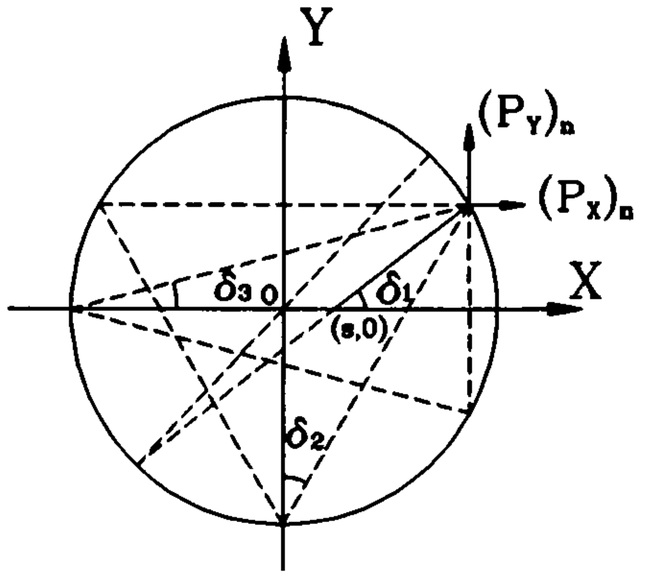

Figure 7.9 Case 3 Problem

When considering all the boundary traction forces acting along the whole disc circumference, we divide the whole disc boundary into **N** discrete elements. The boundary traction stresses are then divided into **N** pairs of boundary traction stresses in the **X** and **Y** directions $(\mathbf{T}_x)_n$ and $(\mathbf{T}_y)_n$ $[n = 1,2,3,\ldots,N]$ respectively. Then the action by these stresses are equated by **N** pairs of concentrated boundary forces $(\mathbf{P}_x)_n$ and $(\mathbf{P}_y)_n$ $(n = 1,2,3,\ldots,N)$ acting at the central points $(\mathbf{x}_n, \mathbf{y}_n)$ of each corresponding small segment. These equivalent concentrated forces are calculated by the following relations:

$$\begin{cases} (P_x)_n = (T_x)_n \cdot l_n \\ (P_y)_n = (T_y)_n \cdot l_n \end{cases} \quad | \, n = 1,2,3,\cdots N \tag{7.26}$$

where $\mathbf{l}_n$ is the length of the **n**-th boundary element.

The stress components of any point inside the disc will then be the resulting values superimposed from all the stresses caused by **N** pairs of the boundary forces $(\mathbf{P}_x)_n$ and $(\mathbf{P}_y)_n$ $(n = 1,2,3,\ldots,N)$. When the elements are small enough (**N** is big enough), this equivalence will be exact. Values of $(\mathbf{T}_x)_n$ and $(T_y)_n$ can be calculated by the method discussed in the last section.

In the following derivation, the minus signs of each pair of boundary traction forces are omitted for clearance reasons in the expression. However we should bear in mind that these are cancelling forces and their directions should be opposite to those obtained directly from the case (2) calculation.

According to the nomenclature in Figure 7.9, we derived the normal and tangential stresses

σ_N and σ_T at any point (s,0) along the pseudo crack line for this problem discussed above as follows:

$$\begin{cases} \sigma_N = -\sum_{n=1}^{N} \left[\frac{2\cdot(P_x)_n}{\pi}\cdot\frac{\cos\delta_1}{r_1} + \frac{2\cdot(P_y)_n}{\pi}\cdot\frac{\sin\delta_1}{r_1} \right]\cdot\sin^2\delta_1 \\ \qquad + \sum_{n=1}^{N} \left[\frac{(P_x)_n}{\pi\cdot D}\cdot\sin2\cdot\delta_2 + \frac{(P_y)_n}{\pi\cdot D}\cdot\sin2\cdot\delta_3\right] \\ \sigma_T = \sum_{n=1}^{N} \left[\frac{(P_x)_n}{\pi}\cdot\frac{\cos\delta_1}{r_1} + \frac{(P_y)_n}{\pi}\cdot\frac{\sin\delta_1}{r_1} \right]\cdot\sin2\cdot\delta_1 \end{cases} \tag{7.27}$$

where,

$$\begin{cases} r_1 = \sqrt{(x_n - s)^2 + y_n^2} \\ \sin\delta_1 = \frac{y_n}{r_1}, \quad \cos\delta_1 = \frac{x_n - s}{r_1} \\ \delta_2 = \arctan\frac{x_n}{y_n + R}, \quad \delta_3 = \arctan\frac{y_n}{x_n + R} \end{cases} \tag{7.27a}$$

During the superimposition procedure, the N pairs of boundary forces acting at the n-th boundary element in the i-th step $(P_x^{(i)})_n$ and $(P_y^{(i)})_n$ [i = 0,1,2,3,...] can be evaluated by the case (2) solutions and Equation (7.26). Therefore the normal and tangential stresses for the next iteration step [(i + 1)-th step] acting on the crack line [-a, + a] to cancel the stresses produced by these i-th step boundary forces $(P_x^{(i)})_n$ and $(P_y^{(i)})_n$ can then be calculated by Equation (7.27), where the corresponding changes of $\sigma_N = \sigma_N^{(i+1)}$, $\sigma_T = \sigma_T^{(i+1)}$, $(P_x)_n = (P_x^{(i)})_n$ and $(P_x)_n = (P_x^{(i)})_n$ should be made, i.e.,

$$\begin{bmatrix} \sigma_N^{(i+1)} \\ \sigma_T^{(i+1)} \end{bmatrix} = \sum_{n=1}^{N} \begin{bmatrix} (\sigma_N^{(i+1)})_n \\ (\sigma_T^{(i+1)})_n \end{bmatrix} \Bigg| \begin{array}{l} n\text{-}th \quad element \\ (P_x)_n = (P_x^{(i)})_n, \quad (P_y) = (P_y^{(i)})_n \\ i = 0,1,2,3,\cdots \end{array} \tag{7.28}$$

Again these set-up stresses need to be cancelled. Therefore the calculation procedure goes back to the case (2) problem again. The whole stepwise iteration procedure continues until some desired degree of accuracy is reached.

§7.3.3 The Evaluations of the Stress Intensity Factors

During the above stepwise superimposition procedure, only case (2) involves the analysis of the crack fracture problem. Therefore it is only this case which should be taken into account when the SIF values K_I and K_{II} of the original problem are going to be evaluated.

Obviously the resulting $\mathbf{K_I}$ and $\mathbf{K_{II}}$ values will be the superimposed SIF values generated by each step of the iteration procedure, i.e.,

$$\left[\begin{array}{c} K_I \\ K_{II} \end{array}\right] = \sum_{i=0}^{I} \left[\begin{array}{c} K_I^{(i)} \\ K_{II}^{(i)} \end{array}\right] \Bigg| \; i\text{-}th\ Step \tag{7.29}$$

where $\mathbf{K_I^{(i)}}$ and $\mathbf{K_{II}^{(i)}}$ are the SIF values produced at the **i**-th superimposition step and they should be calculated according to the normal and tangential stresses $\boldsymbol{\sigma}_N^{(i)}(s)$ and $\boldsymbol{\sigma}_T^{(i)}(s)$ **[i = 0,1,2,3,...]** acting on the crack line to cancel the stresses during the **i**-th iteration step.

The calculations of $\mathbf{K_I}$ and $\mathbf{K_{II}}$ are based on Sih's results. Sih (1962) presented the SIF calculations for an infinite region with a central crack subjected to internal distributed normal and tangential stresses. Combined with our case, the expressions will be:

$$\begin{cases} K_I^{(i)} = \dfrac{1}{\sqrt{\pi \cdot a}} \cdot \int_{-a}^{a} [\,\sigma_N^{(i)}(s)\,] \cdot \sqrt{\dfrac{a+s}{a-s}} \cdot ds \\ K_{II}^{(i)} = \dfrac{1}{\sqrt{\pi \cdot a}} \cdot \int_{-a}^{a} [\,\sigma_T^{(i)}(s)\,] \cdot \sqrt{\dfrac{a+s}{a-s}} \cdot ds \end{cases} \tag{7.30}$$

As the crack line has already been divided, therefore the above calculations can be evaluated numerically.

§7.3.4 Numerical Superimposition Procedure

As with the procedure used in Chapter 3, the crack line **2a** and the disc boundary circumference are divided into **J** and **N** segments respectively. In the dislocation method, the range for the variable $\boldsymbol{\phi}$ $[-\pi/2, +\pi/2]$ has to be divided into **M** segments as well so that the dislocation function $\mathbf{F}(\boldsymbol{\phi})$ and $\mathbf{G}(\boldsymbol{\phi})$ can be numerically expressed. Calculation begins with the evaluation of the normal and tangential stresses $(\sigma_N^{(i)})_j\big|_{i=0}$ and $(\sigma_T^{(i)})_j\big|_{i=0}$ for each of the crack elements **j** (j = 1,2,...,J) set up along the pseudo crack line $\mathbf{s} \in \mathbf{[-a, +a]}$ when the solid disc is loaded with a pair of diametrical loads **P** inclined to the pseudo crack direction with an angle $\boldsymbol{\theta}$ (Figure 7.2.a). When the stresses $(-\sigma_N^{(i)})_j\big|_{i=0}$ and $(-\sigma_T^{(i)})_j\big|_{i=0}$ (j = 1,2,...,J) are superimposed on the crack elements to cancel these induced stresses, the iteration procedure starts. At this stage the SIF values are calculated the first time, $\mathbf{K_I^{(i)}}\big|_{i=0}$ and $\mathbf{K_{II}^{(i)}}\big|_{i=0}$. For dislocation method, the program turns to calculate the dislocation densities $(\mathbf{F}(\boldsymbol{\phi})^{(i)})_m\big|_{i=0}$ and $(\mathbf{G}(\boldsymbol{\phi})^{(i)})_m\big|_{i=0}$ (m = 1,2,...M) values for the **M** $\boldsymbol{\phi}$ elements. Then for all the methods, the boundary traction stresses $(T_x^{(i)})_n\big|_{i=0}$ and $(T_y^{(i)})_x\big|_{i=0}$ (n = 1,2,...,N) on the **N** circumference elements produced by the cancelling surface stresses acting on the crack surface are calculated,

and thereafter so are the boundary concentrated forces $(P_x^{(i)})_n\big|_{i=0}$ and $(P_y^{(i)})_n\big|_{i=0}$ ($n=1,2,3,\ldots,N$). By superimposing the traction forces $(-P_x^{(i)})_n\big|_{i=0}$ and $(-P_y^{(i)})_n\big|_{i=0}$ back on the N circumference elements, these boundary forces can be cancelled. This certainly will set up the normal and tangential stresses $(\sigma_N^{(i)})_j\big|_{i=1}$ and $(\sigma_T^{(i)})_j\big|_{i=1}$ ($j=1,2,\ldots,J$) again on the J crack elements and these can be cancelled by superimposing $(-\sigma_N^{(i)})_j\big|_{i=1}$ and $(-\sigma_T^{(i)})_j\big|_{i=1}$ back on the crack surface. At this step the SIF values $K_I^{(i)}\big|_{i=1}$ and $K_{II}^{(i)}\big|_{i=1}$ are calculated a second time and the values are superimposed on $K_I^{(i)}\big|_{i=0}$ and $K_{II}^{(i)}\big|_{i=0}$ values calculated above to obtain an approximation of the true K_I^T and K_{II}^T values. Then as the iteration procedure goes on the superimposed SIF values approach the true ones, i.e,

$$\begin{cases} K_{I,II}^{(i)} = K_{I,II}^{(0)} + K_{I,II}^{(1)} + K_{I,II}^{(2)} + \cdots + K_{I,II}^{(i)} \\ K_{I,II}^{(i)} \Rightarrow K_{I,II}^{T}, \quad when \ \ i \Rightarrow \infty \end{cases} \tag{7.31}$$

The iteration procedure stops when the approximate SIF values satisfy the accuracy requirement, i.e.,

$$\begin{cases} When \\ \qquad \left| K_{I,II}^{(i)} - K_{I,II}^{(i-1)} \right| \le ESP \\ then \\ \qquad K_{I,II} = K_{I,II}^{(i)} \end{cases}$$

where **ESP** is the accuracy requirement parameter. In the current evaluations, we set **ESP** = 0.008, which means that we have the confidence to say that the results only have an error of within 1%.

§7.4 The Theoretical SIF for the Mixed Mode CSTBD Problem

§7.4.1 Dislocation Method

§7.4.1.1 F(ϕ) and G(ϕ)

The dislocation density $F(\phi)$ and $G(\phi)$ for each iteration step were evaluated by Equation (7.12). One should pay attention to this equation while doing the integration as it is an infinite integrand. Care should be taken at the interrupted point of x^0 which makes the integrated function on the right hand side tend to infinity. x^0 is depending on the value of ϕ with $(x^0 - a\cdot\sin\phi) = 0$. A small infinitesimal value ϵ was introduced in our calculation to replace x^0 with $x^0-\epsilon$ and $x^0+\epsilon$ while the integration is passing this interrupted point and the final integrated value is obtained by taking the limit of ϵ tending to zero.

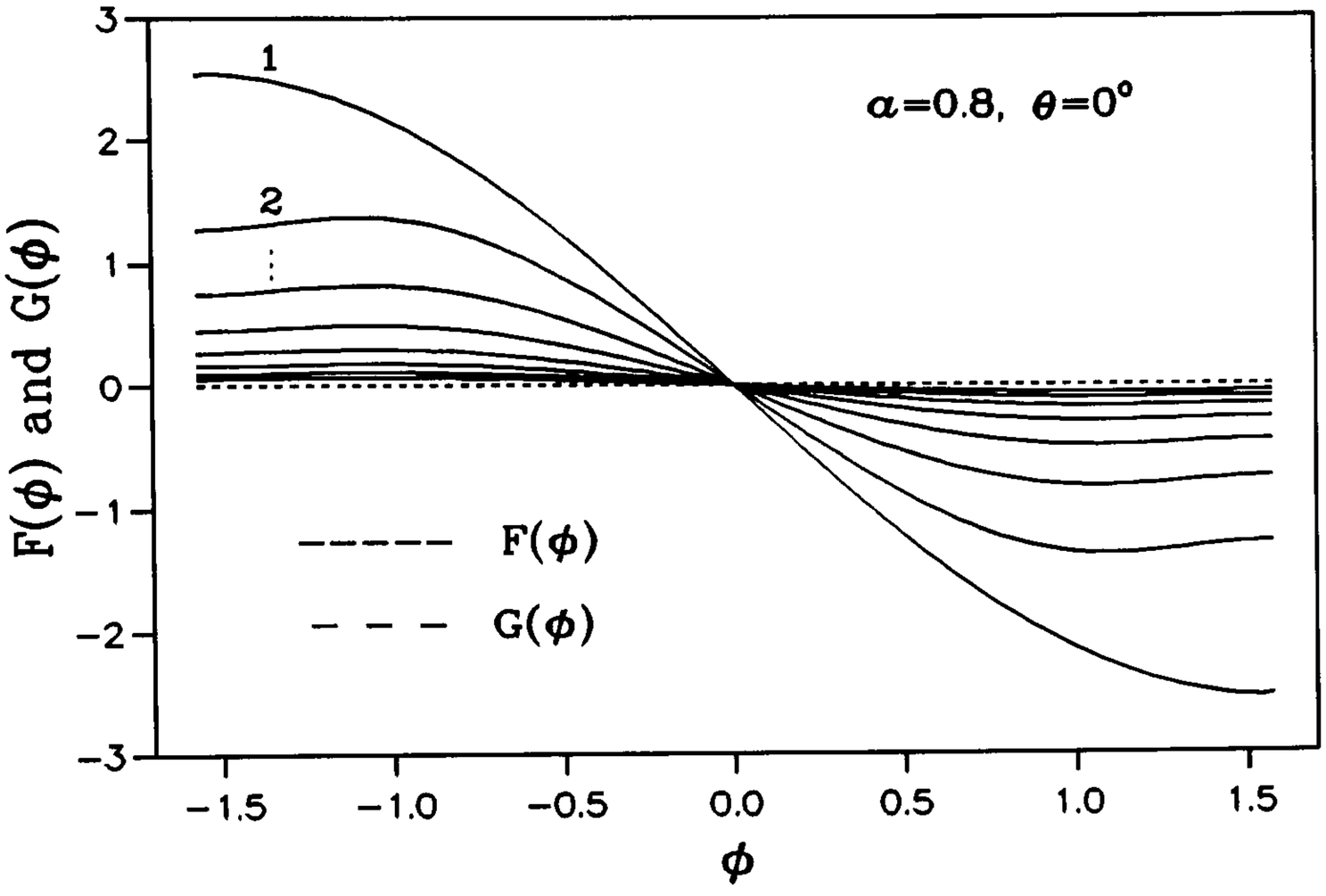

Figure 7.10 a) $F(\phi)$ and $G(\phi)$ for $\alpha = 0.8$, $\theta = 0°$

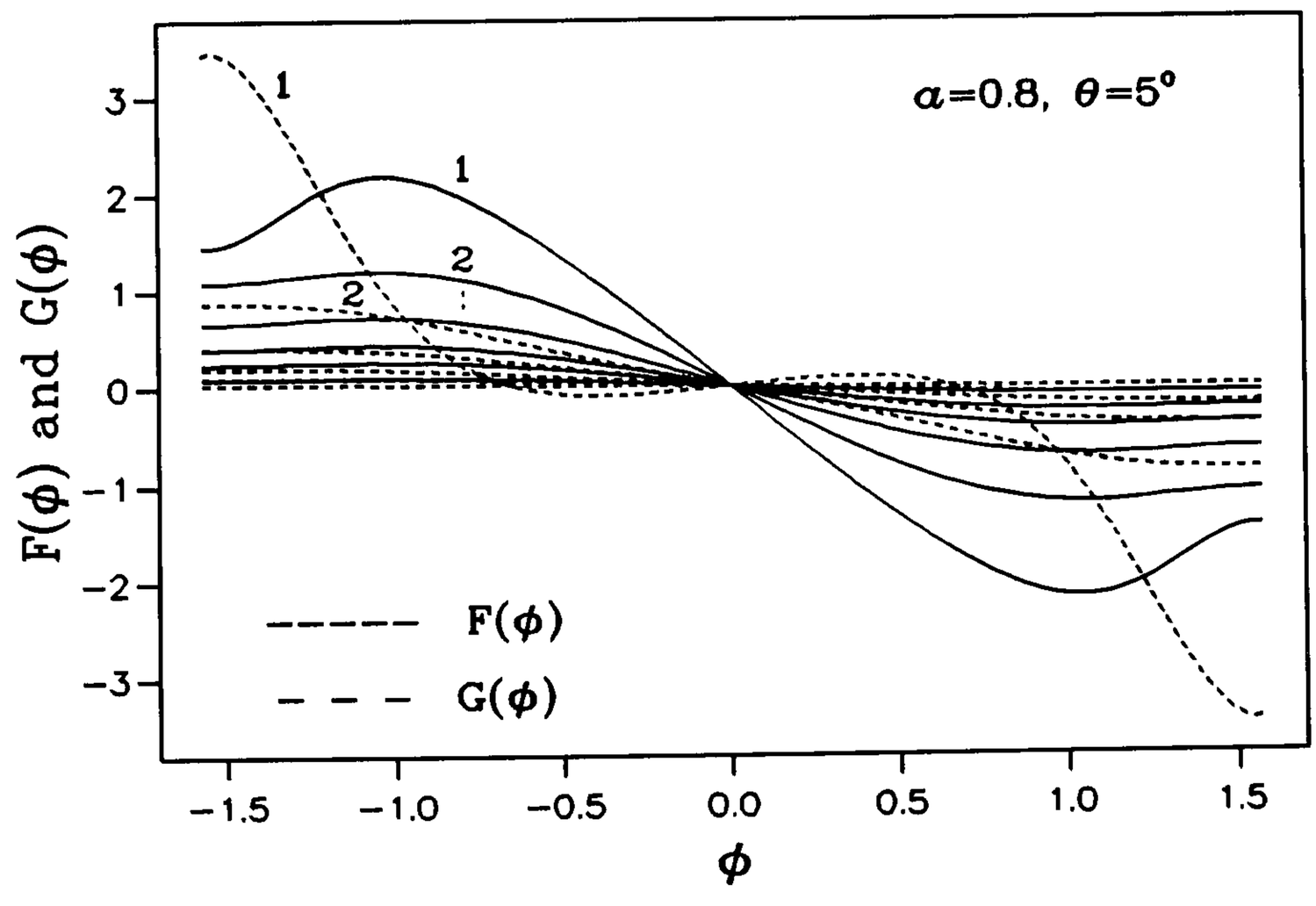

Figure 7.10 b) $F(\phi)$ and $G(\phi)$ for $\alpha = 0.8$, $\theta = 5°$

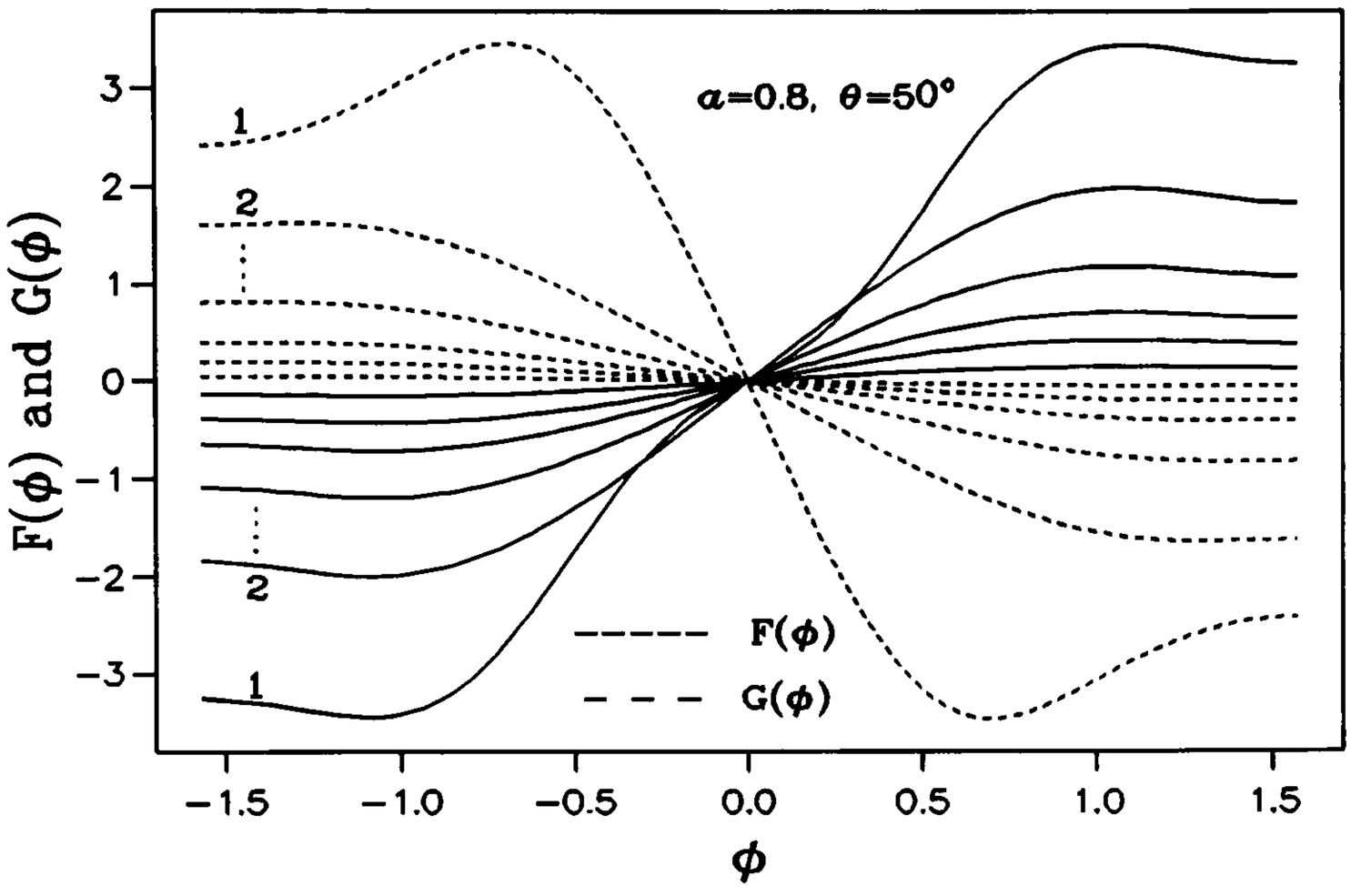

Figure 7.10 c) $F(\phi)$ and $G(\phi)$ for $\alpha = 0.8$, $\theta = 50°$

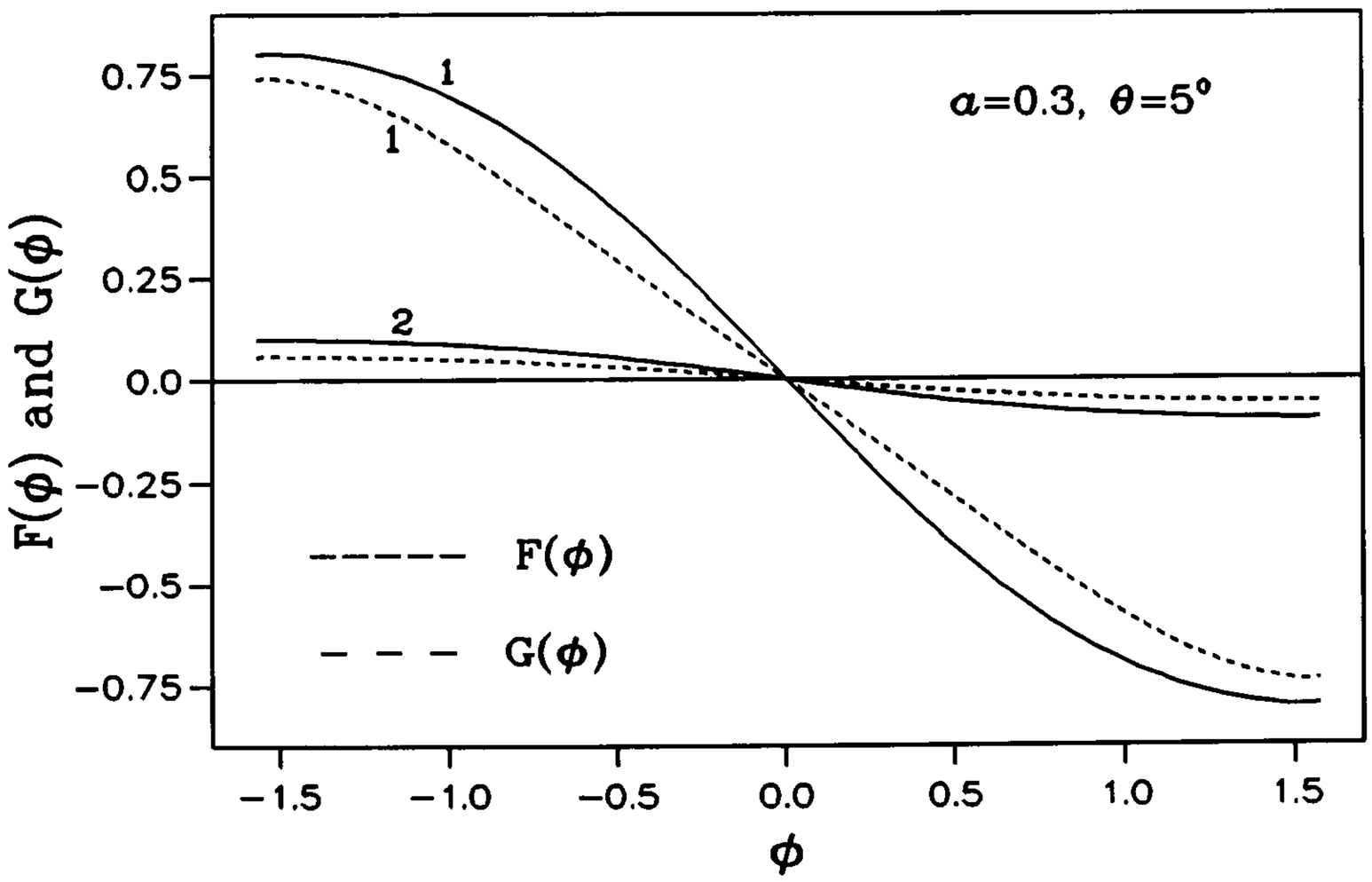

Figure 7.10 d) $F(\phi)$ and $G(\phi)$ for $\alpha = 0.3$, $\theta = 5°$

The $\mathbf{F(\phi)}$ and $\mathbf{G(\phi)}$ values will be dependent on the magnitude and the distribution form of the normal and the tangential stresses acting on the crack surface. For the particular case of the mixed mode CSTBD problem, they will vary according to the crack length **2a** and the inclination angle between the crack orientation and the loading diametrical line θ, (Figure 7.1).

Figure 7.10 a) shows their values for $\theta = 0°$ and $\alpha = 0.8$. As can be seen, $\mathbf{G(\phi)}$ is zero valued because the cancelling tangential stress σ_T is always zero in this case. The numbers shown in the figures means the iteration step number **i** and as can be seen the $\mathbf{F(\phi)}$ value tend to zero as the iteration step tend to infinity, which illustrates the whole iteration procedure is convergent.

Figure 7.10 b) and c) show the $\mathbf{F(\phi)}$ and $\mathbf{G(\phi)}$ values for the same crack length $\alpha = 0.8$ but different inclination angles $\theta = 5°$ and $\theta = 50°$, where the numbers are the iteration step number. As can be seen again, both the $\mathbf{F(\phi)}$ and $\mathbf{G(\phi)}$ values will tend to zero as the iteration step **i** tends to infinity which again proves the convergent conclusion above. Figure 7.10 d) shows the $\mathbf{F(\phi)}$ and $\mathbf{G(\phi)}$ variations for the case of $\theta = 5°$ but the smaller crack length $\alpha = 0.3$. As can be seen, much smaller values are obtained. Compared with the figures shown in a) and b) we know that:

1). Crack length **2a** decides the magnitude of the $F(\phi)$ and $G(\phi)$ functions.

2). It is the inclination angle θ between the crack orientation and the loading direction which mainly determines the shape and the signs of the $\mathbf{F(\phi)}$ and $\mathbf{G(\phi)}$ functions.

3). As θ changes from 0° to 90°, the signs of $\mathbf{F(\phi)}$ will change from positive to negative for $\phi < 0$ and from negative to positive for $\phi > 0$. That means that the edge dislocations for the **Mode I** fracture simulation will change from positive dislocations to negative dislocations. Therefore there should be a turning point of θ at which this simulated **Mode I** dislocations are zero. In other words, a certain angle should exist for θ where the fracture state at the crack tip for the mixed mode CSTBD problem will be just the pure Mode II fracture problem.

§7.4.1.2 T_x and T_y (hence P_x and P_y)

The boundary traction stresses created by the cancelling stresses acting on the crack surface can be evaluated by Equation (7.15) and Equation (3.17). Some of the calculated examples are shown as follows. Figure 7.11 a) illustrates the $\mathbf{T_x}$ and $\mathbf{T_y}$ values along the disc circumference for $\alpha = 0.8$, $\theta = 0°$. The numbers again show the iteration step from which it can be seen that the force values will tend to zero as the step number increases. This demonstrate the convergent iteration procedure by means of the boundary forces. Figure 7.11 b) and c) illustrate the boundary stress variations for the same crack length $\alpha = 0.8$ but for $\theta = 5°$ and $50°$ respectively. Figure 7.11 d) gives the result for $\theta = 5°$ but for a small crack length of $\alpha = 0.3$. From these figures, the following two points can be drawn:

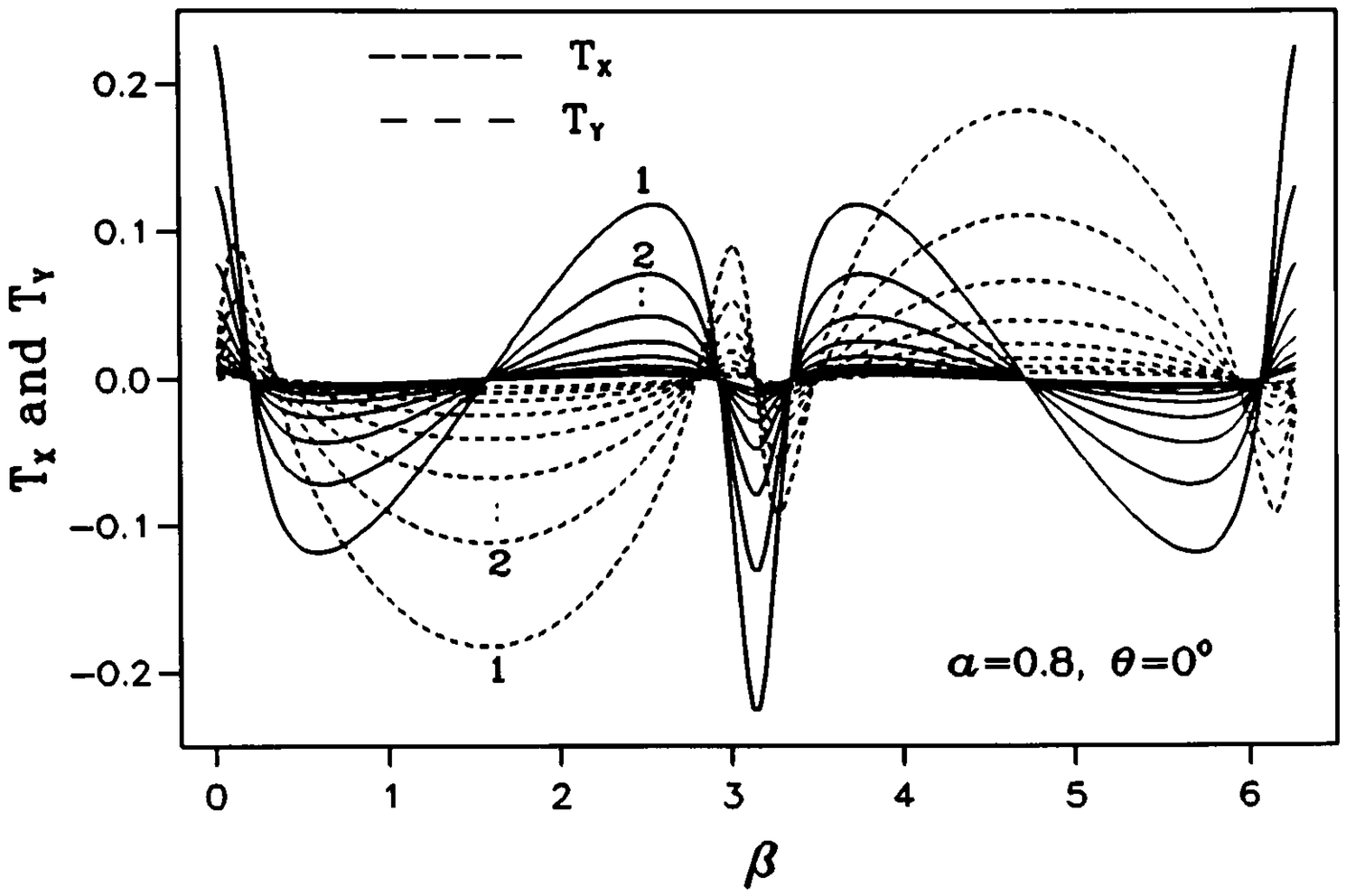

Figure 7.11 a) T_x and T_y for $\alpha = 0.8$, $\theta = 0°$

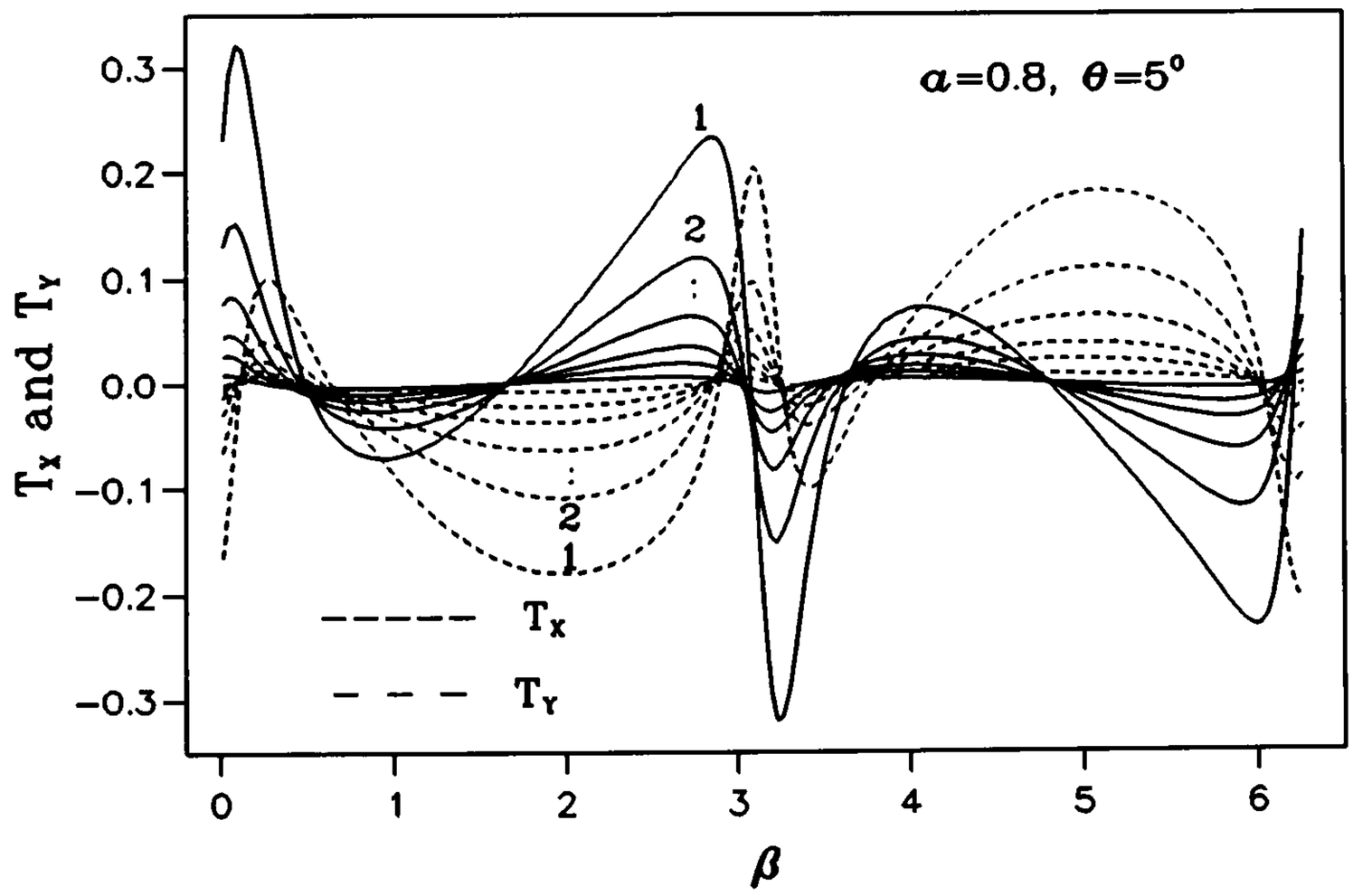

Figure 7.11 b) T_x and T_y for $\alpha = 0.8$, $\theta = 5°$

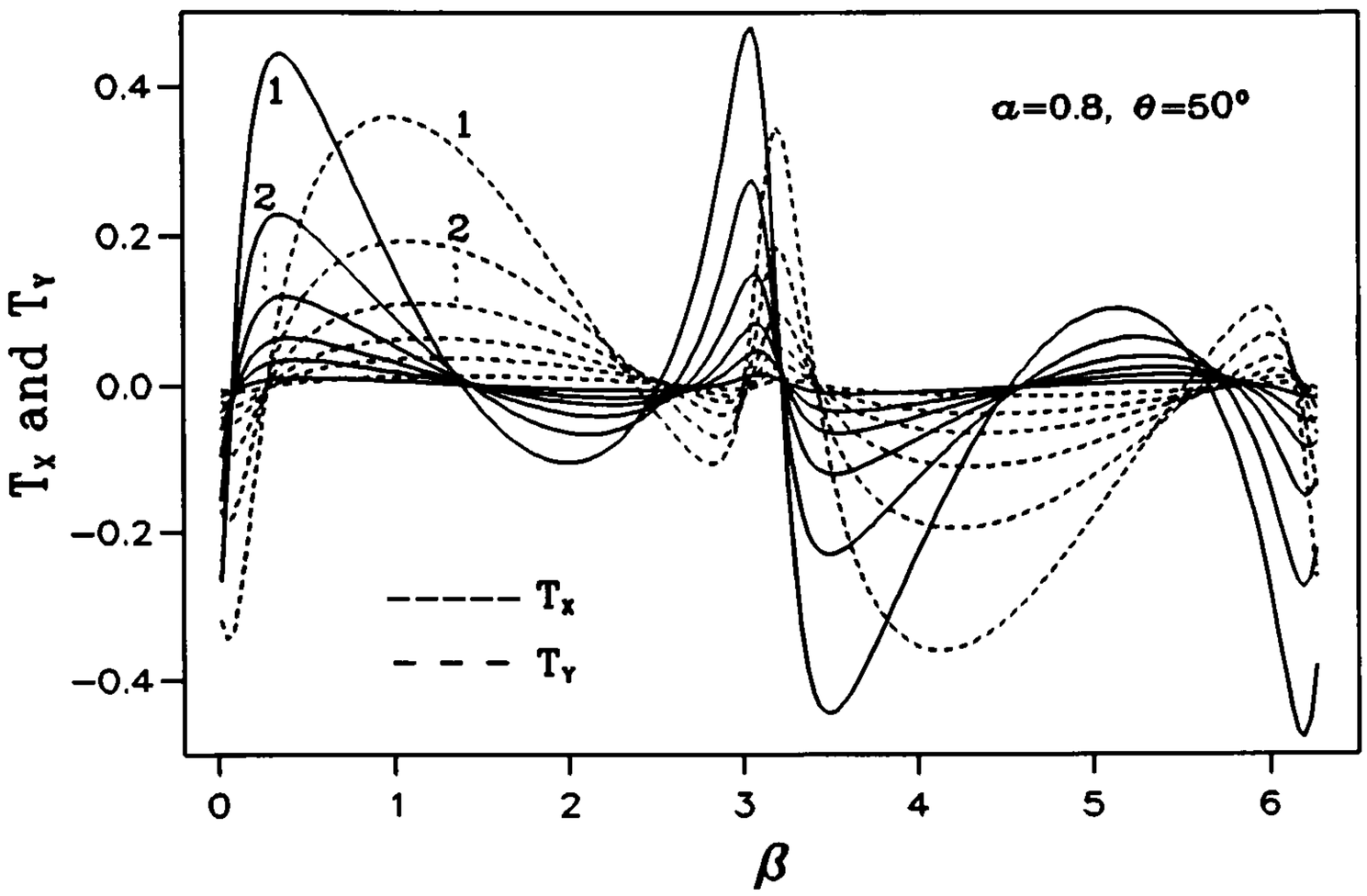

Figure 7.11 c) T_x and T_y for $\alpha = 0.8$, $\theta = 50°$

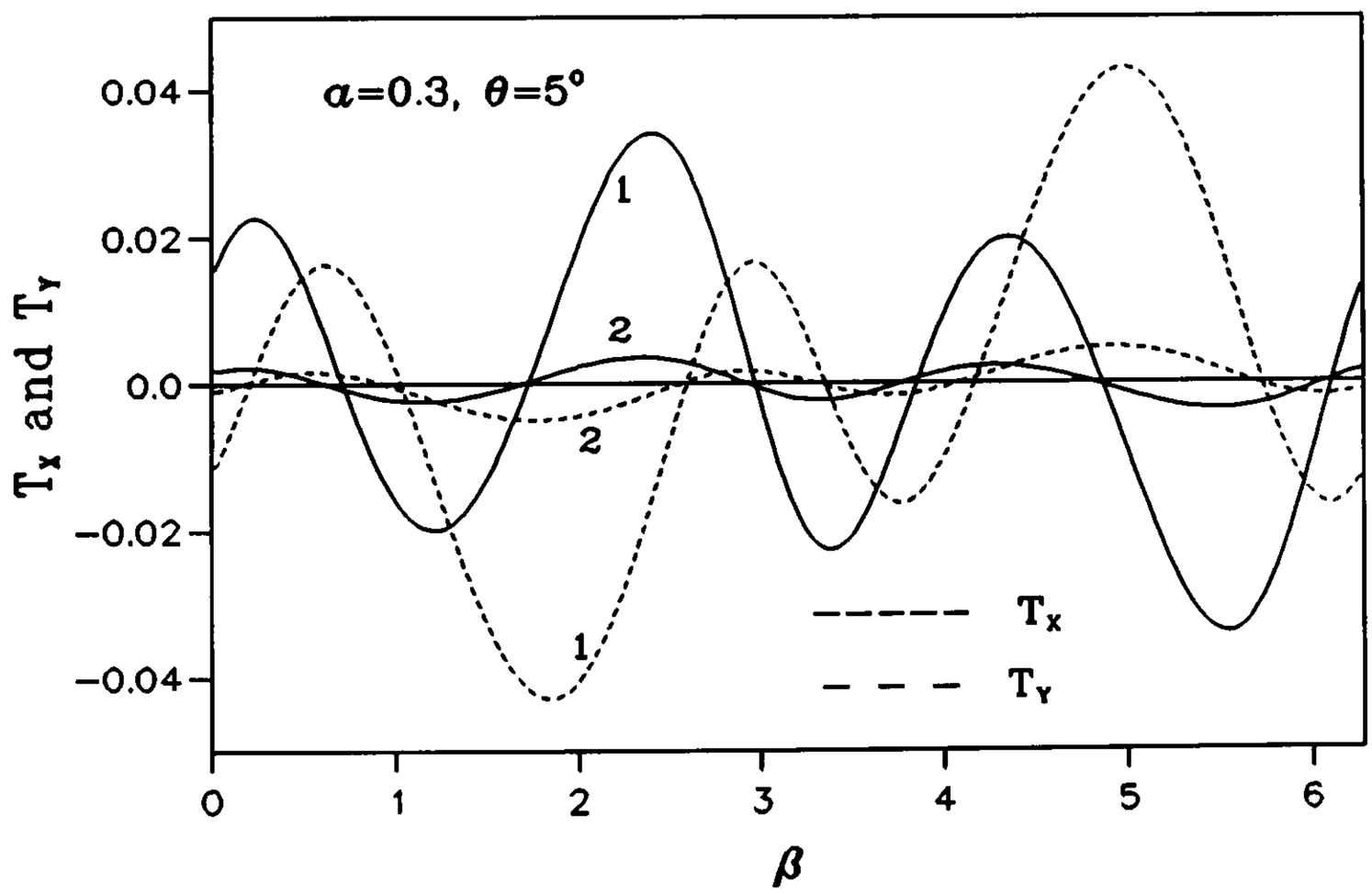

Figure 7.11 d) T_x and T_y for $\alpha = 0.3$, $\theta = 5°$

1) The boundary traction stresses $\mathbf{T_x}$ and $\mathbf{T_y}$ are symmetrical to the **X** and **Y** axes while $\theta = 0°$, but are unsymmetrical generally when $\theta \neq 0°$.

2) For small crack lengths, the variations of $\mathbf{T_x}$ and $\mathbf{T_y}$ are much less severe when compared with the long crack cases.

After the $\mathbf{T_x}$ and $\mathbf{T_y}$ are obtained, $\mathbf{P_x}$ and $\mathbf{P_y}$ can then be calculated from Equation (7.26).

§7.4.1.3 σ_N and σ_T

Figure 7.12 a) - d) show the σ_N and σ_T values for different iteration step number **i** (shown as the numbers in the figures) for a) $\alpha = 0.8$, $\theta = 0°$, b) $\alpha = 0.8$, $\theta = 5°$ c) $\alpha = 0.8$, $\theta = 50°$ and d) $\alpha = 0.3$, $\theta = 5°$. As clearly shown, the iteration steps needed for the σ_N and σ_T to be convergent to zero are much less for the smaller crack case compared with those for the longer crack case. Generally the stress variation patterns of σ_N and σ_T will no longer keep their original forms as can be seen from these four figures.

§7.4.2 Complex Stress Function Method -- I (Z1 Method)

While using the complex stress function method I to do the evaluation, the disc circumference traction stresses $\mathbf{T_x}$ and $\mathbf{T_y}$ (and hence $\mathbf{P_x}$ and $\mathbf{P_y}$) can be calculated directly from Equations (7.16) - (7.21) from the crack surface cancelling stresses σ_N and σ_T as shown in section §7.3.2.2. Similar variation patterns to those by the dislocation method are shown but there is some difference in the magnitude. This difference can be clearly shown when these boundary traction are used to calculate the next step crack surface normal and tangential stresses. Figure 7.13 a) - b) show the σ_N and σ_T values calculated by this method for $\alpha = 0.8$ but $\theta = 0°$ and $50°$ respectively. Compared with those calculated by dislocation method as shown in Figure 7.12, it can be seen that at the crack tip region the "returned" normal stress σ_N has changed sign from its original sign. Even though the iteration procedure can still be convergent, it is suggested that the results will not be able to represent correctly the true fracture status of the crack in the CSTBD as the stress situations in the crack tip region are wrongly expressed. Therefore the $\mathbf{K_I}$ results evaluated this way are considered to be inexact. This point suggests that Erdogan's proposed complex stress function $\Phi(Z)$ and $\Omega(Z)$ may not be perfect. There may be some unimportant terms neglected in the equations in other situations which turn out to be important in our case.

However the above arguments only hold for the normal stress acting on the crack surface σ_N, in other words, only affecting the $\mathbf{K_I}$ value evaluations. For the tangential stress σ_T acting on the surface, it appears to yield similar results compared with the dislocation method (Figure 7.12 c and Figure 7.13 b). Therefore for the $\mathbf{K_{II}}$ evaluations, the results will be valid.

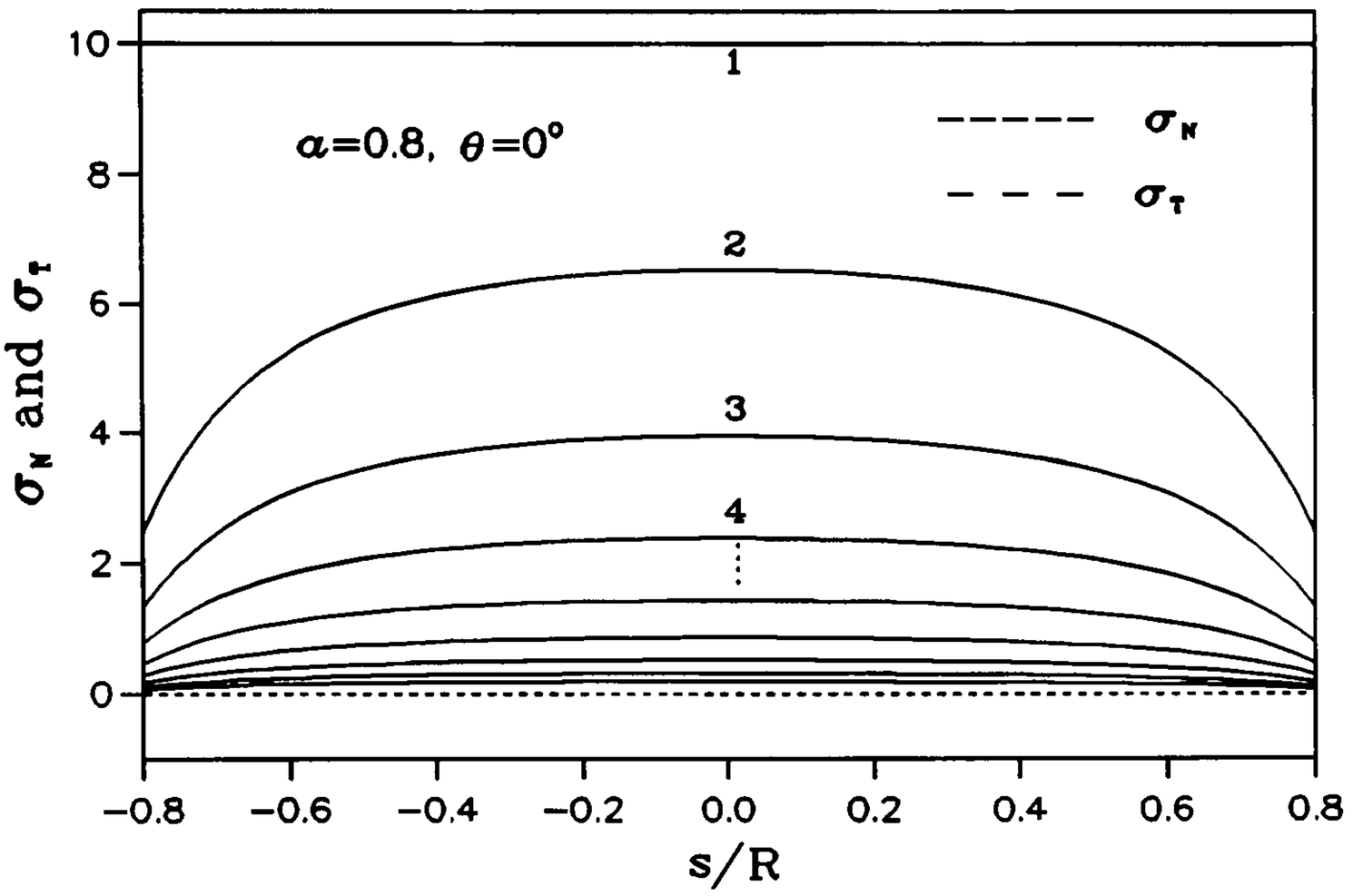

Figure 7.12 a) σ_N and σ_T for $\alpha = 0.8$, $\theta = 0^\circ$

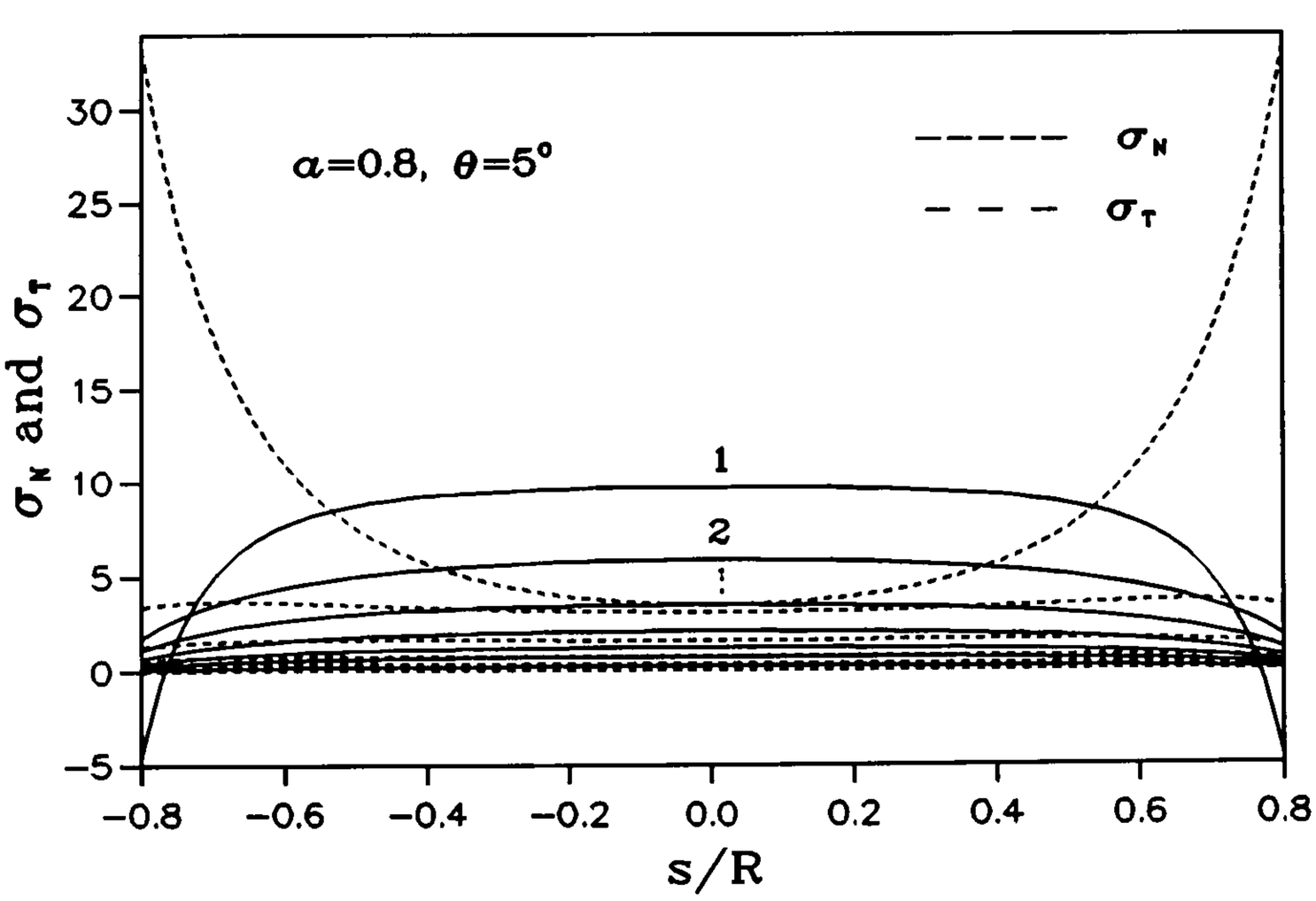

Figure 7.12 b) σ_N and σ_T for $\alpha = 0.8$, $\theta = 5^\circ$

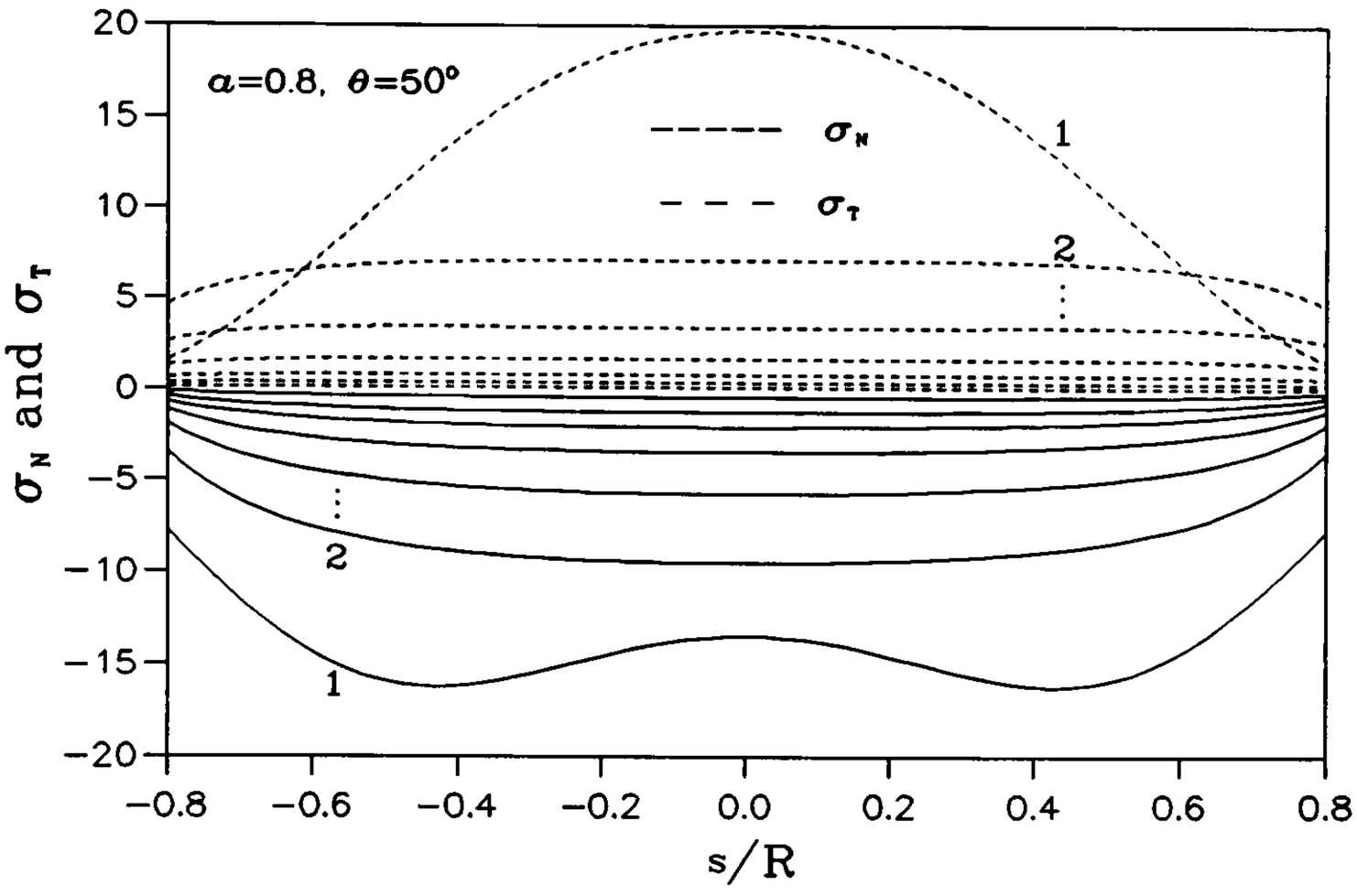

Figure 7.12 c) σ_N and σ_T for $\alpha = 0.8$, $\theta = 50°$

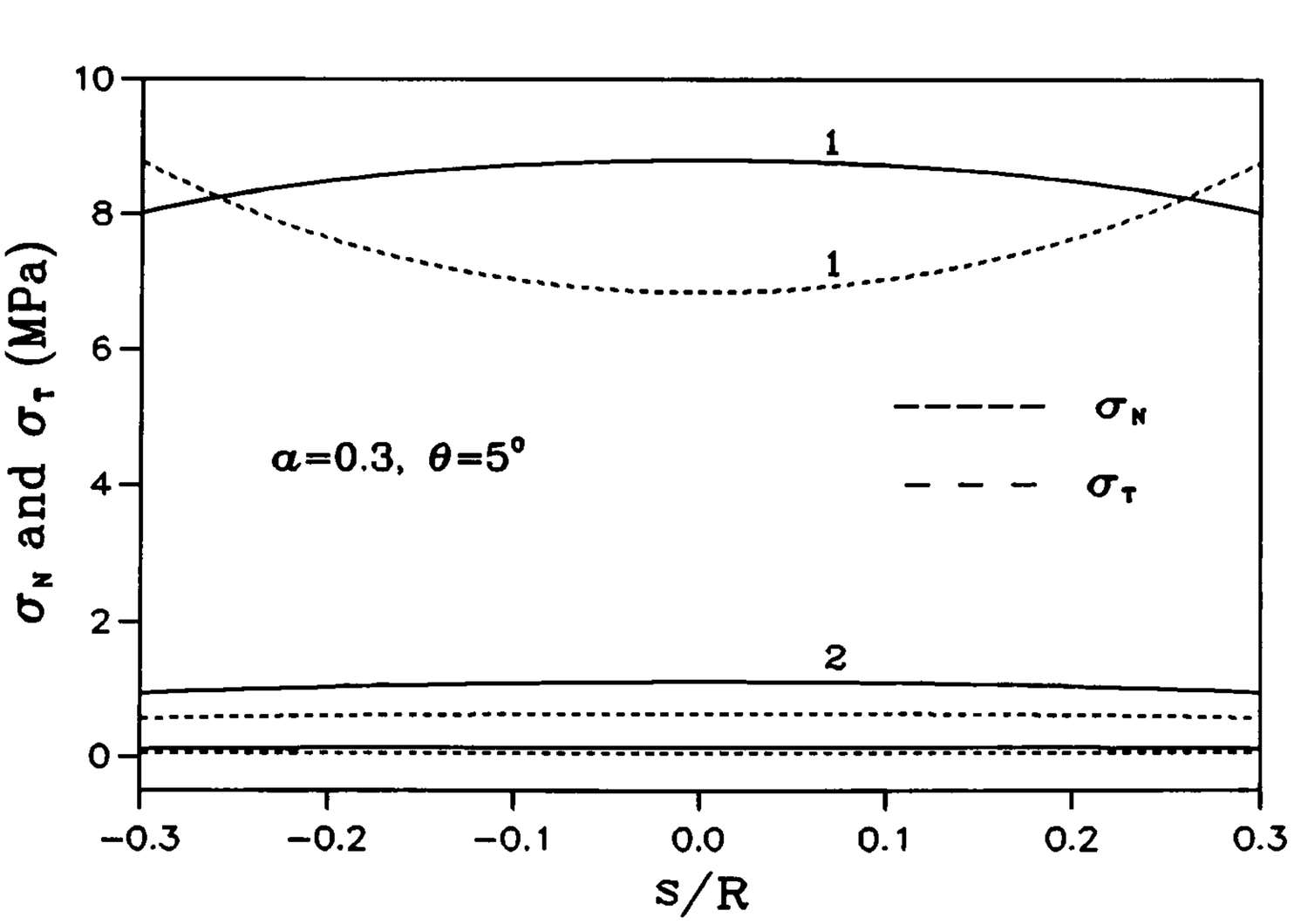

Figure 7.12 d) σ_N and σ_T for $\alpha = 0.3$, $\theta = 5°$

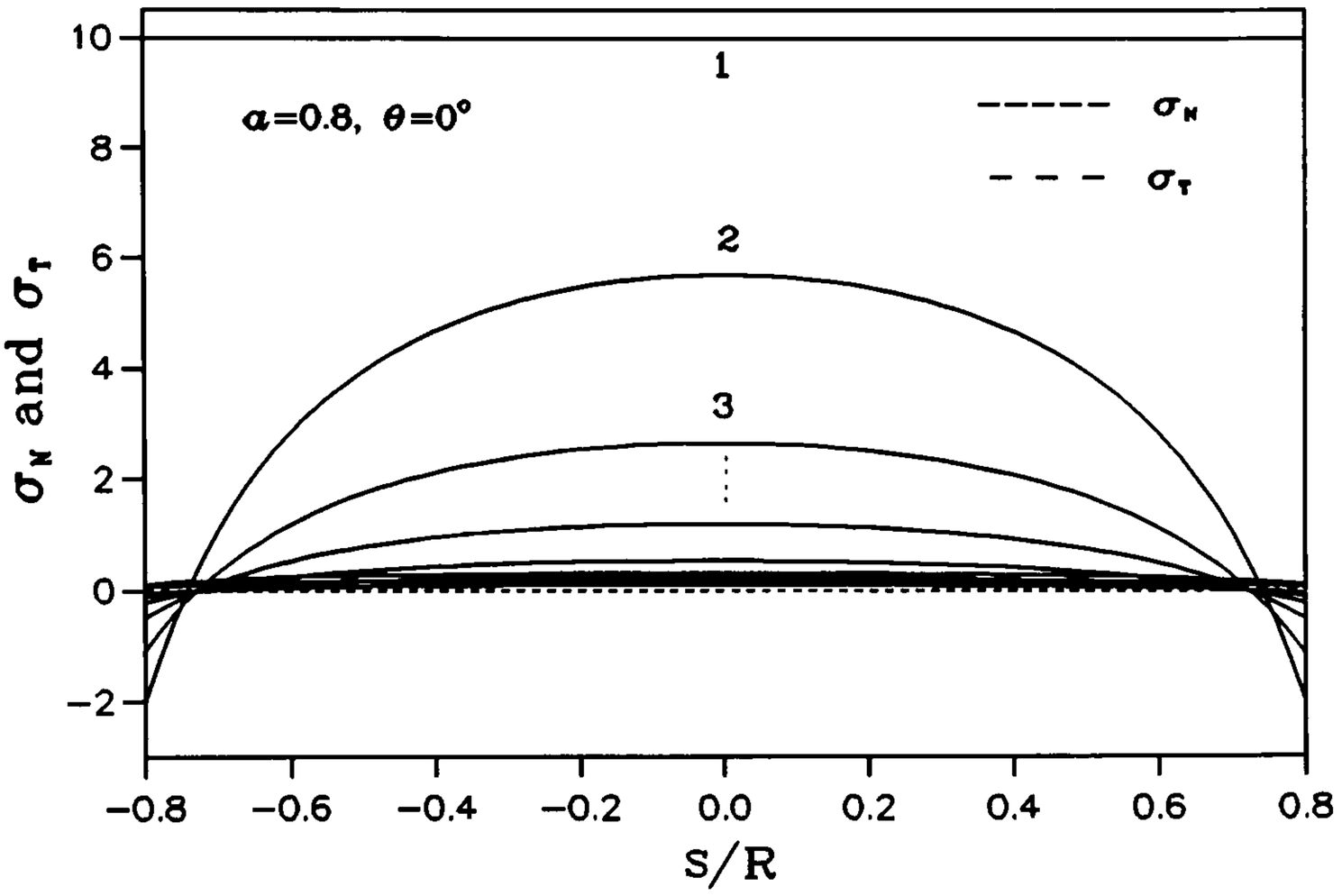

Figure 7.13 a) σ_N and σ_T for $\alpha = 0.8$, $\theta = 0°$ (Z1)

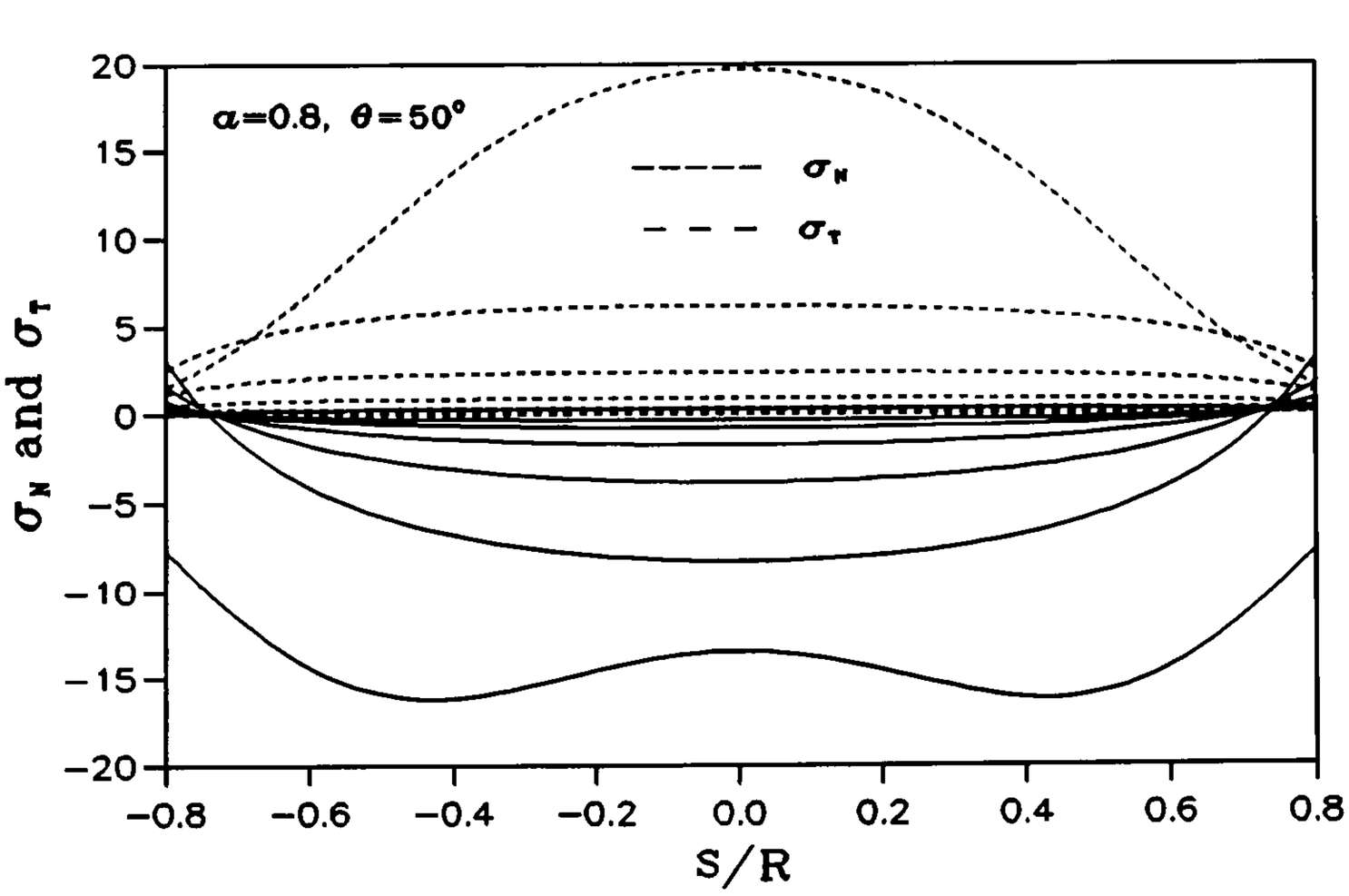

Figure 7.13 c) σ_N and σ_T for $\alpha = 0.8$, $\theta = 50°$ (Z1)

§7.4.3 Complex Stress Function Method -- II (Z2 Method)

As discussed above, the $\mathbf{K_I}$ values calculated by the complex stress function method I are not exact, another complex stress function had to be sought to express the action of normal force on the crack surface. Therefore a complex stress function proposed by Irwin for the Mode I fracture problem is introduced. The $\mathbf{T_x}$ and $\mathbf{T_y}$ (and hence $\mathbf{P_x}$ and $\mathbf{P_y}$) values can be calculated from the cancelling stresses acting on the crack surface directly from Equation (7.22) - (7.25) shown in section §7.3.2.2. Then the normal and tangential stresses on the crack surface due to the boundary cancelling forces can be obtained from the equations shown in section §7.3.2.3. Very encouragingly, the $\mathbf{T_x}$, $\mathbf{T_y}$, $\boldsymbol{\sigma_N}$, $\boldsymbol{\sigma_T}$ and $\mathbf{K_I}$ values calculated by this method yield exactly the same results as those calculated by the dislocation method, i.e., their variations are the same as those shown in Figure 7.11 and Figure 7.12.

§7.4.4 Comments on the SIF Evaluations for Mixed Mode CSTBD Fracture Problem

As the concluding remarks for this section, the following three points are made.

1). It is suggested at this stage that the $\mathbf{K_I}$ value evaluated by the dislocation method and complex stress function method II be the exact solution.

2). Unfortunately a third tool to solve the **Mode II** SIF in the mixed mode CSTBD fracture problem could not be found at this stage. Therefore under the condition of no further proof, the $\mathbf{K_{II}}$ values calculated both by the dislocation method and the complex stress function methods have to be accepted even though there exist some differences. Numerical and experimental calibrations are recommended.

3). One important point should be made which is the crack closure problem in the mixed mode CSTBD fracture problem. As for a crack with ideal zero width, when $\boldsymbol{\theta}$ is greater than a certain angle the $\mathbf{K_I}$ value will change from positive to negative, i.e, the crack tip will be subjected to compressive **Mode I** loading instead of the splitting one. In this case the crack will close. This closure certainly will create extra normal forces on the crack surface and shearing resistance will come to exist when **Mode II** fracture loading is applied. This will then affect the $\mathbf{K_I}$ and $\mathbf{K_{II}}$ values. However in practical applications, the CSTBD is always machined with the central crack having a certain width. In this case it is suggested that the crack surfaces can not close under compressive **Mode I** fracture loading under the condition of LEFM. The specimen will still behave in the LEFM range before the disc fails. Therefore the above evaluations can still be regarded as valid.

§7.5 The Calculated SIF (K_I and K_{II}) Results

The following diagrams show the K_I and K_{II} results calculated by the above three evaluation methods. They are expressed in the forms of $\mathbf{f_I}(\alpha,\theta)$, $\mathbf{f_{II}}(\alpha,\theta)$, $\mathbf{Y_I}(\alpha,\theta)$ and $\mathbf{Y_{II}}(\alpha,\theta)$ variations which are defined as followed:

$$\begin{cases} f_{I,II}(\alpha,\theta) = \dfrac{K_{I,II}}{K_0} \\ \textit{Where } K_{I,II} = \textit{Caliculated SIF Values} \\ K_0 = \dfrac{P}{B\cdot\sqrt{R}}\cdot\sqrt{\dfrac{\alpha}{\pi}} \end{cases} \tag{7.34}$$

and,

$$\begin{cases} Y_{I,II}(\alpha,\theta) = f_{I,II}(\alpha,\theta)\cdot\sqrt{\dfrac{\alpha}{\pi}} \\ (or) = \dfrac{K_{I,II}}{\dfrac{P}{B\cdot\sqrt{R}}} \end{cases} \tag{7.35}$$

The cases of crack length $\alpha = 0.1, 0.3, 0.5, 0.7, 0.8, 0.9$ for different crack inclination angles θ are shown together in the Figure 7.14. As can be seen, for the small crack cases ($\alpha \le 0.5$) the $\mathbf{f_I}$ and $\mathbf{f_{II}}$ results by the three methods basically agree well. If these results are compared with those obtained by Awaji and Sato (1978) and by Atkinson (1982) for short crack cases, it can then be concluded that the current evaluated $\mathbf{K_I}$ and $\mathbf{K_{II}}$ results coincide with theirs for the small crack case as the error in their evaluation results made by the approximation can really be neglected.

As the crack length tends larger, $\alpha > 0.5$, the $\mathbf{K_{II}}$ values by the dislocation method (marked **d** in the figure) and the complex stress function methods (marked with **Z1** and **Z2** respectively) will tend to diverge, and when $\alpha = 0.9$ this difference will be around 30%. However for $\mathbf{K_I}$ values, the same results by these three methods will hold up to a crack length of $\alpha = 0.7$. After that the dislocation method (**d**) and the complex stress function method II (**Z2**) will still yield the same $\mathbf{K_I}$ results for any crack length (less than 2% difference for large values) while the $\mathbf{K_I}$ value by the complex stress function method I (**Z1**) will differ more and more from those obtained by **d** and **Z2** methods as the crack length increases.

From these findings, it is suggested that the $\mathbf{K_I}$ value for mixed mode CSTBD fracture problem should adopt the results by the **d** or the **Z2** method, and the results by **Z1** method

should be discarded. However for $\mathbf{K_{II}}$ values, it is still not possible to conclude which one will yield more precise results for the problem at this stage. A third evaluation method should be sought or a numerical or experimental method should be used to help to judge the correctness of the evaluation. For the sake of clearer illustration, $\mathbf{f_I(\alpha,\theta)}$ and $\mathbf{f_{II}(\alpha,\theta)}$ by **d** and **Z2** methods are displayed in Figure 7.15 a) and b) respectively for all the crack lengths. As can be seen again, the $\mathbf{f_I(\alpha,\theta)}$ values shown in these two figures are generally the same. Only less than 2% difference is shown for the cases of $\alpha = 0.9$ and $\theta = 70° \sim 90°$. $\mathbf{f_I(\alpha,\theta)}$, $\mathbf{f_{II}(\alpha,\theta)}$ can also be expressed in forms of $\mathbf{Y_I(\alpha,\theta)}$ and $\mathbf{Y_{II}(\alpha,\theta)}$ which was defined in Equation (7.35). These transformations will make easier the connection of SIF values to specimen compliance (for the SIF evaluation of the CCNBD specimen) and also make simpler the calculation of fracture toughness value $\mathbf{K_{IC}}$ or $\mathbf{K_{IIC}}$ in practical usage. Figure 7.16 a) and b) clearly illustrate the variations of $\mathbf{Y_I(\alpha,\theta)}$ and $\mathbf{Y_{II}(\alpha,\theta)}$ with α and θ by the dislocation method, where the variation pattern for different α and θ can be easily obtained. The similar diagrams of $\mathbf{Y_I(\alpha,\theta)}$ and $\mathbf{Y_{II}(\alpha,\theta)}$ by **Z2** method are displayed in Figure 7.16 c) and d). The three dimensional variation diagram of them is shown in Figure 7.17.

Based on the results shown above, it is known that the CSTBD specimen can be taken as an ideal specimen to be used to study mixed mode fracture problems. By only fixing the different inclination angle θ between the crack orientation and the loading direction (which is an easy job), different combinations of **Mode I** and **Mode II** fracture intensities can be easily obtained and therefore the mixed mode fracture problem can be investigated.

If we compare the $\mathbf{Y_I(\alpha,\theta)}$ values in Figure 7.16 a) for the case of $\theta = 0°$ with the results evaluated in Chapter 3 for pure **Mode I** SIF values $\mathbf{Y(\alpha)}$ of the CSTBD specimen, we will realize that their difference over the whole crack length range is negligible (less than $\pm 1.1\%$). This again substantiates the correctness of both the evaluations in Chapter 3 and in this chapter. In fact, the evaluation in Chapter 3 is just one of the special cases included in the general solutions discussed here.

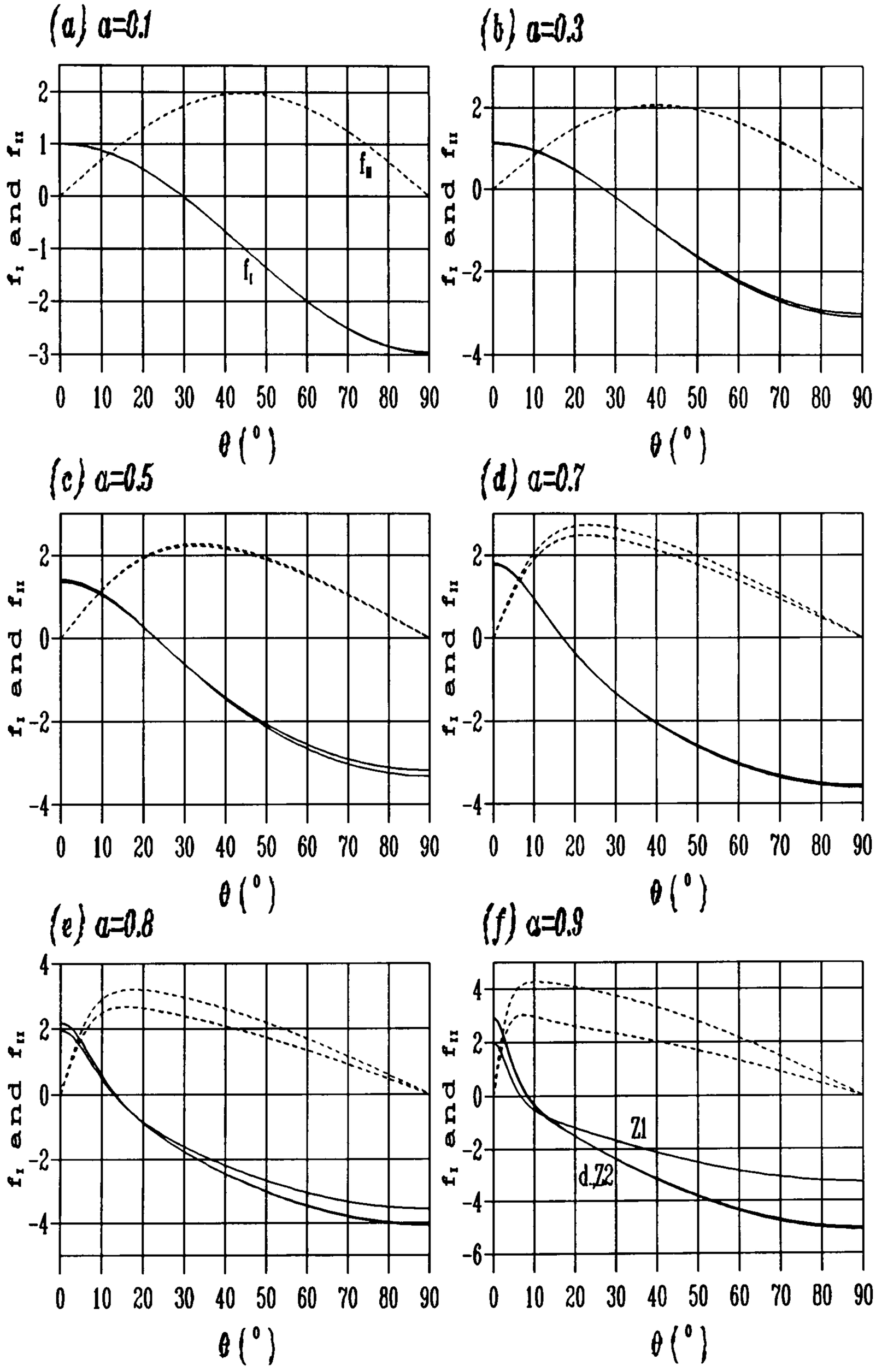

Figure 7.14 $f_I(\alpha,\theta)$ and $f_{II}(\alpha,\theta)$ for mixed mode CSTBD problem by d, Z1 and Z2 Methods

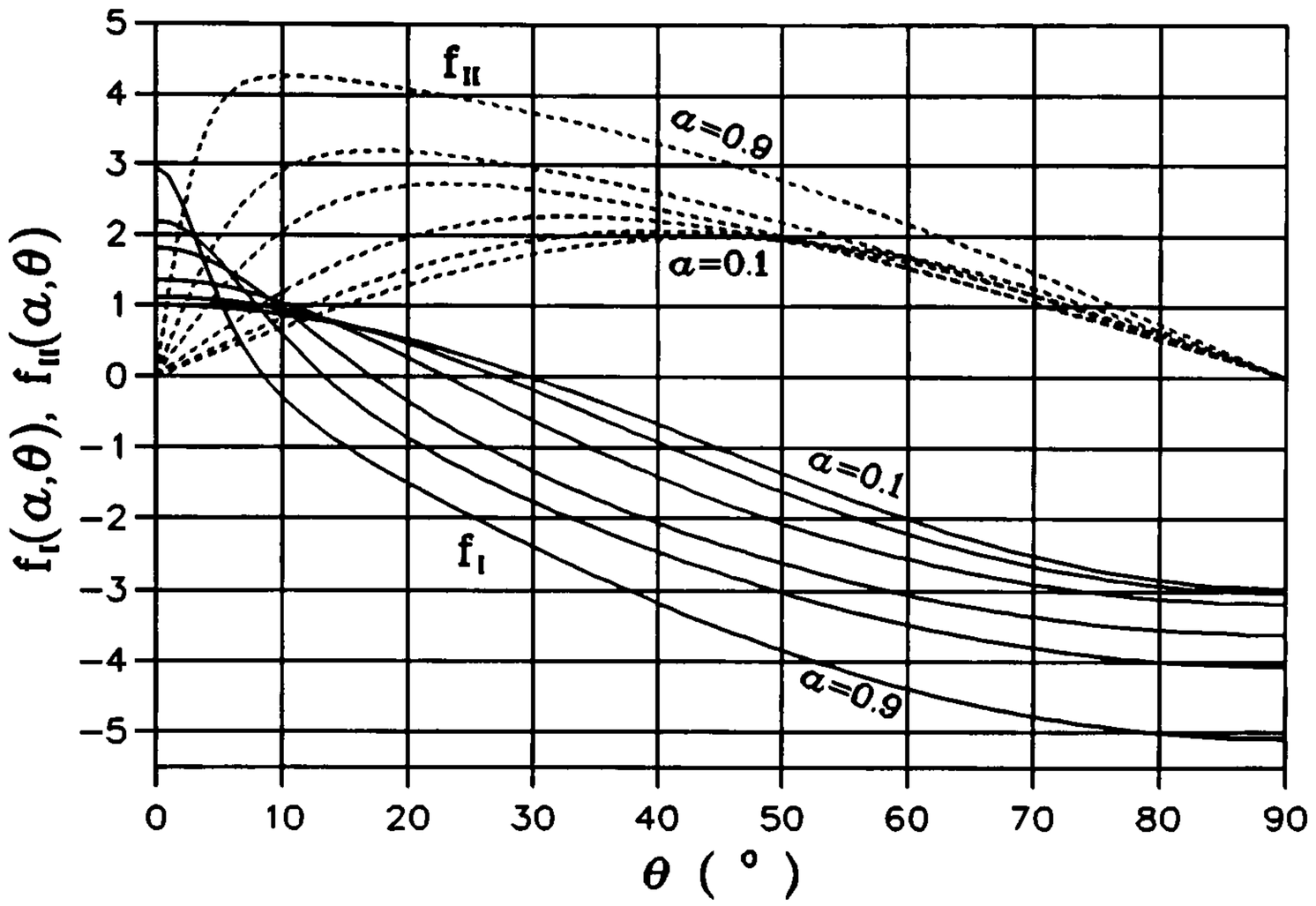

Figure 7.15 a) $f_I(\alpha,\theta)$ and $f_{II}(\alpha,\theta)$ for mixed mode CSTBD problem by dislocation Method

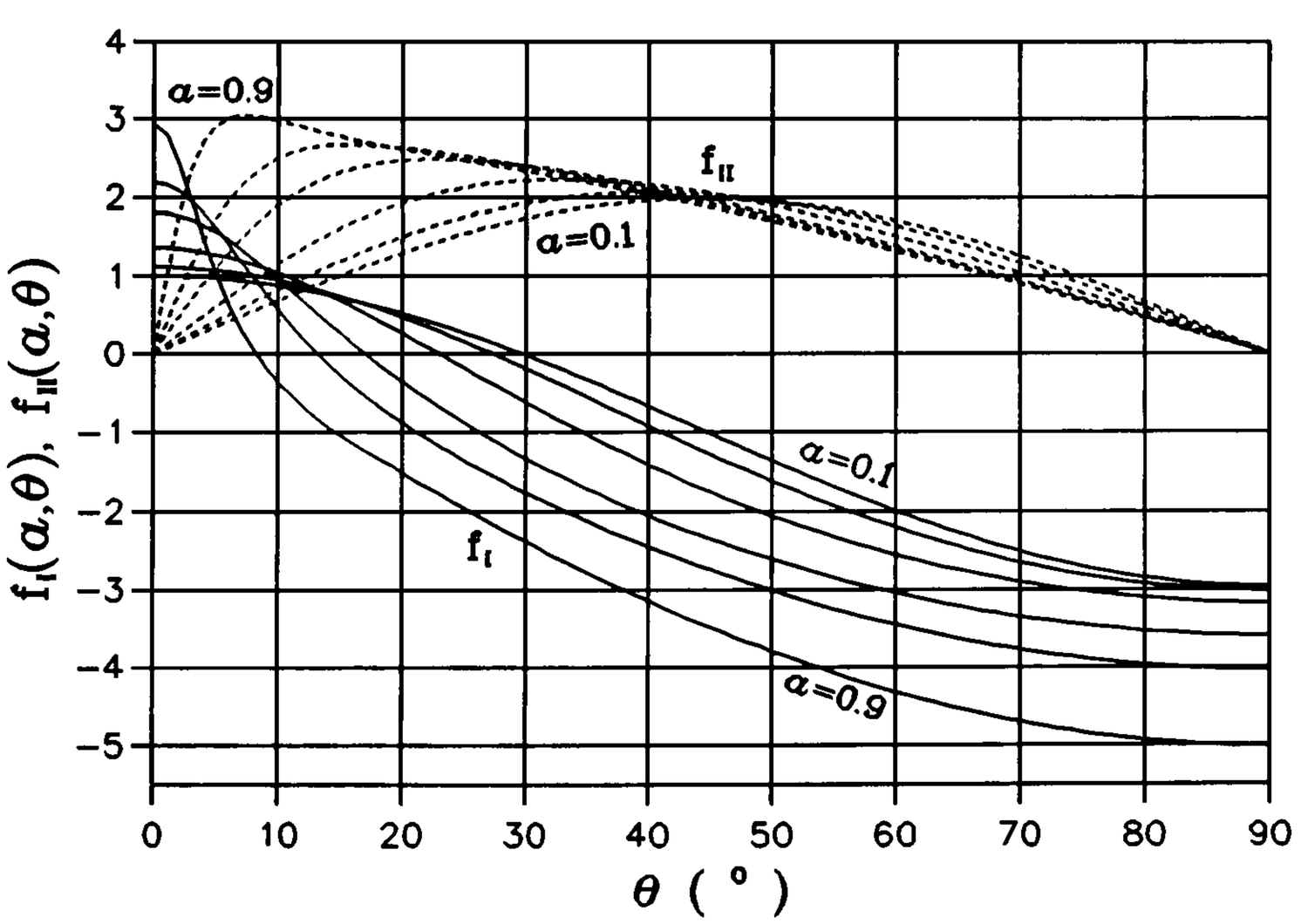

Figure 7.15 b) $f_I(\alpha,\theta)$ and $f_{II}(\alpha,\theta)$ for mixed mode CSTBD problem by Z2 Method

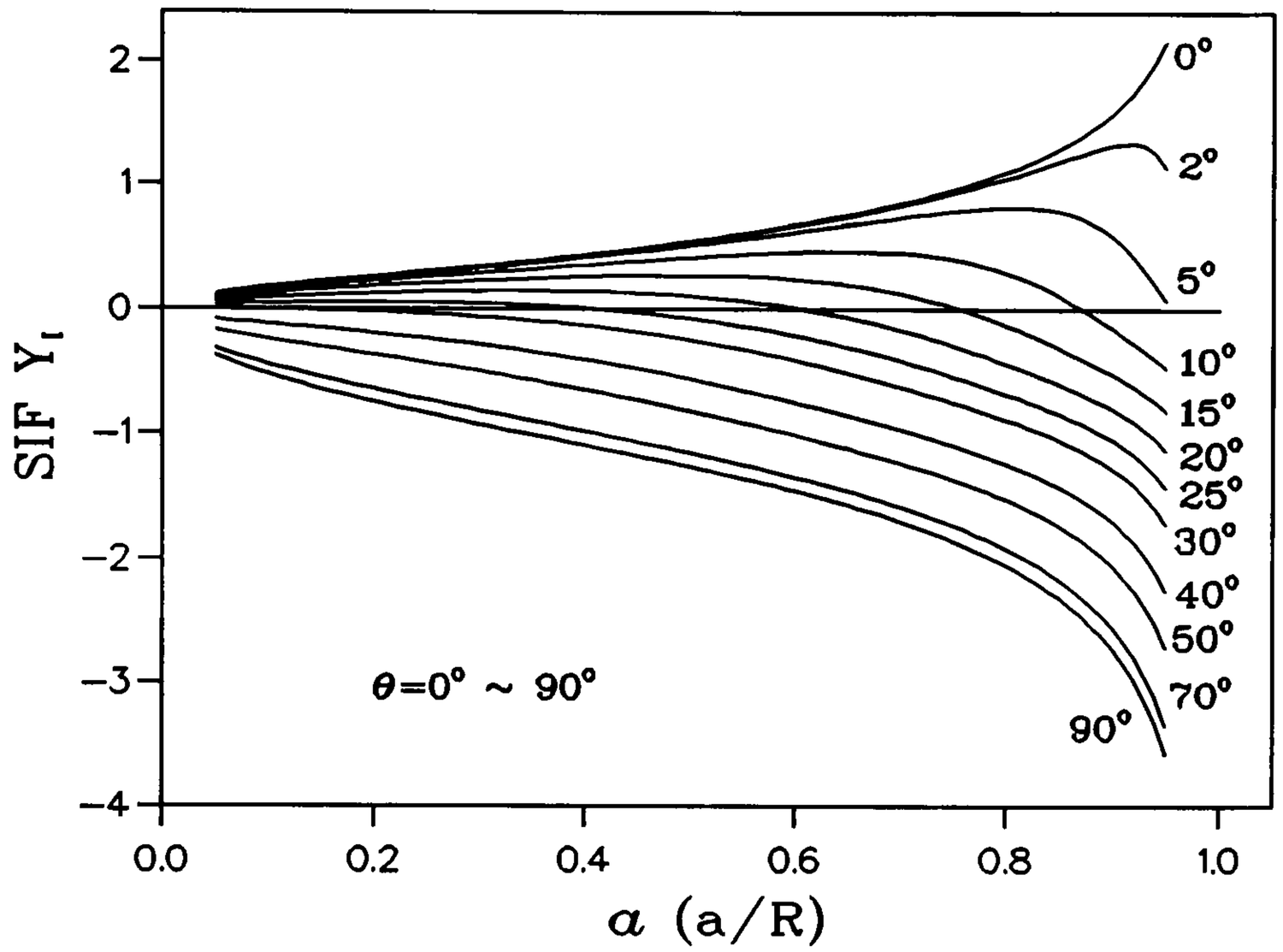

Figure 7.16 a) $Y_I(\alpha,\theta)$ for mixed mode CSTBD problem by Dislocation method

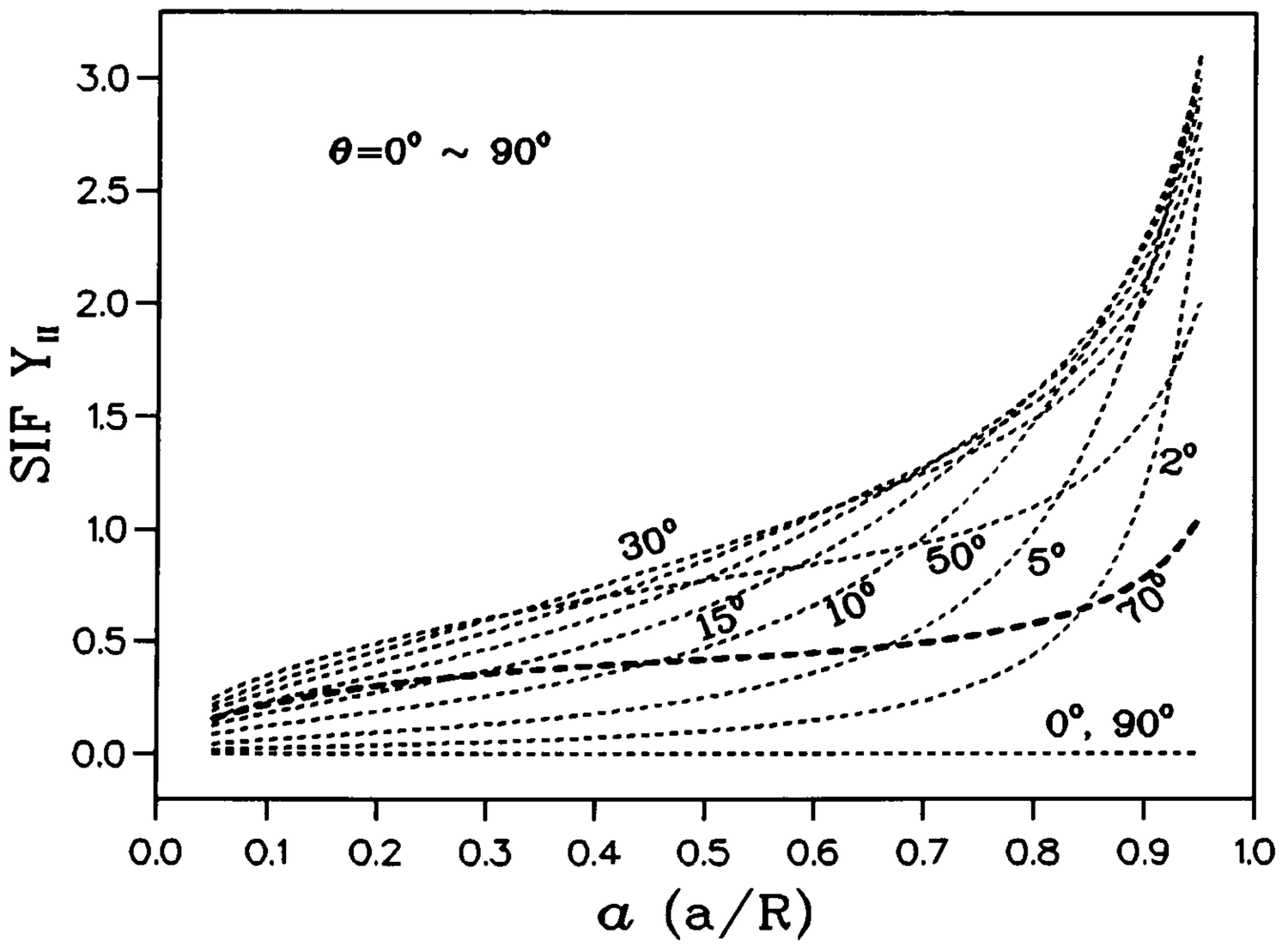

Figure 7.16 b) $Y_{II}(\alpha,\theta)$ for mixed mode CSTBD problem by Dislocation method

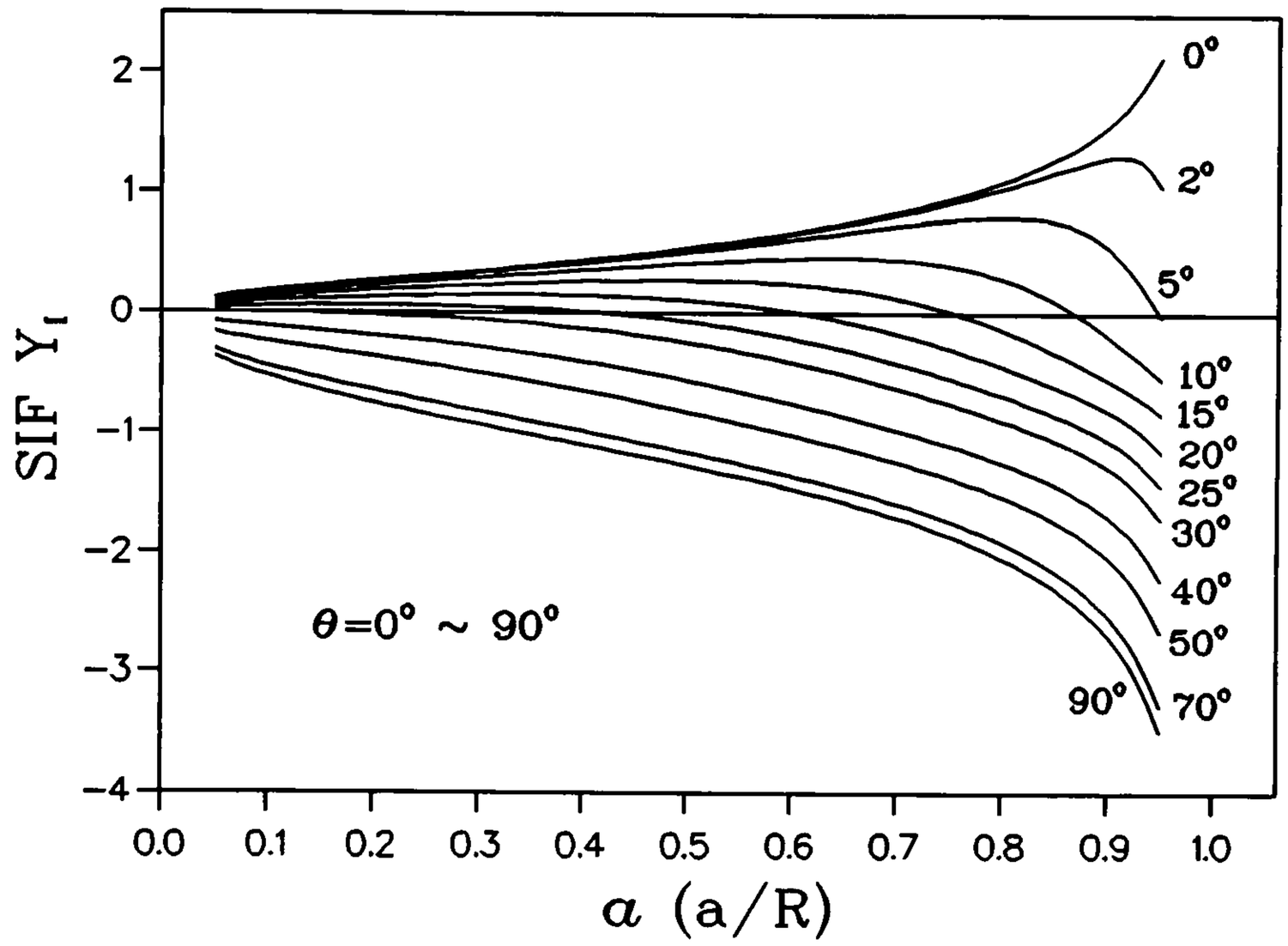

Figure 7.16 c) $Y_I(\alpha,\theta)$ for mixed mode CSTBD problem by Z2 method

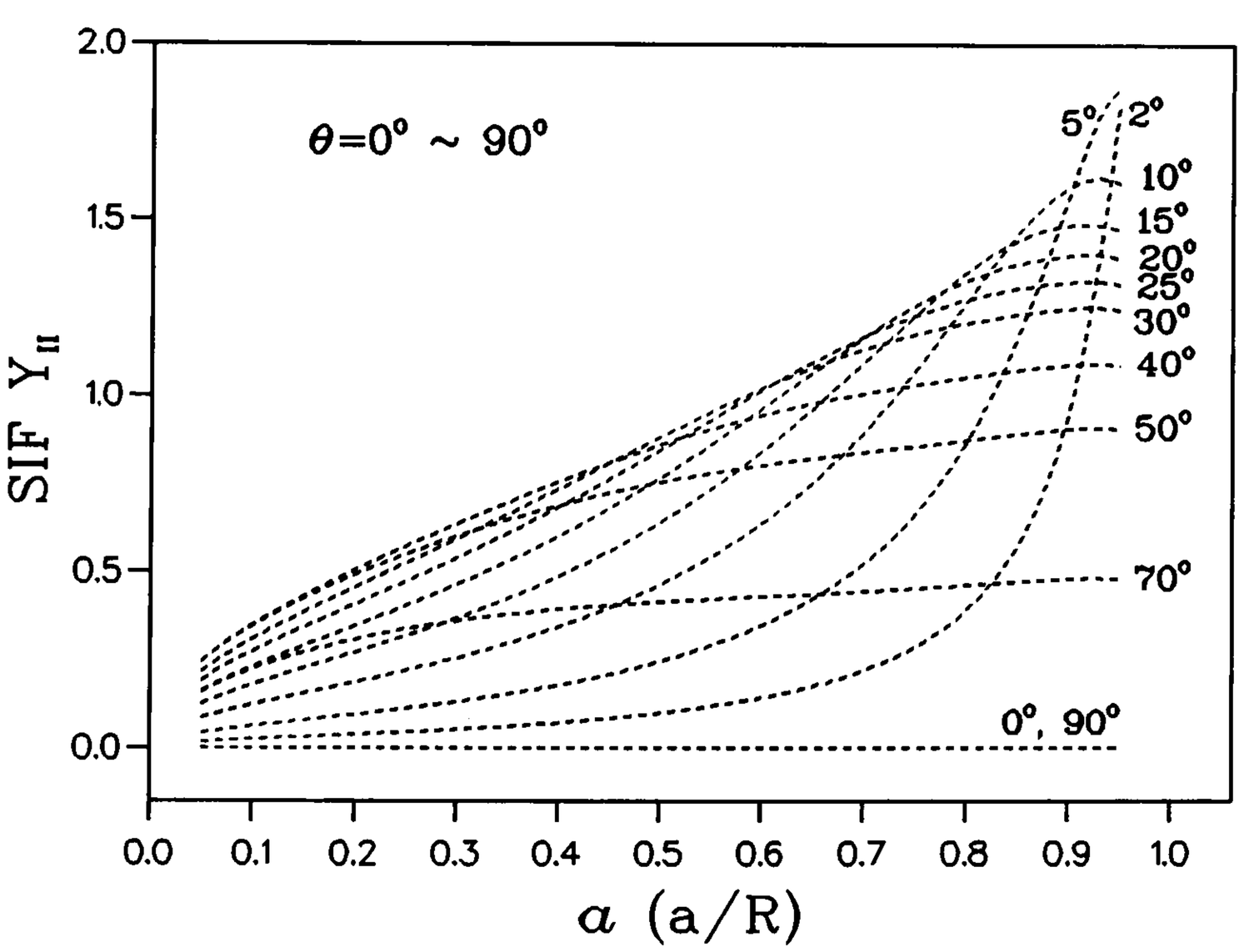

Figure 7.16 d) $Y_{II}(\alpha,\theta)$ for mixed mode CSTBD problem by Z2 method

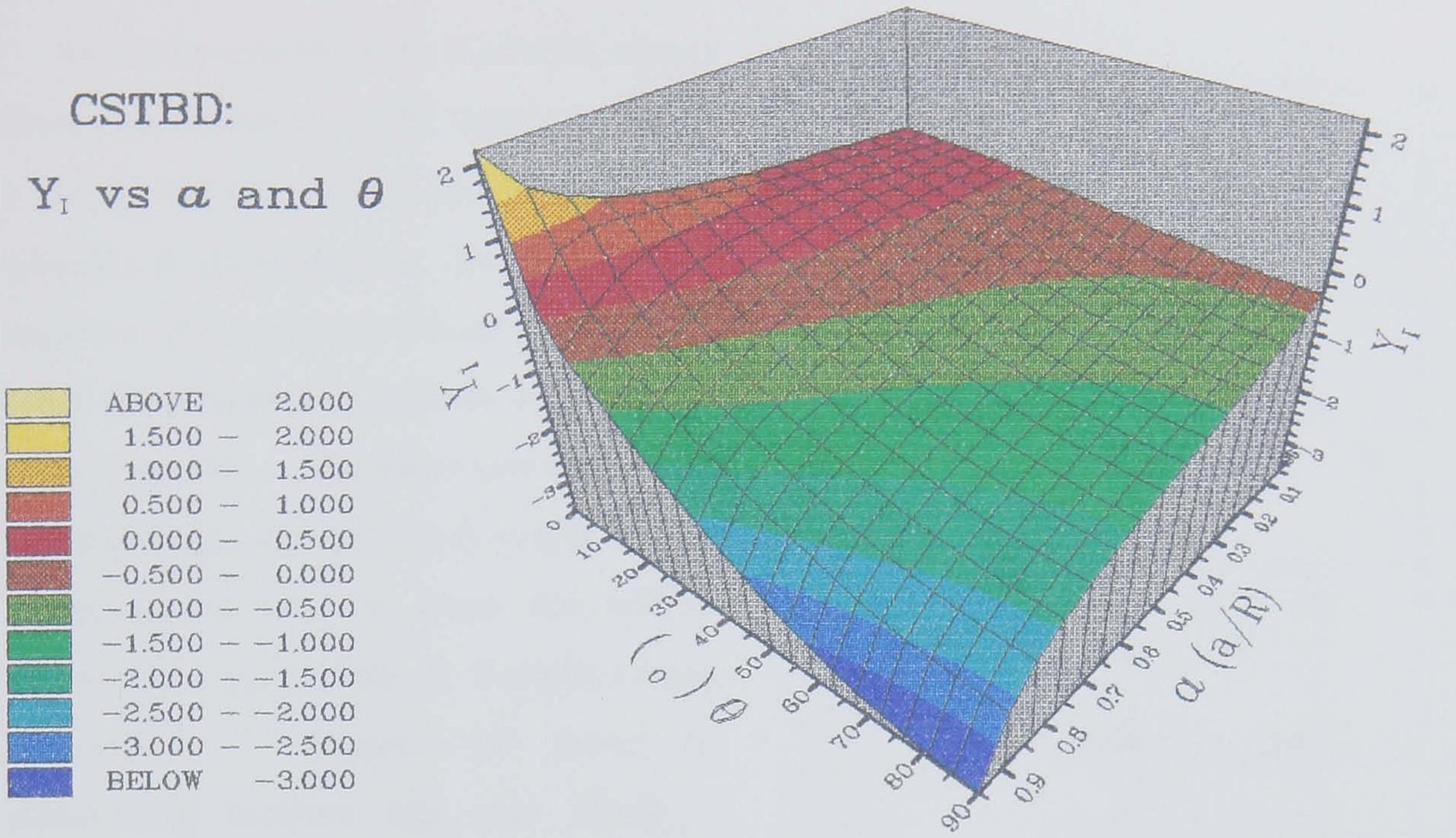

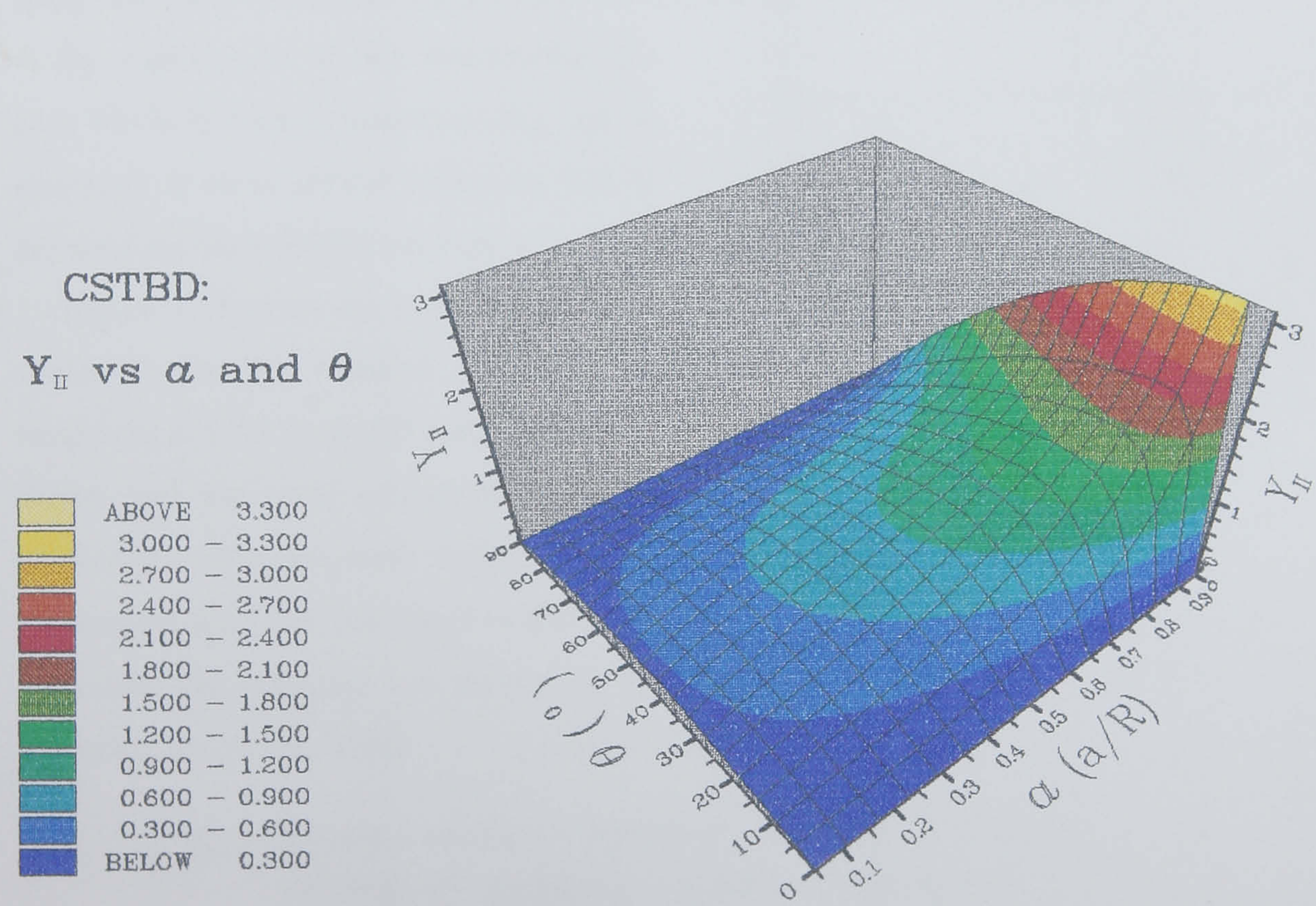

Figure 7.17 $Y_I(\alpha,\theta)$ and $Y_{II}(\alpha,\theta)$ for Mixed Mode CSTBD Fracture Problem by Dislocation Method

§7.6 The Pure Mode II Fracture Problem for The CSTBD Specimen

As can be seen from the $\mathbf{K_I}$ and $\mathbf{K_{II}}$ results shown above, for any crack length, the **Mode I** SIF $\mathbf{K_I}$ will start from a positive maximum when $\theta = 0^o$ (Split **Mode I**), decrease, become negative (Compression **Mode I**) and then reach the negative maximum as θ changes from 0° to 90°. Therefore there should be a certain angle for each crack length α **(a/R)** where $\mathbf{K_I} = 0$, i.e., the crack tips will be subjected to pure **Mode II** fracture loading $\mathbf{K_{II}}$ only. Figure 7.18 shows the relationship between this pure **Mode II** critical crack length α_{II} and the critical crack inclination angle θ_{II}, where the solid line is our evaluation result. Some discrete evaluation results by Atkinson (1982), Sanchez (1979) and Awaji and Sato (1978) for crack length $\alpha \le 0.6$ are also shown in the figure.

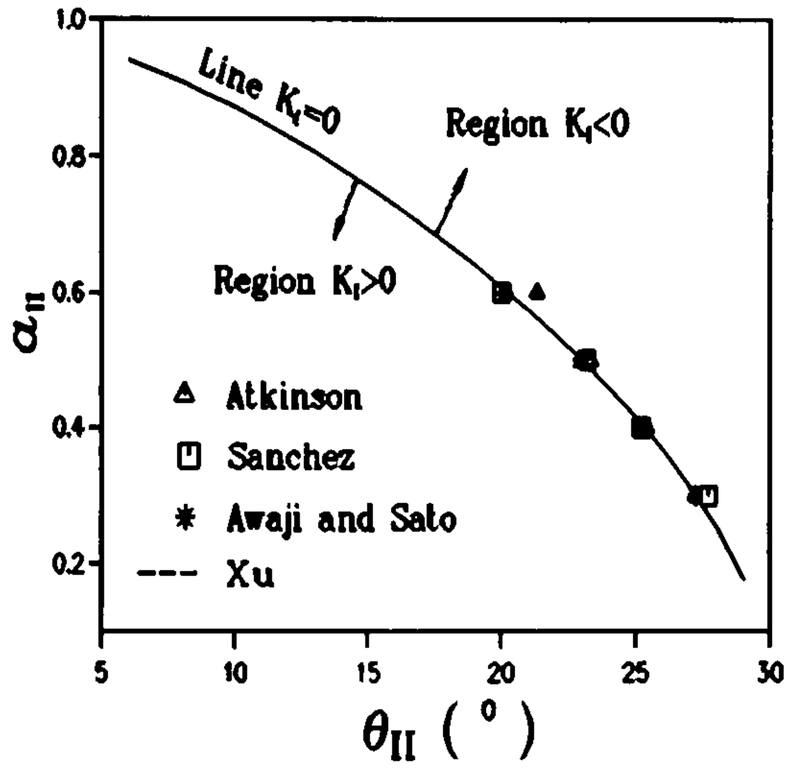

Fig.7.18 Critical α_{II} and θ_{II}

By making use of this relationship, the pure **Mode II** fracture toughness $\mathbf{K_{IIC}}$ can be measured if these critical values α_{II} and θ_{II} are used for the CSTBD test fixture.

Figure 7.19 gives the pure **Mode II** SIF values $\mathbf{Y_{II}}$ for this situation. Again the results for $\alpha \le 0.6$ by Awaji and Sato are also shown and the good agreement is clearly illustrated. For practical usage, 8 order polynomial lines are best fitted to these two lines and the relations are shown in the following functional forms:

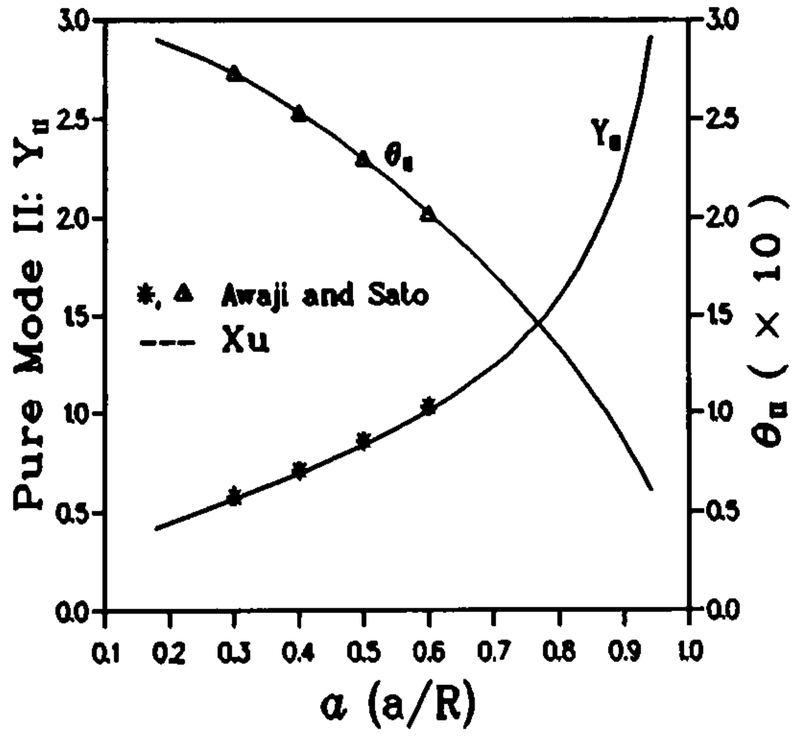

Fig.7.19 Pure Mode II Y_{II}

$$\begin{cases} \theta_{II} = 30.4406 - 4.6734\cdot\alpha - 17.6741\cdot\alpha^2 - 9.6827\cdot\alpha^3 + 3.9819\cdot\alpha^4 \\ \qquad + 12.9163\cdot\alpha^5 - 13.3222\cdot\alpha^6 + 12.8001\cdot\alpha^7 - 13.1239\cdot\alpha^8 \\ Y_{II} = 0.06462 + 2.8956\cdot\alpha - 6.8663\cdot\alpha^2 + 9.8566\cdot\alpha^3 - 0.4455\cdot\alpha^4 - 1.0494\cdot\alpha^5 \\ \qquad - 13.2492\cdot\alpha^6 + 9.0783\cdot\alpha^7 - 10.7354\cdot\alpha^8 + 28.4775\cdot\alpha^9 - 6.3197\cdot\alpha^{10} \\ \qquad + 10.6626\cdot\alpha^{11} - 10.0268\cdot\alpha^{12} - 34.2997\cdot\alpha^{13} + 1.7292\cdot\alpha^{14} + 25.2216\cdot\alpha^{15} \end{cases} \tag{7.36}$$

The calculations of θ_{II} and Y_{II} by these two relations will yield the results within 1% error. With the help of this calculation, the critical fixture for any pure **Mode II** fracture situation of the CSTBD specimen with any crack length can be easily obtained.

§7.7 Mixed Mode Fracture Strength Locus

Fracture strength locus is one of the main subjects in mixed mode fracture research [Whittaker, 1992]. A large number of expressions have been proposed to describe this fracture criteria relationship between the SIF values, K_I and K_{II}, and the fracture toughness, K_{IC} and K_{IIC}, on the foundation of the fracture theories (Maximum Stress Theory -- σ Criterion, Maximum Strain Energy Release Rate Theory -- G Criterion or Minimum Strain Energy Density Theory -- S Criterion) [Whittaker, 1992][9] or simply on the basis of experimental results [10][9]. However they can be summarized in the following form:

$$\left(\frac{K_I}{K_{IC}}\right)^{k_u} + k_c \cdot \frac{K_I \cdot K_{II}}{K_{IC} \cdot K_{IIC}} + \left(\frac{K_{II}}{K_{IIC}}\right)^{k_u} = 1 \qquad (7.37)$$

where k_u is within the range of $1.6 \sim 2.0$ [10], k_c is the interaction coefficient between the two fracture modes and K_{IC} and K_{IIC} are the **Mode I** and **Mode II** fracture toughness. It has been proved experimentally that K_{IIC} is normally around $0\% \sim 20\%$ larger than K_{Ic} value [159][10][9]. If we substitute $K_{IIC} = k_m \cdot K_{IC}$ ($k_m = 1.0 \sim 1.2$) and the relation of $K_{I,II} = Y_{I,II} \bullet P/(B \bullet \sqrt{R})$ into the above relation we will have an alternative form for Equation (7.37) as followed:

$$Y_{MIX} = \left(Y_I\right)^{k_u} + \frac{k_c}{k_m} \cdot Y_I \cdot Y_{II} + \left(\frac{Y_{II}}{k_m}\right)^{k_u} = \left(\frac{P}{B \cdot \sqrt{R}} \cdot K_{IC}\right)^{k_u} \qquad (7.38)$$

where Y_{MIX} can be viewed as the mixed mode SIF value.

Therefore the criteria of fracture will turn to the mixed SIF value Y_{MIX} reaching a certain limit which is connected to the material fracture toughness as $[P \bullet K_{IC}/(B \bullet \sqrt{D})]^{k_u}$. Y_{MIX} will behave like a single SIF and obviously its value will mainly be determined by Y_I and Y_{II} values and will be affected by the coefficients k_u, k_m and k_c. Figure 7.20 a), b), c) and d) are some of the examples of calculated Y_{MIX} based on different coefficients for different crack inclination angles.

In practical application, both the theoretical solutions and experiments are suggested to decide the fracture strength locus of a material. The usage of the CSTBD specimen makes it easier to have different combination of K_I and K_{II} fracture intensities and therefore the fracture strength locus can be easily determined by limited experiments.

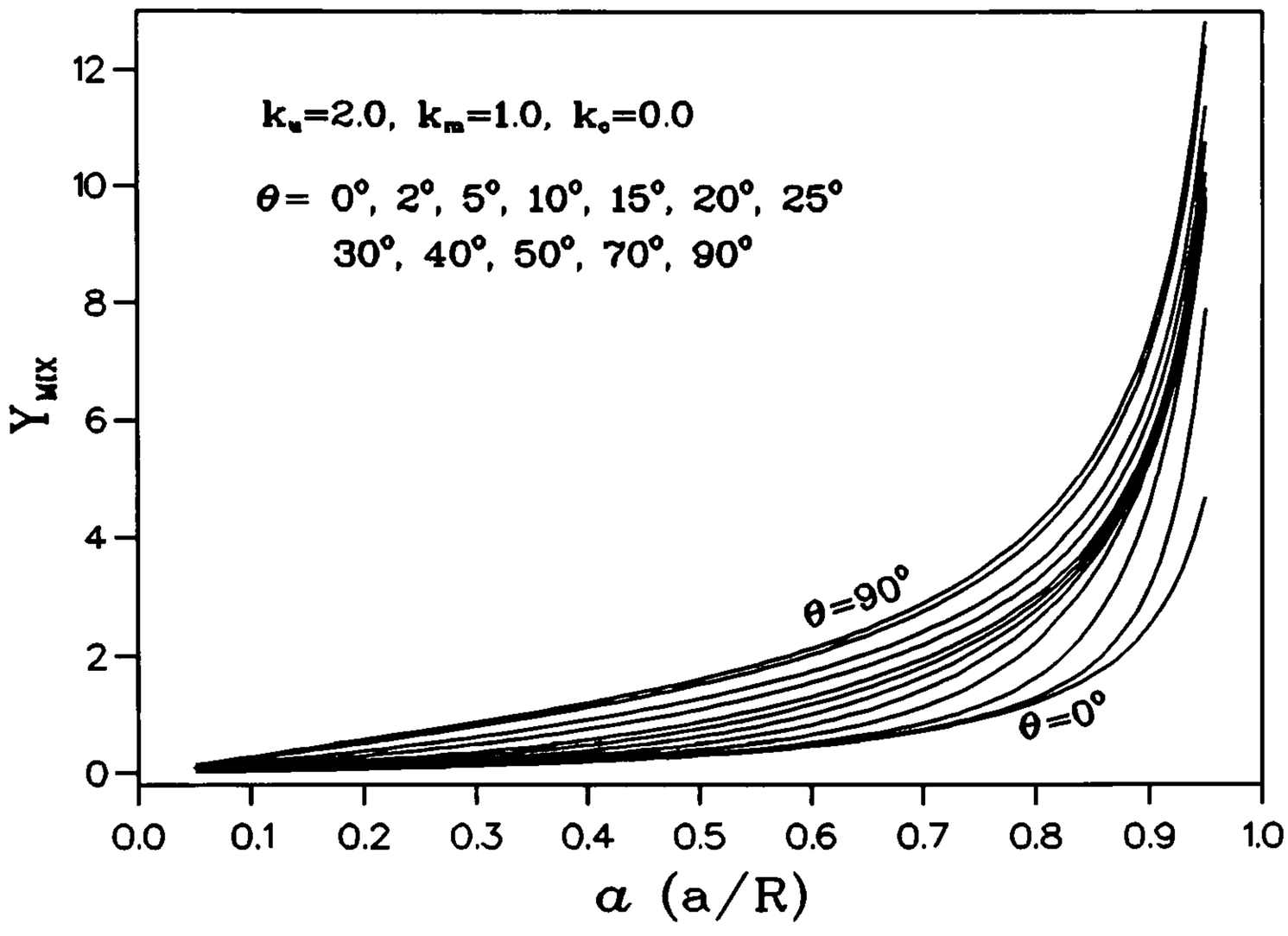

Figure 7.20 a) Y_{MIX} for $k_u = 2.0$, $k_m = 1.0$ and $k_c = 0.0$

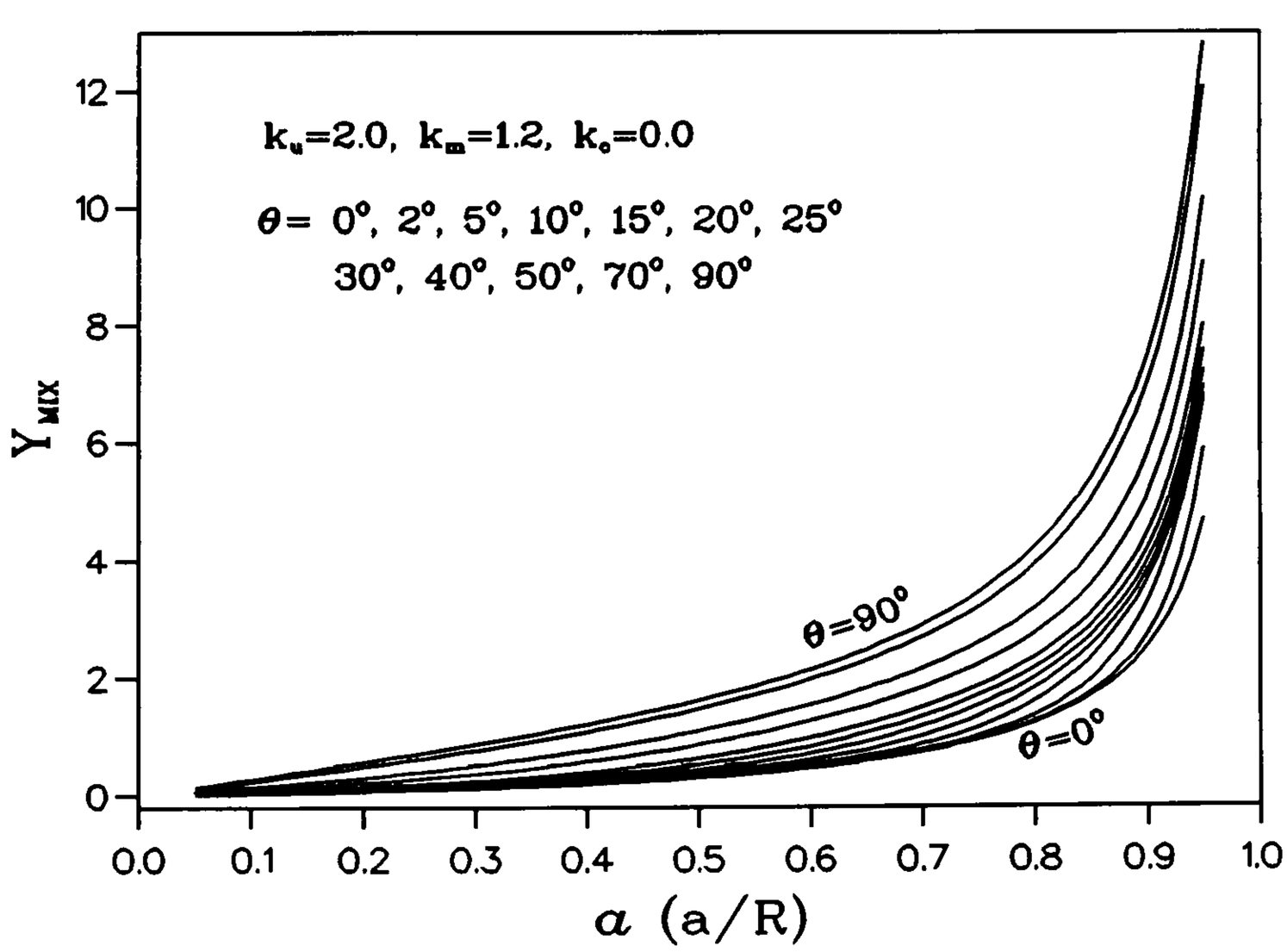

Figure 7.20 b) Y_{MIX} for $k_u = 2.0$, $k_m = 1.2$ and $k_c = 0.0$

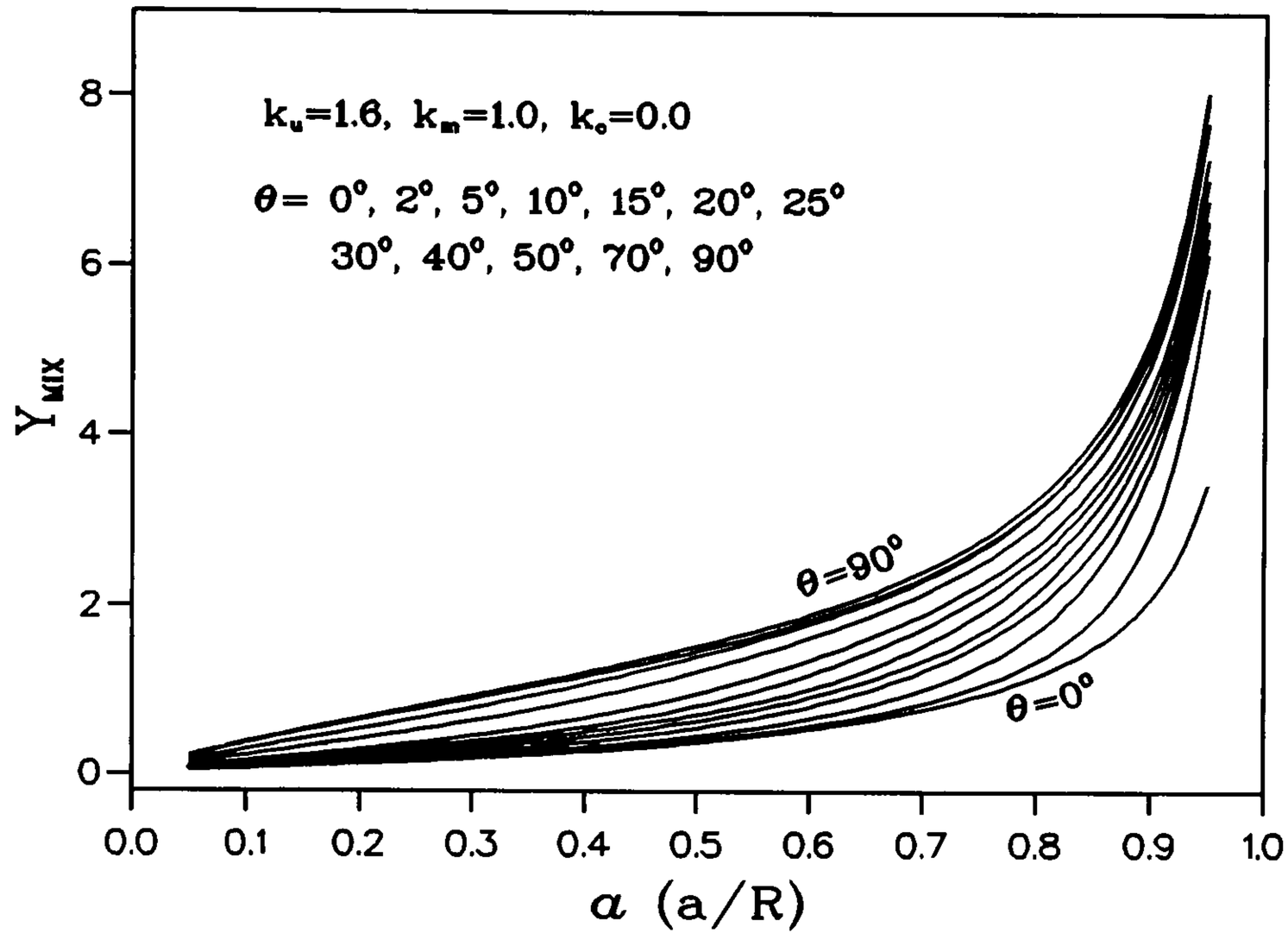

Figure 7.20 c) Y_{MIX} for $k_u = 1.6$, $k_m = 1.0$ and $k_c = 0.0$

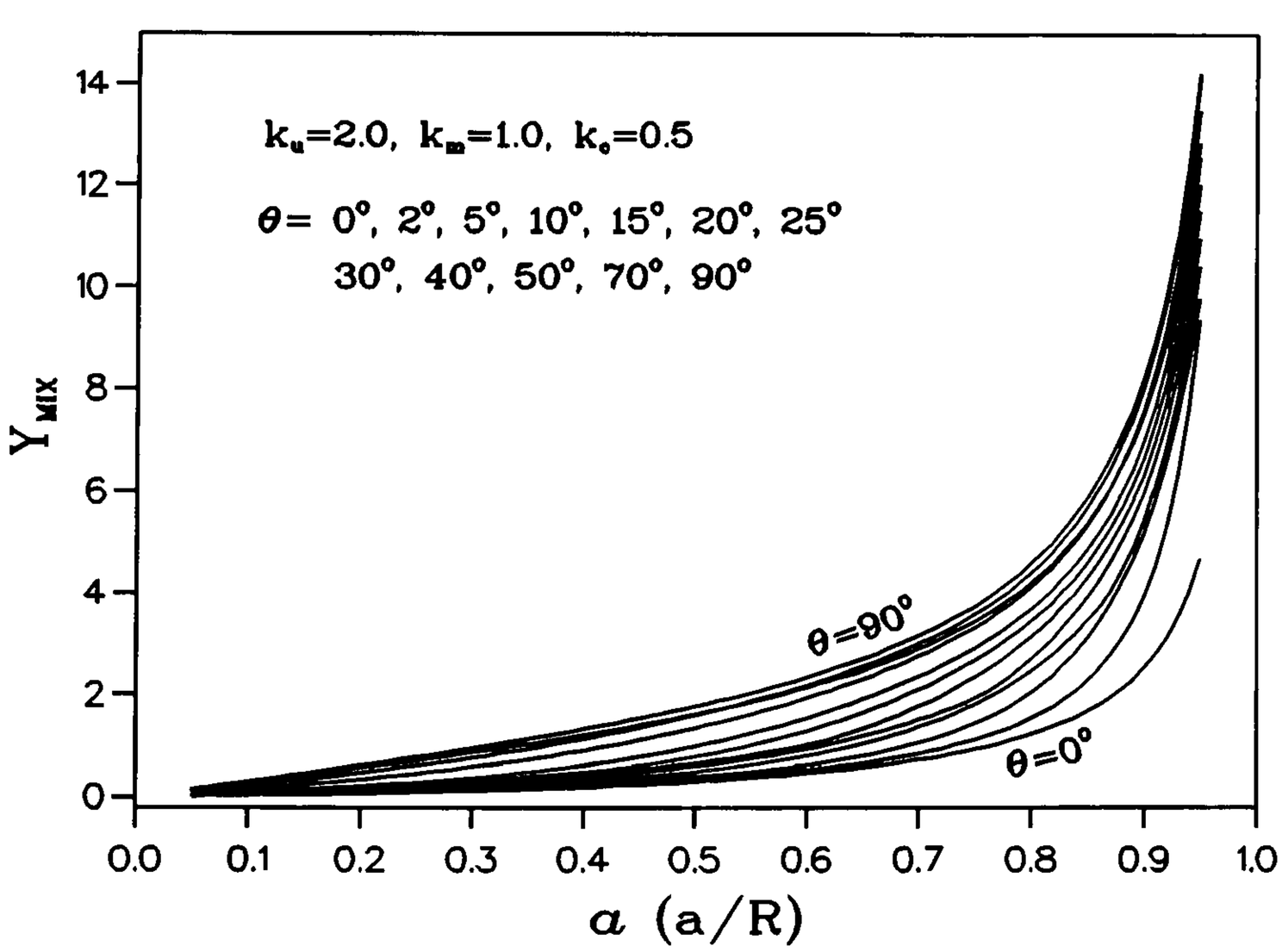

Figure 7.20 d) Y_{MIX} for $k_u = 2.0$, $k_m = 1.0$ and $k_c = 0.5$

§7.8 The Usage of CCNBD Specimen in Mixed Mode Fracture Studies

The good features of the chevron notched crack specimen, especially the CCNBD, appearing in the fracture studies inspire us to introduce the CCNBD for mixed mode fracture studies. As discussed in the last section, the dominated SIF in determining the fracture will be the mixed SIF $\mathbf{Y_{MIX}}$ value. Therefore for the CCNBD geometry, it is the change of this $\mathbf{Y_{MIX}}$ which will decide the critical state of the specimen.

However attention should be paid that in the CCNBD specimen, the propagation of the crack within the chevron part of the specimen is constraint by the notch and cannot behave as freely as the crack front in the CSTBD specimen (where the crack front is not subjected to any constraint and is free to propagate in any direction according to the different combinations of the **Mode I** and **Mode II** fracture intensities). In other words, the crack has to propagate in the chevron notch direction within the chevron part of the crack in the CCNBD specimen. The reason is geometrically obviously as the new crack surface created when the crack is propagating in the chevron notch direction within the chevron part is always less than that created by the propagation in any other direction and therefore the energy needed is certainly a minimum from Griffith's energy theory. As a result, the σ-, **G**- and **S**- mixed mode fracture propagation theories are considered to be valid for the mixed mode CCNBD fracture problem only after the crack propagation front reaches the un-notched part of the specimen.

Based on the above arguments, in chevron crack propagation analysis, if we suggest that the total energy release rate or energy resistance **G** of the constrained propagation is the sum of the energy release rate or energy resistance for each fracture mode $\mathbf{G_I}$ and $\mathbf{G_{II}}$, and that the crack will propagate when the total energy release rate reaches a certain limit $\mathbf{G_C}$, i.e.,

$$G = G_I + G_{II} = G_C \tag{7.39}$$

then within the range of LEFM, from the relation between $\mathbf{G_{I,II}}$ and $\mathbf{K_{I,II}}$ as shown in Equation (2.11), we will soon reach the same crack propagation criteria as Equation (7.37) but with $\mathbf{k_u}=2.0$ and $\mathbf{k_c}=0.0$ in particular.

What is needed to be determined are the variations of SIF $\mathbf{Y^*_{MIX}}$ for the CCNBD specimen as the crack propagates because this will decide the critical situation of the specimen as discussed above. As mentioned in Chapter 3, the equations for the CCNBD SIF $\mathbf{Y^*}$ evaluations are valid for any fracture mode or mixed mode condition. Therefore if we substitute $\mathbf{Y_I}$, $\mathbf{Y_{II}}$ and $\mathbf{Y_{MIX}}$ for the CSTBD specimens determined in the last few sections into the evaluation formulas listed in Chapter 3, we will then get the variations of the **Mode I**, **Mode II** and mixed mode SIF values, $\mathbf{Y^*_I}$, $\mathbf{Y^*_{II}}$ and $\mathbf{Y^*_{MIX}}$, for the mixed mode CCNBD specimen. Based on the

experience of pure **Mode I** fracture analysis, we suggest the usage of Bluhm's slice model to simulate the behaviour of the CCNBD specimen under the mixed mode fracture condition. Therefore Equation (3.53) is used for the Y^*_I, Y^*_{II} and Y^*_{MIX} evaluations.

Figure 7.21 a) and b) are just two of the examples of the variations of Y^*_I, Y^*_{II} and Y^*_{MIX} for the CCNBD specimen as the crack propagates for different crack inclination angles. One should bear in mind that it is the variation of Y^*_{MIX} which will decides the critical state of the specimen. Again the behaviour of chevron crack is shown and therefore an unproven

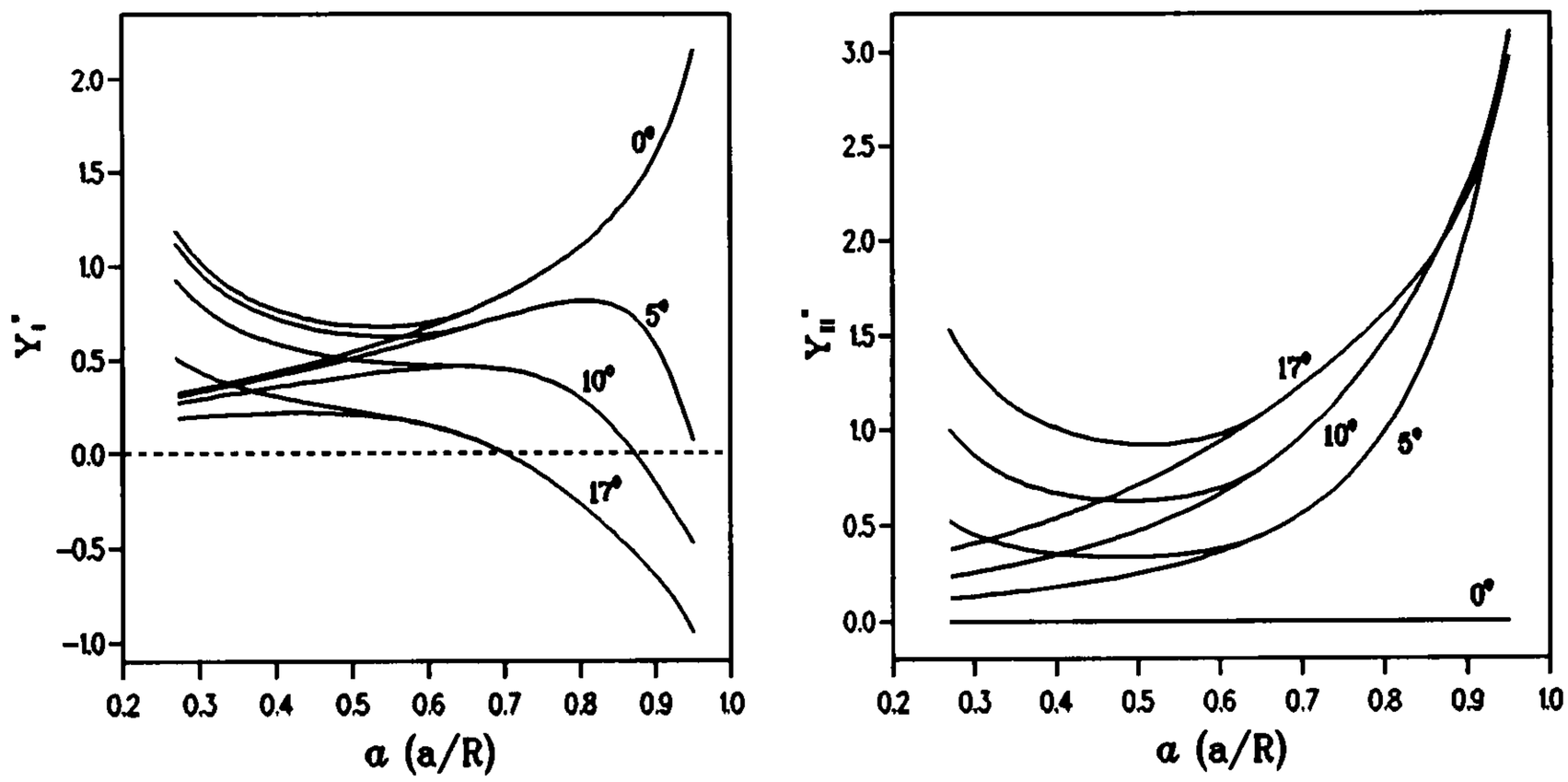

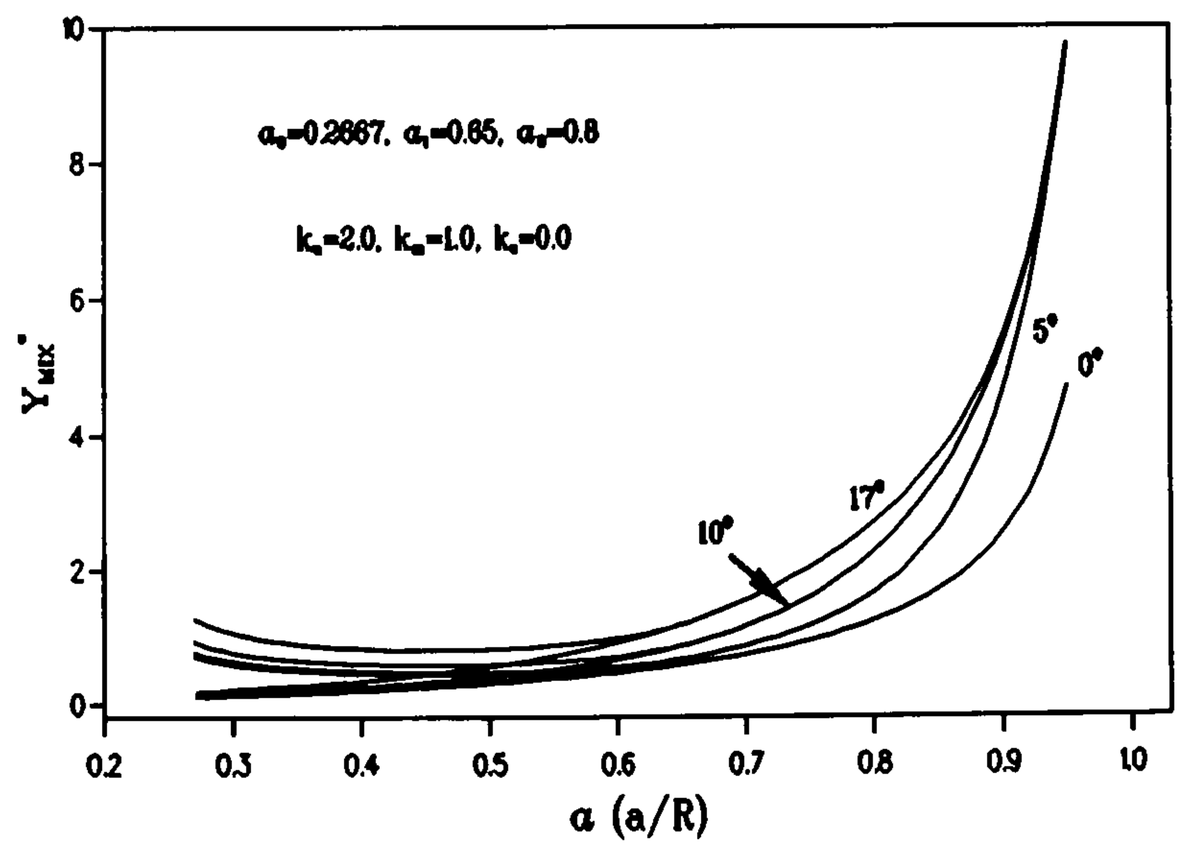

Figure 7.21 a) Y^*_I, Y^*_{II} and Y^*_{MIX} for $k_u = 2.0$, $k_m = 1.0$ and $k_c = 0.0$

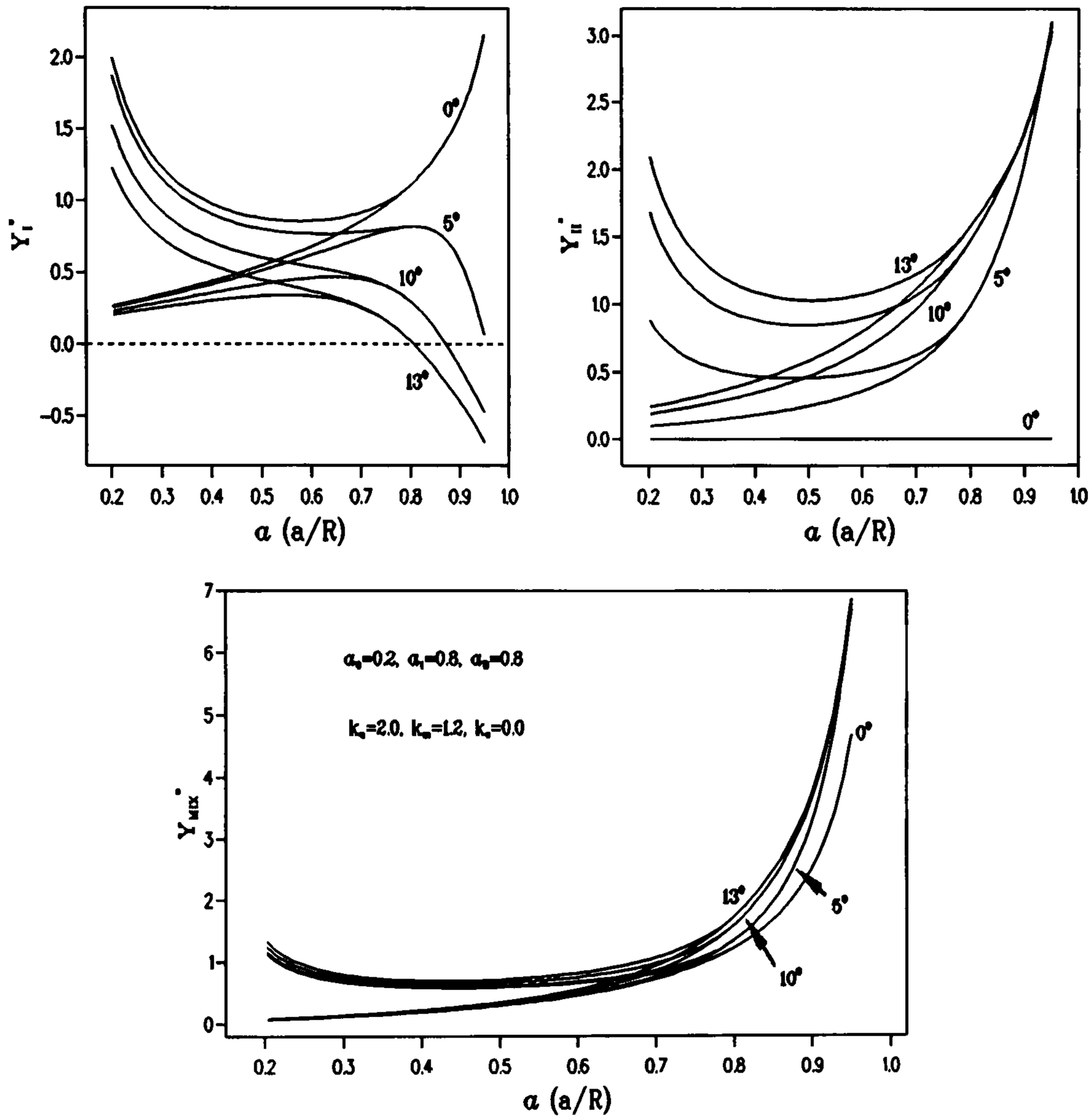

Figure 7.21 b) Y^*_I, Y^*_{II} and Y^*_{MIX} for $k_u = 2.0$, $k_m = 1.2$ and $k_c = 0.0$

suggestion can be made that the CCNBD specimen may still be suitable for use as a mixed mode fracture toughness testing specimen and the good features of the chevron cracked specimen will still hold. Certainly the point needs investigating in more detail.

However one particular point should be taken care of for the CCNBD specimen if we consider the crack closure problem when the crack propagates. As in the CCNBD specimen, the initial part of the chevron crack behaves more or less like a pre-cracking procedure. Therefore the crack can be viewed as being with zero width and when the **Mode I SIF** is negative or the fracture force is compressive, the crack will close. In this case the evaluations based on no crack closure will be no longer valid. Therefore in order to keep the validity of

the results, the crack inclination angle θ should be kept within a certain value to ensure positive $\mathbf{K_I}$ values or split **Mode I** fracture condition. This value can be decided from Figure 7.18 for $\mathbf{K_I > 0}$ according to different crack lengths where the upper limit of the θ value is shown as the solid line. In the two cases shown in Figure 7.21 for $\alpha_1 = 0.65$ and 0.80 respectively the two upper limits of θ to keep the validity of the evaluations within the chevron part of the crack will be 17.3° and 13°.

However if the CCNBD is used for practical mixed mode testing to determine the fracture strength locus, the $\mathbf{Y^*_{MIX}}$ cannot be evaluated beforehand as the coefficients $\mathbf{k_u}$, $\mathbf{k_m}$ and $\mathbf{k_c}$ are unknown. In this case the theoretical values of $\mathbf{k_u} = 2.0$, $\mathbf{k_m} = 1.0$ and $\mathbf{k_c} = 0.0$ can always be suggested.

Much more work has to be done in order to apply the CCNBD specimen to mixed mode fracture testing. The first important thing is to determine the critical state and its corresponding critical $\mathbf{K_I}$ ($\mathbf{Y_I}$) and $\mathbf{K_{II}}$ ($\mathbf{Y_{II}}$) values for the specimens of different geometrical dimensions. Numerical or experimental validations for the theoretical evaluations are also needed. There is certainly much more and complicated work required compared with the pure **Mode I** CCNBD problem. As the period of the current research is limited, it has not been possible to complete these investigation at the moment.

§7.9 Conclusions and Suggestions for further Research

The following conclusions can be drawn from the above sections:

1) The superimposition technique developed in Chapter 3 to solve the crack problem for the CSTBD specimen has been successfully used to solve the mixed mode fracture problem. As a matter of fact, the method is applicable to any crack problem.

2) The long crack cases for $\alpha > 0.6$ for the mixed mode CSTBD fracture problem has been solved using dislocation and complex stress function methods by the technique mentioned in (1). The error in the solution is believed to be within 1%.

3) The CSTBD and CCNBD specimen geometries are believed to be ideal specimens for mixed mode fracture experimental studies of rock materials, fracture toughness ($\mathbf{K_{IC}}$ and $\mathbf{K_{IIC}}$) measurement, material fracture strength locus testing and crack propagation investigation are some examples. It is very easy to obtain the different combinations of the Mode I and Mode II fracture intensities and the loading fixture will still remain as simple as for the Brazilian disc test.

4) The pure **Mode II** fracture condition can be easily realised in the CSTBD specimen geometry by fixing the crack inclination angle to the loading direction with a fixed value. The loading fixture will still remain very simple.

5) The CCNBD specimen will keep the good features of the chevron cracked specimen when used in mixed mode fracture studies.

At the same time, some further researches are strongly suggested:

1) Numerical or experimental validations are needed to validate the above theoretical results.

2) Much more work is needed to investigate the applications of the CSTBD and CCNBD specimens for mixed mode fracture studies.

3) Consideration should be given to drawing a draft for the pure **Mode II** fracture toughness $\mathbf{K_{IIC}}$ and mixed mode fracture test for rock materials by the CSTBD and CCNBD specimen geometries.

Chapter 8

An Initial Probabilistic Fracture Approach to Rock Cutting Mechanics

§8.1 Introduction

In rock excavation engineering, rock cutting performance prediction plays an important role in cutting tool and machine design. Many researches have been carried out on the connections between the cutting parameters (i.e. forces and energy consumed), and the rocks conventional properties (i.e. compressive and tensile strength). However the cutting models have always been theoretically idealized.

Evans (1962), on the basis of investigations into the penetration of wedges into coal, proposed that the breaking of coal is essentially a tensile failure and suggested a tensile theory for coal cutting. The cutting force, $\mathbf{F_C}$, for a symmetrical wedge penetrating into a rectangular buttock of coal can be calculated by the following formula:

$$F_C = \frac{2 \cdot \sigma_t \cdot h \cdot \sin(\Theta + \phi)}{1 - \sin\Theta} \tag{8.1}$$

where σ_t -- coal tensile strength (MPa),

h -- cutting depth (m),

Θ -- half wedge angle and,

ϕ -- the friction angle between the wedge and the coal.

This formula was derived based on the following three assumptions:

1) The failure surface is a circular arc (two dimensional),

2) the tensile stress induced by the wedging is uniformly distributed over the failure surface, and failure occurs when the tensile stress exceeds the tensile strength of the coal, and

3) at the tip of the wedge, the arc is tangential to the bisector of the wedge angle.

Roxborough extended the theory to rock cutting in 1973 with a similar model and calculation formula and provided experimental validation of his conclusions. It has been concluded that the general principles fundamental to coal cutting mechanics and the design of efficient coal cutting systems might be equally tenable in rock cutting engineering.

Late in the 1970s, Evans introduced a three dimensional model based on the same tensile failure assumptions for the point attack cutting geometry and some evaluation formulas were produced. However, the above mentioned two dimensional theory is still popular because of its simplicity and acceptable closeness between the predicted and practical values.

Another cutting model was proposed by Merchant in 1945 for metal cutting and has also been adopted for rock cutting. This theory is based on the following different assumptions:

1) Rock failure under drag tool cutting is a shearing problem, and the shear failure surface is a straight line (two dimensional), or plane (three dimensional),

2) the shear stress is uniformly distributed over the failure line or plane, shear failure occurs when the shear stress exceeds the material's shear strength, and the failure line or plane is decided by the criteria where the cutting force needed is a minimum.

The corresponding calculation formula based on this theory is therefore given as:

$$F_C = 2 \cdot \sigma_s \cdot h \cdot \Omega(\beta, \phi) \tag{8.2}$$

where σ_s -- is the shear strength of the rock,

h -- cutting depth and,

Ω -- is a function determined by the cutting alignment angles.

Nishimatsu in 1972 derived some estimation formula for rock cutting and normal forces based on the same model assumptions as that of Merchant's theory, but taking into account the compressive and tensile stress induced by the tool's cutting and normal action and using the Mohr's strength criteria. Deliac suggested a cutting model based on mixed mode fracture theory in 1990. In addition, Hardy (1973), Ingraffea (1986) and Saouma (1985) have also used the finite element method to simulate the cutting procedure as well.

However all the existing theories approach the problem by assuming that rock is an ideal solid material, i.e., ignoring the rock inhomogeneities, anisotropy, discontinuities and other random influences. Unfortunately the aspects neglected are just the dominating cases in practical engineering. It is this latter point that suggests the introduction of probabilistic fracture mechanics for rock cutting mechanics as it will take into account all the different rock random characteristics and approach the problem from a statistical point of view.

All large solids can be considered to consist of many different smaller parts, called consistent elements, which can behave in the same or different way according to their mineral content and discontinuity size, orientation and distribution. Obviously the behaviour of the whole solid body will be determined by the characteristics of the individual parts and their interactions. This discrete property can easily be seen in brittle materials, especially rock whose composition varies widely and randomly from part to part. When the observed sample size (or the number of the investigated parts) is large enough, there will be a common rule which the consistent parts will tend to follow from the point of statistics. This statistical rule can then be taken as the basic mechanical characteristic of the whole body. If some assumptions about the interaction between the consistent parts are made, thereafter the mechanical behaviour of the whole solid can then be derived.

§8.2 Local Strength Theory, Strength of Elementary Parts, Parent Distribution

For a certain material, supposed there is a "threshold strength" or "lower bound strength", $\mathbf{S_U}$, below which the material consistent elements will never fail, therefore the probability of failure of one element when subjected to an external force **S** can be defined as:

$$\textit{Probability of Failure} = \begin{cases} P(S) & , S > S_U \\ 0 & , S \le S_U \end{cases} \tag{8.3}$$

Different expressions for **P(S)** can be obtained based on different assumptions. **P(S)** is called the element strength distribution, and is also referred to as the local strength distribution or parent strength distribution.

§8.2.1 Weibull Distribution

Weibull suggests an empirical but widely accepted form for the **P(S)** expression as follows:

$$P(S) = \begin{cases} \left(\dfrac{S - S_U}{S_0'}\right)^m & , S > S_U \\ 0 & , S \le S_U \end{cases} \tag{8.4}$$

where $\mathbf{S_U}$, $\mathbf{S_0'}$ and **m** are material dependent constants.

The form has been successfully applied in the probabilistic fracture research field and is believed to be able to satisfactorily describe the strength distribution of the elementary parts over the whole range.

§8.2.2 Type III Extreme Value Distribution Assumption

When investigating the whole solid strength, we can divide the whole solid into **N** small consistent elements. What is important to us is the possible minimum strength value out of the **N** consistent parts which will dominantly determine the failure of the whole body. This is a typical problem for type III extreme value statistics of random variables, i.e., minimum value statistics. Therefore with regard to the element strength distribution equation, what really matters to contribute to the evaluation of the whole solid strength is the low tail of the distribution function. As a result, it is always possible and reasonable to make some simple mathematical approximation to that low tail part because normally it possess a low value of the

probability of failure no matter what the element's real strength distribution is (which can be seen from the general Equation (8.3) where the **P(S)** value will converge to **0** as the **S** approaches the lower bound value $\mathbf{S_U}$ along the low tail of the element strength distribution function). Two general types of approximations are normally introduced as follows. With these two approximations, the evaluation of the minimum strength value out of the **N** elements can be carried out without knowing the exact element strength distribution beforehand.

a) Cauchy Type (Power Equation) Approximation

Suppose the element strength probability distribution falls down approximately in the power pattern when the force S approaches the lowest strength bound $\mathbf{S_U}$ from the right hand side, then the **P(S)** expression can be drawn:

$$P(S) = \begin{cases} \delta \cdot (S - S_U)^m & , S > S_U \\ 0 & , S \le S_U \end{cases} \tag{8.5}$$

This pattern is referred to as the Cauchy type pattern bounded at $\mathbf{S_U}$. The δ, **m** are material constants.

b) Exponential Type Approximation

When the element strength probability distribution in the lower part falls in the same way as an exponential function, an approximation **P(S)** can then be obtained:

$$P(S) = \delta \cdot \exp(-\upsilon \cdot S) \tag{8.6}$$

Again, δ and υ are material constants. It is important to note that there is no lower bound for this approximation, so that its application is only limited to some special occasions.

§8.2.3 Elementary Strength Distribution Derived from Griffith's Theory

We can always divide any solid body into many elementary parts each containing one crack (micro flaw) only. The critical state of the cracked element is, from fracture mechanics, when the stress **S** and the crack length **a** satisfy the following equation:

$$S\sqrt{a} = K_C \tag{8.7}$$

where $\mathbf{K_C}$ is the material fracture toughness. Therefore the probability of failure can be expressed as Equation (8.8), where **Fe(x)** is an artificially specified probability function which describe the probability of finding a crack with the length less than **x** in any arbitrary element. It is presented by Frechet in 1927 [45] in Equation (8.9). Here the δ and ν are material constants.

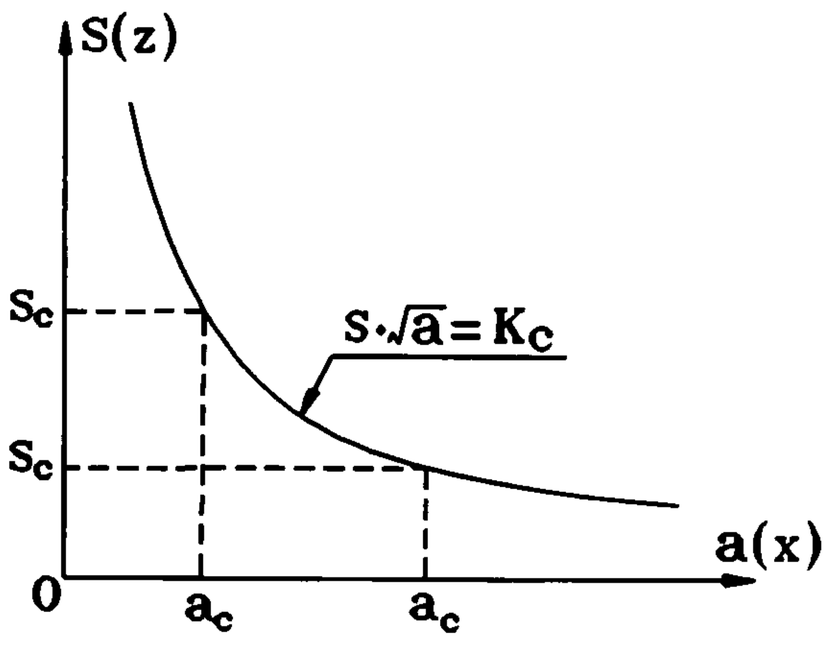

Figure 6.1 Critical State

Submit the equation of **Fe(x)** in Equation (8.8) and make the substitution of

$$P(S) = P\{z \le S\} = P\{x \ge a\} = P\{x \ge \frac{K_C^2}{S^2}\} = 1 - Fe(\frac{K_C^2}{S^2}) \tag{8.8}$$

$$Fe(x) = \exp[-(\frac{x}{\delta})^{-\nu}] \tag{8.9}$$

$\varkappa = \mathbf{K_C}/\sqrt{\delta}$, we can then reach the following distribution:

$$P(S) = 1 - \exp[-(\frac{K_C^2}{S^2 \cdot \delta})^{-\nu}] = 1 - \exp[-(\frac{S}{\kappa})^{2\nu}] \tag{8.10}$$

Here note should be taken that there is no particular fracture mode restriction on the above derivation. But the application conditions for Equation (8.10) should follow the assumptions given below:

1) The flaws of varying severity distribute throughout the whole body,

2) The whole body is divided into elements in such a way that every element contain one flaw only, and there is no interactions between the flaws so the strength of every element can be evaluated independently,

3) the strength of the element is determined by the flaw only according to Griffith's theory of crack instability.

§8.3 Evaluation of the Strength of the Whole Solid Body

In probabilistic strength theory, the interactions between the consistent parts of a solid are always simulated by two different models, weakest link (series link) model and bundle link

(parallel link) model.

§8.3.1 Weakest Link Model

It was first proposed by Weibull in 1923 as an universal engineering mathematical model, and later widely developed by many of the following researchers [45,61,110]. It is founded on the following assumptions:

1) The whole body Ω is isotropic and statistically homogeneous, i.e., the probability of finding a flaw of a given severity within an arbitrary small volume in the body is the same throughout the whole body.

2) The whole Body Ω is divided into N elementary parts V_i (i = 1,2,3,...,N). The local strength distribution of each element V_i is supposed to be identical according to assumption 1), and the failure of each element is an independent random event.

3) All the N elements are connected using the series chain link model to mechanically compose the whole body. Therefore the failure of the whole body will be defined as when any one of the N links (or elements) fails.

Based on these assumptions, the solution for the body strength problem will be mathematically to find the minimum strength value out of the samples of size N.

Suppose S is the smallest out of S_i (i = 1,2,...,N), then,

$$P(S) = P\{S' \le S\} = 1 - P\{S' > S\} \tag{8.11}$$

and from the theory of probability,

$$P\{S' > S\} = P\{(S_1 > S) \cap (S_2 > S) \cap \cdots\cdots \cap (S_N > S)\} \tag{8.12}$$

As the events are mutually independent and possess an identical parent distribution, i.e., $P_1(S) = P_2(S) = \cdots\cdots = P_N(S)$,

$$\begin{aligned} P\{S' > S\} &= P\{S_1 > S\} \cdot P\{S_2 > S\} \cdots P\{S_N > S\} \\ &= 1 - [1 - P_1(S)] \cdot [1 - P_2(S)] \cdots [1 - P_N(S)] \end{aligned} \tag{8.13}$$

and,

$$P(S) = P\{S' > S\} = 1 - [1 - P_i(S)]^N \tag{8.14}$$

Therefore when the sample size **N**, hence the considered body volume **V**, is large enough, the asymptotic form of **P(S)** can be written as:

$$\lim_{N\to\infty} P(S) = 1 - \lim_{N\to\infty} [\,1 - P_i(S)\,]^N = 1 - \exp[\,-N \cdot P_i(S)\,] \tag{8.15}$$

which is under the assumption that $\mathbf{N} \cdot \mathbf{P_i(S)}$ is small enough compared with **N**.

If we substitute the Weibull function as the parent distribution $\mathbf{P_i(S)}$, the final form of the **P(S)** equation will be:

$$P(S) = 1 - \exp[\,-(\frac{S - S_U}{S_0})^m\,] \tag{8.16}$$

where the substitution has been made that $\mathbf{S_0 = S_0'/N^{1/m}}$.

If we substitute the Cauchy type approximation as the parent distribution, the identical form of the probability equation to Equation (8.16) will be obtained. If the element strength distribution derived from Griffith's fracture theory is used as the parent distribution instead, the evaluation equation for the whole body strength probability distribution will be:

$$P(S) = 1 - \exp\{-N[\,1 - \exp(-(\frac{S}{\kappa})^{2\nu})\,]\} \tag{8.17}$$

Freudenthal [45] simplified the above equation by linear transformation and gave the expression in the following simpler form:

$$P(S) = 1 - \exp[\,-(\frac{S}{\omega})^{2\nu}\,] \tag{8.18}$$

where some constant substitution between $\varkappa$ and ω has been made. Again this is another form of Weibull's distribution.

Therefore we can conclude that as long as the weakest link model applies, the body strength distribution will all come out to be in the same form as Equation (8.16) no matter what the parent distribution is.

§8.3.2 Bundle Link Model

This theory was first introduced by Daniels in 1930 when he was investigating the strength of materials consisting of threads. Four basic assumptions are suggested:

1) and 2) The same as assumptions 1) and 2) in the weakest link model.

3) All the **N** elements are connected as a parallel model to mechanically compose the whole body, i.e., all the elements will "work" directly to the external force independently instead of

via the other elements. When one element (link) fractures and fails, a redistribution of load to the remaining ones will occur and the whole body may survive. Henceforth the whole body failure will be defined as when all the elements (links) have fractured and failed.

4) All the elements have the same priority (or responsibility) to take the external load, i.e., when the external load acting on the body will be statistically uniformly distributed over the surviving elements.

Suppose the body is subjected to an external force **S**, then by the above assumptions, failure of the whole body will follow procedures set out below, where $\mathbf{S_i}$ is denoted as the local strength of the **i**-th element,

$$\begin{cases} 0 \le S_N \le \dfrac{S}{N} \\ S_N \le S_{N-1} \le \dfrac{S}{N-1} \\ \vdots \\ S_3 \le S_2 \le \dfrac{S}{2} \\ S_2 \le S_1 \le S \end{cases} \tag{8.19}$$

The reason for using the inequality forms here instead of equality conditions is that during the **i**-th element's fracture step, any external force value between $\mathbf{S_{i-1}}$ and $\mathbf{S_{i+1}}$, from the point of statistics, can possibly cause the element to fracture, and each corresponding to a probability value of failure.

Writing Equation (8.19) in the mathematical form, we can reach the following equation:

$$P(S) = P\{(0 \le S_N \le \frac{S}{N}) \cap (S_N \le S_{N-1} \le \frac{S}{N-1}) \cap \cdots \cap (S_2 \le S_1 \le S)\} \tag{8.20}$$

Substitute the independent condition and the identical parent distribution condition, we have:

$$P(S) = N! \cdot \int_0^{\frac{S}{N}} P_i(S_N) \cdot dS_N \cdot \int_{S_N}^{\frac{S}{N-1}} P_i(S_{N-1}) \cdot dS_{N-1} \cdots \int_{S_2} P_i(S_1) \cdot dS_1 \tag{8.21}$$

where the introduction of **N!** accounts for all the possible orderings of link breakage.

Tracy (1982) use the Weibull function as the parent distribution $\mathbf{P_i(S)}$ and conducted the numerical solution of the body strength distribution for different sample size **N**. The conclusion has been drawn that the body strength will tend to follow the normal distribution when the sample size is large enough ($\mathbf{N > 14}$).

Daniels (1930) simulated the fracture procedure and concluded that for those parent distributions following the law:

the resulting body strength distribution will be normal. Interestingly, the parent distribution

Daniels (1930) simulated the fracture procedure and concluded that for those parent distributions following the law:

$$\lim_{S \to \infty} S \cdot [\, 1 - P(S) \,] = 0 \tag{8.22}$$

the resulting body strength distribution will be normal. Interestingly, the parent distribution function discussed in probabilistic fracture mechanics all satisfy this criteria. Therefore if the bundle link theory applies, the normal (Gaussion) strength probability distribution will be the result.

§8.4 Force Distribution Model for Rock Cutting

Practical cutting problems include different rock fragmentation mechanism which makes it unreasonable to use a single model based on a particular mechanism to describe the whole cutting procedure. However if we approach the problem from the point of statistics based on probabilistic fracture mechanics, we can then view all the results as a combination of all the different cutting mechanisms. Henceforth the cutting performance will be better predicted.

A typical section of cutting force and normal force recorded signals is shown in Figure 8.1. Each peak value (local maximum) corresponds to one chipping event, which represents one rock breakout during the cut. These small chips will be referred to as minor chipping (**MI**) and they are marked as "**x**" in Figure 8.2. Major chipping (**MA**) (marked as boxes "□" and circles "○" in the figure) means the forming of a relatively larger chip, which normally will comprise several minor chipping points. Major chipping length **L** will be the distance the tool moves from the start to the end of the major chipping cycle.

When analysing a particular cut, the rock breakage strength can be denoted by rock cutting strength (notified as **CS**) and rock indentation strength (notified as **IS**), which are the cutting force and normal force magnitudes correspondingly at the points of chipping. Obviously the strength values **CS** and **IS** can be seen as random variables which will be determined by some other random variables at the chipping points, such as the mineral content, micro-structure and tool cutting state. It can be assumed that when the observed sample size **N** is large enough, the strength values will follow some kind of probabilistic distribution.

The defined **CS** value will be contributed to from two main sources. The first is the cutting force needed just to fracture the rock immediately in front of the cutting tool to form the chips. We can denote this part of the cutting strength **CS** as rock cutting fracture strength, or **FS** for short. The other component of **CS** is the force in the cutting direction

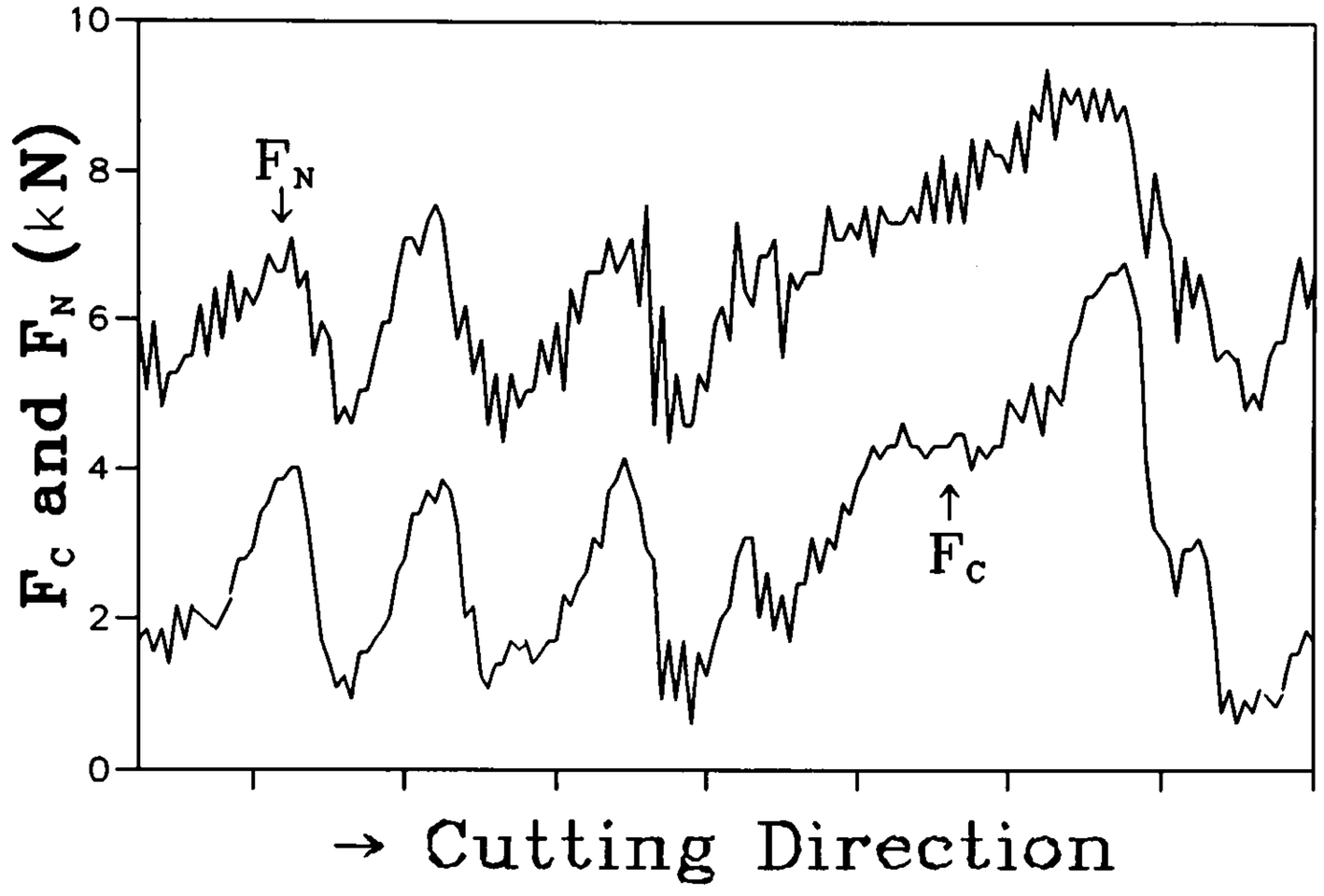

Figure 8.2 Cutting and Normal Forces

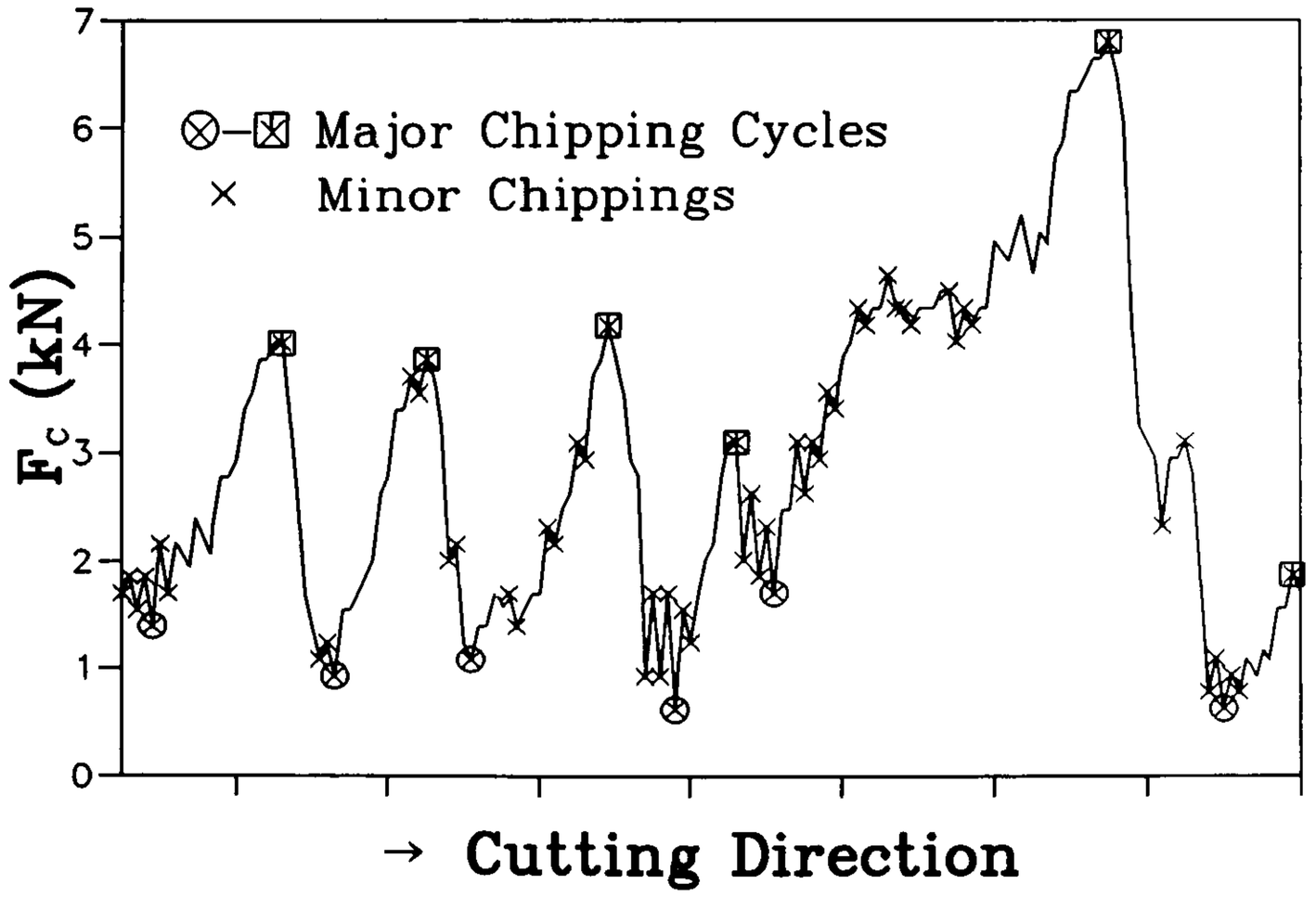

Figure 8.3 Signal Analysis

caused by the friction between tool and rock surface as the tool moves across the rock, which is obviously in proportion to the rock cutting normal force components and the friction coefficient between the tool and the rock surface.

Obviously there will be two different fracture strength **FS** values. When investigating the minor chipping, it is minor chipping fracture strength or **FSMI** for short, and when analysing the major chipping, we can find one maximum **FSMI** during every major chipping cycle and this value will be called the rock major chipping fracture strength or **FSMA** for short.

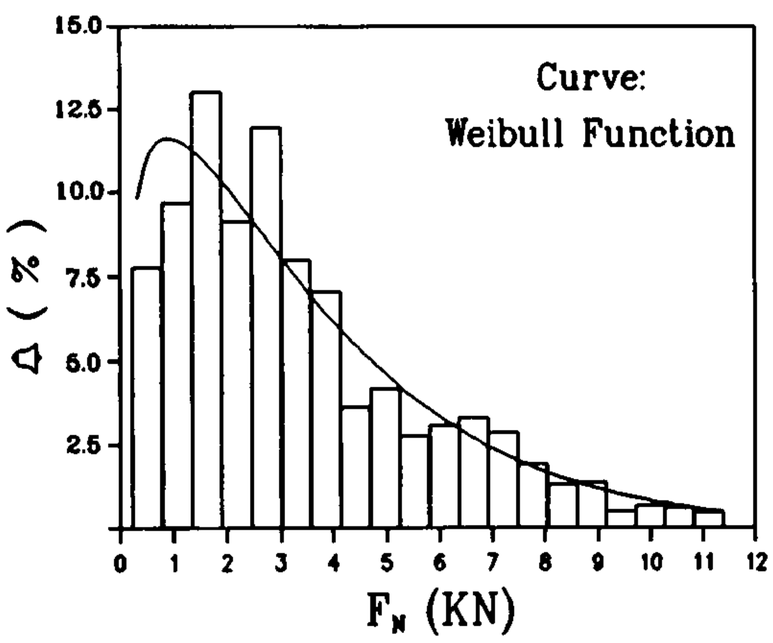

a.

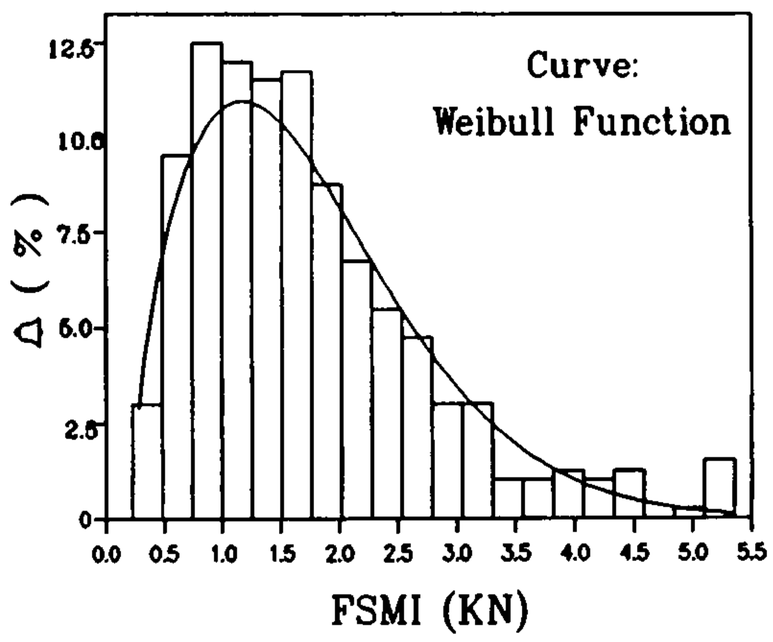

b.

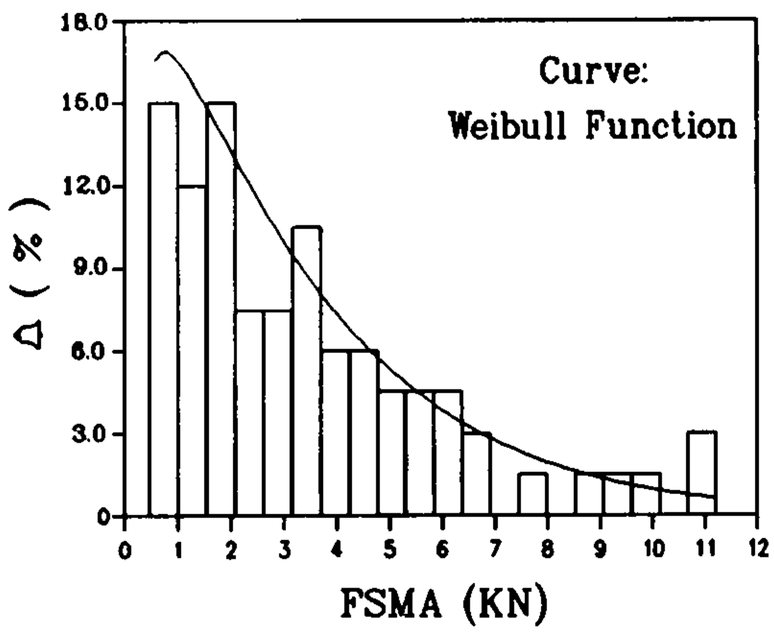

c.

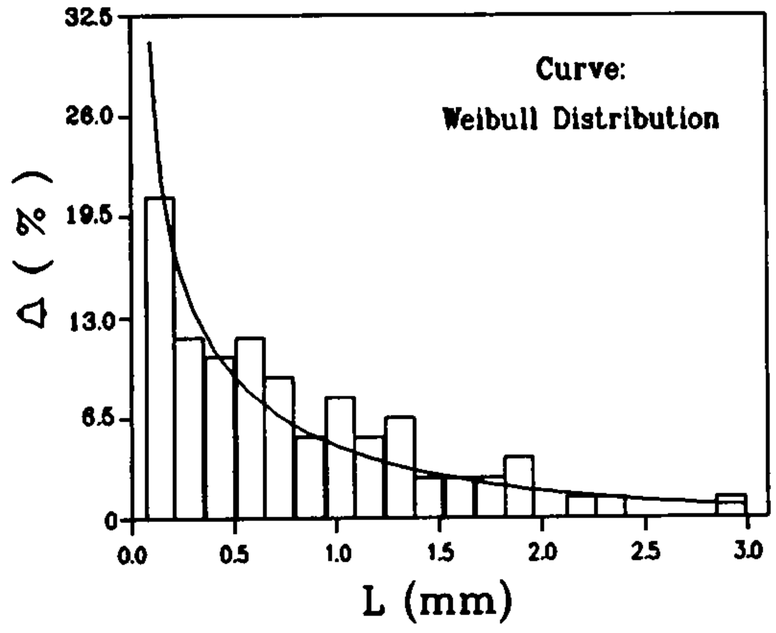

d.

Figure 8.4 Some Typical Distributions of Rock Indentation Strength **IS** (a.), Minor Chipping Fracture Strength **FSMI** (b.), Major Chipping Fracture Strength **FSMA** (c.) and Major Chipping Length **L** (d.)

Nine different rock samples varying from sandstones to granites were chosen to conduct the

instrumented rock cutting test. At least four cuts were made for each rock sample. For every cut, the **IS**, **FSMI**, **FSMA** and the major chipping length **L** were sampled and analyzed along the whole cutting length. Figure 8.4 illustrate some selected typical histograms of their values, where the percentage corresponding to a certain strength value range means the portion of the number of times when the sampled strength values fell in that range out of the total number of the sample.

As clearly shown in Figure 8.4, the strength values and the chip length distribution are skewed to the left. This signifies that during cutting, the chips with smaller breakage strength and smaller chip length will form a higher proportion of all the chips. This result coincides with the practical observation that small chips always dominate in the size distribution of the cut debris. The solid curves shown in Figure 8.4 are the corresponding analogous Weibull distribution curves for the strength values and the chip length. Quite encouragingly, all the investigated values can be satisfactorily expressed by this distribution function.

Based on these distribution illustrations, we can no longer hold the opinion that the variations of the rock cutting and normal forces (or rock cutting strength **CS** and indentation strength **IS**) follow the normal (Gaussion) probabilistic distribution, as is commonly believed. But the Weibull distribution to describe the variations of their values is to be assumed instead. According to the analysis in section §8.3, it is then suggested that rock breaking in rock cutting will follow the weakest link theory.

The coinciding point is that in rock fragmentation, there are always many possible fracturing routes when the rock is subjected to an external load (such as being acted on by the cutting tool bit), as illustrated in Figure 8.5. The actual breaking trace (corresponding to the actual breakage strength) is always the route which requires the lowest energy consumption, in other words, which is the easiest (or weakest) breakage route compared with the others. Certainly this particular route will change from point to point according to the different mineral content, micro structures, external loading conditions and the rock residual (damage) strength owing to the previous loading or breakage history. This causes the random characteristics of the breakage strength.

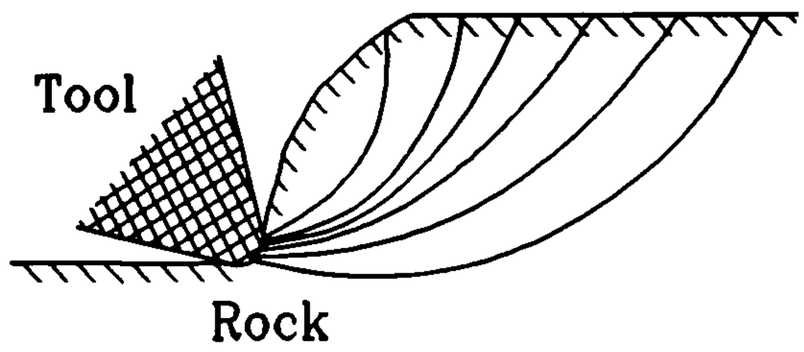

Fig.8.5 Possible Breaking Routes

In practical rock cutting, the studied rock boundary condition is normally supposed to be "infinite". Therefore in the following analysis an identical investigated rock volume will be automatically assumed. That will eliminate the volume influences which are signified as the

value of N in the original Weibull distribution.

Three distribution parameters $\mathbf{S_U}$, $\mathbf{S_O}$ and **m** should be determined in order to use the Weibull's model to express rock cutting performance. The linear goodness of fit estimation method is normally used because of its preferable simplicity over the maximum likelihood method and the other methods. If we rewrite the Weibull function in the following form:

$$1 - P(S) = \exp[-(\frac{S - S_U}{S_O})^m] \tag{8.23}$$

then double log both sides of the equation we finally reach:

$$\log\{-\log[1 - P(S)]\} = -m\cdot\log S_O + m\cdot\log(S - S_U) \tag{8.24}$$

Therefore the relation between $\mathbf{\log\{-\log[1-P(S)]\}}$ and $\mathbf{\log(S-S_U)}$ will be linear as $\mathbf{Y = a + bX}$, and the distribution parameters can then be expressed as $\mathbf{m = b}$ and $\mathbf{S_O = \exp(-a/m)}$. Therefore by fitting in the observed data $\mathbf{S_j}$, $\mathbf{P(S_j)}$ (j = 1,2,3,...,J), the distribution parameters can be calculated.

The calculation of $\mathbf{P(S_j)}$ is normally by the technique of order statistics. Rearrange the **J** sampled values (strength or chip length) in order from the smallest value $\mathbf{S_1}$ to the maximum value $\mathbf{S_J}$ as:

$$S_1 < S_2 < \cdots < S_J \tag{8.25}$$

Then from order statistics, the preferred estimate of $\mathbf{P(S_j)}$ will be:

$$P(S_j) = \frac{j}{J+1} \tag{8.26}$$

Which is considered to be an unbiased statistical estimator.

The estimations of the distribution parameters from all the cuts on the nine rock samples has been conducted and the results are listed in Table 8.2. Table 8.1 lists the related mechanical properties of the samples used for the test, where **E** is the Young's modulus in GPa, σ_c and σ_t are the compressive and tensile strength in MPa, $\mathbf{K_{IC}}$ is the Mode I fracture toughness value in MPa$\sqrt{\text{m}}$, $\mathbf{F_C}$ and $\mathbf{F_N}$ are the average cutting force and normal force in kN, and **SE** is the specific energy in MJ/m^3 obtained from the instrumented cutting test.

Of the three distribution parameters, $\mathbf{S_O}$ is more important as its value determines the magnitude of the distribution and signifies the practical strength value or major chip length.

Table 8.1 Rock Samples and Their Mechanical Properties

Sample	E	σ_c	σ_t	K_{IC}	F_C	F_N	SE
1	10.60	50.93	3.48	0.657	1.81	2.30	10.56
2	15.55	73.23	3.36	0.610	2.22	3.23	16.23
3	11.12	47.61	4.03	0.720	1.39	2.13	10.60
4	13.75	48.48	3.46	0.635	1.81	2.25	10.98
5	12.11	102.64	7.40	0.95	2.66	3.27	13.68
6	7.79	17.53	2.02	0.344	1.06	1.20	8.14
7	22.85	104.31	8.01	1.237	3.43	5.66	27.70
8	56.70	295.55	20.86	2.803	5.55	21.25	53.56
9	40.27	191.71	13.56	2.119	4.40	9.47	28.88

Table 8.2 Indentation Strength and Fracture Strength Distribution Parameters

No.	IS			FSMI			FSMA		
	S_U^C	S_0^C	m^C	S_U^I	S_0^I	m^I	S_U^A	S_0^A	m^A
1		2.454	1.418		1.475	1.395		1.709	1.193
2		3.969	1.327		2.063	1.591		2.456	1.247
3		2.330	1.302		1.250	1.353		1.489	1.200
4		2.465	1.228		1.468	1.416		1.907	1.056
5	0.222	3.553	1.185	0.163	2.450	1.118	0.404	2.912	0.964
6		1.242	1.147		0.901	1.799		0.895	1.401
7		6.439	1.395		3.428	1.063		4.112	1.051
8		25.66	1.442		7.521	1.295		9.200	1.168
9		11.13	1.366		4.947	1.191		5.950	1.120

The m value will change the shape of the distribution and physically it means the scatter of the strength or in terms of rock mechanics, the brittleness of rock materials [Jayatilaka, 1979]. On knowing these distribution parameters, the rock cutting characteristics can be clearly understood. Therefore these parameters can be taken as rock property constants describing rock cuttability.

§8.5 Rock Cutting Performance Prediction from the Point of Probabilistic Statistics

One useful analysis is relating the above distribution parameters with conventional rock properties based on rock fragmentation (fracture) mechanisms so that rock cutting characteristics can be predicted. Of the two force components needed for cutting, normal force is the force required to crush the rock and to keep the tool at the required depth of cut. Its value is mainly decided by the rock compressive strength, cutting depth and tool wear flat (determining the crushing area underneath the tool). If the cutting depth is fixed and the sharp tool state is assumed (which is generally the case when doing rock cuttability assessment), the $\mathbf{S_0}$ for rock indentation strength $\mathbf{S_0^C}$ could be related to rock compressive strength in a simple form. On the other hand, the rock fracture strength will be mainly influenced by rock fracture properties and therefore the rock fracture toughness $\mathbf{K_C}$ value can be taken as the vital variable to determine the $\mathbf{S_0}$ value for minor and major chipping fracture strength **FSMI** and **FSMA**, $\mathbf{S_0^I}$ and $\mathbf{S_0^A}$. If it is assumed that rock fracturing in rock cutting is mainly a tensile (**Mode I**) fracture problem, then the **Mode I** rock fracture toughness $\mathbf{K_{IC}}$ can be used to determine the above mentioned relations. If mixed mode fracturing is suggested to be the main case in rock cutting, then the rock's mixed mode fracture strength $\mathbf{K_C^m}$ should be used instead. In fact, mixed mode fracturing is the dominant situation in rock cutting. However at this stage, we are short of data for rock mixed mode fracture strength values and therefore the $\mathbf{K_{IC}}$ values for rock materials was be used for the current investigation.

Figure 8.6 a. - c. show the relationships of $\mathbf{S_0^C}$, $\mathbf{S_0^I}$ and $\mathbf{S_0^A}$ values with σ_c and $\mathbf{K_{IC}}$. The best fit regressions for these relationships have been conducted. Therefore if we take these results as the basis, the cutting performance can be predicted step by step by following the procedure listed in Table 8.3. Some points about the derivation of the procedure listed in the table are discussed as follows.

1) For a random variable following the Weibull distribution, its expected value (or mean

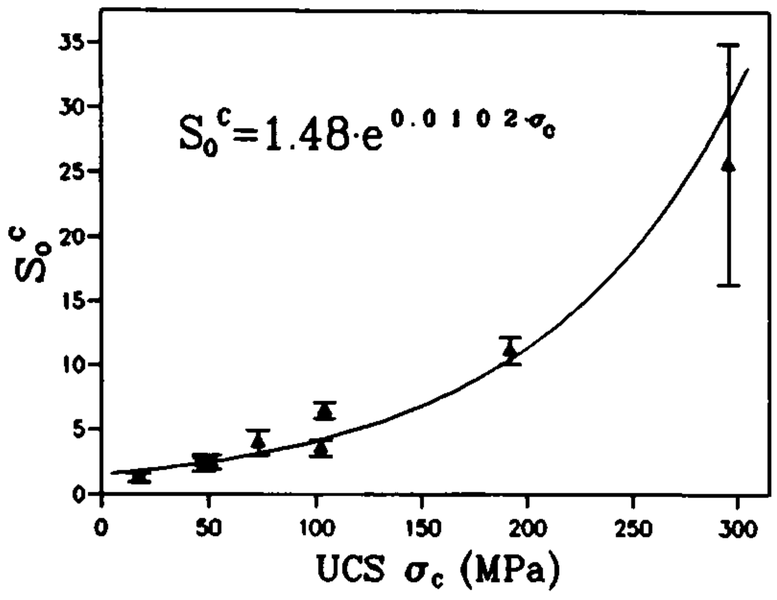

a.

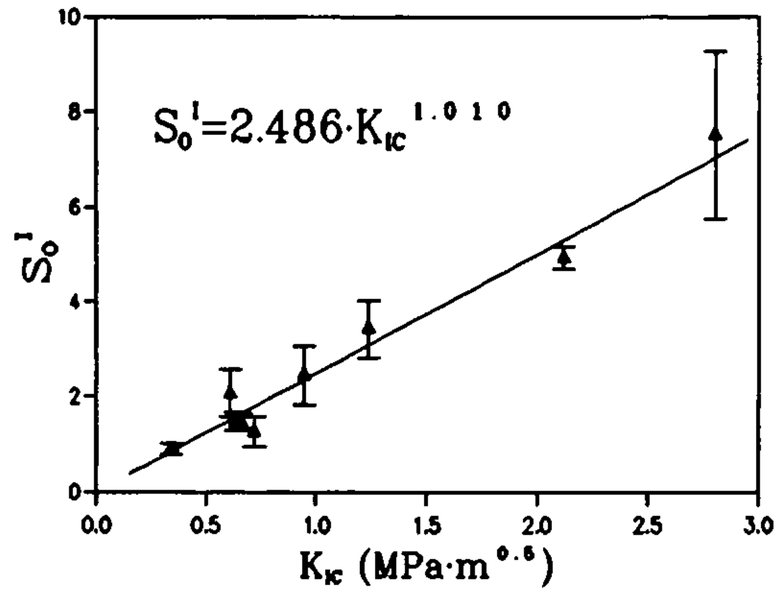

b.

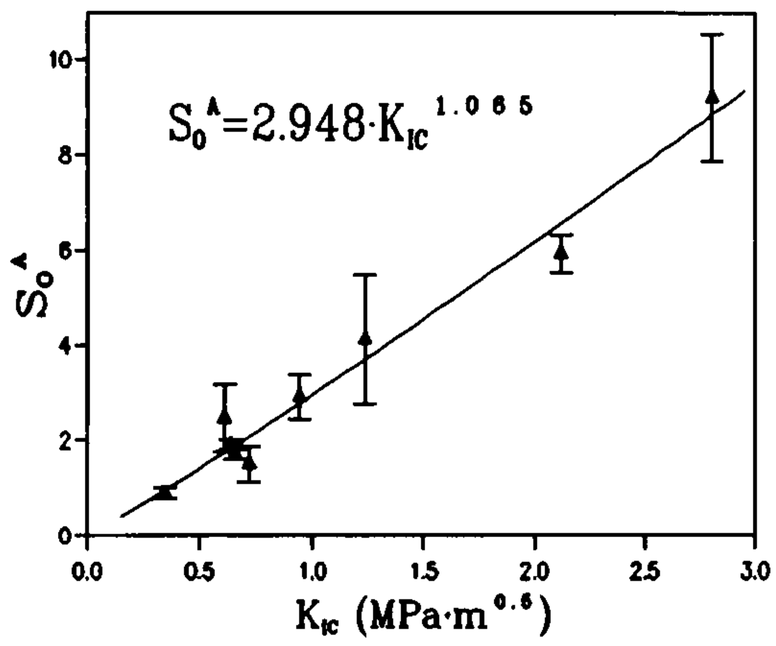

c.

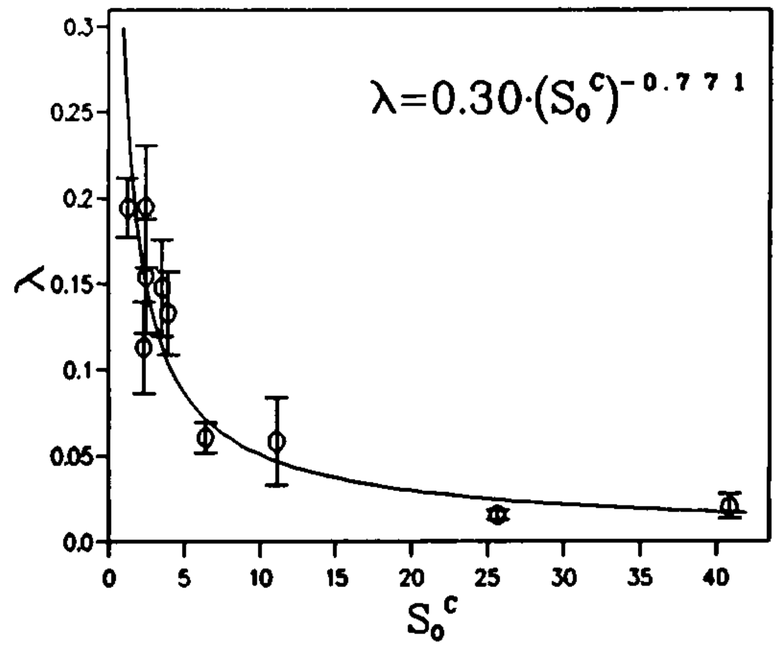

d.

Figure 8.6 Relationships between S_0^C, S_0^I and S_0^A with σ_c and K_{IC} (a, b and c), Relationship between Friction Coefficient λ and S_0^C (d.)

value) is obtained in the following way:

$$E[S] = \bar{S} = \int_0^1 S \cdot dP(S) = \int_0^\infty [1 - P(S)] \cdot dS \tag{8.27}$$

Substitute the **P(S)** equation and the integration will yields:

$$\bar{S} = S_U + S_O \cdot \Gamma\left(1 + \frac{1}{m}\right) \tag{8.28}$$

Table 8.3 Rock Cutting Performance Prediction

No.	Descriptions	Formulas
1	S_0 of IS	$S_0^C = 1.48 \cdot \exp(0.0102 \cdot \sigma_C)$
2	Mean IS, or Normal Force	$F_N = 0.222 + 0.913 \cdot S_0^C$
3	Friction Coefficient	$U = 0.30 \cdot (S_0^C)^{-0.771}$
4	S_0 of FSMI	$S_0^I = 2.486 \cdot K_{IC}^{1.010}$
5	Mean FSMI	$F_{CM} = 0.915 \cdot S_0^I$
6	Proportional Coeff.	$\wp = 1.024 + 0.027 \cdot S_0^I$
7	Mean Peak Cutting Force	$F_{CMAX} = F_{CM} + U \cdot F_N$
8	Mean Cutting Force	$\overline{F_C} = F_{CMAX} / \wp$
9	S_0 of FSMA	$S_0^A = 2.948 \cdot K_{IC}^{1.065}$
10	Major Chipping Length	$\overline{L} = 1.12 \cdot (S_0^A)^{-0.34}$
11	Specific energy	$SE = 3.667 + 4.172 \cdot (\frac{\overline{F_C}}{\overline{L}})$

where $\Gamma(1+1/m)$ is the Gamma function, whose value can be found in a mathematical handbooks.

The value calculated by Equation (8.28) theoretically equals the mean of the investigated strength. If the distribution parameters of **IS**, **FSMI** or **FSMA** are substituted, their mean values will be obtained. The variance of these values can be estimated by the following equation:

$$Var[S] = S_O \cdot \sqrt{\Gamma(1+\frac{2}{m}) - \Gamma^2(1+\frac{1}{m})} \qquad (8.29)$$

2) Based on our experimental results the friction coefficient λ shows a clear variation tendency with respect to the S_O^C, as illustrated in Figure 8.6 d. In the case discussed here, this coefficient is defined as the ratio of the friction force between the tool and the rock cutting surface in the cutting direction over the total tool normal force.

3) The mean major chip length **L** has a power relationship with S_0^A, which is shown in Figure 8.7 a.

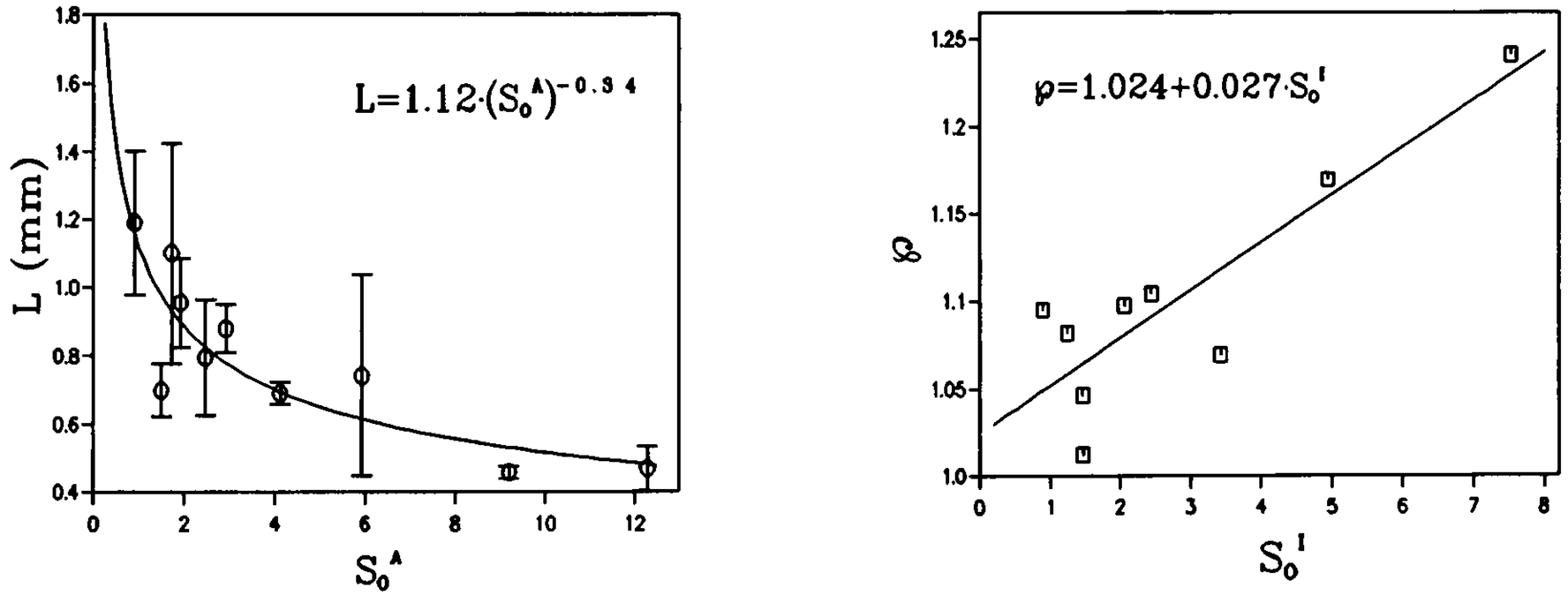

a. b.

Figure 8.7 Values of L and Φ (a. and b.)

4) As has been discussed above, the mean peak cutting force (minor chipping) will be the superimposition of the mean minor chipping fracture strength (mean of **FSMI)** and the friction force caused by the action of normal force, which is shown in Table 8.3 as formula 7.

5) For the mean cutting force evaluation, another proportional coefficient should be introduced which is the ratio of mean peak cutting force (minor chipping) over the mean cutting force. This proportional coefficient Φ can be determined from the distribution parameter S_0^I. Figure 8.7 b. shows their relation.

6) The specific energy will be in proportion to the magnitude of the cutting force. The other determining variable will be the chip (debris) volume which is certainly in proportion to the mean major chip length. It is reasonable to suggest that specific energy is a function of the quotient of mean cutting force divided by the mean major chip length, i.e.,

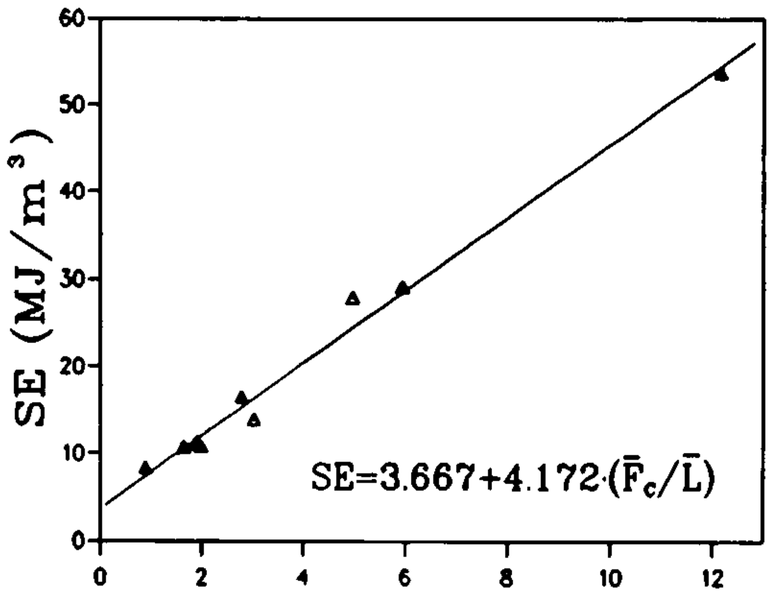

Figure 8.8 SE and F_C/L

$$SE = \Psi\left(\frac{\overline{F_C}}{\overline{L}}\right) \tag{8.30}$$

The current experimental results, which are shown in Figure 8.8, clearly shows a linear relationship for this relation.

6) Due to the limited rock samples tested, the variation of the Weibull distribution parameter **m** value does not show any clear relationship with any conventional rock property. Therefore at this stage its mean value has to be accepted while the model is used to evaluate the cutting performance. Further investigation of the relationship of **m** to rock brittleness properties should be conducted.

§8.6 Application 1 -- Cutting and Normal Force Prediction

Nevertheless, we used the above procedure to predict some cutting parameters. From equation 2 and equation 8 in Table 8.3 the mean normal force and mean cutting force for a rock can be obtained directly. Their values have been calculated for the rock samples used in our experiment and Figure 8.9 shows the predicted relations of normal force with rock compressive strength and the cutting force with rock fracture toughness. As discussed above, the cutting performance parameters are connected to these two conventional rock properties in a complicated way, so we cannot expect to predict the force value knowing only one single property value. The force values should be always viewed as the effect of their combination.

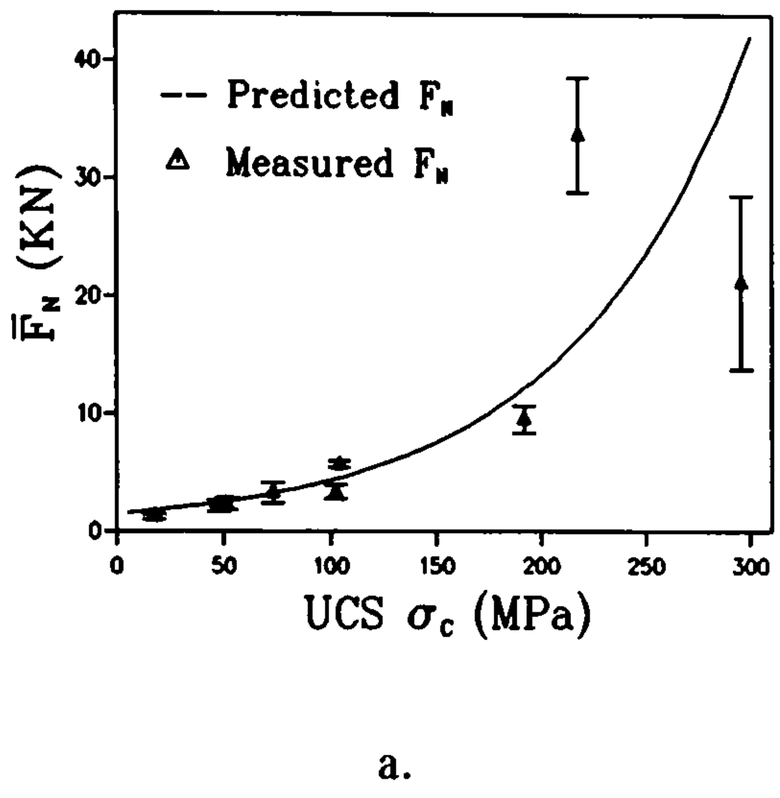

Figure 8.9 Predicted Cutting and Normal Forces

§8.7 Application 2 -- Specific Energy Prediction

Further, we used the above procedure to predict specific energy values from published data [36]. Figure 8.10 shows that the predicted and the measured values are within ±10%. Figure 8.11 shows the predicted and the measured **SE** values varying with two conventional rock properties, compressive strength σ_c and fracture toughness K_{IC}. The data are from the same source as used in Figure 8.10, but some fracture toughness values are estimated from the available Young's modulus value **E**, tensile strength σ_t and compressive strength σ_c of the rock materials according to their relationships discussed in Chapter 5. The results shown in these figures suggest that the above prediction expresses well the intrinsic relations between rock properties and cutting performance parameters. Further investigations are recommended.

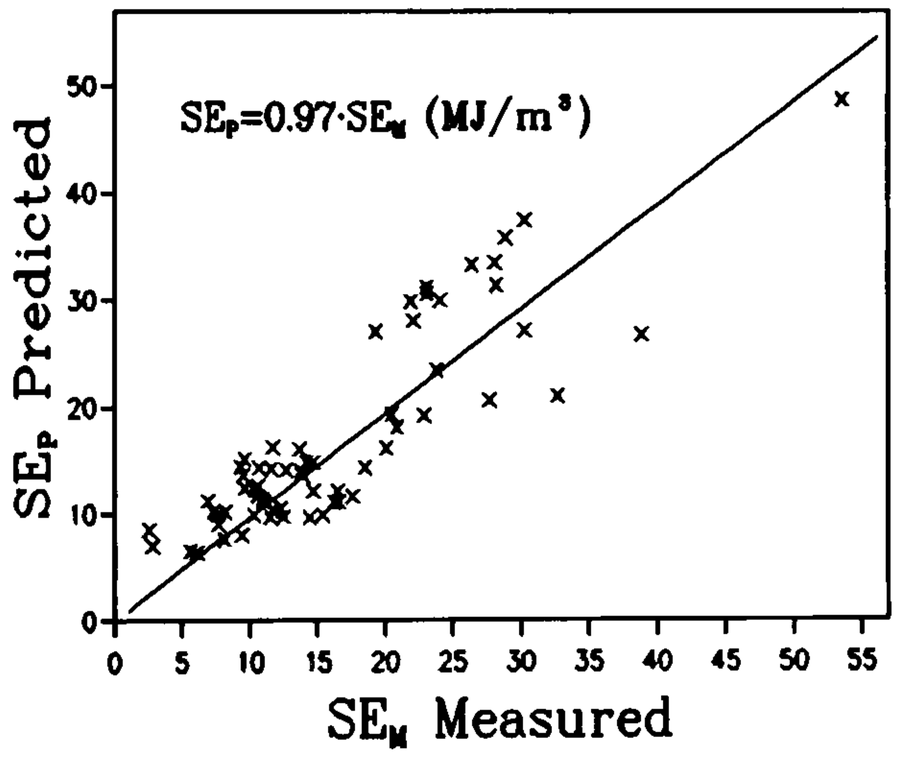

Figure 8.10 SE_P and SE_M

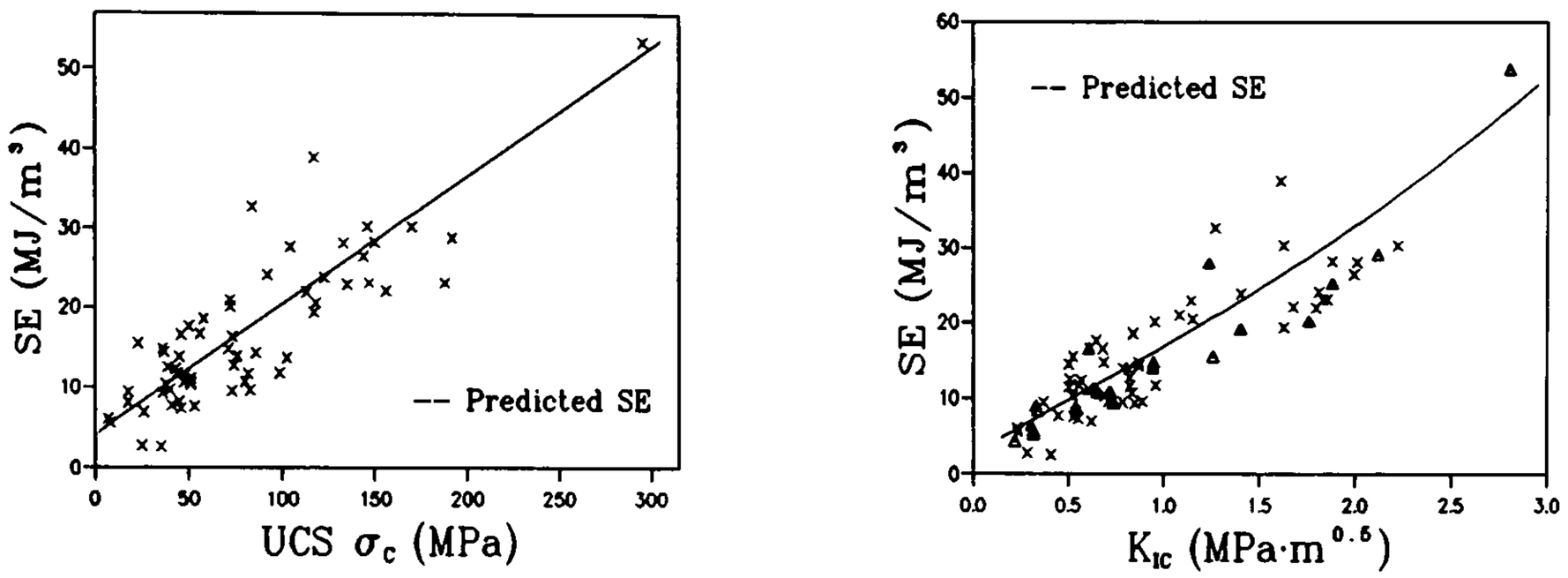

a. b.

Figure 8.11. Predicted SE Values vs σ_c and K_{IC}

§8.8 Some Prospects for the further Applications of the Predictions

The above predictions based on the probabilistic fracture mechanics were especially developed for the rock instrumented cutting test which is widely used for the rock cuttability assessment. However the basic ideas and the whole methodology are generally applicable for different cutting tools. Based on this method, the statistics from a large number of experiments on a wide range of rocks will certainly yield the suitable coefficients and constants which can then be used for further rock cutting performance predictions for that particular cutting tool.

Furthermore, while investigating the combined effects of cutting tools, such as studying the whole cutting head with tools, the statistics of function variables could be used. Some common and useful relations are given below, which allows the prediction of cutting head performance from one instrumented cutting test.

In the following equations, $\mathbf{X}_1$, $\mathbf{X}_2$,..., $\mathbf{X}_n$, $\mathbf{X}$ and $\mathbf{Y}$ are random variables. $\mathbf{Z}$ is the function and $\mathbf{E[Z]}$ and $\mathbf{V[Z]}$ are the corresponding expected (or mean) value and the square of the standard deviation.

1) $Z = aX$,

$$\begin{cases} E[Z] = a \cdot E[X] \\ V[Z] = a^2 \cdot V[X] \end{cases} \tag{8.31}$$

2) $Z = X \pm Y$,

$$\begin{cases} E[Z] = E[X] \pm E[Y] \\ V[Z] = V[X] + V[Y] \pm 2\cdot\rho\sqrt{V[X]\cdot V[Y]} \end{cases} \tag{8.32}$$

3) $Z = XY$,

$$\begin{cases} E[Z] = E[X]\cdot E[Y] + \rho\cdot\sqrt{V[X]\cdot V[Y]} \\ V[Z] = E[X]^2\cdot V[Y] + E[Y]^2\cdot V[X] + 2\cdot\rho\cdot E[X]\cdot E[Y]\sqrt{V[X]\cdot V[Y]} + (1+\rho^2)\cdot V[X]\cdot V[Y] \end{cases} \tag{8.33}$$

4) $Z = Y/X$,

$$\begin{cases} E[Z] = \dfrac{E[Y]}{E[X]}\cdot\left(1 + \dfrac{V[X]}{E[X]^2}\right) \\ V[Z] = \dfrac{E[Y]^2}{E[X]^2}\cdot\left(\dfrac{V[X]}{E[X]^2} + \dfrac{V[Y]}{E[Y]^2} - 2\cdot\rho\cdot\dfrac{\sqrt{V[X]\cdot V[Y]}}{E[X]\cdot E[Y]}\right) \end{cases} \tag{8.34}$$

5) and finally, for a general function, $Z = f(X_1, X_2, \ldots, X_n)$,

$$\begin{cases} E[Z] = f\left(E[X_1], E[X_2], \cdots, E[X_n]\right) + \dfrac{1}{2}\cdot\sum_{i-1}^{n}\dfrac{\partial^2 Z}{\partial X_i^2}\cdot V[X_i] \\ V[Z] = \left(\sum_{i-1}^{n}\left(\dfrac{\partial Z}{\partial X_i}\right)^2\cdot V[X_i]\right)^{\frac{1}{2}} \end{cases} \tag{8.35}$$

Further applications for cutting heads are being carried out. Take the TBM cutting head for instance. It is worth pointing out that when the whole cutting head is considered, the rigidity of the machine should be taken into consideration. Owing to the fact that the rock cutting face is normally very rough because of the brittle fracture properties of rock materials, not every tool on the cutting head is cutting the rock at the same time and no tools are cutting the rock all the time. The number of tools which are cutting the rock out of the whole tool set and the cutting time out of the whole operational time for every single tool can be viewed as a random process. Their distribution parameters can be determined by statistics as well.

Suppose the rock type and the cutting geometries are fixed, the forces needed for the cutting can then be viewed as a function of the cutting depth only, i.e., $\mathbf{F} = \mathcal{L}(\mathbf{h})$ ($\mathbf{F} = \mathbf{F_C}$ or $\mathbf{F_N}$). On the other hand, the rock breakage volume per unit cutting length $\mathbf{Vu}$ is a function of the cutting depth and the cutting breakout angle, or in mathematical form, $\mathbf{Vu} = \mathcal{F}(\mathbf{h}, \boldsymbol{\phi})$ (Figure 8.12). Therefore the specific energy for rock cutting should be in the following form:

$$SE = \frac{F_C}{Vu} = \frac{\mathcal{L}(h)}{\mathcal{F}(h,\phi)} \tag{8.36}$$

The commonly accepted form for **Vu** is based on the assumption that both sides of the cutting slot are up side down triangles (Figure 8.12), and it is expressed as:

$$\mathcal{F}(h,\phi) = b \cdot h + h^2 \tan\phi \tag{8.37}$$

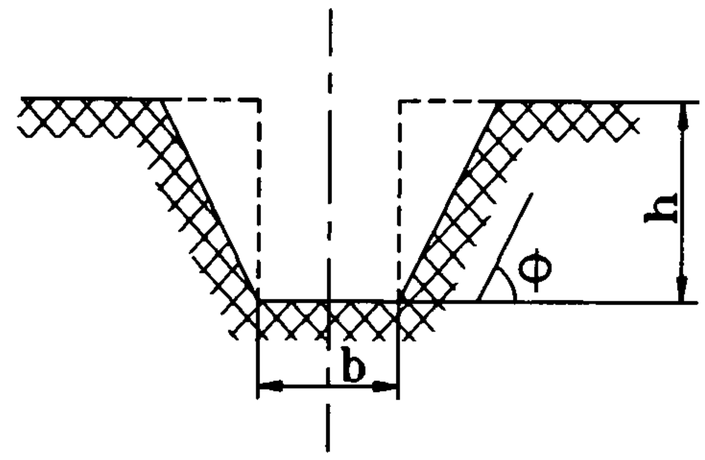

Figure 8.12 Cutting Slot Section

where **b** is the cutting tool width. Practically the extreme form for the specific energy will be infinity as the cutting depth tends to infinity. Therefore combining Equation (8.36) and Equation (8.37), we can predict that the form for the expression of $\mathcal{L}$**(h)** for cutting force should be the exponential type function or the power type function with the power coefficient larger than two.

For reasons of simplicity, we can use the later one. If we introduce the threshold force value, or lower bound force value, whose physical implications have been discussed in Section §8.2, we can then analogously express the force equation as:

$$F_C = F_C(h) = S_U + a \cdot h^b \tag{8.38}$$

where $\mathbf{S_U}$ is the threshold force value, **b** is the power coefficient with a value larger than 2, and its actual value, together with **a**, will be decided by the rock and the cutting alignment, and they can be decided by the Weibull distribution parameters as well. For this purpose, the easier and more precise way is by doing a few rock cutting tests at different cutting depths and then doing the statistical regression analysis.

For the normal force value, theoretically we know that the force value increase rate (or the derivative) increases with the cutting depth **h**. Therefore the power relationship with the power greater than 1 between the normal force and the cutting depth can be assumed, i.e.,

$$F_N = F_N(h) = c \cdot h^d \tag{8.39}$$

Again the constants can be related to the Weibull distribution parameters by the cutting tests at different depths.

After the determination of the relationship of Equation (8.37) to (8.39), the mean force values and their variance can be obtained by the mathematical relationships listed above in this section. Thereafter the mean value and variance of the specific energy can be determined by the following equations:

$$\begin{cases} E[SE] = \dfrac{E[F_C]}{E[Vu]}\cdot\left(1+\dfrac{V[Vu]}{E[Vu]^2}\right) \\ V[SE] = \dfrac{E[F_C]^2\cdot V[Vu]+E[Vu]^2\cdot V[F_C]}{E[Vu]^4} \end{cases} \tag{8.40}$$

where the condition of variable independence is assumed and **E[Vu]** and **V[Vu]** can be obtained by:

$$\begin{cases} E[Vu] = b\cdot h + h^2\cdot E[\tan\phi] \\ V[Vu] = h^4\cdot V[\tan\phi] \end{cases} \tag{8.41}$$

For the cutting tool array performance prediction, the mean total force values and their variance can be derived from the single tool cutting characteristics. As an instructive example, let us take a model of a TBM for instance. Suppose there is a simple model of TBM cutterhead mounted with **N** number of drag tool cutting picks, each with the same cutting geometries and having the rotating radius $\mathbf{r_i}$ (i = 1,2,...,N). Therefore the machine torque value contributed by all the cutting tools can be expressed as:

$$T = \sum_{i-1}^{N} T_i = \sum_{i-1}^{N} F_C^i\cdot r_i \tag{8.42}$$

with the mean and variance,

$$\begin{cases} E[T] = \displaystyle\sum_{i-1}^{N} E[F_C^i]\cdot r_i = E[F_C]\cdot\sum_{i-1}^{N} r_i \\ V[T] = \displaystyle\sum_{i-1}^{N} V[T_i] = \sum_{i-1}^{N} V[F_C^i]\cdot r_i^2 = V[F_C]\cdot\sum_{i-1}^{N} r_i^2 \end{cases} \tag{8.43}$$

Here the non-influenced relationship between the cutting tools is supposed. Based on this same assumption, the total machine thrust force **TR** can be obtained from the following calculations:

$$\begin{cases} E[TR] = \displaystyle\sum_{i-1}^{N} E[F_N^i] = N\cdot E[F_N] \\ V[TR] = \displaystyle\sum_{i-1}^{N} V[F_N^i] = N\cdot V[F_N] \end{cases} \tag{8.44}$$

Note should be taken that the above evaluation account for the force values from the cutting tools only. The friction forces coming from other parts of the machine are not included.

While estimating the tool combination performance for a roadheader cutting head, the cutting force and normal force values for each pick will change from zero to their maximum and then back to zero as the pick cutting depth changes in the same pattern while that pick is cutting the rock, as shown in Figure 8.13. Then the torque value produced by the ith pick will be:

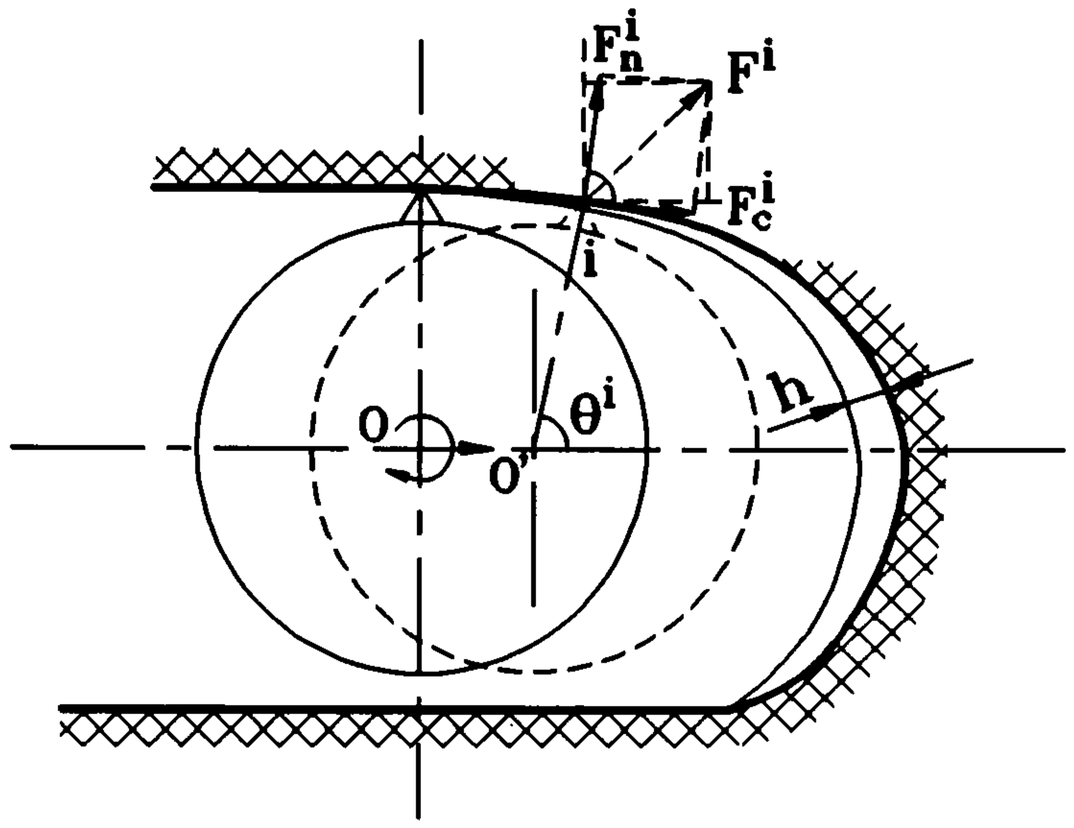

Figure 8.13 Roadheader Pick Cutting

$$\begin{cases} E[T^i] = r_i \cdot F_C^i \\ V[T^i] = r_i^2 \cdot V[F_C^i] \end{cases} \tag{8.45}$$

Where the $\mathbf{F_C^i}$ value is not constant as the cutting depth is changing, and furthermore the equations are only valid when that particular pick is cutting the rock. For the sumping force and the vertical force produced by the **i**-th cutting pick, their values are affected both from the cutting force and the normal force set up by that cutting tool. The following equations demonstrate their relationship.

$$\begin{cases} F_S^i = F_C^i \cdot \sin\theta^i + F_N^i \cdot \cos\theta^i \\ F_V^i = F_C^i \cdot \cos\theta^i + F_N^i \cdot \sin\theta^i \end{cases} \tag{8.46}$$

where θ^i is the angle between the pick position radius and the level axis, which is positive when the pick is over the level axis and negative when under it. Their mean and variance can be evaluated as follows:

$$\begin{cases} E[F_S^i] = E[F_C^i] \cdot \sin\theta^i + E[F_N^i] \cdot \cos\theta^i \\ E[F_V^i] = E[F_C^i] \cdot \cos\theta^i + E[F_N^i] \cdot \sin\theta^i \\ V[F_S^i] = (\sin\theta^i)^2 \cdot V[F_C^i] + (\cos\theta^i)^2 \cdot V[F_N^i] \\ V[F_V^i] = (\cos\theta^i)^2 \cdot V[F_C^i] + (\sin\theta^i)^2 \cdot V[F_N^i] \end{cases} \tag{8.47}$$

Henceforth, the whole cutting torque value, the whole sumping force and the whole vertical force can be obtained simply by summing up the values contributed by different picks.

$$\begin{cases} E[T] = \sum_{i-1}^{n} E[T^i] = \sum_{i-1}^{n} E[F_C^i]\cdot r_i \\ V[T] = \sum_{i-1}^{n} V[F_C^i]\cdot r_i^2 \end{cases} \tag{8.48}$$

and,

$$\begin{cases} E[F_S] = \sum_{i-1}^{n} E[F_S^i], \quad E[F_V] = \sum_{i-1}^{n} E[F_V^i] \\ V[F_S] = \sum_{i-1}^{n} V[F_S^i], \quad V[F_V] = \sum_{i-1}^{n} V[F_V^i] \end{cases} \tag{8.49}$$

It is vitally important to note that the above equations are only valid for the **n** tools which are cutting the rock at the time of evaluation out of the **N** total tools mounted on the cutting drum. As for the roadheader cutting head, the **N** tools are not cutting the rock at the same time. Therefore the rotating phase of the drum will be very important as it will decide the cutting state of different tools at different times.

The above prospects have only approached the problem theoretically. It provides guidelines for related estimations. The practical work is under consideration.

§8.9 Conclusions and Suggestions for further Research

1) Weibull's weakest link strength theory is applicable in rock fragmentation engineering and is believed to be able to better solve the problem from a statistical point of view because of the random characteristics of rock materials. It is suggested that this method can be adopted for some other rock mechanics research.

2) In rock cutting engineering, the rock indentation strength and rock fracture strength are random variables varying from point to point along the rock cutting path determined by many other random variables, and their values follow Weibull probabilistic distribution, instead of the commonly suggested normal (Gaussion) distribution.

3) The Weibull distribution parameters $\mathbf{S_U}$, $\mathbf{S_0}$ and **m** of the above mentioned strength can be taken as material constants particularly for rock cutting. On knowing them, not only can the cutting performance parameters, such as cutting force, normal force and specific energy, be predicted, but their values' scatter and distribution can also be found. Further research is suggested to use the distribution parameters to assess the rock cuttability and to do rock

classification for rock cutting engineering.

4) The prediction procedure discussed in this work is based on the rock cutting mechanism and is therefore believed to be illustrating well the cutting performance parametric relationships. However the experiments that have been conducted are still far too limited. Therefore some error should be allowed for at this stage when using the procedure listed in Table 8.3 for practical prediction. Even though the prediction carried out above is quite satisfactory, a large amount of statistical research is suggested in order to reach the more generally applicable cutting performance prediction. However it is unrealistic to expect a universal prediction estimation. All estimations have their own restrictions.

5) As long as the cutting performance of a single tool has be determined, their combination effect for any kind of tool array, expected value and variance, can be evaluated as well.

Chapter 9
Conclusions

1. The **Mode I** fracture problem for a cracked straight-through Brazilian disc (CSTBD) subjected to a pair of diametrical concentrated loads on the disc boundary directed along the crack orientation has been found to be best solved numerically by a stepwise superimposition technique. The problem can be divided into two simpler problems, an uncracked Brazilian disc subjected to arbitrary boundary loadings and an infinite region with a central crack subjected to internal surface loadings. Then the solution for the original problem can be reached by superimposing the solutions of these two simpler problems continuously (iteratively) until the desired accuracy requirements have been met. The final solution for the **Mode I** stress intensity factor (SIF) for the CSTBD specimen can be expressed by the best fit polynomial given in the following formula in terms of dimensionless SIF values $\mathbf{Y}(\alpha)$ defined as $\mathbf{Y}(\alpha) = \mathbf{K_I}/\mathbf{K_0} = \mathbf{K_I}/[\mathbf{P}/(\mathbf{B}\sqrt{\mathbf{R}})]$, where $\mathbf{K_I}$ is the dimensional SIF value, **B** and **R** are the thickness and the radius of the disc, **P** is the external load and α is the dimensionless crack length **a/R** (**a** is the semi crack length).

$$\begin{aligned} Y(\alpha) = {} & 0.0354 + 2.0394\cdot\alpha - 7.0356\cdot\alpha^2 + 12.8154\cdot\alpha^3 + 8.4111\cdot\alpha^4 \\ & - 30.7418\cdot\alpha^5 - 29.4959\cdot\alpha^6 + 62.9739\cdot\alpha^7 + 66.5439\cdot\alpha^8 \\ & - 82.1339\cdot\alpha^9 - 73.6742\cdot\alpha^{10} + 73.8466\cdot\alpha^{11} \end{aligned} \tag{9.1}$$

The error in this evaluation is within 1%. It is believed that this solution can best represent the true SIF values of the **Mode I** CSTBD problem for the long crack case up to $\alpha = 0.95$ compared with existing solutions by previous researchers.

2. A mixed **Mode I** and **Mode II** fracture situation can be easily obtained from the cracked Brazilian disc problems simply by inclining the crack orientation direction to the diametrical loading direction with a certain angle θ. By changing the value of this angle, different combinations of **Mode I** and **Mode II** fracture intensities can be obtained while the loading fixtHxe still remains very simple. Therefore the cracked Brazilian discs (CSTBD and CCNBD) are obviously the ideal specimen geometries which can be used for mixed mode fracture investigation of brittle materials, especially of rock.

By taking advantage of the same stepwise superimposition technique developed for solving the **Mode I** CSTBD problem, the mixed mode fracture problems of the CSTBD specimen with any crack length has now been solved with the help of dislocation and complex stress function

methods. The stage of the solutions for crack length $\alpha > 0.6$ has not yet been reached by previous researchers. The dimensionless SIF solutions of the problem, $\mathbf{Y_I(\alpha,\theta)}$ and $\mathbf{Y_{II}(\alpha,\theta)}$ (defined as $\mathbf{Y_I(\alpha,\theta) = K_I/K_0}$, $\mathbf{Y_{II}(\alpha,\theta) = K_{II}/K_0}$ and $\mathbf{K_0 = P/(B\sqrt{R})}$, representing the two components of the mixed mode fracture intensity, **Mode I** and **Mode II** fracture intensities respectively), are graphically presented in Figure 7.14 - Figure 7.17.

One of the special cases is when the inclined angle between the crack direction and the loading diameter is zero, i.e., $\theta = 0°$, then the mixed mode fracture problem will come back to the pure **Mode I** CSTBD fracture problem. Quite encouragingly, the SIF $\mathbf{Y_I(\alpha,\theta)}\big|\,\theta = 0°$ value representing the **Mode I** fracture intensity in this special case obtained from mixed mode fracture analysis coincides with the $\mathbf{Y(\alpha)}$ value directly derived from the pure **Mode I** fracture evaluation, i.e., Equation (9.1). This substantiates the correctness of both of the evaluations.

In corresponding to a crack length α **(a)**, a certain inclination angle θ_{II} between the crack direction and the loading direction can always be found under which the mixed mode CSTBD fracture problem will be reduced to pure **Mode II** fracture problem only, i.e., $\mathbf{Y_I(\alpha,\theta) \equiv 0}$ when $\theta = \theta_{II}$. This is another special case of mixed mode fracture problem for the CSTBD specimen. By using this condition, **Mode II** fracture problems can be investigated, such as the **Mode II** fracture toughness measurement and **Mode II** crack propagation studies. θ_{II} and the corresponding pure Mode II SIF values, $\mathbf{Y_{II}(\alpha,\theta)}\big|\,\theta = \theta_{II}$, for the CSTBD can be accurately (error within $\pm 1\%$) calculated by the following equations:

$$\begin{cases} \theta_{II} = 30.4406 - 4.6734\cdot\alpha - 17.6741\cdot\alpha^2 - 9.6827\cdot\alpha^3 + 3.9819\cdot\alpha^4 \\ \qquad + 12.9163\cdot\alpha^5 - 13.3222\cdot\alpha^6 + 12.8001\cdot\alpha^7 - 13.1239\cdot\alpha^8 \\ Y_{II} = 0.06462 + 2.8956\cdot\alpha - 6.8663\cdot\alpha^2 + 9.8566\cdot\alpha^3 - 0.4455\cdot\alpha^4 - 1.0494\cdot\alpha^5 \\ \qquad - 13.2492\cdot\alpha^6 + 9.0783\cdot\alpha^7 - 10.7354\cdot\alpha^8 + 28.4775\cdot\alpha^9 - 6.3197\cdot\alpha^{10} \\ \qquad + 10.6626\cdot\alpha^{11} - 10.0268\cdot\alpha^{12} - 34.2997\cdot\alpha^{13} + 1.7292\cdot\alpha^{14} + 25.2216\cdot\alpha^{15} \end{cases} \tag{9.2}$$

3. The introduction of cracked chevron notched Brazilian disc (CCNBD) specimen brings the advantages of chevron notched geometry into the application of cracked Brazilian disc for rock fracture toughness investigation. It together with the CSTBD specimen form a pair of cracked Brazilian discs ideal for fracture researches of brittle materials, especially for rocks.

The geometrical dimensions for different CCNBD specimens can be expressed and distinguished by three basic dimensionless geometrical parameters, dimensionless crack length α_0 $\mathbf{(a_0/R)}$ and α_1 $\mathbf{(a_1/R)}$ and dimensionless specimen thickness α_B **(B/R)**. On knowing them, all the other geometrical dimensions can be calculated. Their interrelations with each other and with the dimensionless cutting saw radius $\alpha_s\mathbf{(R_s/R)}$ and the cutting depth $\mathbf{h_c}$ are as follows:

$$\begin{cases} \alpha_s = R_s/R = \sqrt{\alpha_0^2 + (\alpha_1^2 - \alpha_0^2 + \alpha_B^2/4)^2 \div \alpha_B^2} \\ h_c = (\alpha_s - \sqrt{\alpha_s^2 - \alpha_1^2})\cdot R = (\alpha_s - \sqrt{\alpha_s^2 - \alpha_0^2})\cdot R + B/2 \\ \alpha_0 = \sqrt{\alpha_s^2 - (\sqrt{\alpha_s^2 - \alpha_1^2} + \alpha_B/2)^2} \\ \alpha_1 = \sqrt{\alpha_s^2 - (\sqrt{\alpha_s^2 - \alpha_0^2} - \alpha_B/2)^2} \\ \alpha_B = 2\cdot(\sqrt{\alpha_s^2 - \alpha_0^2} - \sqrt{\alpha_s^2 - \alpha_1^2}) \end{cases} \tag{9.3}$$

However these three basic dimensions cannot vary freely. They are restricted by each other by the following relations:

$$\begin{cases} \alpha_B \le 2\cdot\sqrt{\alpha_1^2 - \alpha_0^2} \\ \alpha_0 \le \sqrt{\alpha_1^2 - \alpha_B^2/4} \\ \alpha_1 \ge \sqrt{\alpha_0^2 + \alpha_B^2/4} \end{cases} \tag{9.4}$$

One interesting feature about the CCNBD specimen geometry is that, when the CCNBD, CB and SR specimens are machined from the same rock cores, their crack orientation planes can be constructed perpendicular to each other in 3-D space. In other words, these three specimens together form a complete set of specimens for rock anisotropic fracture studies. This will greatly reduce the error caused by the different rock block selections when conducting anisotropic fracture analysis.

4. Combining the SIF solution of the CSTBD problem under any single mode or mixed mode fracture conditions with the compliance method, the fracture problem for the CCNBD specimen under the corresponding fracture mode condition can be solved. It has been concluded that Bluhm's slice superimposition model better simulates the CCNBD fracture problems than any other model. The dimensionless SIF values for the CCNBD fracture problems in terms of $\mathbf{Y}^*(\alpha)$, based on Bluhm's model, can be expressed in the following formula:

$$Y^*(\alpha) = \left[\frac{\alpha_B^4 \cdot g_3(\alpha)}{8 \cdot g_1(\alpha) \cdot g_2(\alpha)}\right]^{\frac{1}{2}} \tag{9.5}$$

where $\mathbf{Y}^*(\alpha)$ is defined as:

$$Y^*(\alpha) = \frac{K^*(\alpha)}{K_0} = \frac{K^*(\alpha)}{\frac{P}{B\sqrt{R}}} \tag{9.6}$$

and,

$$\begin{cases} g_1(\alpha) = (\alpha_1^2 - \alpha_0^2) + \dfrac{\alpha_B^2}{4} - \sqrt{(\alpha_1^2 - \alpha^2)\cdot\alpha_B^2 + (\alpha_1^2 - \alpha_0^2 - \dfrac{\alpha_B^2}{4})^2} \\ g_2(\alpha) = \left[\dfrac{1}{BE'} \cdot \dfrac{g_1(\alpha)}{C(\alpha)} + \dfrac{1}{BE'} \cdot \int_{\alpha}^{\alpha_1} \dfrac{g_4(\xi)}{C(\xi)} \cdot d\xi \right]^2 \\ g_3(\alpha) = \dfrac{2}{(BE')^2} \cdot \dfrac{Y(\alpha)\cdot g_1(\alpha)}{C^2(\alpha)} - \dfrac{(1-c_k)}{BE'} \cdot \dfrac{g_4(\alpha)}{C(\alpha)} \\ g_4(\alpha) = \dfrac{\alpha_B^2 \cdot \alpha}{\sqrt{(\alpha_1^2 - \alpha^2)\cdot\alpha_B^2 + (\alpha_1^2 - \alpha_0^2 - \alpha_B^2/4)^2}} \end{cases} \tag{13}$$

c_k is the interlaminar effect constant in the Bluhm's model. $C(\alpha)$ in the above equations is the dimensionless compliance value for the corresponding CSTBD specimen and it is calculated by the following relation:

$$C(\alpha) = \int_0^{\alpha} \frac{2}{BE'} \cdot Y^2(\alpha) \cdot d\alpha \tag{9.8}$$

The above equations are not restricted to any particular fracture mode. In other words, the SIF $\mathbf{Y^*(\alpha)}$ for the CCNBD fracture problems can be **Mode I**, **Mode II**, **Mode III** or mixed mode SIF values depending on the fracture mode which the original $\mathbf{Y(\alpha)}$ and $\mathbf{C(\alpha)}$ of the CSTBD fracture problem represents. If we substitute the SIF solution for the pure **Mode I** CSTBD fracture problem (Equation (9.1)) into the above expressions, the SIF solution for the CCNBD specimen under **Mode I** fracture condition can then be obtained.

5. Based on these evaluations, it has been concluded that the CCNBD specimen will behave in a way typical of a chevron cracked geometry and most of the applicable CCNBD specimens will fall in the range of medium crack case. The CCNBD specimens with short cracks are difficult to machine and those with long cracks are unsuitable for practical fracture toughness measurement.

In the case of the applicable CCNBD specimens with medium length cracks, they will reach their critical states when the crack fronts are some where between the initial and the final crack length $\mathbf{a_0}$ and $\mathbf{a_1}$. These critical states, hence the critical crack length $\mathbf{a_m}$ and the critical (minimum) SIF values $\mathbf{Y^*_m}$ are specimen geometry dependent only. They are not influenced by the external loading conditions. It is mathematically self-evident that these critical states will correspond to the maximum (or failure) external load under the LEFM conditions. Therefore by recording the maximum external load when the CCNBD specimens are used to measure the fracture toughness of rock materials, the fracture toughness values can then be calculated by the following equations:

$$K_C = \frac{P_{max}}{B\sqrt{R}} \cdot Y_m^* \tag{9.9}$$

Again no particular fracture mode is implied by this calculation so this equation is equally suitable for fracture toughness measurements for any fracture mode condition.

Unless otherwise stated, the following conclusions will be directed to the **Mode I** fracture condition only.

6. Numerical calibration of **Mode I** fracture problems for the CSTBD and CCNBD specimens both by boundary element method (BEM) and by finite element method (FEM) have proved the validity of the theoretical evaluations of the **Mode I** SIF values for the CSTBD and CCNBD fracture problems. The methods used for the SIF calculations are immediate displacement method and compliance method. The differences of the $\mathbf{Y}(\alpha)$ values for the CSTBD specimen and $\mathbf{Y}^*_m$ values for the CCNBD specimens between the theory and the numerical calibration are within $\pm 5\%$.

7. The specimen geometry requirement studies for rock **Mode I** fracture toughness ($\mathbf{K_{IC}}$) measurement by the CCNBD specimens show that the dimensionless specimen geometries α_1 and α_B should be within the range outlined by the following six restrictions in order to obtain satisfactory conditions for plane strain fracturing which is believed to generate constant fracture toughness values dependent on materials only. These requirements are:

$$\begin{cases} \alpha_1 \geq 0.4 , & \textit{Line } 0 \\ \alpha_1 \geq \alpha_B/2 , & \textit{Line } 1 \\ \alpha_B \leq 1.04 , & \textit{Line } 2 \\ \alpha_1 \leq 0.8 , & \textit{Line } 3 \\ \alpha_B \geq 1.1729 \cdot \alpha_1^{1.6666} , & \textit{Line } 4 \\ \alpha_B \geq 0.44 , & \textit{Line } 5 \end{cases} \tag{9.10}$$

These requirements are referred to as valid CCNBD geometrical range.

It is the CCNBD specimens with the specimen geometries within these range which will be used for practical determination of **Mode I** fracture toughness values of rock materials. For these CCNBD specimens, the critical **Mode I** SIF values $\mathbf{Y}^*_m$ which are to be used for fracture toughness calculations can be expressed by the following equation:

$$Y_m^* = u \cdot e^{v \cdot \alpha_1} \tag{9.11}$$

where **u** and **v** are geometrical constants which are dependent on α_0 and α_B only and can be obtained from Table 4.9. Equation (9.11) is substantiated both theoretically and numerically and can therefore be used for practical measurement with confidence.

8. Experiments by 40 different CCNBD specimen geometries on 42 different rock samples have proved that the CCNBD specimens with the geometry dimensions within the range defined by Equation (9.10) will yield consistent fracture toughness ($\mathbf{K_{Ic}}$) values for rock materials, which are believed to be the valid material constants. The fracture toughness values obtained from specimens with geometries far outside the valid range were found to vary considerably. Therefore in order to have a valid rock fracture toughness test, the valid geometry requirements expressed in Equation (9.10) should be strictly observed.

It has been further proved that the rock $\mathbf{K_{IC}}$ values generated by the CCNBD specimens are around 10% lower than the first step (Level I) $\mathbf{K_{IC}}$ values determined by CB and SR methods, see the Equation (9.12). However those determined by the CCNBD specimens are believed to be closer to the actual material fracture toughness values.

$$K_{IC}^{CCNBD} = 0.0521 + 0.8788 \cdot K_{IC}^{ISRM} \tag{9.12}$$

9. Experimental specimen size requirement studies suggest that in order to obtain a valid consistent material constant fracture toughness value $\mathbf{K_{IC}}$, the CCNBD specimen diameter **D** is recommended to be at least 75 mm unless a smaller size has been validated beforehand. For any specimen size, the validation study should be carried out each time before the $\mathbf{K_{IC}}$ value can be taken as a valid material constant. The studies can be conducted easier by comparing the results from different specimen sizes, or alternatively can be approximately validated by the following equation:

$$D_{\min} = 8.88 + 1.4744 \cdot \left(\frac{K_{Ic}}{\sigma_t}\right)^{-2} \tag{9.13}$$

10. Based on the experimental results, good relationships between the measured fracture toughness ($\mathbf{K_{Ic}}$) and the conventional rock properties, Young's modulus **E**, tensile strength σ_t and UCS σ_c, have been obtained. For the purpose of estimation, the $\mathbf{K_{IC}}$ value of a rock material can be jointly predicted by averaging the calculated values from the following three equations:

$$\begin{cases} K_{Ic} = 0.0540 \cdot E^{1.0143} \\ K_{Ic} = 0.2598 \cdot \sigma_t^{0.7728} \\ K_{Ic} = 0.0225 \cdot \sigma_c^{0.8390} \end{cases} \tag{9.14}$$

11. Many good features when using the CCNBD specimens for rock fracture toughness measurement have been shown during the current experimental investigation. Some of the important points are summarized as follows.

a). The critical SIF values $\mathbf{Y^*_m}$ for the CCNBD specimens which are to be used for calculations of fracture toughness values are around 1.0 only, compared with those critical values of 10.42 and 24.0 for the standard CB and SR specimens recommended by the ISRM. This means, by the comparison of Equation (9.9) with Equation (5.5), if the suggested standard geometries for these three specimens are used to measure the $\mathbf{K_{IC}}$ of the same rock material, the maximum (failure) load for CCNBD specimen $\mathbf{P_{max}}$ in kN will be around 6.6 times larger than the measured $\mathbf{K_{IC}}$ in MPa$\sqrt{m}$, while the multiplication factors for the CB and SR specimens are just around 1.0 and 0.44 only. In other words, CCNBD specimens can work as an amplifier to increase the magnitude of the output reading from the generally very small input of fracture toughness value. The failure load of the CCNBD specimen will be around 6.6 times greater than that of the CB specimen and 15.0 times than the SR specimen, if their suggested standard specimen geometries are used for the fracture toughness testing of the same rock material. This is of great significance for practical purposes as the extremely high requirement on the testing machine's low load range test abilities set by the CB and SR methods can be reduced. This will certainly increase the availability, test ability and suitability of the testing apparatus and will make the testing easier to carry out. In addition, larger output reading always means less system error in the experiment. Experimental results have proved these arguments.

b) No complicated setting-up aid and loading fixture are required for the CCNBD test. The testing will be as simple as that for using a normal Brazilian disc to measure the rock tensile strength.

c) Much larger tolerance can be given to the CCNBD geometrical dimensions during specimen preparation. The designed geometrical dimensions $\mathbf{a_0}$, $\mathbf{a_1}$ and $\mathbf{a_B}$ can be just used for the approximate control of the specimen geometries to be prepared but their final values do not have to be strictly the same as the designed values. In fact, the actual CCNBD specimen dimensions do not have to be measured before the prepared specimen are ready for test, and the $\mathbf{a_0}$ value can be more precisely measured after the test when the CCNBD specimens have

been cracked into two halves. The critical SIF value $\mathbf{Y^*_m}$ is only to be decided by Equation (9.11) according the actual specimen dimensions. The specimens are considered to be valid for fracture toughness ($\mathbf{K_{Ic}}$) measurement as long as these measured geometrical dimensions are within the range outlined by Equation (9.10). This flexibility for the sample preparation makes the CCNBD specimen more convenient and easier to prepare compared with other chevron notched specimens, and this is always of great benefit for engineering purposes.

With respect to the accuracy of the specimen dimension measurement after the sample preparation, it has been concluded that amongst the three cardinal dimensionless geometrical dimensions (α_0, α_1 and α_B), α_0 and α_B are less important in the determination of $\mathbf{Y^*_m}$ value for the CCNBD specimen compared with α_1 value. In other words, the induced error in the $\mathbf{Y^*_m}$ values will be mainly influenced by the error in the α_1 determination. Therefore for the determination of α_0 and α_B values, greater tolerance can be given during the measurement. For the determination of $\mathbf{a_1}$ value, the error of ± 0.1mm is accepted.

d). It has been experimentally proved that the CCNBD specimen geometry generates less scattered $\mathbf{K_{IC}}$ values if only one single geometry is used compared with CB and SR methods.

e). Based on theoretical investigation of the mixed mode fracture analysis for the CSTBD and the CCNBD geometries, great potential has been shown for these two geometries to be the ideal specimens to be used for rock pure Mode II and mixed mode fracture research, such as the **Mode II** fracture toughness test, mixed mode fracture strength locus test and the studies of crack propagation in rock materials under mixed mode fracture situations. Different combinations of **Mode I** and **Mode II** fracture intensities can be easily obtained by inclining the crack orientation to the loading direction at a different angle, and the testing will remain the same, simple and convenient to carry out. Besides, these two specimens are believed to be good geometries which can be adapted for rock anisotropic fracture studies.

12. When applied to rock cutting mechanics analysis, rock fracture toughness $\mathbf{K_{IC}}$ can be used jointly with rock UCS, σ_c, for the prediction of rock cutting parameters based on Weibull's probabilistic fracture model. It is believed that Weibull's weakest link strength theory based on statistical (probabilistic) fracture mechanics can better represent the cutting mechanism in rock cutting from a statistical point of view as there are involved many random characteristics of the rock material. It has been experimentally proved that rock indentation strength and rock fracture strength (which represent the rock's resistance to the tool's normal force and cutting force respectively) are random variables, varying from point to point along the rock cutting route and their values follow the Weibull's probabilistic distribution, instead of the commonly suggested normal distribution.

The Weibull distribution parameters obtained above can be taken as rock material constants

for rock cutting. On knowing them, not only the cutting performance parameters, such as the mean cutting force, mean normal force and mean specific energy are known, but also their values' distribution can be predicted. At this stage, it is believed that rock fracture toughness $\mathbf{K_{IC}}$ and rock UCS strength σ_c play the main important roles in determining the rock cutting force and rock normal force respectively and the rock cutting specific energy. Some application of this initial prediction method have yielded quite encouraging results, though much more needs to be done before this prediction method can be accepted as an applicable theory.

Based on the above conclusions, some further researches are strongly recommended.

1. For the **Mode I** rock fracture toughness ($\mathbf{K_{IC}}$) test by the CCNBD specimen, the research results given above are far from complete. More rock samples and a larger specimen size range are suggested for the investigation of the size effect on the $\mathbf{K_{IC}}$ test values so that a more accurate size requirement criteria for a valid CCNBD test can be reached. Attention should also be directed the loading rate effect on the $\mathbf{K_{IC}}$ test values so that more precise valid loading rates can be decided before the test. Compared with the Level II $\mathbf{K_{IC}}$ values determined by the ISRM suggested CB and SR methods, the $\mathbf{K_{IC}}$ values obtained by the CCNBD method are still much lower. Further investigation into this aspect is strongly suggested. In addition, a round robin test by different rock mechanics research laboratory is also strongly suggested to be organized in the near future so that the reproducibility and the repeatity of the fracture toughness values obtained from the tests by the CCNBD specimen geometry can be investigated.

2. Similar to the rock **Mode I** fracture toughness $\mathbf{K_{IC}}$ test, a draft for recommending the CSTBD or the CCNBD specimens for rock pure **Mode II** and mixed mode fracture test, such as fracture toughness $\mathbf{K_{IIC}}$ measurement, fracture strength locus test and mixed mode crack propagation investigation, has to be drawn at some stage. Therefore numerical and experimental calibrations of pure **Mode II** and mixed mode CSTBD and CCNBD fracture problems have to be carried out to substantiate the theoretical evaluations.

3. As it is believed that the CSTBD and the CCNBD are ideal specimens to be used for rock anisotropic fracture studies, further theoretical and experimental investigations in this area are to be conducted.

4. The combination of the probabilistic fracture mechanics with rock cutting mechanics for cutting performance prediction is just a first step approach. Even though encouraging predicted results have been shown, they are based on many mathematically imperfect assumptions. Many more theoretical and experimental investigations have to be carried out before this initial theory can be accepted.

Bibliography and References

1. Akazawa, T., (1953), Tension Test Method for Concrete, *Union of Testing and Research for Materials and Structures*, No. 16.
2. Aoki, S. & Sakata, M., (1980), Statistical Approach to Delayed Failure of Brittle Materials, *International Journal of Fracture*, Vol. 16, No.5, pp. 459-468.
3. ASTM Standard E 399 - 74, (1974), Standard Test Method for Plane-Strain Fracture Toughness of Metallic Materials, ASTM publication.
4. ASTM E561, (1987), *Annual Book of ASTM Standards*, Metal Test Methods and Analytical Procedure, ASTM publication, Philadephia, 03.01.
5. Atkinson, B.K., (1979), Fracture Toughness of Tennessee Sandstone and Carrara Marble Using the Double Torsion Testing Method, *Int. J. Rock Mech. Min. Sci. & Geomech. Abstr.* , Vol. 16, pp. 49-53.
6. Atkinson, B.K., (1987), *Fracture Mechanics of Rock*, Academic Press.
7. Atkinson, C., (1972a), On Dislocation Densities and Stress Singularities Associated with Cracks and Pile ups in Inhomogeneous Media, *International Journal of Engineering Science*, Vol. 10, pp. 45-71.
8. Atkinson, C., (1972b), The Interaction between a Crack and an Inclusion, *International Journal of Engineering Science*, Vol. 10, pp. 127-136.
9. Atkinson, C., (1982), Smelser, R.E. & Sanchez, J., Combined Mode Fracture via the Cracked Brazilian Disk Test, *International Journal of Fracture*, Vol. 18, No. 4, pp. 279-291.
10. Awaji, H. & Sato, S., (1978), Combined Mode Fracture Toughness Measurement by the Disk Test, *Journal of Engineering Materials and Technology*, Vol. 100, pp. 175-182.
11. Bamford, W.E., (1984), Rock Test Indices Are Being Successfully Correlated with Tunnel Boring Machine Performance, 5th Australian Tunnelling Conference, Sydney, Australia.
12. Bamford W.E., (1986), Cuttability and Drillability of Rock, Civil College Technical Report, Engineers, Australia.
13. Barenblett, G.I., (1962), The Mathematical Theory of Equilibrium Cracks in Brittle Fracture, *Adv. Appl. Mech.*, 7, pp. 55-129.
14. Barker, L.M., (1977), A Simplified Method for Measuring Plane Strain Fracture Toughness, *Engineering Fracture Mechanics*, Vol. 9, pp. 361-369.
15. Barker, L.M., (1979), Theory for Determining K_{IC} from Small Non-LEFM Specimens, Supported by Experiments on Aluminum, *International Journal of Fracture*, Vol. 15, No. 6, pp. 515-536.
16. Barker, L.M., (1983), Compliance Calibration of a family of Short Rod and Short Bar Fracture Toughness Specimens, *Engineering Fracture Mechanics*, 17, No. 4, pp.289-312.
17. Barker, L.M., (1984), Specimen Size Effects in Short Rod Fracture Toughness Measurements,

Chevron-Notched Specimens: Testing and Stress Analysis, ASTM STP 855, Philadelphia PA, pp. 117-133.

18. Batdorf, S.B., et. al., (1978), Weakest Link Theory Reformulated for Arbitrary Fracture Criterion, *Journal of The American Ceramic Society*, Vol. 61, N0. 7-8, pp. 355-358.

19. Beech, J.F. & Ingraffea, A.R., (1982), Three Dimensional Finite Element Calibration of the Short Rod Specimen, *International Journal of Fracture*, 18, No. 3, pp. 217-229.

20. Berenbaum & Brodie, (1959), The Tensile Strength of Coal, *J. Inst., Fuel*, 32, pp. 320-327.

21. Bieniawski, Z.T., (1966a), Mechanism of Rock Fracture in Compression, Report of the South African Council of Scientific and Industrial Research, No. MEG 459.

22. Bieniawski, Z.T., (1966b), Stable and Unstable Fracture Propagation in Rock, Report of the South African Council of Scientific and Industrial Research, No. MEG 493.

23. Bieniawski, Z.T., (1967), Mechanism of Brittle Fracture of Rock, Part I -- Theory of the Fracture Process, *Int. J. Rock Mech. Min. Sci. & Geomech. Abstr.*, Vol.4, pp. 395 - 406, Part II -- Experimental Studies, *Int. J. Rock Mech. Min. Sci. & Geomech. Abstr.*, Vol.4, pp. 407 - 423, Part III -- Fracture in Tension and under Long-term Loading, *Int. J. Rock Mech. Min. Sci. & Geomech. Abstr.* Vol. 4, pp. 425 - 430.

24. Bieniawski, Z.T., (1980), Rock Material under Mixed Mode Fracture, *Proceedings of the 1st USA-Greece Symposium on Mixed Mode Crack Propagation*, G.C.Sih & P.S. Theocaris, (Eds), Athens, Greece, pp.333-347.

25. Bluhm, J.I., (1975), Slice Synthesis of a Three Dimensional "Work of Fracture" Specimen, *Engineering Fracture Mechanics*, Vol. 7, pp. 593-604.

26. Bowie, O.L. & Neal, D.M., (1970), A Modified Mapping-Collocation Technique for Accurate Calculation of Stress Intensity Factors, *International Journal of Fracture Mechanics*, 6, No. 2, 199-206.

27. Brooker, C.M., (1979), Theoretical and Practical Aspects of Cutting and Loading by Shearer Drums, *Colliery Guardian Coal International*, January & April.

28. Brown, W.F. & Strawley, J.E., (1966), *Plane Strain Crack Toughness Testing of High Strength Metallic Materials*, ASTP STP 410.

29. Brown, W.F. & Kaufman, J.G., (1976), *Developments in Fracture Mechanics Test Methods Standardization*, ASTM STP632.

30. Bubsey, R.T., et. al., (1982), Compliance Calibration of the Short Rod Chevron-Notch Specimen for Fracture Toughness Testing of Brittle Materials, *International Journal of Fracture*, Vol. 18, No. 2, pp. 125-133.

31. Bush, A.J., (1976), Experimentally Determined Stress-Intensity Factors for Single-edge-crack Round Bars Loaded in Bending, *Experimental Mechanics*, July, pp.249-257.

32. Carneiro, F., (1947), Une Novelle Methode d'essai pour Deternirer la Resistance a la Traction du Beton, Reunion des Laboratories d'Essai de Matheriaux, Paris.

33. Cartwright, D.J. & Rooke, D.P., (1979), Green's Functions in Fracture Mechanics, *Fracture Mechanics -- Current Status, Future Prospects*, ed.: R.A. Smith, Pergamon Press.

34. Chang, S., (1988), Stress Intensity Factors in a Circular Cylinder Containing a Pair of Radial Cracks, *Engineering Fracture Mechanics*, Vol. 30, No. 6, pp. 811-818.

35. Chell, G.G.,et. al., (1977), A Post Yield Fracture Mechanics Analysis of Three-Point Bend Specimens and Its Implications to Fracture Toughness Testing, *Engineering Fracture Mechanics*, Vol. 9, pp. 101-121.

36. Chen, J.F., (1989), The Development of the Cracked-Chevron-Notched Brazilian Disc Method for Rock Fracture Toughness Measurement and Tunnelling Machine Performance Prediction, Ph.D Thesis, The University of Newcastle upon Tyne.

37. Chiang, W.T., (1977), Fracture Criteria for Combined Mode Cracks, *Fracture* IV, ed.: H. Liebowitz , Academic Press, New York, pp. 135-154.

38. Chong, K.P. & Kuruppu, M.D., (1984), New Specimen for Fracture Toughness Determination of Rock and Other Materials, *International Journal of Fracture*, 26, pp. R59-R62.

39. Clifton, R.J., Simonsen, E.R., Jones, A.H. & Green, S.J., (1976), Determination of the Critical Stress Intensity Factor, K_{IC}, from Internally Pressurised Thick-walled Vessels, *Experimental Mechanics*, 16, pp.233-238.

40. Costin L.S., (1981), Static and Dynamic Fracture Behavior of Oil Shale, *Fracture Mechanics for Ceramics, Rocks and Concrete*, ASTM STP 745, eds.: S.W. Freiman et. al..

41. Daniels, H.E., (1930), The Statistical Theory of the Strength of Bundles of Threads I, *Proc. Roy. Soc. (London)* Ser. A. 183, pp. 405-435.

42. Davies, D.G.S., (1973), The Statistical Approach to Engineering Design in Ceramics, *Proceedings of the British Ceramic Society*, 22, pp. 429-452.

43. Deliac, E.P., (1988), Optimization of Rock Breaking Machine, PhD thesis, Mining Tech. and Econ. Dept., Ecole des Mines de Paris, Fontainebleau, France.

44. Erdogan, F., (1962), On the Stress Distribution in Plates with Collinear Cuts under Arbitrary Loads, *Proceedings of the 4th US National Congress of Applied Mechanics*, pp. 547-553.

45. Evans, A.G. & Jones, R.L., (1978a), Evaluation of a Fundamental Approach for the Statistical Analysis of Fracture, *Journal of the Americal Ceramic Society*, Vol. 61, No. 3-4, March - April, pp.156-160.

46. Evans, A.G., (1978b), A General Approach for the Statistical Analysis of Multiaxial Fracture, *Journal of The American Ceramic Society*, Vol. 61, No. 7-8, July - Aug., pp. 302-308.

47. Evans, I. & Pomeroy, C.D., (1966), *The Strength, Fracture and Workability of Coal*, Published by Pergamon Press, 1st edn..

48. Evans, I., (1984), A Theory of Cutting Force for Point-attack Picks. *International Journal of Mining Engineering*, Vol. 2, pp. 63-67.

49. Ewalds, H.L. & Wanhill, R.J.H., (1984), *Fracture Mechanics*, London: Edward Arnold.

50. Fairhurst, C. & Cornet, F.H., (1981), Rock Fracture and Fragmentation, Rock Mechanics from Research to Application, *Proceedings of the 22nd US Symposium on Rock Mechanics*, MIT, pp.21-46.

51. Farmer, I.W., (1986), Energy Based Rock Characterization, *Proceedings of the Symposium held*

at the SME-AIME Annual Meeting, New Orleans, Louisiana, USA.

52. Farmer, I.W. & Garritty, P., (1987), Prediction of Roadheader Cutting Performance from Fracture Toughness Considerations, *6th International Rock Mechanics Conference*, Canada.

53. Fowell, R.J. & McFeat-Smith, I., (1976), Factors Influencing the Cutting Performance of a Selective Tunnelling Machines, *Proceedings of the 1st International Symposium of Tunnelling '76 (London)*, IMM, March.

54. Fowell, R.J. & Xu, C., (1991), The CCNBD Test for Cutting Performance Prediction, *7th International Congress on Rock Mechanics*, Aachen, pp. 467-470.

55. Frechet, M., (1927), On the Law of Probability of Maximum Stress, *Ann. Soc. Polon. Math. (Cracow)*, 6.

56. Freudenthal, A.M., (1968), Statistical Approach to Brittle Fracture, *Fracture* II, ed.: H.Liebowitz, Academic Press, New York, pp. 591-619.

57. Frocht, M.M., (1948), *Photoelasticity*, John Wiley & Sons, Inc..

58. Griffith, A.A., (1921), The Phenomenon of Rupture and Flow in Solids, *Phil. Trans. R. Soc. London*, Series A, 221, pp.163-198.

59. Griffith, A.A., (1924), The Theory of Rupture, *Proceedings of the 1st International Congress of Applied Mechanics*, Delft, pp. 55-63.

60. Hardy, M.P., (1973), Fracture Mechanics Applied to Rock, PhD thesis, The University of Minnesota, USA.

61. Harr, M.E., (1977), *Mechanics of Particulate Media -- A Probabilistic Approach*, McGraw-Hill.

62. Henry, J.P., Paquet, J. & Tancrez, J.P., (1977), Experimental Study of Crack Propagation in Calcite Rocks, *Int. J. Rock Mech. Min. Sci. & Geomech. Abstr.*, 14, pp. 85-91.

63. Hobbs, D.W., (1964), The Tensile Strength of Rocks, *Int. J. Rock. Mech. Min. Sci.*, 1, pp.385-396.

64. Hoek, E. & Bieniawski, Z.T., (1965), Brittle Fracture Propagation in Rock under Compression, *International Journal of Fracture Mechanics*, 1, pp.137-155.

65. Hondros, G., (1959), The Evaluation of Poisson's Ratio and the Modulus of Materials of a Low Tensile Resistance by the Brazilian (Indirect Tensile) Test with Particular Reference to Concrete, *Australian Journal of Applied Science*, Vol. 10., No. 3, pp. 243-268.

66. Howarth, D.F., et. al., (1988), Performance Characteristics of a small scale Rotary Boring Machine Instrumented with Large Drag Picks, *Int. J. Rock Mech. Min. Sci. & Geomech. Abstr.*, Vol. 25, No.1, pp. 25 - 33.

67. Huang, J.A. & Wang, S.J., (1985), An Experimental Investigation Concerning the Comprehensive Fracture Toughness of Some Brittle Rocks, *Int. J. Rock Mech. Min. Sci. & Geomech. Abstr.* , Vol. 22, No. 2, pp. 99 - 104.

68. Hudson, J.A., Brown, E.T. & Rummel,F., (1972), The Controlled Failure of Rock Discs and Rings Loaded in Diametral Compression, *Int. J. Rock Mech. Min, Sci.*, Vol. 9, pp. 241-248.

69. Hull, D. & Bacon, D.J., (1984), *Introduction to Dislocations*, 3rd ed., Pergamon Press.

70. Hunt, R.A. & McCartney, L.N., (1979), A New Approach to Weibull's Statistical Theory of

Brittle Fracture, *International Journal of Fracture*, Vol. 15, No. 4, pp. 365-375.

71. Inglis, C.E., (1913), Stresses in a Plate due to the Presence of Cracks and Sharp Corners, *Trans. Institute Naval Architects*, LV, pp. 219-230.

72. Ingraffea, A.R., Perucchio, R., Han, T.Y., Gerstle, W.H. & Huang, Y.P., (1984a), Three-dimensional Finite Element and Boundary Element Calibration of the Short-rod Specimen, *Chevron-Notched Specimens: Testing and Stress Analysis*, ASTM STP 855, J.H. Underwood, S.W. Freiman & G.I. Baratta (eds.), American Society for Testing and Materials, Philadelphia, pp. 49-68.

73. Ingraffea, A.R., Gunsallus, K.L., Beech, J.F. &Nelson, P.P., (1984b), A Short Rod Based System for Fracture Toughness Testing of Rock, *Chevron-Notched Specimens: Testing and Stress Analysis*, ASTM STP 855, J.H. Underwood, S.W. Freiman & G.I. Baratta (eds.), American Society for Testing and Materials, Philadelphia, pp. 152-166.

74. Ingraffea, A.R., Gunsallus, J.F. & Nelson, P.P., (1986), A Fracture Toughness System for Prediction of Tunnelling Boring Machine Performance, *27th U.S. Rock Mechanics Symposium*.

75. Ioakimidis, N.I., (1982), Bounds for the Dislocation Densities and the Stress Intensity Factors in Elastic Crack Problems, *International Journal of Fracture*, Vol. 20, pp. 133-145.

76. Irwin, G.R., (1948), Fracture Dynamics, *Fracture of Metals*, American Society of Metals, pp.147-166.

77. Irwin, G.R., (1957), Analysis of Stresses and Strains Near the End of a Crack Tranversing a Plate, *Journal of Applied Mechanics*, pp. 361-364.

78. Irwin, G.R., (1958a), Fracture, *Handbuch der Physik*, 6, Springer-Verlag, Heidelberg, pp. 551-590.

79. Irwin, G.R., (1958b), Discussion of the Paper on the Dynamic Stress Distribution Surrounding a Running Crack: a photoelastic analysis, *Proc. SESA*, 16, pp. 93-96.

80. Irwin, G.R., (1960), Fracture Mechanics, *Structural Mechanics*, Goodier and Hoff. (eds.), Pergamon Press, pp. 557-592.

81. Jaeger, J.C. & Cook, N.G.W., (1979), *Fundamentals of Rock Mechanics*, 3rd edn., Fletcher & Son Ltd, Norwich, Great Britain.

82. Jayatilaka, S.A., (1979), *Fracture of Engineering Brittle Materials*, Applied Science Publishers Ltd, London.

83. Johnson, J.N., Clifton, R.J., Simonson, E.R. & Green, S.J., (1973), Analysis of Fracture for Hollow Cylindrical and Spherical Rock Specimens subjected to Internal Pressure with Application to Underground Containment, Terra Tek Report on Contract No. DNA 001-73-C-0153, Salt Lake City, Utah.

84. Jones, D.L. & Chisholm, D.B., (1975), An Investigation of the Edge-Sliding Mode in Fracture Mechanics, *Engineering Fracture Mechanics*, Vol. 7, No. 3, pp. 261-270.

85. Kanninen, M.F. & Popelar, C.H., (1985), *Advanced Fracture Mechanics*, Oxford University Press.

86. Karfakis, M.G., Chong, K.P., et. al., (1986), A Critical Review of Fracture Toughness Testing

of Rocks, *Rock Fracture Mechanics -- Key to Energy Production*, 27th US Symposium on Rock Mechanics, Jostens Publications, Chapter 1, pp. 3-10.

87. Kenny, P. & Johnson, S.N., (1982), The Effect of Wear on the Performance of Mineral-cutting Tools, *Rock Breaking and Mechanical Excavation*, ed.: P. Baumgartner, CIM Special Volume 30, The Canadian Institute of Mining & Metallurgy.

88. Knott, J.F., (1973), *Fundamentals of Fracture Mechanics*, Butterworths, London.

89. Labuz, J.F., et. al., (1987), The Fracture Process Zone in Granite: Evidence and Effect, *Int. J. Rock Mech. Min. Sci. & Geomech. Abstr.* , Vol. 24, N0. 4, pp. 235-246.

90. Lajtai, E.Z., (1977), A Theoretical and Experimental Evaluation of The Griffith Theory of Brittle Fracture, *Tectonophysics*, 11, pp. 129 - 156.

91. Lawn, B.R. & Wilshaw, T.R., (1975), *Fracture of Brittle Solids*, Cambridge University Press, Cambridge.

92. Libatskii, L.L. & Kovchik, S.E., (1967), *Soviet Materials Science*, 3, pp.334-339.

93. Lidiard, A.B., (1979), Probabilistic Fracture Mechanics, *Fracture Mechanics, Current Status, Future Prospects*, ed.: R.A. Smith, Proceedings of a Conference held at Cambridge University, March 16, 1979, Pergamon Press, pp. 149-178.

94. Lindqvist, P.A., (1984), Indentation Fracture Development in Rock Continuously Observed with a Scanning Electron Microscope, *Int. J. Rock Mech. Min. Sci. & Geomech. Abstr.* , Vol. 21, No. 4, pp.165-182.

95. Lundborg, N., (1972), A Statistical Theory of the Polyaxial Compressive Strength of Materials, *Int. J. Rock Mech. Min. Sci*. Vol. 9, pp. 617-624.

96. McCabe, D.E., et. al., (1978), Elastic-Plastic R-Curves, *Journal of Engineering Materials and Technology*, Transactions of the ASME, Vol. 100, pp. 258-266.

97. McCartney, L.N., (1979), Extensions of a Statistical Approach to Fracture, *International Journal of Fracture*, Vol. 15, No. 5, pp. 477-486.

98. McClintock, F.A. & Walsh, J.B., (1962), Friction on Griffith Cracks in Rock under Pressure, *Proc. 4th US Nat. Congr. Appl. Mech.* ,Berkeley, pp. 1021-1051.

99. McClintock, F.A. & Zaverl, (1979), F., An Analysis of the Mechanics and Statistics of Brittle Crack Inition, *International Journal of Fracture*, Vol.15, No. 2, pp. 107-118.

100. McFeat-Smith, I., (1977), Rock Property Testing for the Assessment of Tunnelling Machine Performance, *Tunnels and Tunnelling*, pp. 29-33.

101. Merchant, M.E., (1945), Basic Mechanics of the Metal Cutting Process, *J. Applied Mechanics*, 11, pp.168.

102. Munz, D.G., et. al., (1980a), Compliance and Stress Intensity Coefficients for Short Bar Specimens with Chevron Notches, *International Journal of Fracture*, Vol. 16, No. 4, pp. 359-374.

103. Munz, D.G. & Shannon, J.L., (1980b), Fracture Toughness Calculation from Maximum Load in Four Point Bend Tests of Chevron Notch Specimens, *International Journal of Fracture*, Vol. 16, pp. R137-R141.

104. Murakami, Y., et. al., (1987), *Stress Intensity Factors Handbook*, Pergamon Press.

105. Muskhelishvili, N.I., (1953a), *Singular Integral Equations*, translated by Radok, J.R.M., Noordhoff, Netherlands.

106. Muskhelishvili, N.I., (1953b), *Some Basic Problems of the Mathematical Theory of Elasticity*, 4th Edn., English translated by J.R.M.Rodak, Groningen, The Netherlands, P.Noordhoff Ltd..

107. Nelson, P.P. & Fong, L.C., (1986), Characterization of Rock for Boreability Evaluation Using Fracture Material Properties, *27th U.S. Rock Mechanics Symposium*.

108. Newman, J.C.Jr., (1984), A Review of Chevron-Notched Specimens, *Chevron-Notched Specimens: Testing and Stress Analysis*, ASTM STP 855, J.H. Underwood, S.W. Freiman & G.I. Baratta (eds.), American Society for Testing and Materials, Philadelphia, pp. 5-31.

109. Nishimatsu, Y., (1972), The Mechanics of Rock Cutting, *Int. J. Rock Mech. Min. Sci. & Geomech. Abstr.* , Vol. 9, pp.261-270.

110. Olofsson, T., (1978), Evaluation of Fracture Parameters and Elastic Properties of Rock Materials, Report 195E, University of Lulea, Sweden.

111. Orowan, E., (1949), Fracture and Strength of Solids, *rep. Prog. Phys.*, 12, p.185.

112. Orowan, E., (1955), Energy Criteria of Fracture, *Weld J. Res. Suppl.* , 20, p.157.

113. Ouchterlony, F., (1980a), Compliance Measurement on Notched Rock Cores in Bending, Report DS 1980:2, Swedish Detonic Research Foundation, Stockholm, Sweden.

114. Ouchterlony, F., (1980b), A New Core Specimen for the Fracture Toughness Testing of Rocks, Report DS P10, Swedish Detonic Research Foundation, Stockholm, Sweden.

115. Ouchterlony, F., (1981), Extension of the Compliance and Stress Intensity Formulas for the Single Edge Crack Round Bar in Bending, *Fracture Mechanics for Ceramics, Rocks and Concrete*, ASTM STP 745, eds.: S.W.Freiman, et. al..

116. Ouchterlony, F., (1982), Review of Fracture Toughness Testing of Rock, *SM Archives* 7, pp. 131-211.

117. Ouchterlony, F., (1986), A Core Based Specimen with Chevron Edge Notch for Fracture Toughness Measurement, *Rock Mechanics -- Key to Energy Production, 27th US Symposium on Rock Mechanics*, Jostens Publications.

118. Ouchterlony, F., (1989), On the Background to the Formulae and Accuracy of Rock Fracture Toughness Measurements Using ISRM Standard Core Specimens, *Int. J. Rock Mech. Min. Sci. & Geomech. Abstr.* , Vol. 26, No. 1, pp. 13-23.

119. Ouchterlony, F. & Takahashi, H., et. al., (1991), Experiences from Fracture Toughness Testing of Rock According to the ISRM Suggested Methods, Report DS 1991:2, SveDeFo.

120. Owen, D.J.R. & Fawkes, A.J., (1983), *Engineering Fracture Mechanics: numerical methods and application*, Pineridges Press Ltd..

121. Pook, L.P., (1971), The Effect of Crack Angle on Fracture Toughness, *Engineering Fracture Mechanics*, Vol. 3, No. 3, pp. 205-218.

122. Rice, R.J., (1971), Mathematical Analysis in the Mechanics of Fracture, *Fracture* II, ed.:, H. Liebowitz , Academic Press.

123. Rich, T.P., et. al., (1977), Probability Based Fracture Mechanics for Impact Penetration Damage, *International Journal of Fracture*, Vol. 13, No. 4, pp. 409-430.

124. Rooke, D.P. & Tweed, J., (1972), The Stress Intensity Factors of a Radial Crack in a Finite Rotating Elastic Disc, *International Journal of Engineering Science*, Vol. 10, pp. 709-714.

125. Rooke, D. P. & Tweed, J., (1973), The Stress Intensity Factors of a Radial Crack in a Point Loaded Disc, *International Journal of Engineering Science*, Vol. 11, pp. 285-290.

126. Rooke, D.P. & Cartwright, D.J., (1976), *Compendium of Stress Intensity Factors*, The Hillingdon Press, London, Her Majesty's Stationary Office.

127. Roxborough, F. F. , (1973), Cutting Rock With Picks, *The Mining Engineer*,pp. 445-455.

128. Roxborough, F.F., Phillips, H.R., (1980), Rock Excavation by Disc Cutter, course notes, The University of Newcastle upon Tyne.

129. Sanchez, J., (1979), Application of the Disk Test to Mode I-II Fracture Analysis, MSc Thesis, Mechanical Engineering Department, University of Pittsburgh, Pittsburgh, Pa.

130. Sangha, C.M., (1974), Microfracturing of a Sandstone in Uniaxial Compression, *Int. J. Rock Mech. Min. Sci. & Geomech. Abstr.* , Vol. 11, pp. 107 - 113.

131. Saouma, V.E. & Kleinosky, M.J., (1985), Finite Element Simulation of Rock Cutting, Fracture Mechanics Approach, *Rock Mechanics in Productivity*.

132. Schmidt, R.A., (1975), Fracture Testing of Rock, Closed Loop, MTS System Corp., 5., 5., pp. 3-12.

133. Schmidt, R.A., (1976), Fracture Toughness Testing of Limestone, *Experimental Mechanics*, pp.161-167.

134. Schmidt, R.A. & Lutz, T.J., (1978), K_{IC} and J_{IC} of Westerly Granite - Effects of Thickness and in-plane Dimension, *Fracture Mechanics Applied to Brittle Materials*, Part 2.

135. Schmidt, R.A., (1980), A Microcrack Model and its Significance to Hydraulic Fracturing and Fracture Toughness Testing, *Proc. 21st US Symp. on Rock Mech.*, pp. 581-590.

136. Shetty, D.K., Rosenfield, A.R. & Duckworth, W.H., (1985), Fracture Toughness of Ceramics Measured by a Chevron-notched Diametral-Compression Test, *Journal of The American Ceramic Society*, Vol. 68, No. 12, pp. c325-c443.

137. Shetty, D.K., Rosenfield, A.R. & Duckworth, W.H., (1986), Mixed-mode Fracture of Ceramics and Diametral Compression, *Journal of The American Ceramic Society*, Vol. 69, No. 6, pp. 437-443.

138. Shetty, D.K., Rosenfield, A.R. & Duckworth, W.H., (1987), Mixed mode Fracture in Biaxial Stress State, *Engineering Fracture Mechanics*, Vol. 26, pp. 825-845.

139. Sih, G.C., Paris, P.C. & Erdogan, F., (1962), Crack-Tip Stress-Intensity Factors for Plane Extension and Plate Bending Problems, *Journal of Applied Mechanics*, Transactions of the ASME, pp. 306-312.

140. Singh, R.N. & Pathan, A.G., (1988), Fracture Toughness of Some British Rocks by Diametral Loading of Discs, *Mining Science and Technology*, Elsevier Science Publishers B.V. Amsterdam, 6, pp.179-180.

141. Sneddon, I.N., (1946), The Distribution of Stress in the Neighbourhood of a Crack in am Elastic Solid, *Proc. Roy. Soc. (London)* Ser. A-187, pp. 229 - 260.

142. Sneddon, I.N. & Lowengrub, M., (1969), *Crack Problems in the Classical Theory of Elasticity*, Chapter 2.

143. Stanley, P., et. al., (1973), An Engineer's Approach to the Prediction of Failure Probability of Brittle Components, *Proceedings of the British Ceramic Society*, 22, pp. 453-487.

144. Sun, Z. & Ouchterlony, F., (1986), Fracture Toughness of Stripa Granite Cores, *Int. J. Rock Mech. Min. Sci. & Geomech. Abstr.* , Vol. 23, No. 6, pp. 399-409.

145. The ISRM Testing Commission, (1988), Suggested Methods for Determining the Fracture Toughness of Rock.

146. Timoshenko, S.P. & Goodier, J.N., (1970), *Theory of Elasticity*, 3rd ed., McGraw-Hill, New York.

147. Towers, O.L. & Garwood, S.J., (1980), Maximum Load Toughness, *International Journal of Fracture*, Vol. 16, pp. R85-R91.

148. Tracy, P.G., et. al., (1982), On the Statistical Nature of Fracture, *International Journal of Fracture*, Vol. 18, No. 4, pp. 253-277.

149. Tranter, C.J., (1948), The Use of the Mellin Transform in Finding the Stress Distribution in an Infinite Wedge, *Q. J. Mech. appl. Math.*, 1, pp. 125.

150. Trustrum, K. & Jayatilaka, A.D., (1979), On Estimating the Weibull Modulus for a Brittle Material, *Journal of Materials Science*, Vol. 14, pp.1080-1084.

151. Tweed, J. & Das, S.C., (1972a), The Stress Intensity Factors of a Radial Crack in a Finite Elastic Disc, *International Journal of Engineering Science*, Vol. 10, pp. 323-335.

152. Tweed, J., (1972b), Some Dual Integral Equations Involving Inverse Finite Mellin Transforms, *Q. J. Mech. appl. Math.*, pp. 179-184.

153. Tweed, J., Das, S.C. & Rooke, D.P., (1972c), The Stress Intensity Factors of a Radial Crack in a Finite Elastic Disc, *Int. J. Engng. Sci.*, Vol. 10, pp. 323-335.

154. Visalvanish, K., et. al., (1981), Compliance Measured Fracture Toughness of Morter and Fiber Reinforced Morter, *Fracture Mechanics for Ceramics, Rocks and Concrete*, ASTM STP 745, ed.: S.W. Freiman, et. al..

155. Weibull, W., (1951), A Statistical Distribution Function of Wide Applicability, *Journal of Applied Mechanics*, pp. 293-297.

156. Weil, N.A. & Daniel, I.M., (1964), Analysis of Fracture Probabilities in Nonuniformly Stressed Brittle Materials, *Journal of the American Ceramic Society*, Vol. 47, No. 6, June, pp. 268-274.

157. Wessel, E.T. & Loss, F.J., (1983), *Elastic-Plastic Fracture Test Methods*, ASTM STP 856.

158. Westergaard, H.M., (1939), Bearing Pressures and Cracks, *Journal of Applied Mechanics*, 61, A49-53.

159. Whittaker, B.N., Singh, R.N. & Sun, G., (1992), *Rock Fracture Mechanics -- Principles, Design and Applications*, Elsevier.

160. Williams, M.L., et. al., (1957), On the Stress Distribution at the Base of a Stationary Crack,

Journal of Applied Mechanics, pp. 109-114.

161. Wong, T.F., (1982), Micromechanics of Faulting in Westerly Granite, *Int. J. Rock Mech. Min. Sci. & Geomech. Abstr.* , Vol. 19, pp. 49 - 64.

162. Yanagidani, T. & Sano, O., (1978), The Observation of Cracks Propagating in Diametrically-Compressed Rock Disc, *Int. J. Rock Mech. Min. Sci. & Geomech. Abstr.* , Vol. 15, pp.225-235.

163. Yarema, S. Ya. & Krestin, G.S., (1966), *Soviet Materials Science*, 2, pp. 7-10.

164. Yatomi, C., (1980), On Griffith's Theory, *International Journal of Fracture Mechanics*, Vol. 16., pp R239-R241.

165. Zdenek, P.B., et. al., (1987), Size Effect Tests and Fracture Characteristics of Aluminum, *Engineering Fracture Mechanics*, Vol. 26, No. 1, pp. 45-57.

166. Zoback, M.D., (1978), A Simple Hydraulic Fracturing Technique for Determining Rock Fracture Toughness, *Proc. 19th US Symp. on Rock Mechanics*, University of Nevada, Reno, pp. 83-85.

Appendix A: An Input Data File for BEASY Numerical Calibration

```
BE3DTE 0 0
TITLE D = 75,R' = 26,B = 30,a0 = 10,a1 = 24.39262,
            a = 15.00,b = 5.526479
BP 1 0 0 0
BP 2 0 0 15.00
BP 3 0 0 37.5
BP 4 15.0 0 0
BP 5 15.0 0 24.392622
BP 6 15.0 0 37.5
BP 7 2.763239 0 0
BP 8 2.763239 0 15.00
BP 9 2.763239 0 37.5
BP 10 15.0 37.5 0
BP 11 0 37.5 0
BP 12 0 1.3087310 37.4771560
BP 13 15.0 1.3087310 37.4771560
BP 14 2.763239 0 24.392622
BP 20 24.00000 0 0
BC 1 11 12 1 1
BC 2 12 3 1 1
BC 3 10 13 4 1
BC 4 13 6 4 1
BC 5 8 5 20 1
BC 6 10 6 4 1
BR 1 1 2 8 7 408 2
BR 2 7 8 5 4 408 5
BR 3 2 3 9 8 -408 1
BR 4 14 9 6 5 5 5
BD 5 8 14 5 4 5
BR 6 10 13 12 11 6 3
BR 7 13 6 3 12 1 5
BD 8 4 6 10 4 6
ZN 1
ZP 0.3
ZE 10000
ZX 1
ZZ 1
ZB 1-8
PL 0
PD 3 2 0 0 0 0
PD 4 2 0 0 0 0
PD 5 2 0 0 0
PP 7 -1 -100 -100 -100 -100
LF 1
EN
```

Appendix B: Programs for the SIF Evaluation of the CSTBD and CCNBD Fracture Problems

1. Program SIFE
(for SIF Evaluation of Mode I CSTBD Fracture Problem)

```
      PROGRAM SIFE
C
C          THE STRESS INTENSITY FACTOR
C      EVALUATION OF THE CRACKED STARIGHT-
C         THROUGH BRAZILIAN DISK SUBJECTED
C           TO A PAIR OF DIAMETRICAL LOADS
C         UNDER MODE I FRACTURE CONDITION
C
      DIMENSION CET(100),CET1(100),CET2(100),
                     RCC1(100),RCC2(100)
      DIMENSION TXX(100),TYY(100),SYY(100),
                     SYY1(100),SYY2(100)
      DIMENSION SIFF(100),SIFF0(100)
C
      OPEN(1,FILE = 'data3')
      OPEN(2,FILE = 'data4')
      READ (1,*) DIAM,RID,THICK,PER
      READ (1,*) NUMBI,NUMBJ,EPS
      READ (1,*) CETBEG,CETEND
C
      DO 1500 III = 1,99
      SIF = 0.
      PC0 = 0.
      PC1 = 0.
      PC2 = 0.
      PC3 = 0.
      PCC = 0.
      PI = 3.1415926
      CRACK = CRACK + 0.01
C
C     COMPUTE THE INITIAL STRESSES ALONG
C                   THE XX-AXIS
C
      SYY0 = 2.*PER/(PI*THICK*DIAM)
      PC0 = SYY0
      SIF = SIF + SYY0*SQRT(PI*CRACK)
C
C      COMPUTE THE BOUNDARY GEOMETRIES
C
      WRITE (6,20)
 20   FORMAT (//,'THE BOUNDARY GEOMETRIES')
      WRITE (6,30)
 30   FORMAT (/,'J   CET(I)   LENGTH  CET1(I)   CET2(I)
     *          RCC1(I)    RCC2(I)')
C
      CETB1 = CETBEG
      STEP1 = (CETEND-CETB1)/NUMBJ
      DO 100 I = 1,NUMBJ
      CET(I) = (CETB1 + STEP1/2.)*PI/180.
C
      CETB1 = CET(I)*180./PI + STEP1/2.
```

```
      ALEN = 2.*RID*SIN(STEP1*PI/360.)
      CET1(I) = ATAN2((RID*SIN(CET(I))),
                      (RID*COS(CET(I))-CRACK))
      CET2(I) = ATAN2((RID*SIN(CET(I))),
                      (RID*COS(CET(I)) + CRACK))
      RCC1(I) = SQRT((RID*SIN(CET(I)))**2
                      + (RID*COS(CET(I))-CRACK)**2)
      RCC2(I) = SQRT((RID*SIN(CET(I)))**2
                      + (RID*COS(CET(I)) + CRACK)**2)
      CET5 = CET(I)*180./PI
      CET6 = CET1(I)*180./PI
      CET7 = CET2(I)*180./PI
C
      WRITE(6,40)I,CET5,ALEN,CET6,CET7,RCC1(I),RCC2(I)
 40   FORMAT (I5,6F9.4)
C
 100  CONTINUE
 105  CONTINUE
      SIF00 = SIF
C
C     COMPUTE THE SHEAR AND NORMAL FORCE
C                  ON THE BOUNDARY
C
      WRITE (6,110)
 110  FORMAT (//,'THE SHEAR AND NORMAL FORCE
                  ON THE BOUNDARY')
      WRITE (6,120)
 120  FORMAT (/,'NUMBJ   CET(I)   ALEN    TXX(I)
     * TYY(I)')
C
      DO 200 I = 1,NUMBJ
      CET3 = CET(I)-CET1(I)/2.-CET2(I)/2.
      CET4 = 3.*(CET1(I) + CET2(I))/2.
      A1 = RID*PC0/SQRT(RCC1(I)*RCC2(I))
      A2 = CRACK*CRACK/(RCC1(I)*RCC2(I))
C
      SIGXX = A1*(COS(CET3)-A2*SIN(CET(I))
                      *SIN(CET4))-PC0
      SIGYY = A1*(COS(CET3) + A2*SIN(CET(I))
                      *SIN(CET4))-PC0
      SIGXY = A1*A2*SIN(CET(I))*COS(CET4)
      TXX(I) = SIGXX*COS(CET(I)) + SIGXY*SIN(CET(I))
      TYY(I) = SIGXY*COS(CET(I)) + SIGYY*SIN(CET(I))
      IF (JJJJ.EQ.1) GOTO 200
      WRITE (2,130) I,CET(I),TXX(I),TYY(I)
 130  FORMAT (I5,3F9.4)
 200  CONTINUE
      JJJJ = 1
C
C     COMPUTE STRESSES ON THE XX-AXIS DUE
C               TO THE BOUNDARY FORCE
C
      WRITE (6,210)
 210  FORMAT (//,'STRESS ALONG THE X-AXIS DUE
C               TO THE BOUNDARY FORCE')
      WRITE (6,220)
 220  FORMAT (/,'NUMBI     XJ     STEP     SYY1(I)
     * SYY2(I)')
C
      XBEG = -CRACK
      STEP2 = 2.*CRACK/NUMBI
      DO 400 I = 1,NUMBI
      XJ = XBEG + STEP2/2.
      XBEG = XJ + STEP2/2.
C
      DO 300 J = 1,NUMBJ
      ALFA1 = PI/2.-CET(J)
      ALFA2 = CET(J)
      X1 = RID*COS(CET(J))
      Y1 = RID*SIN(CET(J))
      R1 = SQRT((XJ-X1)**2 + Y1*Y1)
      SINC1 = (XJ-X1)/R1
      COSC1 = Y1/R1
      R21 = SQRT((X1 + XJ)**2 + Y1*Y1)
      R22 = SQRT((X1-XJ)**2 + Y1*Y1)
      COSC11 = Y1/R1
      COSC21 = (X1 + XJ)/R21
      SINC21 = -Y1/R21
      COSC22 = (X1-XJ)/R22
      SINC22 = -Y1/R22
      A3 = COSC21*SINC21**2/R21
      A4 = COSC22*SINC22**2/R22
C
      SYY11 = -4.*TYY(J)*ALEN*(COSC1**3/R1
                      -COS(ALFA1)/(2.*DIAM))
      SYY22 = -2.*TXX(J)*ALEN*(A3 + A4-COS(ALFA2)/DIAM)
      SYY11 = SYY11/PI
      SYY22 = SYY22/PI
      PC1 = PC1 + SYY11
      PC2 = PC2 + SYY22
 300  CONTINUE
C
      SYY1(I) = PC1
      SYY2(I) = PC2
      WRITE (6,310) I,XJ, STEP2,PC1,PC2
 310  FORMAT (I5,4F10.4)
      PC1 = 0.
      PC2 = 0.
      PC3 = 0.
 400  CONTINUE
C
      WRITE (6,410)
 410  FORMAT (/,' NUMBI    SYY(I)')
C
      DO 500 I = 1,NUMBI
      NUM1 = NUMBI-I + 1
      SYY(I) = 2.*SYY2(I) + SYY1(I) + SYY1(NUM1)
      PCC = PCC + SYY(I)
      WRITE (6,420) I,SYY(I)
 420  FORMAT (I5,F10.4)
 500  CONTINUE
C
      PC0 = PCC/FLOAT(NUMBI)
      PCC = 0.
      SIF = SIF + PC0*SQRT(PI*CRACK)
      P0 = PER/(THICK*SQRT(RID))
      SIF0 = SIF/P0
      WRITE (6,900) CRACK,SIF,SIF0
 900  FORMAT ('CRACK = ',F9.4,'      SIF = ',F10.6,'
                      SIF0 = ',F9.4)
      IF (ABS(SIF-SIF00).LT.EPS) GOTO 1000
      GOTO 105
 1000 CONTINUE
      SIFF(III) = SIF
      SIFF0(III) = SIF/(SYY0*SQRT(PI*CRACK))
      WRITE (6,1B00)
 1100 FORMAT (//)
 1500 CONTINUE
C
      DO 1520 JJ = 1,99
```

```
      CRACK1 = 0.01*FLOAT(JJ)*RID
      ALFA1 = CRACK1/RID
      SIFF0(JJ) = SIFF0(JJ)*SQRT(ALFA1/PI)
      WRITE (2,1505) ALFA1,SIFF0(JJ)
 1505 FORMAT (2F9.4)
      WRITE (6,1510) CRACK1,SIFF(JJ),CRACK1,SIFF0(JJ)
 1510 FORMAT (' SIFF(',F4.2,') = ',F12.5,'
                    SIFF0(',F4.2,') = ',F12.5)
 1520 CONTINUE
C
      CLOSE(1)
      CLOSE(2)
      STOP
      END
```

2. Program SIFCN (for SIF Evaluation of Mode I CCNBD Fracture Problem)

```
      PROGRAM SIFCN
C
C     STRESS INTENSITY FACTOR EVALUATION OF
C          THE CRACKED CHEVRON-NOTCHED
C          BRAZILIAN DISK SUBJECTED TO
C          DIAMETRICAL COMPRESSION
C
      implicit double precision (a-h,o-z)
      OPEN (1,FILE = 'data9')
      OPEN (2,FILE = 'data10')
      WRITE (6,10)
 10   FORMAT ('STRESS INTENSITY EVALUATION
                    OF CCNBD SPECIMEN',/)
      AK = 1.0
      DELTA = 0.0004
      READ (*,*) ALFA0,ALFA1,ALFAB,K
      DO 2000 IJ = 1,25
      ALFA1 = ALFA1 + 0.02
      IF (ALFAB.GT.BMAX) GOTO 3000
C
 40   A0 = ALFA0
      STEP = (ALFA1-ALFA0)/FLOAT(K)
      STEP0 = STEP/2.
      WRITE (6,70)
 70   FORMAT (' ALFA      YALFA      YSIF1    YSIF2
                    YSIF3')
C
      DO 1000 I = 1,K
      ALFA = A0 + STEP
      A0 = ALFA
      A1 = ALFA1**2-ALFA0**2 + ALFAB**2/4.
      A1A = (ALFA1**2-ALFA0**2-ALFAB**2/4.)**2
      A2 = (ALFA1**2-ALFA**2)*ALFAB**2
C
      A8 = 0.5717*SQRT(ALFA)-0.385*SQRT(ALFA**3)
                    + 5.2946*SQRT(ALFA**5)
      A9 = -17.1177*SQRT(ALFA**7) + 19.9932*SQRT(ALFA**9)
      A10 = 11.0711*SQRT(ALFA**11)-16.2871*SQRT(ALFA**13)
      A11 = -29.0685*SQRT(ALFA**15)
                    + 29.5453*SQRT(ALFA**17)
C
      AA = ALFA
      AY1 = 0.03537 + 2.0394*AA-7.0356*AA**2
                    + 12.8154*AA**3 + 8.4111*AA**4
      AY2 = -30.7418*AA**5-29.4959*AA**6
                    + 62.9739*AA**7 + 66.5439*AA**8
      AY3 = -82.1339*AA**9-73.6742*AA**10 + 73.8466*AA**11
      AY = AY1 + AY2 + AY3
C
      F1 = A1-SQRT(A2 + A1A)
      F2 = ALFA*ALFAB**2/SQRT(A2 + A1A)
      YALFA = A8 + A9 + A10 + A11
      IF (I.NE.1) GOTO 300
      CALFA = 0.
      CY = 0.
      AA = 0.
      JJ = INT(ALFA0/STEP0)
      DO 250 III = 1,JJ
      AFAB = AA + STEP0/2.
      AA = AFAB + STEP0/2.
      A8B = 0.5717*SQRT(AFAB)-0.385*SQRT(AFAB**3)
                    + 5.2946*SQRT(AFAB**5)
      A9B = -17.1177*SQRT(AFAB**7) + 19.9932*SQRT(AFAB**9)
      A10B = 11.0711*SQRT(AFAB**11)
                    -16.2871*SQRT(AFAB**13)
      A11B = -29.0685*SQRT(AFAB**15)
                    + 29.5453*SQRT(AFAB**17)
C
      AB = AFAB
      AY1B = 0.03537 + 2.0394*AB-7.0356*AB**2
                    + 12.8154*AB**3 + 8.4111*AB**4
      AY2B = -30.7418*AB**5-29.4959*AB**6
                    + 62.9739*AB**7 + 66.5439*AB**8
      AY3B = -82.1339*AB**9-73.6742*AB**10 + 73.8466*AB**11
      AYB = AY1B + AY2B + AY3B
C
      YAFAB = A8B + A9B + A10B + A11B
      CALFA = CALFA + 2.*STEP0*YAFAB**2
      CY = CY + 2.*STEP0*AYB**2
C
 250  CONTINUE
 300  CALFA = CALFA + 2.*STEP*YALFA**2
      CY = CY + 2.*STEP*AY**2
C
      J = INT((ALFA1-ALFA)/DELTA)
      A00 = ALFA
      A99 = 0.
      CALFAA = CALFA
      B99 = 0.
      CYC = CY
C
      DO 500 II = 1,J
      AFAC = A00 + DELTA/2.
      A00 = AFAC + DELTA/2.
C
      A11 = ALFA1**2-ALFA0**2 + ALFAB**2/4
      A11A = (ALFA1**2-ALFA0**2-ALFAB**2/4)**2
      A22 = (ALFA1**2-AFAC**2)*ALFAB**2
      A8C = 0.5717*SQRT(AFAC)-0.385*SQRT(AFAC**3)
                    + 5.2946*SQRT(AFAC**5)
      A9C = -17.1177*SQRT(AFAC**7)
                    + 19.9932*SQRT(AFAC**9)
      A10C = 11.0711*SQRT(AFAC**11)
                    -16.2871*SQRT(AFAC**13)
      A11C = -29.0685*SQRT(AFAC**15)
```

```
                    +29.5453*SQRT(AFAC**17)
      YAFC = A8C + A9C + A10C + A11C
C
      AC = AFAC
      AY1C = 0.03537 + 2.0394*AC-7.0356*AC**2
                    +12.8154*AC**3 + 8.4111*AC**4
      AY2C = -30.7418*AC**5-29.4959*AC**6
                    +62.9739*AC**7 + 66.5439*AC**8
      AY3C = -82.1339*AC**9-73.6742*AC**10 + 73.8466*AC**11
      AYC = AY1C + AY2C + AY3C
C
      F22 = AFAC*ALFAB**2/SQRT(A22 + A11A)
      CALFAA = CALFAA + 2.*DELTA*YAFC**2
      A99 = A99 + F22*DELTA/CALFAA
      CYC = CYC + 2.*DELTA*AYC**2
      B99 = B99 + F22*DELTA/CYC
C
 500  CONTINUE
C
      F3 = (F1/CALFA + A99)**2
      C3 = (F1/CY + B99)**2
      F4 = 2.*F1*YALFA**2/(CALFA**2)-(1.-AK)*F2/CALFA
      C4 = 2.*F1*AY**2/CY**2-(1.-AK)*F2/CY
C
      YSIF1 = SQRT(ALFAB**2/(2.*F1))*YALFA
      YSIF2 = SQRT(F4*ALFAB**4/(8.*F1*F3))
      YSIF3 = SQRT((ALFA1-ALFA0)/(ALFA-ALFA0))*YALFA
      YC1 = SQRT(ALFAB**2/(2.*F1))*AY
      YC2 = SQRT(C4*ALFAB**4/(8.*F1*C3))
C
      AKK = 0.7982 + 0.3806*ALFAB
      YALFAK = YALFA/AKK
      YSIF2K = YSIF2/AKK
      YALFAK = 1.3087*YALFAK
      YSIF2K = 1.3087*YSIF2K
      CC = YALFA/AY
C
      WRITE (2,600) ALFA,YALFA,YSIF1,YSIF2
 600  FORMAT (4F10.5)
C
 1000 CONTINUE
 2000 CONTINUE
C
 3000 CLOSE (1)
      CLOSE (2)
C
      STOP
      END
```

3. Program MIXCSTBD (for SIF Evaluation of Mixed Mode CSTBD Fracture Problem) (Dislocation Method)

```
 PROGRAM MIXCSTBD
DIMENSION FFI(300),GFI(300)
DIMENSION SXX(300),SYY(300),SXY(300),
                TXX(300),TYY(300)
      DIMENSION PP(300),QQ(300)
      OPEN (2,FILE = 'data10')
      OPEN (3,FILE = 'data11')
      OPEN (4,FILE = 'data12')
      OPEN (7,FILE = 'data13')
      OPEN (8,FILE = 'data14')
C
      IX = 80
      IFI = 100
      IB = 180
      EPSK = 0.008
      R = 1.0
      D = 2.0
      P = 31.4159
      READ (*,*) CETA
      PI = 3.1415926
C
      RCET = CETA*PI/180.
      C = 0.04
      DO 2000 IJ = 1,91
      C = C + 0.01
C
C     RCET = CETA*PI/180.
      DX = 2.*C/FLOAT(IX)
      XX = -C-DX
      DO 5 I = 1,IX + 1
      XX = XX + DX
      R1 = SQRT(XX**2*(SIN(RCET))**2
                    + (XX*COS(RCET)-R)**2)
      R2 = SQRT(XX**2*(SIN(RCET))**2
                    + (XX*COS(RCET) + R)**2)
      SINB1 = XX*SIN(RCET)/R1
      COSB1 = (R-XX*COS(RCET))/R1
      SINB2 = XX*SIN(RCET)/R2
      COSB2 = (R + XX*COS(RCET))/R2
      SINC1 = SIN(RCET)*COSB1 + COS(RCET)*SINB1
      COSC1 = COS(RCET)*COSB1-SIN(RCET)*SINB1
      SINC2 = SIN(RCET)*COSB2-COS(RCET)*SINB2
      COSC2 = COS(RCET)*COSB2 + SIN(RCET)*SINB2
      SIGMA1 = -2.*P*COSB1/(PI*R1)
      SIGMA2 = -2.*P*COSB2/(PI*R2)
      SIGN1 = SIGMA1*SINC1**2
      SIGT1 = SIGMA1*SINC1*COSC1
      SIGN2 = SIGMA2*SINC2**2
      SIGT2 = SIGMA2*SINC2*COSC2
      PP(I) = SIGN1 + SIGN2 + 2.*P/(PI*D)
      QQ(I) = SIGT1 + SIGT2
      QQ(I) = -QQ(I)
      WRITE (3,3) XX,PP(I),QQ(I)
3     FORMAT (3F11.5)
 5    CONTINUE
C
      ALFAC = C/R
      AK0 = P*SQRT(ALFAC/PI)/SQRT(R)
      FFAK1 = 0.
      FFAK2 = 0.
      YYAK1 = 0.
      YYAK2 = 0.
      YAK10 = 0.
      YAK20 = 0.
C
      V = 0.3
      W = 3.-4.*V
 20   III = 0
      DX = 2.*C/FLOAT(IX)
```

```
      DELTX = DX/1000.
      DELTFI = PI/FLOAT(IFI)
      FI = -PI/2.-DELTFI
C
      AK1 = 0.
      AK2 = 0.
      XX = -C-DX
      DO 30 I = 1,IX
      XX = XX + DX
      IF (I.NE.IX) GOTO 25
      DEX = DX/10.
      XX = XX-DEX
      DPP = (PP(IX + 1)-PP(IX))/10.
      DQQ = (QQ(IX + 1)-QQ(IX))/10.
      PB = PP(IX)-DPP
      QB = QQ(IX)-DQQ
      DO 23 J = 1,10
      XX = XX + DEX
      X1 = XX + DEX/2.
      PB = PB + DPP
      QB = QB + DQQ
      PE = PB + DPP
      QE = QB + DQQ
      PM = (PB + PE)/2.
      QM = (QB + QE)/2.
      AK1P = DEX*PM*SQRT((C + X1)/(C-X1))/SQRT(PI*C)
      AK2Q = DEX*QM*SQRT((C + X1)/(C-X1))/SQRT(PI*C)
      AK1 = AK1 + AK1P
      AK2 = AK2 + AK2Q
23    CONTINUE
      GOTO 30
25    X1 = XX + DX/2.
      PM = DX*(PP(I) + PP(I + 1))/2.
      QM = DX*(QQ(I) + QQ(I + 1))/2.
      AK1P = PM*SQRT((C + X1)/(C-X1))/SQRT(PI*C)
      AK2Q = QM*SQRT((C + X1)/(C-X1))/SQRT(PI*C)
      AK1 = AK1 + AK1P
      AK2 = AK2 + AK2Q
30    CONTINUE
      FAK1 = AK1/AK0
      FAK2 = AK2/AK0
      YAK1 = FAK1*SQRT(ALFAC/PI)
      YAK2 = FAK2*SQRT(ALFAC/PI)
      FFAK1 = FFAK1 + FAK1
      FFAK2 = FFAK2 + FAK2
      YYAK1 = YYAK1 + YAK1
      YYAK2 = YYAK2 + YAK2
      WRITE (7,32) ALFAC,FFAK1,FFAK2,YYAK1,YYAK2
32    FORMAT (5F11.5)
      ABS1 = ABS(YAK10-YYAK1)
      ABS2 = ABS(YAK20-YYAK2)
      IF ((ABS1.LT.EPSK).AND.(ABS2.LT.EPSK))GOTO 1000
      YAK10 = YYAK1
      YAK20 = YYAK2
C
      DO 100 I = 1,IFI + 1
      FI = FI + DELTFI
      X0 = C*SIN(FI)
      X01 = X0-DELTX
      X02 = X0 + DELTX
      XX = -C-DX
      FFI(I) = 0.
      GFI(I) = 0.
      DO 90 J = 1,IX
      XX = XX + DX
      XMIN = -C
      IF (XX.GT.XMIN) GOTO 38
      XX = -C
38    X1 = XX + DX/2.
      X2 = XX + DX
      IF (X2.LT.C) GOTO 40
      X2 = C
40    IF ((I.EQ.1).AND.(J.EQ.1))GOTO 74
      IF ((I.EQ.(IFI + 1)).AND.(J.EQ.IX))GOTO 45
      IF (X0.GT.X2) GOTO 80
      IF (X0.LT.XX) GOTO 80
      IF (ABS(X0-X2).GT.DELTX) GOTO 73
      IF (I.NE.(IFI + 1)) GOTO 50
45    X01 = C-DELTX
      X02 = X2
      III = 1
      GOTO 78
50    DXX = X2-X0
      IF (DXX.NE.0.) GOTO 55
      X02 = X2
      III = 1
55    X02 = X0 + DXX/2.
      X01 = X0-DXX/2.
      GOTO 78
73    IF (ABS(X0-XX).GT.DELTX) GOTO 78
      IF (I.NE.1) GOTO 75
74    P2 = PP(1) + (PP(2)-PP(1))*DELTX/DX
      Q2 = QQ(1) + (QQ(2)-QQ(1))*DELTX/DX
      X02 = -C + DELTX
      DX2 = X2-X02
      GOTO 79
75    DXX = X0-XX
      X01 = X0-DXX/2.
      X02 = X0 + DXX/2.
      IF (DXX.NE.0.) GOTO 78
      P2 = PP(J) + (PP(J + 1)-PP(J))*DELTX/DX
      Q2 = QQ(J) + (QQ(J + 1)-QQ(J))*DELTX/DX
      X02 = XX + DELTX
      DX2 = X2-X02
      GOTO 79
78    DX1 = X01-XX
      DX2 = X2-X02
      P1 = PP(J) + (PP(J + 1)-PP(J))*DX1/DX
      P2 = PP(J) + (PP(J + 1)-PP(J))*(DX-DX2)/DX
      Q1 = QQ(J) + (QQ(J + 1)-QQ(J))*DX1/DX
      Q2 = QQ(J) + (QQ(J + 1)-QQ(J))*(DX-DX2)/DX
      BETAF = PP(J)-XX*(P1-PP(J))/DX1
      BETAG = QQ(J)-XX*(Q1-QQ(J))/DX1
      ALFAF = (P1-PP(J))/DX1
      ALFAG = (Q1-QQ(J))/DX1
      C1F = SQRT(C**2-XX**2)*(ALFAF*XX/2.
     +  + C*ALFAF*SIN(FI) + BETAF)
      C1G = SQRT(C**2-XX**2)*(ALFAG*XX/2.
     +  + C*ALFAG*SIN(FI) + BETAG)
      C2F = SQRT(C**2-X01**2)*(ALFAF*X01/2.
     +  + C*ALFAF*SIN(FI) + BETAF)
      C2G = SQRT(C**2-X01**2)*(ALFAG*X01/2.
     +  + C*ALFAG*SIN(FI) + BETAG)
      DF = -ALFAF*C**2*(SIN(FI))**2
     +  -BETAF*C*SIN(FI) + ALFAF*C**2/2.
      DG = -ALFAG*C**2*(SIN(FI))**2
     +  -BETAG*C*SIN(FI) + ALFAG*C**2/2.
      D1F = DF*ASIN(XX/C)
      D2F = DF*ASIN(X01/C)
      D1G = DG*ASIN(XX/C)
```

```
      D2G = DG*ASIN(X01/C)
      EF = C*COS(FI)*(ALFAF*C*SIN(FI) + BETAF)
      EG = C*COS(FI)*(ALFAG*C*SIN(FI) + BETAG)
      F1 = 2.*C**2-2.*C*XX*SIN(FI)
                        + 2.*C*SQRT(C**2-XX**2)*COS(FI)
      F2 = 2.*C**2-2.*C*X01*SIN(FI)
                        + 2.*C*SQRT(C**2-X01**2)*COS(FI)
      F1 = ABS((XX-C*SIN(FI))/F1)
      F2 = ABS((X01-C*SIN(FI))/F2)
      E1F = EF*ALOG(F1)
      E1G = EG*ALOG(F1)
      E2F = EF*ALOG(F2)
      E2G = EG*ALOG(F2)
      FFI(I) = FFI(I) + C2F + D2F + E2F-C1F-D1F-E1F
      GFI(I) = GFI(I) + C2G + D2G + E2G-C1G-D1G-E1G
      IF (III.NE.1) GOTO 79
      III = 0
      GOTO 90
C
79    BETAF = P2-X02*(PP(J + 1)-P2)/DX2
      BETAG = Q2-X02*(QQ(J + 1)-Q2)/DX2
      ALFAF = (PP(J + 1)-P2)/DX2
      ALFAG = (QQ(J + 1)-Q2)/DX2
      C1F = SQRT(C**2-X02**2)*(ALFAF*X02/2.
                        + C*ALFAF*SIN(FI) + BETAF)
      C1G = SQRT(C**2-X02**2)*(ALFAG*X02/2.
                        + C*ALFAG*SIN(FI) + BETAG)
      C2F = SQRT(C**2-X2**2)*(ALFAF*X2/2.
                        + C*ALFAF*SIN(FI) + BETAF)
      C2G = SQRT(C**2-X2**2)*(ALFAG*X2/2.
                        + C*ALFAG*SIN(FI) + BETAG)
      DF = -ALFAF*C**2*(SIN(FI))**2
                        -BETAF*C*SIN(FI) + ALFAF*C**2/2.
      DG = -ALFAG*C**2*(SIN(FI))**2
                        -BETAG*C*SIN(FI) + ALFAG*C**2/2.
      D1F = DF*ASIN(X02/C)
      D2F = DF*ASIN(X2/C)
      D1G = DG*ASIN(X02/C)
      D2G = DG*ASIN(X2/C)
      EF = C*COS(FI)*(ALFAF*C*SIN(FI) + BETAF)
      EG = C*COS(FI)*(ALFAG*C*SIN(FI) + BETAG)
      F1 = 2.*C**2-2.*C*X02*SIN(FI)
                        + 2.*C*SQRT(C**2-X02**2)*COS(FI)
      F2 = 2.*C**2-2.*C*X2*SIN(FI)
                        + 2.*C*SQRT(C**2-X2**2)*COS(FI)
      F1 = ABS((X02-C*SIN(FI))/F1)
      F2 = ABS((X2-C*SIN(FI))/F2)
      E1F = EF*ALOG(F1)
      E1G = EG*ALOG(F1)
      E2F = EF*ALOG(F2)
      E2G = EG*ALOG(F2)
      FFI(I) = FFI(I) + C2F + D2F + E2F-C1F-D1F-E1F
      GFI(I) = GFI(I) + C2G + D2G + E2G-C1G-D1G-E1G
      GOTO 90
80    BETAF = PP(J)-XX*(PP(J + 1)-PP(J))/(X2-XX)
      BETAG = QQ(J)-XX*(QQ(J + 1)-QQ(J))/(X2-XX)
      ALFAF = (PP(J + 1)-PP(J))/(X2-XX)
      ALFAG = (QQ(J + 1)-QQ(J))/(X2-XX)
      C1F = SQRT(C**2-XX**2)*(ALFAF*XX/2.
                        + C*ALFAF*SIN(FI) + BETAF)
      C1G = SQRT(C**2-XX**2)*(ALFAG*XX/2.
                        + C*ALFAG*SIN(FI) + BETAG)
      C2F = SQRT(C**2-X2**2)*(ALFAF*X2/2.
                        + C*ALFAF*SIN(FI) + BETAF)
      C2G = SQRT(C**2-X2**2)*(ALFAG*X2/2.
                        + C*ALFAG*SIN(FI) + BETAG)
      DF = -ALFAF*C**2*(SIN(FI))**2-BETAF*C*SIN(FI)
                        + ALFAF*C**2/2.
      DG = -ALFAG*C**2*(SIN(FI))**2-BETAG*C*SIN(FI)
                        + ALFAG*C**2/2.
      D1F = DF*ASIN(XX/C)
      D2F = DF*ASIN(X2/C)
      D1G = DG*ASIN(XX/C)
      D2G = DG*ASIN(X2/C)
      EF = C*COS(FI)*(ALFAF*C*SIN(FI) + BETAF)
      EG = C*COS(FI)*(ALFAG*C*SIN(FI) + BETAG)
      F1 = 2.*C**2-2.*C*XX*SIN(FI)
                        + 2.*C*SQRT(C**2-XX**2)*COS(FI)
      F2 = 2.*C**2-2.*C*X2*SIN(FI)
                        + 2.*C*SQRT(C**2-X2**2)*COS(FI)
      F1 = ABS((XX-C*SIN(FI))/F1)
      F2 = ABS((X2-C*SIN(FI))/F2)
      E1F = EF*ALOG(F1)
      E1G = EG*ALOG(F1)
      E2F = EF*ALOG(F2)
      E2G = EG*ALOG(F2)
      FFI(I) = FFI(I) + C2F + D2F + E2F-C1F-D1F-E1F
      GFI(I) = GFI(I) + C2G + D2G + E2G-C1G-D1G-E1G
90    CONTINUE
      FFI(I) = FFI(I)/PI**2
      GFI(I) = GFI(I)/PI**2
105   WRITE (2,110) FI,FFI(I),GFI(I)
110   FORMAT (3F10.5)
100   CONTINUE
      DELTB = 2.*PI/FLOAT(IB)
      B = -DELTB
      DO 300 I = 1,IB + 1
      B = B + DELTB
      XB = R*COS(B)
      YB = R*SIN(B)
      SXX(I) = 0.
      SYY(I) = 0.
      SXY(I) = 0.
      FI = -PI/2.-DELTFI
      DO 300 J = 1,IFI
      FI = FI + DELTFI
      F = (FFI(J) + FFI(J + 1))/2.
      G = (GFI(J) + GFI(J + 1))/2.
      SINFI = (SIN(FI) + SIN(FI + DELTFI))/2.
      CX = F*(XB-C*SINFI)*(YB**2-(XB-C*SINFI)**2)
      DX = -G*YB*(3.*(XB-C*SINFI)**2 + YB**2)
      EX = ((XB-C*SINFI)**2 + YB**2)**2
      CY = -F*(XB-C*SINFI)*(3.*YB**2 + (XB-C*SINFI)**2)
      DY = G*YB*((XB-C*SINFI)**2-YB**2)
      EY = ((XB-C*SINFI)**2 + YB**2)**2
      CT = F*YB*(YB**2-(XB-C*SINFI)**2)
      DT = G*(XB-C*SINFI)*((XB-C*SINFI)**2-YB**2)
      ET = ((XB-C*SINFI)**2 + YB**2)**2
      SXX(I) = SXX(I) + DELTFI*(CX + DX)/EX
      SYY(I) = SYY(I) + DELTFI*(CY + DY)/EY
      SXY(I) = SXY(I) + DELTFI*(CT + DT)/ET
300   CONTINUE
      B = -DELTB
      AL = 4.*PI*R/(2.*FLOAT(IB))
      DO 400 I = 1,IB
      B = B + DELTB
      BB = B + DELTB/2.
      SXX(I) = (SXX(I) + SXX(I + 1))/2.
      SYY(I) = (SYY(I) + SYY(I + 1))/2.
      SXY(I) = (SXY(I) + SXY(I + 1))/2.
```

```
      TXX(I) = (SXX(I)*COS(BB) + SXY(I)*SIN(BB))*AL
      TYY(I) = (SXY(I)*COS(BB) + SYY(I)*SIN(BB))*AL
      WRITE (3,350) BB,TXX(I),TYY(I)
  350  FORMAT (3F10.5)
  400  CONTINUE
C
      DB = 2.*PI/FLOAT(IB)
      B = -DB
      SIG = 0.
      DO 450 I = 1,IB
      B = B + DB
      BB = B + DB/2.
      XB = R*COS(BB)
      YB = R*SIN(BB)
      XXX = R + ABS(YB)
      YYY = R + ABS(XB)
      XCET = 2.*ATAN(XB/XXX)
      YCET = 2.*ATAN(YB/YYY)
      SIG = SIG + TXX(I)*SIN(XCET)/(2.*PI*R)
      SIG = SIG + TYY(I)*SIN(YCET)/(2.*PI*R)
  450  CONTINUE
C
      DX = 2.*C/FLOAT(IX)
      XX = -C-DX
      DO 600 I = 1,IX + 1
      XX = XX + DX
      B = -DELTB
      PP(I) = 0.
      QQ(I) = 0.
      DO 500 J = 1,IB
      B = B + DELTB
      BB = B + DELTB/2.
      XP = R*COS(BB)
      YP = R*SIN(BB)
      R1 = SQRT((XP-XX)**2 + YP**2)
      SINC1 = YP/R1
      COSC1 = (XP-XX)/R1
      SIG1 = -2.*TXX(J)*COSC1/(PI*R1)
      SIG2 = -2.*TYY(J)*SINC1/(PI*R1)
      PP(I) = PP(I) + (SIG1 + SIG2)*SINC1**2
      QQ(I) = QQ(I)-(SIG1 + SIG2)*SINC1*COSC1
  500  CONTINUE
      PP(I) = PP(I) + SIG
      WRITE (4,510) XX,PP(I),QQ(I)
  510  FORMAT (3F11.5)
  600  CONTINUE
C
      GOTO 20
C
 1000  CONTINUE
      WRITE (8,1001) C,CETA,FFAK1,FFAK2,YYAK1,YYAK2
 1001  FORMAT (6F11.5)
C
 2000  CONTINUE
C
      CLOSE (2)
      CLOSE (3)
      CLOSE (4)
      CLOSE (7)
      CLOSE (8)
      STOP
      END
```

4. Program Z1
(for SIF Evaluation of Mixed Mode CSTBD Fracture Problem)
(Complex Stress Function Method - I)
(Z1 Method)

```
      PROGRAM Z1
      DIMENSION PP(150),QQ(150),SXX(400),
                SYY(400),SXY(400)
      DIMENSION SXXP(400),SXXQ(400),SYYP(400),SYYQ(400)
      DIMENSION SXYP(400),SXYQ(400)
      DIMENSION TXX(400),TYY(400)
C
      OPEN (3,FILE = 'data11')
      OPEN (4,FILE = 'data12')
      OPEN (7,FILE = 'data13')
      IX = 80
      IB = 180
      PI = 3.1415926
      D = 2.0
      R = 1.0
      P = 31.415926
      V = 0.3
      W = 3.-4.*V
      EPSK = 0.01
C
      READ (*,*) C,CET
      RCET = CET*PI/180.
      DX = 2.*C/FLOAT(IX)
      DB = 2.*PI/FLOAT(IB)
C
      XX = -C-DX
      DO 5 I = 1,IX + 1
      XX = XX + DX
      R1 = SQRT(XX**2*(SIN(RCET))**2
                + (XX*COS(RCET)-R)**2)
      R2 = SQRT(XX**2*(SIN(RCET))**2
                + (XX*COS(RCET) + R)**2)
      SINB1 = XX*SIN(RCET)/R1
      COSB1 = (R-XX*COS(RCET))/R1
      SINB2 = XX*SIN(RCET)/R2
      COSB2 = (R + XX*COS(RCET))/R2
      SINC1 = SIN(RCET)*COSB1 + COS(RCET)*SINB1
      COSC1 = COS(RCET)*COSB1-SIN(RCET)*SINB1
      SINC2 = SIN(RCET)*COSB2-COS(RCET)*SINB2
      COSC2 = COS(RCET)*COSB2 + SIN(RCET)*SINB2
      SIGMA1 = -2.*P*COSB1/(PI*R1)
      SIGMA2 = -2.*P*COSB2/(PI*R2)
      SIGN1 = SIGMA1*SINC1**2
      SIGT1 = SIGMA1*SINC1*COSC1
      SIGN2 = SIGMA2*SINC2**2
      SIGT2 = SIGMA2*SINC2*COSC2
      PP(I) = SIGN1 + SIGN2 + 2.*P/(PI*D)
      QQ(I) = SIGT1 + SIGT2
      QQ(I) = -QQ(I)
  5   CONTINUE
C
      ALFAC = C/R
```

```
      AK0 = P*SQRT(ALFAC/PI)/SQRT(R)
C
      FFAK1 = 0.
      FFAK2 = 0.
      YYAK1 = 0.
      YYAK2 = 0.
      YAK10 = 0.
      YAK20 = 0.
C
 20   DX = 2.*C/FLOAT(IX)
      DELTX = DX/1000.
C
      AK1 = 0.
      AK2 = 0.
      XX = -C-DX
      DO 30 I = 1,IX
      XX = XX + DX
      IF (I.NE.IX) GOTO 25
      DEX = DX/10.
      XX = XX-DEX
      DPP = (PP(IX + 1)-PP(IX))/10.
      DQQ = (QQ(IX + 1)-QQ(IX))/10.
      PB = PP(IX)-DPP
      QB = QQ(IX)-DQQ
      DO 23 J = 1,10
      XX = XX + DEX
      X1 = XX + DEX/2.
      PB = PB + DPP
      QB = QB + DQQ
      PE = PB + DPP
      QE = QB + DQQ
      PM = (PB + PE)/2.
      QM = (QB + QM)/2.
      AK1P = DEX*PM*SQRT((C + X1)/(C-X1))/SQRT(PI*C)
      AK2Q = DEX*QM*SQRT((C + X1)/(C-X1))/SQRT(PI*C)
      AK1 = AK1 + AK1P
      AK2 = AK2 + AK2Q
 23   CONTINUE
      GOTO 30
 25   X1 = XX + DX/2.
      PM = DX*(PP(I) + PP(I + 1))/2.
      QM = DX*(QQ(I) + QQ(I + 1))/2.
      AK1P = PM*SQRT((C + X1)/(C-X1))/SQRT(PI*C)
      AK2Q = QM*SQRT((C + X1)/(C-X1))/SQRT(PI*C)
      AK1 = AK1 + AK1P
      AK2 = AK2 + AK2Q
 30   CONTINUE
      FAK1 = AK1/AK0
      FAK2 = AK2/AK0
      YAK1 = FAK1*SQRT(ALFAC/PI)
      YAK2 = FAK2*SQRT(ALFAC/PI)
      FFAK1 = FFAK1 + FAK1
      FFAK2 = FFAK2 + FAK2
      YYAK1 = YYAK1 + YAK1
      YYAK2 = YYAK2 + YAK2
      WRITE (7,32) ALFAC,FFAK1,FFAK2,YYAK1,YYAK2
 32   FORMAT (5F11.5)
      ABS1 = ABS(YAK10-YYAK1)
      ABS2 = ABS(YAK20-YYAK2)
      IF ((ABS1.LT.EPSK).AND.(ABS2.LT.EPSK))GOTO 1000
      YAK10 = YYAK1
      YAK20 = YYAK2
C
      B = -DB
      DO 300 I = 1,IB + 1
      SXX(I) = 0.
      SYY(I) = 0.
      SXY(I) = 0.
C
      SXXP(I) = 0.
      SXXQ(I) = 0.
      SYYP(I) = 0.
      SYYQ(I) = 0.
      SXYP(I) = 0.
      SXYQ(I) = 0.
C
      B = B + DB
      XB = R*COS(B)
      YB = R*SIN(B)
      XX = -C-DX
      DO 200 J = 1,IX
      XX = XX + DX
      PM = DX*(PP(J) + PP(J + 1))/2.
      QM = DX*(QQ(J) + QQ(J + 1))/2.
      CET = B
      XB1 = XB-C
      XB2 = XB + C
      XB3 = XB-XX
      CET1 = ATAN2(YB,XB1)
      CET2 = ATAN2(YB,XB2)
      CET3 = ATAN2(YB,XB3)
      IF (CET1.GT.0.) GOTO 120
      CET1 = CET1 + 2.*PI
120   IF (CET2.GT.0.) GOTO 121
      CET2 = CET2 + 2.*PI
121   IF (CET3.GT.0.) GOTO 122
      CET3 = CET3 + 2.*PI
122   IF (I.EQ.1) CET1 = 0.
      IF (I.EQ.1) CET2 = 0.
      IF (I.EQ.1) CET3 = 0.
      RR = SQRT(XB**2 + YB**2)
      R1 = SQRT((XB-C)**2 + YB**2)
      R2 = SQRT((XB + C)**2 + YB**2)
      R3 = SQRT((XB-XX)**2 + YB**2)
C
      C1 = (CET1 + CET2 + 2.*CET3)/2.
      C2 = SQRT(C**2-XX**2)
      PRE1 = PM*C2*COS(C1)/(4.*PI*R3*SQRT(R1*R2))
      PIM1 = -PM*C2*SIN(C1)/(4.*PI*R3*SQRT(R1*R2))
      QRE1 = QM*C2*SIN(C1)/(4.*PI*R3*SQRT(R1*R2))
      QIM1 = QM*C2*COS(C1)/(4.*PI*R3*SQRT(R1*R2))
      PRE2 = -PM*SIN(CET3)/(4.*PI*R3)
      PIM2 = -PM*COS(CET3)/(4.*PI*R3)
      QRE2 = QM*COS(CET3)/(4.*PI*R3)
      QIM2 = -QM*SIN(CET3)/(4.*PI*R3)
      C1 = (CET1 + CET2)/2.
      C2 = (W-1.)/(W + 1)
      PRE3 = PM*C2*SIN(C1)/(4.*PI*SQRT(R1*R2))
      PIM3 = PM*C2*COS(C1)/(4.*PI*SQRT(R1*R2))
      QRE3 = -QM*C2*COS(C1)/(4.*PI*SQRT(R1*R2))
      QIM3 = QM*C2*SIN(C1)/(4.*PI*SQRT(R1*R2))
      FIREP = PRE1 + PRE2 + PRE3
      FIREQ = QRE1 + QRE2 + QRE3
      FIIMP = PIM1 + PIM2 + PIM3
      FIIMQ = QIM1 + QIM2 + QIM3
C
      OMREP = PRE1-PRE2 + PRE3
      OMREQ = QRE1-QRE2 + QRE3
      OMIMP = PIM1-PIM2 + PIM3
      OMIMQ = QIM1-QIM2 + QIM3
```

```
C
      C1 = (CET1 + CET2 + 4.*CET3)/2.
      C2 = SQRT(C**2-XX**2)/(4.*PI*R3**2*SQRT(R1*R2))
      PRE1 = -PM*C2*COS(C1)
      PIM1 = PM*C2*SIN(C1)
      QRE1 = -QM*C2*SIN(C1)
      QIM1 = -QM*C2*COS(C1)
      PRE2 = PM*SIN(2.*CET3)/(4.*PI*R3**2)
      PIM2 = PM*COS(2.*CET3)/(4.*PI*R3**2)
      QRE2 = -QM*COS(2.*CET3)/(4.*PI*R3**2)
      QIM2 = QM*SIN(2.*CET3)/(4.*PI*R3**2)
      C1 = (2.*CET-3.*CET1-3.*CET2-2.*CET3)/2.
     C2 = SQRT(C**2-XX**2)*RR/(4.*PI*R3*SQRT((R1*R2)**3))
      PRE3 = -PM*C2*COS(C1)
      PIM3 = -PM*C2*SIN(C1)
      QRE3 = QM*C2*SIN(C1)
      QIM3 = -QM*C2*COS(C1)
      C1 = (2.*CET-3.*CET1-3.*CET2)/2.
      C2 = (W-1.)*RR/((W + 1.)*4.*PI*SQRT((R1*R2)**3))
      PRE4 = -PM*C2*SIN(C1)
      PIM4 = PM*C2*COS(C1)
      QRE4 = -QM*C2*COS(C1)
      QIM4 = -QM*C2*SIN(C1)
      FDREP = PRE1 + PRE2 + PRE3 + PRE4
      FDREQ = QRE1 + QRE2 + QRE3 + QRE4
      FDIMP = PIM1 + PIM2 + PIM3 + PIM4
      FDIMQ = QIM1 + QIM2 + QIM3 + QIM4
C
      ZFREP = 2.*FDIMP*RR*SIN(CET)
      ZFREQ = 2.*FDIMQ*RR*SIN(CET)
      ZFIMP = -2.*FDREP*RR*SIN(CET)
      ZFIMQ = -2.*FDREQ*RR*SIN(CET)
C
      OMIMP = -OMIMP
      OMIMQ = -OMIMQ
      AAP = 4.*FIREP
      AAQ = 4.*FIREQ
      BBP = 2.*(ZFREP-FIREP + OMREP)
      BBQ = 2.*(ZFREQ-FIREQ + OMREQ)
      SXYP(I) = SXYP(I) + ZFIMP-FIIMP + OMIMP
      SXYQ(I) = SXYQ(I) + ZFIMQ-FIIMQ + OMIMQ
      SYYP(I) = SYYP(I) + (AAP + BBP)/2.
      SYYQ(I) = SYYQ(I) + (AAQ + BBQ)/2.
      SXXP(I) = SXXP(I) + (AAP-BBP)/2.
      SXXQ(I) = SXXQ(I) + (AAQ-BBQ)/2.
C
 200  CONTINUE
 300  CONTINUE
C
      DO 320 I = 1,IB + 1
      J = IB + 2-I
      SXY(I) = SXYP(I)-SXYP(J) + SXYQ(I) + SXYQ(J)
      SYY(I) = SYYP(I) + SYYP(J) + SYYQ(I)-SYYQ(J)
      SXX(I) = SXXP(I) + SXXP(J) + SXXQ(I)-SXXQ(J)
 320  CONTINUE
C
      B = -DB
      AL = 2.*PI*R/FLOAT(IB)
      DO 400 I = 1,IB
      B = B + DB
      BB = B + DB/2.
      SXX(I) = (SXX(I) + SXX(I + 1))/2.
      SYY(I) = (SYY(I) + SYY(I + 1))/2.
      SXY(I) = (SXY(I) + SXY(I + 1))/2.
      TXX(I) = (SXX(I)*COS(BB) + SXY(I)*SIN(BB))*AL
      TYY(I) = (SXY(I)*COS(BB) + SYY(I)*SIN(BB))*AL
      WRITE (3,433) BB,TXX(I),TYY(I)
 433  FORMAT (3F10.5)
 400  CONTINUE
C
      B = -DB
      SIG = 0.
      DO 450 I = 1,IB
      B = B + DB
      BB = B + DB/2.
      XB = R*COS(BB)
      YB = R*SIN(BB)
      XXX = R + ABS(YB)
      YYY = R + ABS(XB)
      XCET = 2.*ATAN(XB/XXX)
      YCET = 2.*ATAN(YB/YYY)
      SIG = SIG + TXX(I)*SIN(XCET)/(2.*PI*R)
      SIG = SIG + TYY(I)*SIN(YCET)/(2.*PI*R)
 450  CONTINUE
C
      DX = 2.*C/FLOAT(IX)
      XX = -C-DX
      DO 600 I = 1,IX + 1
      XX = XX + DX
      B = -DB
      PP(I) = 0.
      QQ(I) = 0.
      DO 500 J = 1,IB
      B = B + DB
      BB = B + DB/2.
      XP = R*COS(BB)
      YP = R*SIN(BB)
      R1 = SQRT((XP-XX)**2 + YP**2)
      SINC1 = YP/R1
      COSC1 = (XP-XX)/R1
      SIG1 = -2.*TXX(J)*COSC1/(PI*R1)
      SIG2 = -2.*TYY(J)*SINC1/(PI*R1)
      PP(I) = PP(I) + (SIG1 + SIG2)*SINC1**2
      QQ(I) = QQ(I)-(SIG1 + SIG2)*SINC1*COSC1
 500  CONTINUE
      PP(I) = PP(I) + SIG
      WRITE (4,510) XX,PP(I),QQ(I)
 510  FORMAT (3F11.5)
 600  CONTINUE
C
      GOTO 20
C
 1000 CLOSE (3)
      CLOSE (4)
      CLOSE (7)
      STOP
      END
```

5. Program Z2
(for SIF Evaluation of Mixed Mode CSTBD Fracture Problem)
(Complex Stress Function Method - II)
(Z2 Method)

```
      PROGRAM Z2
      DIMENSION PP(150),QQ(150),SXX(400),
     $                  SYY(400),SXY(400)
      DIMENSION SXXP(400),SXXQ(400),SYYP(400),SYYQ(400)
      DIMENSION SXYP(400),SXYQ(400)
      DIMENSION TXX(400),TYY(400)
C
      CHARACTER IC1*1,IC3*5,ICJ*8
      INTEGER JC
C
      IX = 80
      IB = 180
      PI = 3.1415926
      D = 2.0
      R = 1.0
      P = 31.415926
      V = 0.3
      W = 3.-4.*V
      EPSK = 0.008
C
C     READ (*,*) C
      CETA = -1.0
      CT0 = 0.
C
      ICA = -1
      IC1 = 'c'
      IC3 = 'z.dat'
C
      DO 3000 KC = 1,61
C
      JC = ICA + KC
      IF (KC.GT.31) JC = 30 + 2*(KC-31)
      OPEN (1,FILE = 'DD')
      IF (KC.GT.10) GOTO 2
      JCC = 0
      WRITE (1,1) IC1,JCC,JC,IC3
 1    FORMAT (A1,I1,I1,A5)
      GOTO 4
 2    WRITE (1,3) IC1,JC,IC3
 3    FORMAT (A1,I2,A5)
 4    CLOSE (1)
      OPEN (1,FILE = 'DD')
      READ (1,*) ICJ
      CLOSE (1)
      OPEN (2,FILE = ICJ)
C
      IF (KC.GT.31) CT0 = 1.0
      CETA = CETA + 1.0 + CT0
C
      RCET = CETA*PI/180.
      C = 0.04
      DO 2000 IJ = 1,91
      C = C + 0.01
C
C     WRITE (*,*) KC,IJ,C
C     RCET = CETA*PI/180.
      DX = 2.*C/FLOAT(IX)
      DB = 2.*PI/FLOAT(IB)
C
      XX = -C-DX
      DO 5 I = 1,IX + 1
      XX = XX + DX
      IF (XX.LT.-C) XX = -C
      IF (XX.GT.C) XX = C
      R1 = SQRT(XX**2*(SIN(RCET))**2
     $          + (XX*COS(RCET)-R)**2)
      R2 = SQRT(XX**2*(SIN(RCET))**2
     $          + (XX*COS(RCET) + R)**2)
      SINB1 = XX*SIN(RCET)/R1
      COSB1 = (R-XX*COS(RCET))/R1
      SINB2 = XX*SIN(RCET)/R2
      COSB2 = (R + XX*COS(RCET))/R2
      SINC1 = SIN(RCET)*COSB1 + COS(RCET)*SINB1
      COSC1 = COS(RCET)*COSB1-SIN(RCET)*SINB1
      SINC2 = SIN(RCET)*COSB2-COS(RCET)*SINB2
      COSC2 = COS(RCET)*COSB2 + SIN(RCET)*SINB2
      SIGMA1 = -2.*P*COSB1/(PI*R1)
      SIGMA2 = -2.*P*COSB2/(PI*R2)
      SIGN1 = SIGMA1*SINC1**2
      SIGT1 = SIGMA1*SINC1*COSC1
      SIGN2 = SIGMA2*SINC2**2
      SIGT2 = SIGMA2*SINC2*COSC2
      PP(I) = SIGN1 + SIGN2 + 2.*P/(PI*D)
      QQ(I) = SIGT1 + SIGT2
      QQ(I) = -QQ(I)
 5    CONTINUE
C
      ALFAC = C/R
      AK0 = P*SQRT(ALFAC/PI)/SQRT(R)
C
      FFAK1 = 0.
      FFAK2 = 0.
      YYAK1 = 0.
      YYAK2 = 0.
      YAK10 = 0.
      YAK20 = 0.
C
 20   DX = 2.*C/FLOAT(IX)
      DELTX = DX/1000.
C
      AK1 = 0.
      AK2 = 0.
      XX = -C-DX
      DO 30 I = 1,IX
      XX = XX + DX
      IF (XX.LT.-C) XX = -C
      IF (XX.GT.C) XX = C
      IF (I.NE.IX) GOTO 25
      DEX = DX/10.
      XX = XX-DEX
      DPP = (PP(IX + 1)-PP(IX))/10.
      DQQ = (QQ(IX + 1)-QQ(IX))/10.
      PB = PP(IX)-DPP
      QB = QQ(IX)-DQQ
      DO 23 J = 1,10
      XX = XX + DEX
      X1 = XX + DEX/2.
      PB = PB + DPP
      QB = QB + DQQ
```

```
      PE = PB + DPP
      QE = QB + DQQ
      PM = (PB + PE)/2.
      QM = (QB + QE)/2.
      AK1P = DEX*PM*SQRT((C + X1)/(C-X1))/SQRT(PI*C)
      AK2Q = DEX*QM*SQRT((C + X1)/(C-X1))/SQRT(PI*C)
      AK1 = AK1 + AK1P
      AK2 = AK2 + AK2Q
   23  CONTINUE
      GOTO 30
   25  X1 = XX + DX/2.
      PM = DX*(PP(I) + PP(I + 1))/2.
      QM = DX*(QQ(I) + QQ(I + 1))/2.
      AK1P = PM*SQRT((C + X1)/(C-X1))/SQRT(PI*C)
      AK2Q = QM*SQRT((C + X1)/(C-X1))/SQRT(PI*C)
      AK1 = AK1 + AK1P
      AK2 = AK2 + AK2Q
   30  CONTINUE
      FAK1 = AK1/AK0
      FAK2 = AK2/AK0
      YAK1 = FAK1*SQRT(ALFAC/PI)
      YAK2 = FAK2*SQRT(ALFAC/PI)
      FFAK1 = FFAK1 + FAK1
      FFAK2 = FFAK2 + FAK2
      YYAK1 = YYAK1 + YAK1
      YYAK2 = YYAK2 + YAK2
C     WRITE (7,32) ALFAC,FFAK1,FFAK2,YYAK1,YYAK2
C32   FORMAT (5F11.5)
      ABS1 = ABS(YAK10-YYAK1)
      ABS2 = ABS(YAK20-YYAK2)
      IF ((ABS1.LT.EPSK).AND.(ABS2.LT.EPSK)) GOTO 1000
      YAK10 = YYAK1
      YAK20 = YYAK2
C
      B = -DB
      DO 300 I = 1,IB + 1
      SXX(I) = 0.
      SYY(I) = 0.
      SXY(I) = 0.
C
      SXXP(I) = 0.
      SXXQ(I) = 0.
      SYYP(I) = 0.
      SYYQ(I) = 0.
      SXYP(I) = 0.
      SXYQ(I) = 0.
C
      B = B + DB
      XB = R*COS(B)
      YB = R*SIN(B)
      XX = -C-DX
      DO 200 J = 1,IX
      XX = XX + DX
      IF (XX.LT.-C) XX = -C
      IF (XX.GT.C) XX = C
      PM = DX*(PP(J) + PP(J + 1))/2.
      QM = DX*(QQ(J) + QQ(J + 1))/2.
      CET = B
      XB1 = XB-C
      XB2 = XB + C
      XB3 = XB-XX
      CET1 = ATAN2(YB,XB1)
      CET2 = ATAN2(YB,XB2)
      CET3 = ATAN2(YB,XB3)
      IF (CET1.GT.0.) GOTO 120
      CET1 = CET1 + 2.*PI
  120 IF (CET2.GT.0.) GOTO 121
      CET2 = CET2 + 2.*PI
  121 IF (CET3.GT.0.) GOTO 122
      CET3 = CET3 + 2.*PI
  122 IF (I.EQ.1) CET1 = 0.
      IF (I.EQ.1) CET2 = 0.
      IF (I.EQ.1) CET3 = 0.
      RR = SQRT(XB**2 + YB**2)
      R1 = SQRT((XB-C)**2 + YB**2)
      R2 = SQRT((XB + C)**2 + YB**2)
      R3 = SQRT((XB-XX)**2 + YB**2)
C
      C1 = (CET1 + CET2 + 2.*CET3)/2.
      C2 = SQRT(C**2-XX**2)
      QRE1 = QM*C2*SIN(C1)/(4.*PI*R3*SQRT(R1*R2))
      QIM1 = QM*C2*COS(C1)/(4.*PI*R3*SQRT(R1*R2))
      QRE2 = QM*COS(CET3)/(4.*PI*R3)
      QIM2 = -QM*SIN(CET3)/(4.*PI*R3)
      C1 = (CET1 + CET2)/2.
      C2 = (W-1.)/(W + 1)
      QRE3 = -QM*C2*COS(C1)/(4.*PI*SQRT(R1*R2))
      QIM3 = QM*C2*SIN(C1)/(4.*PI*SQRT(R1*R2))
      FIREQ = QRE1 + QRE2 + QRE3
      FIIMQ = QIM1 + QIM2 + QIM3
C
      OMREQ = QRE1-QRE2 + QRE3
      OMIMQ = QIM1-QIM2 + QIM3
C
      C1 = (CET1 + CET2 + 4.*CET3)/2.
      C2 = SQRT(C**2-XX**2)/(4.*PI*R3**2*SQRT(R1*R2))
      QRE1 = -QM*C2*SIN(C1)
      QIM1 = -QM*C2*COS(C1)
      QRE2 = -QM*COS(2.*CET3)/(4.*PI*R3**2)
      QIM2 = QM*SIN(2.*CET3)/(4.*PI*R3**2)
      C1 = (2.*CET-3.*CET1-3.*CET2-2.*CET3)/2.
      C2 = SQRT(C**2-XX**2)*RR/(4.*PI*R3*SQRT((R1*R2)**3))
      QRE3 = QM*C2*SIN(C1)
      QIM3 = -QM*C2*COS(C1)
      C1 = (2.*CET-3.*CET1-3.*CET2)/2.
      C2 = (W-1.)*RR/((W + 1.)*4.*PI*SQRT((R1*R2)**3))
      QRE4 = -QM*C2*COS(C1)
      QIM4 = -QM*C2*SIN(C1)
      FDREQ = QRE1 + QRE2 + QRE3 + QRE4
      FDIMQ = QIM1 + QIM2 + QIM3 + QIM4
C
      ZFREQ = 2.*FDIMQ*RR*SIN(CET)
      ZFIMQ = -2.*FDREQ*RR*SIN(CET)
C
      OMIMQ = -OMIMQ
      AAQ = 4.*FIREQ
      BBQ = 2.*(ZFREQ-FIREQ + OMREQ)
      SXYQ(I) = SXYQ(I) + ZFIMQ-FIIMQ + OMIMQ
      SYYQ(I) = SYYQ(I) + (AAQ + BBQ)/2.
      SXXQ(I) = SXXQ(I) + (AAQ-BBQ)/2.
C
      C1 = (CET1 + CET2 + 2.*CET3)/2.
      C2 = SQRT(C**2-XX**2)/(PI*R3*SQRT(R1*R2))
      FIRE = PM*C2*COS(C1)
      FIIM = -PM*C2*SIN(C1)
C
      C1 = (CET1 + CET2 + 4.*CET3)/2.
      C2 = SQRT(C**2-XX**2)/(PI*R3**2*SQRT(R1*R2))
      PRE1 = -PM*C2*COS(C1)
      PIM1 = PM*C2*SIN(C1)
```

```
      C1 = (2.*CET-3.*CET1-3.*CET2-2.*CET3)/2.
      C2 = SQRT(C**2-XX**2)*RR/(PI*R3*SQRT((R1*R2)**3))
      PRE2 = -PM*C2*COS(C1)
      PIM2 = -PM*C2*SIN(C1)
C
      FDRE = PRE1 + PRE2
      FDIM = PIM1 + PIM2
C
      SXXP(I) = SXXP(I) + FIRE-YB*FDIM
      SYYP(I) = SYYP(I) + FIRE + YB*FDIM
      SXYP(I) = SXYP(I)-YB*FDRE
C
  200 CONTINUE
  300 CONTINUE
C
      DO 320 I = 1,IB + 1
      J = IB + 2-I
      SXY(I) = SXYQ(I) + SXYQ(J) + SXYP(I)
      SYY(I) = SYYQ(I)-SYYQ(J) + SYYP(I)
      SXX(I) = SXXQ(I)-SXXQ(J) + SXXP(I)
  320 CONTINUE
C
      B = -DB
      AL = 2.*PI*R/FLOAT(IB)
      DO 400 I = 1,IB
      B = B + DB
      BB = B + DB/2.
      SXX(I) = (SXX(I) + SXX(I + 1))/2.
      SYY(I) = (SYY(I) + SYY(I + 1))/2.
      SXY(I) = (SXY(I) + SXY(I + 1))/2.
      TXX(I) = (SXX(I)*COS(BB) + SXY(I)*SIN(BB))*AL
      TYY(I) = (SXY(I)*COS(BB) + SYY(I)*SIN(BB))*AL
C     WRITE (3,433) BB,TXX(I),TYY(I)
C433  FORMAT (3F10.5)
  400 CONTINUE
C
      B = -DB
      SIG = 0.
      DO 450 I = 1,IB
      B = B + DB
      BB = B + DB/2.
      XB = R*COS(BB)
      YB = R*SIN(BB)
      XXX = R + ABS(YB)
      YYY = R + ABS(XB)
      XCET = 2.*ATAN(XB/XXX)
      YCET = 2.*ATAN(YB/YYY)
      SIG = SIG + TXX(I)*SIN(XCET)/(2.*PI*R)
      SIG = SIG + TYY(I)*SIN(YCET)/(2.*PI*R)
  450 CONTINUE
C
      DX = 2.*C/FLOAT(IX)
      XX = -C-DX
      DO 600 I = 1,IX + 1
      XX = XX + DX
      IF (XX.LT.-C) XX = -C
      IF (XX.GT.C) XX = C
      B = -DB
      PP(I) = 0.
      QQ(I) = 0.
      DO 500 J = 1,IB
      B = B + DB
      BB = B + DB/2.
      XP = R*COS(BB)
      YP = R*SIN(BB)
      R1 = SQRT((XP-XX)**2 + YP**2)
      SINC1 = YP/R1
      COSC1 = (XP-XX)/R1
      SIG1 = -2.*TXX(J)*COSC1/(PI*R1)
      SIG2 = -2.*TYY(J)*SINC1/(PI*R1)
      PP(I) = PP(I) + (SIG1 + SIG2)*SINC1**2
      QQ(I) = QQ(I)-(SIG1 + SIG2)*SINC1*COSC1
  500 CONTINUE
      PP(I) = PP(I) + SIG
C     WRITE (4,510) XX,PP(I),QQ(I)
C510  FORMAT (3F11.5)
  600 CONTINUE
C
      GOTO 20
C
 1000 CONTINUE
C
      WRITE (2,1001) C,CETA,FFAK1,FFAK2,YYAK1,YYAK2
 1001 FORMAT (6F11.5)
C
 2000 CONTINUE
      CLOSE (2)
C
 3000 CONTINUE
C
      STOP
      END
```

6. Program MIXCN
(for SIF Evaluation of Mixed Mode CCNBD Fracture Problem)

```
      PROGRAM MIXCN
C
C     STRESS INTENSITY FACTOR EVALUATION OF
C THE CRACKED CHEVRON-NOTCHED BRAZILIAN DISK
C     SUBJECTED TO DIAMETRICAL COMPRESSION
C
      implicit double precision (a-h,o-z)
      DIMENSION C(100),Y1(100),Y2(100),Y3(100)
      OPEN (11,FILE = 'c00my.dat')
      OPEN (12,FILE = 'c02my.dat')
      OPEN (13,FILE = 'c05my.dat')
      OPEN (14,FILE = 'c08my.dat')
      OPEN (15,FILE = 'c10my.dat')
      OPEN (16,FILE = 'c13my.dat')
      OPEN (17,FILE = 'c15my.dat')
      OPEN (18,FILE = 'c17my.dat')
      OPEN (19,FILE = 'c20my.dat')
C
      OPEN (21,FILE = 'c00myn.dat')
      OPEN (22,FILE = 'c02myn.dat')
      OPEN (23,FILE = 'c05myn.dat')
      OPEN (24,FILE = 'c08myn.dat')
      OPEN (25,FILE = 'c10myn.dat')
      OPEN (26,FILE = 'c13myn.dat')
      OPEN (27,FILE = 'c15myn.dat')
      OPEN (28,FILE = 'c17myn.dat')
```

```
      OPEN (29,FILE = 'c20myn.dat')
C
      AK = 1.0
      DELTA = 0.0004
      READ (*,*) ALFA0,ALFA1,ALFAB,K
C
      A0 = ALFA0
      STEP = (ALFA1-ALFA0)/FLOAT(K)
      STEP0 = STEP/2.
C
      DO 2000 IC = 1,9
C
      DO 30 I = 1,91
      GO TO (1,2,3,4,5,6,7,8,9)IC
    1 READ (11,20) C(I),CETA,Y1(I),Y2(I),Y3(I)
      GOTO 30
    2 READ (12,20) C(I),CETA,Y1(I),Y2(I),Y3(I)
      GOTO 30
    3 READ (13,20) C(I),CETA,Y1(I),Y2(I),Y3(I)
      GOTO 30
    4 READ (14,20) C(I),CETA,Y1(I),Y2(I),Y3(I)
      GOTO 30
    5 READ (15,20) C(I),CETA,Y1(I),Y2(I),Y3(I)
      GOTO 30
    6 READ (16,20) C(I),CETA,Y1(I),Y2(I),Y3(I)
      GOTO 30
    7 READ (17,20) C(I),CETA,Y1(I),Y2(I),Y3(I)
      GOTO 30
    8 READ (18,20) C(I),CETA,Y1(I),Y2(I),Y3(I)
      GOTO 30
    9 READ (19,20) C(I),CETA,Y1(I),Y2(I),Y3(I)
   20 FORMAT (5F11.5)
   30 CONTINUE
C
      AAA = ALFA0-STEP
      STEPCS = (0.95-ALFA0)/FLOAT(K)
      ACS = ALFA0-STEPCS
      DO 1000 I = 1,K + 1
C
      IF (I.EQ.K + 1) GOTO 550
C
      ACS = ACS + STEPCS
      ACST = ACS + STEPCS/2.
      IA = INT((ACST-0.04)/0.01)
      AI = 0.01*FLOAT(IA) + 0.04
      IF (ACST.GE.AI) GOTO 32
      Y1B = Y1(IA-1)
      Y1E = Y1(IA)
      Y2B = Y2(IA-1)
      Y2E = Y2(IA)
      Y3B = Y3(IA-1)
      Y3E = Y3(IA)
      AAB = AI-0.01
      GOTO 35
   32 Y1B = Y1(IA)
      Y1E = Y1(IA + 1)
      Y2B = Y2(IA)
      Y2E = Y2(IA + 1)
      Y3B = Y3(IA)
      Y3E = Y3(IA + 1)
      AAB = AI
   35 YCST1 = Y1B + (Y1E-Y1B)*(ACST-AAB)/0.01
      YCST2 = Y2B + (Y2E-Y2B)*(ACST-AAB)/0.01
      YCST3 = Y3B + (Y3E-Y3B)*(ACST-AAB)/0.01
C
      AAA = AAA + STEP
      ALFA = AAA + STEP/2.
C
      A1 = ALFA1**2-ALFA0**2 + ALFAB**2/4.
      A1A = (ALFA1**2-ALFA0**2-ALFAB**2/4.)**2
      A2 = (ALFA1**2-ALFA**2)*ALFAB**2
      F1 = A1-SQRT(A2 + A1A)
      F2 = ALFA*ALFAB**2/SQRT(A2 + A1A)
C
      IA = INT((ALFA-0.04)/0.01)
      AI = 0.01*FLOAT(IA) + 0.04
      IF (ALFA.GT.AI) GOTO 40
      Y1B = Y1(IA-1)
      Y1E = Y1(IA)
      Y2B = Y2(IA-1)
      Y2E = Y2(IA)
      Y3B = Y3(IA-1)
      Y3E = Y3(IA)
      AAB = AI-0.01
      GOTO 45
   40 Y1B = Y1(IA)
      Y1E = Y1(IA + 1)
      Y2B = Y2(IA)
      Y2E = Y2(IA + 1)
      Y3B = Y3(IA)
      Y3E = Y3(IA + 1)
      AAB = AI
   45 Y1A = Y1B + (Y1E-Y1B)*(ALFA-AAB)/0.01
      Y2A = Y2B + (Y2E-Y2B)*(ALFA-AAB)/0.01
      Y3A = Y3B + (Y3E-Y3B)*(ALFA-AAB)/0.01
C
      IF (I.NE.1) GOTO 300
      CALFA1 = 0.
      CALFA2 = 0.
      CALFA3 = 0.
      AFAB = -STEP0
      JJ = INT(ALFA0/STEP0)
      QY1 = Y1(1)/SQRT(0.05)
      QY2 = Y2(1)/SQRT(0.05)
      QY3 = Y3(1)/SQRT(0.05)
C
      DO 250 III = 1,JJ
      AFAB = AFAB + STEP0
      AB = AFAB + STEP0/2.
      IF (AB.GE.0.05) GOTO 60
      Y1B = QY1*SQRT(AB)
      Y2B = QY2*SQRT(AB)
      Y3B = QY3*SQRT(AB)
      GOTO 70
   60 IA = INT((AB-0.04)/0.01)
      AI = 0.01*FLOAT(IA) + 0.04
      IF (AB.GE.AI) GOTO 62
      Y1B = Y1(IA-1)
      Y1E = Y1(IA)
      Y2B = Y2(IA-1)
      Y2E = Y2(IA)
      Y3B = Y3(IA-1)
      Y3E = Y3(IA)
      AAB = AI-0.01
      GOTO 65
   62 Y1B = Y1(IA)
      Y1E = Y1(IA + 1)
      Y2B = Y2(IA)
      Y2E = Y2(IA + 1)
      Y3B = Y3(IA)
```

```
      Y3E = Y3(IA + 1)
      AAB = AI
 65   Y1B = Y1B + (Y1E-Y1B)*(AB-AAB)/0.01
      Y2B = Y2B + (Y2E-Y2B)*(AB-AAB)/0.01
      Y3B = Y3B + (Y3E-Y3B)*(AB-AAB)/0.01
C
 70   CALFA1 = CALFA1 + 2.*STEP0*Y1B**2
      CALFA2 = CALFA2 + 2.*STEP0*Y2B**2
      CALFA3 = CALFA3 + 2.*STEP0*Y3B**2
C
 250  CONTINUE
 300  CALFA1 = CALFA1 + 2.*STEP*Y1A**2
      CALFA2 = CALFA2 + 2.*STEP*Y2A**2
      CALFA3 = CALFA3 + 2.*STEP*Y3A**2
C
      J = INT((ALFA1-ALFA)/DELTA)
      AFAC = ALFA-DELTA
      A991 = 0.
      A992 = 0.
      A993 = 0.
      CAA1 = CALFA1
      CAA2 = CALFA2
      CAA3 = CALFA3
C
      DO 500 II = 1,J
      AFAC = AFAC + DELTA
      AAC = AFAC + DELTA/2.
C
      A11 = ALFA1**2-ALFA0**2 + ALFAB**2/4.
      A11A = (ALFA1**2-ALFA0**2-ALFAB**2/4.)**2
      A22 = (ALFA1**2-AAC**2)*ALFAB**2
C
      IA = INT((AAC-0.04)/0.01)
      AI = 0.01*FLOAT(IA) + 0.04
      IF (AAC.GE.AI) GOTO 72
      Y1B = Y1(IA-1)
      Y1E = Y1(IA)
      Y2B = Y2(IA-1)
      Y2E = Y2(IA)
      Y3B = Y3(IA-1)
      Y3E = Y3(IA)
      AAB = AI-0.01
      GOTO 75
 72   Y1B = Y1(IA)
      Y1E = Y1(IA + 1)
      Y2B = Y2(IA)
      Y2E = Y2(IA + 1)
      Y3B = Y3(IA)
      Y3E = Y3(IA + 1)
      AAB = AI
 75   Y1C = Y1B + (Y1E-Y1B)*(AAC-AAB)/0.01
      Y2C = Y2B + (Y2E-Y2B)*(AAC-AAB)/0.01
      Y3C = Y3B + (Y3E-Y3B)*(AAC-AAB)/0.01
C
      F22 = AAC*ALFAB**2/SQRT(A22 + A11A)
      CAA1 = CAA1 + 2.*DELTA*Y1C**2
      CAA2 = CAA2 + 2.*DELTA*Y2C**2
      CAA3 = CAA3 + 2.*DELTA*Y3C**2
      A991 = A991 + F22*DELTA/CAA1
      A992 = A992 + F22*DELTA/CAA2
      A993 = A993 + F22*DELTA/CAA3
C
 500  CONTINUE
C
      F31 = (F1/CALFA1 + A991)**2
      F32 = (F1/CALFA2 + A992)**2
      F33 = (F1/CALFA3 + A993)**2
      F41 = 2.*F1*Y1A**2/(CALFA1**2)-(1.-AK)*F2/CALFA1
      F42 = 2.*F1*Y2A**2/(CALFA2**2)-(1.-AK)*F2/CALFA2
      F43 = 2.*F1*Y3A**2/(CALFA3**2)-(1.-AK)*F2/CALFA3
C
      IF (ABS(CALFA1).LT.0.0000001)F31 = 1.0
      IF (ABS(CALFA1).LT.0.0000001)F41 = 0.0
      IF (ABS(CALFA2).LT.0.0000001)F32 = 1.0
      IF (ABS(CALFA2).LT.0.0000001)F42 = 0.0
      IF (ABS(CALFA3).LT.0.0000001)F33 = 1.0
      IF (ABS(CALFA3).LT.0.0000001)F43 = 0.0
C
C     YSA1 = SQRT(ALFAB**2/(2.*F1))*Y1A
C     YSA2 = SQRT(ALFAB**2/(2.*F1))*Y2A
C     YSA3 = SQRT(ALFAB**2/(2.*F1))*Y3A
      YSB1 = SQRT(F41*ALFAB**4/(8.*F1*F31))
      YSB2 = SQRT(F42*ALFAB**4/(8.*F1*F32))
      YSB3 = SQRT(F43*ALFAB**4/(8.*F1*F33))
      IF (Y1A.LT.0.) YSB1 = -YSB1
      IF (Y2A.LT.0.) YSB2 = -YSB2
      IF (Y3A.LT.0.) YSB3 = -YSB3
      GOTO 590
C
 550  ALFA = ALFA1
      IA = INT((ALFA-0.04)/0.01)
      AI = 0.01*FLOAT(IA) + 0.04
      IF (ALFA.GE.AI) GOTO 572
      Y1B = Y1(IA-1)
      Y1E = Y1(IA)
      Y2B = Y2(IA-1)
      Y2E = Y2(IA)
      Y3B = Y3(IA-1)
      Y3E = Y3(IA)
      AAB = AI-0.01
      GOTO 575
 572  Y1B = Y1(IA)
      Y1E = Y1(IA + 1)
      Y2B = Y2(IA)
      Y2E = Y2(IA + 1)
      Y3B = Y3(IA)
      Y3E = Y3(IA + 1)
      AAB = AI
 575  YSB1 = Y1B + (Y1E-Y1B)*(ALFA-AAB)/0.01
      YSB2 = Y2B + (Y2E-Y2B)*(ALFA-AAB)/0.01
      YSB3 = Y3B + (Y3E-Y3B)*(ALFA-AAB)/0.01
      ACST = 0.95
      YCST1 = Y1(91)
      YCST2 = Y2(91)
      YCST3 = Y3(91)
 590  GO TO (81,82,83,84,85,86,87,88,89)IC
 81   WRITE (21,600) ALFA,YSB1,YSB2,YSB3,
                     ACST,YCST1,YCST2,YCST3
      GOTO 1000
 82   WRITE (22,600) ALFA,YSB1,YSB2,YSB3,
                     ACST,YCST1,YCST2,YCST3
      GOTO 1000
 83   WRITE (23,600) ALFA,YSB1,YSB2,YSB3,
                     ACST,YCST1,YCST2,YCST3
      GOTO 1000
 84   WRITE (24,600) ALFA,YSB1,YSB2,YSB3,
                     ACST,YCST1,YCST2,YCST3
      GOTO 1000
 85   WRITE (25,600) ALFA,YSB1,YSB2,YSB3,
                     ACST,YCST1,YCST2,YCST3
```

```
      GOTO 1000
86    WRITE (26,600) ALFA,YSB1,YSB2,YSB3,
                     ACST,YCST1,YCST2,YCST3
      GOTO 1000
87    WRITE (27,600) ALFA,YSB1,YSB2,YSB3,
                     ACST,YCST1,YCST2,YCST3
      GOTO 1000
88    WRITE (28,600) ALFA,YSB1,YSB2,YSB3,
                     ACST,YCST1,YCST2,YCST3
      GOTO 1000
89    WRITE (29,600) ALFA,YSB1,YSB2,YSB3,
                     ACST,YCST1,YCST2,YCST3
600   FORMAT (8F11.5)
C
1000  CONTINUE
2000  CONTINUE
      CLOSE (11)
      CLOSE (12)
      CLOSE (13)
      CLOSE (14)
      CLOSE (15)
      CLOSE (16)
      CLOSE (17)
      CLOSE (18)
      CLOSE (19)
      CLOSE (21)
      CLOSE (22)
      CLOSE (23)
      CLOSE (24)
      CLOSE (25)
      CLOSE (26)
      CLOSE (27)
      CLOSE (28)
      CLOSE (29)
C
      STOP
      END
```

Appendix C: Program CUT for Rock Cutting Performance Analysis

```
      PROGRAM CUT
DIMENSION FC(3000),FN(3000),FCMAX(3000),
                FCMIN(3000)
DIMENSION FNMAX(3000),FNMIN(3000),ICMAX(3000),
                ICMIN(3000)
DIMENSION INMAX(3000),INMIN(3000)
DIMENSION FCPMA(2000),FCPMI(2000),ICPMA(2000),
                ICPMI(2000)
DIMENSION FNPMA(2000),FNPMI(2000),INPMA(2000),
                INPMI(2000)
DIMENSION U(3000),U1(3000)
DIMENSION XCMAX(300),YCMAX(300),XNMAX(300),
                YNMAX(300)
DIMENSION XCPMA(200),YCPMA(200),XNPMA(200),
                YNPMA(200)
DIMENSION FCA(2000),FCCA(2000),WFC(2000),
                WFCC(2000)
DIMENSION XFCA(200),YFCA(200),XFCCA(200),
                YFCCA(200)
DIMENSION XWFC(200),YWFC(200),XWFCC(200),
                YWFCC(200)
DIMENSION XC(300),YC(300),XN(300),YN(300)
DIMENSION XU(300),YU(300),XU1(200),YU1(200)
DIMENSION DL(2000),FCCA1(2000),WFCC1(2000)
DIMENSION XDL(200),YDL(200),XFCA1(200),YFCA1(200)
      DIMENSION XWFC1(200),YWFC1(200)
      DIMENSION FCX(3000),XFCX(100),YFCX(100)
      DIMENSION FCY(3000),XFCY(100),YFCY(100)
C
      OPEN (1,FILE='dat')
      OPEN (2,FILE='ofd')
      OPEN (3,FILE='omd')
      OPEN (4,FILE='opd')
      OPEN (7,FILE='owd')
      OPEN (8,FILE='ofcn')
      OPEN (9,FILE='omax')
      OPEN (10,FILE='opeak')
      FCBIG=0.
C
      READ (1,*) II,ALENG,NS,NC,WEIGHT
      DELL=ALENG/FLOAT(II)
      DO 100 I=1,II
      READ (1,2) IFC,IFN
2     FORMAT (2I5)
      FC(I)=FLOAT(2048-IFC)*0.154460
      FN(I)=FLOAT(IFN-2048)*0.087772
      IF (FC(I).LT.FCBIG) GOTO 100
      FCBIG=FC(I)
100   CONTINUE
C
      MINFC=0.04*FCBIG
      J=0
      JI=0
      JII=0
      DO 110 I=1,II
      IF (FC(I).GT.MINFC) GOTO 105
      J=J+1
      GOTO 110
105   JI=JI+1
```

```
      FC(JI) = FC(I)
      FN(JI) = FN(I)
      WRITE (8,106) JI,FC(JI),FN(JI)
  106  FORMAT (I8,2F8.4)
      IF (FN(JI).LT.0.01) GOTO 110
      JII = JII + 1
      U(JII) = FC(JI)/FN(JI)
  110  CONTINUE
C
      P = FLOAT(J)/FLOAT(II)
C
      II = JI
      JS = 20
      CALL STAT (II,FC,FCMEAN,FCSTD)
      CALL STAT (II,FN,FNMEAN,FNSTD)
      CALL STAT (JII,U,UMEAN,USTD)
      CALL DIST (II,FC,XC,YC,JS,DCC)
      CALL DIST (II,FN,XN,YN,JS,DNN)
      CALL DIST (JII,U,XU,YU,JS,DUU)
      FCMAX(1) = FC(1)
      FCMIN(1) = FC(1)
      FNMAX(1) = FN(1)
      FNMIN(1) = FN(1)
C
      FCM = FC(1)
      FNM = FN(1)
      IC = 0
      IN = 0
      ICM = 0
      INM = 0
C
      DO 200 I = 2,II
      IF (FC(I).GT.FCM) GOTO 120
      IF (IC.LT.1) GOTO 115
      FCMAX(ICM) = FCM
      ICMAX(ICM) = I-1
      FCM = FC(I)
      IC = 0
      GOTO 116
  115  FCM = FC(I)
  116  GOTO 130
  120  IF (IC.GT.1) GOTO 125
      ICM = ICM + 1
      FCMIN(ICM) = FCM
      ICMIN(ICM) = I-1
      FCM = FC(I)
      IC = 2
      GOTO 130
  125  FCM = FC(I)
  130  CONTINUE
      IF (FN(I).GT.FNM) GOTO 140
      IF (IN.LT.1) GOTO 135
      FNMAX(INM) = FNM
      INMAX(INM) = I-1
      FNM = FN(I)
      IN = 0
      GOTO 200
  135  FNM = FN(I)
      GOTO 200
  140  IF (IN.GT.1) GOTO 145
      INM = INM + 1
      FNMIN(INM) = FNM
      INMIN(INM) = I-1
      FNM = FN(I)
      IN = 2
      GOTO 200
  145  FNM = FN(I)
  200  CONTINUE
C
      CALL STAT (ICM,FCMIN,FCMINM,FCMINS)
      CALL STAT (ICM,FCMAX,FCMAXM,FCMAXS)
      CALL STAT (INM,FNMIN,FNMINM,FNMINS)
      CALL STAT (INM,FNMAX,FNMAXM,FNMAXS)
      CALL DIST (ICM,FCMAX,XCMAX,YCMAX,JS,DCMAX)
      CALL DIST(INM,FNMAX,XNMAX,YNMAX,JS,DNMAX)
      IJ = 0
      IP = 0
      ICMP = 0
      FCPM = FCMIN(1)
      ICPM = ICMIN(1)
      DO 300 I = 1,ICM
      IF (IJ.GT.1) GOTO 225
      IF (FCMIN(I).GT.FCPM) GOTO 220
      FCPM = FCMIN(I)
      ICPM = ICMIN(I)
      IP = 0
      GOTO 300
  220  IP = IP + 1
      IF (IP.LT.1) GOTO 300
      ICMP = ICMP + 1
      FCPMI(ICMP) = FCPM
      ICPMI(ICMP) = ICPM
      FCPM = FCMAX(I)
      ICPM = ICMAX(I)
      IJ = 2
      IP = 0
      GOTO 300
  225  IF (FCMAX(I).LT.FCPM) GOTO 240
      FCPM = FCMAX(I)
      ICPM = ICMAX(I)
      IP = 0
      GOTO 300
  240  FCP = 0.90*FCPM
      IF (FCMAX(I).LT.FCP) GOTO 241
      GOTO 300
  241  IP = IP + 1
      IF (IP.LT.1) GOTO 300
      FCPMA(ICMP) = FCPM
      ICPMA(ICMP) = ICPM
      IJ = 0
      IP = 0
      FCPM = FCMIN(I)
      ICPM = ICMIN(I)
  300  CONTINUE
C
      IJ = 0
      IP = 0
      INMP = 0
      FNPM = FNMIN(1)
      INPM = INMIN(1)
      DO 390 I = 1,INM
      IF (IJ.GT.1) GOTO 375
      IF (FNMIN(I).GT.FNPM) GOTO 370
      FNPM = FNMIN(I)
      INPM = INMIN(I)
      IP = 0
      GOTO 390
  370  IP = IP + 1
      IF (IP.LT.1) GOTO 390
      INMP = INMP + 1
```

```
      FNPMI(INMP) = FNPM
      INPMI(INMP) = INPM
      FNPM = FNMAX(I)
      INPM = INMAX(I)
      IJ = 2
      IP = 0
      GOTO 390
  375  IF (FNMAX(I).LT.FNPM) GOTO 380
      FNPM = FNMAX(I)
      INPM = INMAX(I)
      IP = 0
      GOTO 390
  380  FNP = 0.90*FNPM
      IF (FNMAX(I).LT.FNP) GOTO 381
      GOTO 390
  381  IP = IP + 1
      IF (IP.LT.1) GOTO 390
      FNPMA(INMP) = FNPM
      INPMA(INMP) = INPM
      IJ = 0
      IP = 0
      FNPM = FNMIN(I)
      INPM = INMIN(I)
  390  CONTINUE
C
      CALL STAT (ICMP,FCPMA,FCPMAM,FCPMAS)
      CALL STAT (INMP,FNPMA,FNPMAM,FNPMAS)
      CALL DIST (ICMP,FCPMA,XCPMA,YCPMA,JS,DCPMA)
      CALLDIST(INMP,FNPMA,XNPMA,YNPMA,JS,DNPMA)
      JJ = 0
      DO 400 I = 1,ICMP
      J = ICPMI(I)
      IF (FN(J).EQ.0.) GOTO 400
      JJ = JJ + 1
      U1(JJ) = FC(J)/FN(J)
  400  CONTINUE
      CALL STAT (JJ,U1,U1M,U1S)
      CALL DIST (JJ,U1,XU1,YU1,JS,DU1)
      DO 600 I = 1,ICMP
      JA = ICPMA(I)
      JI = ICPMI(I) + 1
      SUM = FC(JI-1)
      SUMC = FC(JI-1)-UMEAN*FN(JI-1)
      SUMC1 = FC(JI-1)-U1M*FN(JI-1)
      W1 = 0.
      W2 = 0.
      W3 = 0.
      DO 550 J = JI,JA
      FCC0 = FC(J-1)-UMEAN*FN(J-1)
      FCC1 = FC(J)-UMEAN*FN(J)
      FCC01 = FC(J-1)-U1M*FN(J-1)
      FCC2 = FC(J)-U1M*FN(J-1)
      SUM = SUM + FC(J)
      SUMC = SUMC + FCC1
      SUMC1 = SUMC1 + FCC2
      W1 = W1 + DELL*(FC(J) + FC(J-1))/2.
      W2 = W2 + DELL*(FCC0 + FCC1)/2.
      W3 = W3 + DELL*(FCC01 + FCC2)/2.
  550  CONTINUE
C
      FCA(I) = SUM/FLOAT(JA-JI + 2)
      FCCA(I) = SUMC/FLOAT(JA-JI + 2)
      FCCA1(I) = SUMC1/FLOAT(JA-JI + 2)
      DL(I) = DELL*FLOAT(JA-JI + 1)
      WFC(I) = W1
      WFCC(I) = W2
      WFCC1(I) = W3
  600  CONTINUE
C
      CALL STAT (ICMP,FCA,FCAM,FCAS)
      CALL STAT (ICMP,FCCA,FCCAM,FCCAS)
      CALL STAT (ICMP,FCCA1,FCCA1M,FCCA1S)
      CALL DIST (ICMP,FCA,XFCA,YFCA,JS,DCA)
      CALL DIST (ICMP,FCCA,XFCCA,YFCCA,JS,DCCA)
      CALL DIST (ICMP,FCCA1,XFCA1,YFCA1,JS,DCCA1)
      CALL STAT (ICMP,WFC,WFCM,WFCS)
      CALL STAT (ICMP,WFCC,WFCCM,WFCCS)
      CALL STAT (ICMP,WFCC1,WFCC1M,WFCC1S)
      CALL DIST (ICMP,WFC,XWFC,YWFC,JS,DFC)
      CALL DIST (ICMP,WFCC,XWFCC,YWFCC,JS,DFCC)
      CALL DIST (ICMP,WFCC1,XWFC1,YWFC1,JS,DFCC1)
      CALL STAT (ICMP,DL,DLM,DLS)
      CALL DIST (ICMP,DL,XDL,YDL,JS,DDL)
C
      CHF = 10000.*FLOAT(ICM)/FLOAT(II)
      CHFM = 10000.*FLOAT(ICMP)/FLOAT(II)
      WRITE (2,3000) FCMEAN,FCSTD,FNMEAN,FNSTD,
                     UMEAN,USTD,P,CHF,CHFM
 3000  FORMAT (7F8.4,2F8.2)
      DO 3010 I = 1,JS
      WRITE (2,3001) XC(I),YC(I),XN(I),YN(I),XU(I),YU(I)
 3001  FORMAT (6F8.2)
 3010  CONTINUE
      WRITE (7,3042) FCAM,FCAS,FCCA1M,FCCA1S,WFCM,
     * WFCS,WFCC1M,WFCC1S,DLM,DLS
 3042  FORMAT (10F8.4)
      DO 3050 I = 1,JS
      WRITE (7,3044) XFCA(I),YFCA(I),XFCA1(I),YFCA1(I),
     * XWFC(I),YWFC(I),XWFC1(I),YWFC1(I),XDL(I),YDL(I)
 3044  FORMAT (10F8.2)
 3050  CONTINUE
      DO 3060 I = 1,ICM
      WRITE (9,3055) ICMIN(I),FCMIN(I),ICMAX(I),FCMAX(I)
 3055  FORMAT (I8,F9.4,I8,F9.4)
 3060  CONTINUE
      DO 3070 I = 1,ICMP
      WRITE (10,3065) ICPMI(I),FCPMI(I),ICPMA(I),FCPMA(I)
 3065  FORMAT (I8,F9.4,I8,F9.4)
 3070  CONTINUE
      CLOSE (1)
      CLOSE (2)
      CLOSE (7)
      CLOSE (8)
      CLOSE (9)
      CLOSE (10)
C
      ICMS = 0
      ICPS = 0
      DO 3900 I = 1,ICM
      IF (FCMAX(I).LT.0.01) GOTO 3900
      ICMS = ICMS + 1
      ICMAX(ICMS) = ICMAX(I)
      FCMAX(ICMS) = FCMAX(I)
      ICMIN(ICMS) = ICMIN(I)
      FCMIN(ICMS) = FCMIN(I)
 3900  CONTINUE
      ICM = ICMS
      DO 3990 I = 1,ICMP
      IF (FCPMA(I).LT.0.01) GOTO 3990
      ICPS = ICPS + 1
```

```
      ICPMA(ICPS) = ICPMA(I)
      FCPMA(ICPS) = FCPMA(I)
      ICPMI(ICPS) = ICPMI(I)
      FCPMI(ISPS) = FCPMI(I)
 3990 CONTINUE
      ICMP = ICPS
      CALL WBUL (ICM,FCMAX,SUM,S0M,SMM,RM,S0M1,
                 SMM1,RM1)
      CALL WBUL (ICMP,FCPMA,SUP,S0P,SMP,RP,S0P1,
                 SMP1,RP1)
      DO 4900 I = 1,ICMP
      J = ICPMA(I)
      FCY(I) = FCPMA(I)-U1M*FN(J)
 4900 CONTINUE
      CALL STAT (ICMP,FCY,FCYM,FCYS)
      CALL DIST (ICMP,FCY,XFCY,YFCY,JS,DCY)
      CALL WBUL (ICMP,FCY,SUY,S0Y,SMY,
                 RY,S0Y1,SMY1,RY1)
      WRITE (4,3030) FCPMAM,FCPMAS,FNPMAM,
                 FNPMAS,U1M,U1S,FCYM,FCYS
 3030 FORMAT (8F9.4)
      DO 3040 I = 1,JS
      WRITE (4,3031) XCPMA(I),YCPMA(I),XNPMA(I),
           YNPMA(I),XU1(I),YU1(I),XFCY(I),YFCY(I)
 3031 FORMAT (8F8.2)
 3040 CONTINUE
      CLOSE (4)
      DO 5000 I = 1,ICM
      J = ICMAX(I)
      FCX(I) = FCMAX(I)-U1M*FN(J)
 5000 CONTINUE
      CALL STAT (ICM,FCX,FCXM,FCXS)
      CALL DIST (ICM,FCX,XFCX,YFCX,JS,DCX)
      CALL WBUL (ICM,FCX,SUMM,S0MM,SMMM,
                 RMM,S0MM1,SMMM1,RMM1)
      WRITE (3,5002) SUM,S0M,SMM,RM,S0M1,SMM1,RM1
 5002 FORMAT (7F8.4)
      WRITE (3,5004) SUP,S0P,SMP,RP,S0P1,SMP1,RP1
 5004 FORMAT (7F8.4)
      WRITE (3,5006) SUMM,S0MM,SMMM,RMM,S0MM1,
                 SMMM1,RMM1
 5006 FORMAT (7F8.4)
      WRITE (3,5007) SUY,S0Y,SMY,RY,S0Y1,SMY1,RY1
 5007 FORMAT (7F8.4)
      WRITE (3,3020) FCMINM,FCMINS,FCMAXM,FCMAXS
 3020 FORMAT (4F9.4)
      WRITE (3,3021) FNMINM,FNMINS,FNMAXM,FNMAXS,
                 FCXM,FCXS
 3021 FORMAT (6F9.4)
      DO 3025 I = 1,JS
      WRITE (3,3022) XCMAX(I),YCMAX(I),XNMAX(I),
                 YNMAX(I),XFCX(I),YFCX(I)
 3022 FORMAT (6F9.3)
 3025 CONTINUE
      CLOSE (3)
C
      SUX = SUMM
      S0X = S0MM
      SMX = SMMM
      S0X1 = S0MM1
      SMX1 = SMMM1
C
      JMA = 0
      JPA = 0
      JXA = 0
      JYA = 0
      JMB = 0
      JPB = 0
      JXB = 0
      JYB = 0
      SUMMA = 0.
      SUMPA = 0.
      SUMXA = 0.
      SUMYA = 0.
      SUMMB = 0.
      SUMPB = 0.
      SUMXB = 0.
      SUMYB = 0.
      DO 8700 I = 1,JS
      XM = XCMAX(I)
      XP = XCPMA(I)
      XX = XFCX(I)
      XY = XFCY(I)
      FSMA1 = SMM*((XM-SUM)/S0M)**(SMM-1.)/S0M
      FSPA1 = SMP*((XP-SUP)/S0P)**(SMP-1.)/S0P
      FSXA1 = SMX*((XX-SUX)/S0X)**(SMX-1.)/S0X
      FSYA1 = SMY*((XY-SUY)/S0Y)**(SMY-1.)/S0Y
      FSMA2 = EXP(0.-((XM-SUM)/S0M)**SMM)
      FSPA2 = EXP(0.-((XP-SUP)/S0P)**SMP)
      FSXA2 = EXP(0.-((XX-SUX)/S0X)**SMX)
      FSYA2 = EXP(0.-((XY-SUY)/S0Y)**SMY)
      FSMB1 = SMM1*((XM-SUM)/S0M1)**(SMM1-1.)/S0M1
      FSPB1 = SMP1*((XP-SUP)/S0P1)**(SMP1-1.)/S0P1
      FSXB1 = SMX1*((XX-SUX)/S0X1)**(SMX1-1.)/S0X1
      FSYB1 = SMY1*((XY-SUY)/S0Y1)**(SMY1-1.)/S0Y1
      FSMB2 = EXP(0.-((XM-SUM)/S0M1)**SMM1)
      FSPB2 = EXP(0.-((XP-SUP)/S0P1)**SMP1)
      FSXB2 = EXP(0.-((XX-SUX)/S0X1)**SMX1)
      FSYB2 = EXP(0.-((XY-SUY)/S0Y1)**SMY1)
      FSMA = FSMA1*FSMA2
      FSPA = FSPA1*FSPA2
      FSXA = FSXA1*FSXA2
      FSYA = FSYA1*FSYA2
      FSMB = FSMB1*FSMB2
      FSPB = FSPB1*FSPB2
      FSXB = FSXB1*FSXB2
      FSYB = FSYB1*FSYB2
      IF (FSMA.LT.0.10) GOTO 8690
      JMA = JMA + 1
      SUMMA = SUMMA + YCMAX(I)/FSMA
 8690 IF (FSPA.LT.0.01) GOTO 8691
      JPA = JPA + 1
      SUMPA = SUMPA + YCPMA(I)/FSPA
 8691 IF (FSXA.LT.0.01) GOTO 8692
      JXA = JXA + 1
      SUMXA = SUMXA + YFCX(I)/FSXA
 8692 IF (FSYA.LT.0.01) GOTO 8693
      JYA = JYA + 1
      SUMYA = SUMYA + YFCY(I)/FSYA
 8693 IF (FSMB.LT.0.01) GOTO 8694
      JMB = JMB + 1
      SUMMB = SUMMB + YCMAX(I)/FSMB
 8694 IF (FSPB.LT.0.01) GOTO 8695
      JPB = JPB + 1
      SUMPB = SUMPB + YCPMA(I)/FSPB
 8695 IF (FSXB.LT.0.01) GOTO 8696
      JXB = JXB + 1
      SUMXB = SUMXB + YFCX(I)/FSXB
 8696 IF (FSYB.LT.0.01) GOTO 8700
      JYB = JYB + 1
```

```
      SUMYB = SUMYB + YFCY(I)/FSYB
 8700 CONTINUE
      YMA = SUMMA/FLOAT(JMA)
      YPA = SUMPA/FLOAT(JPA)
      YXA = SUMXA/FLOAT(JXA)
      YYA = SUMYA/FLOAT(JYA)
      YMB = SUMMB/FLOAT(JMB)
      YPB = SUMPB/FLOAT(JPB)
      YXB = SUMXB/FLOAT(JXB)
      YYB = SUMYB/FLOAT(JYB)
C
      X1M = XCMAX(1)-DCMAX/2.
      X1P = XCPMA(1)-DCPMA/2.
      X1X = XFCX(1)-DCX/2.
      X1Y = XFCY(1)-DCY/2.
      X2M = XCMAX(JS) + DCMAX/2.
      X2P = XCPMA(JS) + DCPMA/2.
      X2X = XFCX(JS) + DCX/2.
      X2Y = XFCY(JS) + DCY/2.
      DM = (X2M-X1M)/100.
      DP = (X2P-X1P)/100.
      DX = (X2X-X1X)/100.
      DY = (X2Y-X1Y)/100.
      XM = X1M
      XP = X1P
      XX = X1X
      XY = X1Y
      OPEN (2,FILE = 'odist')
      DO 9000 I = 1,100
      XM = XM + DM
      XP = XP + DP
      XX = XX + DX
      XY = XY + DY
      FSMA1 = SMM*((XM-SUM)/S0M)**(SMM-1.)/S0M
      FSPA1 = SMP*((XP-SUP)/S0P)**(SMP-1.)/S0P
      FSXA1 = SMX*((XX-SUX)/S0X)**(SMX-1.)/S0X
      FSYA1 = SMY*((XY-SUY)/S0Y)**(SMY-1.)/S0Y
      FSMA2 = EXP(0.-((XM-SUM)/S0M)**SMM)
      FSPA2 = EXP(0.-((XP-SUP)/S0P)**SMP)
      FSXA2 = EXP(0.-((XX-SUX)/S0X)**SMX)
      FSYA2 = EXP(0.-((XY-SUY)/S0Y)**SMY)
      FSMB1 = SMM1*((XM-SUM)/S0M1)**(SMM1-1.)/S0M1
      FSPB1 = SMP1*((XP-SUP)/S0P1)**(SMP1-1.)/S0P1
      FSXB1 = SMX1*((XX-SUX)/S0X1)**(SMX1-1.)/S0X1
      FSYB1 = SMY1*((XY-SUY)/S0Y1)**(SMY1-1.)/S0Y1
      FSMB2 = EXP(0.-((XM-SUM)/S0M1)**SMM1)
      FSPB2 = EXP(0.-((XP-SUP)/S0P1)**SMP1)
      FSXB2 = EXP(0.-((XX-SUX)/S0X1)**SMX1)
      FSYB2 = EXP(0.-((XY-SUY)/S0Y1)**SMY1)
      FSMA = FSMA1*FSMA2*YMA
      FSPA = FSPA1*FSPA2*YPA
      FSXA = FSXA1*FSXA2*YXA
      FSYA = FSYA1*FSYA2*YYA
      FSMB = FSMB1*FSMB2*YMB
      FSPB = FSPB1*FSPB2*YPB
      FSXB = FSXB1*FSXB2*YXB
      FSYB = FSYB1*FSYB2*YYB
      WRITE (2,8990) XM,FSMA,FSMB,XP,FSPA,FSPB,
     * XX,FSXA,FSXB,XY,FSYA,FSYB
 8990 FORMAT (13F9.3)
 9000 CONTINUE
      CLOSE (2)
C
      OPEN (2,FILE = 'oprm')
      WRITE (2,2000)
 2000 FORMAT (/,20X,'Cutting Test Analysis Results',//)
      WRITE (2,2010) NS,NC
 2010 FORMAT ('Sample No:',I3,27X,'Cut No:',I3)
      WRITE (2,2020) ALENG,WEIGHT
 2020 FORMAT ('Cutting Length L = ',F9.4,' (mm)',9X,'Weight
     * of Debris W = ',F9.4,' ( g )')
      WRITE (2,2022) P
 2022 FORMAT ('Probability of Cutting Action P = ',F7.4)
      WRITE (2,2024) CHF
 2024 FORMAT ('Minor Chipping Frquency CHF = ',F8.2,' (Hz)')
      WRITE (2,2026) CHFM
 2026 FORMAT ('Major Chipping Frquency CHFM = ',F8.2,'
     * (Hz)')
      WRITE (2,2028) U1M,U1S
 2028 FORMAT ('Friction Coefficient U = ',F8.4,9X,'Standard
     * Deviation = ',F8.4)
      WRITE (2,2030) FCMEAN,FCSTD
 2030 FORMAT ('Mean Cutting Force = ',F8.4,'
     * (KN)',7X,'Standard Deviation = ',F8.4)
      WRITE (2,2040) FNMEAN,FNSTD
 2040 FORMAT ('Mean Normal Force = ',F8.4,'
     * (KN)',8X,'Standard Deviation = ',F8.4)
      WRITE (2,2050) FCMAXM
 2050 FORMAT ('Mean Minor Chipping Maximun Cutting Force
     * = ',F8.4)
      WRITE (2,2060) FCMAXS
 2060 FORMAT (40X,'Standard Deviation = ',F8.4)
      WRITE (2,2070) FNMAXM
 2070 FORMAT ('Mean Minor Chipping Maximun Normal Force
     * = ',F8.4)
      WRITE (2,2080) FNMAXS
 2080 FORMAT (40X,'Standard Deviation = ',F8.4)
      WRITE (2,2090) FCXM
 2090 FORMAT('Mean Minor Chipping Maximun Active Cutting
     * Force = ',F8.4)
      WRITE (2,2100) FCXS
 2100 FORMAT (40X,'Standard Deviation = ',F8.4)
      WRITE (2,2105) FCPMAM
 2105 FORMAT ('Mean Major Chipping Maximun Cutting Force
     * = ',F8.4)
      WRITE (2,2106) FCPMAS
 2106 FORMAT (40X,'Standard Deviation = ',F8.4)
      WRITE (2,2110) FCYM
 2110 FORMAT('Mean Major Chipping Maximun Active Cutting
     * Force = ',F8.4)
      WRITE (2,2120) FCYS
 2120 FORMAT (40X,'Standard Deviation = ',F8.4)
      WRITE (2,2125) FNPMAM
 2125 FORMAT ('Mean Major Chipping Maximun Normal Force
     * = ',F8.4)
      WRITE (2,2126) FNPMAS
 2126 FORMAT (40X,'Standard Deviation = ',F8.4)
      WRITE (2,2130) FCAM
 2130 FORMAT ('Major Chipping Cycle Mean Cutting Force
     * = ',F8.4)
      WRITE (2,2140) FCAS
 2140 FORMAT (40X,'Standard Deviation = ',F8.4)
      WRITE (2,2150) FCCA1M
 2150 FORMAT ('Major Chipping Cycle Mean Active Cutting
     * Force = ',F8.4)
      WRITE (2,2160) FCCA1S
 2160 FORMAT (40X,'Standard Deviation = ',F8.4)
      WRITE (2,2170) WFCM
 2170 FORMAT ('Major Chipping Cycle Mean Total Work Done
     * = ',F8.4)
```

```
      WRITE (2,2180) WFCS
2180  FORMAT (40X,'Standard Deviation = ',F8.4)
      WRITE (2,2190) WFCC1M
2190  FORMAT ('Major Chipping Cycle Mean Active Work Done
     * = ',F8.4)
      WRITE (2,2200) WFCC1S
2200  FORMAT (40X,'Standard Deviation = ',F8.4)
      WRITE (2,2300) DLM,DLS
2300  FORMAT ('Mean Major Chipping Length
     * = ',F8.4,4X,'Standard Deviation = ',F8.4)
      WRITE (2,2400)
2400  FORMAT(/,'Followings are the Weibull Distribution
     * Parameteres',/)
      WRITE (2,2410) SUM
2410  FORMAT ('Minor Chipping Maximun Cutting Force
     * Su = ',F8.4)
      WRITE (2,2420) S0M,S0M1
2420  FORMAT (40X,'S0 = ',F8.4,5X,'S01 = ',F8.4)
      WRITE (2,2430) SMM,SMM1
2430  FORMAT (40X,'m = ',F8.4,5X,'m1 = ',F8.4)
      WRITE (2,2435) RM,RM1
2435  FORMAT (40X,'R = ',F8.4,5X,'R1 = ',F8.4)
      WRITE (2,2440) SUX
2440  FORMAT ('Minor Chipping Maximun Active Cutting Force
     * Su = ',F8.4)
      WRITE (2,2450) S0X,S0X1
2450  FORMAT (45X,'S0 = ',F8.4,5X,'S01 = ',F8.4)
      WRITE (2,2460) SMX,SMX1
2460  FORMAT (45X,'m = ',F8.4,5X,'m1 = ',F8.4)
      WRITE (2,2465) RMM,RMM1
2465  FORMAT (45X,'R = ',F8.4,5X,'R1 = ',F8.4)
      WRITE (2,2470) SUP
2470  FORMAT ('Major Chipping Maximun Cutting Force
     * Su = ',F8.4)
      WRITE (2,2480) S0P,S0P1
2480  FORMAT (39X,'S0 = ',F8.4,5X,'S01 = ',F8.4)
      WRITE (2,2483) SMP,SMP1
2483  FORMAT (39X,'m = ',F8.4,5X,'m1 = ',F8.4)
      WRITE (2,2485) RP,RP1
2485  FORMAT (39X,'R = ',F8.4,5X,'R1 = ',F8.4)
      WRITE (2,2490) SUY
2490  FORMAT ('Major Chipping Maximun Active Cutting Force
     * Su = ',F8.4)
      WRITE (2,2500) S0Y,S0Y1
2500  FORMAT (45X,'S0 = ',F8.4,5X,'S01 = ',F8.4)
      WRITE (2,2510) SMY,SMY1
2510  FORMAT (45X,'m = ',F8.4,5X,'m1 = ',F8.4)
      WRITE (2,2600) RY,RY1
2600  FORMAT (45X,'R = ',F8.4,5X,'R1 = ',F8.4)
      CLOSE (2)
      STOP
      END
      SUBROUTINE STAT (JJ,F,FMEAN,STD)
      DIMENSION F(3000)
      SUM = 0.
      SUMU = 0.
      DO 1500 M = 1,JJ
      SUM = SUM + F(M)
1500  CONTINUE
      FMEAN = SUM/FLOAT(JJ)
      SUM = 0.
      DO 1510 M = 1,JJ
      SUM = SUM + (F(M)-FMEAN)**2
1510  CONTINUE
      STD = SQRT(SUM/FLOAT(JJ-1))
      RETURN
      END
      SUBROUTINE DIST (JJ,F,X,Y,JS,DEL)
      DIMENSION F(3000),X(100),Y(100)
      FMAX = F(1)
      FMIN = F(1)
      DO 1600 M = 2,JJ
      IF (F(M).GT.FMIN) GOTO 1520
      FMIN = F(M)
1520  IF (F(M).LT.FMAX) GOTO 1600
      FMAX = F(M)
1600  CONTINUE
      DEL = (FMAX-FMIN)/FLOAT(JS)
      XX = FMIN
      DO 1700 M = 1,JS
      XX = XX + DEL
      X(M) = XX
      Y(M) = 0.
1700  CONTINUE
      DO 1800 M = 1,JJ
      DO 1710 N = 1,JS
      IF (N.EQ.JS) GOTO 1705
      IF (X(N).LT.F(M)) GOTO 1710
1705  Y(N) = Y(N) + 1.
      GOTO 1800
1710  CONTINUE
1800  CONTINUE
      DO 1900 M = 1,JS
      X(M) = X(M)-DEL/2.
1900  CONTINUE
      RETURN
      END
      SUBROUTINE WBUL (IQ,SQ,SU,S0,SM,R,S01,SM1,R1)
      DIMENSIONS(3000),SS(3000),SA(3000),S1(3000),SQ(3000)
      II = IQ
      DO 5089 I = 1,II
      S(I) = SQ(I)
5089  CONTINUE
      J = 0
      IIJ = II
      SM = S(1)
5090  DO 6000 I = 1,II
      IF (S(I).GT.SM) GOTO 6000
      SM = S(I)
      IS = I
6000  CONTINUE
      J = J + 1
      SS(J) = SM
      IJ = 0
      DO 6010 I = 1,II
      IF (I.EQ.IS) GOTO 6010
      IJ = IJ + 1
      S(IJ) = S(I)
6010  CONTINUE
      II = II-1
      SM = S(1)
      IF (II.NE.1) GOTO 5090
      J = J + 1
      SS(J) = SM
      IF (J.EQ.IIJ) GOTO 6020
      OPEN (11,FILE = 'owarn')
      WRITE (11,6015)
6015  FORMAT (/,'WARNING: J NOT EQUAL II',/)
      CLOSE (11)
6020  IF (SS(1).GT.0.) GOTO 6021
```

```
      SU = 1.05*SS(1)
      GOTO 6022
6021  SU = 0.95*SS(1)
6022  DO 6040 I = 1,J
      IF (I.EQ.J) GOTO 6023
      SA(I) = FLOAT(I)/FLOAT(J)
6023  S1(I) = FLOAT(I)/FLOAT(J + 1)
      IF (I.EQ.J) GOTO 6024
      SA(I) = ALOG(0.-ALOG(1.-SA(I)))
6024  S1(I) = ALOG(0.-ALOG(1.-S1(I)))
      SS(I) = ALOG(SS(I)-SU)
6040  CONTINUE
      JQ = J-1
      CALL REG (JQ,SS,SA,A,B,R)
      CALL REG (J,SS,S1,A1,B1,R1)
      SM = B
      SM1 = B1
      S0 = EXP(-A/B)
      S01 = EXP(-A1/B1)
      RETURN
      END
      SUBROUTINE REG (N,XX,YY,A,B,R)
      DIMENSION XX(3000),YY(3000)
      SX = 0.
      SY = 0.
      SQX = 0.
      SQY = 0.
      SQXY = 0.
      DO 8000 I = 1,N
      SX = SX + XX(I)
      SY = SY + YY(I)
8000  CONTINUE
      XM = SX/FLOAT(N)
      YM = SY/FLOAT(N)
      DO 8010 I = 1,N
      SQX = SQX + (XX(I)-XM)**2
      SQY = SQY + (YY(I)-YM)**2
      SQXY = SQXY + (XX(I)-XM)*(YY(I)-YM)
8010  CONTINUE
      B = SQXY/SQX
      A = YM-B*XM
      R = SQXY/SQRT(SQX*SQY)
      RETURN
      END
```